Dissertation zur Erlangung
des naturwissenschaftlichen Doktorgrades
der Bayerischen Julius-Maximilians-Universität
Würzburg

Fracture dynamics in silicate glasses

vorgelegt von

Tobias Dürig

aus Aschaffenburg

Würzburg 2011

Eingereicht am: ....
bei der Fakultät für Physik und Astronomie

1. Gutachter: Prof. V. Dyakonov

2. Gutachter: Prof. B. Zimanowski

3. Gutachter: ....
der Dissertation.

1. Prüfer: ....

2. Prüfer: ....

3. Prüfer: ....
im Promotionskolloquium.

Tag des Promotionskolloquiums: ....

Doktorurkunde ausgehändigt am: ....

Der Hammer ist ein primitives Werkzeug -
der Computer würde aber unterliegen.
(Georg Skrypzak)

Zusammenfassung

Forschungen mit dem Ziel die Abhängigkeiten und Mechanismen von Bruchprozessen in amorphen silikatischen Materialien exakt verstehen zu lernen, sind nicht nur in den Materialwissenschaften, sondern darüber hinaus auch in der Vulkanologie von größter Bedeutung, vor allem auch im Hinblick auf thermohydraulische Schmelze-Wasser-Wechselwirkungen (sog. "molten fuel coolant-interactions", MFCIs). Aus diesem Grund wurden Hammerschlagexperimente (HIEs) durchgeführt, um unter Verwendung einer Cranz-Schardin Funkenzeitlupe die Bruchdynamiken in exakt definierten Versuchsmaterialien zu analysieren. Die vorliegende Arbeit stellt die Ergebnisse dieser Versuchsreihen vor und beleuchtet detailliert die zeitlichen Abläufe während der Fragmentation, wobei sie ihr Hauptaugenmerk besonders auf die energetischen Dissipationsprozesse beim Rissfortschritt richtet.

In den HIEs können zwei Hauptklassen von Rissen identifiziert werden, welche durch vollkommen unterschiedliche Rissmechanismen gekennzeichnet sind: Stoßwelleninduzierte "Schadensrisse" ("damage cracks") und "Normalrisse" ("normal cracks"), welche ihre Ursachen ausschließlich in Scherspannungen haben. Diesem parallelen Vorhandensein beider Rissklassen wurde mit einem neu entwickelten Konzept Rechnung getragen: Ihm zufolge sind die rissklassenspezifischen Bruchenergien direkt proportional zur jeweiligen Bruchfläche, wobei die entsprechenden Proportionalitätskonstanten als Bruchflächenenergiedichten ("fracture surface energy densities", FSEDs) bezeichnet werden. Ihre Werte wurden für alle untersuchten Targets unter verschiedenen, genau definierten Randbedingungen ermittelt. Die Auswertungen der Zeitlupenaufnahmen und die Einführung neuer bruchdynamischer Parameter ermöglichten nicht nur eine detaillierte Beschreibung der Rissentwicklung im Target, sondern darüber hinaus auch quantitative Aussagen zur Dynamik der Bruchenergiedissipationsraten.

Mit Hilfe umfassender multivariater statistischer Analysen war es zudem möglich, die allgemeinen Abhängigkeiten aller relevanten Bruchparameter sowie die Einflüsse auf die kennzeichnenden Merkmale der bei der Fragmentation erzeugten Partikel herauszufinden. Auf diese Weise konnte ein wichtiges Prinzip der Bruchdynamik nachgewiesen werden, das in dieser Arbeit als "lokaler Anisotropieeffekt" ("local anisotropy effect") bezeichnet wird. Diesem Prinzip zufolge wird die Bruchdynamik in einem Material signifikant durch die Lage von gerichteten Spannungen beeinflusst: Hohe örtliche Spannungsgradienten senkrecht zur Bewegungsrichtung des Risses bewirken eine stabilere Rissausbreitung und damit eine Verringerung der Energiedissipationsraten.

In einem letzten Schritt beschäftigt sich die vorliegende Arbeit mit der Frage, welche vulkanologischen Schlussfolgerungen man aus den vorgestellten Versuchsergebnissen ziehen kann. Dazu wurden die erzeugten HIE-Fragmente mit natürlichen und experimentellen vulkanischen Aschen verglichen, welche von rhyolitischen Tepexitl- und basaltischen Grimsvötn-Schmelzen entstammten. Auf Grundlage dieser Partikelvergleiche konnte gezeigt werden, dass die Hammerschlagsversuche eine geeignete Methode darstellen, um genau jene Belastungsbedingungen zu reproduzieren, welchen Magmen während eines MFCI ausgesetzt sind. Zudem wurde damit der Nachweis erbracht, dass das in dieser Arbeit vorgestellte FSED-Konzept sich adäquat auf vulkanische Fragmentationsprozesse übertragen lässt.

Abstract

Understanding the mechanisms of fragmentation within silicate melts is of great interest not only for material science, but also for volcanology, particularly regarding molten fuel coolant-interactions (MFCIs). Therefore edge-on hammer impact experiments (HIEs) have been carried out in order to analyze the fracture dynamics in well defined targets by applying a Cranz-Schardin highspeed camera technique. This thesis presents the corresponding results and provides a thorough insight into the dynamics of fragmentation, particularly focussing on the processes of energy dissipation.

In HIEs two main classes of cracks can be identified, characterized by completely different fracture mechanisms: Shock wave induced “damage cracks” and “normal cracks”, which are exclusively caused by shear-stresses. This dual fracture situation is taken into account by introducing a new concept, according to which the crack class-specific fracture energies are linearly correlated with the corresponding fracture areas. The respective proportionality constants - denoted “fracture surface energy densities” (FSEDs) - have been quantified for all studied targets under various constraints.

By analyzing the corresponding high speed image sequences and introducing useful dynamic parameters it has been possible to specify and describe in detail the evolution of fractures and, moreover, to quantify the energy dissipation rates during the fragmentation.

Additionally, comprehensive multivariate statistical analyses have been carried out which have revealed general dependencies of all relevant fracture parameters as well as characteristics of the resulting particles.

As a result, an important principle of fracture dynamics has been found, referred to as the “local anisotropy effect”: According to this principle, the fracture dynamics in a material is significantly affected by the location of directed stresses. High local stress gradients cause a more stable crack propagation and consequently a reduction of the energy dissipation rates.

As a final step, this thesis focusses on the volcanological conclusions which can be drawn on the basis of the presented HIE results. Therefore fragments stemming from HIEs have been compared with natural and experimental volcanic ash particles of basaltic Grimsvötn and rhyolitic Tepexitl melts.

The results of these comparative particle analyses substantiate HIEs to be a very suitable method for reproducing the MFCI loading conditions in silicate melts and prove the FSED concept to be a model which is well transferable to volcanic fragmentation processes.

Contents

Part I.

Motivation and Objectives

In 2009, on the south coast of Iceland a subglacial volcano system named after its covering glacier Eyjafjallajökull increasingly showed seismic and volcanic activities after decades of silence [66, 116]. On April 14, 2010 a series of eruptions started beneath the glacier. The rising magma encountered the melt water, driving "phreatomagmatic" explosions and a large plume of glass-rich ash [57], which was transported up to a height of 8 km in the atmosphere [119]. These fine fragmentated magmatic particles became the focus of international attention, as due to northeastern jet streams, they were transported over the northern, western and central parts of Europe [81, 108]. As a consequence in many countries of Europe air traffic was completely disrupted for several days [122]. It is estimated that the resulting economic losses amounted to at least more than € 1,5 billion[1] [124].

These events emphasize impressively, that understanding the processes of explosive phreatomagmatic volcanism is of utmost importance not only for geophysical and volcanological science, but also for the globalized society.

Phreatomagmatic explosions are a type of molten fuel-coolant interaction (MFCI), which have been the subject of scientific investigation of the Physikalisch Vulkanologische Labor (PVL) of Würzburg University for several years [19, 50].

Based on conducted experiments a thorough insight into the driving mechanisms was achieved, which can be summarized as follows [137]:

MFCI explosions are driven by a rapid transfer of heat from the magmatic melt (as the "fuel") to water (as a coolant). When the melt comes into contact with the coolant, nearly instantanously a mm-thick vapor film separates those two immiscible substances, limiting the heat transfer through the magma/water interface drastically and creating a premix. The vapor film is very unstable and can easily collapse [139]. In the experimental runs this breakdown of the seperating layer is triggered by the initiation of a shock wave. In this stage there is a strong thermal and mechanical coupling of the melt and the coolant. As a consequence the water expands, and the melt is facing a rapidly increasing thermohydraulic pressure, resulting in an "overload" situation [137]. Under these conditions the silicate melt is behaving like a brittle solid: Cracks are initiating and proceeding, and creating new surfaces, which cause an increase in the contact area between melt and coolant. The growth of fracture surface forces the cycle of transfer of heat, thermohydraulic expansion and further fragmentation [19]. This mechanism is schematically depicted in Fig. 1.

In the end of this phase of melt fragmentation the overheated water changes the state of aggregation. The resulting steam drives the expansion of the system to atmospheric pressure, expelling the fragments [50].

From the energetic point of view, the processes which lead to the creation of new surfaces are the key mechanisms of the entire MFCI process [18]. Therefore it is decisive to study and understand in detail the fragmentation behavior of silicate melts and its fracture dynamics.

However, comprehensive evaluations in this matter are scarce [19, 123], as several circumstances substantially complicate quantitative analysis of fragmentation processes:

- First of all these processes are running very rapidly (the decisive steps happen in a few hundred microseconds [135]), which means a big challenge to get experimental data by developing and using sensors with a very high temporal and spatial resolution.

- A moving crack tip is by definition a proceeding singularity in the material, and therefore it is difficult to get a description of the interrelationship between a propagating crack and the respective energy transfer. Because of this, fracture mechanics problems are

[1] For technical reasons, in this thesis a comma (",") is used for decimal separation rather than a decimal point ("."), according to central european standards.

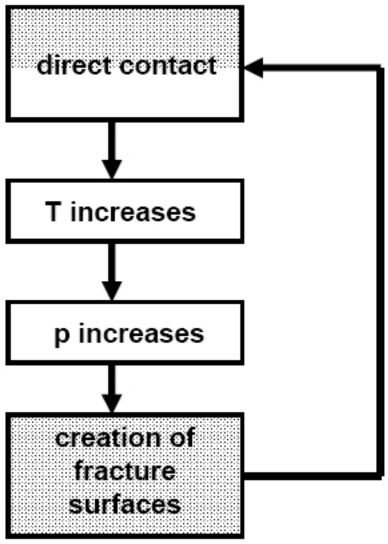

Fig. 1: Diagram of the MFCI processes in the phase of melt fragmentation: The melt is schematically depicted as a hatched area, the coolant as a solid white one. If those two substances come into direct contact, the temperature of the coolant rises, it expands and applies a rapidly increasing thermohydraulic pressure on the melt. As a consequence the magmatic melt shows the fracture behavior of a brittle solid, which results in the creation of new contact areas between melt and coolant.

often seen as being "among the most difficult (ones) to solve with reasonable numeric accuracy" [27].

- All existing models in fracture mechanics are based on empirical results under very specific conditions, usually describing a single crack under quasistatic loading [55]. In real situations, with simultaneous propagating and interacting cracks, fragmentation processes are by far more complex.

- Up to now, the only way to get information about the fragmentation history of phreatomagmatic explosions is to recover and analyze the resulting particles [15]. The dynamics of energy dissipation[2] processes, however, cannot be described yet, as in the critical fragmentation phase, there is no possibility to get a high-resolution "look in the inside" of the melt, neither in a magma chamber nor in a "hot" laboratory crucible during a MFCI experiment.

- Magmatic melts have an amorphous structure, which means that their molecular structure is irregular [59]. This leads to a very complex mechanical behavior [120]. Additionally on a molecular scale the local material conditions show uncontrollable small variances. To obtain general knowledge of the fracture dynamics, one has to make a large number of experiments to enable statistically significant evaluations, which costs time.

- The fracture behavior of amorphous silicate materials depends -among other things- distinctly on its loading velocity [23, 97]. As a consequence one has to study the material

[2]According to a common convention in fracture mechanics (see e.g. [113]), in this thesis the term "energy dissipation" is used to describe all energy transformation processes that are linked to fragmentation.

response under the same loading conditions as the melt is facing during the MFCI. It is not possible to transfer existing simple "quasistatic loading" models.

- In materials science, there exists a whole branch of research, dealing solely with "impact physics". However, due to the close integration of this kind of research and the armaments industry, access to empirical data and results, which could be helpful to solve the mentioned energy problems of MFCI, is strongly restricted.

Hence empirical models which specify *in situ* the dynamic energy dissipation processes in silicate melts, under MFCI loading conditions, during the creation of new surfaces do not exist yet.

Against this backdrop, the main objective of this thesis is to tread new pragmatic paths and find innovative methods to describe the fracture dynamics in glasses, focussing especially on the aspect of energy dissipation processes. Therefore it is required to conduct fundamental research in suitable materials and to check if these results are transferable to "real" magmatic melts.

In particular the following questions are to be investigated:

- How can MFCI loading conditions be reproduced in transparent glasses?
- How do amorphous silicate materials break under these loading velocities?
- What different kinds of crack mechanisms result in material failure?
- How do boundary conditions influence the generation of new surface and energy dissipation processes?
- Is it possible to find a useful physical parameter, which is suitable to describe fracture dynamics from the thermodynamical point of view?
- What are the general empirical results?
- Is there a possibilty to obtain a fundamental fragmentation model in silicate glasses?
- Are the resulting models in general transferable to phreatomagmatic processes?

To answer these questions, we begin by taking a closer look at the current state of fracture mechanics and my own preliminary research (see part II). This part is based on considerations mentioned within the scope of my diploma thesis [40], in which edge-on hammer impact experiments (HIEs) with thermally stress-relieved glass panes have been conducted in order to study the development of cracks. A high-speed photographic technique was used.

However, due to the new objectives with focus on energetic aspects, the original experimental setup had to be distinctly modified.

Part III describes new as well as enhanced measurement techniques and analysis methods which have been applied in the present study. This includes a brief overview on the used methods of multivariate statistics which are needed, as fragmentation is a stochastical process on a microscopic scale [40], and furthermore boundary conditions have been comprehensively varied in the experiments. Additional background information on these variations and attendant circumstances of the test series are also presented in this part as well.

In part IV the results of subsidiary experimental studies are shown.

Part V is the core of this thesis, thoroughly describing fragmentation and energetic dissipation processes in glass and glass ceramics, giving direct answers to most of the questions mentioned above. In a next step (part VI) these results are applied to volcanic materials, comparing different products of fragmented magmatic melts with fragments produced by HIEs.

Finally, part VII summarizes the main results and considerations of this thesis and provides suggestions on future application of the insights gained in fracture processes.

The fracture surface energy density concept presented in this thesis was also outlined by the author in the *Journal of Geophysical Research* [42]. The procedure and some of the findings of the comparative particle analysis were published in the *Bulletin of Volcanology* [41].

Part II.

State of Research and Results of Own Spadeworks

1. Fundamentals of Fracture Mechanics

Parts of this chapter are based on an overview of fracture mechanics I provided in my diploma thesis [40]. More detailed and supplementary information can be found there.

1.1. Elasticity Theory

In the classical theory of deformation, the mechanical effects of external forces applied to a solid body can be described with a simple continuum theory approach: The loaded material is then regarded as a continuum, atomic bindings and forces are ignored [40, 82]. The applied force $\mathbf{F}$ acting on a surface area A can be split up in a normal component $\mathbf{F}_n$ and a tangential component $\mathbf{F}_t$.

$$\mathbf{F} = \mathbf{F}_n + \mathbf{F}_t \tag{II.1-1}$$

To quantify the effect of these forces, the components are normalized to the surface area [126]. The resulting physical quantities are denominated as “normal stress” σ and “shear stress” τ and defined as follows:

$$\sigma = \frac{F_n}{A} \tag{II.1-2}$$

$$\tau = \frac{F_t}{A} \tag{II.1-3}$$

The deformation as a result of pure normal stress applied on a material is called “strain” ε [77]:

$$\varepsilon = \frac{\triangle l}{l} \tag{II.1-4}$$

where l represents the original length of the respective object, and $\triangle l$ gives the resulting change of length [82]. If a sample is stretched in one direction this usually also effects a contraction strain ε_{contr} perpendicular to the applied load σ_{axial}. The ratio of transverse contraction and axial strain is defined as the “Poisson’s ratio” μ by [126]:

$$\mu = -\frac{\varepsilon_{contr}}{\varepsilon_{axial}} \tag{II.1-5}$$

Under an increasing loading of an applied external force $\mathbf{F_n}$ a sample passes through different stages [82].

In the first stage, under low loading, the material usually shows a linear elastic behavior, described by Hooke’s law:

$$\sigma = E \cdot \varepsilon \tag{II.1-6}$$

E represents a material property, called the “modulus of elasticity”. This implies that deformation grows linearly with an increasing stress.

At higher loadings the deformation is not longer linear and the proportionality range ends. Nevertheless the strain in this “elastic range” remains reversible, until the stress exceeds a certain limit, which is called “yield strength” [82, 126].

At this point there are two different possibilities of material behavior [105] (see Fig. 2):

The first type of material behavior is called “ductile”: The stress relaxes by causing a plastic, i.e. irreversible deformation, characterized by deformation mechanisms like for example the movement of atomic dislocations in a lattice [59].

The second kind of materials fails “brittle”, showing fractures instead of plastic deformation [105, 118]. An ideal brittle material does not show any plastic deformation at all, when the yield stress is exceeded [70].

In reality the failure behavior of a sample depends distinctly on its loading velocity [25]. Therefore it is useful to describe a material as “ductile” or “brittle” only in context with the analyzed loading conditions.

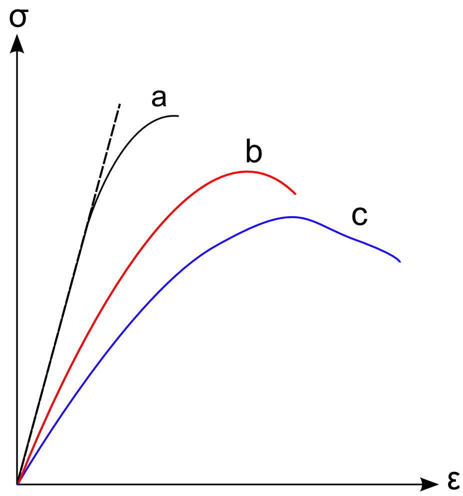

Fig. 2: Stress-strain curves for a brittle (a) and two ductile (b and c) samples.

1.2. General Properties of Silicate Materials

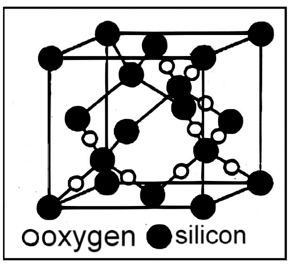

Fig. 3: Basic structure of silicate melts (ad. [109]).

Magmatic melts vary greatly in chemical composition [68] and mechanical behavior [44, 117], even if they originate from the same magma chamber (but at another time) [117]. Although they can have multifarious crystalline inclusions, all magmatic melts have in principle a similar silicate basic structure without an atomic long-range order (see Fig. 3).

This noncrystalline structure is denominated “amorphous” [8] or also “glassy”, as an anorganic melt, which solidifies substantially without crystallisation, is refered to as “glass” [59].

In general, there are three main categories for silicate glasses [53, 111]: soda lime glasses, borosilicate glasses and lead glasses.

Silicate materials which have a crystalline short range order but are amporphous on larger scales are called “glass-ceramics” [65, 107]. As the crystallic components in these materials reduce thermal expansion [7] the susceptibilty to thermal gradients is much lower than in “real” glasses [58]. For this reason, glass-ceramics are the focus of current industrial research [90].

In Fig. 4 the atomic arrangement of an amorphous silicate melt is depicted in plane view, according to the most accepted [111] structural theory of glass, which is commonly known as “random network theory” [136].

Glasses structurally resemble a liquid, but a very viscous one, effectively showing a solid-like behavior under short term loadings [106, 109]. Due to these characteristics, amorphous materials can be seen as frozen “supercooled liquids” [52].

It is important to note, that during cooling and solidification glass is most probably going through different structural phases [65]. Therefore, it is to be expected that the fracture behavior of silicate melts depend strongly on their “cooling history” [111].

Theoretical [14, 43, 53] and experimental [40, 70] results suggest that glasses can be seen as “ideal brittle” under overcritical loadings. Nevertheless, some models try to explain unanswered phenomena (see section II.1.5) in glass by plastic deformation on the nanometer scale [79]. However, this theory has not been experimentally proved up to now.

Due to their missing long range order the material properties of relaxed glasses are in general macroscopically isotropic [111].

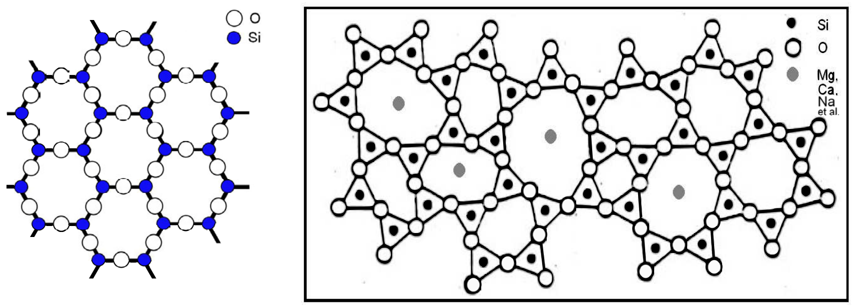

Fig. 4: Chemical structures of silicates: On the left one can see the “ideal” structure of a pure silicate crystal in plane view. On the right (ad. [109]) the highly disordered “amorphous” structure of soda lime glass is shown.
Materials, which have a X-ray amorphous structure but a crystalline short range order, are called “glass-ceramics”.

1.3. Notch Stress Concept

In the beginning of materials science, engineers experienced huge differences between the theoretically predicted and the empirical material strengths [26]. Researchers detected that the strength of a sample is substantially reduced by intrinsic flaws in the material [8]. Today, it is a well-known fact that also seemingly homogeneous materials are in fact interspersed with microscopic flaws, called “microcracks” [106].

The notch stress concept was developed to study and quantify the stress distribution in the surrounding area of a single flaw in an otherwise homogeneous material, by a mathematical approach [87].

The basic idea is that in an ideal-brittle material crack opening and propagation occurs if - and only if - the calculated local stress $\sigma(x)$ exceeds a specific limit, the molecular material strength σ_F [79]:

$$\sigma(x) > \sigma_F \tag{II.1-7}$$

On the above mentioned assumptions it is then possible to make predictions of the crack path by calculating the local stress distribution.

The notch stress model describes an elliptical notch in a loaded isotropic sample in two dimensions. The edge of the crack is therefore described via plane two-dimensional coordinates.

1.3.1. Crack Edge Results

As a boundary condition one considers a load at a large distance from the notch, given by two principal normal stress components σ_A and σ_B [55]. The elliptical notch is described by the semi-major axis a and the semi-minor axis b. Therefore the crack length is given by $2a$. The center of the ellipse is selected as the origin of the coordinate system, so that the x'-axis coincides with a, and the y'-axis coincides with b. The rotation angle between the positive x'-axis and σ_B is given by ϑ_o (see Fig. 5).

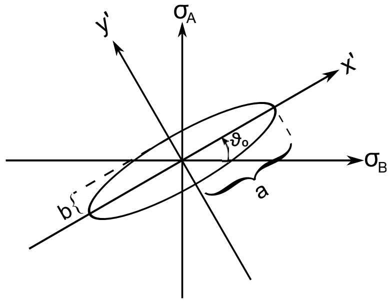

Fig. 5: Two-dimensional notch stress model: Elliptical notch in a biaxial stress field (σ_A, σ_B).

It is helpful to introduce elliptic coordinates (ξ, η) by the following transformation equations [87]:

$$x' = c \cdot cosh\,\xi cos\,\eta \tag{II.1-8}$$

$$y' = c \cdot sinh\,\xi sin\,\eta \tag{II.1-9}$$

$$c^2 = a^2 - b^2 \tag{II.1-10}$$

The edge of the notch is given by $\xi = \xi_0$, and:

$$a = c \cdot cosh\,\xi_0 \tag{II.1-11}$$

$$b = c \cdot sinh\,\xi_0 \tag{II.1-12}$$

First of all the stress at the notch edge itself is calculated. In this case one can suppose as boundary conditions [87]:

$$(\sigma_\xi)_R = 0, (\tau_{\xi\eta})_R = 0 \tag{II.1-13}$$

The index R indicates the edge of the crack.

After a lengthy calculation one gains finally a general expression, which quantifies the stress at the crack edge $\sigma_R = (\sigma_\eta)_{\xi=\xi_0}$ [87]:

$$\sigma_R = \frac{(\sigma_A + \sigma_B) sinh\,2\xi_0 + (\sigma_A - \sigma_B) \cdot \left[e^{2\xi_0} \cdot cos\,2(\eta + \vartheta_0) - cos\,2\vartheta_0\right]}{cosh\,2\xi_0 - cos\,2\eta} \tag{II.1-14}$$

With (II.1-14) one obtains a maximum edge stress $\sigma_M = \mathrm{Max}(\sigma_R)$ for $\eta = 0, \pi$. In other words: the maximum of σ_R is always located at the tip of the crack [54]. Therefore an investigation of the stress field has to focus on the surrounding area of the crack tip, the so called "notch root" [87].

1.3.2. Normal Stress Law

One can introduce the radius of curvature r_K at the crack tip:

$$r_K = \frac{b^2}{a} \tag{II.1-15}$$

Under the conditions that $\sigma_A > \sigma_B$, $3\sigma_A + \sigma_B \geq 0$ and $b \ll a$ one obtains with (II.1-11), (II.1-12), (II.1-14) and (II.1-15) a resulting maximum tensile edge stress of [54, 89]:

$$\sigma_M = 2\sigma_A\sqrt{\frac{a}{r_K}} \tag{II.1-16}$$

under the orientation angle:

$$(\vartheta_o)_M = 0 \tag{II.1-17}$$

One substantial conclusion of (II.1-16) is that the stress at the notch root increases, when r_K is reduced, that means when the crack tip is becoming "sharper".

Another fundamental consequence directly results from (II.1-17): Considering a group of statistically distributed, arbitrary orientated extendable cracks of similar length, one obtains crack-openings for those which are orientated perpendicularly to the maximum principal tensile stress (i.e. $\sigma_A > 0$).

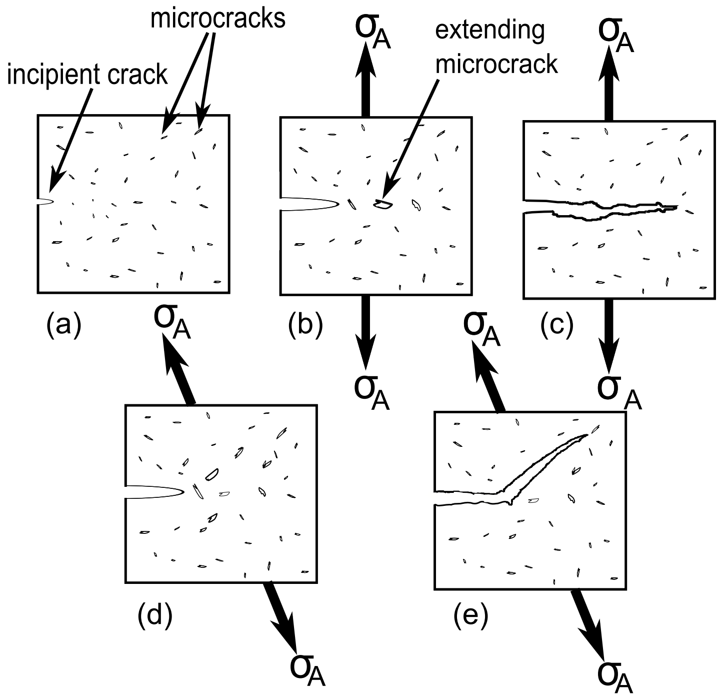

Fig. 6: Crack propagation due to the normal stress law: A crack always propagates perpendicularly to the axis of principal stress σ_A.

Fig. 6 demonstrates its consequences: A material sample with an incipient notch and interspersed with microcracks is shown (a). Under a tensile stress σ_A the incipient notch extends perpendicularly to σ_A, the same happens with all microcracks, which satisfy (II.1-17) (b). The material strength is diminished in this direction and therefore becoming highly anisotropic. As a result the propagating macroscopic crack is running normally to σ_A, coalescing with all extended microcracks on its way (c).

If the angle of σ_A changes (d), other microcracks are extending: Those, which are perpendicular to the new direction of the tensile principle stress. Thus the macroscopic crack is gradually "diverted", directed by the new anisotropy of material strength (e).

According to these considerations a crack in an ideal-brittle material is predicted to extend always in such a way that the resulting fracture surface is normal to the driving maximum principal tensile stress σ_A.

This basic law of fracture mechanics is sometimes denominated "Normal stress law" [70] and is supported by further considerations, based on the notch stress concept, as explained in the following sections.

1.3.3. Investigation of the Far-Field

A big problem in the notch stress concept is that it is not possible to obtain an exact mathematical expression of the stress field outside of the notch's interface, as - among other things - the boundary conditions (II.1-13) cease, and subsequently too much degree of freedom remains undetermined [87].

Nevertheless, there are two ways to achieve satisfying results: One possibility is to use approximations. These models deliver good results especially in the near-field of the crack tip [54].

Another option is to study accurately defined cases. The latter method is now used to investigate the stress distribution in the far-field of the crack [87].

The following considerations are based on the assumption, that an elliptical notch is under an uniaxial load with the conditions $\xi_0 = 0, \sigma_B = 0, \sigma_A \neq 0$. Then the expression (II.1-14) is simplified to:

$$\sigma_R = \sigma_A \frac{sinh\, 2\xi_0 + e^{2\xi_0} \cdot cos\, 2\eta - 1}{cosh\, 2\xi_0 - cos\, 2\eta} \tag{II.1-18}$$

With this, (II.1-11), (II.1-12) and (II.1-15) one obtains at $\eta = 0$ the maximum stress:

$$\sigma_M = \sigma_A \left(1 + 2\sqrt{\frac{a}{r_K}}\right) \tag{II.1-19}$$

The resulting stress distribution in the prolongation of the semi-major axis is demonstrated in Fig. 7 (right). In the far-field in front of the crack tip (i.e. $r \gg a$) one easily recognizes that the stress components σ_x and σ_y, which are directed along the respective axis, are converging towards:

$$\sigma_x \rightarrow 0 \tag{II.1-20}$$

$$\sigma_y \rightarrow \sigma_A \tag{II.1-21}$$

As one has a similar stress behavior in the far-field of a crack tip in more complex cases, (II.1-20) and (II.1-21) can be seen as a representative result [87].

1.3.4. Modes of Crack Opening

A fundamental idea for a near-field approximation is to suppose that the stress field substantially depends on the type of crack separation, i.e. on how the applied forces enable the crack to propagate. Irwin [67] suggested that every loading of a crack can be described as a superposition of three basic "modes", which are shown in Fig. 8.

Mode I is characterized by tensile stress perpendicular to the plane of the propagating crack. This is a mode of direct crack opening. Mode II is a mode of in-plane shear, where a shear stress is applied normal to the crack front and parallel to the crack plane. Mode III,

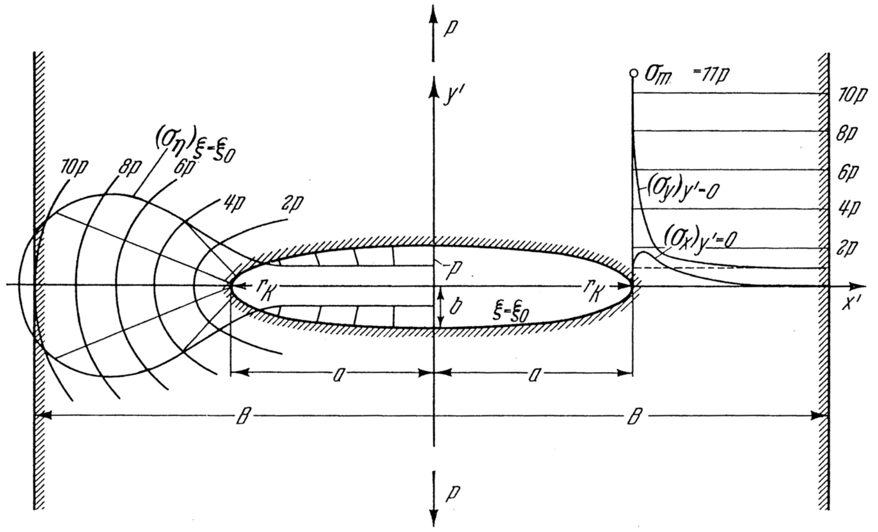

Fig. 7: Stress distribution at the edge and in the surrounding area of an elliptical notch of the width B under a tensile loading $\sigma_A = p$ (ad. [87]). Only Cartesian coordinates are shown.
On the left side, the distribution of the edge stress given by (II.1-14) is depicted.
The curves on the right show the stress components σ_x and σ_y along the prolongation of the semi-major axis, coinciding with the x'-axis, computed with (II.1-18). In this example $\frac{a}{r_K} = 25$ is selected as a representative value. With (II.1-19) one then obtains $\sigma_M = 11p$.

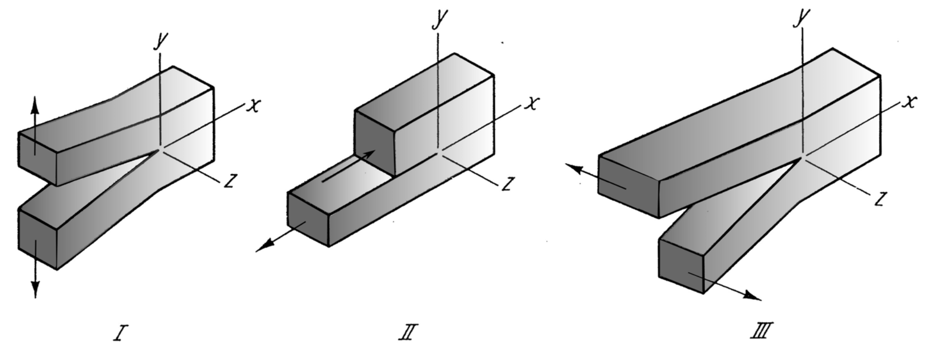

Fig. 8: Types of crack separation, denoted by mode I, II and III.

a mode of transverse shear, is characterized by a shear stress acting parallel to both: crack front and crack pane [67].

Due to the conclusions drawn in section II.1.3.2 and as this thesis is tackling primary brittle fracture, it is reasonable to focus on the most important mode of direct crack opening (mode I) [70].

1.3.5. Approximate Near-Field Solutions

Again one examines an elliptical notch with a loading σ_A applied in a far distance and perpendicular to the semi-major axis a. Initially the notch is assumed to be infinitely small, with $r_K \to 0$. The length of the crack is given by $2a$. The stress field in front of the crack tip is investigated in a range r (see Fig. 9) with $r \ll a$. On the other hand the material is seen as a continuum, therefore r has to be large compared to molecular sizes [67].

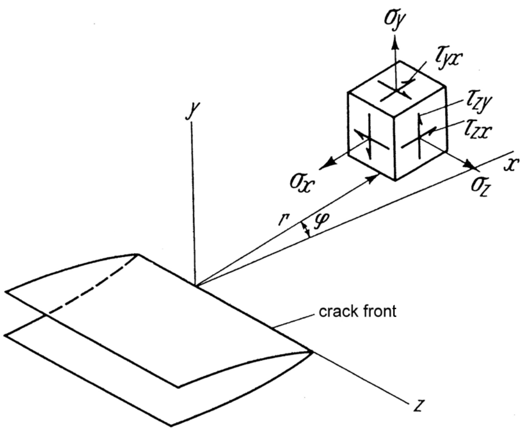

Fig. 9: Notation of the coordinates and stress components used in (II.1-22) to (II.1-26). Note that in this case the coordinates x, y and z are related to the crackfront (ad. [70]).

Using the notation shown in Fig. 9 one obtains the following results for mode I cracks [70]:

$$\sigma_x = \frac{K_I}{\sqrt{2\pi r}} \cdot cos\frac{\varphi}{2}\left[1 - sin\frac{\varphi}{2}sin\frac{3\varphi}{2}\right] \tag{II.1-22}$$

$$\sigma_y = \frac{K_I}{\sqrt{2\pi r}} \cdot cos\frac{\varphi}{2}\left[1 + sin\frac{\varphi}{2}sin\frac{3\varphi}{2}\right] \tag{II.1-23}$$

$$\sigma_z = \mu\left(\sigma_x + \sigma_y\right) \tag{II.1-24}$$

$$\tau_{xy} = \frac{K_I}{\sqrt{2\pi r}} \cdot sin\frac{\varphi}{2}cos\frac{\varphi}{2}cos\frac{3\varphi}{2} \tag{II.1-25}$$

$$\tau_{zx} = \tau_{zy} = 0 \tag{II.1-26}$$

K_I is a fundamental parameter in fracture mechanics and is refered to as “stress intensity factor” [55]. This factor describes the amplification of the magnitude of the applied stress due to the existing flaws. It depends on the load σ_A, on the geometry of the sample as well as on the size and location of the crack [79]. It is given by:

$$K_I = Y \cdot \sigma_A \cdot \sqrt{2a} \tag{II.1-27}$$

with Y being a geometrical parameter.

As one considers only mode I crack opening, it is useful to calculate the principal stress components by doing a principal component analysis, using the following defining equation [61]:

$$\sigma_{1,2} = \frac{\sigma_x + \sigma_y}{2} \pm \sqrt{\left(\frac{\sigma_x - \sigma_y}{2}\right)^2 + \tau_{xy}^2} \tag{II.1-28}$$

which implies with (II.1-22) and (II.1-23):

$$\sigma_{1,2} = \frac{K_I}{\sqrt{2\pi r}} \cdot cos\frac{\varphi}{2}\left[1 \pm sin\frac{\varphi}{2}\right] \tag{II.1-29}$$

Regarding a small central crack under an uniaxial load σ_A perpendicular to the plane of the crack, one obtains [79]:

$$K_I = \sigma_A\sqrt{\pi a} \tag{II.1-30}$$

Irwin [67] presented his approximation equations as a result of (II.1-30) in combination with a more accurate analysis of the boundary conditions:

$$\sigma_x = \sigma_A \sqrt{\frac{a}{2r}} \cdot cos\frac{\varphi}{2} \left[1 - sin\frac{\varphi}{2} sin\frac{3\varphi}{2}\right] - \sigma_A \tag{II.1-31}$$

$$\sigma_y = \sigma_A \sqrt{\frac{a}{2r}} \cdot cos\frac{\varphi}{2} \left[1 + sin\frac{\varphi}{2} sin\frac{3\varphi}{2}\right] \tag{II.1-32}$$

$$\tau_{xy} = \sigma_A \sqrt{\frac{a}{2r}} \cdot sin\frac{\varphi}{2} cos\frac{\varphi}{2} cos\frac{3\varphi}{2} \tag{II.1-33}$$

Note that the only difference between these equations and (II.1-22), (II.1-23) and (II.1-25) is the added summand $-\sigma_A$ in (II.1-31).

As mentioned above, this approximation can only be applied in a distinct range. Küppers [76] appointed the scope of validity of the Irwin equations by numerical methods, implying:

$$15r_K \leq r \leq 0,05a \tag{II.1-34}$$

Assuming for example $2a = 0{,}5\,\mathrm{mm}$ and $\frac{a}{b} = 500$ one obtains $15\,\mathrm{nm} \leq r \leq 12{,}5\,\mathrm{\mu m}$ as a typical scope of application.

In a range $15r_K \leq r \leq 10^{-3}a$ very close to the crack tip, σ_x and σ_y are becoming equal. Therefore the stress field in this area is isotropic, and the summand in (II.1-31) can be neglected. In this case the expression (II.1-31) matches (II.1-22).

1.3.6. Resulting Model of Crack Propagation

Now it is possible to determine the dynamic crack propagation by calculating the differential modification of the stress field in the surrounding area of the crack tip and using (II.1-7) to predict the locations of material failure.

However, the results of the near-field approximation soon revealed an apparent contradiction which was not solved for a long time: If the length variation of a continuous extending crack exceeds a certain limit, the results of (II.1-31) to (II.1-33) predict the highest stress values passing σ_F not at the notch root itself, but some distance ahead under a certain angle $\varphi \neq 0$ [55]. To let an existing crack propagate, σ_F must be exceeded at the crack tip, which means that, before this happens, further cracks are nucleated in front of the original crack itself.

Therefore a theoretical model has been developed, which predicts that a primary crack does not extend continuously, but in an act of coalescence with new created and extending "daughter cracks" [14].

The maximum distance between the primary mother cracks and the secondary daughter cracks is called "cross-over-length" [14]. In glass this distance is estimated at 1 nm [76] and is therefore beyond the local resolution of optical methods which were used in this thesis.

This model is totally compatible with the considerations made about the normal stress law (see section II.1.3.2): Now the predicted crack deflection in a changed external loading situation can be described in an easy way: Assume a mother crack, which is not perpendicular to the new loading direction (see Fig. 6 (d) and (e)). This model predicts daughter cracks, which are due to the normal stress law nucleating and extending preferentially perpendicular to the changed stress field. Following the reduced material strength in this preferential direction the resulting crack makes a turn.

Another important phenomena is at least qualitatively [55] explained by this model: The phenomena of crack instability [46, 79] and crack bifurcation [40], which is detailed in section II.3.2.

Considering the randomly distributed interspersed microcracks additionally to the opening daughter cracks “out of plane” at nanometer scale makes it now clear, that a crack path is never predictible in every detail, even if an ideal-brittle fracture is assumed. For the objectives in this thesis, however, it is important to obtain a general, not a microscopic description of the dynamical energy dissipation during the crack propagation.

1.4. Energy Considerations: Griffith Theory of Brittle Fracture

Even with the approximation equations (II.1-22) to (II.1-26), describing the stress field is a complex process, as K_I is depending on size and geometry of the propagating crack and therefore is a dynamic parameter [88]. Numerical calculations need large computer capacities, and for this reason developing crack simulation methods is a task, which still preoccupies the experts today (cf. [14, 39, 60, 80, 88, 130]).

Another approach was developed by A. A. Griffith , starting from energy balance considerations at the crack tip [54]:

The energy U needed to enlarge an existing crack by the length a is composed of the energy, which is transformed into new surface U_S and the mechanical energy U_M. The latter is the sum of the energy U_E, which is stored elastically in the sample, and the potential energy U_A of the external stress σ_A:

$$U = U_S + U_M = U_S + U_E + U_A \tag{II.1-35}$$

If σ_A is quasi-static, the mechanical energy decreases with the extension of the crack. On the other side the surface energy increases. Griffith's basic idea was to postulate, that a crack propagates in a way, that the total energy does not alter with the length of the crack:

$$\frac{dU}{da} = 0 \tag{II.1-36}$$

Furthermore (cf. [40]):

$$\frac{d^2U}{da^2} < 0 \tag{II.1-37}$$

In the case of a differential crack progress, the displacement of the flanks of the cracks under the effect of σ_A can be neglected. As a consequence, no work is done by external forces, and:

$$U_A = 0 \tag{II.1-38}$$

As a result of linear elastic fracture mechanics one gains the release of the energy which was elastically stored in the medium before:

$$U_E = -\frac{\pi \cdot a^2 \cdot \sigma_A^2}{E} \tag{II.1-39}$$

The surface energy which has to be expended to obtain a crack of the length $2a$ and a unit width of 1 is given by:

$$U_S = 4 \cdot a \cdot \gamma \tag{II.1-40}$$

where γ is the material dependent free surface energy per unit area [79]. Dealing with (II.1-38), (II.1-39) and (II.1-40) in combination with (II.1-35) one can solve the resulting equation for σ_A and determine in consideration of (II.1-36) the critical material-specific stress σ_{crit}, under which a crack propagates spontaneously and unstably:

$$\sigma_{crit} = \sqrt{\frac{2 \cdot E \cdot \gamma}{\pi \cdot a}} \tag{II.1-41}$$

for constant load and under plane stress conditions.

With (II.1-41) the material strength of a sample can be estimated. This expression is known in literature as the "Griffith criterion" [54, 91].

Fig. 10 schematically illustrates the coherence of energies due to Griffith's approach. At

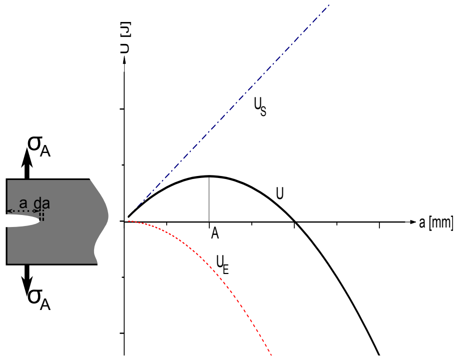

Fig. 10: Griffith energy-balance concept: On the left the plane stress situation of an uniaxial loading is shown. On the right all energies are schematically depicted, which are due to this model relevant for crack propagation (ad. [40]).

the equilibrium point A the total energy U reaches its maximum, and the system is in a stable balanced state. If the crack length a is overrunning this threshold, the crack starts to propagate unstably and without stopping. This case of $\sigma_A > \sigma_{crit}$ is called stage of "catastrophic crack propagation" [55].

Finally the strain-energy-release-rate G can be determined. It is also called "crack extension force" [79] and quantifies the total energy per crack length, released by the elastically pre-stressed sample. G is defined:

$$G = -\frac{dU_M}{da} \tag{II.1-42}$$

Assuming a brittle mode I fracture, (II.1-30) can be solved for σ_A. Inserting this result in (II.1-42) in consideration of (II.1-35), (II.1-38) and (II.1-39) one wins the following expression:

$$G = \frac{K_I^2}{E} \tag{II.1-43}$$

The according stress intensity factor, which is causing the overrun of σ_{crit} is referred to as critical stress-intensity value or plain-strain "fracture toughness" K_{Ic} [26]. This is an important matter constant and quantifies the specific resistance of the material against crack propagation. With (II.1-43), (II.1-35), (II.1-36) and (II.1-40) one obtains the so-called "crack resistance" G_c:

$$G_c = \frac{K_{Ic}^2}{E} = 2 \cdot \gamma \tag{II.1-44}$$

Therefore to achieve a definite fracture criterion of a sample one just has to determine one of the three values: the crack resistance G_c, the fracture toughness K_{Ic}, or the critical stress σ_{crit}, respectively.

1.5. Fracture Criterion Limitations and New Approach

Several methods were developed to determine one of the above mentioned fracture criteria of a sample: Indentation tests basing on methods of Hertz [62, 63], Vickers [20] and Roesler [103, 104]. These methods have been continuously modified [47, 85] and are today used in a lot of different variations to study the hardness of brittle presumed materials [95].

Alternatively, a number of other experimental methods has been developed to determine fracture toughness mostly by applying a quasi-static load on a notched sample in a three-point bending test configuration [29, 55, 95].

Nevertheless, the significance of the resulting values is always restricted due to a number of methodical disadvantages and limitations:

- As K_{Ic} depends strongly on the geometrical boundary conditions (see also [30]), all these tests have to be conducted with standardized devices and samples (e .g. DIN EN 1288 [36]). This is adequate to win basic information about the strength of materials with a certain level of security for engineering applications [106], but not sufficient to make detailed predictions of the energetic dynamics during complex fracture processes of material failure [20, 133, 134].

- Material failure is a statistical process, therefore a large number of samples is required for each testing method [77, 99]. Thus its result is just providing an average expectation value of a parameter, which may vary significantly.

- In most of the testing methods, only a single predetermined crack is studied. With those standardized experiments the complex interaction of energies, which accompanies the propagation of several cracks and crack types in a "real" fracture situation, cannot be examined, as it is not easily possible to transfer the results of the above mentioned notch stress theory to a complex multi-crack "reality" [20, 93, 94].

- Shock wave induced cracks are totally disregarded in these models. Nevertheless shock waves [18] and the interaction between shock wave induced cracks and brittle cracks caused by propagating elastic waves play a decisive role in MFCI processes [97].

- Furthermore, by using notched samples, the quantity of energy, which dissipates into the initiation of cracks is not considered in those standardized tests.

- The most important difficulty is a huge gap between the theoretically predicted and experimentally determined values, which is still puzzling the experts [55]: For a glass with $E = 7,3 \cdot 10^{10}\,\frac{\mathrm{N}}{\mathrm{m}^2}$ for example, the theoretical value of 2γ is predicted to be $2,4\,\frac{\mathrm{J}}{\mathrm{m}^2}$ [79]. However, the determined value of such a notched glass sample under a three point bending experiment with quasi-static loading was revealed to be $4\,\frac{\mathrm{J}}{\mathrm{m}^2}$ [79] (due to this contradiction, some researchers suppose that glass is not ideal-brittle but ductile at nanometer scale [22, 55]) and the measured surface energy under dynamic loading is even distinctly higher, strongly depending on the loading velocity [23, 92].

Due to these facts, although many fracture phenomena can be qualitatively explained by conclusions drawn from notch stress models, the above mentioned parameters G_c, K_{Ic} and σ_{crit} are quite cumbersome and not too useful for our purpose to describe the energy dynamics of fracture processes in magmatic melts.

Therefore, in this thesis a new experimental approach is proposed, taking the only known linear correlation of fracture processes into account: The linear correlation of "fracture energy" and fracture surface, which is theoretically predicted by (II.1-40), and experimentally verified [16].

The according proportionality factor is sometimes denominated by the (misleading) term "specific critical shear stress" (cf. [98]) or "critical fragmentation energy" [97]. To prevent misunderstandings I will use another term: "fracture surface energy density" (FSED) η . It is defined by:

$$\eta = \frac{E_{frac}}{A_{frac}} \tag{II.1-45}$$

where E_{frac} is the fracture energy and A_{frac} is the resulting fracture surface.

It is important to note, that E_{frac} describes all energies which affect fracture processes (see also chapter V.6). Hence this term considers energy dissipation not only into new surfaces but also into heat and even possibly ductile deformation. Therefore η is *not* identical with γ in (II.1-40), but much handier to be determined by representative experiments.

2. Basics of Shock Waves

A shock wave is induced under an impact load. It is a very fast propagating singularity [78], which is established within a "few microseconds" [74], in water within 1 µs [51]. Although there exist some basic models of shock wave propagation in gases [78] and liquids [51], comprehensive evaluations about the nature of shock waves in solid states are scarce [127].

Therefore to start with the basics of shock waves, consider a model of a perfect fluid without friction (cf. [78], unless otherwise stated):

An expression for the law of conservation of mass is given by the continuity equation:

$$\frac{\partial \varrho}{\partial t} + div\left(\varrho \cdot \mathbf{v}\right) = 0 \tag{II.2-1}$$

where ϱ is the mass density of the fluid and $\mathbf{v}$ the velocity of flow. Energy conservation for a volume element is expressed by:

$$\frac{\partial}{\partial t}\left(\frac{\varrho \cdot v^2}{2} + \varrho \cdot \epsilon\right) = -div\left[\varrho \cdot \mathbf{v} \cdot \left(\frac{v^2}{2} + w\right)\right] \tag{II.2-2}$$

with ϵ denoting the liquid's intrinsic energy and w its enthalpy per mass unit. Hence the equation of motion in an ideal fluid is given by the Euler equation:

$$\frac{d\mathbf{v}}{dt} = \frac{\partial \mathbf{v}}{\partial t} + \left(\mathbf{v}\nabla\right)\mathbf{v} = -\frac{1}{\varrho}\nabla p \tag{II.2-3}$$

The change of the pressure p, which takes effect on each volume element dV is equal to the product of the fluid's density per volume unit and its acceleration $\frac{d\mathbf{v}}{dt}$.

Sound waves as oscillations of low amplitude in a compressible fluid have a low velocity $\mathbf{v}$. In this case the term $\left(\mathbf{v}\nabla\right)\mathbf{v}$ can be neglected. Also the changes in pressure and density are quite low, and hence:

$$\varrho = \varrho_0 + \varrho' \tag{II.2-4}$$

$$p = p_0 + p' \tag{II.2-5}$$

The index 0 denotes the constant value of the liquid, which is in an equilibrium. Small variations in the sound wave are marked by apostrophes. By neglecting the second order terms, the continuity equation (II.2-1) turns to:

$$\frac{\partial \rho'}{\partial t} + \varrho_0 \cdot \nabla \mathbf{v} = 0 \tag{II.2-6}$$

and (II.2-3) turns to:

$$\frac{\partial \mathbf{v}}{\partial t} + \frac{1}{\varrho_0} \cdot \nabla p' = 0 \tag{II.2-7}$$

These linearized state equations can be applied to sound waves of moderate or low amplitude. As the propagation of a sound wave in an ideal fluid takes place under adiabatic conditions, the correlation between pressure and density is given by:

$$p' = \left(\frac{\partial p}{\partial \varrho_o}\right)_S \rho' \tag{II.2-8}$$

With (II.2-6) results:

$$\frac{\partial p'}{\partial t} + \varrho_0 \cdot \left(\frac{\partial p}{\partial \varrho_o}\right)_S \cdot \nabla \mathbf{v} = 0 \tag{II.2-9}$$

Therefore a sound wave is totally described by (II.2-7) and (II.2-9) with its variables $\mathbf{v}$ and p.

By introducing a velocity potential ϕ, defined as:

$$grad\, \phi = \mathbf{v} \tag{II.2-10}$$

one achieves with (II.2-7) and (II.2-9):

$$p' = -\varrho \cdot \frac{\partial \phi}{\partial t} \tag{II.2-11}$$

$$\frac{\partial^2 \phi}{\partial t^2} - c^2 \triangle \phi = 0 \tag{II.2-12}$$

In this linear wave equation (II.2-12), c is the propagation velocity:

$$c = \sqrt{\left(\frac{\partial p}{\partial \varrho}\right)_S} \tag{II.2-13}$$

Hence, the speed of sound of a certain matter is defined as the propagation velocity of harmonic waves i.e. with not too high amplitudes.

At high pressure amplitudes all these simplifications, *inter alia* those of (II.2-3) to (II.2-7), are no longer allowed. One obtains anharmonic effects and as a consequence a correlation between the amplitude of the pressure wave and its velocity: The higher the amplitude of a pressure peak, the higher its propagation velocity [74].

If the initial pressure peak exceeds a certain limit, a front of discontinuity is established, which propagates with supersonic speed (as defined above) through the material. This propagating front is called "shock wave". It is followed by waves of rapid pressure alternations [102].

The pressure amplitude of a shock wave front can be approximately described as the dynamic pressure at a planar plate (cf. [74], unless otherwise stated): By considering the Bernoulli equation of an ideal flow (constant density ϱ and intrinsic energy ϵ) one obtains:

$$p_1 + \frac{1}{2}\varrho_1 v_1^2 = p_0 + \frac{1}{2}\varrho_0 v_0^2 = const \tag{II.2-14}$$

Presume that the flow is perpendicularly hitting a static planar plate. That means that at the plate's surface the flow is coming to a stop. The variables of the undisturbed flow are indicated by the index 0, and 1 denotes the flow's variables at the plate's interface. As $v_1 = 0$:

$$p_1 - p_0 = \frac{1}{2}\varrho_0 v_0^2 \tag{II.2-15}$$

The left term describes the dynamic pressure (also called "stagnation point pressure"), which is acting on the plate. To quantify the effective pressure p_{eff} on an object of arbitrary shape a pressure coefficient C_p is introduced and defined by:

$$C_p = \frac{p_{eff} - p_0}{\frac{1}{2}\varrho v^2} \tag{II.2-16}$$

At the front of the shock wave the maximum pressure is given by:

$$p_{max} = C_p \cdot \frac{1}{2}\varrho v^2 \tag{II.2-17}$$

The pressure decrease in a distance r from the point of maximum pressure (e.g. the point of impact) can be expressed by:

$$p \sim p_{max} \cdot \left(\frac{1}{r}\right)^n \tag{II.2-18}$$

If the source of the shock wave is punctiform, a spherical wave can be considered. In this case:

$$n = 2 \tag{II.2-19}$$

If the source is linear, the shock wave can be described as a cylindrical wave with:

$$n = 1 \tag{II.2-20}$$

Assuming that a shock wave is composed of a number of plane high-frequency waves, the shock wave energy E_{shock} in an ideal fluid is a function [51, 78]:

$$E_{shock} = E_{shock}(c; \varrho; A; v_p^2) \tag{II.2-21}$$

where v_p denotes the velocity of the projectile whose impact had caused the shock wave, and A is its contact area.

Hence, two additional characteristics of shock waves can be derived from (II.2-21):

1. The intensity of shock waves depends on the impact velocity.
2. Furthermore it depends on the contact area, which implies a dependency on the geometry of the projectile.

These dependencies have been experimentally substantiated by investigations on shock waves in water [51].

As general models of shock waves in silicate melts do not exist, the only possibility is to conduct fundamental research (i.e. damage evaluation) [127] and to transfer the knowledge of shock waves in fluids [74].

The admissibility of this method is at least qualitatively supported by empirical results [74, 102].

3. Results of Own Preliminary Investigations

As explained in section II.1.5, it is absolutely essential to study fracture processes in representative experiments, which means under loading conditions that are similar to “real” MFCI situations.

For this reason a low velocity hammer impact edge-on experiment in a three-point bending test configuration was selected, with which the gap in fracture research between standardized three-point bending tests under quasi-static load [101] and high velocity impact experiments (cf. e.g. [69, 112, 128]) is closed.

This thesis can thereby base on some fundamental findings, preliminarily gathered in my diploma thesis [40], where high speed cinematographic visualization and analysis methods of fracture processes in impacted float glass targets have been introduced and established. Its most relevant conclusions have been a good starting point and are hence summarized in this chapter.

3.1. Phenomenology of Cracks and Fracture Dynamics

As the classification of cracks has been substantially extended and modified in the present thesis (see V.1), obsolete designations are not used here.

- In principle, after impact two completely different classes of cracks occur: One crack class is propagating semi-circularly from the point of impact in the plane of observation, creating a complex conchoidal fracture structure. Its nature and appearance conditions let strongly suppose that these crack types are - at least indirectly - induced by shock waves.

- The other class of cracks is characterized by a propagation perpendicular to the plane of observation. Only the two most prominent subtypes of this kind of cracks have been studied in detail: On the one hand the subtype of cracks, which propagate between the three contact points of the target with the bearings and the hammer tip. These cracks form an “A”-like shape and are therefore referred to as “A-cracks”. Another subtype of cracks was named “W-cracks” as those cracks seem to track the outer flanks of a capital letter “W”. Conchoidal cracks, A-cracks and W-cracks show significant differences in appearance and also in their dynamics.

- The dynamics of crack tip propagation is characterized by distinct velocity fluctuations. As a maximum, the measured speed was found to be limited to 65 % of Rayleigh velocity for A-cracks and to 71 % for W-cracks.

- A new parameter denoted “fracture area velocity” (FAV) was introduced. It quantifies the new created surface area per time and provides a tool to describe fracture dynamics. With an innovative method (see III.5.2.5), this value can now be determined by means of high speed cinematographic crack image sequences. As explained later, this parameter is crucial, as it is the foundation for energy dissipation analysis.

3.2. Crack Instabilities and Branching

An important mechanism which limits the velocity of crack propagation is an effect that can be observed especially at A-cracks:

At high velocities, A-crack propagation is becoming increasingly unstable, marked by deviations from the original course in the crack path and finally by branching events. Some of the branching cracks are only of a depth of about 200 µm. This effect is referred to as "micro-branching" [11, 115]. Other crack branches are severing the material completely and are therefore called "macro-branching" [40].

Studies of crack velocity as well as FAV uncover the context between crack instability and crack dynamics: when the crack exceeds a critical velocity, its speed suddenly drops. Simultaneously, the crack tip forms a bulge, which becomes a branching point (see Fig. 11).

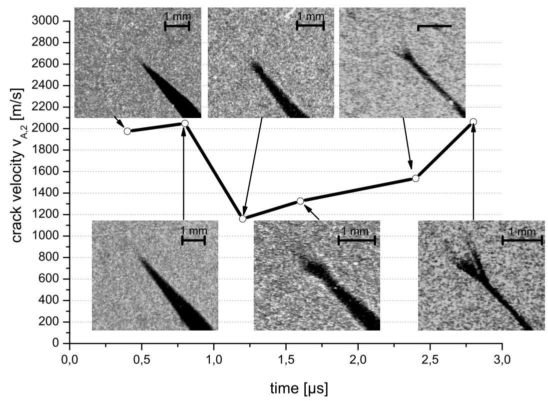

Fig. 11: Crack dynamics during branching: A crack tip propagates with a rather high velocity of more than 2000 m/s. Then (at 1,2 µs) the crack velocity drops. Simultaneously a "bulge" is formed at the crack tip, which shows to be the basis point of a branching crack (ad. [40]).

The increasing instability close to the branching point can also be reconstructed by morphological investigations of the fracture surface (see Fig. 12).

Although several approaches have been suggested in the recent past [10, 80, 114], a general accepted quantitative model for crack instability effects is still lacking [55].

However a qualitative model may explain the deviations from the path predicted by the normal stress law:

As a consequence of the near-field solution, presented in section II.1.3.5, the principal stress close to the crack tip is given by (II.1-29), hence:

$$\sigma_1 = \frac{K_I}{\sqrt{2\pi r}} \cdot cos\frac{\varphi}{2}\left[1 + sin\frac{|\varphi|}{2}\right] \tag{II.3-1}$$

Considering (II.3-1) as a function of φ with constant r, one achieves a maximum of σ_1 not at $\varphi = 0°$ but at $\varphi = \pm 60°$. Under this angle σ_1 is 30 % greater than in the prolongation of the fracture surface (under $\varphi = 0°$, which also is denoted "ligament" [70]), as:

$$\sigma_1\left(\pm 60°\right) = 1{,}30 \cdot \frac{K_I}{\sqrt{2\pi r}} \tag{II.3-2}$$

Due to this characteristic feature of the stress distribution, the normal stress law has to be modified within the scope of (II.1-34), as already indicated in section II.1.3.6.

In Fig. 13 the behavior of a crack tip under an increasing stress is schematically shown.

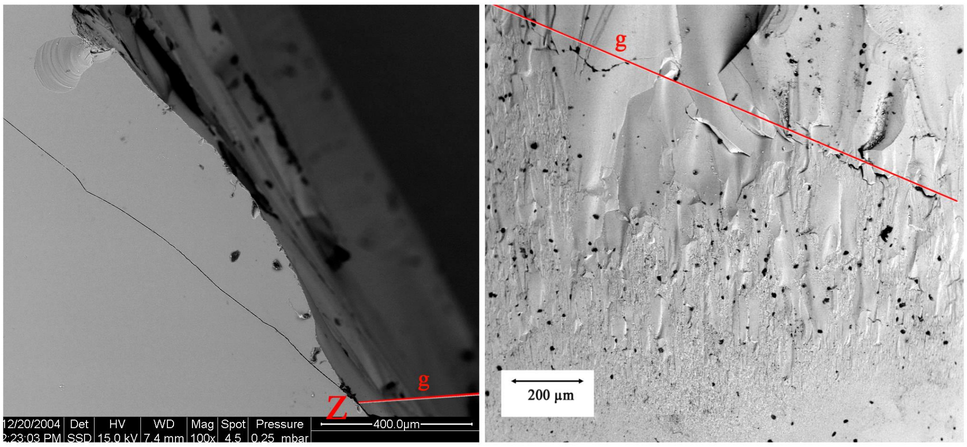

Fig. 12: SEM-Images of a fracture surface at a branching point: On the left the breaking edge of a fragment is depicted. A second crack appears as a sharp line, which branches from the point Z under an angle of approx. 25°. On the right the surface of the same fragment is shown in top view. The crack tip was propagating from below, became increasingly unstable implying a growing surface roughness, and was finally branching at the level of the red plotted line g. (These SEM images were made at the Bundeskriminalamt, Wiesbaden [40].)

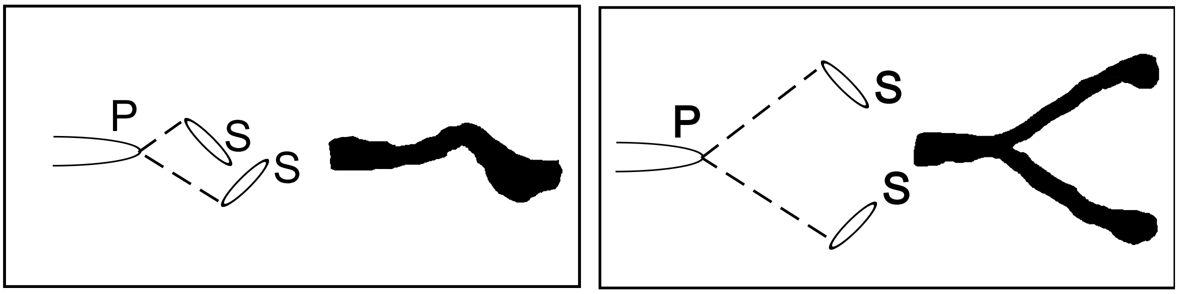

Fig. 13: Qualitative model of crack instabilities: Due to the near-field solution (II.3-2) inclined secondary cracks S extend under a certain angle in front of the primary crack P. If the stress increases, the distance between the tip of the primary crack and the opening secondary cracks grows, which leads to an increasingly rough surface (left) and finally to crack branching (ad [40]).

If σ_1 and therefore K_I increases in front of the crack tip, secondary cracks extend at a growing distance under the depicted angle, which are subsequently fusing with the primary "mother" crack. Due to the normal stress law, the orientation of the opening secondary cracks is inclined towards the direction of the original ligament. As a result of the growing distance one obtains a more and more unstable crack path and hence a fracture surface with an increasing roughness. Branching occurs, if the level of stress is finally high enough to let K_I exceed K_{Ic} at a certain distance from the crack tip, resulting in an opening of secondary cracks fairly wide apart.

In this model, the crucial point is that K_I in the near-field of the crack tip is not solely depending on the crack geometry, but also considerably on the crack velocity v [40, 70]. As on the other side the crack velocity itself is a function of K_I [70] one obtains a complex feedback correlation, which continues to preoccupy the experts [10].

Although this model seems to provide at least a reasonable qualitative explanation for the effects of crack instability, it has to be noted that some empirical results raise fundamental doubts [55]: In some materials, crack branching also occurs even at rather low crack velocities. Furthermore the empiric angles between two crack branches are always significantly smaller than predicted, as one can also easily reconsider for example in Fig. 12.

3.3. Concept of Directed and Fluctuating Stress

Under a polariscope, statically loaded targets reveal regions of high tension called "principal stress zones" (PSZ, see e.g. Fig. 43). In broad outline the course of A-cracks and the onset of W-cracks can be predicted by this photoelastic method. At smaller scales, however, crack propagation seems to be a stochastic process. Consequently a qualitative model presents two mechanisms, which affect the process of crack propagation after the moment of impact:

On the one hand, there is an increasing "directed stress" supposed, which is forcing the crack to propagate in a "macroscopic" locatable zone within the PSZ.

On the other hand, at the moment of impact strongly fluctuating stress waves are rushing through the material, causing stochastic effects on the propagating cracks: At smaller scales, the location and the dynamics of cracks are massively affected by those chaotic (in the sense of unpredictable) stress waves.

It has to be stressed, that this model was a suggestion solely based on the phenomenology of cracks and photoelastic examinations under static loading.

For technical reasons dynamic stress investigations by means of photoelasticity have not been conducted in the past. The present thesis has to close this gap by presenting detailed studies of stress dynamics during fragmentation and providing more comprehensive considerations about the decisive driving mechanisms of fracture.

Part III.

Experimental Setup, Measurement and Evaluation Methods

1. The Hammer Impact Experiment (HIE)

Based on the previously described experiences and considerations, an experimental setup was developed and constructed allowing a comprehensive insight into energetic dissipation processes during fragmentation of samples, which have been overloaded in an edge-on impact configuration by a hammer. In this section its features are detailed.

1.1. Impact configuration

1.1.1. Bearings

The target samples are positioned on two half-cylindrical bearings of C45E steel [37], mounted at a fixed distance of 50 mm apart from each other. The half-cylindrical shape is selected to minimize the area of contact and thus to reduce uncontrollable side effects due to friction between the loaded sample and the bearings. The underside of the bearings are constructed in a way to provide an optimal mechanical coupling to the force transducers underneath (see Fig. 14). The diameter of each half-cylinder is 21,05 mm.

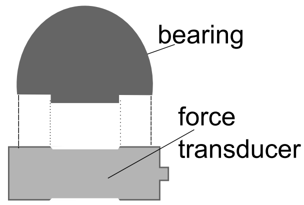

Fig. 14: Bearing.

1.1.2. Hammer

A stainless steel tube with a square cross-section serves as the shaft of the hammer. It is pivoted between two ball bearings, which are mounted on a massive metal platform on the top of a height adjustable tripod (see Fig.15). A metal billet weighing 4,8 kg is held freely

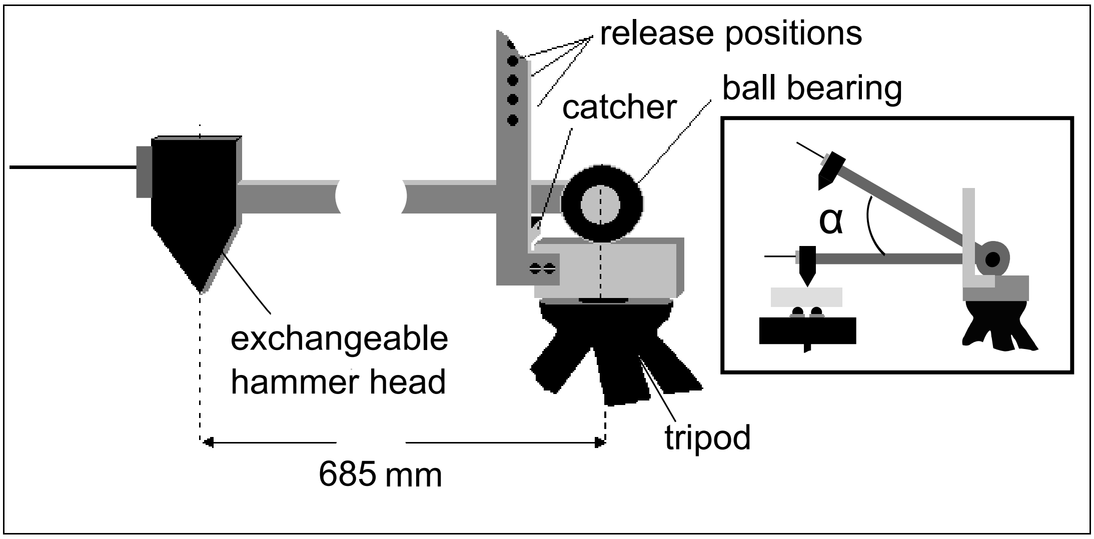

Fig. 15: Hammer setup (see text).

suspended between the tripod's feet to provide a stable stand during the impact.

On the other end of the shaft, the exchangeable hammer head is fixed with a firm Allen screw. Before each experiment care is taken to ensure that the impact of the hammer tip is central. That means that the point of impact was precisely equidistant to each bearing. Furthermore the tripod is always adjusted to a height, at which the hammer hits the target perpendicularly, and thus the shaft of the hammer is exactly horizontal. The position of the hammer tip is described by a rotational angle α, which is defined to be 0 degree at the point of impact. In this position the distance between the point of impact and the center of rotation is 685 mm.

Also attached to the metal platform, is an L-shaped arm including six drilled slots. With this construction the hammer can be released from six different heights by pulling a metal bolt.

To prevent damage to hammer and ball bearings a shock adsorbing “catcher” dampens the further movement after the target's last stage of fragmentation and the hammer's breakthrough.

Until the moment of impact both systems, hammer and sample mount are totally decoupled from mechanical point of view, in order to avoid disturbing effects like the transmission of vibrations when the hammer is falling.

The total loading mass m_H of the respective hammer is around 2290 g and is determined before each HIE series.

1.2. Visualization and Imaging Systems

1.2.1. Cranz-Schardin High Speed Camera System

The central element of the HIE is a Cranz-Schardin multiple spark high speed camera from Drello[1]. With this camera, it is possible to achieve high-speed recordings, which allows to evaluate in detail crack propagation and fragmentation processes. The camera system consists of several components, which are described below [38]:

On the one side of the setup, there is a camera from Linhof[2], consisting of 24 object lenses with a focal length of 550 mm. These lenses are arranged in a matrix of six rows and four columns. In the optimal case one obtains 24 pictures, which are projected to the image plane on the reverse side. As this camera does not contain shutters, it is an open system, and therefore sensible to exposure. As a consequence, experiments with the Cranz-Schardin camera have to be conducted in total darkness.

On the reverse side of the camera, a cassette is attached, containing a 18 x 24 cm panchromatic sheet film of the type Plus-X-Professional (Type 4147), produced by Kodak[3] with a very fine grain size and an ISO sensitivity of 125/22°.

The counterpart of the camera is the flash unit, which faces the camera from the other side of the setup. It is equipped with 24 spark gaps, which can be fired in sequences. Upstream to each flash device a capacitor is connected with an applied voltage of 10 kV, provided by a stand-alone control unit.

This control unit also relays an additional chronological staggered voltage pulse of 600 V amplitude, using a quartz-stabilized high frequency oscillator. The resulting over-voltage initiates a spark discharge, which lasts 100 ns. This period defines the exposure time of a single flash. The frame rate can be specified at the control unit, by adjusting intervals between maximum 4 ms (250 Hz) and minimum 400 ns (2,5 MHz).

The schematic setup of the Cranz-Schardin camera is illustrated in Fig. 16. A spark gap

[1] Drello Ing. Paul Drewell GmbH & Co. KG, Mönchengladbach, Germany
[2] Linhof Präzisions-Systemtechnik GmbH, München, Germany
[3] Kodak GmbH, Stuttgart, Germany

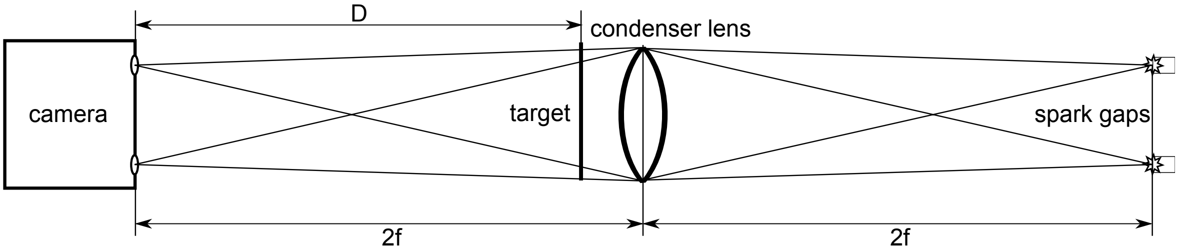

Fig. 16: Optical path of a Cranz-Schardin camera system: The spark gaps are depicted sharply via a condenser lens of $f = 100\,\text{cm}$ on the object lenses. Hence the distance between the flash plane and the object lens plane is 4 m. As the distance D between the object lens plane and the target to be photographed is about 192 cm, the latter one is very close to the condenser lens.

is depicted sharply on the appropriate object lens via a special condenser lens of 150 mm diameter. The latter lens has a focal length f of 100 cm, the distance between the plane of the spark gaps and the object lens plane is $4f$.

The sample, which is to be studied under high frame rates, is positioned close to the condenser lens.

Due to this proximity to the scene of HIE impact, an additional 5 mm thick cover glass plate is installed to protect the condenser lens (see also Fig. 19).

The camera is focused on the target plane, which is therefore sharply depicted on the sheet film. The spark gaps are fired top down and column by column (see Fig. 17).

With the selected condenser lens, due to space limitations it was not possible to project the top row of spark gaps on the image plane. As a consequence the images with the running number 0, 6, 12 and 18 are missing (gray color in Fig. 17). These gaps have to be taken into account in the evaluation of the image sequences.

After exposure, the films were developed manually by myself in a photo laboratory.

0	6	12	18
1	7	13	19
2	8	14	20
3	9	15	21
4	10	16	22
5	11	17	23

Fig. 17: Numbering of an image sequence (see text).

A selection of the most significant images (3600 out of 28120) have been framed and scanned via a 3600 dpi slide scanner from Reflecta[4].

The other images have been scanned with the aid of a Kodak film scanner with a resolution of 2800 dpi.

1.2.2. Triggering

For a successful HIE it is crucial to use a reproducible and accurate trigger. Best results were achieved with a closing circuit system [40]. The trigger circuit is powered by a 12 V battery.

One pole is connected to a trigger pole, a 299 mm long rod of 7 mm diameter, which is attached to the head of the hammer as an extension (e.g. see Fig. 19). A plastic flange separates the pole and the hammer head, serving as an electrical insulator.

Under a certain angle α_{Tr} the trigger pole touches a 150 mm long leaf spring, which is connected to the second pole of the trigger circuit. This leaf spring is attached to a holder, which is adjustable in height via a high-precision micrometer screw. It is not very useful to choose $\alpha_{Tr} = 0°$, i.e. to trigger at the moment of impact, as the control unit's electronics shows an intrinsic delay and hence the sequence would start too late. For this reason the leaf spring is adjusted a certain distance (normally 0,8 mm) over the upper edge of the target. An

[4]Reflecta GmbH, Rottenburg, Germany

additional delay, i.e. the time period between the trigger signal and the first flash event, can be preset at the control unit.

The experimenter's challenge is to predict the correct delay needed to record the first stage of fragmentation.

1.2.3. IR-Video Camera

An additional camera was deployed to study slower concomitants of fragmentation, like the movement of the resulting fragments. As an HIE has to be conducted in total darkness, a Panasonic[5] type NV-DS 15 digital video camera was used in IR night vision mode with a frame rate of 25 fps (50 fps by deinterlacing).

A white screen with a scale encloses the condenser lens to ensure a good contrast between the fragments and the background.

1.2.4. Modified Setup for Photoelastic Investigations

As mentioned in II.3.3, to understand fracture processes it is essential to gain knowledge about the specific stress distribution in the target.

Thus the setup was constructed in a way that allows also photoelastic investigations. To conduct these experiments, two crossed polarizers are mounted (see Fig. 18): One is attached

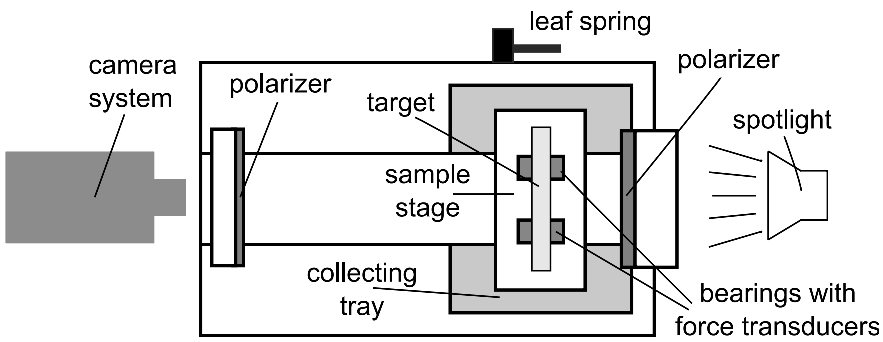

Fig. 18: Bird's eye view of the setup for photoelastic experiments (hammer is not depicted).

at the condenser lens, converting the passing light into plane polarized light, which is subsequently passing through the sample.

In glass, the magnitude of the refractive indices is a local function of the local stress [49]. Consequently, stressed samples show birefringence effecting a local rotation of the plane of polarization.

With the aid of another polarizer, which is crossed mounted as an analyzer, the stressed regions of the sample becomes visible as fringes, known as "isoclinics" [49]. This polarizer is attached in front of the respective camera.

The Cranz-Schardin camera system is not useful for this kind of examination, as the flash intensity is not sufficient.

Instead, a bright spotlight (Reflecta 5005 with 2 x 1000 W) is used as light source.

In principle, with the described setup three kind of photoelastic experiments can be conducted:

1. Photoelastic investigations of unloaded samples: Before each HIE the respective target is checked in the polariscope for pre-stressed regions.

[5]Panasonic Corporation, Osaka, Japan

2. Examinations under static loading: A defined load of 100 N is applied to the sample to visualize the principal stress zone and the regions of directed stress (see II.3.3).

3. Photoelastic studies under impact conditions: In these special HIE series digital high speed camera systems are used instead of the Cranz-Schardin camera. The specifications of these cameras are described below.

1.2.5. Supplementary High Speed Camera Systems

Two further high speed cameras are deployed to study in detail:

- The movement of the hammer.
- The kinetics of the fragments.
- The dynamics of stress distribution in samples under an impact loading.

For these jobs the following camera systems are used:

- A NAC[6] HotShot 512 SC digital high speed camera (monochrome version; resolution: 512 x 512 px; frame rate at 1:1 aspect ratio: up to 4000 fps), kindly provided by Prof. Taddeucci[7] (J-series).
- A NAC Memrecam GX1 digital high speed camera system (pixel bit depth: 12 bit; resolution: 1280 x 1024 px; frame rate at 1:1 aspect ratio: up to 3000 fps) (N-series).

1.2.6. Additional Photo Cameras

In the list below, all the used digital photo cameras and their purposes are as follows:

1. Nikon Coolpix 990 camera (2048 x 1536 px): Used in photoelastic experiments to record stress fringes of targets under no, as well as under static loading.
2. Canon EOS 350D (3456 x 2304 px) digital reflex camera: Deployed in photoelastic experiments and to record fracture surfaces, fragments and particles also by means of a microscope.
3. Casio Exilim EX-F1 (2816 x 2112 px) camera: Used for supplementary impact studies.

1.3. Sensors and Data Acquisition Systems

1.3.1. Displacement Transducer

A continuous high precision carbon rotary potentiometer of the type Radiohm[8] CIP 162 with a maximum resistance of 10 kΩ is adjusted in alignment with the rotation axis.

In a supplementary test series the linearity of the potentiometer was checked obtaining an empirical fault tolerance of less than 0,1 %.

As in this configuration, the voltage at the potentiometer is directly related to the angle of the hammer α, it can serve as a displacement transducer.

With the aid of a voltage divider circuit, powered by a 12 V battery, the displacement curve of the hammer tip can be accurately determined by recording the voltage signal via a 1GS/s

[6] NAC Image Technology, Simi Valley (CA), USA
[7] Prof. Jacobo Taddeucci, Istituto Nazionale di Geofisica e Vulcanologia (INGV), Rome, Italy
[8] Radiohm, Fabrique de Materiel Electrotechnique, Paris, France

two-channel digital storage oscilloscope PCS 500 from Velleman[9], which is connected to a PC. Unless otherwise stated the setting for the displacement signal was 0,1 $\frac{\mathrm{ms}}{\mathrm{div}}$ and 0,05 $\frac{\mathrm{V}}{\mathrm{div}}$.

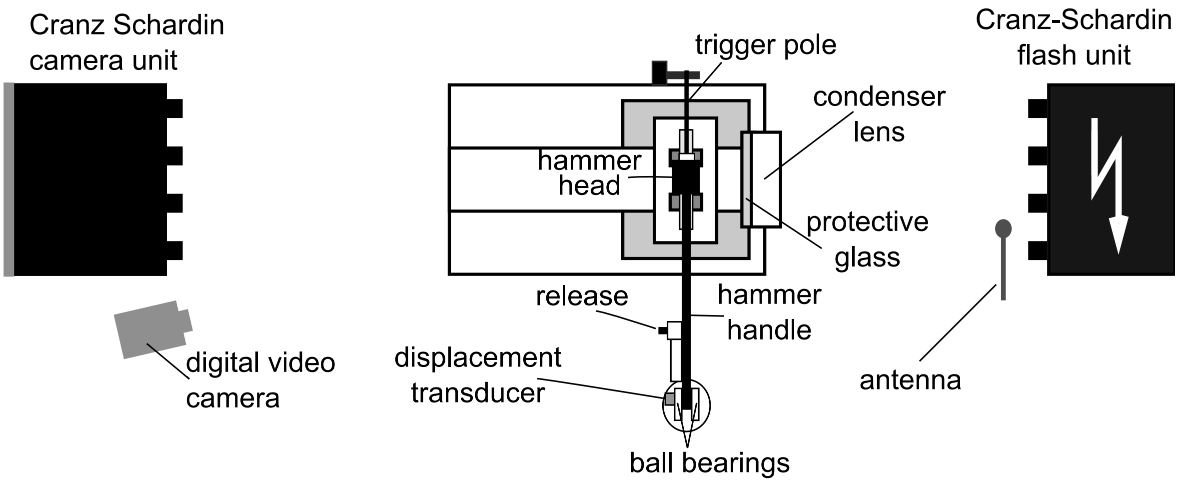

Fig. 19: HIE setup (bird's eye view).

1.3.2. Force Transducers

As indicated in sec. III.1.1.1, an annular quartz crystal force sensor type 9031A from Kistler[10] was mounted under each bearing (see Fig. 14). By this means information on force signals out-coupled from the target is obtained. Each force transducer transforms the acting force to be measured into an electric charge Q [73].

Two charging amplifiers type 5006 from Kistler convert the charges into a proportional voltage and provide an amplified output signal [72].

In the aftermath of a hammer impact, large forces occur. Therefore an amplification of 1 $\frac{\mathrm{kN}}{\mathrm{V}}$ was selected at the HIEs.

The signals are recorded by a second digital storage oscilloscope PCS 500, which was connected to another PC (see sec. III.1.3.4). Unless otherwise stated the force signal settings were 0,05 $\frac{\mathrm{ms}}{\mathrm{div}}$ and 1,5 $\frac{\mathrm{V}}{\mathrm{div}}$ for both channels (left and right force signal).

1.3.3. Electromagnetic Signal

An antenna was adjusted close to the flash unit, to detect the electromagnetic pulse of the spark gaps, and is directly connected to a storage oscilloscope type Philips[11] PM 3335 60 MHz. A flash appears on the screen as a sharp peak. Hence, each frame from the image sequence can be assigned to the exact time of exposure. In each HIE, the EMP settings are adapted to the selected flash interval.

1.3.4. Coordinated Data Acquisition System (CODAS)

The configuration of the recording systems is shown in Fig. 21.

[9]Velleman Inc., Fort Worth (TX), USA
[10]Kistler Instrumente AG, Winterthur, Switzerland
[11]Koninklijke Philips Electronics N.V., Eindhoven, Netherlands

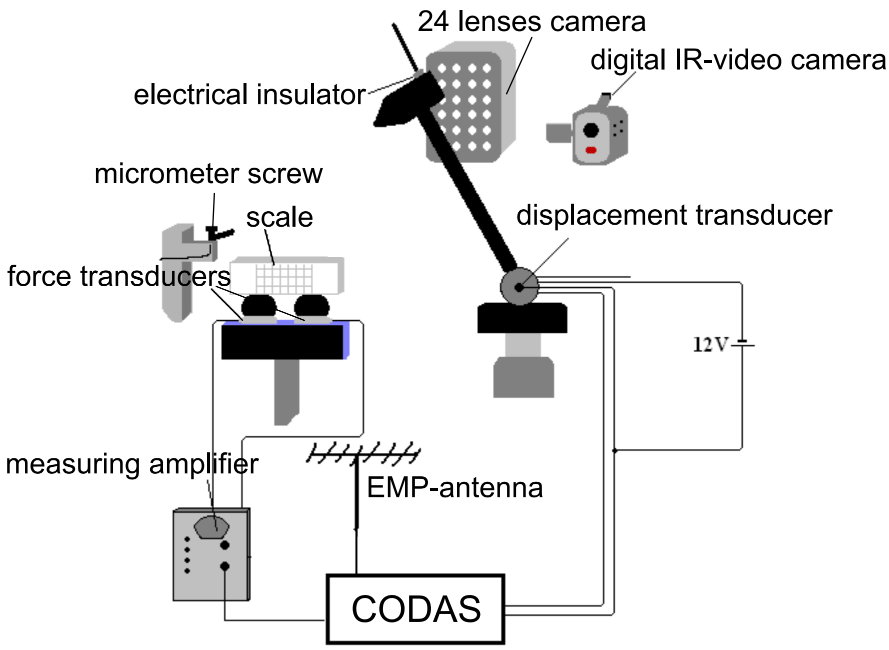

Fig. 20: Setup of the HIE (perspective illustration).

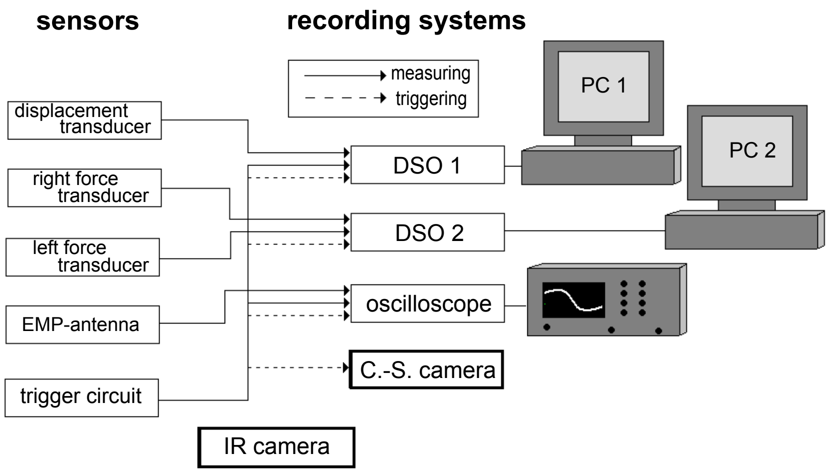

Fig. 21: Coordinated data acquisition system (CODAS). DSO 1 and DSO 2 stand for the two two-channel digital storage oscilloscopes PCS 500, which are connected to different PCs. "Oscilloscope" denotes the stand-alone storage oscilloscope PM 3335 from Philips, "C.-S. camera" is an abbreviation for the Cranz-Schardin camera system.

The two force signals are recorded by a digital oscilloscope (DSO 2), the signal from the displacement transducer by another one (DSO 1). Additionally the trigger signal was recorded by the DSO 1. The stand-alone oscilloscope records the electromagnetic pulse received by the antenna.

The aim of this specific setup (denoted as CODAS) was to synchronize all data on the same time axis. Therefore the trigger signal of the Cranz-Schardin-camera (showing the contact between the trigger pole of the hammer and the leaf spring) is also used to trigger the other data acquisition systems.

2. Target Preparation

2.1. Raw Materials

All samples used as targets in the HIEs have been prepared under precisely defined conditions before. Two types of glasses have been used as basic material: Glass prisms of the type "Optifloat®" from Pilkington[1] and lucent "Robax®" glass ceramics panes from Schott[2] produced in 2005. The panes delivered by the manufacturer are of the size 150 mm (width) and 40 mm (height).

The properties of the raw materials are specified according to DIN 1249-10 and DIN 13316 [48, 131]. The specifications (Thickness according to the manufacturer information d, Young's modulus E, density ϱ, Poisson's ratio μ and softening temperature T_G) are given in Table 1.

Raw material	d [mm]	E [GPa]	ϱ [$\frac{g}{cm^3}$]	μ	T_G [°C]	Products
"Optifloat®"	5	73	2,5	0,23	≈600	FG, T5, T10, TK, AS
"Robax®"	4	93	2,6	0,248	≈650	RX

Table 1: Specifications of the target's raw materials.

2.2. Setup for Target Preparation

A three-point bending setup was constructed in a high-temperature furnace type KK 55.19 from Linn[3] to temper and prepare the targets under temperatures near the softening temperature T_G. The increase of the furnace temperature is controlled by a thermostat TC 50 from Bentrup[4].

To create a defined pre-stress in a sample, it is positioned on two cylindrical bearings of the same material and diameter (21,05 mm) as those used in the HIEs. The distance b of the two bearings is free adjustable. For pre-stress purposes a distance of 5 cm or 10 cm was selected, depending on the type of target to be prepared.

A rod passes through the floor of the furnace (see Fig. 22). At its end, a hook made of high-temperature resistant steel (material number HT 1.484 [132]) with a pointed blade (width of contact area: 0,6 mm) is mounted. The hook is centrally aligned between the two bearings.

The rod is linked to a lever, which in turn is moved by a computer controlled linear stepper motor. A force sensor type 9051A from Kistler is attached between the end of the rod and the lever. It is connected to a Kistler charge amplifier type 5006, which in turn is linked to a 16 bit PC data acquisition DAQ card 6036E from National Instruments[5]. The force signal is recorded by means of the software "LabView 6.0" of National Instruments on the same PC which controls the stepper motor.

[1] Pilkington Deutschland AG, Gelsenkirchen, Germany
[2] Schott AG, Mainz, Germany
[3] Linn High Therm GmbH, Eschenfelden, Germany
[4] Bentrup Industrie Steuerungen, Fernwald, Germany
[5] National Instruments Cooperation, Austin (TX), USA

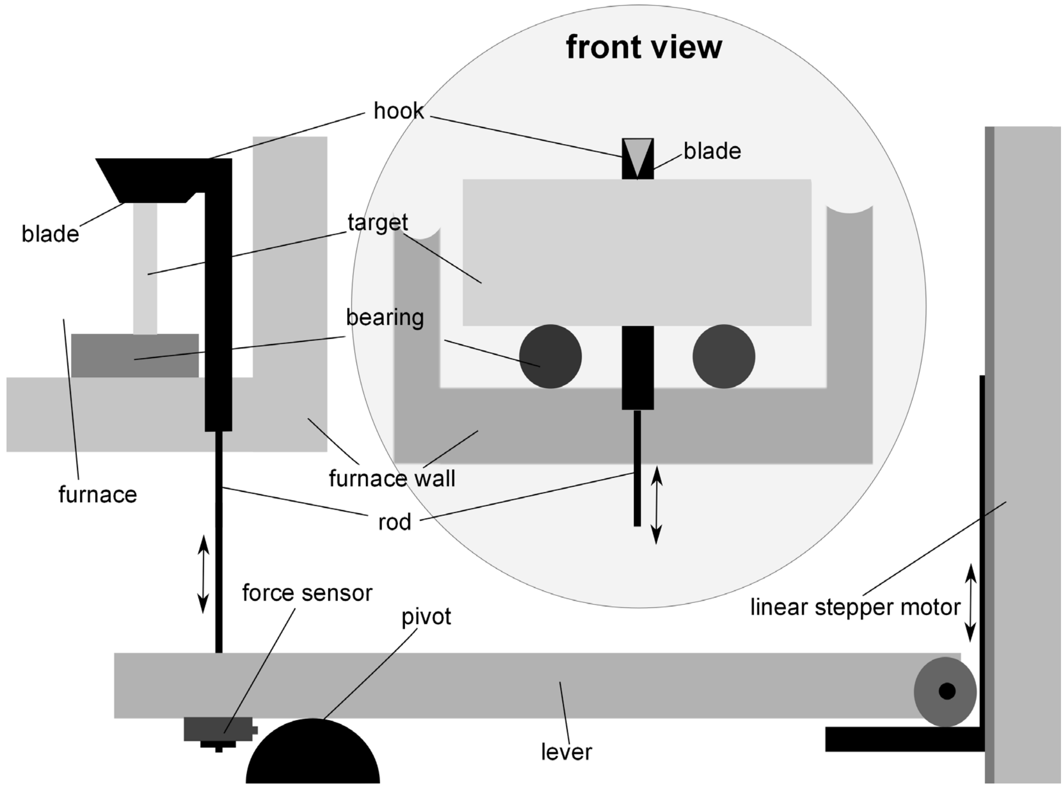

Fig. 22: Setup for creating pre-stresses in glass samples.

Due to this construction the hook can perform an uniaxial displacement with high accuracy, acting a precisely defined force on the sample.

2.3. Preparation Procedures

Due to technical reasons, the real size of a sample varies from piece to piece. Thus, in a first step, the raw panes have been reground in the thin section laboratory of the Geological Institute. The resulting targets had parallel edges with a height-related tolerance of 5 µm per 1,00 cm length.

Six different target types are created, based on the raw material panes. Their respective preparation procedures are described below (see also Table 2):

FG: Stress-Relieved Float Glass

These types of targets have been tempered to ensure targets with a total absence of interior pre-stress. To do this, the unloaded samples are put in the furnace and heated to 500 degrees Celsius. Under this condition, close to the T_G, the material shows relaxation processes, and potentially contained pre-stressings are relieved. The subsequent cooling is very slowly with a duration t_{cool} of about 24 hours. Stress-relieved float glass targets are referred to as “FG”.

T5: Thermally Pre-Stressed Float Glass ($b = 50\,\mathrm{mm}$)

These targets are denoted T5 to indicate the bearing distance b of 5 cm. That means the loading condition during the preparation procedure is identical to the later impact configuration.

To create a defined pre-stressing, the float glass panes are heated to 500 degrees Celsius. Then the hook is set into motion with an effective speed v_{load} of 0,1 $\frac{\text{mm}}{\text{s}}$. The stepper motor is stopped, when the applied loading force F_{load} of 400 N is achieved. After that, the loaded sample is rapidly cooled down to room temperature by opening the furnace door and injecting cool air with the aid of a fan. After this treatment, due to thermal shrinkage, the target shows pre-stressed regions. In the end, the loading is released by an effective speed v_{unload} of 1,0 $\frac{\text{cm}}{\text{s}}$.

T10: Thermally Pre-Stressed Float Glass ($b = 100\,\text{mm}$)

The preparation of these float glass panes is very similar to that of T5 targets. The only difference is the broader bearing distance of 10 cm, which is part of the identifier "T10".

TK: Upside Down Thermally Pre-Stressed Float Glass

These targets are identical to T5 targets. Unlike the T5 targets, however, the "TK" denominated targets are positioned upside down in the HIEs.

AS: Stress-Relieved Float Glass Covered By A Silver Contact Layer

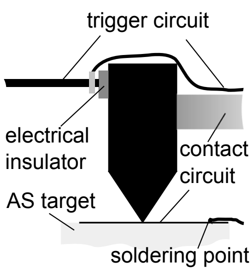

Fig. 23: Contact sensor.

These types of targets are based on FG targets and hence are tempered in an identical way. Additionally a thin electrically conductive silver layer is manually applied to the upper edge of the samples. This kind of target is denoted "AS" and is used to determine the exact time of the hammer impact. A wire is therefore soldered to the silver layer, leading to a pole of a 12 V battery. The other pole was connected to the hammer (see Fig. 23). By joining up the storage oscilloscope in circuit, the detected contact signal gives the precise time of the impact.

RX: Robax Glass Ceramics

These samples are not thermally treated at all.

Target	Raw material	b [mm]	T_{heat} [°C]	F_{load} [N]	v_{load} [$\frac{mm}{s}$]	v_{unload} [$\frac{cm}{s}$]	t_{cool}
FG	Optifloat	-	500	-	-	-	24 h
T5	Optifloat	50	500	400	0,1	1,00	8 min
T10	Optifloat	100	500	400	0,1	1,00	8 min
TK	Optifloat	50	500	400	0,1	1,00	8 min
AS	Optifloat	-	500	-	-	-	24 h
RX	Robax	-	-	-	-	-	-

Table 2: Parameters for target preparation: The distance of the bearings b, the applied loading force F_{load}, the used loading and unloading velocities (v_{load} and v_{unload}) as well as the duration t_{cool} of cooling the sample from T_{heat} to room temperature are presented.

In a last step, the "real" size of each target is measured by means of a micrometer caliper and documented.

3. Examined Boundary Conditions

The HIE setup is optimized to study fragmentation processes in different targets under a wide range of defined altered boundary conditions. Impact velocity, hammer geometry and target types can easily be permuted and are described by an introduced dummy variable for reasons of simplification. This nominally scaled index $\{xyz\}$ is always given in curly brackets and consists of three digits according to the following system:

- The first digit x indicates the slot from which the hammer was released. This induces the height of fall and therefore the hammer velocity. As six different slots are available, x can vary from 1 to 6. The highest initial position is indicated by the highest value (see Table 3).

{x..}	$\bar{v}_H$ $\left[\frac{m}{s}\right]$	$\sigma\left(v_H\right)\left[\frac{m}{s}\right]$
1	1,79	0,02
2	1,94	0,01
3	2,09	0,02
4	2,22	0,01
5	2,35	0,02
6	2,46	0,02

Table 3: Release slots of the hammer, average impact velocities $\bar{v}_H$ and standard deviations $\sigma\left(v_H\right)$.

- The second digit y indicates the hammer geometry. The assignment of these values is shown in Fig. 24. The hammer heads consist of HT-steel 1.484 [132], the rounded tip of the hammer is formed by an half cylindrical piece of the same material and diameter as the bearings (C45E steel [37], see also sec. III.1.1.1), which is attached to the head by two Allen screws. The width of the contact area of the pointed hammer head is 0,4 mm. The broad heads show a width of 4,5 mm and 8,3 mm.

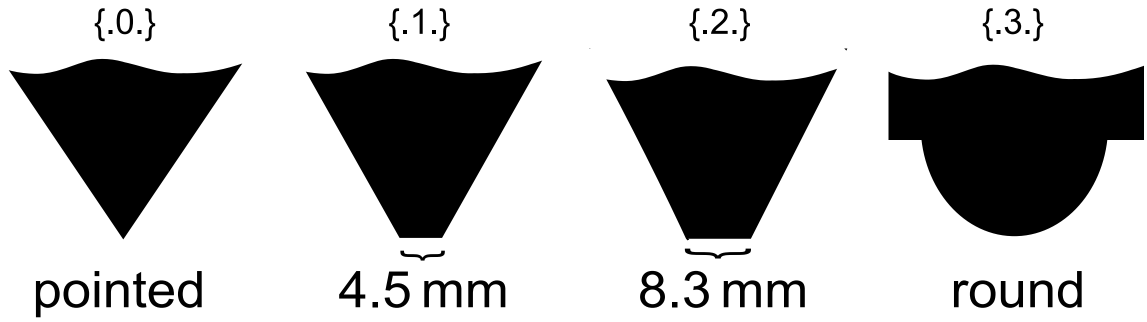

Fig. 24: Hammer geometry: Four different types of hammer heads have been used, which are indicated by the second digit in the dummy variable. The associated values for y are in order from left to right 0, 1, 2 and 3.

{..z}	Target
1	FG
2	T5
3	T10
4	TK
5	AS
6	RX

Table 4: Assignment of target types.

- The third digit z describes the target and is assigned in Table 4.

For the application of multivariate statistical analysis methods it is often useful to use pooled data sets. Aggregated data sets of arbitrary configurations are indicated by the capital letters X and Y.

For example "{1X1}" includes {101}, {111}, {121} and {131}, while "{X0Y}" incorporates all experiments with a pointed hammer head.

4. Some Basics of Particle Analysis

4.1. General Remarks

Particle shape analysis and the study of grain size distributions play an important role in Geology and related sciences [125].

The basic idea is to find unique signatures of particle distributions, which can identify the underlying fragmentation and transport processes [21]. Therefore extensive studies have also been carried out to analyze and trace particles resulting from MFCI processes (e.g. [140]).

By applying these volcanological methods and standard techniques, HIE particle analysis does not only provide a detailed description of the resulting fragments, but also allows comparative studies with volcanic ash particles and their generation processes.

Information about the grain size distribution of particles is provided by sieve analysis, which was performed according to the specification of VDI guideline 2031 and DIN ISO 3310 [100] using a set of sieves from Retsch[1], arranged in downwards decreasing mesh size.

In Geology ϕ is introduced as a grain size parameter:

$$\phi = -log_2 l \tag{III.4-1}$$

where l denotes the actual grain size in mm. In Table 5 all resulting screening fractions are listed.

ϕ	-4	-3	-2	-1	0	1	>1
l [mm]	16	8	4	2	1	0,5	$<0,5$

Table 5: Mesh sizes and resulting screening fractions.

4.2. The Heywood Factor

The specific surface area S_V of a sphere is given by:

$$S_V = \frac{A_{sphere}}{V_{sphere}} = \frac{x^2\pi}{\frac{1}{6}x^3\pi} = \frac{6}{x} \tag{III.4-2}$$

where A_{sphere} denotes the area, V_{sphere} the volume and x the diameter of a sphere. The specific surface of a non-spherical shaped object is bigger and can be generally described by:

$$S_V = \frac{A}{V} = \frac{6}{x} \cdot f_H \tag{III.4-3}$$

where f_H is a form factor, in literature also known as "Heywood factor" [1], with:

$$f_H \rightarrow \begin{cases} = & 1\, for\, spheres \\ \geq & 1\, for\, arbitrary\, objects \end{cases} \tag{III.4-4}$$

[1] Retsch GmbH, Haan, Germany

The mass specific area S_m of an arbitrary object is then described by:

$$S_m = \frac{A}{m} = \frac{6}{x \cdot \rho} \cdot f_H \tag{III.4-5}$$

Hence the Heywood factor can be determined by:

$$f_H = \frac{\rho \cdot x}{6} \cdot S_m \tag{III.4-6}$$

4.3. Image Particle Analysis (IPA)

The IPA concept is a tool to compare shape and surface features of particle samples. It has been specifically developed at the Geomineralogic Department in Bari in order to compare and discriminate volcanic glass particles [15, 33] and has proven to provide significant results [6, 16, 140]. To guarantee a high degree of comparability, IPA of the recovered HIE fragments has been carried out there, performing the same procedures and using the same tools as described in literature.

In IPA, four adimensional parameters are calculated to give a quantitative description of a particle's shape:

These four shape parameters are denoted compactness *com*, circularity *cir*, elongation *elo* and rectangularity *rec*. Their definition equations are [15]:

$$com = \frac{Particle\,area}{Breadth \cdot Width} \tag{III.4-7}$$

where *Breadth* denotes the horizontal side and *Width* the vertical side of the smallest rectangle circumscribed by the digital object.

$$elo = \frac{Max.\,intercept}{Mean\,intercept\,perpendicular} \tag{III.4-8}$$

where $Max.\,intercept$ denotes the maximum intercept of the object (i.e. the longest segment in the object parallel to the long side of the minimum rectangle circumscribing it) and $Mean\,intercept\,perpendicular$ is calculated by the ratio $Particle\,area/Max.\,intercept$.

$$cir = \frac{Particle\,perimeter}{Perimeter\,of\,the\,circle\,with\,the\,same\,area\,of\,the\,particle} \tag{III.4-9}$$

$$rec = \frac{Particle\,perimeter}{2 \cdot Breadth + 2 \cdot Width} \tag{III.4-10}$$

For comparison studies it is important to use images of identical resolution. Therefore high resolution SEM images (600 dpi) of particles have been chosen to apply IPA. All shape parameters have been determined by means of the image analysis software Optilab Pro 2.6 from Graftek[2].

[2]Graftek Imaging Inc., Austin (TX), USA

5. Devices and Methods Used for Fragment Analysis

5.1. Microscopes

Morphological analyses of fragment surfaces have been performed in Italy at the Geomineralogic Department of the University of Bari thanks to the kind cooperation of Prof. Dellino[1].

These investigations have been carried out by means of a scanning electron microscope (SEM) type S-360 from Cambridge, allowing also quantitative material analysis by energy-dispersive X-ray spectroscopy (EDX).

For the purpose of optical microscopy a stereo microscope M5A from Wild Heerbrugg[2] was applied.

5.2. Planimetrical Methods

Due to the FSED concept (see sec. III.1.5), it is essential to quantify the generated fracture surface A_{frac}. As each method has its own limited application range, a variety of different methods have to be used.

In this section all used planimetrical methods are outlined.

5.2.1. Planimetrical Epihalsy (TEH)

This method has been introduced at the suggestion of Prof. Reents[3] as an innovative technique to quantify fragment areas within the scope of my diploma thesis and was formerly denoted by the neologism "Topometrical Epihalsy" [40]. Several changes and modifications have been performed to reduce interference effects and to optimize this method for quick, precise and reliable area quantification of fragments. It is now referred to as "Planimetrical Epihalsy" but still abbreviated as "TEH". The development of its setup and TEH measurements have been performed in the PVL.

5.2.1.1. Principle and Setup of TEH

TEH bases on the principle of adhesion:

The setup consists of two separated basins: A dipping basin with an ion-containing solution, and a basin containing distilled water, denoted "measurement basin" as it serves as the actual measuring system.

The TEH procedure steps are illustrated in Fig. 25. At first, the sample to be measured is plunged into a dipping basin (a) with a saline solution, and pulled out (b). The best results were achieved by using a saline (NaCl) solution with an added surfactant (a detergent). This adhesive solution has to be prepared daily, as the detergent decomposes within a few days.

[1] Prof. Pierfrancesco Dellino, Dipartimento Geomineralogico, Università degli studi di Bari, Italy

[2] Wild Heerbrugg GmbH, München, Germany

[3] Prof. Georg Reents, Lehrstuhl für theoretische Physik III, Physikalisches Institut, Julius-Maximilians-Universität Würzburg, Germany

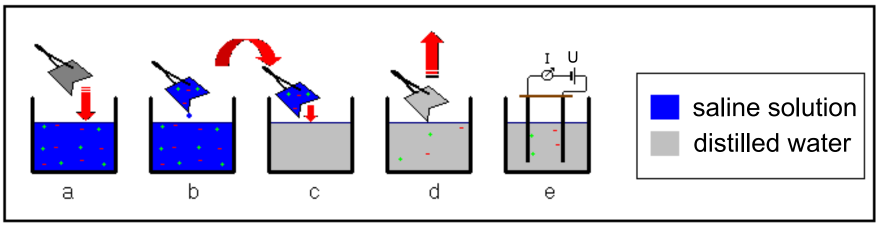

Fig. 25: TEH measurement of surface areas (ad. [40]). Each step of this procedure is described in the text.

After a reproducible dripping off procedure, due to the wetting effect, the sample is covered by a film, containing a certain amount n of the liquid.

It has been shown that, under the condition that the samples are of comparable size, material and surface morphology, the amount of the adhesive liquid n is directly proportional to the surface area A of the respective sample [40].

$$A \sim n \qquad \text{(III.5-1)}$$

The covered fragment is subsequently dipped into the second basin containing distilled water (c). The ions on the sample's surface dissolve (d) and effect a great increase of electrical conductivity in the testing liquid, which can be quantified by means of electrolysis (e).

The setup for this electrical measurement is schematically depicted in Fig. 26.

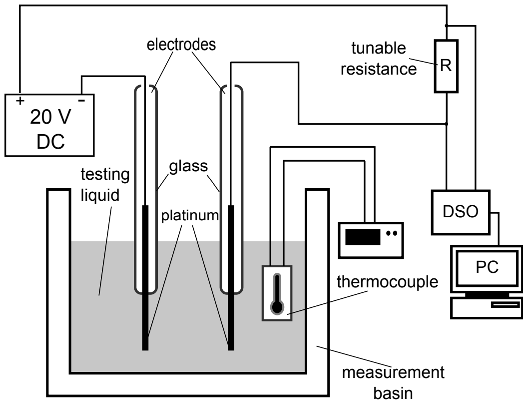

Fig. 26: Setup to determine the electrical conductivity within the scope of TEH area quantification. Using the shown circuit, the increase of conductivity in the test liquid effects an increasing current I, which can be quantified by means of a precisely tuned resistance and a digital storage oscilloscope (DSO).

A thermocouple (NiCr-Ni type K [35]) in connection with a SIKA[4] display unit shows the temperature of the testing liquid. This feature is important for controlling purposes as the temperature of the testing liquid affects the mobility of the ions and hence I. Therefore calibrations and measurements have to be performed under the same thermal conditions.

Two platinum electrodes are centrally mounted, at a distance of 35 mm from tip to tip. The upper parts of the electrodes are water-tightly shrink-wrapped in glass covers. Thus an always identical contact surface with the testing liquid is guaranteed.

The testing circuit is powered by a 20 V DC voltage source. The resulting current I between both electrodes is quantified by measuring the applied voltage U on a precisely tunable

[4] Dr. Siebert & Kühn GmbH & Co. KG, Kaufungen, Germany

resistance R (in most cases $10\,k\Omega$ is selected). This data is recorded by a Voltcraft[5] DSO-2100 USB digital PC oscilloscope with a sampling rate of 10 Hz. Knowing R and U, it is trivial to calculate I, which is related to the area of the dipped in sample as shown below:

5.2.1.2. Electrochemical Background and Calibration

The specific conductivity σ_{spec} depends on the concentration c of the dissolved ions. NaCl dissolves completely in a polar liquid [52] and therefore [86]:

$$n \sim c \tag{III.5-2}$$

In this case the relation is described by the empirical Kohlrausch square root law [9]:

$$\Lambda(c) = \Lambda_0 - k \cdot \sqrt{c} \tag{III.5-3}$$

where Λ is denoted “equivalent conductivity”, which is defined by [9]:

$$\Lambda = \frac{\sigma_{spec} \cdot 1000}{c} \left[\frac{cm^2}{\Omega mol}\right] \tag{III.5-4}$$

In (III.5-3) Λ_0 is the limiting value for $\Lambda(c \to 0)$ and k is an empirical constant.

With (III.5-4) and (III.5-3) the specific conductivity is given by:

$$\sigma_{spec}(c) = \frac{\Lambda_0}{1000} \cdot c - \frac{k}{1000} \cdot c^{\frac{3}{2}} \tag{III.5-5}$$

On the basis of these results the relation between the surface area of the sample A and the experimentally determined current I is given by:

$$I = j + a \cdot A - b \cdot A^{\frac{3}{2}} \tag{III.5-6}$$

where a, b and j are constants, which have to be found by calibration measurements:

Standard samples of a well-known surface area are used to get calibration curves (see Fig. 27).

The constants a, b and j are then calculated by a curve fitting operation with the aid of the software OriginPro[6] 8G SR1.

Due to the restrictions of (III.5-1), the size and shape of the standard samples used for calibration have to be appropriate to the fragments to be measured.

For coarse grained fragments ($\phi \leq -2$) a single standard sample of $64\,mm^2$ area is selected for calibration. For finer fractions glass beads with 2, 1 or 0,5 mm diameter are used. In these cases of high area resolution, best results are achieved by the application of an adhesive solution with an increased salinity (see Fig. 27, right).

5.2.2. Measurements by Nitrogen Adsorption (BET)

BET stands for the surnames of Stephen Brunauer, Paul Hugh Emmett und Edward Teller, who developed a model to describe the adsorption of gas molecules on solid surfaces [13]. This theory of surface physisorption is used to determine the specific area of a sample by the measurement of its adsorption-desorption isotherm under a defined gas (usually nitrogen) atmosphere [3] and is described by DIN 66 131 and 66 132 [1].

[5] Voltcraft Eurodiscount GmbH, Hirschau, Germany
[6] OriginLab Corporation, Northampton (MA), USA

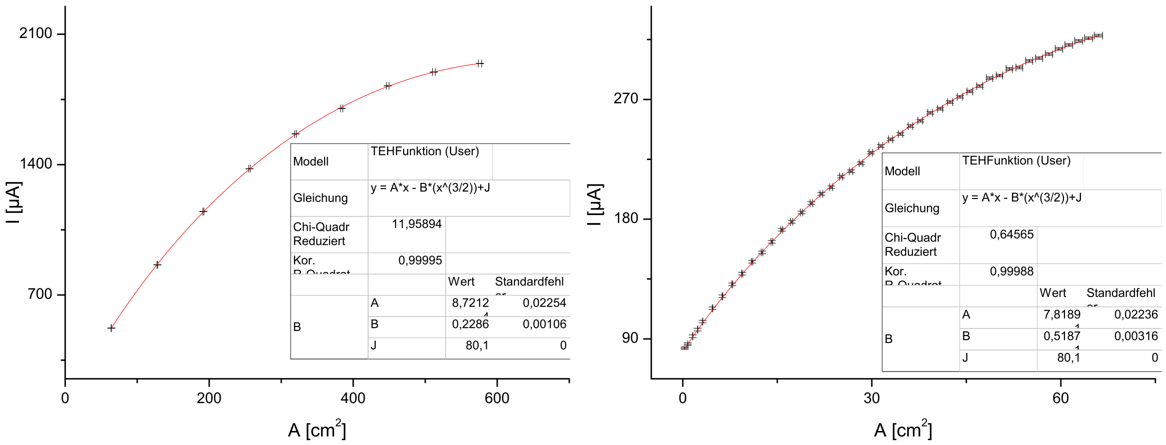

Fig. 27: Calibration curves: The correlation between the measured current I and the area A of standard samples is plotted and fit to (III.5-6). On the left, a calibration curve for coarse grained fragments is depicted [TEHeich112]. A finer calibration method is used to determine the area of smaller fragments (right) [TEHeich223].

The BET measurement method is a reliable tool for particles with a sufficient big specific area [3, 98].

However, as most of the particles resulting from HIE fragmentation are rather coarse-grained with a low specific surface (see V.5.2) BET can only be applied to the smallest sieve fraction of particles. Therefore this method is only marginally used to compare and control the results of the finest fragments achieved by TEH.

These supplementary control measurements have been performed in Mainz[7] by means of a gas sorption analyzer type NOVA 1200 from Quantachrome[8].

5.2.3. Planimetry by CAD Modeling (CAD)

First, the fragment, which is to be reconstructed by CAD modeling, is positioned on a scale paper and photographed from two precisely defined angles.

With the aid of the CAD software “FormZ RenderZone Plus 6.5.6 (demo version)” from AutoDesSys[9] the outlines and contour lines are drawn to scale under the respective angles. In a third step, a wire frame model is generated, which is finally rendered (see Fig. 28). The program then provides the total surface area of the reconstructed object as well as the volume and - if density and the axis of rotation of this fragment are assigned by the user - even the mass and the moment of inertia under the respective axis. As these values are needed to calculate the kinetic energy of the fragments, planimetry by CAD was a central method used in this thesis.

Comparative studies with TEH results have shown that this method provides reliable results with very small measurement errors, for rather big fragments.

A precise reconstruction of small particles with complex surfaces however is a very time-consuming procedure. Thus for those types of fragments, TEH has shown to be more useful.

[7]Hydrochemisches Labor, Institut für Geowissenschaften, Universität Mainz; Germany
[8]Quantachrome GmbH & Co. KG, Odelzhausen, Germany
[9]AutoDesSys Inc., Columbus (OH), USA

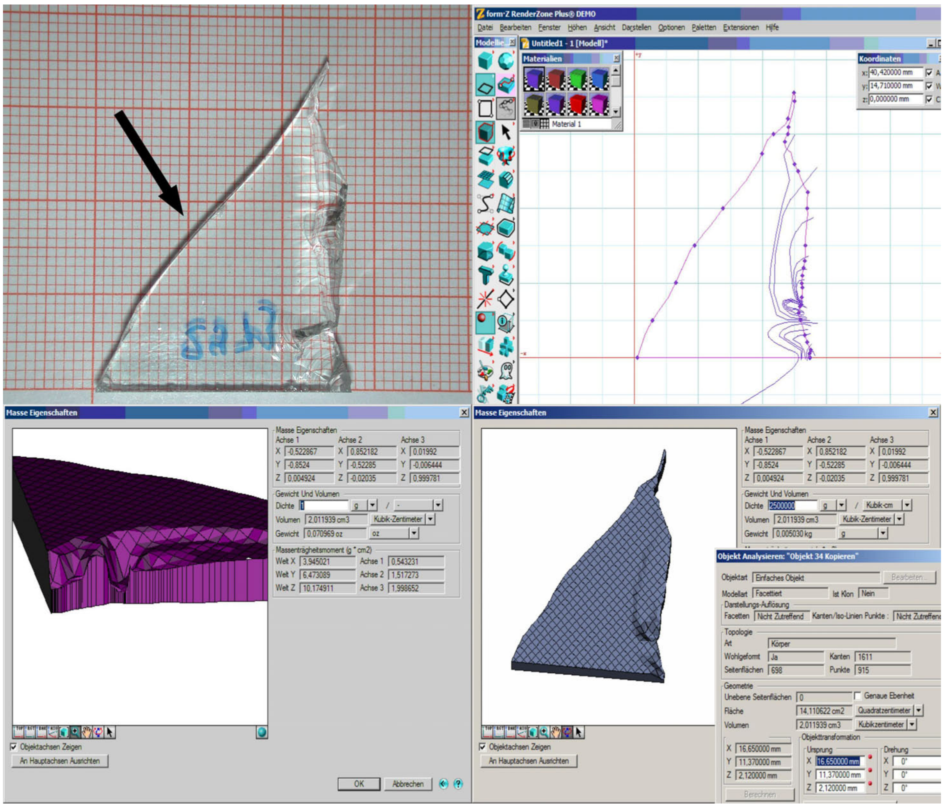

Fig. 28: Reconstruction of a fragment (top left) by CAD: At first (top right) the projected perimeters of the fragment are drawn to scale from two well defined angle of views. By means of the program "FormZ RenderZone Plus 6.5.6" it is then possible to construct a wire-frame model, to render it, and to determine all relevant parameters of the object (bottom row), such as for example its total surface area, its volume and - if the density of the material and an axis of rotation is defined - its respective mass moment of inertia.

5.2.4. Photographic Planimetry (OPT)

This simple method is used to determine pre-fracture surfaces. The examined fragments are photographed from all sides, lying on scale paper. With an image analysis software, Adobe[10] Acrobat Professional 7.0, all surfaces are measured which do not belong to the net area of fracture surface generated by the HIEs.

As CAD, BET and TEH methods provide only total (i.e. gross) areas, the resulting value by means of OPT is needed to calculate the net post-fracture surface areas (see V.5.3.5).

5.2.5. Optical Area Projection Concept (OPC)

This planimetrical method has been specifically developed to quantify the dynamics of fracture surface areas during fragmentation by means of high speed cinematography [40] (see also II.3.1) and plays therefore a crucial role in this thesis.

In the image sequences, cracks appear as two dimensional projected shadows. At a time t_i a crack, which shows at least piecewise smooth surfaces, can be equidistantly dissected in n parts of the length l_j. It is:

$$l(t_i) = n \cdot l_j \tag{III.5-7}$$

In Fig. 29 the situation of the part j of a crack is illustrated. As a result of geometrical

[10] Adobe Systems; San Jose (CA); USA

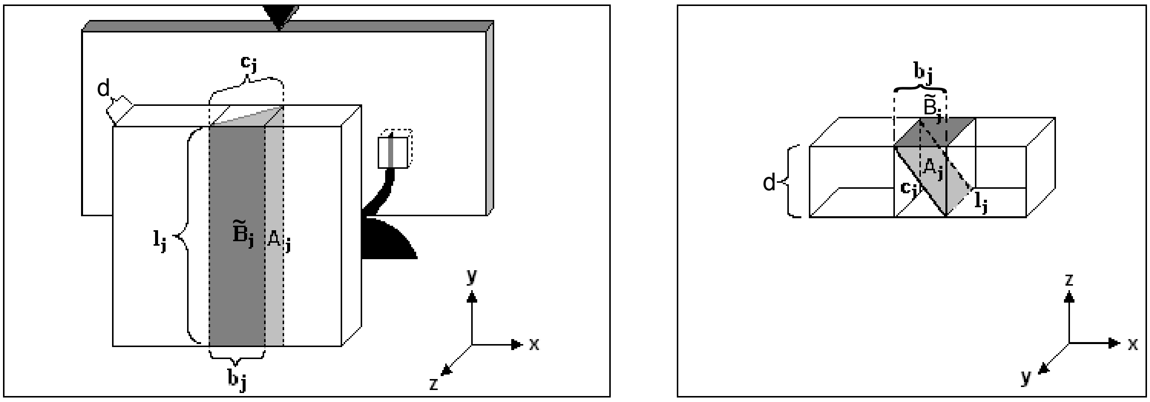

Fig. 29: Optical area projection concept (OPC): A crack in a target of the thickness d is presumed to be composed of many rectangular parts of width c_j and length l_j. In the image sequences the plane of view is given by the xy-plane, and the real fracture area A_j (both crack interfaces to be considered) is depicted as the projected area $\widetilde{B}_j$ (ad. [40]).

considerations the "real" fracture area A_j of crack part j is given by:

$$A_j = 2 \cdot l_j \cdot c_j = 2 \cdot l_j \cdot \sqrt{d^2 + b_j^2} \tag{III.5-8}$$

The total fracture area at time t_i can then be expressed by:

$$A(t_i) = \sum_j A_j = 2 \cdot l_j \cdot \sum_j \sqrt{d^2 + b_j(t_i)^2} \tag{III.5-9}$$

As the determination of $b_j(t_i)$ is a complex issue, one has to develop this expression [40]: Due to (III.5-7) follows:

$$A(t_i) = 2 \cdot n \cdot l_j \cdot \frac{\sum_j \sqrt{d^2 + b_j(t_i)^2}}{n} = 2 \cdot l(t_i) \cdot \bar{c}(t_i) \tag{III.5-10}$$

where $\bar{c}(t_i)$ denotes the average depth of the crack, which can be approximately determined by the average projection width $\bar{b}(t_i)$, introduced by:

$$\bar{c}(t_i) = \sqrt{d^2 + \bar{b}(t_i)^2} \tag{III.5-11}$$

In a suitable coordinate system, the projected area $\widetilde{B}(t_i)$, which appears black in the image sequences, can be expressed by:

$$\widetilde{B}(t_i) = \int_{\tilde{x}_1}^{\tilde{x}_2} b(\tilde{x}, t_i) d\tilde{x} \tag{III.5-12}$$

where $\tilde{x}_1$ denotes the initial point and $\tilde{x}_2$ the end point of the crack in the used coordination system. $b(\tilde{x}, t_i)$ specifies the exact projection width $b_j(t_i)$ at the point $\tilde{x}$. The average projection width $\bar{b}(t_i)$ is then defined by:

$$\int_0^{l(t_i)} \bar{b}(t_i) dx \equiv \int_{\tilde{x}_1}^{\tilde{x}_2} b(\tilde{x}, t_i) d\tilde{x} \tag{III.5-13}$$

And thus:

$$\bar{b}(t_i) = \frac{\widetilde{B}(t_i)}{l(t_i)} \tag{III.5-14}$$

Therefore, the average projection width $\bar{b}(t_i)$ describes the width of a rectangle, which has the same area $\widetilde{B}(t_i)$ and the same length $l(t_i)$ as the projected crack area.

Using (III.5-10), (III.5-11) and (III.5-14), the crack surface $A(t_i)$ is given in a good approximation by:

$$A(t_i) = 2 \cdot l(t_i) \cdot \sqrt{d^2 + \frac{\widetilde{B}(t_i)^2}{l(t_i)^2}} \tag{III.5-15}$$

By measuring the crack length $l(t_i)$ and the projected crack area $\widetilde{B}(t_i)$ with the aid of an image analysis software, it is now possible to quantify the actual crack surface.

Hence, the OPC provides a reliable tool to determine quantitatively the fracture area development.

Furthermore, OPC can be applied to determine post-fracture surface areas of fragments by analyzing photographs, taken in top view, under the condition that the crack surface is rather smooth. For example the area of the smooth left edge (indicated by an arrow) of the fragment shown in Fig. 28 (top left) can be quantified by means of the OPC method.

6. Implemented Multivariate Statistical Methods

A number of multivariate statistical methods applied in this thesis are listed below. The selected level of significance is always 5 %, which means that the term "significant" describes an error probability of less than 5 % [12]. Results with a significance level of less than 1% are denoted "highly significant".

A detailed description of the applied statistical methods would go far beyond the scope of this thesis. Instead, references are given for detailed background information. All tests have been conducted by using the software SPSS 11.0[1].

- Correlation analysis [12, 75, 121]: As a characterizing correlation coefficient, the Pearson's product-moment coefficient (also "Pearson's correlation coefficient") ρ is determined. Furthermore for each analysis the error probability p is issued. In some cases partial correlation analyses are applied to reveal spurious or hidden correlations.

- Levene-test for the equality of variances [12, 121]: Many statistical tests are solely valid under the condition of equal variances. The Levene-test is a useful test to check if this condition is satisfied. It is conducted automatically by SPSS in combination with other relevant tests.

- F-test [96]: An alternative method used to check the equality of variances, based on the Fisher-Snedecor distribution ("F-distribution").

- T-tests [12, 31, 121]: In many cases it is important to verify that the mean values of two independent samples are significantly different. T-tests are applied as a useful and well developed statistical method [32], named after the Student's t-distribution, which is followed by the test statistic under the assumption that the null hypothesis: "The mean values of the two populations are equal" is true. By calculating the error probability *Sig.* with the aid of SPSS, the null hypothesis can be significantly rejected if *Sig.* is less than 5%. In this case the result reads: "The mean values of the tested populations are significantly different."
  At least two conditions are necessary to perform a t-test: The samples have to be selected at random. Additionally the populations from which the samples have been drawn have to be normally distributed. Both conditions are always proved to be satisfied for HIE particles.
  SPSS provides two different types of t-tests [12]: A t-test using a single, "pooled" variance, calculated by the formula [71]:

$$\sigma_p^2 = \frac{(N_1 - 1) \cdot \sigma_1^2 + (N_2 - 1) \cdot \sigma_2^2}{N_1 + N_2 - 2} \tag{III.6-1}$$

  where σ_p^2 denotes the pooled variance, $\sigma_{1,2}$ the standard deviations and $N_{1,2}$ the sizes

[1] SPSS Inc., Chicago (Il), USA

of both samples. The t-value is then defined by:

$$t = \frac{\overline{X_1} - \overline{X_2}}{\sqrt{\frac{\sigma_P^2}{N_1} + \frac{\sigma_P^2}{N_2}}} \tag{III.6-2}$$

where $\overline{X_1}$ and $\overline{X_2}$ are the measured mean values of the samples. This "pooled variance t-test" only provides reliable results for equal variances.
If the variances differ significantly, another kind of t-test has to be conducted: the "separate variance t-test", in which t is calculated by:

$$t = \frac{\overline{X_1} - \overline{X_2}}{\sqrt{\frac{\sigma_1^2}{N_1} + \frac{\sigma_2^2}{N_2}}} \tag{III.6-3}$$

Thus, an additional Levene test has to be performed to determine which of both t-test results is actually valid.

- Equivalence test (ET): If the t-tests do not show significant differences between the mean values of two samples, it is a strong indication of a similarity between both samples. From the mathematical point of view, however, this is not automatically a strict "significant" proof, a fact which is often overseen in scientific studies [96].
  To prove two samples to be of "significant" equivalence I used a testing method described in [96], comparing two sets of data (mean values $\overline{X_1}$ and $\overline{X_2}$) with the same standard deviation σ and sample sizes N_1 and N_2. In fact this "equivalence test" (ET) does not test the "identity" of two samples, but reveals if the confidence level of a sample is in a given threshold limit value of the compared one.
  At first a maximal difference range ($-D$ to $+D$) from the mean of the sample has to be selected, giving the maximum allowed threshold of mean values. Then - with p being the error probability - the $(1-2p)$ Confidence levels $C_{max,min}$ can be calculated by:

$$C_{max,min} = \overline{X_1} - \overline{X_2} \pm t_{(1-p),\,(N_1+N_2-2)} \cdot \sigma \cdot \sqrt{\frac{1}{N_1} + \frac{1}{N_2}} \tag{III.6-4}$$

  where $t_{(1-p),\,(N_1+N_2-2)}$ is the $(1-p)$ quantile of the central t-distribution function with $(N_1 + N_2 - 2)$ degrees of freedom [96]. The mean values of two samples are denoted "significantly equal" if:

$$-D < C_{min} < C_{max} < D \tag{III.6-5}$$

  Note that an ET only provides reliable results if the variances of both analyzed data sets are equal. This precondition has been checked by F-tests.

- Nonparametric tests [12, 121]: In contrast to t-tests, the requirements for nonparametric tests are considerably less strict [75]. Therefore these kinds of tests are always applied as complementary tests and in situations when the conditions for t-tests are not fulfilled. The term "nonparametric tests" summarizes a number of different statistical testing methods, including in particular Chi-square, Kolmogorov-Smirnov, Mann-Whitney, Moses, Wald-Wolfowitz and Kruskal-Wallis tests [12]. When applied, each method is specified.

- One way analysis of variance (ANOVA): As t-tests, this technique is used to compare mean values and to check if they show significant differences. But in contrast to the first, the ANOVA is based on the F-distribution [12]. This tool is especially useful for multivariate statistical studies [83].

- Discriminant analysis [12, 56, 75, 121]: This method is used to classify cases based on a set of "explaining" independent variables. This technique is applied several times in the Daisy Chain Discriminant Analysis Concept to find unique signatures in the force signals (see V.2).
- Principal Component Analysis (PCA) [12, 75, 121]: This statistical method is used to reduce the number of variables. For this purpose correlations between the environmental variables are revealed, and more "useful" - i.e. uncorrelated describing variables - are created by linearly combining the original ones. These new variables are referred to as "principal components" [12].

Part IV.

Results of Supplementary Measurements

1. Results of EDX-Analyses

The composition of all targets has been analyzed under the SEM via EDX spectroscopy. FG, T5, T10, TK and AS show no significant difference in their atomic composition. Hence it can be deduced that preparation procedures do not affect the targets' chemical structures. The composition of Optifloat glass, which is the raw material of all of these targets, is given in Table 6 and Table 7. Additionally the results for RX are shown there. Both materials have a similar SiO_2 content, but significant differences in the contents of other elements, especially of Na, Mg, Ca and Al.

Element	Optifloat® (2004) [weight %]	Robax® (2004) [weight %]
Na	10,00	
Mg	2,45	
Al	0,48	12,61
Si	33,88	33,06
Ca	6,49	
O	46,70	51,43
P		0,97
Ti		0,82

Table 6: Composition of Optifloat glass and Robax glass ceramics according to EDX-analysis.

Compounds	Optifloat® (2004) [weight %]	Robax® (2004) [weight %]
SiO_2	72,47	70,74
Al_2O_3	0,91	23,82
Na_2O	13,48	
MgO	4,05	
CaO	9,08	
P_2O_5		2,23
TiO_2		3,21

Table 7: Results of EDX compound analysis of Optifloat glass and Robax.

Multiple EDX measurements at different spots of the targets show no significant alternations of the Optifloat glass composition, so the chemical structure of these targets can be presumed to be ideally homogeneous. The composition of Robax, however, differs slightly from place to place, due to its nanocrystalline structure.

Comparative EDX investigations at fracture surfaces and crack edges have not revealed any significant chemical anomalies.

2. Impact Behavior of the Hammer

Considering the motion sequence of the hammer at the time of the impact, three relevant stages can be identified (see Fig. 30):

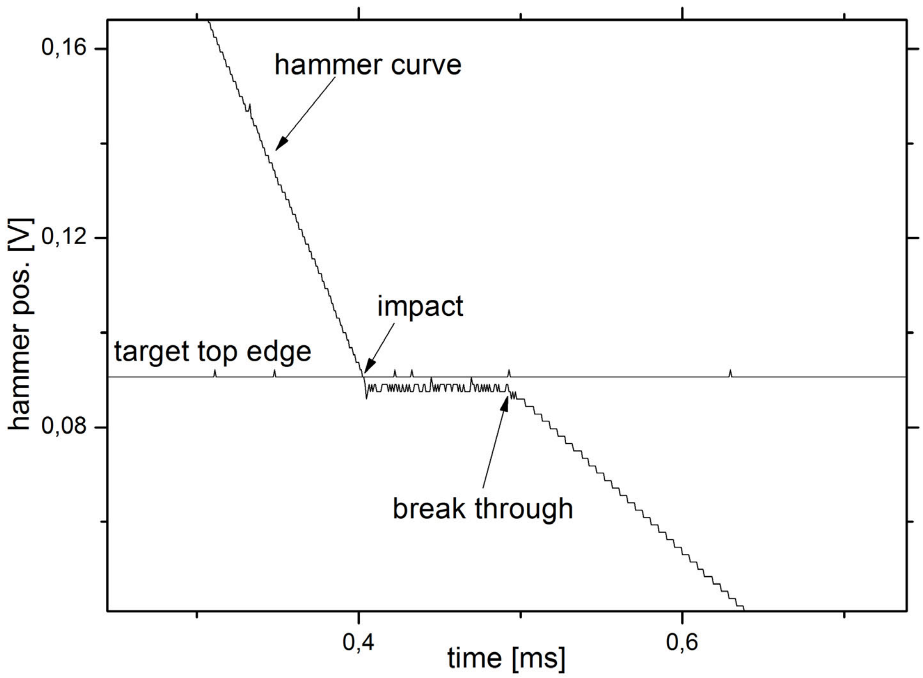

Fig. 30: Representative path-time diagram of the hammer [652td]: By means of this curve the impact velocity v_H and the break through velocity v_b of the hammer can be easily determined. In this case, $v_H = 2{,}46\,\frac{m}{s}$ and $v_b = 1{,}20\,\frac{m}{s}$. The corresponding image sequence of this HIE can be found in Appendix I.

1. The hammer impacts with a velocity v_H, which can be easily determined, as in the observed time frame the gravitational acceleration remains negligible. Thus, the impact energy E_{impact} is given by:

$$E_{impact} = \frac{1}{2} m_H v_H^2 \qquad \text{(IV.2-1)}$$

   It is defined as the maximum energy, which can be provided by the impacting hammer.

2. Almost immediately after impact, all path-time-diagrams show a plateau phase, which means that the hammer seems to stop for some time. A closer inspection of the diagrams, however, reveals that the hammer is in fact not staying at the top edge of the target, but some 10 µm below. This fact agrees very well with the results of comparative high speed cinematographic studies using AS-targets, which indicate that virtually instantly with

the impact a small notch appears at the point of contact. Thus, the hammer slightly indents the target before stopping. At this stage all relevant energies are transferred into the target and the principal fragmentation processes take place (see e.g. Fig. 31).

3. After plain formation of primary cracks and extensive fragmentation, the hammer breaks through and moves with a velocity v_b. With this value, the total energy input E_{tot} can be calculated. This important parameter is defined as the total energy which was actually provided by the impacting hammer, and is given by:

$$E_{tot} = \frac{1}{2} \cdot m_H \cdot \left(v_H^2 - v_b^2\right) \qquad \text{(IV.2-2)}$$

The values of v_H and v_b have been checked and verified by comparative Cranz-Schardin and high speed video analyses. The calculated accuracy of hammer velocities measured by the displacement transducer was determined to be $\pm 0{,}005\,\frac{m}{s}$. Nevertheless, taking into account possible artifacts occurring during the impact, a value of $\pm 0{,}01\,\frac{m}{s}$ was selected as a realistic measurement uncertainty.

The standstill of the hammer, however, could not be verified by optical speed detection methods, due to its comparatively low resolution in time and space. Yet two facts support the existence of the "standstill effect":

Investigations of the plateau time periods $t_{plateau}$ reveal some reproducible patterns: Next to other factors, this parameter depends significantly on the crack geometry. In Table 8 the mean values for two kinds of cracks are presented, under variation of the target types: Primary cracks, which severe the target centrically between both bearings are compared to A-cracks, which start from the bearings (see chapter V.1).

$t_{plateau}$ [µs]	FG	T5	T10	RX
Centrical cracks	$108{,}5 \pm 13{,}3$	$104{,}4 \pm 9{,}0$	$115{,}5 \pm 18{,}1$	$94{,}6 \pm 6{,}9$
A-cracks	$130{,}8 \pm 12{,}8$	$123{,}3 \pm 21{,}4$	$125{,}6 \pm 11{,}5$	$127{,}8 \pm 13{,}9$

Table 8: Mean values and standard deviations of plateau time periods $t_{plateau}$ of different targets and crack geometries. Cracks which are severing the target centrically between both bearings ("centrical cracks") are faster established than A-cracks. Consequently the hammer shows significant shorter plateau stages.

When centrical cracks have been established in the target, the measured values for $t_{plateau}$ are significantly shorter than those of experiments showing A-cracks. This result is consistent with geometrical considerations: The length of a centrical crack is shorter than that of an A-crack. Hence in the first case the target is faster severed, and the hammer's breakthrough happens at an earlier juncture.

Additionally to that, dynamic photoelastic impact studies provide further indications that the plateau stage shown in the path-time diagram is a real effect and not an inherent artifact:

A representative image sequence is shown in Fig. 31. According to the frame rate, the time period between each frame is approx. 59,5 µs. It can be clearly seen, that it takes some time between the first contact (top left) and first considerable fragmentation, in this case approx. 119 µs after impact (top right). This result coincides very well with the usual time of the plateau stage: During this short period the hammer applies a strong loading until the target is severed. Subsequently the hammer breaks through, while the target shows further fragmentation and a decreasing stress distribution (bottom row).

It is remarkable that no distinct acceleration can be detected in the stage of the breakthrough. According to the knowledge of the author, such a mechanical boundary layer effect

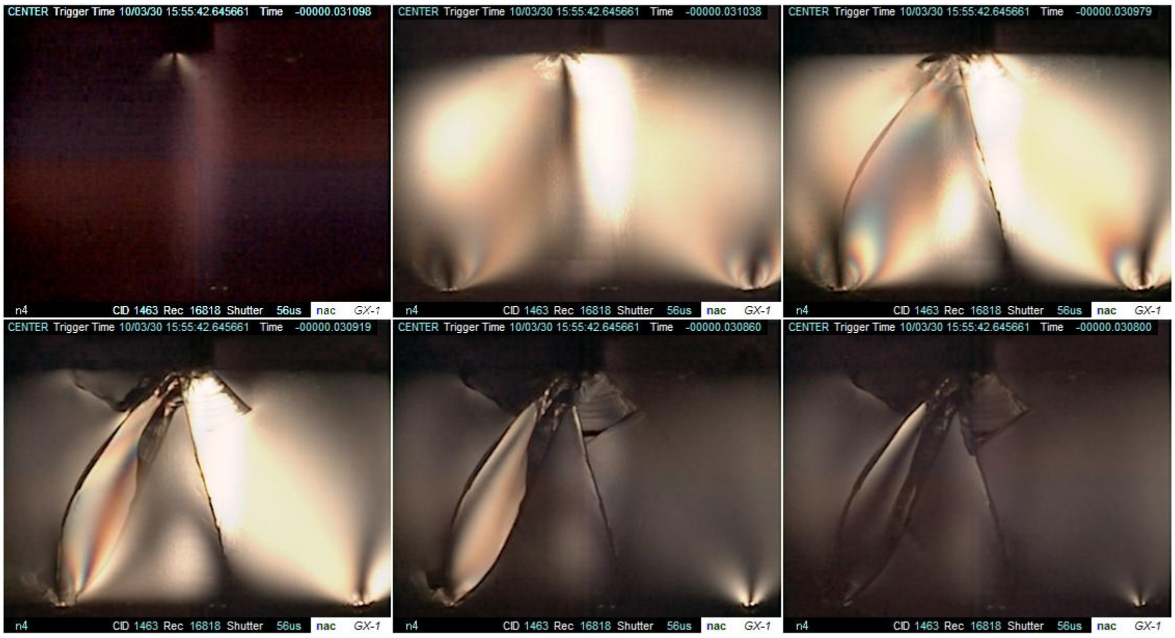

Fig. 31: Dynamic stress distribution in the PSZ after impact ([N4], HIE {126}; frame rate: 16.818 fps).

has not been described in literature yet, and it still remains unclear, how the required residual energy could be stored during the fragmentation stage, particularly as resonance analysis of the hammer shows solely resonant frequencies in the range of a few kHz.

However, it is important to note that this effect does not affect energetic considerations at all: The relevant parameters v_H, v_b, E_{impact} and E_{tot} have been proved to be measured correctly by analyzing the data of the displacement transducer, and can therefore be used for energy balance.

Part V.

Discussion of HIE Results

1. Classification of Cracks

For a systematic phenomenological description and comprehensive statistical analysis of crack patterns, a useful classification system has been developed for this thesis.

Although at first glance the abundance of different designations might be a bit confusing, the division in main classes, subclasses, types and subtypes follows a pragmatic principle: The nomenclature is determined by the presumed driving mechanisms of the cracks, their forms of appearance, and their points of nucleation. Every mentioned kind of crack shows its own significant dependency and propagation behavior, which specifically affects the dissipation of fracture energy. The classification system is shown in Table 9.

<table>
<tr><th>Main class</th><th>Subclass</th><th>Type</th><th>Subtype</th></tr>
<tr><td rowspan="3">Damage cracks</td><td rowspan="3"></td><td>Impact notch</td><td rowspan="3"></td></tr>
<tr><td>Conchoidal cracks (CCs)</td></tr>
<tr><td>Intermediate cracks</td></tr>
<tr><td rowspan="13">Normal cracks</td><td rowspan="5">Primary cracks</td><td rowspan="2">A-cracks</td><td>from the bearings (ACB)</td></tr>
<tr><td>from the top (ACT)</td></tr>
<tr><td rowspan="3">Centrical cracks</td><td>Straight cracks (SCM)</td></tr>
<tr><td>Branching cracks (BCM)</td></tr>
<tr><td>Top cracks (TCM)</td></tr>
<tr><td rowspan="4">Secondary cracks</td><td>B-cracks</td><td rowspan="8"></td></tr>
<tr><td>C-cracks</td></tr>
<tr><td>V-cracks</td></tr>
<tr><td>Y-cracks</td></tr>
<tr><td rowspan="4">Special cracks</td><td>D-cracks</td></tr>
<tr><td>E-cracks</td></tr>
<tr><td>X-cracks</td></tr>
<tr><td>Z-cracks</td></tr>
</table>

Table 9: Phenomenological classification of cracks: Only the most prominent kinds of cracks are listed. This classification system allows to perform detailed statistical analysis in order to study the influence of boundary conditions on crack geometry.

1.1. Main Classes and Subclasses of Cracks

As already mentioned in II.3.1 two principally different kinds of fractures occur in the HIEs series:

- On the one hand cracks are initiated at the point of impact, characterized by a propagation within the plane of observation and showing a complex conchoidal structure. These kind of cracks are generally denoted “damage cracks”. Please note that this term is defined as a generic term and is not identical to similar expressions in some literature (cf. e.g. [112]).

- On the other hand a variety of cracks can be identified, which propagate perpendicularly to the plane of observation. These cracks are summarized by the generic term “normal cracks”.

All indications suggest that the driving mechanisms of damage cracks and normal cracks are totally different (see also below).

Normal cracks can be phenomenologically subdivided in three subclasses by the stage of their emergence:

1. Primary cracks: This term summarizes all normal cracks which appear in the initial phase of fracture. As the starting geometry of a crack has a great influence on the further crack development as well as on the total energy dissipation, fracture studies focus particularly on this subclass of fracture.
2. Secondary cracks: All normal cracks which can be identified in the subsequent stages of fragmentation are denoted by this generic term.
3. Special cracks: This term includes all exceptional forms of cracks.

1.2. Phenomenological Description of Damage Crack Types

Impact Notch

As shown above, this fracture type nucleates virtually immediately after the hammer impact. Thus, the impact notch is always the first crack to occur and its appearance in an image sequence can be used to determine the exact moment of impact.

Conchoidal Cracks (CCs)

This type of fracture is already described in II.3.1: Conchoidal cracks start from the point of impact and are characterized by a complex surface structure (e.g. see Fig. 32). They propagate in the plane of view, which makes it difficult to quantify the real fracture area development. To a much lower extent, conchoidal cracks can sometimes be also detected at the contact points of the bearings. The process of conchoidal crack development is usually initiated some 10 µs before the first primary cracks are observed and can last till the latest stage of fragmentation.

Intermediate Cracks

Cracks which show characteristics of both damage and normal cracks, are referred to as “intermediate cracks”. This fracture type is a result of interacting crack mechanisms and can often be observed in the late stages of fragmentation, when normal cracks and damage cracks locally overlap (see Fig. 32 (center)). Its characteristics strongly resemble those of conchoidal cracks. Hence, the latter can be presumed to play a dominant role in the creation of intermediate cracks and in the generation of the resulting particles. Thus, intermediate cracks are assigned to damage cracks.

1.3. Characteristics of Primary Crack Types and Subtypes

In general, four points in a target have shown to be especially predestinated for crack nucleation: The three contact points between the target, the hammer and the bearings, plus the central spot at the bottom edge between the two contact points. Starting from these nucleation points, various distinguishable primary cracks are observed:

1.3.1. W-cracks

W-cracks are initiated at the contact points with the bearings, and run upwards on the outer flanks of the principal stress zone (see II.3.1 and Fig. 32 (right)). Usually, the non-branching W-cracks are initiated in the first stage of normal crack development and are characterized by high crack velocities. In many cases, however, the propagation of this crack type stops before the tip reaches the target's top edge ("incomplete W-cracks").

1.3.2. A-cracks

As already introduced in II.3.1, A-cracks are fracture structures extending from the bearings to the point of impact, forming a reversed "V". For a more detailed description, two subtypes can be discriminated, depending on the point of nucleation:

A-cracks from the Bearings (ACBs)

The frequently occurring ACBs start at the bearings and are usually characterized by intensive crack branching (see Fig. 32 (right)).

A-cracks from the Top (ACTs)

In contrast, ACTs are initiated at the point of impact and show no or few bifurcations. Usually this rarer A-crack subtype is attended by a distinct formation of damage crack structures (see Fig. 32 (left)). The dynamic features of ACTs show notable differences to that of ACBs (see e.g. Fig. 99 in V.9.6.1).

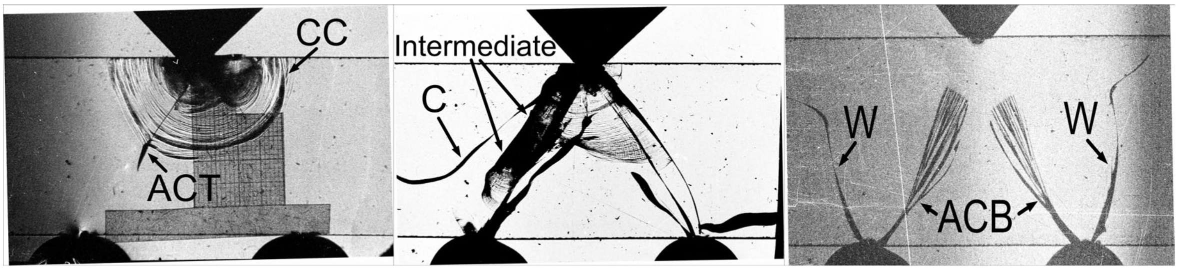

Fig. 32: Typically observed crack types: Conchoidal cracks (CCs, left) and intermediate cracks (center) are classified as "damage cracks" and differ significantly from "normal cracks", which are shown in the shape of A-cracks from the top (ACTs, left) and from the bottom (ACBs, right). Also W-cracks are depicted (right) as well as C-cracks (center). The latter crack type is occurring in the late stages of fragmentation and thus belongs to the subclass of secondary cracks ([V263B11], [V287B14], [V248B08]).

1.3.3. Centrical Cracks

The generic term "centrical crack" summarizes all primary cracks, which propagate centrically between the two contact points with the bearings, thus running in the middle of the PSZ triangle. Centrical cracks can be divided in three subtypes:

Branching Cracks in the Middle (BCMs)

BCMs start at the bottom edge between both bearings and show intensive crack branching.

Straight Cracks in the Middle (SCMs)

Contrary to the BCMs, this subtype shows no branching and is characterized by its straight profile. SCMs are almost exclusively observed in TK targets.

Top Cracks in the Middle (TCMs)

This kind of crack is observed only occasionally and is closely related to ACTs and D-cracks: TCMs show a non-branching profile and run straight from the point of impact to the center of the bottom edge.

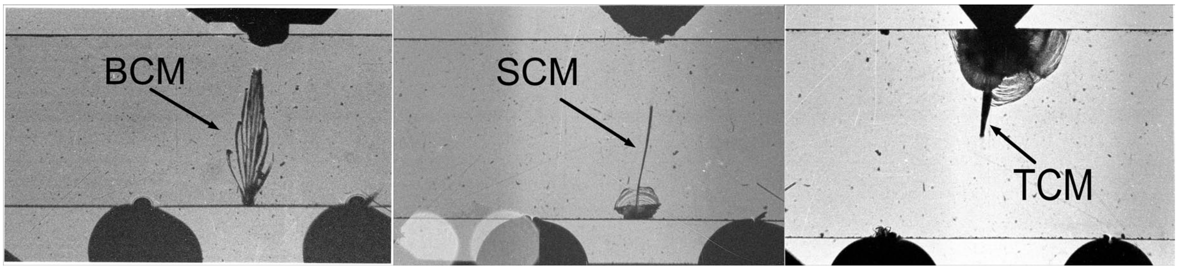

Fig. 33: Centrical cracks: Cracks which run centrically can be subdivided in BCMs, SCMs and TCMs ([V622B07], [V362B16], [V275B11]).

1.4. List of Secondary Crack Types

In the later stages of fragmentation a great number of different crack types can be observed. As a comprehensive and detailed description would lead us too far, only the most prominent secondary cracks are briefly outlined.

V-cracks

All cracks, which connect the primary crack structures (see Fig. 34 (left)), are referred to as “V-cracks”.

B-cracks

Often fracture structures develop parallel to already completed A-cracks on the outside of the primary fracture triangle. These cracks are denoted “B-cracks” (see Fig. 34 (center)).

C-cracks

Similar to B-cracks, these fractures start parallel to A-cracks, but then swivel to the side which faces away from the PSZ (see Fig. 32 (center) and Fig. 34 (right)). Thus, in contrast to B-cracks, C-cracks do not reach the points contacting the bearings.

Y-cracks

Often sickle-shaped, Y-cracks are nucleated at the edges of already existing normal cracks and start perpendicularly to their mother cracks, creating a prominent kink (see Fig 34). In many cases, these cracks stop after a small distance, seemingly creating a dead end. Most probably, these cracks are driven by residual stress release of the material.

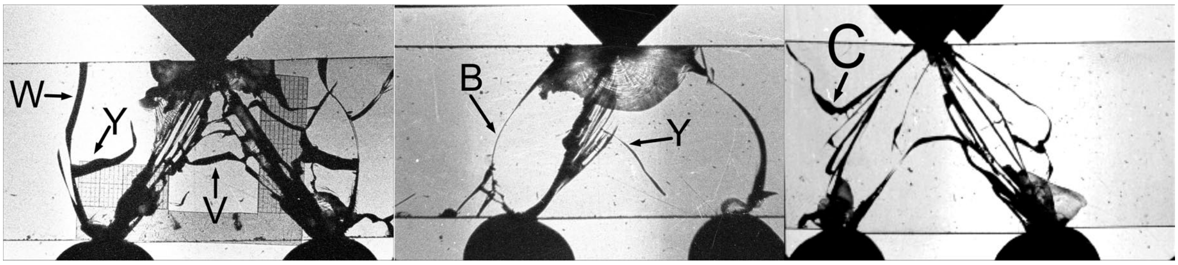

Fig. 34: Secondary cracks: Note that in all three examples ACBs had been established as primary cracks, before the secondary crack types shown have been nucleated ([V241B17], [V292B13], [V513B15]).

1.5. List of Special Crack Types

Three of the most prominent special cracks are shown below (see also Fig. 35):

D-cracks

This crack propagates in the first stages of normal fracture, starts at the point of impact and shows a straight profile. In contrast to ACTs or TCMs, this crack type severs the target asymmetrically, ending at an arbitrary point on the bottom edge of the sample. D-cracks are rare and have been sporadically observed in FG, T5 and RX.

E-cracks

Very similar to W-cracks, these rare cracks start at the bearings and run on the outer flanks of the PSZ. But in contrast to the former crack types, E-cracks turn to the outside and not to the upper edge of the target.

Z-cracks

Z-cracks are fractures which are initiated at unusual points in the sample and propagate very rapidly. It can be strongly presumed that the nucleation points of Z-cracks are a consequence of local material defects.

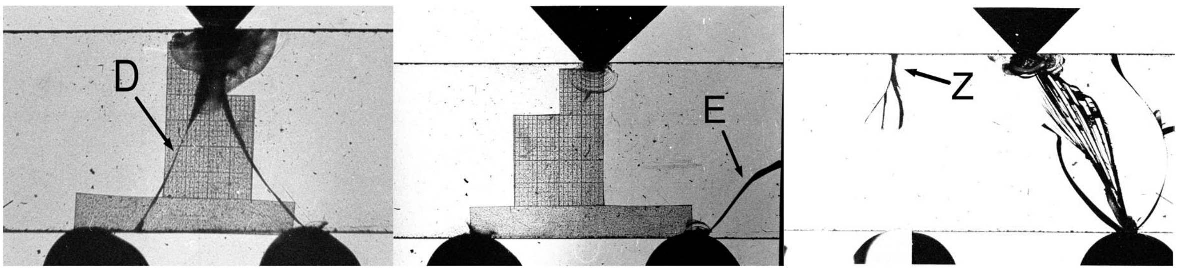

Fig. 35: Prominent special cracks: D-cracks are cracks halfway between TCMs and ACTs (left), E-cracks are bending W-cracks (center) and Z-cracks are characterized by unusual nucleation points (right). All crack types shown occur rarely under the examined conditions ([V264B07], [V270B14], [V323B16]).

2. Force Signal Analysis

2.1. General Aspects about Force Signals

Force signals typically show a number of peaks, which are arranged in up to three peak packets, referred to as “peak groups”. Fig. 36 depicts a representative example: Within a time slot of approx. 200 µs the right force transducer recorded a peak group of two peaks (36 - 91,8 µs) and a subsequent peak group with one peak (156 - 176 µs). The left signal shows three peak groups. Note that both signals show significant differences, for example the maximum force on the left is distinctly higher than the maximum peak of the right signal. This is a very typical result for HIEs.

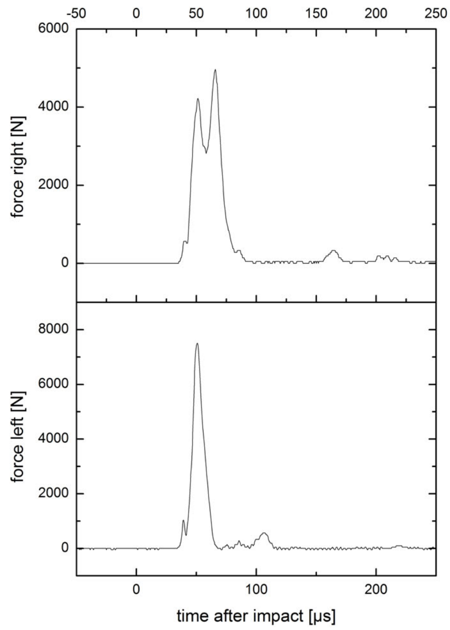

Fig. 36: Typical force signals of an HIE ([RL281], {103}): The signal consists of several peaks, which show significant variations.

An additional example is given in Fig. 37. As before, the time axis is set to the moment of impact as zero point. The theoretical runtime of a signal can be calculated by considering the transmission lengths (schematically depicted in Fig. 37 (A)) and the respective speed of sounds in target and bearings. Thus, for the depicted case the theoretical runtime is determined to be approx. 10,9 µs. The actually detected runtime offset, however, given by the time interval between the moment of impact and the first signal slope, is approx. 36,0 µs (see Fig. 37 (C, D)), and hence differs significantly from the calculated value. This delay does not alter for FG and T5 targets and only slightly for RX (35,1 µs). It can be explained by the specific coupling conditions, which are distinctly affected by complex interface phenomena between hammer and target as well as between target and bearings.

Furthermore, an additional source of the observed delay can be found in the electrical data recording systems and especially in the charge amplifiers.

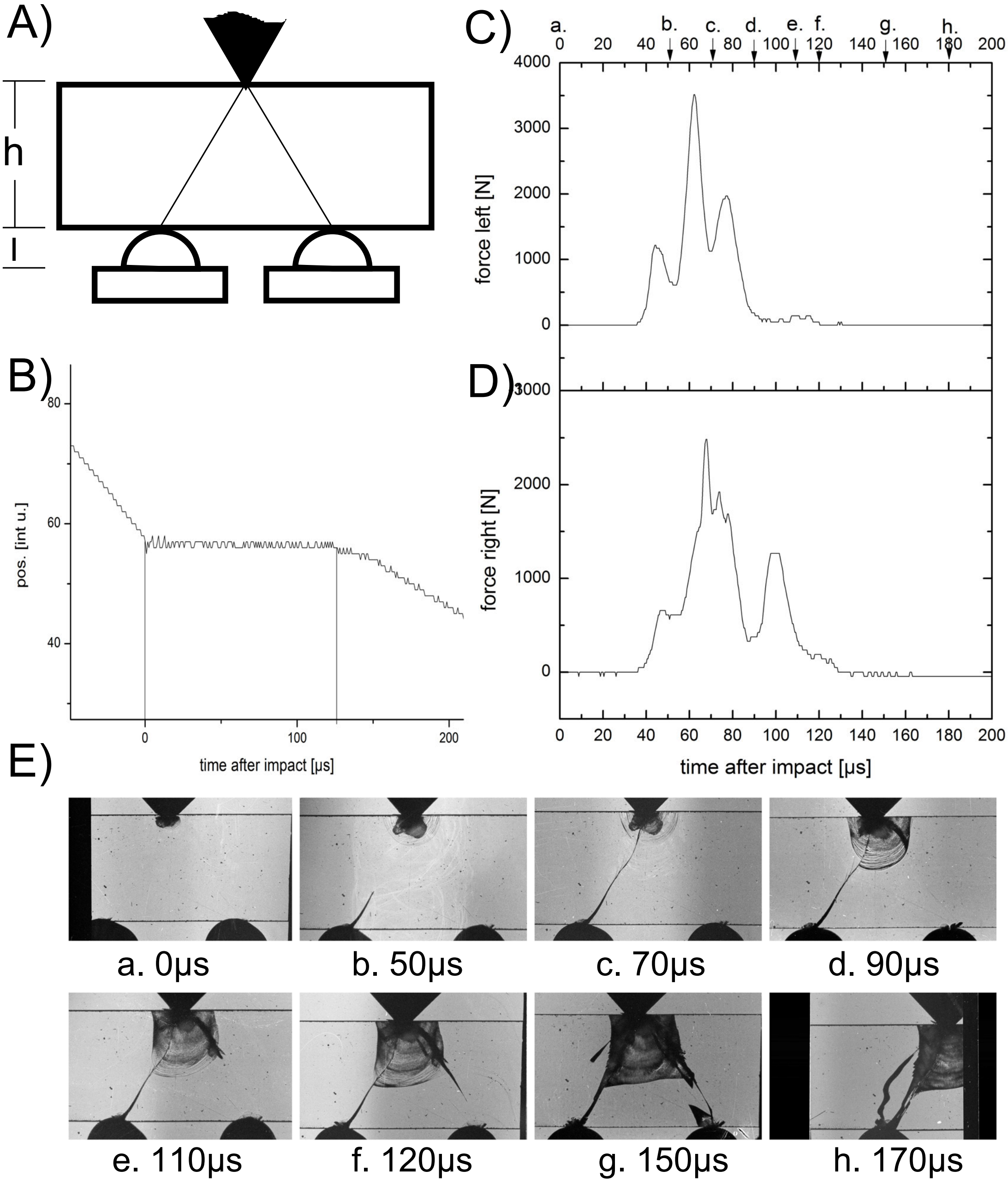

Fig. 37: Hammer impact, force signals and crack development [V290], {103}: Considering the respective transmission distances of the target and the bearings (A), the runtime of an impact signal can be calculated. In this case, the corresponding features are: T10, speed of sound $c_L = 5818\,\frac{\mathrm{m}}{\mathrm{s}}$, $h = 38,99\,\mathrm{mm}$ for the target and $c_L = 5782\,\frac{\mathrm{m}}{\mathrm{s}}$, $l = 17,00\,\mathrm{mm}$ for the bearings. As a result one obtains a theoretical runtime of 10,9 µs. However, the experimentally determined value is 36,0 µs (C and D). All peak groups of the force signals are arranged in a time slot, which is consistent with the period of the hammer's plateau stage (B). The fracture processes of the considered case can be observed in the image sequence shown below (E, excerpt).

Another interesting fact about force signals is that all significant peak groups are arranged in a time slot of less than 200 µs after the first signal slope. The dimension of this time interval is well consistent with the hammer's contact period with the target (see chapter IV.2). In Fig. 37 (B) the respective motion sequence of the hammer is depicted, showing a contact period of 125 µs, which is perfectly in line with both force signals.

It has to be stated, that in some cases after the breakthrough of the hammer, fragments are "jammed" a second time between the hammer head and the bearings, inducing further fragmentation processes.

As those secondary fragmentation and energy dissipation processes are totally out of detection, all those experimental records have to be omitted. Analyzing the force signals provides an easy way to identify unwanted "jammed" experiments: These are characterized by additional intensive peaks (> 2000 N) in the later stages beyond the mentioned time slot. The empirical ratio between "jammed" HIEs to successful ones is about 4,2 % (see Appendix B).

Resonance frequencies of the setup are determined to be in the range of some kHz, which hence does not affect the measuring signal during the observed period.

On the other hand, the frame rate of the measuring amplifiers is limited to 100 kHz [72]. Thus, due to their high velocities, shock waves cannot be detected by the force transducers.

2.2. Influences on Force Signals

Studying the influences on the characteristics of force signals, a strong correlation between the impact velocity and the maximum amplitude is expected. Correlation analysis between v_H and the maximum amplitude of the first peak group provide values of 0,302 (left), resp. 0,303 (right) for the Pearson coefficients, which have been verified to be highly significant with an error probability $p < 0,05\,\%$ (see Appendix B). Although this implies a distinct linear correlation in the examined range of impact velocities, the signal is clearly affected by additional and more dominant influences.

Comprehensive analysis has been performed to study the nature of these influences. In short, the results indicate:

- Force signals are not at all affected by the hammer geometry. This conclusion has been verified for all used target types.
- There is a significant dependency between the force signal's characteristics and the type of target. Especially pre-stresses seem to have a big influence.
- Conchoidal cracks have shown to affect force signals significantly. This effect can be explained by seismic reflections and scattering effects at the complex structure of the expanding conchoidal fracture surfaces and by damping effects in the damage crack zone.

The most interesting feature of force signals is revealed by considering the corresponding images of fracture propagation (Fig. 37 (E)): In the depicted case an ACB has started from the left side (b.), about 50 µs after the impact. At this moment the left signal shows a clear drop, which can be explained by the local stress release in the target, driving the propagating crack. The growth of load on the opposite, right side is slightly reduced as well, but the right force signal still shows an increasing slope in this stage.

When the left flank of the ACB is completed (c.), a significant drop of loading is detected on the left side, contrary to the right signal, which shows at this moment its maximum peak. Due to this asymmetric loading situation, another crack is initiated - this time on the right side - which can be detected as a pronounced drop of the right force signal (d.). After the primary fragmentation stage is finished, and the target is severed (h.), the fragments diverge and lose the contact to the bearings. Thus, secondary fracture processes are not detectable for the force transducers.

Following this interpretation, the existence of several peaks in the signals reveals that the dynamic stress and energy dissipation situation in the target during the propagation of a single crack is quite intricate, and cannot be explained just by a simple model presuming a “quasi static” load: A developing crack shows complex fluctuations in its force signals, which are very similar to those of its propagation behavior.

2.3. The Daisy Chain Discriminant Analysis Concept

Evidently, the initial fracture development has a complicated, but significant influence on the signal’s characteristics. This can be used to determine the primary crack type just by means of the detected force signals, which would be especially helpful for data records with missing or incomplete image sequences.

Therefore an innovative technique of signal analysis was developed, which provides the possibility to make statements about the initial fracture situation in the target. This method mainly bases on a sequence of different discriminant analyses. These procedures are schematically depicted in Fig. 38.

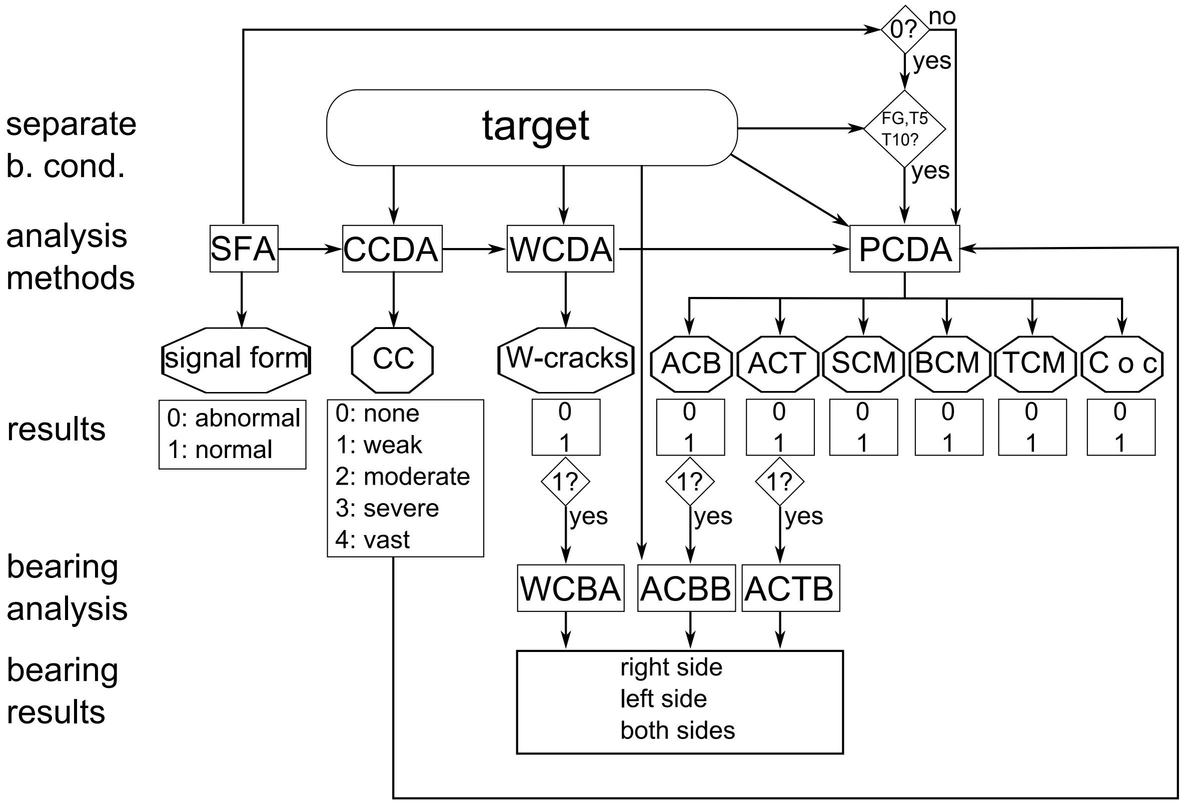

Fig. 38: Schematic diagram of the Daisy Chain Discriminant Analysis Concept: First of all, a signal form analysis (SFA) is performed, then follows a series of discriminant analysis tests (see text and Appendix B for details).

A comprehensive description of all procedures is provided in Appendix B and is briefly outlined below:

First of all, each force signal is parametrized: Characteristic parameters, like for example the number of peak groups, the number of peaks in each peak group, the maximum peak values and the area under each peak are quantified, thus providing a "finger print" of each signal.

The basic idea of this classification method is now to use discriminant analysis to "decipher" this signature and to find useful characteristic discriminant functions, by which means the primary crack type can be determined.

It has to be noted that due to its considerable influence on force signals the type of target has to be taken into account in all tests. As a consequence, most of the discriminant analyses have to be carried out specifically for each material.

In a first step, an optical signal form analysis (SFA) is performed to filter unwanted "jammed" HIEs (see above) and find out unusual data records.

Then a material specific conchoidal crack discriminant analysis (CCDA) is performed, which provides a quantitative description of the intensity of conchoidal fractures by the ordinal index M_R, which is defined as follows:

- $M_R = 0$: no conchoidal cracks
- $M_R = 1$: weak conchoidal fracture intensity, area less than 50 mm^2 in projection
- $M_R = 2$: moderate conchoidal fracture intensity, area less than 200 mm^2 in projection
- $M_R = 3$: severe conchoidal fracture intensity, area less than 400 mm^2 in projection
- $M_R = 4$: vast conchoidal fracture intensity, area more than 400 mm^2 in projection

Subsequently, another material specific discriminant analysis is performed in order to identify W-cracks (W-crack discriminant analysis, WCDA). By means of further analysis (W-crack bearing analysis, WCBA) it is even possible to draw conclusions about the symmetry of W-cracks.

In the next step a material specific primary crack discriminant analysis (PCDA) is conducted, which is the main item of the Daisy Chain Discriminant Analysis Concept, and provides reliable results for all signals, classified in the SFA as "normal".

As mentioned above, force signals are distinctly affected by the intensity of conchoidal fracture development. Therefore good results for PCDA have been achieved by determining the respective discriminant functions separately:

- for "normal conchoidal crack intensities": $M_R < 3$
- and for "particularly pronounced conchoidal crack intensities": $M_R \geq 3$

All data records can be classified, using the results of the CCDA carried out before. Then the corresponding PCDA is selected.

As a result, one obtains the information about the primary crack type occurred in the HIE ("C o c" in Fig. 38 stands for a "combination of crack types"). In the case of ACBs and ACTs, additional discriminant analyses (ACBB and ACTB) reveal the location of the respective crack type.

The non-standardized and standardized discriminant coefficients, as well as characteristic statistical values for all mentioned discriminant analyses are listed in Appendix B.

To check the quality of this method, a number of datasets have been used as a control group, by applying the described concept and comparing the calculated results with the actual primary crack situation, in so-called “hit-miss tables” [12]. The control group consisted of: 67 HIE datasets for FG, 36 for T5, 38 for T10, 21 for TK, 11 for AS and 34 datasets for RX.

Table 10 shows the results of this “hit-miss” control procedure.

[%]	FG	T5	T10	TK	AS	RX
CCDA	88,1	88,9	89,5	90,5	81,8	94,1
WCDA	97,0	94,4	100			97,1
WCBA	100	100	100			100
PCDA ($M_R < 3$)	97,6	100	95,8	100	100	100
ACBB	100	100	100		72,7	100
ACTB	100	100	90,0		100	100
total hit ratio	86,6	88,9	86,8	90,5	72,7	94,1

Table 10: ”Hit-miss” table of the Daisy Chain Discriminant Analysis Concept: This method achieves high hit ratios for nearly all targets. Only for AS targets is the hit ratio significantly lower (approx. 73 %), possibly because of interfering effects of the silver layer - although this result should not be overrated, in respect of the comparatively low number of experimental data specifically for this target type.

3. Influences on Crack Propagation Paths

3.1. Crack-Mapping

To determine how the location of crack paths is affected by constraints, comprehensive statistical examinations have been carried out.

In addition to those methods based on frequency analysis, innovative graphical techniques have been developed as easy tools to detect and describe repeating crack patterns. In this thesis, these procedures are referred to as "crack-mapping". It is based on the principle of image stacking: Therefore the final images, i.e. pictures which show the final stage of crack development, are taken into account. In a first step, those images have been sorted by respective boundary conditions, cropped to the same size and equalized.

Then the images are stacked and analyzed by means of the freeware program "ImageJ 1.43t"[1]. There are several methods to win graphical information about the statistical distribution of crack patterns, depending on the projection type of the stacks:

- AVG-mapping: For each pixel, the local average intensity over all images in the stack is calculated. In false color representation, regions which are very frequently crossed by cracks appear as bright orange areas, whereas regions of low fracture path frequencies are colored deep blue. Thus, AVG-mapping is a reliable tool to describe the likelihood of specific crack types.

- MAX-mapping: Each pixel stores the local maximum value (i.e. the brightest color) over all images in the stack. As a result one obtains a projection of distinctly pronounced patterns, that means of crack structures which can be observed without exception in every image of the stack. Those patterns are displayed as white areas contrasting a blue background in false color representation. As damage cracks feature big variations even under identical initial conditions, it is difficult to resolve its extension in AVG-maps. Thus, MAX-mapping provides a useful complementary tool to study especially this type of fracture.

- MIN-mapping: Each pixel contains the local minimum value (i.e. the darkest color) over all images in the stack. Consequently one gains a map of all regions, which have been crossed by a crack at least once (displayed in yellow and green color). Hence, MIN-mapping is a utile method to identify regions, which are very unlikely to be affected by cracks.

- STD-mapping: For each pixel, the local standard deviation is calculated: In false color representation, high values for the standard deviation are displayed in bright orange and red. STD-mapping is a very useful tool to compare two different results, e.g. two AVG-maps under different conditions.

[1] http://rsb.info.nih.gov/ij

3.2. General Material-Specific Correlations of Crack Paths

Fig. 39 provides an impression of the material's influence on the appearance of fracture patterns.

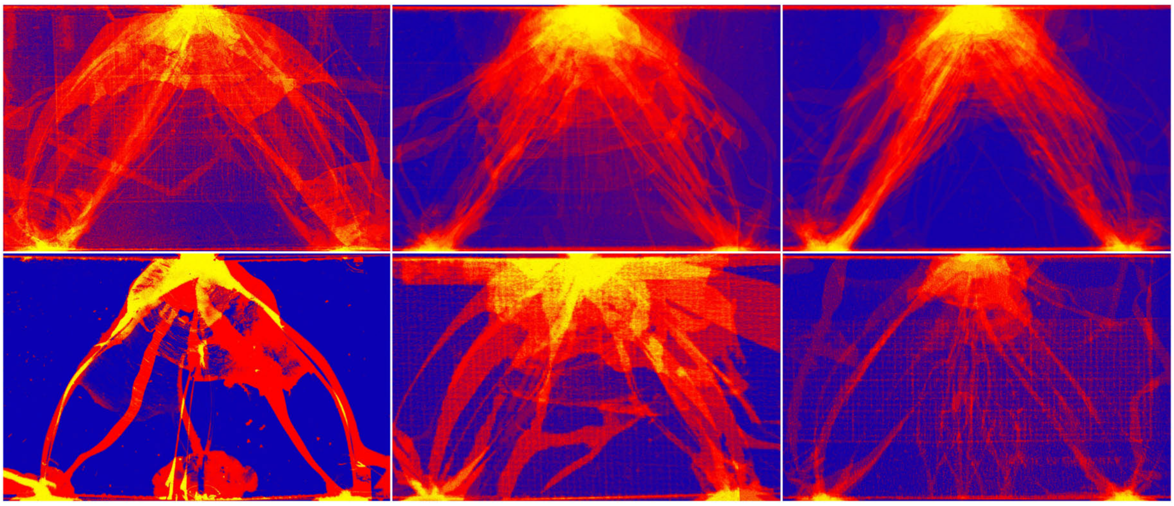

Fig. 39: AVG-mapping results for different target types: The average crack paths of the stacked cases (from top left to bottom right) {101}, {102}, {103}, {104}, {105} and {106} are depicted. The corresponding sample size has been 25, 21, 23, 17, 11, and 22 respectively.

It is clear that A-cracks play a dominant role in FG, T5 and T10 targets, whereas TK are marked by SCMs. AS-targets show dissolved A-crack structures, as well as RX, which for their part also seem to be especially susceptible to BCMs. Fig. 40 shows the corresponding MIN-mapping results.

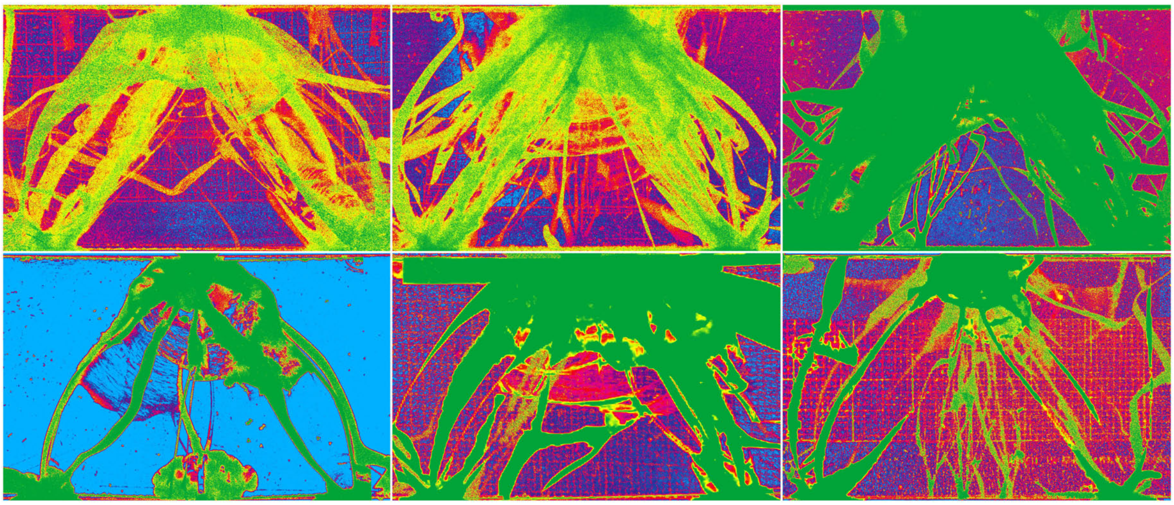

Fig. 40: MIN-mapping results for the cases depicted in Fig. 39.

The best insight in the material-specific behavior of damage cracks is offered by the MAX-mapping results, which are depicted in Fig. 41.

The susceptibility to damage cracks clearly depends on the material: RX has shown to be comparatively insensitive against conchoidal cracks. Also T10 samples show lower damage crack extensions than FG, T5 and TK.

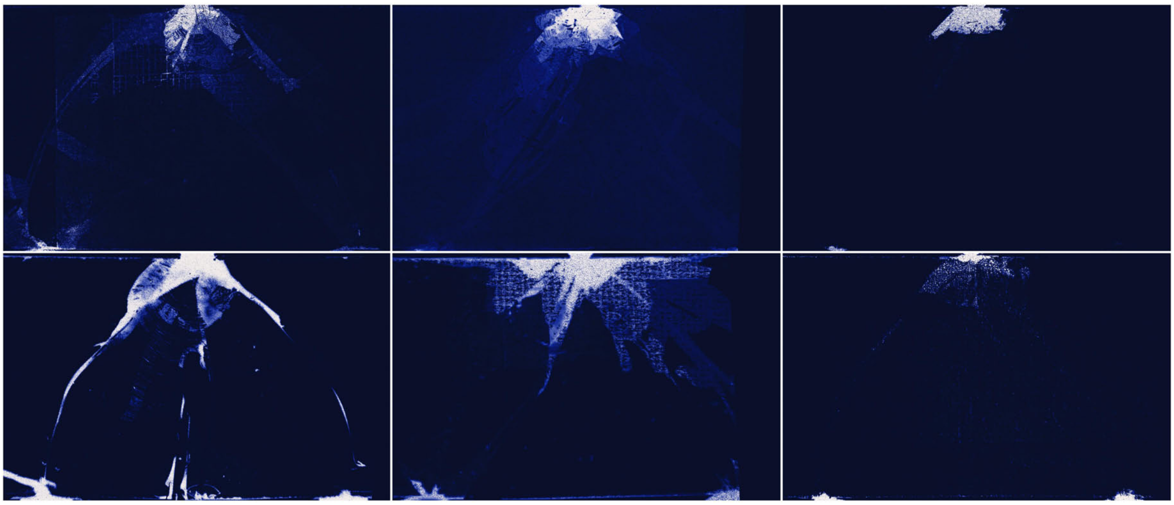

Fig. 41: MAX-mapping results for the cases depicted in Fig. 39. The white structures depict fractures, which have been occurred in every case.

It is of interest, that in AS the areas of damage cracks are mainly located directly beneath the top edge of the sample.

An explanation could be that the boundary silver layer of AS targets acts as an extended interface during the impact: Shock waves are coupled into the material not only at the point of impact, but also in its surrounding along the silver layer. As a consequence, conchoidal crack areas are primarily located near the edge and its form differs significantly from the usual semicircular shape of conchoidal crack fronts occurring in other target types.
In Fig. 42 all standard deviations between each AVG-map are depicted.

A statistical overview of primary crack frequencies is given in Table 11.

[%]	ACB	ACT	SCM	BCM	TCM	C o c
FG	52,2	17,8		25,6	4,4	
T5	43,3	16,4		29,9	9,0	1,5
T10	60,0	20,0	4,6	15,4		
TK			90,6	9,4		
AS	63,0	25,9		11,1		
RX	47,1	13,2		29,4	4,4	5,9

Table 11: Frequencies of primary crack types. “C o c” denotes a combination of various crack types.

In general, one can state that each target type shows its own typical distribution of crack types and that pre-stresses distinctly affect crack geometry. Also the dependency on other factors (hammer geometry and impact velocity) is specific for each material, which is examined in the following pages.

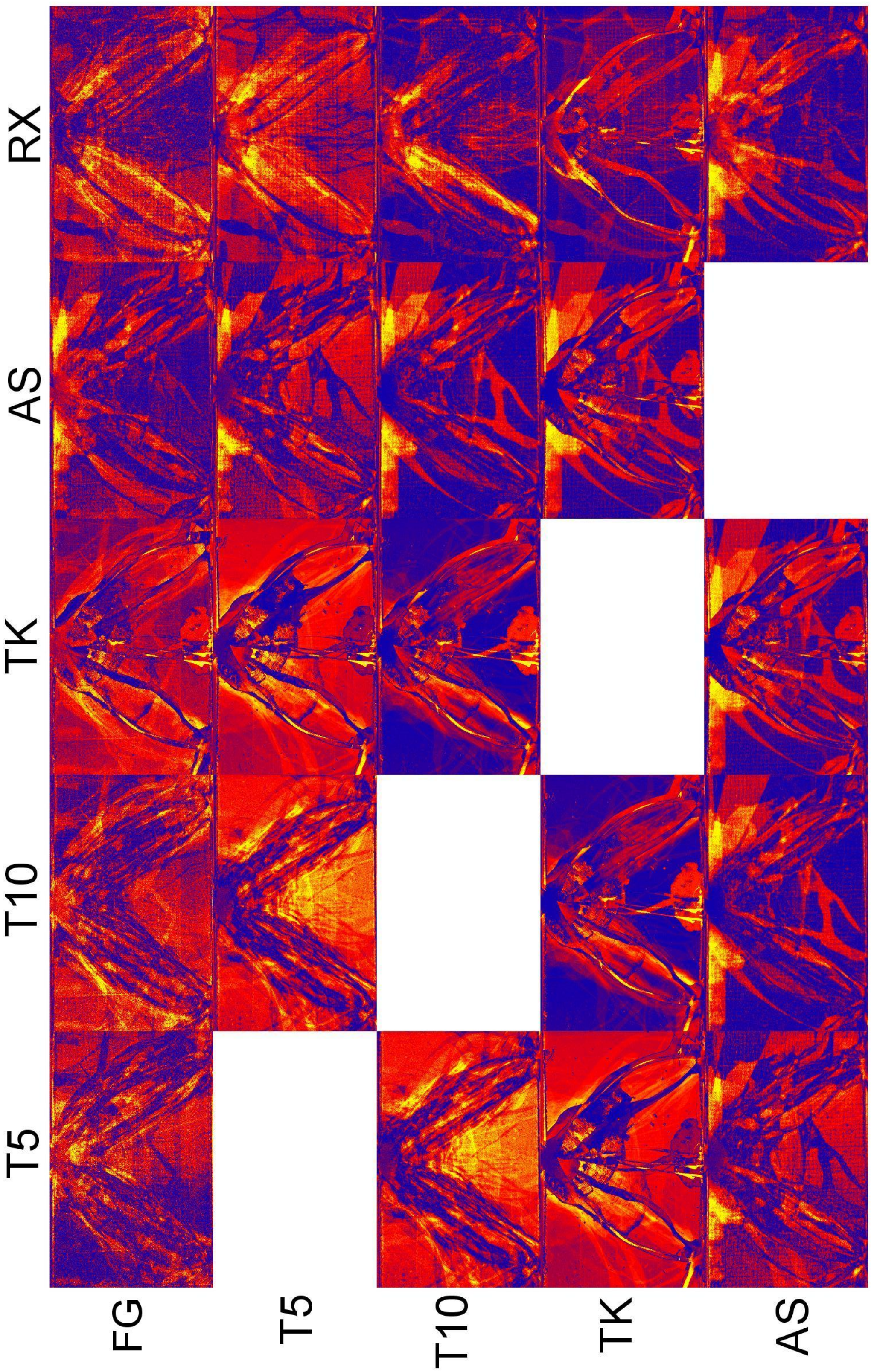

Fig. 42: Results of STD-mapping between all AVG-maps, depicted in Fig. 39: Regions which show major changes in their crack paths are highlighted by bright colors.

3.3. Effects on Crack Patterns in FG

As already pointed out in II.3.3, there is a significant correlation between the location of "directed" stresses in FG under static loadings and the crack patterns resulting from HIEs. A detailed study on this topic is presented in [40]. Comprehensive experimental results indicate that all conclusions drawn from experiments with FG and a pointed hammer tip can principally be transferred also for other hammer geometries. Fig. 43 shows the respective stress distributions in FG under static loadings.

Fig. 43: Results of photoelastic investigations for FG: The stress distribution under static loading is depicted, using different hammer geometries (from left to right: {X11}; {X21} and {X31}).

Note that in principle the typical triangular shaped principal stress zone (PSZ) does not change. Furthermore it can be seen, that the PSZ in FG under loading of a hammer of 8,3 mm width (Fig. 43, center) shows to some degree an asymmetrical distribution. This effect can be explained by microscopic irregularities in the interfaces between hammer and target: An increasing contact area increases the influence of arbitrary morphological structures, slightly deforming the zone of directed stresses.

There is a significant correlation between impact velocities and intensities of damage cracks: The faster the hammer hits the target, the more damage cracks tend to occur, a conclusion which is verified by the results of AVG- (see Fig. 44) and MAX-mapping (see Fig. 45).

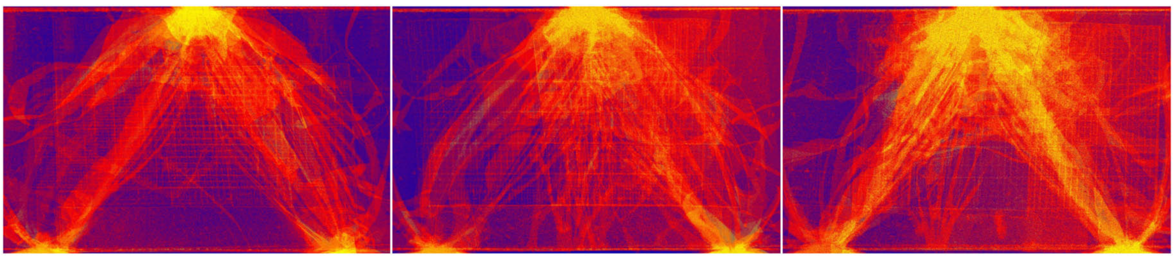

Fig. 44: AVG-mapping results for HIEs using FG under variation of the impact velocity: From left to right, the stacked cases {101} and {201}, {301} and {401}, {501} and {601} are depicted.

This correlation can be easily explained by the consideration of shock waves and the relationship (II.2-21): A more rapid impact initiates higher shock wave amplitudes, which are probably the primary cause of damage cracks.

Another fact that is revealed by Fig. 44, is that under higher impact velocities, BCMs are more likely to occur.

Changing the hammer tip geometry significantly affects the frequency distribution of primary crack types, which is shown in Table 12.

Using a pointed hammer head, most of the initiated primary cracks are ACBs, which agrees well with the location of the PSZ. Experiments with flat hammer heads show a significant drop of ACB frequencies. Instead, ACTs and TCMs appear, which are associated with vast damage crack structures. Nevertheless, ACBs remain to be the most prominent fracture types

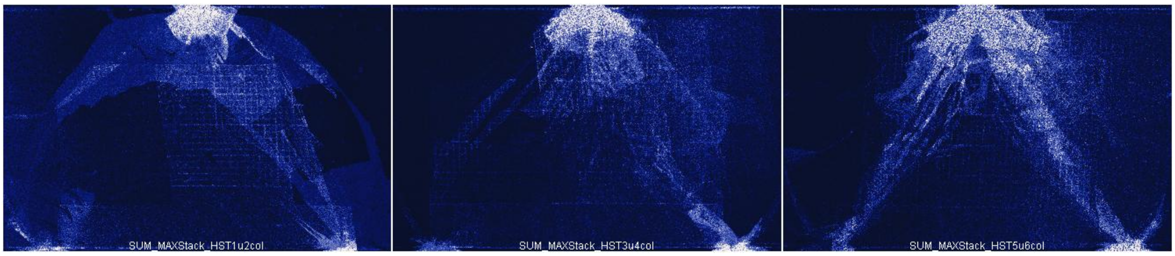

Fig. 45: MAX-mapping result for FG from low (left) to high (right) impact velocities: The stacked cases {101} and {201} are compared with those of {301} and {401} (center) and {501} and {601}. The influence of impact rapidity on the expansion of damage cracks is clearly visible.

[%]	ACB	ACT	SCM	BCM	TCM
pointed	64,3	16,7		19,0	
4,5 mm	46,2	30,8		23,1	
8,3 mm	45,0	15,0		30,0	10,0
round	33,3	13,3		40,0	13,3

Table 12: Influence of hammer geometry on frequencies of primary crack types in FG ({1X1}).

in FG under these impact conditions.

Contrarily, in the case of a round hammer head, BCMs are more likely to be initiated than ACBs. Thus it is clear, that the shape of the contact area during the impact distinctly affects the mechanical coupling conditions and the initiation of primary cracks.

3.4. Situation in T5 and its Effects on Crack Patterns

The situation of pre-stresses and their influence on the PSZ in T5 targets is illustrated in Fig. 46.

Fig. 46: Stress distribution in T5 targets: The situation of an unloaded pre-stressed sample (left) is depicted, as well as the stress distribution under the load of a 4,5 mm wide (center) and a round (right) hammer head.

The areas of high pre-stresses fuse with the well known directed stress zone appearing under static loading. Although in principle the PSZ in T5 resembles that of FG (cf. Fig. 43), the unstressed zone between the bearings in the lower half of the loaded T5 sample is more extended than in a stress-relieved FG target. Furthermore, the gradients between stressed and unstressed zones appear to be more prominent.

As a consequence of this specific stress situation in T5, the frequency of TCMs rises significantly up to 9,0 % (see Table 11). Also BCMs are more likely to appear. The latter result indicates that not only the location of the pre-stressed zones affects crack geometry, but also the gradients between stressed and unstressed regions.

Complementary to the simple model presented in II. 3.3, one can presume that the stress waves, propagating through the material from the point of impact, are virtually channeled by interferences with directed stresses located in the PSZ. This modified model is also supported by the results of dynamic photoelastic HIEs, which are illustrated in Fig. 47.

The influences of hammer geometry are presented in Table 13.

[%]	ACB	ACT	SCM	BCM	TCM	C o c
pointed	41,9	29,0		9,7	16,1	3,2
4,5 mm	57,1	14,3		28,6		
8,3 mm	52,9			47,1		
round	25,0	8,3		58,3	8,3	

Table 13: Influence of hammer geometry on frequencies of primary crack types in T5 ({1X2}).

Using a flat or round hammer head instead of a pointed one, results in a significantly increasing number of occurring BCMs. As already pointed out for FG, it is demonstrated that the hammer geometry directly affects the input of stress waves, and one can conclude, that using a hammer of an increasing width enhances their dynamic influence, to the detriment of that of the fixed, "directed" PSZ.

Furthermore, it is of interest that, as in FG, this effect is even more prominent for HIEs with a round hammer head, although for this case, the theoretical contact area between hammer and target is distinctly lower: This indicates that the latter is an insufficient parameter to describe its influence on fragmentation.

In fact, at the moment of stress wave initiation, the actual contact area is determined by the structure of the immediately nucleated impact notch and as a consequence, by the three

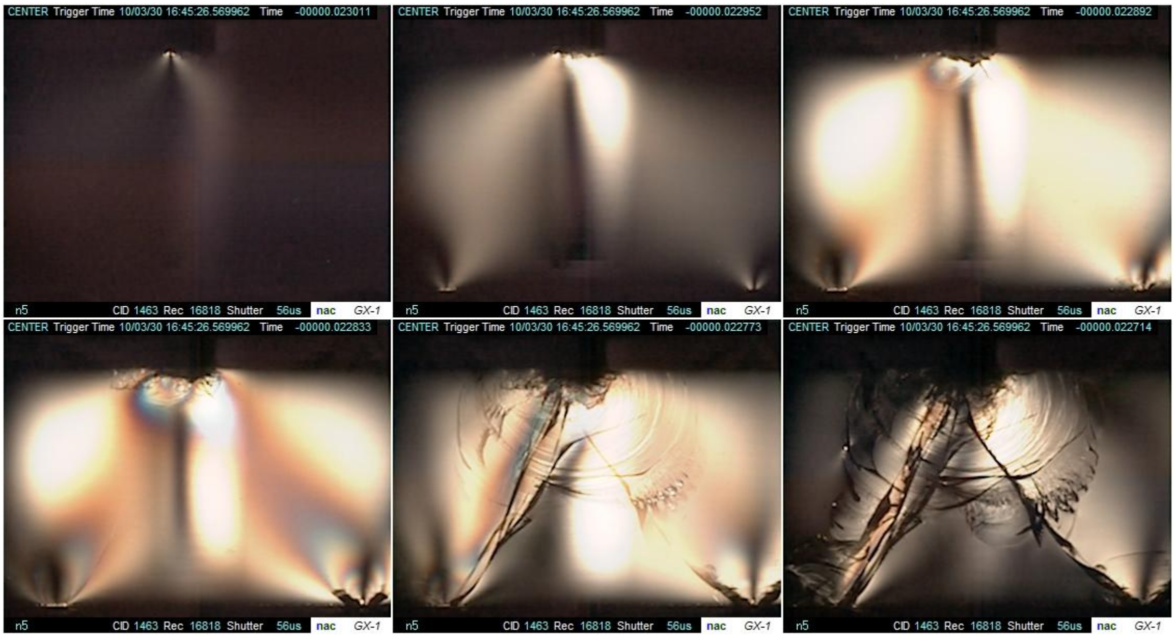

Fig. 47: Results of photoelastic experiments under impact conditions, using a T5 sample (settings: 16.818 fps, HIE {122}, [N5]): The typical PSZ known from static loading experiments is now superimposed by incoupled stress waves, which cause interferences. Note that after the completion of ACBs, there are still zones showing residual loads, which subsequently drive the establishment of secondary cracks.

dimensional shape of the hammer tip.

This inference is also supported by Fig. 48, in which the results for a pointed hammer tip are compared with that for a flat one of 8,3 mm width.

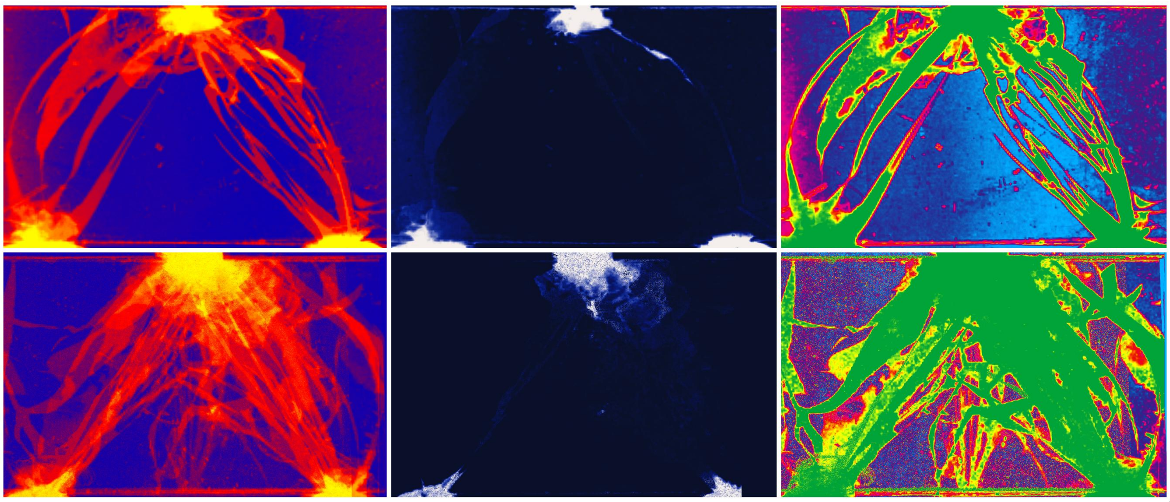

Fig. 48: AVG-, MAX- and MIN-mapping (from left to right) results for the cases {602} (top row) and {622} (bottom row).

Note that the use of a flat hammer instead of a pointed one clearly enhances the creation of conchoidal cracks. This effect has also been described for FG in [40] and is universal for all examined target types. Considering (II.2-21), this material-independent effect is another strong indication for shock waves to be the primary cause of conchoidal cracks.

Again, as observed for FG, an increasing impact velocity also causes an intensification of conchoidal cracks. The STD-mapping results for T5 in Fig. 49 (center) gives a good impression of the dimension of this effect.

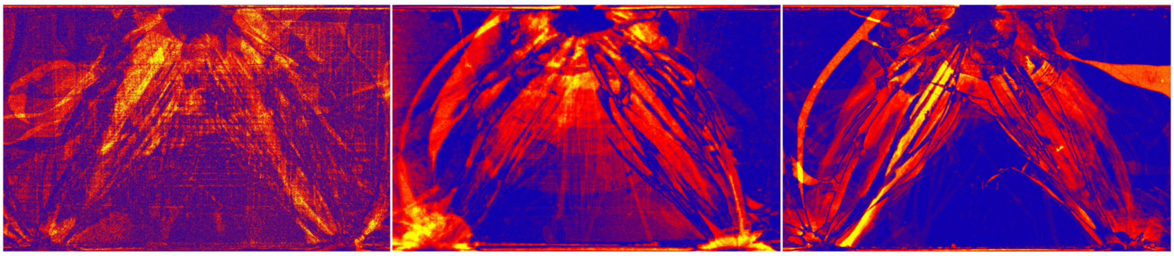

Fig. 49: Comparison of low and high impact velocities in (from left to right) FG, T5 and T10 targets: The standard deviations of the AVG-mapping results are illustrated for the cases {101} compared with {601}, {102} compared with {602} and {103} compared with {603}.

3.5. Situation in T10 Targets

Fig. 50 gives a photoelastic insight into the situation of unloaded and loaded T10 targets. Complementarily, the stress distribution on the periphery of the PSZ is provided by Fig. 51.

Fig. 50: Stress situation in T10 targets: An unloaded pre-stressed sample (left) is depicted as well as samples loaded by a pointed (center) and a round (right) hammer head.

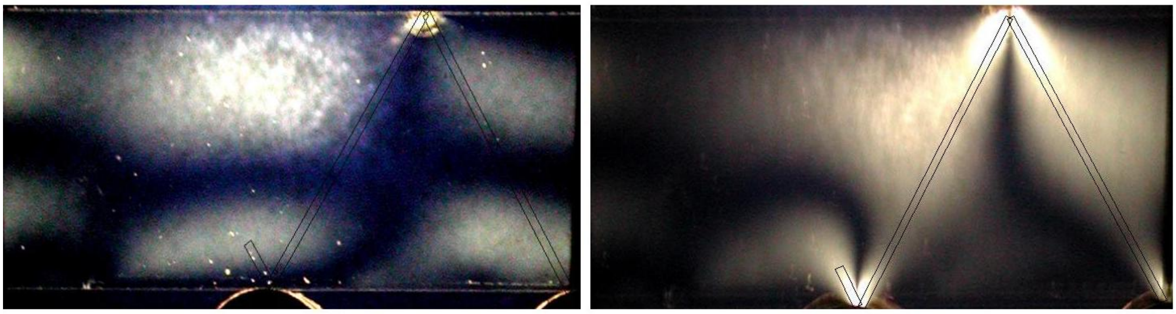

Fig. 51: Stress distribution at the PSZ and its outlying areas of T10 targets: An unloaded sample is compared with a target under the load of a 4,5 mm wide hammer head. One can clearly see, how the pre-stressed areas fuse to a complex stress pattern. In both pictures, the typical position of the PSZ is marked by thin black lines.

Again, the pre-stressed zones fuse to form a PSZ, which shows the typical triangular shape plus the onset of W-flanks (these regions are marked by thin black lines in Fig. 51). By considering the circumference of the PSZ, however, a complex stress pattern is revealed, which is specific only to T10 targets. Consequently, the stress is quasi partly “deflected”, away from the zone between the bearings and the hammer tip. As we will see (cf. chapter V.9.6.5), this fact will be crucial for the understanding of fracture energetics.

HIEs with T10 targets feature a comparable low frequency of BCMs (cf. Table 11), most of the primary cracks are concentrated in the A-crack corridor (see Fig. 39 (top right)).

It is interesting that this bunching effect is observed for damage cracks, too: As for the other kinds of targets, an increasing impact velocity is positively correlated to an enhancement of damage cracks. But in contrast to T5 and FG, the resulting damage cracks in T10 samples tend to develop anisotropically, in form of intermediate cracks which propagate in the zone of A-cracks.

As in all other targets, damage crack intensities are also correlated to the shape of the hammer tip. Considering this feature in connection with the frequencies of ACTs (see Table 14), it reveals some crucial information about the nature of the latter ones.

[%]	ACB	ACT	SCM	BCM
pointed	59,5	24,3	5,4	10,8
4,5 mm	100,0			
8,3 mm	54,5	9,1		36,4
round	53,8	23,1	7,7	15,4

Table 14: Influence of hammer geometry on frequencies of primary crack types in T10 ({1X3}).

Although ACTs are always associated with pronounced conchoidal crack structures, they do not show the same dependencies as the latter ones: Using a flat hammer tip instead of a pointed one enhances conchoidal crack development, but decreases the frequency of occurring ACTs.

This implies that conchoidal cracks are a feature, but not the only cause for ACTs. Instead, the specific pre-stress situation in the target also plays an important role, as well as the shape of the hammer tip affecting the coupling conditions between hammer and target.

3.6. Situation in TK Targets

The pre-stress situation of TK samples is that of vertically flipped T5, as TK targets are just T5 samples, which are positioned upside down for HIEs. Due to these specific circumstances, a loaded TK sample shows a complex stress pattern (see Fig. 52). The positions of those areas of high stress can be explained by a superimposition of the original PSZ emanating from the process of preparation (marked in red in Fig. 52 (center)), and the additional primary stress zone of actual loading (marked in green).

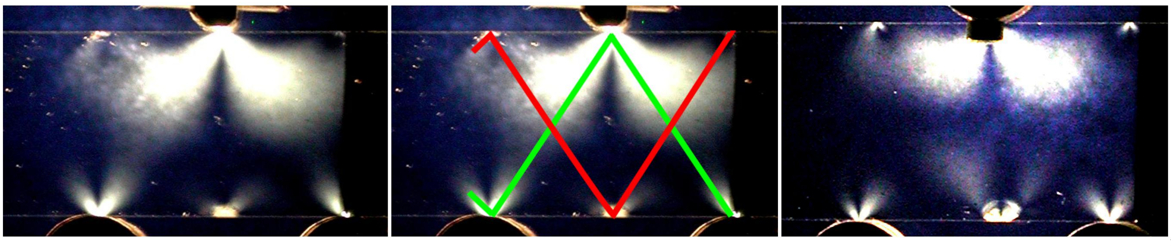

Fig. 52: Stress distribution in TK targets: The pre-stressed samples are identical to T5, but positioned upside down under loading. Thus under the load of a flat (4,5 mm wide, left and center) or round (right) hammer head, TK shows a complex stress pattern, which results from a superimposition of two typical primary stress zones, marked in green and red (center).

This specific stress situation ensures nucleation and propagation of SCMs (which are characteristic for TK in HIEs, see Fig. 39 bottom left) and in some rarer cases BCMs (see Table 15) as primary cracks. Thus, it can be presumed that the dynamic tensional stress waves initiating and driving those cracks are exclusively "channeled" in the central zone.

[%]	pointed	4,5 mm	8,3 mm	round
SCM	100,0	100,0	88,9	80,0
BCM			11,1	20,0

Table 15: Frequencies of BCMs and SCMs depending on the shape of the hammer head ({1X4}).

Finally, comparative studies of damage cracks in TK have revealed no significant differences in their dependencies compared with those of FG: Conchoidal crack intensities are enhanced by higher impact velocities and a flat or round geometry of the hammer head.

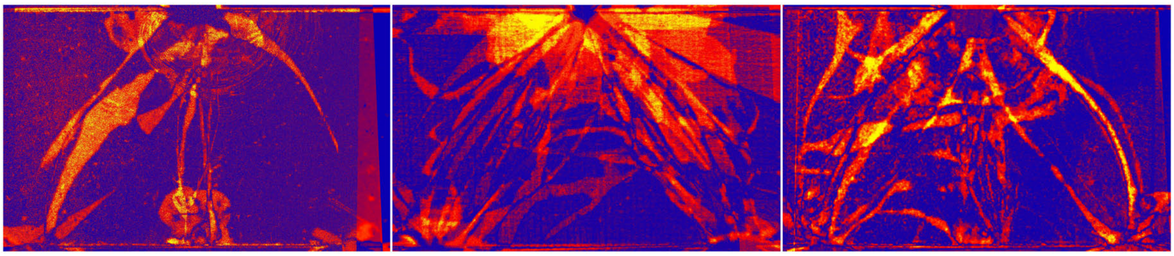

Fig. 53: Comparison of low and high impact velocities in (from left to right) TK, AS and RX targets: The standard deviations of the AVG-mapping results are illustrated for the cases {104} compared with {604}, {105} compared with {605} and {136} compared with {636}. It has to be considered, however, that the size of the database for TK targets is comparatively low.

3.7. Situation in AS Targets

Although in an AS target the PSZ under static load is identical to that of a FG target, there are some indications, that the coupling between hammer and target as well as the dynamics of stress waves are significantly affected by the additional silver layer on the sample's upper edge.

As pointed out above, compared to other target types, the position of damage crack expansion is distinctly different in AS targets (see also Fig. 53 (center)). Nevertheless, the dependencies of this crack class on impact velocities and hammer geometry remain the same.

Fig. 54 gives a clear impression of the stress wave dynamics in an AS sample, made during an HIE.

The additional interface between hammer and target evidently influences the initiation of primary cracks, as AS targets are characterized by very high frequencies of A-cracks: Compared to all other target types, they show the highest rates of ACBs as well as of ACTs and the lowest rates of BCMs (see Table 11 and Table 16).

[%]	ACB	ACT	BCM
pointed	66,7	23,8	9,5
round	50,0	33,3	16,7

Table 16: Influence of the hammer geometry on frequencies of primary crack types in AS ({1X5}).

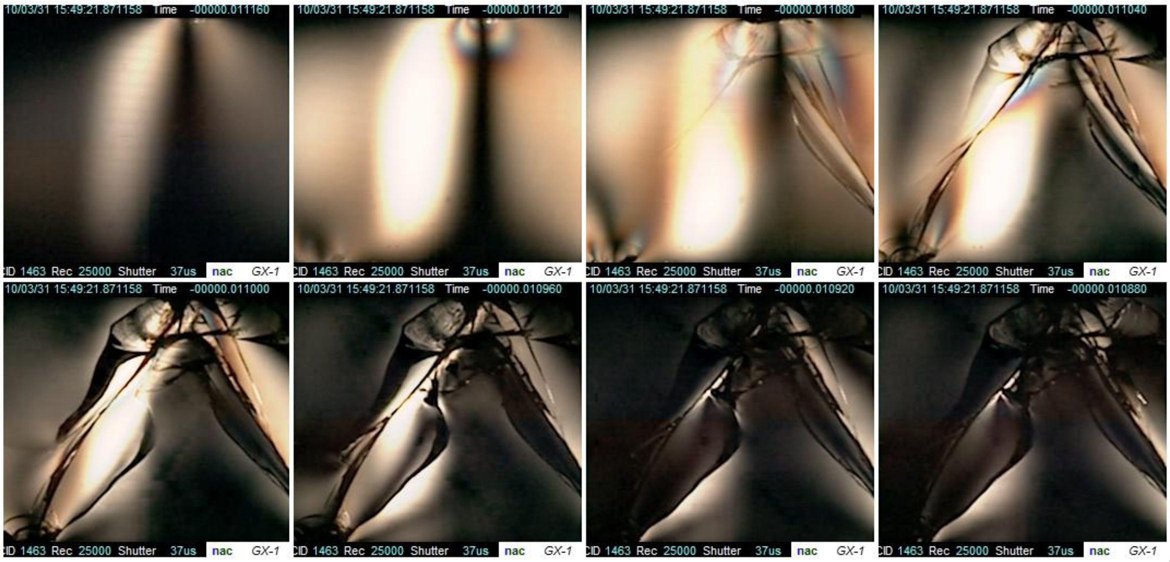

Fig. 54: Photoelastic image sequence examining an AS sample under impact conditions (settings: 25.000 fps, HIE {125}, [N18]).

3.8. Situation in RX Targets

Under static load, the stress distribution in RX shows a typical PSZ, which is comparable to that of a FG (see Fig. 55). Contrary to those, however, the stressed zones are vaster and appear to be more diffused than in float glass samples. This could be explained by the nanocrystalline structure of the examined glass ceramics.

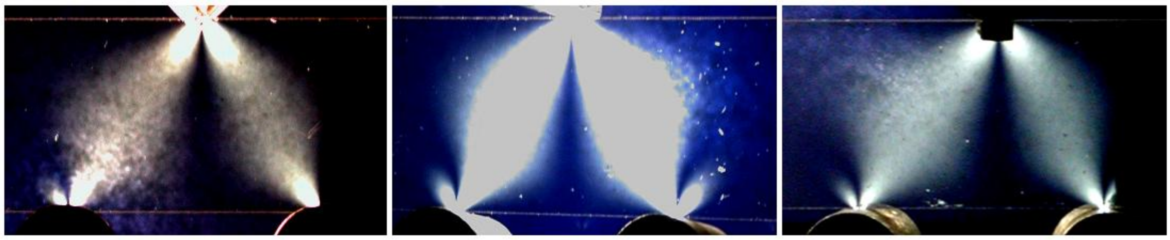

Fig. 55: Stress situation in loaded RX targets: The samples are loaded by a pointed (left), a flat (4,5 mm width, center) and a round (right) hammer head, respectively.

A representative example for the dynamic stress development of RX under impact loading can be studied in Fig. 31.

The impression of stress scattering in the PSZ coincides well with the results, considering the frequencies of primary cracks: In RX, the rate of A-cracks (ACBs as well as ACTs) is lower than for example for FG (cf. Table 11). Instead, primary cracks occur comparatively often in the shape of BCMs, TCMs, or as a combination of various crack types.

Furthermore, the rates of bifurcation for ACBs have shown to be significantly lower than in any other crack types. It is notable, that this effect is not observed for BCMs. Thus one can conclude, that the dynamics of BCMs are less affected by the nanocrystalline structure of the material, than that of ACBs. This conclusion will be confirmed below (see V.9).

Another characteristic of RX can be observed under high impact velocities: Under specific circumstances, a vast amount of secondary cracks (especially Y-cracks) is created, forming marbled crack paths and virtually causing total disintegration of the sample (see Fig. 56 (bottom row)). This “disintegration effect” has been exclusively observed for RX targets. It is also revealed by Fig. 53: Higher impact velocities bring about not only higher damage crack intensities, but also higher rates of secondary cracks (marked in the STD-map by orange color).

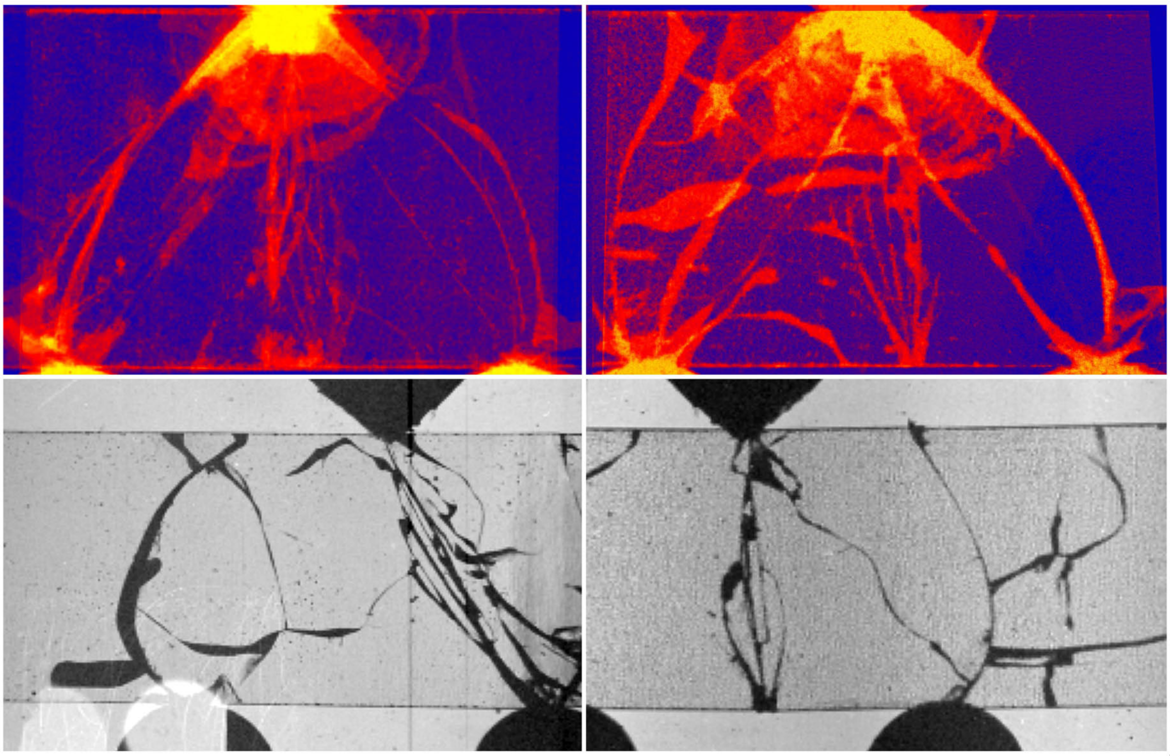

Fig. 56: AVG-mapping results for RX under low ({136}, top left) and high ({636}, top right) impact velocities. Additionally, two examples for the disintegration effect under high impact velocities are depicted (bottom row: [V429B22] and [V430B23], both {606}).

As indicated above (see Fig. 41), Robax is less vulnerable for damage cracks, compared to the other target types: Intermediate cracks and conchoidal cracks are less predominant. Nevertheless, damage cracks show the well known dependencies on hammer geometry and impact velocity (see Fig. 56 (top row)).

[%]	ACB	ACT	SCM	BCM	TCM	C o c
pointed	45,5	9,1		27,3	9,1	9,1
4,5 mm	50,0	20,0		30,0		
8,3 mm	30,0	20,0		50,0		
round	60,0	13,3		20,0		6,7

Table 17: Influence of the hammer geometry on the frequencies of primary crack types in RX ({1X6}).

4. Linear FSED Models

Basic Linear FSED Model

As pointed out in section II.1.5, fracture surface energy density (FSED) is introduced as a crucial parameter to describe energy dissipation processes during fragmentation. In this basic FSED model the respective determination equation is given by (II.1-45). The corresponding "total" FSED η_{tot} of an HIE can be calculated by:

$$\eta_{tot} = \frac{E_{frac}}{A_{frac}} \tag{V.4-1}$$

Crack Class-Specific FSED Model

Yet, one has to bear in mind the results of the studies mentioned above, which indicate that damage cracks and normal cracks differ distinctly in their natures:

Damage cracks are evidently created in zones, which have been passed previously by shock waves. Those for their part have effected a total modification of local material properties, leaving the material susceptible for shear stresses, which finally cause the complex conchoidal crack structures.

These considerations imply, that the respective FSED for damage cracks are most probably significantly different from that for normal cracks.

Therefore as an advanced approach, a second linear ansatz is conducted, assuming two location-independent FSED instead of one: η_{DC} for damage cracks and η_{NC} for normal cracks. Hence, the determination equation for the total energy dissipation due to fracture is given by:

$$E_{frac} = \eta_{NC} \cdot A_{NC} + \eta_{DC} \cdot A_{DC} \tag{V.4-2}$$

where A_{NC} stands for the fracture area of normal cracks, and A_{DC} describes the area of damage crack surfaces.

Under identical constraints, the fragmentation processes of i hammer impact experiments are thus energetically described by the equation:

$$\mathbf{A} \cdot \vec{\eta} = \vec{E} \tag{V.4-3}$$

where $\mathbf{A}$ specifies the resulting amounts of A_{NC} and A_{DC} for each single HIE:

$$\mathbf{A} = \begin{pmatrix} A_{NC\,1} & A_{DC\,1} \\ A_{NC\,2} & A_{DC\,2} \\ \dots & \dots \\ A_{NC\,i} & A_{DC\,i} \end{pmatrix} \tag{V.4-4}$$

The corresponding FSED and fracture energies are given by the vectors $\vec{\eta}$ and $\vec{E}$, which are defined by:

$$\vec{\eta} = \begin{pmatrix} \eta_{NC} \\ \eta_{DC} \end{pmatrix} \tag{V.4-5}$$

$$\vec{E} = \begin{pmatrix} E_{frac\,1} \\ E_{frac\,2} \\ \dots \\ E_{frac\,i} \end{pmatrix} \tag{V.4-6}$$

Note that to determine the fracture surface energy densities $\vec{\eta}$ of a specific material, the data set of an HIE has to be compared to (at least) a second one, which has been recorded under identical constraints.

Furthermore, it is not only necesseary to quantify the amounts of fracture areas A_{frac} and the fracture energies E_{frac}, but also to distinguish between the fracture areas created by normal cracks A_{NC} and damage crack induced areas A_{DC}.

Considerations, ways and results of those procedures are pointed out in the following chapters.

5. Fragment Analysis

5.1. Findings of Morphological Investigations on Fracture Surfaces

To read the traces of fragmentation, thorough SEM investigations on fragments have been performed. The main objective is to obtain additional information about fracturing processes and to find out material-specific characteristics of surface generation. Furthermore, a close look at the surface morphology raises the possibility to check the applicability of some optical planimetrical methods (especially of OPC).

5.1.1. Morphology of Damage Cracks

Damage cracks are characterized by their conchoidal structures, fine radial pits, which are referred to as "radial cracks" and "Wallner lines" in literature [70], plus small parallel cracks, denoted "fracture lances" [84, 118]. A closer examination of conchoidal fracture surfaces, however, reveals the existence of significantly distinguishable zones, depending on the distance to the point of impact: At least four characteristic zones can be identified, denoted in this thesis as "Zone 0" to "Zone 3" (see Fig. 57). Below, each zone is described.

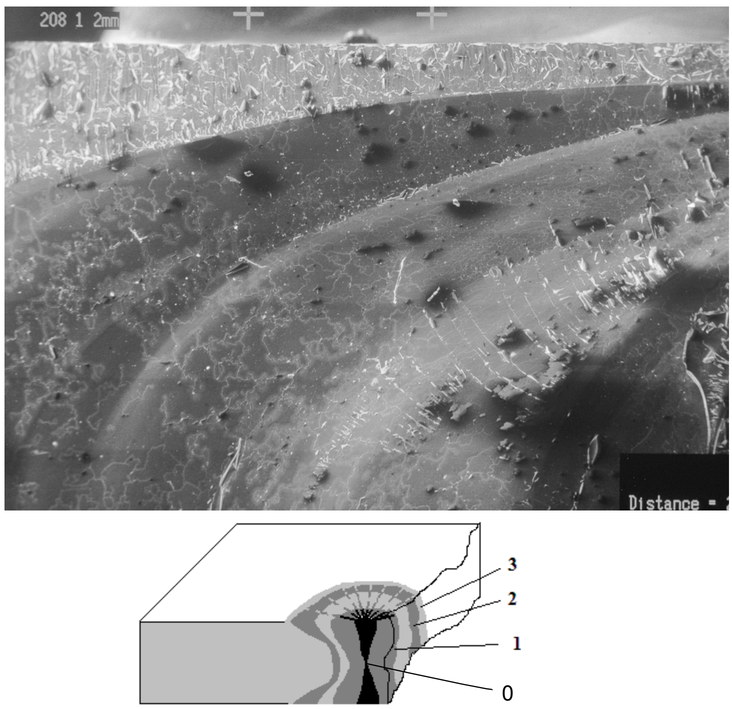

Fig. 57: Discrete zones of conchoidal cracks: At least four specific zones can be identified (schematically depicted below). The SEM image on top shows the surface of a FG fragment. Discrete borders separate the zones 1, 2 and 3 (SE, [V208], {101}). "2 mm" denotes the distance between both hair crosses.

Zone 0: Impact Notch

As pointed out above, a notch is initiated immediately at the moment of impact. SEM studies reveal that the surroundings of the point of impact are a zone of total decomposition (see Fig. 58). This specific “Zone 0” surface morphology is exclusively observed in the vicinity of the point of impact and can thus be presumed to be a feature of highest energy release rates.

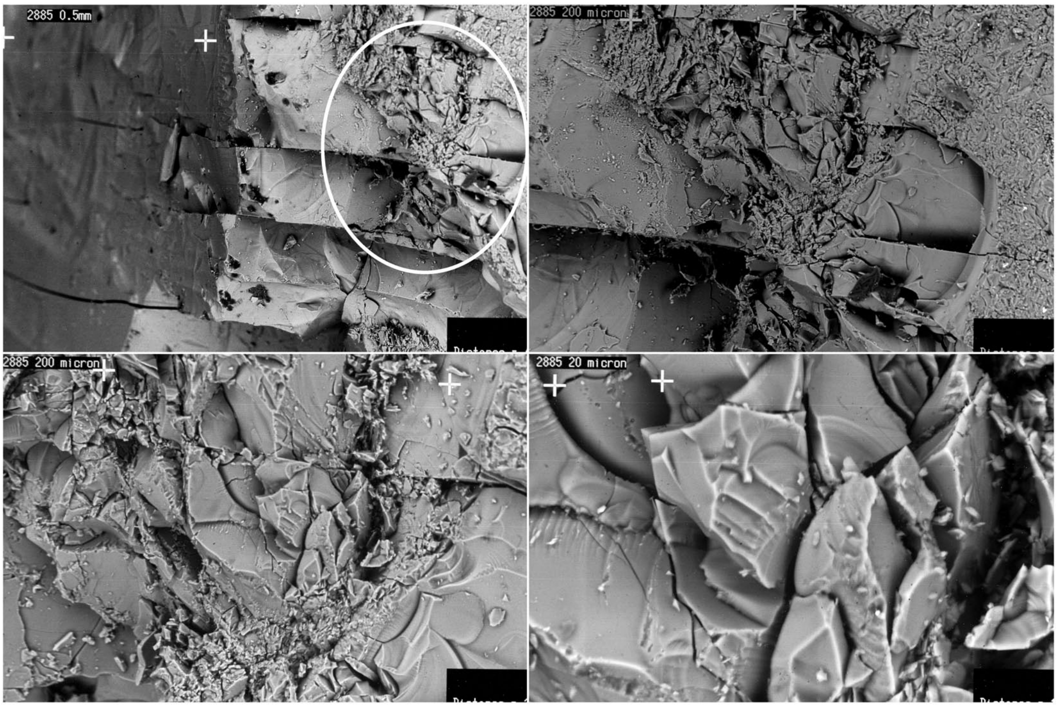

Fig. 58: SEM images showing Zone 0 of a T10 target under various magnifications (BSE, [V288], {103}): The impact notch is marked by a white ellipse in the upper left image. For each image, the scale is given by the distance between two hair crosses.

Due to the model of V.3.4 the subsequent fragmentation is *inter alia* caused by stress waves, which are in fact seismic wave fronts of great pressure gradients.

Evidently, the conditions of mechanical coupling between hammer and sample strongly depend on the extension and the geometry of Zone 0: The initiation of stress waves is significantly affected by the actual contact area as well as by damping effects in this zone.

With this in mind, it becomes clear why HIEs are not reproducible in all details: Even small variations in size and geometry of Zone 0 might have big effects on stress waves.

The fragments generated in this zone are of extraordinary fine grain size and mostly found as deposit particles on “carrier” fragments (see Fig. 64). Due to electrostatic attraction, free isolated particles of this size are very rare.

Zone 1: Trichips

Zone 0 is followed by a fracture zone characterized by small triangular formed, pointed fragments (see Fig. 59), which indicate that this has been a region of high energy release.

It is notable that for all targets, Zone 1 is framed by clearly visible borders. Due to these distinct local limitations of Zone 0, 1 and 2, respectively, one can conclude that energy dissipation in regions, which have been passed previously by shock waves, is not a process linearly depending on the distance to the point of impact, but a discrete, stepped process.

Furthermore, the existence of material-specific parameters can be presumed, which specify the minimum energy density needed for the establishment of each zone, thus confining their extension.

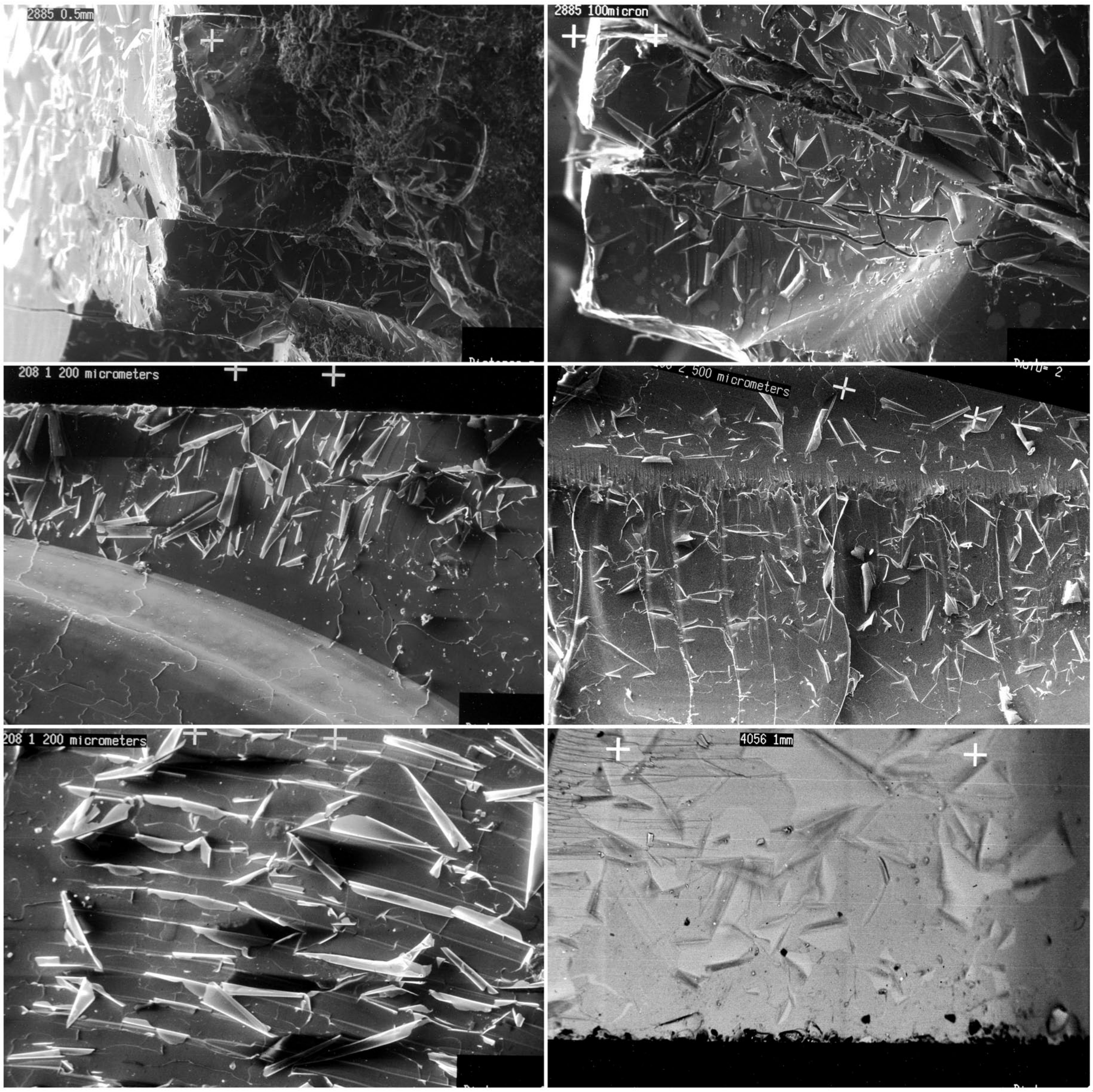

Fig. 59: Zone 1 in different samples: Trichips can be observed in T10 targets (top row: SE, [V288], {103}) as well as in FG (center row and bottom left: SE, [V208], {101}) and in RX (bottom right: BSE, [V405], {106}). The first picture (top left) has been taken from the same position as Fig. 58 (top left), this time detecting secondary instead of back-scattered electrons. Note that Zone 1 is clearly differentiated from the other zones.

Zone 2: Tessellate cracks

The next zone is characterized by very peculiar, shallow microscopic fractures, reminiscent of mosaic patterns (see Fig. 60). Due to this phenomenology, this kind of fracture is denoted "tessellate cracks". In rarely observed cases, those cracks are deep enough to create isolated fragments, which are hence of small size and of flaked shape. It has to be noted that the dimension of "Zone 2" is generally much greater than that of Zone 0 and 1. Furthermore, the transition to Zone 3 is considerably smoother than the transition to Zone 1.

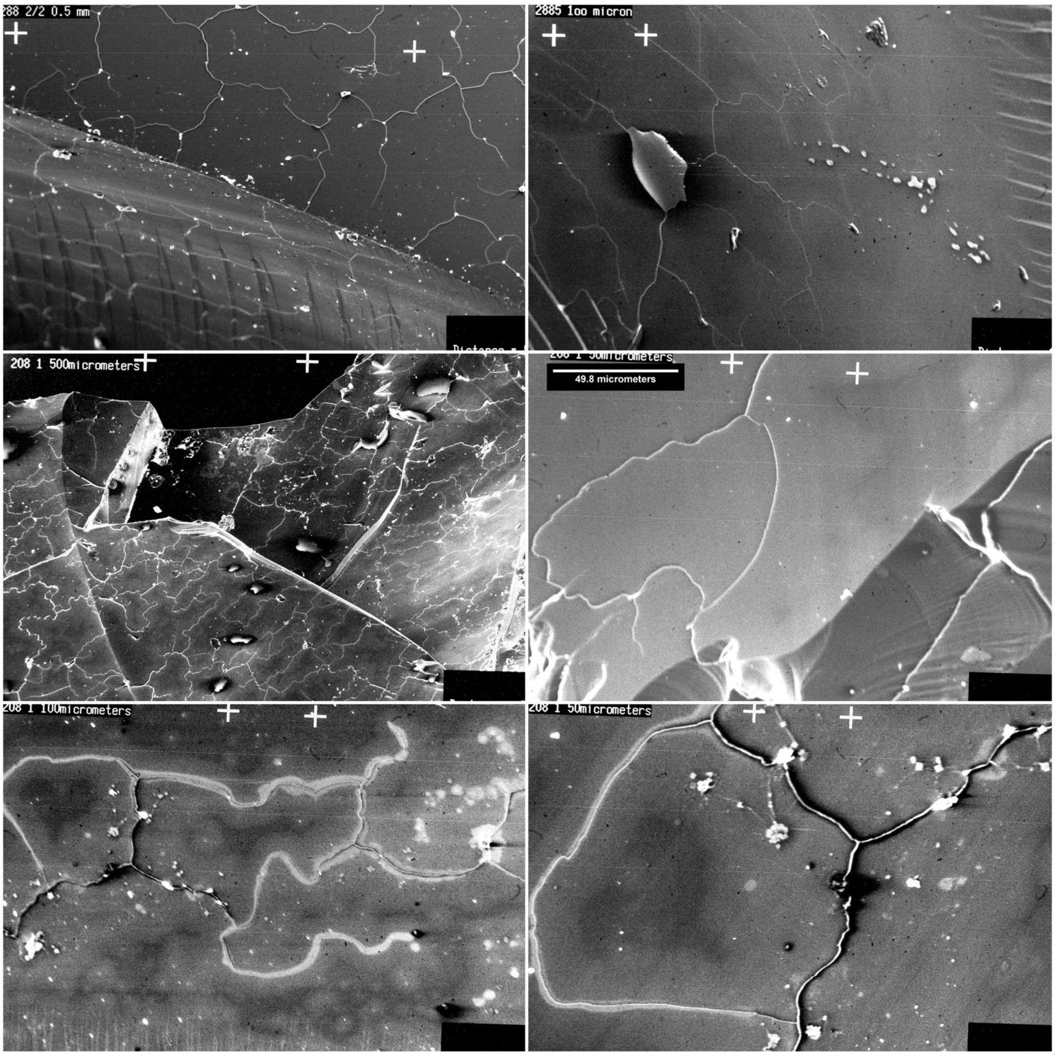

Fig. 60: Zone 2 characterized by tessellate cracks: These kind of fractures have been found in all targets. Here, tessellate cracks in T10 (top row, SE, [V288], {103}) and FG (center and bottom row: SE, [V208], {101}) are depicted. As one can see in the first picture (top left), tessellate cracks are very shallow. The top right image shows the transition between Zone 2 and Zone 3.

Zone 3: "Conventional" conchoidal fracture surface

At least for FG, the features of Zone 3 are already described in literature (e.g. [70, 84, 118]): This zone is characterized by fracture lances and small pits, denoted "Wallner lines" and "radial cracks". The macroscopic shape of conchoidal fracture is referred to as "Hertzian cone fracture" [47, 62, 63], which is a characteristic feature of quasi-static indentation on brittle materials [24]. Fig. 61 provides some morphological insights into the typical structure of Zone 3.

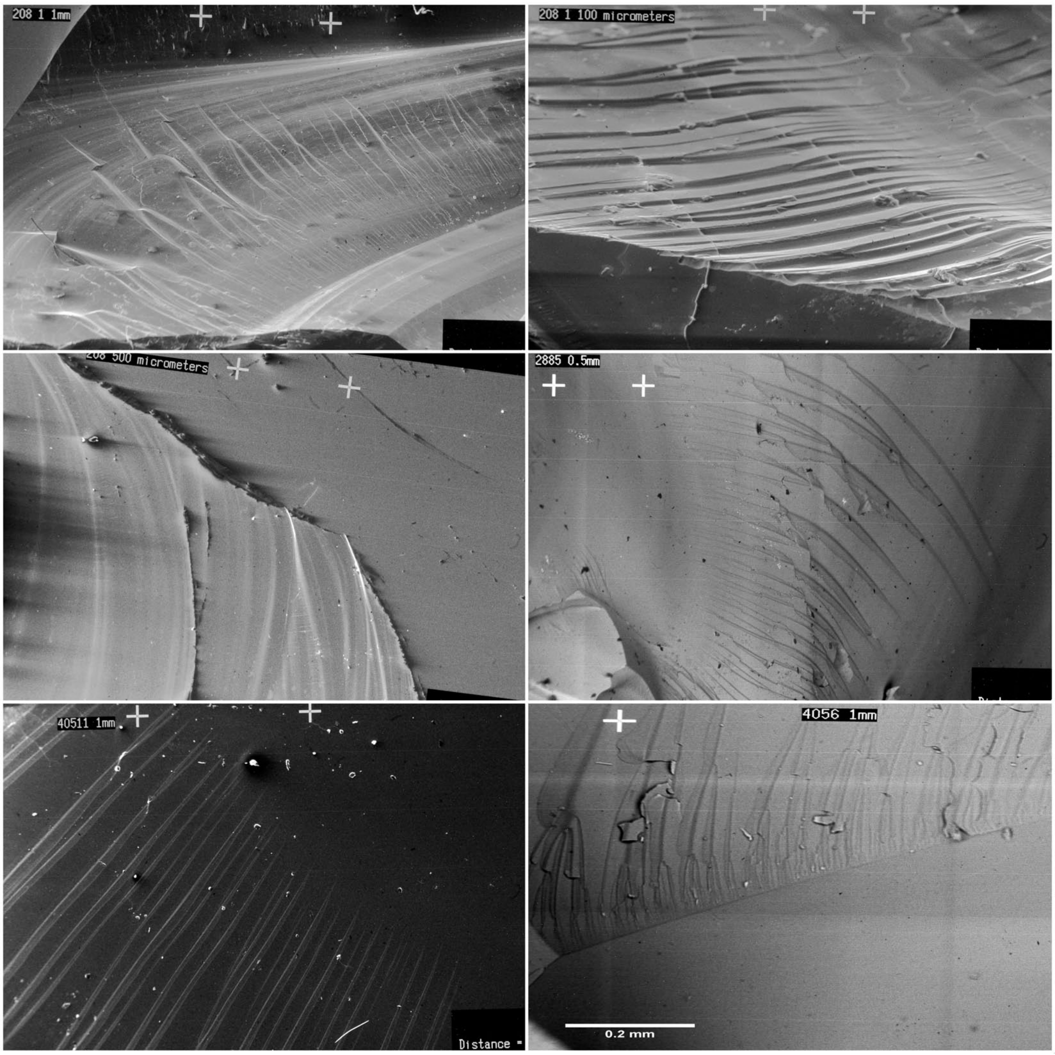

Fig. 61: Zone 3: (Top row and center left: FG: SE, [V208], {101}; center right: T10: SE, [V288], {103}; bottom row: RX: SE, [V405], {106}) In the first picture (top left), the transition from Zone 2 to 3 in FG is depicted. Zone 3 is characterized by the lack of tessellate cracks and by the typical complex conchoidal crack structure, showing stepped surfaces (top right), Wallner lines (center left) and fracture lances (bottom left). The end of Zone 3 determines the perimeter of the damage crack zone (bottom right).

5.1.2. Morphology of Normal Cracks

The breaking edges of all fragments, generated by normal cracks, are characterized by mostly even surfaces (cf. Fig. 62). Only in the vicinity of bifurcation is the fracture mirror marked by a rougher topographical structure (see e.g. Fig. 12). This typical feature is verified for all examined target types. Thus, an important precondition for the applicability of the OPC method is met. In contrast, due to their complexity, the actual surface areas of damage crack structures cannot be determined by optical projection methods.

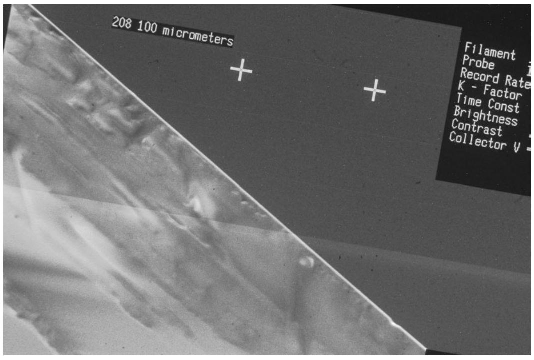

Fig. 62: Fracture mirror, generated by a normal crack in a FG sample (SE, [V208], {101}): The breaking edge shows a nearly even surface.

5.1.3. Material-Specific Features of Fracture Mirrors

The fracture morphology of T10 fragments is very similar to that of FG particles.

One characteristic feature, however, which has only been observed in thermally pre-stressed float glasses, is depicted in Fig. 58 (top left): The fragment consists of several parallel superposed layers, which are shifted against each other. As a consequence, one can detect rather deep parallel cracks running through the fragments (see also Fig. 59 (top row)). It has to be stated that these "foliation fractures" are only observed in central fragment pieces near the point of impact, which are always marked by distinct damage crack structures. Normal crack surfaces never appear to be affected.

In general, RX fragments are characterized by a significantly "smoother" surface, as depicted in Fig. 63. Additionally trichips and tessellate cracks are much less pronounced in RX than in float glass fragments.

The smooth structure of fracture mirrors in RX is a strong indication, that the amount of energy needed to generate fracture surfaces is distinctly higher in these samples than in other target types. As a consequence one expects significant higher values for the RX-specific FSED.

5.1.4. Backtracking of Particles

Considering the zoning of conchoidal cracks makes it possible to determine the origin of fragments (see Fig. 64): Zone 0-particles are extraordinarily small and can usually be found only on carrier fragments (a and b). Particles stemming from Zone 1 are marked by a typical jagged shape due to trichips (c), whereas Zone 2 particles are characterized by tessellate cracks on their surfaces (d).

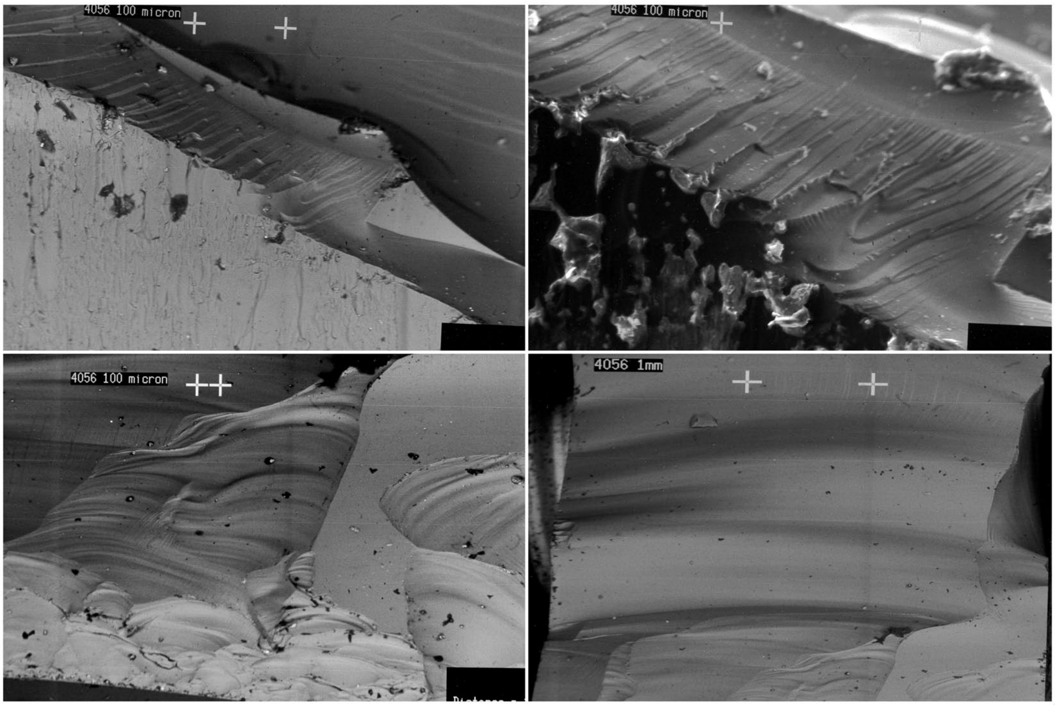

Fig. 63: Fracture mirrors of RX fragments: Note that the breaking edges in glass ceramic targets are distinctly smoother than in float glass samples (top left and bottom row: BSE; top right: SE; all: [V405], {106}).

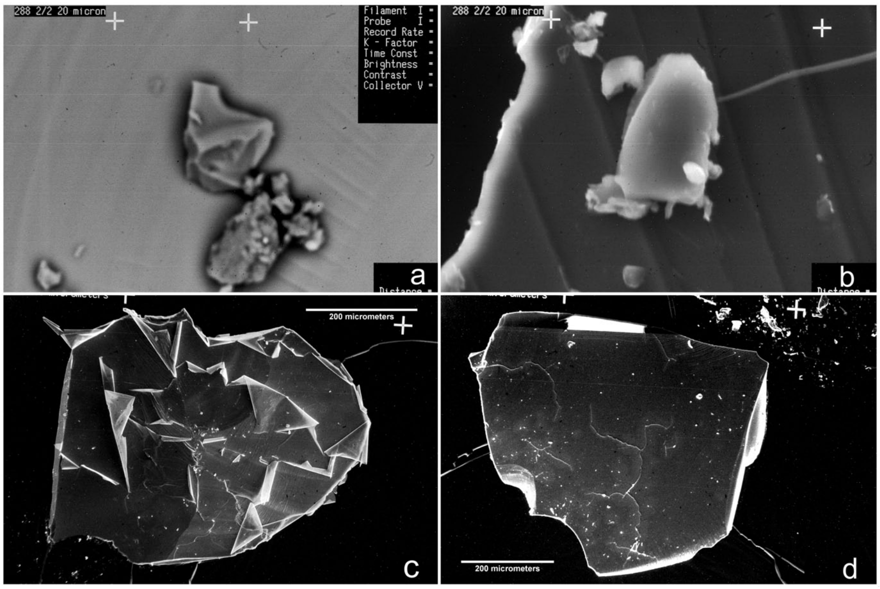

Fig. 64: Backtracking of particles: Fragments can easily be traced back to their origins. As representative examples, Zone 0-particles are depicted (top row: [V208], {101}; a: BSE, b: SE). Note that the shape of these particles is very similar to that of larger scaled fragments, indicating self-similarity. The bottom row (both: SE, [V288], {103}) shows typical particles, which stem from Zone 1 (c), and from a region localized at the border of Zone 2 next to Zone 3 (d), respectively.

5.2. Results of Sieving Analyses

All screen analyses provide grain size distributions of distinct skewness (e.g. Fig. 65): Very few large fragments (with very low fracture areas, as we will see later) make up the bulk of the particle masses. As shown below, this characteristic skewness is also of great importance in the consideration of the kinetic energies of fragments.

An exhaustive description of sieving analysis results would go far beyond the scope of this thesis, which focuses on the energetic dissipation processes of fragmentation. Instead, in this section only the most conspicuous effects of impact velocity, hammer geometry and target type on grain size distributions are briefly outlined and demonstrated by representative examples. Comprehensive data of sieving analysis can be found in Appendix C.

5.2.1. Grain Size Distribution and Impact Velocity

Fig. 65 shows typical grain size distributions of HIE fragments, generated under low and high impact velocity respectively.

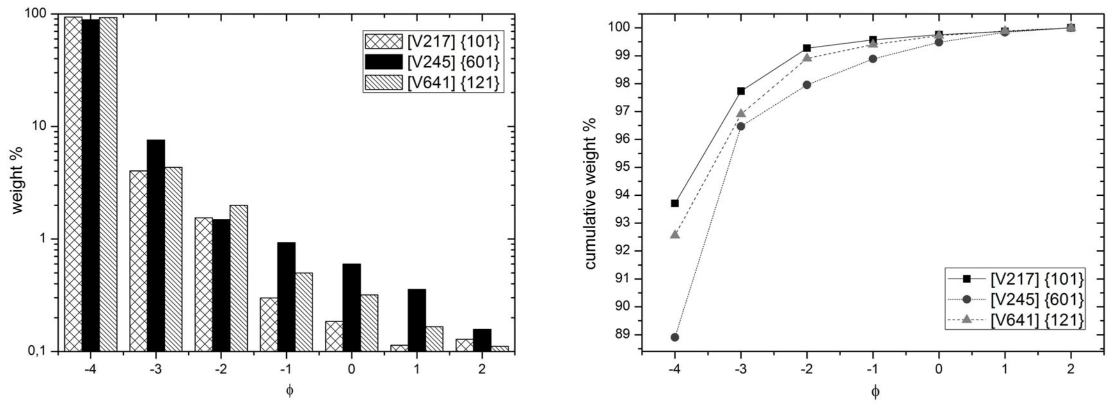

Fig. 65: Sieving analysis results for FG fragments: The grain size distribution (left) and cumulative mass fractions (right) of representative examples are plotted (see keys and text).

V		ϕ :	-4	-3	-2	-1	0	1	>1
	m_ϕ	[g]	65,68	2,82	1,08	0,21	0,13	0,08	0,09
217	$n\,(m_\phi)$	[%]	93,71	4,02	1,54	0,30	0,19	0,11	0,13
	$N\,(m_\phi)$	[%]	93,71	97,73	99,27	99,57	99,76	99,87	100,00
	m_ϕ	[g]	62,16	5,29	1,04	0,65	0,42	0,25	0,11
245	$n\,(m_\phi)$	[%]	88,9	7,57	1,49	0,93	0,60	0,36	0,16
	$N\,(m_\phi)$	[%]	88,9	96,47	97,96	98,89	99,49	99,85	100,00
	m_ϕ	[g]	66,69	3,13	1,44	0,36	0,23	0,12	0,08
641	$n\,(m_\phi)$	[%]	92,56	4,34	2,00	0,50	0,32	0,17	0,11
	$N\,(m_\phi)$	[%]	92,56	96,9	98,9	99,4	99,72	99,89	100,00

Table 18: Mass distribution data represented in Fig. 65: Mass m_ϕ, mass fraction $n\,(m_\phi)$ and cumulative mass fraction $N\,(m_\phi)$ are displayed for each sieve fraction.

It is evident, that in the case of high impact velocity ({601}) the mass of coarse particles (i.e. $\phi \leq -2$) is lower than in the case of low impact velocity, whereas the mass of "fine" particles (defined as $\phi \geq -1$) is significantly greater. The growing mass of fine particles coincides very well with the results for conchoidal cracks (see chapter V.3): Under higher impact velocities damage cracks are distinctly more pronounced. This significant interrelationship is a strong indication that the fractions of fine particles are dominated by damage cracks, a fact which is of utmost importance for the determination of FSED.

5.2.2. Grain Size Distribution and Hammer Geometry

This conclusion is also confirmed by the results of comparative grain size studies, in which the effect of the hammer geometry was analyzed (cf. Fig. 66).

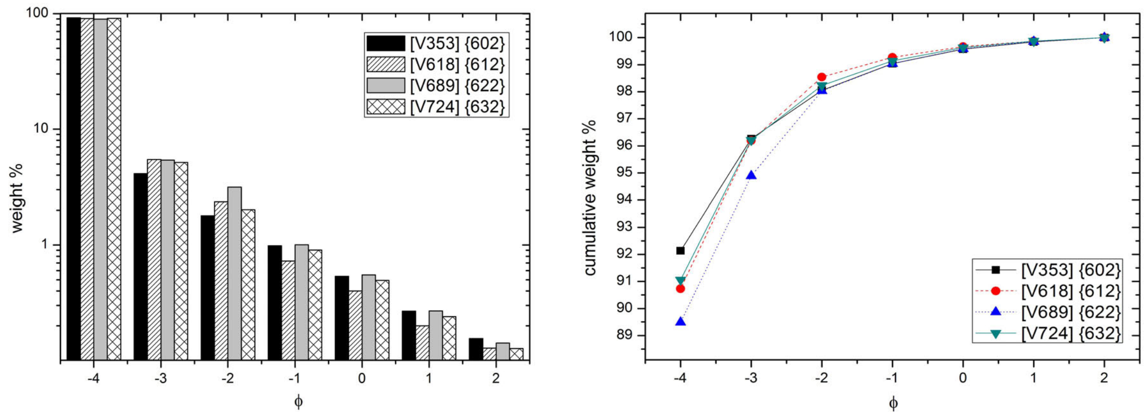

Fig. 66: Sieving analysis results of HIEs with T5 targets under the use of various hammer geometries: The grain size distribution (left) and cumulative mass fractions (right) of representative examples are plotted (see keys and text).

V		ϕ :	-4	-3	-2	-1	0	1	>1
	m_ϕ	[g]	65,33	2,93	1,27	0,70	0,38	0,19	0,11
353	$n(m_\phi)$	[%]	92,13	4,13	1,79	0,99	0,54	0,27	0,16
	$N(m_\phi)$	[%]	92,13	96,26	98,05	99,04	99,58	99,85	100,00
	m_ϕ	[g]	63,63	3,83	1,65	0,51	0,28	0,14	0,09
618	$n(m_\phi)$	[%]	90,73	5,46	2,35	0,73	0,40	0,20	0,13
	$N(m_\phi)$	[%]	90,73	96,19	98,54	99,27	99,67	99,87	100,00
	m_ϕ	[g]	63,18	3,81	2,22	0,71	0,39	0,19	0,10
689	$n(m_\phi)$	[%]	89,49	5,40	3,14	1,01	0,55	0,27	0,14
	$N(m_\phi)$	[%]	89,49	94,89	98,03	99,04	99,59	99,86	100,00
	m_ϕ	[g]	64,45	3,65	1,43	0,64	0,35	0,17	0,09
724	$n(m_\phi)$	[%]	91,06	5,16	2,02	0,90	0,49	0,24	0,13
	$N(m_\phi)$	[%]	91,06	96,22	98,24	99,14	99,63	99,87	100,00

Table 19: Mass distribution data represented in Fig. 66: Mass m_ϕ, mass fraction $n(m_\phi)$ and cumulative mass fraction $N(m_\phi)$ are displayed for each sieve fraction.

Although the coarse fractions $\phi \leq -2$ show quite inconclusive results and large deviations, the finer fractions $-1 \leq \phi \leq 1$ are significantly distributed in correlation to the hammer geometry: In general, the mass of these particles m_f increases due to the order given by:

$$m_{f,pointed} < m_{f,round} < m_{f,4{,}5\,mm} < m_{f,8{,}3\,mm} \tag{V.5-1}$$

where the second index describes the hammer geometry. This dependency is identical to that for conchoidal crack intensities shown in chapter V.3.

An important exception to this empirical rule is observed for the finest fraction: An explanation could be given by the fact, that the fraction $\phi > 1$ is dominated by Zone 0-particles and trichips, whose generation is correlated to the amount of locally prevailing energy density at the moment of impact. This local density of mechanical energy is presumed to be distinctly greater for a pointed hammer than in case of a flat hammer, which exerts a lower local pressure under otherwise identical conditions.

5.2.3. Material-Specific Effects on Grain Size Distribution

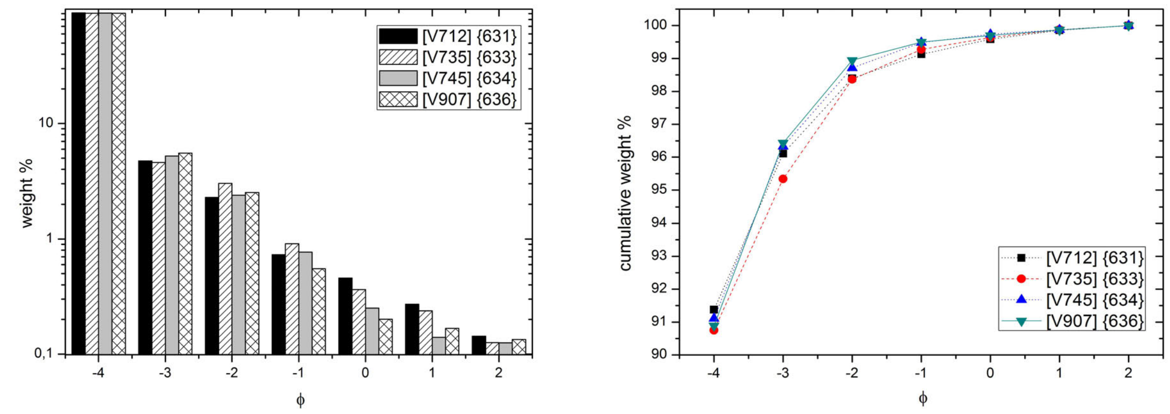

Fig. 67: Sieving analysis results of HIEs with various target types: The grain size distribution (left) and cumulative mass fractions (right) of representative examples are plotted (see keys and text).

V	ϕ :	ϕ :	-4	-3	-2	-1	0	1	>1
	m_ϕ	[g]	63,89	3,31	1,60	0,51	0,32	0,19	0,10
712	$n\,(m_\phi)$	[%]	91,38	4,73	2,29	0,73	0,46	0,27	0,14
	$N\,(m_\phi)$	[%]	91,38	96,11	98,40	99,13	99,59	99,86	100,00
	m_ϕ	[g]	63,76	4,44	1,57	0,68	0,27	0,16	0,10
735	$n\,(m_\phi)$	[%]	90,75	4,59	3,02	0,91	0,36	0,24	0,13
	$N\,(m_\phi)$	[%]	90,75	95,34	98,36	99,27	99,63	99,87	100,00
	m_ϕ	[g]	65,27	3,74	1,71	0,55	0,18	0,10	0,09
745	$n\,(m_\phi)$	[%]	91,11	5,22	2,39	0,77	0,25	0,14	0,13
	$N\,(m_\phi)$	[%]	91,11	96,33	98,72	99,49	99,74	99,88	100,00
	m_ϕ	[g]	54,27	3,31	1,50	0,33	0,12	0,10	0,08
907	$n\,(m_\phi)$	[%]	90,89	5,54	2,51	0,55	0,20	0,17	0,13
	$N\,(m_\phi)$	[%]	90,89	96,43	98,94	99,49	99,69	99,86	100,00

Table 20: Mass distribution data represented in Fig. 67: Mass m_ϕ, mass fraction $n\,(m_\phi)$ and cumulative mass fraction $N\,(m_\phi)$ are displayed for each sieve fraction.

This "smallest fraction effect" has been observed for all target types. For RX targets, however, it is less pronounced, which probably could be a consequence of the fact that in RX samples significantly less Zone 0-particles and trichips are generated.

Thus, the finest fraction (which is in fact the screen underflow through the finest mesh size) of RX particles is less dominated by those particle types than in case of other materials.

Fig. 67 shows representative grain size distributions of HIE particles under the use of different target types: The total mass fraction of fine particles (i.e. $\phi \geq -1$, as defined above) reaches slightly higher values for T10 targets than in the case of HIEs with FG, but significantly lower values for TK and RX targets. In the displayed comparison (see Fig. 67, Table 20) the respective results for the total mass fractions of fine particles are for FG: 1,60 %, for T10: 1,64 %, for TK: 1,29 %, and for RX: 1,05 %.

The low values for glass ceramics coincide well with the previously determined distinctly lower sensitivity of RX to damage cracks and thus -due to the above mentioned damage crack theory- to shock waves.

It is of interest, that also TK targets show significantly lower mass fraction values for fine particles. This result indicates, that the location of existing pre-stresses has a big influence on the target's susceptibility to shock waves and on the generation processes of fine fragments.

Apart from these material-specific features, screen analyses have provided very similar results. For all target types the grain size distribution of HIE particles shows the same dependencies on impact velocity as well as on hammer geometry. These results of sieving analysis suggest that it is just the level of these influences, which depends on the target type.

5.3. Fracture Area Quantification Model

5.3.1. Quality Control

A simple method was used to check the quality of the examined set of fragments: The total mass of the target was determined before and after the HIEs. If the deviation was more than 1 % of the total mass, the concerning set of particles was not used for evaluation. The quota of "valid" cases has amounted to 93 % of the total quantity.

5.3.2. Classification of Fragments

According to chapter V.4 one has to segregate fracture areas according to their underlying fracture processes, in order to quantify the matrix components A_{NC} and A_{DC} in (V.4-4). This is facilitated by categorizing all fragments and performing class-specific area planimetry.

Therefore an approach is adopted, which has been partially proposed in [40]: The fragments are segregated in four fragment classes, denoted by Roman numerals (see also Fig. 68):

- Class I-fragments are particles of coarse grain size, which are generated exclusively by normal cracks. Thus, these fragments are characterized by breaking edges with plane surface morphology.

- Class II-fragments are very similar to class I-fragments, but they additionally show traces of damage cracks.

- Class III-fragments are the result of intensive crack branching: The interior of these coarse particles are traversed by parallel normal cracks (see Fig. 69 for details). Consequently, all fracture areas of these fragments are assigned to A_{NC}.

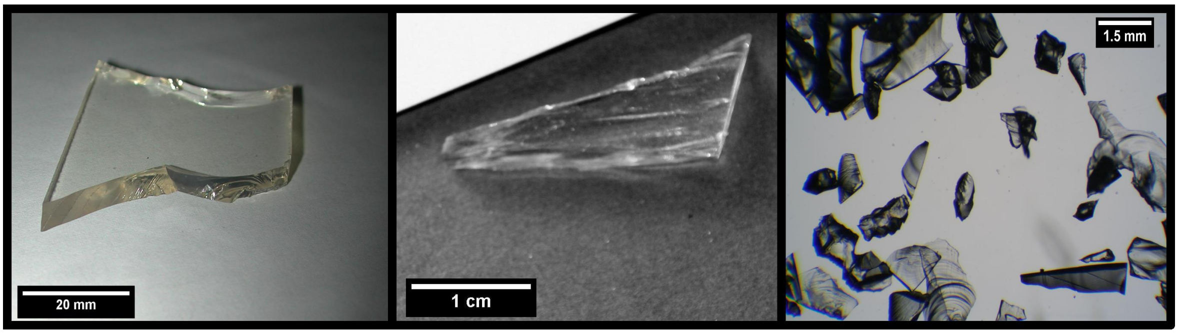

Fig. 68: Fragment classes: From left to right typical fragments of class I, III and IV are depicted. An example for a class II-fragment is shown in Fig. 28.

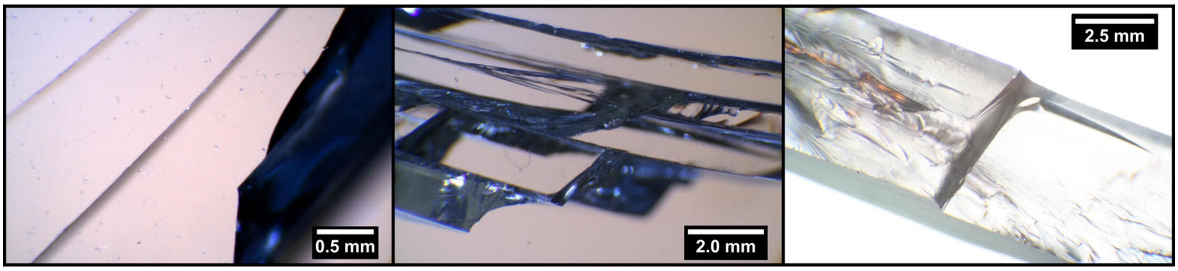

Fig. 69: Microscope photographs of class III-fragments: These particles are traversed by parallel normal cracks (left). A closer look at the breaking edges reveals, that fracture areas of these fragments are comparatively plane (center and right). Therefore, OPC can be used to quantify the fracture area.

- Due to the sieving analysis results, it makes sense to assign all particles $\phi \geq -1$ (hence particles of a grain size less than 4 mm) to a specific class. These fragments which have previously been subsumed "fine particles", are also denoted "class IV-fragments".

Fragment class	Grain size	Generation
I	$\phi \leq -2$ ($\geq 4\,\mathrm{mm}$)	exclusively by normal cracks
II	$\phi \leq -2$ ($\geq 4\,\mathrm{mm}$)	by normal cracks as well as by damage cracks
III	$\phi \leq -2$ ($\geq 4\,\mathrm{mm}$)	by bifurcating normal cracks
IV	$\phi > -2$ ($< 4\,\mathrm{mm}$)	predominantly by damage cracks

Table 21: Fragment classes (see also text).

5.3.3. Gross Areas

In many cases, it is not possible to measure the actual fracture area A. Instead, one obtains the "gross" area B of the sample, which is the total sum of both "pre-" and "post-fracture" surface areas. From this one has to subtract the "pre-fracture" areas N, which are the areas already existing before the HIE.

Quantifying crack-specific fracture areas is quite a complex problem, as a combination of different planimetrical methods have to be used, depending on the fragment classes.

In principal, the fragment class is indicated by a Roman numeral, and the applied planimetrical method is given by the initials introduced in chapter III.5.2.

The total gross area B_{tot} is given by the sum of the areas of all fragment classes:

$$B_{tot} = B_I + B_{II} + B_{III} + B_{IV} \tag{V.5-2}$$

In detail, the components of this equation are determined as follows:

- B_I is quantified by TEH or CAD. This interchangeability of methods is used to check the measuring accuracy of both planimetrical methods and is also expressed by a slash.

$$B_I = B_I^{(TEH/CAD)} \tag{V.5-3}$$

- B_{II} is quantified by TEH or CAD. As for B_I this interchangeability is used to check the respective measuring accuracy. Usually, TEH has been used as the standard measuring method.

$$B_{II} = B_{II}^{(TEH/CAD)} \tag{V.5-4}$$

- B_{III} can be quantified by a combination of TEH and OPC. As TEH provides only results for free surface areas $B_{III,free}^{(TEH)}$, additional measurements have to be performed to get also the internal fracture areas $A_{III\,intern}$. Therefore OPC was applied:

$$B_{III} = B_{III,free}^{(TEH)} + A_{III,intern}^{(OPC)} \tag{V.5-5}$$

  As shown below, there is a simpler way to quantify A_{III}, and hence B_{III} is only determined for control purposes.

- B_{IV} is quantified by TEH or by a combination of TEH and BET. As BET only provides good results for the finest fraction $\phi > 1$, it is useful to distinguish between the gross area of finest class IV-fragments $B_{IV,\phi>1}$ and the residual gross areas of this class $B_{IV,\phi\leq 1}$. The results of BET are used to check the accuracy of the TEH method for the finest particles.

$$B_{IV} = B_{IV,\phi\leq 1}^{(TEH)} + B_{IV,\phi>1}^{(TEH/BET)} \tag{V.5-6}$$

Before each HIE, the dimensions of the target have been quantified (sample width b, height h, thickness d). Thus, determining the actual total fracture surface A_{tot} is simply:

$$A_{tot} = B_{tot} - N_{tot} = B_{tot} - 2 \cdot b \cdot h - 2 \cdot d \cdot h - 2 \cdot b \cdot d \tag{V.5-7}$$

5.3.4. The Finest Fraction

As pointed out in chapter V. 5.2.2, the screen analysis results indicate, that the finest particles $\phi > 1$ are dominated by Zone 0-particles and trichips. This conclusion is confirmed by the results of additional granulometric studies, which reveal that there is no linear correlation between the finest mass fraction $n\,(m_{\phi>1})$ and the extension of damage crack, nor between $n\,(m_{\phi>1})$ and the number of crack branches Z. These results strongly support the theory that the finest particles are generated exclusively in areas of high energy density, which means in the vicinity of the impact notch.

This affected area is confined to a very small region of the target. Hence, compared to the generated amount of post-fracture area (see below), the values for the pre-fracture areas of the impact notch and trichips zone are at least two orders of magnitude lower.

Therefore the pre-fracture area $N_{IV,\phi>1}$ can be neglected, and thus:

$$A_{IV,\phi>1} = B_{IV,\phi>1} - N_{IV,\phi>1} \approx B_{IV,\phi>1} \tag{V.5-8}$$

Furthermore, the proportion of $N_{IV,\phi>1}$ to the total pre-fracture area of class IV-fragments N_{IV} is negligibly small, and as a consequence one can approximate:

$$N_{IV} = N_{IV,\phi>1} + N_{IV,\phi\leq 1} \approx N_{IV,\phi\leq 1} \tag{V.5-9}$$

5.3.5. Approach to Determine A_{DC} and A_{NC}

The fracture area caused by damage cracks A_{DC} can be calculated by:

$$A_{DC} = A_{II,DC} + A_{IV,DC} \tag{V.5-10}$$

with $A_{II,DC}$ and $A_{IV,DC}$ describing the amount of fracture area, which was exclusively generated by damage cracks in class II- and class IV- fragments, respectively.

By introducing κ:

$$\kappa = \frac{A_{IV,\phi\leq 1,DC}}{A_{IV,\phi\leq 1}} \tag{V.5-11}$$

as a factor which quantifies the ratio between the damage crack induced fracture area of $\phi \leq 1$ class IV-particles and the total fracture area of these particles, one obtains the following general equation for A_{DC}:

$$A_{DC} = \kappa \cdot (B_{IV,\phi\leq 1} - N_{IV,\phi\leq 1}) + (B_{IV,\phi>1} - N_{IV,\phi>1}) + A_{II,DC} \tag{V.5-12}$$

which can be simplified by the approximations (V.5-8) and (V.5-9):

$$A_{DC} \approx \kappa \cdot (B_{IV,\phi\leq 1} - N_{IV}) + B_{IV,\phi>1} + A_{II,DC} \tag{V.5-13}$$

The fracture area induced by normal cracks A_{NC} is described by:

$$A_{NC} = A_I + A_{II,NC} + A_{III} + (1-\kappa) \cdot A_{IV,\phi\leq 1} \tag{V.5-14}$$

Taking into account (V.5-3) the fracture area of class I-fragments can easily be determined by:

$$A_I = B_I^{(TEH/CAD)} - N_I^{(OPT)} \tag{V.5-15}$$

For class II-fragments, however, the fracture area $A_{II;all}$ is a composition of $A_{II,NC}$ and $A_{II,DC}$:

$$A_{II,all} = A_{II,NC} + A_{II,DC} = B_{II}^{(TEH)} - N_{II}^{(OPT)} \tag{V.5-16}$$

and thus by means of TEH, OPT and OPC:

$$A_{II,DC} = B_{II}^{(TEH)} - N_{II}^{(OPT)} - A_{II,NC}^{(OPC)} \tag{V.5-17}$$

There are two possible ways to quantify the fracture area of class III-fragments: One possibility is to conduct a combination of TEH, OPC and OPT measurements, using a relation derived from:

$$A_{III} = B_{III} - N_{III}^{(OPT)} \tag{V.5-18}$$

Considering (V.5-5) one obtains:

$$A_{III} = B_{III,free}^{(TEH)} + A_{III,intern}^{(OPC)} - N_{III}^{(OPT)} \tag{V.5-19}$$

This method however is quite elaborate. Alternatively, A_{III} can be determined by quantifying free and internal fracture areas exclusively by means of OPC:

$$A_{III} = A_{III}^{(OPC)} \tag{V.5-20}$$

This way has been selected as a standard method, whereas the measurements needed for (V.5-19) have only been taken to check the accuracy of OPC.

The fracture area of class IV-particles is given by:

$$A_{IV} = B_{IV} - N_{IV} \tag{V.5-21}$$

Determining the pre-fracture area of class IV-fragments N_{IV}, which is needed to obtain the fracture area of fine particles, is quite a complex task. With (V.5-7) a solution for this problem is given by the expression:

$$\begin{aligned} N_{IV} &= N_{tot} - N_I^{(OPT)} - N_{II}^{(OPT)} - N_{III}^{(OPT)} && \text{(V.5-22)} \\ &= 2 \cdot (b \cdot h + d \cdot h + b \cdot d) - N_I^{(OPT)} - N_{II}^{(OPT)} - N_{III}^{(OPT)} && \text{(V.5-23)} \end{aligned}$$

Considering (V.5-13), as well as (V.5-4), (V.5-6), (V.5-16), (V.5-17) and (V.5-23), the following expression is obtained for damage crack induced fracture areas:

$$\begin{aligned} A_{DC} &\approx \kappa \cdot \left[B_{IV,\phi\leq 1}^{(TEH)} - 2 \cdot (b \cdot h + d \cdot h + b \cdot d) + N_I^{(OPT)} + N_{II}^{(OPT)} + N_{III}^{(OPT)} \right] \\ &+ B_{IV,\phi>1}^{(TEH/BET)} + B_{II}^{(TEH)} - N_{II}^{(OPT)} - A_{II,NC}^{(OPC)} && \text{(V.5-24)} \end{aligned}$$

Taking into account (V.5-3), (V.5-9), (V.5-15) and (V.5-14), normal crack induced fracture areas are given by:

$$\begin{aligned} A_{NC} &\approx B_I^{(TEH/CAD)} - N_I^{(OPT)} + A_{II,NC}^{(OPC)} + A_{III}^{(OPC)} + (1 - \kappa) \cdot \\ &\cdot \left[B_{IV,\phi\leq 1}^{(TEH)} - 2 \cdot (b \cdot h + d \cdot h + b \cdot d) + N_I^{(OPT)} + N_{II}^{(OPT)} + N_{III}^{(OPT)} \right] && \text{(V.5-25)} \end{aligned}$$

5.3.6. Approximate Solutions for A_{DC} and A_{NC}

The only parameter in (V.5-24) and (V.5-25), which cannot readily be quantified, is κ. Nevertheless, considering the occurring cracks, there are just two possible sources for fine particles of a diameter less than 4 mm:

- Damage cracks, which evidently generate particles smaller than the target thickness d.
- Regions of intensive normal crack branching.

To check the influence of these two possible generation sources, correlation analyses have been conducted for all targets (see e.g. Table 22 for FG):

		$m_{\phi=-1}$	$m_{\phi=0}$	$m_{\phi=1}$	$B_{IV,\phi=-1}$	$B_{IV,\phi=0}$	$B_{IV,\phi=1}$	$B_{IV,\phi>1}$
Z	ρ	0,231	0,228	0,261	0,236	0,235	0,267	0,178
	p	13,1 %	13,6 %	8,7 %	12,3 %	12,5 %	8,0 %	24,8 %
M_R	ρ	0,585*	0,719*	0,634*	0,583*	0,714*	0,630*	0,300*
	p	$<$ 0,05 %	$<$ 0,05 %	$<$ 0,05 %	$<$ 0,05 %	$<$ 0,05 %	$<$ 0,05 %	0,5 %

Table 22: Results of bivariate correlation analyses for FG: The Pearson correlation coefficients ρ are shown as well as the corresponding error probability p. Significant linear correlations are marked by an asterisk. There is no significant correlation between the number of crack branches Z and the mass m, nor the measured area of various fractions for class IV-fragments B_{IV}. In contrast to these results, the latter data sets are linearly correlated to the intensity of conchoidal cracks M_R with high significance. The sample size of these studies has been $N = 44$ in the case of Z and $N = 85$ in the case of M_R.

The results show no significant correlation between the data sets of fine particles and the intensity of crack branching, which is specified by the number of crack branches Z. Nevertheless, there is a highly significant linear correlation between the intensity of conchoidal cracks

M_R on the one hand and the mass and area of all fine particle fractions on the other hand. These results coincide well with the conclusions drawn before on the basis of sieving analyses (cf. section V.5.2.2): The bulk of fine particles $\phi \geq -1$ are generated by damage cracks, the influence of normal crack induced particles in these fractions is negligible.

Thus, κ is approximately given by:

$$\kappa \approx 1 \tag{V.5-26}$$

As a consequence, the expressions (V.5-24) and (V.5-25) can be substantially simplified. Thus, an approximation for A_{DC} is given by:

$$\begin{aligned} A_{DC} \quad \approx \quad & B_{IV,\phi\leq 1}^{(TEH)} - 2\cdot(b\cdot h + d\cdot h + b\cdot d) + N_I^{(OPT)} + N_{III}^{(OPT)} \\ + \quad & B_{IV,\phi>1}^{(TEH/BET)} + B_{II}^{(TEH)} - A_{II,NC}^{(OPC)} \end{aligned} \tag{V.5-27}$$

Furthermore, A_{NC} is determined by:

$$A_{NC} \approx B_I^{(TEH/CAD)} - N_I^{(OPT)} + A_{II,NC}^{(OPC)} + A_{III}^{(OPC)} \tag{V.5-28}$$

A_{DC} and A_{NC} can now be calculated by means of (V.5-27) and (V.5-28) and applying the specified methods to quantify the required parameters.

5.4. Planimetrical Concept for Fine Particles

Performing TEH analyses for class IV-fragments is quite an elaborate job, because each fraction has to be calibrated by similar sized standard samples. Furthermore, the measuring accuracy depends on the screen fraction.

Therefore a concept was developed to simplify planimetrical measurements, exploiting the fact that the particles in most fractions are self-similar.

5.4.1. Considerations for the Heywood Factor

If within a specific fraction, the grain size of particles is distributed symmetrically (which is the case, e.g. for normal or also for uniform distributions), in (III.4-6) x can be replaced by the average grain size $\bar{x}$ of the observed fraction, which is given by:

$$x \rightarrow \bar{x} = \frac{1}{2}\cdot(x_u + x_l) \tag{V.5-29}$$

where x_u and x_l denote the upper and the lower screen diameters of the observed fraction. For example, for $\phi = 1$, $\bar{x}$ is assigned a value of $0,75\,mm$. Thus, (III.4-6) can be modified:

$$f_H = \frac{1}{12}\cdot(x_u + x_l)\cdot\rho\cdot S_m \tag{V.5-30}$$

Transformation of (III.4-5) and (V.5-30) provides:

$$A = \frac{12\cdot f_H\cdot m}{\rho\cdot(x_u + x_l)} \tag{V.5-31}$$

Under the condition of self-similarity, the Heywood factor f_H is invariant towards grain size. This implies, that if f_H has been calculated for one fraction, the areas of all other fractions, which are self-similar to the first one, can be calculated by means of (V.5-31). The only measurement to conduct is to perform a screen analysis and to quantify the fraction mass.

As pointed out, the presented planimetrical Heywood concept is valid under two conditions:

1. Within a fraction, the grain size distribution has to be symmetrical, so that (V.5-29) is validated.

2. The concept bases substantially on self-similarity of the studied fractions.

Therefore, both conditions have to be checked for all fractions.

5.4.2. Grain Size Investigations within a Fraction

For various cases the grain size distribution within different fractions has been determined by means of microscopic measurements. The results for {101} are displayed in Fig. 70 and are representative for all studied cases. The grain sizes of the fractions $\phi = -1$, 0 and 1 always appear to be equally distributed.

In contrast to that, the grain size distribution of the finest particles $\phi > 1$ show significant differences: They assume normal distribution.

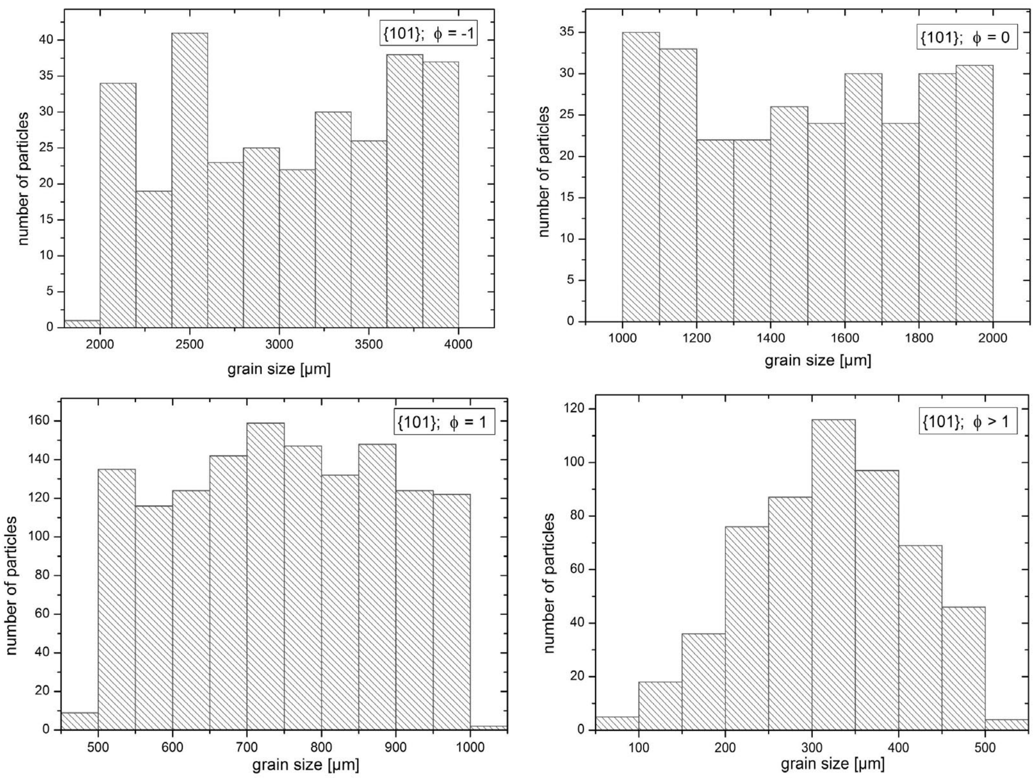

Fig. 70: Typical grain size distribution within the fractions of fragments, resulting from an HIE: The grain size distribution of the finest particles $\phi > 1$ is significantly different from the other fractions.

These results confirm the conclusions drawn above: The finest fraction is predominantly composed of particles, which have been generated by totally different mechanisms compared to those responsible for the production of coarser class IV-fragments. This coincides well with the previously described theory, that the particles $\phi > 1$ mainly originate from the impact notch region and Zone 1, respectively.

These impressions are mathematically substantiated by the results of Kolmogorov-Smirnov uniform distribution tests and other nonparametric tests (detailed in Appendix H). Table 23 compares for various examined fractions representative values of the empirical mean grain size $\hat{x}$ with the theoretical mean values $\bar{x}$, which have been calculated by equation (V.5-29).

Sample No.	{...}	ϕ	N	$\bar{x}$ [µm]	$\hat{x}$ [µm]	$\sigma(x)$ [µm]
1	101	>1	554	-	320,40	92,73
2	601	>1	545	-	315,19	80,22
3	621	>1	579	-	314,74	84,17
4	602	>1	537	-	310,11	79,83
6	101	1	486	750	742,55	142,66
7	102	1	361	750	753,80	147,28
8	601	1	433	750	749,12	147,59
9	111	1	268	750	753,63	138,38
10	121	1	297	750	748,88	147,91
11	131	1	309	750	756,83	138,11
12	103	1	259	750	743,53	153,43
13	104	1	234	750	730,70	151,39
14	106	1	269	750	738,16	149,74
15	101	0	277	1500	1494,76	303,72
16	601	0	264	1500	1500,91	279,14
17	102	0	231	1500	1513,38	283,29
18	103	0	244	1500	1501,76	285,11
19	104	0	207	1500	1483,48	301,62
20	106	0	211	1500	1490,27	282,31
21	101	-1	172	3000	3083,25	617,66
22	601	-1	164	3000	2983,72	578,78
23	121	-1	124	3000	2963,64	602,17
24	103	-1	119	3000	2954,32	546,43
25	106	-1	98	3000	2948,08	592,74

Table 23: Representative results of empirical ($\hat{x}$) and theoretical mean values ($\bar{x}$), calculated by (V.5-29). Additionally, the standard deviation $\sigma(x)$ of each data set is given.

These results validate (V.5-29) for nearly all class IV-fractions of all HIEs, except the finest ones.

Considering the nature of the smallest fraction $\phi > 1$, it is evident that (V.5-29) is not very useful for these particles, as it is not easily possible to determine x_l.

As a consequence, the planimetrical Heywood concept cannot be applied, and $B_{\phi>1}^{(TEH/BET)}$ has always been determined directly, by means of TEH and controlled by spot check BET measurements.

5.4.3. IPA and Self-Similarity

Particle shape comparisons between fragments of different fractions $-1 \leq \phi \leq 1$ under the SEM reveal continuously recurring forms, which are scale-independent. According to these findings, self-similarity of particles can be presumed.

In order to quantitatively substantiate these conclusions, image particle analysis (IPA) has been performed. An additional advantage of this method is that the determined form parameters can be used for a direct comparison with volcanic ash particles [6].

In a first step IPA has been conducted on the basis of SEM images, in order to find recurring shapes and thus to identify specific subpopulations. All determined shape factors are listed in Appendix D and are illustrated (as standardized values) in the ternary diagrams of Fig. 71.

It is not easy to identify subpopulations on the basis of ternary diagrams.

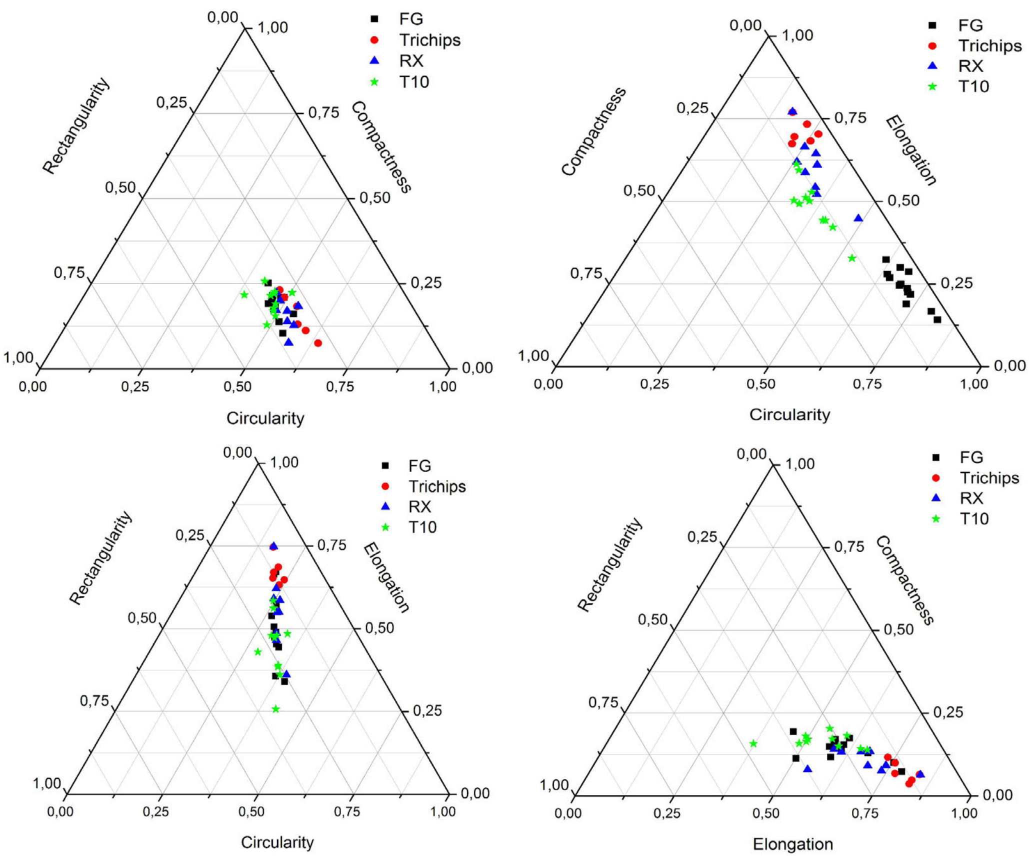

Fig. 71: IPA results of various samples: Note that for this kind of data presentation, standardized values have been used.

A proven method to reduce the number of IPA parameters is to find optimal parameters by means of principal component analysis (cf. [32] and III.6). The best results have been achieved by the aid of a principal component analysis followed by a Varimax rotation method with Kaiser [12] normalization. Fig. 72 presents a diagram for FG, using the principal components F1 and F2, which are computed due to the component matrix shown in Table 24.

	Components		Rotated components	
	1	2	1	2
circularity	0,988	0,150	0,990	0,138
elongation	$-3{,}443 \cdot 10^{-2}$	0,782	$-2{,}532 \cdot 10^{-2}$	0,783
compactness	$-1{,}246 \cdot 10^{-2}$	$-0{,}766$	$-2{,}139 \cdot 10^{-2}$	$-0{,}766$
rectangularity	0,991	$-0{,}132$	0,989	$-0{,}143$

Table 24: Results of principal component analysis with the IPA data set for FG, using a Varimax rotation method with Kaiser normalization: The original component matrix (left) as well as the rotated component matrix (right) are depicted.

As a result, three distinctly different kinds of particle shapes can be identified:

- The bulk of particles are mainly characterized by a flaked appearance (see e.g. also in Fig. 74, Fig 75 and Fig. 76) and low elongation. The component values of these fragments vary from -1,25 to 0,25 for F1 and from -1,25 to 1,1 for F2, respectively. This cluster is denoted subpopulation (class) A.

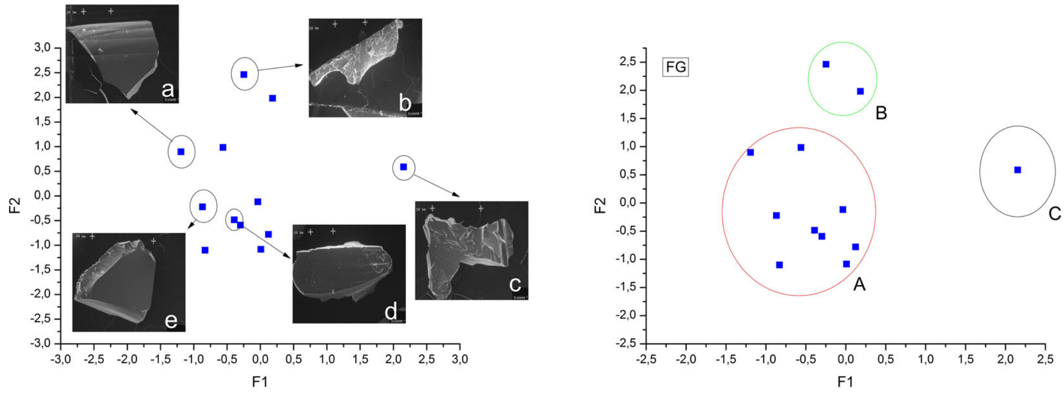

Fig. 72: IPA results for FG due to a principal component analysis: F1 and F2 are computed as a linear combination of the original IPA parameters and its loadings given in Table 24. Additionally, for some representative cases the corresponding particles are depicted (left). Most of the particles belong to subpopulation class A ((a), (d) and (e)). Nevertheless, there are also distinctly elongated particles (b), which are associated to subpopulation class B. Furthermore, angular particles (c) can be identified and are classified as subpopulation class "C". The same diagram is also shown on the right, this time illustrating how those subpopulation classes are allocated.

- Subpopulation B particles are evidently very elongated fragments, and are thus mainly characterized by large elongation values of at least 4,5.
- Particles with high values for F1 (more than 2,0) are characterized by a conspicuous angular shape. Those fragments are denoted subpopulation (class) C particles.

These three subpopulation classes can be found in all studied fractions and for all target types and can be optically identified with ease, which allows comprehensive statistical investigations by means of reflected-light microscope images. In order to prove self-similarity, it is necessary to check that their ratio is independent from the grain size. This has been statistically verified (see Appendix H) by performing chi-square tests, which have never shown a significant difference in the ratio of subpopulation classes under variation of fractions $-1 \leq \phi \leq 1$.

Consequently, it can be strongly presumed that the particles of the fractions $-1 \leq \phi \leq 1$ are in all cases self-similar. Thus, the planimetrical Heywood concept has proven to be applicable.

5.5. Considerations for Subpopulation Classes

Typical examples showing particles from different target types are presented in Fig. 74 to Fig. 76. IPA allows to reveal significant differences in their shapes.

Alternatively to principal component analysis, another possibility to reduce the number of IPA parameters is to plot "contour-shape" diagrams, which are quite simple to create: Considering the definition equations (III.4-7) to (III.4-10) reveals that circularity and rectangularity are very sensitive to the perimeter of an object, whereas compactness strongly depends on its area [15].

Therefore, two further parameters are defined:

$$contour = circularity \cdot rectangularity \tag{V.5-32}$$

$$shape = compactness \cdot elongation \tag{V.5-33}$$

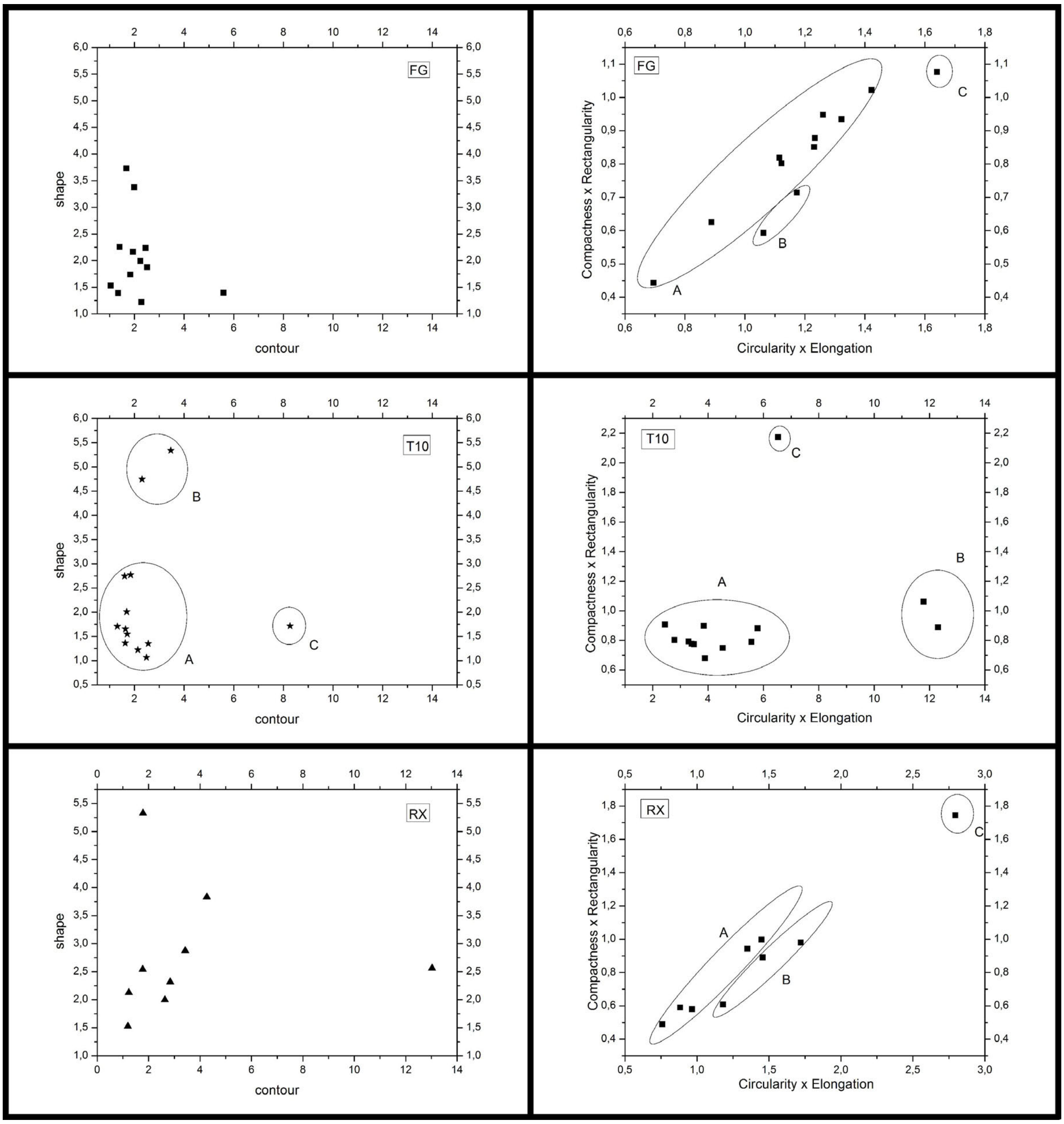

Fig. 73: Illustration methods of IPA results: Contour-shape diagrams (left column) and the corresponding complementary diagrams (right column) are depicted. In the latter diagrams also the positions of the subpopulation clusters are illustrated.

Fig. 73 (left column) shows contour-shape diagrams of several samples. It is notable, that the distributions of data points are - in principle - quite similar to those resulting from a principal component analysis (see above). A closer look in Table 24 provides a simple explanation for that: The principal component F1 in Fig. 72 is almost exclusively made up of circularity and rectangularity. Thus, due to (V.5-32), F1 is nearly identical to the introduced contour parameter. In contrary, F2 is a linear combination of all four IPA parameters, but is mainly dominated by compactness (loaded with the factor $-0,766$) and elongation (loaded with the factor $0,783$).

Nevertheless, it has to be stated, that the IPA parameters are not independent from each other. As a consequence, e.g. a high "contour" value could indicate a great irregularity of the contour, but it is not a compulsory proof. Therefore, additional plots have to be analyzed, showing the product of circularity and elongation plotted over the product of rectangularity and compactness. These complementary plots allow the discrimination of objects in terms of differences in shape and contour [15] and are also presented in Fig. 73 (right column).

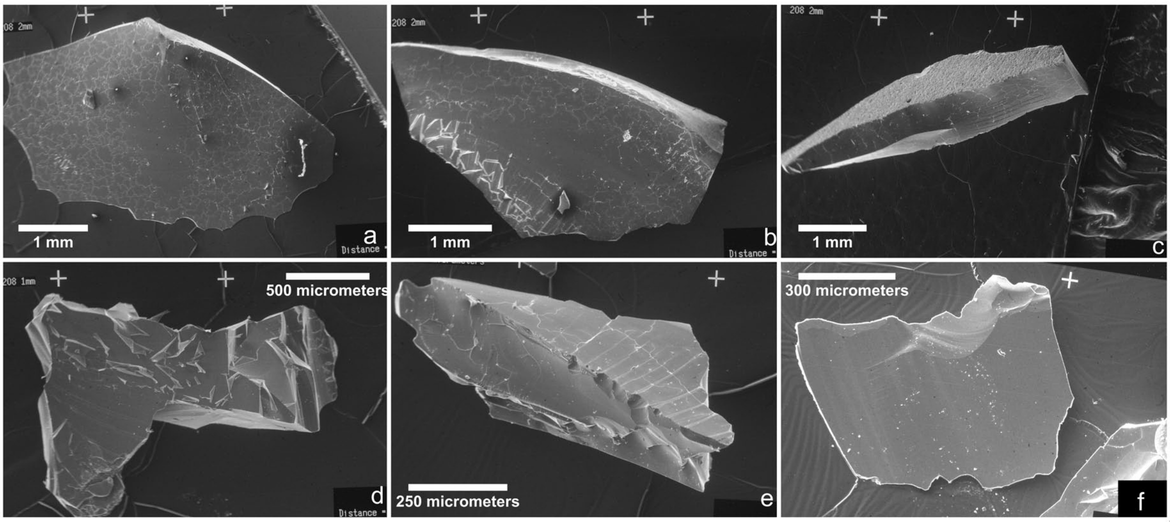

Fig. 74: Representative examples for particles stemming from FG [V208], {101}: Most of the particles (a, b, e, f) are allocated to subpopulation A, but also typical elongated subpopulation B (c) and C (d) class particles are shown.

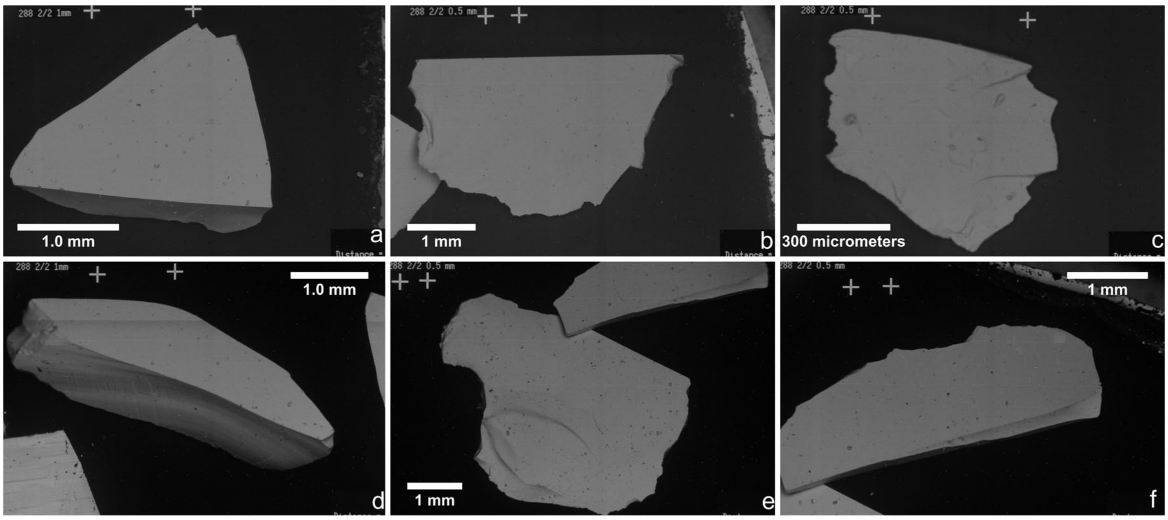

Fig. 75: Typical examples for T10 particles [V288], {103}.

Three facts are evident:

- The diagrams of the latter kind are not always useful to discriminate A and B subpopulation class particles, as those are clustered quite closely. Thus, for discrimination purposes, contour-shape diagrams are preferable.
- Contour-shape diagrams are roughly similar for all target types, which could be explained by the fact that for all those targets, comparable subpopulations are observed. A closer look, however, reveals the notable fact, that the positions and diameters of the subpopulation clusters are divergent:

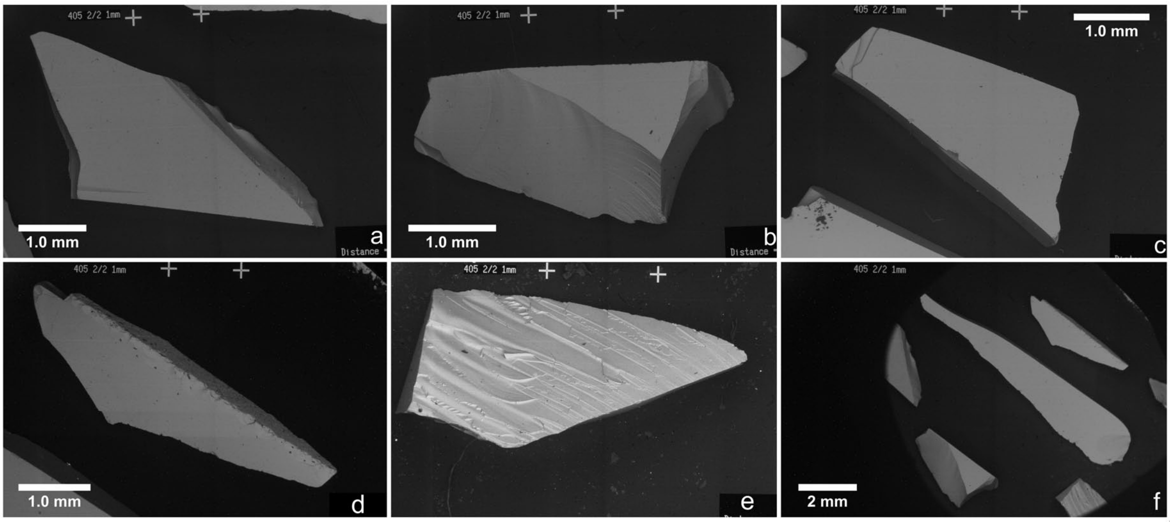

Fig. 76: Representative examples for RX particles [V405], {106}: Note that these particles are characterized by regular, smooth contours.

For example, B-class particles originating from T10 targets seem to feature significantly more differences to "normal" A subpopulation class particles than in the case of FG particles. Additionally, subpopulation C particles from RX targets seem to have very pronounced shapes, compared to the corresponding type of particles, which stem from FG or T10.

- Also the complementary plots show significant differences, especially for T10 targets. It is of interest that the subpopulation clusters of FG and RX show significant less differences in their positions. Thus it can be considered proven, that thermal pre-stresses have a great effect on the shape of particles.

Some boundary conditions affect not only the shape of particles, but also the frequency distribution of particles in the subpopulation classes: Table 25 shows the frequency distributions for various cases.

Sample No.	{...}	N	$n(A)$ [%]	$n(B)$ [%]	$n(C)$ [%]	χ^2	As. sig. [%]
1	101	1129	79,27	18,95	1,77	0,000	100,0
2	301	900	79,44	18,67	1,89	0,119	94,2
3	601	900	79,33	18,22	2,44	2,576	27,6
4	111	900	80,33	16,89	2,78	7,344	2,5
5	121	900	80,22	16,67	3,11	11,761	0,3
6	131	900	79,00	18,89	2,11	0,602	74,0
7	102	900	75,89	22,22	1,89	6,388	4,1
8	103	900	76,11	21,78	2,11	5,464	6,5
9	104	900	79,33	19,00	1,67	0,055	97,3
10	106	900	73,56	25,89	0,56	33,924	$<$0,05
11	636	900	73,89	25,11	1,00	24,198	$<$0,05

Table 25: Subpopulation frequency distributions: For various boundary conditions $-1 \leq \phi \leq 1$ particles of the sample size N are examined. The frequencies n of subpopulation A, B and C, respectively are listed as well as the results of χ^2-tests, by means of which all data sets have been compared to sample No. 1 (see also Appendix H).

To detect significant influences, by means of χ^2-tests each data set has been statistically compared with the theoretical expectation values, assuming no significant changes to the first case {101} as null hypothesis H_0. As results, the values for χ^2 are shown together with the asymptotic significance (As. sig.). The latter parameter quantifies the error probability, if H_0 is rejected. Due to a common convention, H_0 can be "significantly" rejected, if the significance is lower than 5 %.

Fig. 77 shows the corresponding relative frequencies of class B particles under varying boundary conditions.

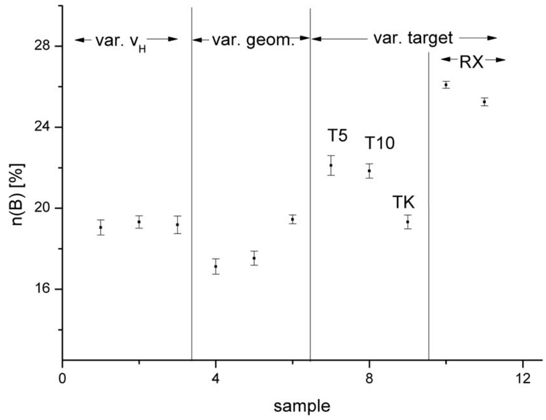

Fig. 77: Relative frequencies of subpopulation B particles $n(B)$, shown for all cases listed in Table 25 (see also text).

Based on Fig. 77 and on the results given in Table 25 the following important conclusions can be drawn:

- At least for FG, the impact velocity does not have a significant influence on the frequency distribution of particles.
- The distribution itself, however, significantly depends on the hammer geometry: If a broader hammer head is used, the frequency of class C particles $n(C)$ distinctly increases and the amount of subpopulation B particles shows a significant drop. In contrast, a round hammer head affects no significant change.
- Samples from T5 targets show significant higher values for $n(B)$. It is evident, that the anisotropic situation in the target due to thermal pre-stresses has a great influence on the creation of elongated class B particles: A stronger anisotropy causes a higher amount and - due to the results mentioned above - more pronounced particles allocated to subpopulation B. Note that this implies, that the mechanisms which induce damage cracks, do not extinguish pre-existing anisotropies in the material.
- This effect is also observed for T10 targets, as the determined significance value of 6,5 % is quite close to the 5 % limit.
- The χ^2-test results for RX glass ceramics reveal differences of high significance. Probably due to their nanonanocrystalline nature, RX particles show the highest values for $n(B)$ and the lowest values for $n(C)$. Furthermore, the elongation of B class particles show comparably high deviations. This can be explained by the fact that glass ceramics are

interspersed with crystal faces, which are according to energetic aspects more susceptible for fracture processes. This phenomenon is known as "transcrystalline cleavage" [55].

Considering these results, the following fundamental statements can be made:

1. In all examined cases, particles allocated to class A are the dominating subpopulation. These fragments originate from all zones of damage cracks.

2. It can be strongly presumed, that particles belonging to subpopulation class B originate mainly from areas of pronounced anisotropies in the material.
   Hence, $n(B)$ can be used as a useful indicator, which provides also quantitative information about the extent of these pre-fracture stress anisotropies, thus giving a valuable insight into the loading situation of the target immediately before fragmentation has taken place.

3. The specific shape of C class particles as well as empirically verified linear correlations indicate, that fragments of this subpopulation class originate from areas of intermediate cracks.

4. Material properties have a significant and reproducible influence on the shape of particles. Thus, the Heywood factor f_H is affected by them as well as by thermal pre-stresses.

5.6. Results of Fracture Area Analysis

5.6.1. Heywood Factor f_H: Results and Dependencies

Table 26 shows mean values for f_H under some important HIE configurations. They give an impression of the influences on the shape of particles, which are statistically verified by correlation analyses and t-tests (raw data and test results are presented in the corresponding folder of Appendix H on the attached DVD):

	{101}	{111}	{131}	{102}	{103}	{104}	{105}	{106}	{601}	{603}
$\bar{f_H}$	12,13	12,41	12,21	11,33	11,37	11,94	11,87	8,47	12,13	11,33
$\sigma(f_H)$	0,05	0,08	0,05	0,09	0,12	0,12	0,11	0,06	0,04	0,12

Table 26: Mean values of Heywood factors $\bar{f_H}$ for the fractions $-1 < \phi < 1$ and corresponding standard deviations $\sigma(f_H)$ under various HIE configurations.

- There is no significant linear correlation between the impact velocity v_H and $\bar{f_H}$. Furthermore, t-tests reveal no significant differences between those values under different impact velocities at all. This implies that, at least for the fractions $-1 < \phi < 1$, the particle shape is independent from the impact energy E_{impact}, a result which is in good agreement with the findings of Raue [98].

- Table 27 shows significant differences of f_H under the use of different hammer geometries. For most target types, there is a strong dependency on the impact situation. An explanation for this effect can possibly be found in the influences on shock wave energies, described by (II.2-21). Furthermore, as already mentioned above, a broader hammer effects significantly lower frequencies of subpopulation class B particles, which implies higher values for S_m in (V.5-30). As a consequence, one obtains higher values for f_H.

	pointed	4,5 mm	8,3 mm	round
pointed		all (lower)	all (lower)	FG, TK, RX (lower)
4,5 mm	all (higher)		FG, T10, TK, RX (higher)	all (higher)
8,3 mm	all (higher)	FG, T10, TK, RX (lower)		all (higher)
round	FG, TK, RX (higher)	all (lower)	all (lower)	

Table 27: Significant differences of f_H, verified by t-tests: To understand this table correctly, read the left column first. For example it says: "For a pointed hammer head the values of f_H are for all examined targets significantly lower than for a 4,5 mm wide hammer head."

- It is evident, that f_H strongly depends on the material (see Table 26). The lowest values have been determined for RX targets, which coincides well with the SEM results mentioned above: RX targets are characterized by a smooth and rounded surface morphology and have hence a significant lower surface-volume ratio. Also thermal pre-stresses result in significant lower values for f_H, which is evidently a consequence of the higher rates of elongated subpopulation B particles in the cases of T5 and T10.
  A very interesting fact is that TK samples, though also thermally pre-stressed target types, show significantly higher values for f_H than for example T5 targets. An explanation for this effect could be, that due to the specific "upside down" impact configuration, the damage cracks expand in a zone, which is de facto not affected by pre-stresses and thus isotropic. As a consequence, the values for the Heywood factor of TK particles are closer to those of FG than of T10 or T5. Nevertheless, during the process of target preparation, arbitrary thermal pre-stresses as well as the generation of microcracks cannot be completely avoided. This explains why the values for f_H of TK targets are not identical to those of FG targets.

5.6.2. Results for the Finest Particles $\phi > 1$

The mass specific areas S_m of the finest particles have been calculated on the basis of the determined fracture area $B_{IV,\phi>1}$ and the corresponding mass $m_{IV,\phi>1}$. Additionally these values have been checked by means of BET measurements. Representative mean values of S_m under various HIE configurations are presented in Table 28.

$[\frac{m^2}{kg}]$	{101}	{601}	{102}	{103}	{104}	{105}	{106}	{116}	{126}	{136}
$\overline{S_m}$	134,2	134,5	124,5	122,9	133,1	134,6	106,0	105,6	105,4	105,6
$\sigma(S_m)$	0,6	0,5	0,7	0,6	0,6	1,1	0,7	0,9	0,6	0,5

Table 28: Mean values of mass specific areas $\overline{S_m}$ for particles $\phi > 1$ and corresponding standard deviations $\sigma(S_m)$ under various HIE configurations.

The influences on S_m have been checked by multivariate statistical tests (see Appendix H) and are summarized in the following:

- There is no significant linear correlation between S_m and the impact velocity v_H. The mass specific area is hence completely independent from E_{impact}.

- The hammer geometry does not significantly affect S_m, which also implies that the mass specific area does not depend on the intensity of damage cracks.
  This is in contrast to the previous findings for f_H of the coarser fractions $-1 < \phi < 1$ and underpins once more the above mentioned theory (see also V.5.4.2): The finest particles $\phi > 1$ mainly originate from the impact notch and Zone 1, and are hence generated by other mechanisms than the coarser ones.

- With the exception of the case AS - FG, comparisons between different target types reveal always significant differences in S_m. Thus the dominating influence on S_m is clearly exerted by the material properties. Pre-stresses evidently cause a reduction of mass specific areas of $\phi > 1$ particles. As for f_H, the lowest S_m values of all target types are featured by RX particles.
  Considering these results, and taking also the findings of V.5.4.2 into account, one can conclude, that the amount and the shape of the finest particles originating from Zone 0 and Zone 1 are considerably dominated by the influence of the material properties, and not significantly affected by the specific impact situation itself.

5.6.3. Resulting Fracture Areas

Typical mean values for A_{DC} and A_{NC} under various HIE configurations are shown in Table 29.

	$\bar{A}_{DC}[mm^2]$	$\bar{A}_{NC}[mm^2]$	$\sigma(A_{DC})[mm^2]$	$\sigma(A_{NC})[mm^2]$
{101}	20605 ± 620	3365 ± 74	4146 ± 130	631 ± 14
{111}	23086 ± 710	2620 ± 58	1558 ± 68	740 ± 16
{601}	33026 ± 1036	5023 ± 111	5481 ± 171	1809 ± 40
{102}	20231 ± 623	3117 ± 69	3638 ± 123	822 ± 18
{103}	20895 ± 619	3204 ± 70	2320 ± 79	640 ± 14
{123}	22340 ± 667	2747 ± 60	1102 ± 40	670 ± 15
{603}	27558 ± 808	4274 ± 94	6822 ± 228	1015 ± 22
{106}	12451 ± 365	2783 ± 61	2980 ± 84	715 ± 16

Table 29: Mean values of A_{DC} and A_{NC} under various HIE configurations: Additionally the corresponding standard deviations σ are listed. For detailed information about the calculation of measurement uncertainties, see Appendix A.

The complete list of all resulting fracture areas can be found in Appendix E. Fig. 78 shows representative fracture area distributions.

It is important to note, that the values for A_{DC} and A_{NC} vary considerably - even under identical HIE configurations. Thus all subsequent statements only describe statistical tendencies, which may not be valid for an individual case.

In summary, the following conclusions concerning HIE generated fracture areas can be drawn:

- The percentage of A_{DC} varies between 62,4 % and 94,7 %, and averages 86,0 % of the total fracture area. This implies that damage cracks always play a major role in the generation of new surfaces.

- RX targets show significant lower values (and ratios) for A_{DC} than any other target type. This coincides well with the considerations mentioned above: The nanocrystalline structure of the examined glass ceramics apparently reduces the susceptibility to shock wave induced fragmentation processes.

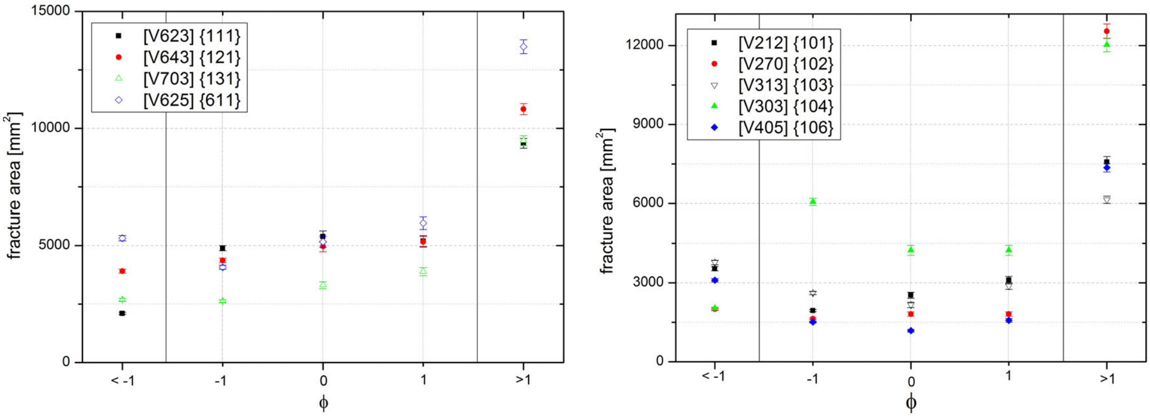

Fig. 78: Representative fracture area values of HIEs under various configurations: The left diagram illustrates the influence of v_H and hammer geometry on the fracture area. The right plot shows the resulting fracture areas of different target types. Note that in both diagrams the first value on the left specifies the total sum of the fracture area of all particles $\phi < -1$, which is by definition identical to A_{NC}.

- It is noteworthy, that the finest particles $\phi > 1$ always feature the highest values and hence have a considerable influence on the total fracture area of damage crack A_{DC}.
- In principle, there is a distinct influence of the hammer geometry on A_{DC}. This is in compliance with the dependencies of f_H and the results of the sieving analysis (see section V.5.2): A wider hammer head causes more fine particles plus higher values of f_H and consequently also higher values of A_{DC}.
- Higher impact velocities and higher impact energies E_{impact} correlate significantly with higher values of A_{DC} (the corresponding analysis results are presented in Appendix H). Also this effect can be explained by the results of sieving analysis: Higher impact velocities cause more fine particles.

6. Energy Balances

The total energy balance of an HIE is described by:

$$E_{tot} = E_{kin} + E_{setup} + E_{air} + E_{def} + E_{frac} \tag{V.6-1}$$

where E_{tot} denotes the total energy input in the target, E_{kin} the kinetic energy of the fragments after fragmentation, E_{setup} the energy component that dissipates in the HIE setup in the form of seismic waves, E_{air} the acoustical energy which is released into the surrounding air, and E_{def} the plastic deformation energy, absorbed by the hammer head. The residual forms of energies (including heat) are presumed to contribute to fracture processes and are covered by the term "fracture energy" E_{frac} (see also section II.1.5).

In this chapter each energy term is determined, quantified and - if possible - analyzed for its dependencies and influences. All conclusions are based on the results of multivariate statistical tests, performed with the program SPSS. These outputs are presented in the corresponding folders in Appendix H.

6.1. Total Energy Input E_{tot}

6.1.1. Overview of Results

For each HIE data set, E_{tot} has been quantified by means of equation (IV.2-2). The determined values for each HIE can be found in Appendix F. Table 30 presents a statistical description of these results.

	E_{tot} [mJ]	HIE
minimum value	1730 ± 51	[V223], {101}
maximum value	5406 ± 63	[V653], {621}
mean value	3340	
standard deviation	645	

Table 30: Overview of the determined values for E_{tot}: The corresponding HIE number and configuration is displayed in the right column.

6.1.2. Dependencies

Multivariate statistical analyses have revealed the following dependencies of E_{tot}:

- There is a strong and highly significant linear correlation between E_{tot} and E_{impact} (as well as between E_{tot} and v_H). The corresponding total Pearson correlation coefficient, for which all cases (i.e. all HIE configurations) have been taken into account, has shown to be 0,633 with an error probability of less than 0,05 %.
  It is important to remember the difference in information provided by E_{tot} and E_{impact}: The term "impact energy" denotes the energy, which has been potentially available for all relevant processes during the HIE. In contrast, the amount of energy, which has actually been transformed is specified by E_{tot}.

It is evident that in the examined scope of impact velocities, an increasing impact energy brings about a growing energy input in the observed system.

- This phenomenon is even more pronounced under constrained HIE configurations, which implies a considerable additional influence of hammer geometry and material properties. Table 31 displays the determined specific Pearson correlation coefficients, which have been verified to be significant. Only results for test samples $N > 6$ are presented. For additional illustration, two of these cases are also plotted (see Fig. 79).

$\rho(E_{tot}; E_{impact})$	FG	T5	T10	TK	AS	RX
pointed	0,752**	0,573**	0,622**		0,835**	0,355*
4,5 mm wide	0,668*	0,842*				
8,3 mm wide	0,798**	0,766**	0,870**	0,671*		
round	0,516*	0,773**	0,894**			0,849**

Table 31: Determined Pearson correlation coefficients ρ for the linear correlation between E_{tot} and E_{impact} under various HIE configurations: Only significant results for sample sizes $N > 6$ are presented. Asterisks indicate the level of significance:
* indicates that the result is significant at the 5 % level.
** indicates that the result is "highly significant" at the 1 % level.

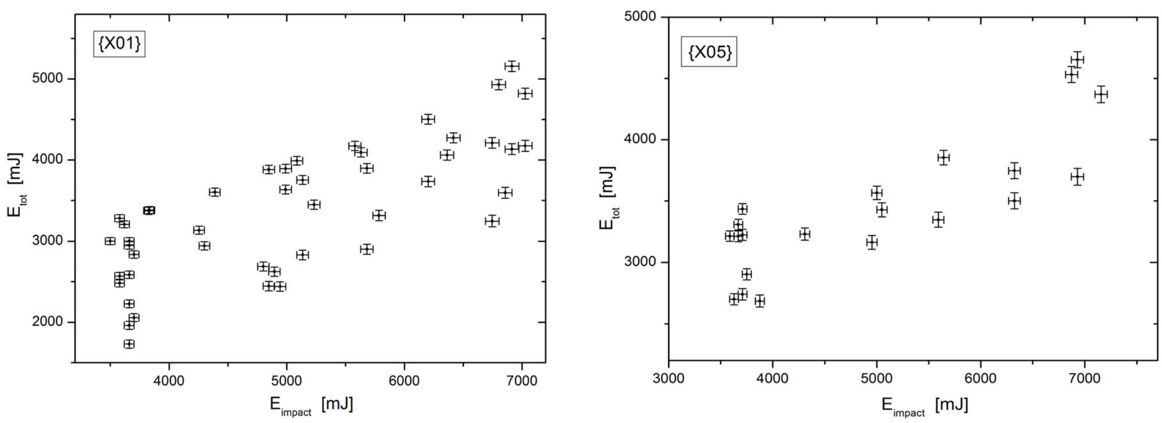

Fig. 79: Plots, illustrating the correlation between E_{tot} and E_{impact}: The cases {X01} (left) and {X05} (right) are presented, where "X" denotes an arbitrary value. The uncertainties are calculated by the results of the error analysis, shown in Appendix A.

- The influence of the hammer geometry on E_{tot} has been verified to be significant by means of t-tests in a number of comparisons (e.g. {102} - {122}; {421} - {431}, {424} - {434}; {126} - {136}). This effect also coincides well with the fact, that the geometry of the hammer head has a big influence on the intensity of damage cracks as well as on the amount and fracture area of generated class IV particles, which evidently affects the energy balance.

- The theory of a fundamental interrelationship between hammer geometry, damage crack induced fracture areas and E_{tot} is finally supported by the statistical results for nearly all boundary conditions. This is shown by a distinct linear correlation between E_{tot} and the damage crack intensities M_R (e.g. in case of {2X1} the highly significant correlation coefficient is 0,931), thus closing the chain of proof:
Put simply, a wider hammer head causes - due to an enhanced generation of shock waves

- higher damage crack intensities and growing fracture areas, so that the energy input in the system E_{tot} has to increase.

- As mentioned above, the material properties also have a considerable influence on E_{tot}: Different target types have been proven to show significant deviations in E_{tot}. Particularly notable are the distinctly lower values of E_{tot} for TK and RX targets.
  In this context, it has to be kept in mind that the dimensions of the used RX targets have been different: These samples have been of considerably lower volume and masses. This and the lower contact area between hammer and target might serve as an explanation, why in these cases less energy has been transformed during the HIE.

6.2. Kinetic Energies of Fragments E_{kin}

6.2.1. Determination of E_{kin}

In order to determine the kinetic energies of fragments, it is necessary to distinguish between coarse fragments and finer ones:

$$E_{kin} = E_{kin,\phi<-2} + E_{kin,\phi\geq-2} \tag{V.6-2}$$

By means of mass measurements, CAD reconstruction and video analysis of the movies recorded by the digital video camera, it is possible to quantify $E_{kin,\phi<-2}$ as the sum of all kinetic energy terms of each of n coarse fragments:

$$E_{kin,\phi<-2} = \sum_{i=1}^{n} \left(\frac{1}{2} \cdot m_i \cdot v_i^2 + \frac{1}{2} \cdot \Theta_i \cdot \omega_i^2 \right), \tag{V.6-3}$$

where each fragment is characterized by its mass m_i, moment of inertia Θ_i, initial translational velocity v_i and initial rotational velocity ω_i. As in an HIE only a few coarse fragments are generated (usually $3 < n < 8$), the measurement effort has been manageable.

Of course, this method is not applicable for finer fragments, for three reasons:

1. The high numbers of finer fragments make this determination concept ineffective and time-consuming.
2. It is nearly impossible to identify all these smaller fragments in the image sequences.
3. Due to the local resolution of the digital video camera, it is quite difficult to determine the dynamic parameters of fragments with a diameter smaller than 8 mm ($\phi \geq -2$).

Therefore, two approaches have been made to determine the kinetic energy of finer fragments:

Three-level Valuation Model

This model uses the basic conclusions on class IV particles: As mentioned before, approximately all of these particles ($\phi \geq -1$) are generated in the damage crack zone. After the breakthrough of the hammer, these fragments propagate as an expanding "particle cloud", which is illustrated in Fig. 80.

In a number of supplementary HIEs, the expansion of these particle clouds has been studied by means of a digital high-speed camera. It can be presumed, that the velocity v_{pf} of the expanding particle front gives a maximum value of the translational velocity of fine particles. An empirical value for HIEs under the configuration {622} is given by:

$$v_{pf} = (2{,}12 \pm 0{,}19)\,\frac{m}{s}$$

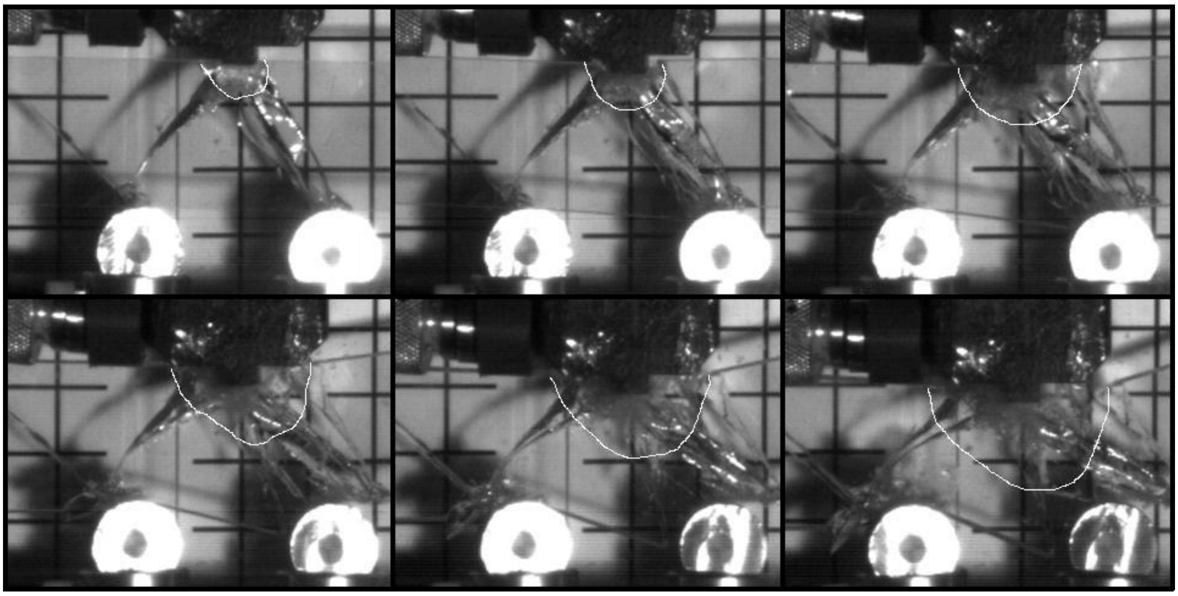

Fig. 80: Movement of class IV fragments: The front of the expanding particle cloud is highlighted by a white line ([J101]; frame rate: 1000 fps).

The total mass of class IV particles is given by $m_{\phi \geq -1}$ after sieving analysis. For arbitrary class IV particles, which are self-similar in the fractions $-1 \leq \phi \leq 1$, the values of the moment of inertia have been determined to be between $0{,}5 \cdot 10^{-7} kg\, m^2$ and $5{,}0 \cdot 10^{-7} kg\, m^2$. Compared to the translational energies $E_{trans,\phi \geq -1}$, it turns out that the rotational energy of those particles $E_{rot,\phi \geq -1}$ is considerably smaller:

$$E_{rot,\phi \geq -1} \approx (6{,}33\,\% \pm 3{,}13\,\%) \cdot E_{kin,\phi \geq -1} \approx (6{,}87\,\% \pm 3{,}66\,\%) \cdot E_{trans,\phi \geq -1} \qquad \text{(V.6-4)}$$

In fact, the values of $E_{rot,\phi \geq -1}$ would have been only comparable to those of the corresponding $E_{trans,\phi \geq -1}$, if the particles had rotated with rotational velocities ω_i of several hundred revolutions per second. In reality the values for ω have been distinctly (by one to two orders of magnitude) lower.

It is evident, that due to the great skewness of particle mass distribution, by far the biggest part of the kinetic energy is that transformed into the movement of the coarse fragments.

This effect is confirmed by additional experiments, which have been conducted to study the kinetic energy of the residual particles with the size $\phi = -2$. In order to estimate the average kinetic energy of this kind of fragments, a mass-specific energy value $e_{resi,\phi=-2}$ has been empirically determined:

$$e_{resi,\phi=-2} = \frac{E_{kin,\phi=-2}}{m_{\phi=-2}} \qquad \text{(V.6-5)}$$

For HIEs under the configuration {622} it has proven to be:

$$e_{resi,\phi=-2} = (0{,}46 \pm 0{,}30)\ \frac{mJ}{g} \qquad \text{(V.6-6)}$$

With these results, in a three-level model the total kinetic energy of all fragments can be estimated by:

$$E_{kin} \approx E_{kin,\phi<-2} + 1{,}0687 \cdot \left(\frac{1}{2} \cdot m_{\phi \geq -1} \cdot v_{pf}^2\right) + e_{resi,\phi=-2} \cdot m_{\phi=-2} \qquad \text{(V.6-7)}$$

Two-level Valuation Model

It is notable, that - within the examined scope - $e_{resi,\phi=-2}$ does not significantly change in the case of altering boundary conditions, and that this value is even also in good agreement with the determined mass-specific energy values for the finer fragments.

This empirically proved universality of e_{resi} allows to simplify the determination equation (V.6-7):

$$E_{kin} \approx E_{kin,\phi<-2} + e_{resi,\phi=-2} \cdot m_{\phi\geq-2} \tag{V.6-8}$$

A conclusive explanation for this universality of $e_{resi,\phi=-2}$ could be its comparatively big variation and the low figures of $m_{\phi\geq-2}$, which usually do not exceed 5 g. In fact, the average value of $m_{\phi\geq-2}$ is 2,65 g (standard deviation: 0,62 g), so that $E_{kin,\phi\geq-2}$ is orders of magnitude lower than $E_{kin,\phi<-2}$. In particular of course, this applies to class IV fragments (featuring a mean value $\bar{m}_{\phi\geq-1}$ of 0,84 g).

Due to the better results of comparative error analysis (see Appendix A) and the considerably lower measuring expenditure, the two-level valuation model based on (V.6-8) has been selected to quantify E_{kin}.

6.2.2. Overview of Results

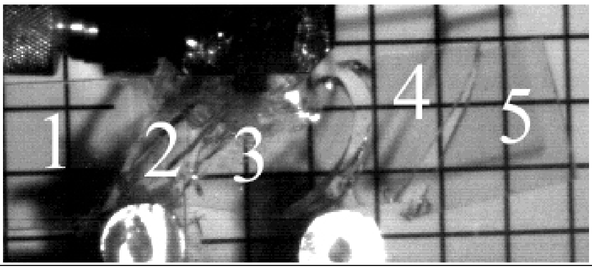

i	m_i [g]	Θ_i $\cdot 10^{-6}$ [kg m^2]	$E_{kin,i}$ [mJ]	$\frac{E_{trans,i}}{E_{kin}}$ [%]	$\frac{E_{rot,i}}{E_{kin}}$ [%]	$\frac{E_{kin,i}}{E_{kin}}$ [%]	$\frac{m_i}{m}$ [%]
1	27,21	7,26	$47{,}55 \pm 1{,}01$	95,7	4,3	19,8	40,0
2	3,36	0,46	$4{,}50 \pm 0{,}11$	$> 99{,}9$	$< 0{,}1$	1,9	4,9
3	10,91	3,44	$11{,}64 \pm 0{,}31$	92,1	7,9	4,8	16,0
4	9,63	2,58	$83{,}71 \pm 0{,}81$	99,3	0,7	34,8	14,1
5	13,80	2,88	$91{,}48 \pm 1{,}01$	97,8	2,2	38,1	20,3
$\phi \geq -2$	3,19		$1{,}47 \pm 0{,}02$			0,6	4,7

Table 32: Occurring kinetic energies for coarse and finer HIE fragments calculated by means of the two-level model: In this example, the rotational energy plays a minor role for all particles. It has to be remarked that this is not always the case, as coarse particles can feature considerable rotational movements.
What is representative in this example, however, is that the bulk of kinetic energy has been dissipated in few coarse fragments, while $E_{kin,\phi\geq-2}$ is of a nearly negligible small amount.

A representative example for typical translational and rotational energies of the dispersing fragments is given in Table 32. The corresponding numbers of the coarse fragments are displayed in the image at the top of the table.

Furthermore, a conclusive overview of the kinetic energies occurring in the HIEs is given in Table 33. The kinetic energies of the particles, which disperse after fragmentation, make up between 1,4 and 8,1 % of the total energy input E_{tot}. It is a very interesting fact, that these results are quite comparable to those of (more fierce) MFCI experiments, which have been determined to be between 5,1 and 12,5 % [18].

	E_{kin} [mJ]	HIE
minimum value	$43{,}4 \pm 3{,}0$	[V312], {103}
maximum value	$291{,}2 \pm 11{,}3$	[V618], {612}
mean value	124,7	
standard deviation	44,9	

Table 33: Overview of the resulting values for E_{kin}: The corresponding HIE number and configuration is displayed in the right column.

6.2.3. Dependencies

The following dependencies of E_{kin} have been revealed by multivariate statistical analyses:

- There is a strong and highly significant linear correlation between v_H and E_{kin} (e.g. in the case of {X31}, ρ has been determined to be 0,698 with an error probability p of 0,4 %).
- As there is also a verified linear correlation between E_{tot} and E_{kin}, and on the other hand E_{tot} depends on v_H as well, partial correlation analyses have been conducted. As a result, one obtains a significant linear correlation for v_H, but none for E_{tot}. These results indicate strongly, that the actual relevant parameter for E_{kin} is v_H (as well as E_{impact}) and *not* E_{tot}.
- Box plots and the results of statistical tests suggest, that there is no significant dependency of E_{kin} on the hammer geometry.
- Due to great variations of E_{kin}, no significant influence of the material has been verified. However, TK targets are an exception: For low impact velocities (lowest height of hammer fall: {1XY} with X and Y arbitrary values) the kinetic energies of TK fragments are significantly lower than E_{kin} of AS fragments.
- Taking a closer look at the dependency on the geometry of the primary crack gives an explanation for this anomaly: For example, it has been verified by t-tests that for {1XY} E_{kin} is significantly higher (with an error probability of 2,2 %), when ACTs had been established as primary cracks than in the case of SCMs. In the first case, the empirical mean value of E_{kin} has been 121,9 mJ, in the latter case only 96,8 mJ.
  If the primary crack is a SCM, the material is cut only into two big fragments, a situation which evidently results in lower kinetic energy balances.
  As pointed out in chapter V.3.6, SCMs are the predominant primary crack types, which occur in TK targets - and nearly exclusively there. Under these considerations, it becomes clear why TK targets are characterized by lower kinetic energies.

6.3. Energies Dissipating into the Setup E_{setup}

6.3.1. Models of Determination

E_{setup} describes the amount of energy, which has been dissipated into the HIE setup in form of elastic waves and is quantified by means of force signal analysis.

In principle, the used force sensors can be seen in the observed range ideally as Hookean springs of great rigidity, featuring a modulus of resilience D, which has been experimentally determined to $6,0\,\frac{\mathrm{kN}}{\mu\mathrm{m}}$. The corresponding linear-elastically stored energy E_{elast} is given by:

$$E_{elast} = \int_{x_o}^{x_1} \vec{F}(\vec{x})d\vec{x} \tag{V.6-9}$$

where $\vec{x}$ is the displacement and $\vec{F}$ denotes the restoring force exerted by the "spring", for which - due to Hook's law:

$$\vec{F}(\vec{x}) = D \cdot \vec{x} \tag{V.6-10}$$

Due to the known spring rate, the corresponding displacement of the force sensor can be calculated at any given time (see Fig. 81).

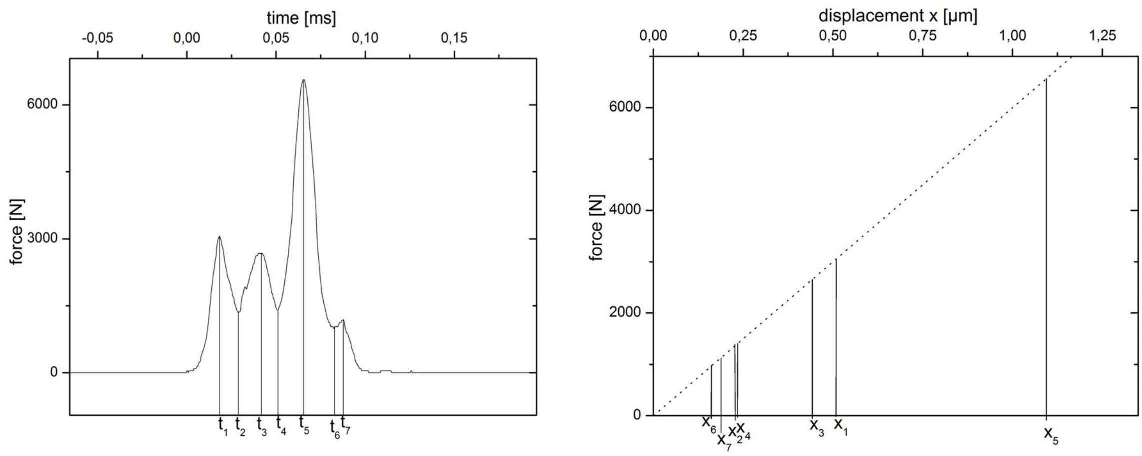

Fig. 81: Representative example to illustrate the correlation between force, time and displacement [V290R].

As pointed out in chapter V.2, force signals are in the relevant period characterized by a number of grouped peaks (see e.g. Fig. 36 and Fig. 81). For an energetic consideration, the crucial point is to know in what direction the elastic energy is released in each case of sensor relaxation. Obviously, there are always two possibilities:

1. The energy is released back into the target in form of seismic waves, which contribute to crack propagation. Thus, by definition, this kind of energy is included in the fracture energy E_{frac} and irrelevant for E_{setup}.

2. The elastic energy of the relaxing force sensor dissipates into the setup. In this case, the term of energy is relevant for E_{setup}.

Without further information, a precise discrimination is not possible. As a consequence, three different valuation models have been developed, in order to approximate the quantity of E_{setup}.

Pulsed Force Peak Model

This model postulates that a recorded force signal is simply composed of a sequence of single pulsed force peaks, which completely and instantly dissipates into the setup. Thus, it is assumed that between each recorded force peak, the sensor completely relaxes.

Consequently, the resulting seismic energy E_{pulse} of the example shown in Fig. 81 is given by:

$$E_{pulse} = \int_{0}^{x_1} \vec{F}(\vec{x})d\vec{x} + \int_{0}^{x_3} \vec{F}(\vec{x})d\vec{x} + \int_{0}^{x_5} \vec{F}(\vec{x})d\vec{x} + \int_{0}^{x_7} \vec{F}(\vec{x})d\vec{x} \tag{V.6-11}$$

Although its assumption is not very realistic, this model provides at least an approximation for the maximum limit of E_{setup}.

One Way Model of Incomplete Relaxation

As the pulsed force peak model, this model also postulates that every form of released elastic energy dissipates exclusively into the setup.

However, in contrast to the first one, in this model it is presumed that the force sensor does *not* completely relax between each peak. Thus, in the case of the example presented in Fig. 81 the resulting energy E_{1way} can be calculated by:

$$E_{1way} = \int_{x_2}^{x_1} \vec{F}(\vec{x})d\vec{x} + \int_{x_4}^{x_3} \vec{F}(\vec{x})d\vec{x} + \int_{x_6}^{x_5} \vec{F}(\vec{x})d\vec{x} + \int_{0}^{x_7} \vec{F}(\vec{x})d\vec{x} \tag{V.6-12}$$

Also this model provides a (probably more accurate) approximation for the maximum limit of E_{setup}.

Two Way Model of Incomplete Relaxation

In the two way model of incomplete relaxation it is presumed that only the maximum elastic energy dissipates into the setup, and all additional components are a consequence of a complex interaction between force sensors and evolving fractures. Thus, this model postulates that the elastic energy stored in the force sensor is released back into the target, until the force signal reaches its maximum F_{max}. In our example of Fig. 81 the resulting energy E_{2way}, which has been dissipated into the setup, can be quantified by:

$$E_{2way} = \int_{0}^{x_5} \vec{F}(\vec{x})d\vec{x} = \frac{1}{2} \cdot \frac{F_{max}^2}{D} \tag{V.6-13}$$

where F_{max} specifies the value of the force in the moment of highest loading.

As this model coincides well with the considerations made in chapter V.2, its results can be regarded as the most realistic approximations for E_{seis}, and hence:

$$E_{pulse} > E_{1way} > E_{2way} \approx E_{setup} \tag{V.6-14}$$

A quantitative comparison of the resulting values for E_{pulse}, E_{1way} and E_{2way} is presented in Table 34.

It is of interest, that all models - even those, which suggest the maximum limit of possible values - provide very low approximate results for E_{setup} with ratios considerably less than 1 % of the total energy input. Hence, E_{setup} can be regarded as a nearly irrelevant term in the energy balance (V.6-1).

	E_{pulse} [mJ]	E_{1way} [mJ]	E_{2way} [mJ]
[V290R]	5,1	4,7	3,6
[V290L]	2,1	2,0	1,1
total [V290]	7,2	6,7	4,7
percentage of E_{tot}	0,27 %	0,25 %	0,18 %

Table 34: Resulting energy values for a representative example: The results of the right ([V290R], plotted in Fig. 81) and left ([V290L]) force signal, calculated according to the corresponding model, are shown as well as the total sum of both and the corresponding ratio of the total energy input.

Nevertheless, E_{setup} has been approximately determined for all HIE data sets, using the two way model of incomplete relaxation (all results can be found in Appendix F). For the sake of completeness, the most important issues about the results and dependencies of E_{setup} are briefly outlined.

6.3.2. Overview of Results and Dependencies of E_{setup}

Table 35 gives a statistical summary of the resulting values for E_{setup}. In no instance has the energetic ratio $\frac{E_{setup}}{E_{tot}}$ exceeded 0,52 %.

	E_{setup} [mJ]	HIE
minimum value	$0{,}14 \pm 0{,}07$	[V213], {101}
maximum value	17 ± 8	[V686], {622}
mean value	5,6	
standard deviation	3,5	

Table 35: Overview of the resulting values for E_{setup}: The corresponding HIE number and configuration is displayed in the right column.

The following statements on the dependencies of E_{setup} are supported by the results of multivariate statistic analyses (those are displayed in detail in Appendix H):

- Box plots reveal no systematical dependency of the impact velocity v_H on E_{setup}. Only for some few constraints, it appears that there is a significant positive linear correlation (e.g. in the case {X01} the correlation coefficient is 0,572 with an error probability of less than 0,05 %). This indicates that the influence of impact coupling conditions (i.e. the hammer geometry) and material properties is much higher than the influence of E_{impact}.

- In fact, the influence of the hammer geometry on E_{setup} has been verified to be significant by means of t-tests in a number of comparisons (e.g. {101} - {111}; {201} - {211}; {101} - {131}; {606} - {616}; {602} - {622}).

- T-tests have also revealed the significant dependency of the target type (e.g. for the comparison {601} - {602}; {601} - {603}; {601} - {604}; {601} - {606}). These results are well consistent with the findings of chapter V.2: Evidently, the specific material properties of a target significantly affects the force signal as well as the resulting energy E_{setup}.

6.4. Plastic Deformation Energy E_{def}

First of all, it has to be stated, that all HIE targets behave in an ideally brittle way, so that if plastic deformation occurs, only the hammer head will be affected.

For most cases of HIEs, however, there is no measurable plastic deformation of the hammer tip. In fact, the only configuration, under which the hammer head is significantly notched, is {X06}, i.e. when a pointed hammer hits a RX target.

To quantify the corresponding energies E_{def}, which have been dissipated into the plastic deformation of the hammer tip, comparative (and *de facto* totally inelastic) hammer impact studies on B_4C samples of the same dimensions as RX targets have been conducted. By determining the impact energy as well as the seismic energy, one obtains the dissipated deformation energy. These energy values have been plotted over the determined notch depth, so that the resulting curve could be used as a calibration curve (see Fig. 82).

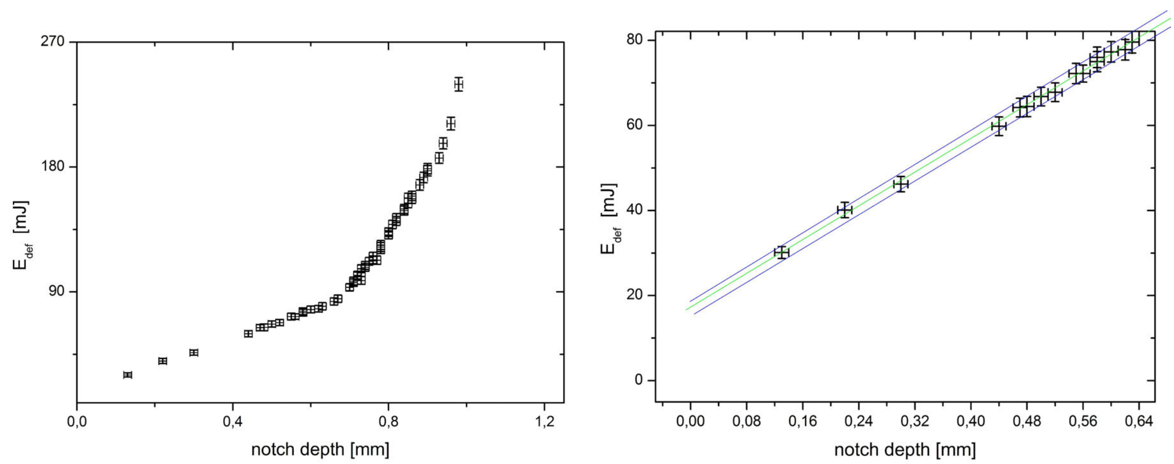

Fig. 82: Empirical correlation between plastic deformation energy E_{def} and the notch depth of the hammer head, based on inelastic impact studies on B_4C samples: On the right, the relevant part of the calibration curve for lower notch depth values is presented, which can be approximated as a linear correlation with a slope of approx. 99 $\frac{mJ}{mm}$. The respective range of inaccuracy is displayed as well.

The measured notch depths for HIEs under the condition {X06} have been between 0,11 mm and 0,64 mm. For these values, the energy in the calibration curve shows an approximately linear correlation (see Fig. 82, right) with a fault tolerance of $\triangle E_{def} = \pm 2$ mJ (cf. Appendix A). Due to the empirical results, plastic deformation needs a minimum energy value, which is approximately (by extrapolation) determined to be $E_{def,0} = (13 \pm 2)$ mJ.

A statistical overview of the resulting E_{def} is provided by Table 36.

{X06}	E_{def} [mJ]	HIE
minimum value	$28{,}0 \pm 2{,}0$	[V410], {106}
maximum value	$80{,}0 \pm 2{,}0$	[V434], {606}
mean value	51,6	
standard deviation	16,6	

Table 36: Overview of the resulting values for E_{def}: Note that this energy term is only relevant for HIEs under the constraints {X06}, otherwise E_{def} is presumed to be zero. Thus, for statistical statements only the cases {X06} have been taken into account.

Below, the fundamental findings for E_{def} are summarized, based on the results of multivariate statistical analyses (see also Appendix H):

- Plastic deformation processes are mostly negligible. Only under the HIE constraints {X06}, E_{def} has to be considered in the energy balance. Under these conditions its resulting values vary between 1,0 % and 3,1 % of E_{tot}.
- Evidently, there is a strong dependency on the material: Glass ceramic samples have proven to be considerably harder (i.e. more resistant against the impact of a steel hammer) than float glass targets.
- Also the contact area between hammer and target has a significant influence on E_{def}: As pointed out above, wide and round hammer heads are much less affected by the impact.
- There is a highly significant linear correlation between v_H and E_{def} ($\rho = 0,953$, $p < 0,05\,\%$). This result is also confirmed by the results of partial correlation analyses, which have verified that in fact E_{def} is only indirectly affected by E_{tot}, and primarily depends on E_{impact}.

6.5. Acoustic Energies E_{air}

Due to empirical findings published in literature (e.g. [16, 45, 98]) for blasting experiments as well as for MFCI, it can be presumed that the amount of acoustic energy which is released into the surrounding air in form of sound waves, does not exceed 5 % of the total energy input.

As a consequence, E_{air} has been determined by:

$$E_{air} \approx 0,05 \cdot E_{tot} \tag{V.6-15}$$

It has to be stated that this is an approximation to obtain the maximum value for E_{air}, and its actual amount is probably lower. This fact has also to be considered in the error analysis (see Appendix A).

6.6. Fracture Energies E_{frac}

6.6.1. Determination and Overview of Results

Under all these considerations and by means of (V.6-1), it is now possible to quantify E_{frac}, using the determination equation:

$$E_{frac} = E_{tot} - E_{kin} - E_{setup} - E_{air} - E_{def} \tag{V.6-16}$$

As this thesis especially focuses on the energetic aspects of fragmentation, E_{frac} is seen as a crucial quantity and has hence been comprehensively studied. Table 37 presents a statistical summary of its values.

	E_{frac} [mJ]	HIE
minimum value	1589 ± 66	[V223], {101}
maximum value	5003 ± 102	[V653], {621}
mean value	3055	
standard deviation	603	

Table 37: Overview of the resulting values for E_{frac}: The corresponding HIE number and configuration is displayed in the right column.

Experiment	E_{DC} [%]	E_{NC} [%]	E_{shock} [%]	E_{surf} [%]	E_{frac} [%]	$E_{residual}$ [%]
[V406] {106}	75,0	10,9			85,9	14,1
[V222] {101}	84,3	6,7			91,0	9,0
[V665] {123}	89,2	4,3			93,6	6,4
MFCI (a)			37,5	50,0	87,5	12,5
MFCI (b)			58,9	36,0	94,9	5,1

Table 38: Percentages of fracture energies in relation to the total energy input: Representative results of HIEs are compared to data of MFCI, published in [18]. The resulting ratios of E_{frac} of MFCI and HIEs coincide very well.

The percentage of E_{frac} in relation to E_{tot} varies between 85,9 % and 93,6 %. A comparison between the fracture energies of HIEs and MFCI is presented in Table 38:

On the one hand, E_{frac} is composed of damage crack and normal crack energies, E_{DC} and E_{NC}, which are calculated by the corresponding FSED (see chapter V.8.3).

In the published case of MFCI [18], however, the values of shock wave energy E_{shock} and of surface generating fragmentation energy (including all classes of cracks) E_{surf} are given. Note that these terms of energy are - due to their definition - not identical and thus not comparable to E_{DC} and E_{NC}.

Nevertheless, the sum of E_{shock} and E_{surf} results in E_{frac} as well, so that this term of energy can be used for comparative studies between both types of experiments.

It is notable, that the resulting values coincide very well. This good agreement of experimental results can be seen as strong and convincing evidence, that MFCI and HIEs are based on comparable fragmentation processes.

6.6.2. Dependencies

Due to the results of multivariate statistic analyses (in detail presented in Appendix H), the following conclusions can be drawn:

- A scatter plot (see Fig. 83) and statistical tests reveal a highly significant and virtually ideal linear correlation between E_{frac} and E_{tot}. Without constraints, ρ amounts to 0,997 ($p <$ 0,05 %). This highly significant correlation has been also validated for every single HIE configuration.

- Due to the interrelationship between E_{tot} and v_H, it is no surprise that E_{frac} is correlated to impact velocity (and impact energy) with a high significance, too.
  Nevertheless, the results of partial correlation analyses have revealed that it is E_{tot}, on which in fact E_{frac} depends: As the corresponding correlation coefficient (checking the partial correlation between E_{frac} and E_{tot} controlling for v_H) is 0,9959 ($p <$ 0,05 %), while on the other hand, the partial correlation coefficient between E_{frac} and v_H controlled for E_{tot} is -0,3264 ($p <$ 0,05 %).
  Put simply, this result implies that if the dominating influence of E_{tot} is mathematically removed, E_{frac} is even negatively correlated to the impact energy! Although at first glance possibly puzzling, this effect could be coherently explained by the damping influence of the impact notch, which extends in the case of increasing impact velocities.

- Besides these factors, there is also a weak but not negligible influence of the hammer geometry on E_{frac} (e.g. significant differences between {X23} and {X33} are verified by t-tests in the case of E_{tot} ranging between 3,5 J and 4,0 J). This influence is consistent with the suggested impact notch damping model, as well.

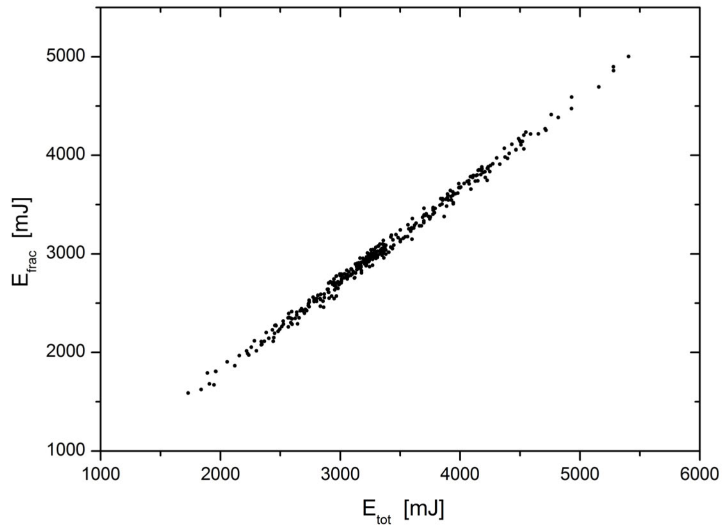

Fig. 83: HIE results of E_{frac} plotted over E_{tot}: The clear linear correlation is also supported by bivariate and partial correlation analysis (see Appendix H).

- The strong linear correlation with E_{tot} effects also a similar target type dependency on E_{frac}. Especially in the case of higher impact velocities RX and TK targets show significantly lower fracture energy mean values (see Table 39).

Y (target)	{1XY} $\bar{E}_{frac}$ [mJ]	{4XY} $\bar{E}_{frac}$ [mJ]	{6XY} $\bar{E}_{frac}$ [mJ]	{6XY} $\frac{\bar{E}_{frac}}{V_{target}}$ $[\frac{J}{m^3}]$
1 (FG)	2591 ± 66	3377 ± 88	3880 ± 99	136,70
2 (T5)	2626 ± 66	3364 ± 86	3676 ± 96	129,52
3 (T10)	2804 ± 67	3643 ± 87	3829 ± 97	134,90
4 (TK)	2782 ± 66	2909 ± 86	3119 ± 96	109,90
5 (AS)	2774 ± 67	3274 ± 84	3952 ± 95	139,24
6 (RX)	2493 ± 67	3050 ± 88	3089 ± 95	135,71

Table 39: Target specific mean values and uncertainties of E_{frac} under various hammer fall heights and arbitrary hammer geometries: Especially for cases of higher impact velocities, the values for $\bar{E}_{frac}$ of TK and RX samples are significantly lower than for the other target types.

- Once again, it has to be mentioned that RX samples have been thinner and thus have been of a smaller volume V_{target}. To get an idea about the effect of this issue, the amounts of standardized volume-specific fracture energy E_{frac}/V_{target} have been calculated and are displayed in Table 39 as well.
  It is an interesting fact, that the resulting values of RX are very close to those of FG. At least all results impressively underline, that the existence as well as the geometry of pre-stresses have a distinct influence on E_{frac}, and that the specific stress situation in TK targets significantly effects lower fracture energy dissipation.

- In contrast, no significant linear correlation has been found between E_{frac} and the type of primary crack. This result is quite interesting, as it can be seen as a first indication, that, at least in regard to normal cracks, E_{frac} - and thus also the corresponding fracture surface energy density - is generally not a location-depending parameter.

7. Complementary Results of Multivariate Statistical Analysis

By additional multivariate statistical analyses it is now possible to check the previously made assumptions, as well as to gain further valuable insight in the interdependencies of parameters, which help to describe fracture processes.

All results can be found in the corresponding output files of SPSS, which are presented in the respective folder of Appendix H on the attached DVD.

Based on these statistical results, the following conclusions can be drawn:

- The correlation between M_R an v_H has been verified to be significant linear for FG (ρ = 0,290; p = 0,7 %). This result validates the corresponding crack mapping observations made in chapter V.3.3: A higher impact velocity (and thus a higher amount of E_{impact}) results in a higher damage crack intensity M_R, a finding which supports the fundamental theory of shock wave induced damage cracks.

- Considering the nature of damage cracks, it is appropriate to take once again a closer look at Table 22 in chapter V. 5.3.6, which presents the highly significant correlation results between M_R and fragment areas B for various fractions.
  It is evident, that the corresponding correlation coefficient ρ is distinctly lower for the finest fraction $\phi > 1$. This phenomenon is not only observed for FG, but also for all other target types (in fact for T5, T10, and RX, there is no significant correlation for the finest fraction at all). It coincides very well with the considerations, presented in chapter V.5.3.4 and underpins the theory, that the finest fraction is dominated by Zone 0 particles and trichips in every respect.

- There is also a slight but significant linear correlation (e.g. for FG: ρ = 0,247; p = 1,6 %) between v_H and the number of crack branches Z. The latter parameter can be seen as an indicator, which quantifies the stability of primary cracks. Evidently, the crack stability is affected by the impact energy.

The key issue of this thesis - the description of energetic dissipation processes by using the FSED concept - is based on the presumption that there is a linear correlation between the fracture energy E_{frac} and the generated surface area A_{frac}, which has already been theoretically predicted and experimentally verified for MFCI processes (see chapter II.1.5).
Now it is possible to validate this presumption also for HIEs, by means of correlation and regression analyses:
In fact all tests confirm, that E_{frac} and A_{frac} are linearly correlated with high significance for all targets (see Table 40) and for all hammer geometries. This clear linear correlation is exemplarily illustrated for FG and RX by Fig. 84, too.

Furthermore, also the crack class-specific fracture areas A_{NC} and A_{DC} show highly significant linear correlations to E_{frac} for all targets as well (with one exception: the correlation between A_{NC} and E_{frac} in the case of TK targets is slightly above the 5 % level of significance).

$\rho(E_{frac};\ ...)$		FG	T5	T10	TK	AS	RX
A_{frac}	ρ	0,994	0,991	0,991	0,988	0,991	0,968
	p	$< 0{,}05\,\%$	$< 0{,}05\,\%$	$< 0{,}05\,\%$	$< 0{,}05\,\%$	$< 0{,}05\,\%$	$< 0{,}05\,\%$
A_{NC}	ρ	0,416	0,407	0,566	0,315	0,672	0,433
	p	$< 0{,}05\,\%$	$< 0{,}05\,\%$	$< 0{,}05\,\%$	7,9 %	$< 0{,}05\,\%$	$< 0{,}05\,\%$
A_{DC}	ρ	0,995	0,993	0,995	0,992	0,990	0,984
	p	$< 0{,}05\,\%$	$< 0{,}05\,\%$	$< 0{,}05\,\%$	$< 0{,}05\,\%$	$< 0{,}05\,\%$	$< 0{,}05\,\%$

Table 40: Linear correlation for various target types between E_{frac} and A_{frac}. The latter parameter describes the total sum of A_{NC} and A_{DC}, which as well have proved to be linearly correlated with high significance. The first row denotes always the amount of the respective Pearson's correlation coefficient ρ, while the corresponding error probability is denoted p.

It is evident that the determined values of ρ are distinctly lower for A_{NC} than for A_{DC} and slightly lower for A_{frac} than for A_{DC}. This might be an indication, that the advanced fracture-specific FSED model (see chapter V.4) is superior and closer to the reality of fracture processes than the basic FSED model described by (V.4-1).
Yet, this result should not be overrated, as one has to consider that the areas A_{DC} show always significantly higher values than the respective A_{NC}. As a consequence this effect could also be caused by a stronger scattering influence due to A_{NC} measurement uncertainties.

In conclusion, one can state that all experimental results of HIEs verify the presumptions made above, allowing to apply the FSED concept.

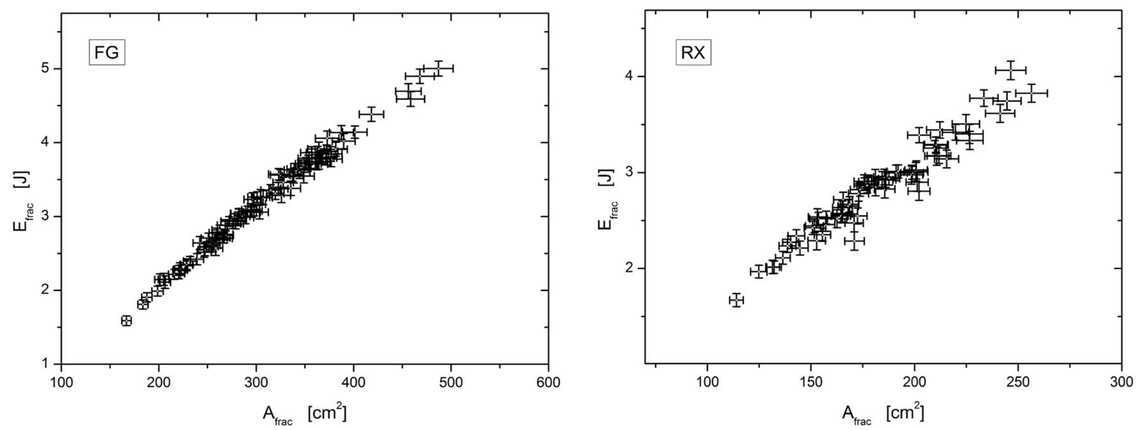

Fig. 84: Linear correlation between E_{frac} and A_{frac}, illustrated for HIEs with FG and RX targets. The corresponding slope is given by the respective FSED parameter η_{tot} (see Table 42).

8. Fracture Surface Energy Densities

On the basis of the results presented above, it is now possible to quantify the corresponding FSED parameters η_{tot} and $\vec{\eta}$ for each HIE as well as to examine the quality of both FSED models.

All statements below are based on the results of multivariate statistical analyses, which can be found in detail in the corresponding folders of Appendix H.

8.1. Results for the Basic FSED Model and η_{tot}

The total FSED η_{tot} for each HIE has been quantified by means of (V.4-1) and are listed in Appendix F. Additionally a least square linear regression has been carried out with the aid of the software SPSS. Those results are denoted $\tilde{\eta}_{tot}$. A statistical overview of the occurring values is given in Table 41.

	$\eta_{tot}\ \left[\frac{J}{m^2}\right]$	HIE	$\tilde{\eta}_{tot}\ \left[\frac{J}{m^2}\right]$
minimum value	$95{,}2 \pm 6{,}7$	[V223], {101}	$94{,}6 \pm 2{,}5$
maximum value	$167{,}6 \pm 8{,}5$	[V423], {306}	$147{,}9 \pm 4{,}8$
mean value	116,9		112,5
standard deviation	19,8		18,8

Table 41: Overview of the resulting values for η_{tot}: The corresponding HIE number and configuration is displayed in the center column. In the right column the results of target type-specific linear regression analyses $\tilde{\eta}_{tot}$ are presented as well.

The following conclusions about η_{tot} can be drawn due to the results of multivariate statistic analyses:

- No general linear correlation between η_{tot} and v_H has been found within the studied scope. However, it has to be kept in mind that the range of impact velocities in the HIEs has been relatively small ($1{,}75\ \frac{\mathrm{m}}{\mathrm{s}} \leq v_H \leq 2,50\ \frac{\mathrm{m}}{\mathrm{s}}$), so that it might just be superimposed by the effects of measurement inaccuracies of η_{tot}. It has to be stressed that a general dependency of v_H cannot be ruled out for wider velocity ranges.
  In fact, published results [23, 92] indicate a significant influence of the impact energy, if the studied range is substantially larger, as already pointed out in chapter II.1.5.

- In this respect, it is notable that at least FG and T5 targets show a significant but not very strong linear correlation between η_{tot} and the fracture energy E_{frac} (e.g. ρ amounts to 0,301 ($p = 1{,}4\,\%$) for T5). This result can be seen as an indication that the parameter η_{tot} is only comparable under similar experimental conditions.

- The hammer geometry appears to have no significant influence on η_{tot} at all.
  The only exception to this empirical finding has been found for RX targets: In the case of a 8,3 mm wide hammer, the respective values of η_{tot} have been significantly higher than for all other hammer geometries (η_{tot} {X26}: $(161{,}8 \pm 3{,}3)\ \frac{\mathrm{J}}{\mathrm{m}^2}$ is for example with a high significance of $p < 0{,}05\,\%$ different to η_{tot} {X06}: $(153{,}3 \pm 4{,}4)\ \frac{\mathrm{J}}{\mathrm{m}^2}$). This phenomenon

is also the reason for the comparatively large standard deviation for η_{tot} of RX, presented in Table 42.
As this "outlier" effect is exclusively observed for the HIE configuration {X26}, this might be a resonance effect. However, due to the comparatively low data size number ($N = 12$ under this configuration), this finding could also be a coincidental artifact and should not be overrated, particularly as this effect is not detectable any more in the advanced FSED model (see there).

- As expected, there is a clear and highly significant dependency on the material. The determined results η_{tot} and $\tilde{\eta}_{tot}$ for various target types are shown in Table 42.

	$\bar{\eta}_{tot}\ \left[\frac{J}{m^2}\right]$	$\sigma(\eta_{tot})\left[\frac{J}{m^2}\right]$	$\tilde{\eta}_{tot}\ \left[\frac{J}{m^2}\right]$	$s(\tilde{\eta}_{tot})\left[\frac{J}{m^2}\right]$
FG	105,1	1,2	104,3	2,6
T5	112,6	1,9	110,2	3,2
T10	113,9	1,8	116,4	2,9
TK	100,9	2,9	102,2	2,5
AS	94,6	2,5	99,9	2,3
RX	147,9	4,8	155,9	6,4

Table 42: Resulting total FSED for various target types: The mean values $\bar{\eta}_{tot}$ and the respective standard deviations $\sigma(\eta_{tot})$, as well as the results of linear regression $\tilde{\eta}_{tot}$ plus the corresponding standard errors $s(\tilde{\eta}_{tot})$ are presented (see also text).

- AS targets show significantly lower total FSED values than FG samples (at least within the studied scope). This implies that adding a silver layer to a target decreases the costs of energy needed to generate a certain amount of fracture area. Although these results are based on a rather low sample size (N = 27), this effect might be explained by the specific coupling conditions between the hammer and the silver layer, which clearly affects the extension of damage cracks (see chapter V.3.2).

- Also the specific pre-stress situation in TK targets evidently effects significantly lower values for η_{tot}. This is especially notable, as it has been previously verified that at the same time the dissipated fracture energy $\bar{E}_{frac}$ has been significantly lower for these target types (see chapter V.6.6.2). Thus, in TK targets the amount of the generated total fracture area has been distinctly smaller, *although* their total FSED is significantly lower.

- According to the basic FSED model, the pre-stress geometries in T5 as well as in T10 targets effect an increase of η_{tot}: Compared to FG, more energy is needed to create the same amount of fracture area.

- The highest values of total FSED are determined for RX targets. This finding is a further indication that due to the specific nanocrystalline structure, glass ceramics show a distinctly reduced susceptibility to material failure processes.

8.2. Results for the Fracture-Specific FSED Model and $\vec{\eta}$

8.2.1. FSED Determination Concepts

According to (V.4-3), in the case of two data sets ($i = 2$), the FSED for damage cracks η_{DC} can be calculated by:

$$\eta_{DC} = \frac{E_{frac\,2} - \eta_{NC} \cdot A_{NC\,2}}{A_{DC\,2}} \tag{V.8-1}$$

where η_{NC} is given by:

$$\eta_{NC} = \frac{E_{frac\,1} A_{DC\,2} - E_{frac\,2} A_{DC\,1}}{A_{NC\,1} A_{DC\,2} - A_{NC\,2} A_{DC\,1}} \tag{V.8-2}$$

If there are more than two data sets on hand (i.e. i > 2), the equation system (V.4-3) is over-determined, and statistical methods can be used to specify $\vec{\eta}$.

For this purpose two different approaches have been conducted:

General Determination of FSED by Linear Regression

Especially for large sample sizes $i \gg 2$, (V.4-3) can be statistically solved by a linear regression applying a least squares approach. This “classical” solution is a generally used method, which has been developed by Gauss (see e.g. [34]) and provides not only reliable results, but also allows to make profound statistical statements on the quality of the presumed linear model as well as the respective uncertainties [12, 121].

Furthermore this method has the advantage of being insensitive to numerical instabilities, thus all data sets can be used. All linear regression operations have been conducted by means of the statistical analysis software SPSS.

The FSED values quantified by means of linear regression are denoted $\tilde{\eta}_{NC}$ and $\tilde{\eta}_{DC}$.

Individual FSED Determination Concept

This determination concept is used in cases of too low sample sizes, in which the standard errors resulting from the classical linear regression are too large to allow statistical comparative analysis.

In the alternative FSED determination concept, $\vec{\eta}$ is calculated individually for each HIE data set, using (V.8-2) and (V.8-1) as well as the average values of all residual data sets under identical HIE configurations as complementary reference records $i = 2$.

For the calculation of the corresponding mean value it is useful to consider data sets, for which the resulting denominator in (V.8-2) - which in fact is identical to the determinant of (V.4-3) for $i = 2$ - is as large as possible, in order to avoid numeric instabilities and to reduce uncertainties.

A closer look reveals that numeric instabilities are only significant for HIE data sets, which are “too similar” to the observed one. These records have been omitted before the average has been computed.

Due to the considerable fluctuation of the parameters A_{NC}, A_{DC} and E_{frac} even under identical HIE configuration (see chapters 5 and 6), the number of “usable” data sets has in all cases been more than 90 % of the total sample size and has hence been sufficient for representative statistical analysis.

Note that - from a strict mathematical point of view - due to this method the quantification for each case has based on an (although slightly) different pool of data sets, so that if there is a choice, the statistical results by means of the linear regression method are preferable.

All resulting individual FSED calculated by this method are listed in the tables of Appendix F.

8.2.2. Normal Crack-Specific FSED η_{NC}: Results and Dependencies

Table 43 presents a statistical summary of the determined values for η_{NC}. Evidently both FSED determination methods provide similar results, which indicates that the individual determination concept is an admissible alternative to the linear regression.

	η_{NC} $\left[\frac{J}{m^2}\right]$	HIE	$\tilde{\eta}_{NC}$ $\left[\frac{J}{m^2}\right]$
minimum value	37,46	[V605], {114}	$(41{,}66 \pm 3{,}51)$
maximum value	67,02	[V421], {306}	$(65{,}09 \pm 2{,}30)$
mean value	50,08		49,82
standard deviation	8,58		8,16

Table 43: Overview of the resulting values for η_{NC}, calculated by the individual FSED determination concept: The corresponding HIE number and configuration is displayed in the center column. In the right column also the corresponding results of target type-specific linear regression analyses $\tilde{\eta}_{NC}$ are displayed.

Due to the results of multivariate statistical analyses the following conclusions can be drawn (see Appendix H):

- There is no significant linear correlation between η_{NC} and v_H within the considered scope.
- Furthermore η_{NC} shows no significant dependency on the hammer geometry. It is of interest that there is also no significant "outlier"-effect for the case {X26} as recorded for η_{tot}.
- The normal crack-specific FSED depends significantly on the material type (see Table 44).

	$\bar{\eta}_{NC}$ $\left[\frac{J}{m^2}\right]$	$\sigma\left(\eta_{NC}\right)\left[\frac{J}{m^2}\right]$	$\tilde{\eta}_{NC}$ $\left[\frac{J}{m^2}\right]$	$s\left(\tilde{\eta}_{NC}\right)\left[\frac{J}{m^2}\right]$
FG	47,05	0,42	47,79	1,55
T5	43,04	0,38	44,47	1,24
T10	51,96	0,52	49,62	2,95
TK	38,04	0,38	41,66	3,51
AS	48,92	0,43	50,32	4,41
RX	65,91	0,61	65,09	2,30

Table 44: Normal crack-specific FSED values for various target types: The mean values $\bar{\eta}_{NC}$, calculated by the individual FSED determination concept and the respective standard deviations $\sigma\left(\eta_{NC}\right)$ are shown, as well as the results of linear regression $\tilde{\eta}_{NC}$ plus the corresponding standard errors $s\left(\tilde{\eta}_{NC}\right)$. Please note that by definition standard deviations and standard errors are different parameters.

- It is evident that TK targets show the lowest values for η_{NC}: The specific pre-stress geometry in these targets apparently reduces the amount of energy needed to create normal crack induced fracture surfaces.
- Also the pre-stress situation in T5 targets appears to facilitate energy dissipation in normal cracks. This result is quite plausible, as the pre-stress configuration had been

identical to the situation of the later HIE. Thus, there has already been some energy dissipation during the procedure of target preparation, which effects an energetic reduction of the fracture threshold.

- In this regard, it is particularly notable that - in contrast to T5 and TK - normal crack-specific FSED of T10 targets show significant higher values than FG. The broader pre-stress geometry clearly increases the amounts of energy needed to expend in order to generate normal crack induced fracture surfaces.
- Also AS targets show significantly higher amounts of η_{NC} than FG targets. It is clear that the coupling situation between hammer and target is distinctly affected by the attached silver layer. This result indicates that the interfacial condition plays an important role in impact experiments and hence always has to be considered in fracture studies.
- The highest values for η_{NC} are those featured by RX targets. For the examined glass ceramics, the necessary expenditure of energy to create a certain amount of fracture area in form of normal cracks is about 40 % higher than for FG targets. This result clearly confirms our considerations on the significant influence of the nanocrystalline structure on fracture processes (see above).
- The amount of total energy input E_{tot} does not significantly affect η_{NC}.

8.2.3. Results and Dependencies of Damage Crack-Specific FSED η_{DC}

A statistical overview of the resulting η_{DC} and $\tilde{\eta}_{DC}$ is given in Table 45.

	η_{DC} $\left[\frac{J}{m^2}\right]$	HIE	$\tilde{\eta}_{DC}$ $\left[\frac{J}{m^2}\right]$
minimum value	104,60	[V505], {605}	(105,91 ± 1,32)
maximum value	181,85	[V424], {306}	(178,96 ± 1,13)
mean value	128,14		125,07
standard deviation	24,80		27,44

Table 45: Overview of the resulting values for η_{DC}, calculated by the individual FSED determination concept: The corresponding HIE number and configuration is displayed in the center column. In the right column the respective results of target type-specific linear regression analyses $\tilde{\eta}_{DC}$ are presented as well.

The following statements on the dependencies of η_{DC} are supported by the results of multivariate statistic analyses:

- Like for η_{NC}, there is also no significant linear correlation between η_{DC} and v_H within the studied scope.
- In general, the hammer geometry has no significant influence on η_{DC}. Also - like for η_{NC} - no significant "outlier"-effect has been detected for the case {X26}.
- It is evident that η_{DC} significantly depends on the target type-specific material properties of the target (see Table 46).
- The lowest damage crack-specific FSED values have been detected for AS targets. Evidently, the specific interfacial situation of those targets facilitates the generation of

	$\bar{\eta}_{DC}$ $\left[\frac{\mathrm{J}}{m^2}\right]$	$\sigma\left(\eta_{DC}\right)\left[\frac{\mathrm{J}}{m^2}\right]$	$\tilde{\eta}_{DC}$ $\left[\frac{J}{m^2}\right]$	$s\left(\tilde{\eta}_{DC}\right)\left[\frac{\mathrm{J}}{m^2}\right]$
FG	112,09	1,48	111,35	0,30
T5	120,86	1,59	119,80	0,30
T10	125,90	1,59	125,95	0,72
TK	109,76	1,47	108,46	0,81
AS	106,71	1,51	105,91	1,32
RX	177,97	2,30	178,96	1,13

Table 46: Damage crack-specific FSED values for various target types: The mean values $\bar{\eta}_{DC}$, calculated by the individual FSED determination concept and the respective standard deviations $\sigma\left(\eta_{DC}\right)$ are shown, as well as the results of linear regression $\tilde{\eta}_{DC}$ plus the corresponding standard errors $s\left(\tilde{\eta}_{DC}\right)$.

fracture surfaces in form of damage cracks. This implies that due to the silver layer, shock waves seem to be more “effective” in AS targets than in any other target type. It is an interesting fact that the coupling conditions of those targets affect η_{NC} and η_{DC} in completely different ways, which can be seen as a further indication that in principle damage cracks and normal cracks are based on different fracture mechanisms.

- Highly significant higher values for η_{DC} are featured by TK targets. Note that in these targets, the damage crack zone is in large parts not affected by thermal pre-stresses. This could explain why the damage crack-specific values of TK targets are rather close (yet still significantly lower) to those of FG.

- Pre-stressed T5 targets and T10 targets show distinctly higher amounts for η_{DC} than any other float glass targets. It is evident that the generation of damage crack-induced surfaces, is from an energetic point of view, more “cost intensive” in those cases. This coincides well with the crack mapping results (see Fig. 41): T10 targets, in particular, show significantly lower damage crack intensities.

- Again, as in the case of AS targets, it is notable that the thermal pre-stress configuration in T5 targets effect an increase in η_{DC} and at the same time a decrease in η_{NC}. As we will see later, understanding this behavior might be the key to further comprehension of fracture mechanisms.

- The examined glass ceramic samples have featured the highest damage crack-specific FSED values of all target types. The amounts of η_{DC} for RX are roughly about 60 % higher than for FG, which indicates once more that this material has a particular low susceptibility towards the effects of shock waves.

- E_{tot} has shown no significant influence on η_{DC} in the studied scope.

8.2.4. Checking for Local Dependencies

As mentioned above, η_{NC} and η_{DC} are not dependents of E_{tot}. This is quite an important fact, as it implies that they are - at least in the studied scope of HIEs - very handy parameters in order to describe energy dissipation processes.

Yet, to use the FSED parameters also for a dynamical description, it is necessary to check if η_{NC} and η_{DC} are constants, or a locally dependent function of the respective crack tip.

Local Dependency of η_{DC}

Due to the discrete structure of the conchoidal crack zone, it is very unlikely, that η_{DC} is locally independent. In fact, this parameter probably gives the average amount of several discrete density values $\eta_{DC\,0}$, $\eta_{DC\,1}$, $\eta_{DC\,2}$, $\eta_{DC\,3}$.

It would be a very elaborate and difficult task to determine the zone-specific values of this parameter.

Nevertheless, there is an elegant possibility to obtain at least an idea of how large the local dependency of the determined "overall" FSED parameter η_{DC} finally is:

It has been checked by means of statistical t-tests if the damage crack intensity M_R has a significant influence on the damage crack-specific FSED parameter η_{DC} under otherwise identical HIE constraints.

Remarkably enough, there is in *no* instance any significant difference in η_{DC} (see Appendix H).

Maybe the values of the zonal FSED parameters are too close for this method and thus beyond the resolution limit.

Another, more likely explanation for this rather astonishing result might be, that one of the specific FSED parameters (most probably that of Zone 0: $\eta_{DC\,0}$, as a considerable part of the fracture area is generated there, suggesting that this is the zone of maximum energy dissipation) has a dominating influence on η_{DC}. As a consequence the other terms $\eta_{DC\,i}$ effect only a variation, which is too low to be detected by this approach.

On any account, these results imply that it is admissible to apply η_{DC} in good approximation as a locally independent constant, to describe the energy dissipation processes in HIEs.

Local Dependency of η_{NC}

One fundamental result of the previous section is that not only the existence, but also the geometry of pre-stresses significantly affects the value for FSED of normal cracks.

Hence it could be assumed that η_{NC} depends on the position of the propagating crack tip: The FSED for cracks in the pre-stressed regions might be different compared to those propagating on the non pre-stressed periphery. Fig. 85 illustrates this situation, by showing a representative example:

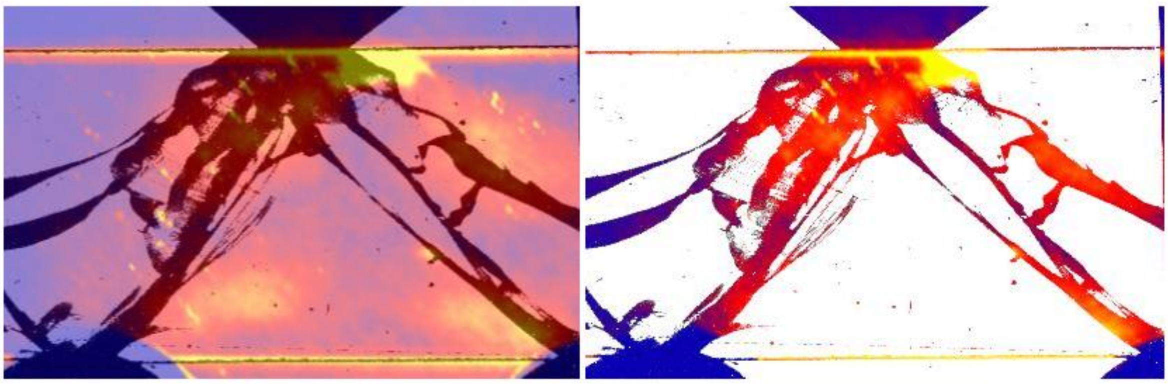

Fig. 85: Considerations on the local dependency of η_{NC}: A photoelastic picture of a pre-stressed T5 target is superposed with an image of the same target in a late state of HIE fragmentation ([V293], {102}).

An image of pre-stresses (marked by bright colors) in a T5 target is crossfaded with an image of the same target in a late state of HIE fragmentation. If η_{NC} was locally depending on the pre-stress properties of the material, the FSED of cracks in the previously pre-stressed regions would be different from those in the non pre-stressed areas. The latter cracks propagating in the isotropic zone are marked blue in the right image of Fig. 85.

To check if this presumption is valid, an analytical approach can be conducted. Therefore, the linear normal crack-specific FSED model is extended, by now considering three different FSED parameters:

- η_{DCZ} describes the FSED for all normal cracks, which propagate in the zone that has been finally affected by damage cracks.
- η_{PZ} is the FSED parameter, which specifies energy dissipation in the anisotropic pre-stressed areas.
- η_{IZ} describes the FSED for normal crack propagation in the isotropic zones of the target.

The corresponding regions are marked in Fig. 86.

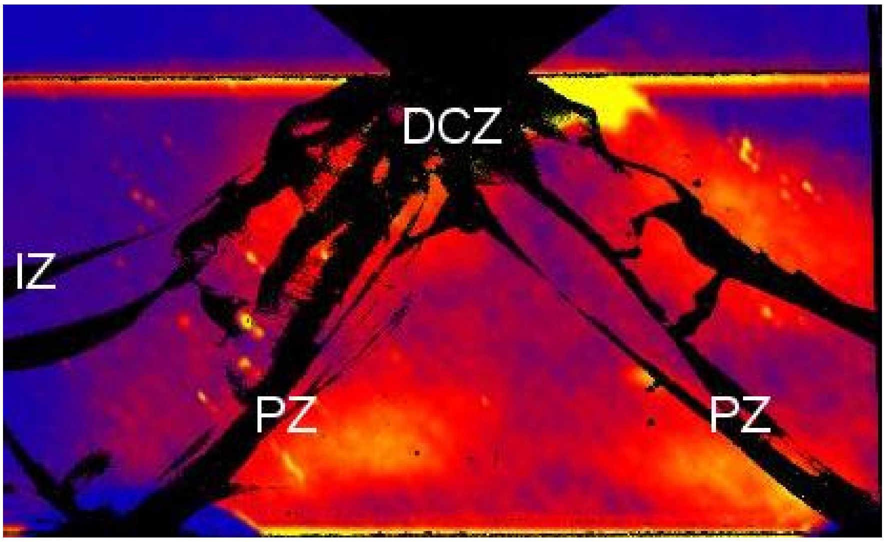

Fig. 86: Zonal model to check the local dependency of η_{NC}: In this model, it is presumed that the damage crack zone (DCZ), the pre-stressed zone (PZ) and the isotropic zone (IZ) are characterized by significantly different FSED.

By means of OPC, the resulting fracture areas A_{DCZ}, A_{PZ} and A_{IZ} can be quantified as well as the normal crack-specific fracture energy E_{NC} (see section V.8.3).

The linear ansatz:

$$E_{NC\,i} = \eta_{DCZ} \cdot A_{DCZ\,i} + \eta_{PZ} \cdot A_{PZ\,i} + \eta_{IZ} \cdot A_{IZ\,i} \tag{V.8-3}$$

can again be solved by means of linear regression. An analytical solution for three recorded data sets is given by the equations:

$$\eta_{DCZ} = \frac{\psi_{321} + \psi_{132} + \psi_{213} - \psi_{231} - \psi_{312} - \psi_{123}}{\Omega_{321} + \Omega_{132} + \Omega_{213} - \Omega_{231} - \Omega_{312} - \Omega_{123}} \tag{V.8-4}$$

$$\eta_{IZ} = \frac{E_{NC\,2} \cdot A_{PZ\,3} - E_{NC\,3} \cdot A_{PZ\,2} + \eta_{DCZ} \cdot (A_{PZ\,2} \cdot A_{DCZ\,3} - A_{PZ\,3} \cdot A_{DCZ\,2})}{A_{PZ\,3} \cdot A_{IZ\,2} - A_{PZ\,2} \cdot A_{IZ\,3}} \tag{V.8-5}$$

$$\eta_{PZ} = \frac{E_{NC\,2} - \eta_{DCZ} \cdot A_{DCZ\,2} - \eta_{IZ} \cdot A_{IZ\,2}}{A_{PZ\,2}} \tag{V.8-6}$$

where:

$$\psi_{ijk} = E_{NC\,i} \cdot A_{PZ\,j} \cdot A_{IZ\,k} \tag{V.8-7}$$

and:

$$\Omega_{ijk} = A_{PZ\,i} \cdot A_{IZ\,j} \cdot A_{DCZ\,k} \tag{V.8-8}$$

Thus it is possible to calculate and compare the resulting FSED parameters.

Yet this method is very elaborate and time consuming, as in practice a large data base is needed to achieve an acceptable accuracy.

Therefore, a more pragmatic approach has been conducted as well: A series of t-tests have been performed in order to check if η_{NC} significantly depends on the occurring primary crack type.

Fig. 87 helps to understand the significance of this test: A BCM, for example, always propagates between the regions of high pre-stresses and also between the flanks of the resulting PSZ.

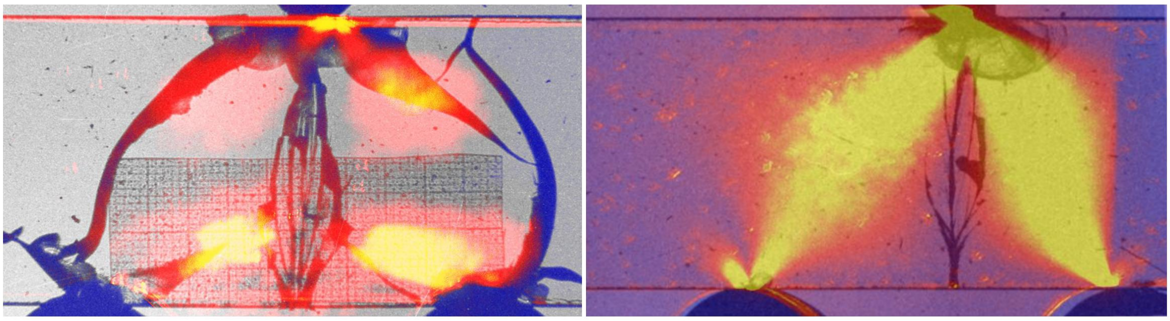

Fig. 87: Location of a BCM in a pre-stressed T5 target (left: [V271], {102}) and in a loaded FG sample (right: [V640], {121}): If η_{NC} was a parameter, which distinctly depends on the position of the propagating crack tip towards the regions of pre-stresses or the PSZ, the corresponding fracture surface energy density of BCMs would be significantly different from that of samples which have been fragmented by ACBs (as shown e.g. in Fig. 85).

Presume that η_{PZ} and η_{IZ} are distinctly different and that η_{NC} is a parameter, which shows a considerable local dependency.

In contrast to A-cracks, large parts of the BCMs do not cross the pre-stressed regions (see Fig. 87, left) nor the resulting PSZ (see Fig. 87, right).

As a consequence, the resulting amount of η_{NC} in the case of BCMs would show significant differences compared to those experiments, for which ACBs as primary cracks have been detected.

Yet, the results of the statistical tests, as well as spot-checks made by the analytical method, have shown that this presumption has to be rejected:

Virtually none of the comparative t-tests has revealed a significant dependency of η_{NC} on the primary crack type (see Appendix H).

The only exception is given by slightly lower values of η_{NC} for RX targets, if ACTs have been involved (for ACTs: $\bar{\eta}_{NC} = (65{,}53 \pm 0{,}61)\ \frac{\mathrm{J}}{\mathrm{m}^2}$, for BCMs: $\bar{\eta}_{NC} = (66{,}12 \pm 0{,}62)\ \frac{\mathrm{J}}{\mathrm{m}^2}$, significance by t-test: 3,6 %).

These type of cracks are always associated with extensive damage crack structures (see chapter V.1.3.2), and are characterized by large amounts of intermediate cracks, so it is very likely that this is - if not a coincidence - just an effect caused by the applied method of area quantification.

In this regard it has to be kept in mind that those fracture areas generated by normal cracks which have crossed the damage crack zone, always have been finally handled as "intermediate crack areas" in the quantification model (see chapter V.5.3) and have therefore been allocated to the area of *damage* cracks.

This could explain, why in virtually no studied case η_{DCZ} affects the determined FSED for normal cracks η_{NC} at all, although energy dissipation in this zone is most probably a significantly different process.

Furthermore, the local influence of anisotropic pre-stressed zones η_{PZ} on the process of energy dissipation is - due to our considerations above - not significantly different from that of η_{IZ}. Thus - at least in the studied scope of the HIEs - η_{NC} can be applied as a locally independent parameter, even in pre-stressed targets, with the only restriction that this parameter has probably a limited significance in the damage crack zone.

The fundamental consequences of this conclusion are discussed in section V.8.5.

8.3. Crack Class-Specific Fracture Energies E_{NC} and E_{DC}

Within the crack class-specific model, it is now possible to allocate the corresponding amount of energy, which has dissipated in form of normal crack areas or in form of damage crack induced fracture areas.

These terms are denoted E_{NC} and E_{DC}, respectively. Due to the linear equation (V.4-2) they are determined by:

$$E_{NC} = \eta_{NC} \cdot A_{NC} \tag{V.8-9}$$

and:

$$E_{DC} = \eta_{DC} \cdot A_{DC} \tag{V.8-10}$$

The resulting amounts for each HIE are listed in Appendix F.

The following sections summarize the results and dependencies of these energy terms, based on multivariate statistical analyses, which can be found in detail in the corresponding folder of Appendix H.

8.3.1. Results and Dependencies of E_{NC}

Table 47 presents a statistical summary of the resulting E_{NC}.

	E_{NC} [mJ]	HIE
minimum value	$(61{,}9 \pm 2{,}1)$	[V741], {134}
maximum value	$(430{,}0 \pm 12{,}4)$	[V433], {606}
mean value	179,2	
standard deviation	71,0	

Table 47: Summary of the resulting values for E_{NC}. The corresponding HIE number and configuration is displayed in the right column.

In short, the following facts about E_{NC} are revealed by multivariate statistical methods:

- There is a highly significant dependency on E_{impact} and E_{tot}: Without constraints, the corresponding results of linear correlation analyses have been $\rho = 0{,}533$; $p < 0{,}05\,\%$ and $\rho = 0{,}363$; $p < 0{,}05\,\%$, respectively.

- Partial correlation analyses reveal that the actually relevant parameter is evidently E_{impact} ($\rho = 0{,}421$; $p < 0{,}05\,\%$, if controlled for E_{tot}) and not E_{tot}.

- This clear linear correlation between E_{NC} and E_{impact} is even more conspicuous, when the data sets are separated by target types: For example for RX targets, ρ amounts to 0,723 ($p < 0{,}05\,\%$).
- Box plots as well as one-way analyses of variances (ANOVA, see chapter II.6) reveal no consistent dependency of the hammer head geometry on E_{NC}.
- There is a rather large variation of E_{NC} even under identical HIE configurations.
- Furthermore, there is an evident dependency on the target type: E_{NC} clearly depends on the properties of the material, which is confirmed by ANOVA results. Especially RX targets with significantly higher and TK targets with significantly lower amounts of E_{NC} show considerable differences to the corresponding values of the other targets. The respective results are listed in Table 49.
- Finally, box plots and ANOVA results reveal that E_{NC} is not significantly influenced by the type of the primary crack. This result coincides well with the findings for η_{NC}: The process of energy dissipation in form of normal crack induced fracture areas is locally independent.

8.3.2. Results of E_{DC} and Impact Notch Theory

A statistical overview of the calculated amounts of E_{DC} is given in Table 48.

	E_{DC} [mJ]	HIE
minimum value	(1386 ± 61)	[V223], {101}
maximum value	(4688 ± 112)	[V652], {621}
mean value	2876	
standard deviation	582	

Table 48: Summary of the resulting values for E_{DC}. The corresponding HIE number and configuration is displayed in the right column.

Before turning attention to the dependencies of E_{DC}, it is useful to take a closer look at the content of this energy term:

Due to the definition of E_{frac} and due to our considerations on the primary causes of damage cracks, it can be presumed that E_{DC} includes *inter alia* the dissipated shock wave energy E_{shock}.

The amount of this energy term in an impact experiment - according to the conclusions of chapter II.2 - depends on the contact area of the impacting object as well as on the impact velocity.

The percentage of E_{shock} within E_{DC} is unknown for HIEs. Nevertheless, referring to empirical results for MFCI [18] (see also Table 38 in chapter V.6.6.1), one can assume that the amount of E_{shock} will be in the range of 40 to 60 % of E_{tot} or even higher (cf. chapter V.9.3.4). Thus E_{shock} is most probably a relevant magnitude for the total damage crack-specific fracture energy and it can be expected that E_{DC} is significantly (or at least visibly) influenced by the hammer head geometry as well as by E_{impact}.

A first indication that supports these conclusions, can be found in Table 48: Both extrema belong to HIEs with the same target type (FG). It is clear that it is not the target type, but hammer geometry and impact velocity, which have a dominant influence on E_{DC}: Its amount is considerably higher in the case of a high velocity impact of an 8,3 mm wide hammer than for a pointed hammer with low impact velocities.

Nevertheless, as pointed out in chapter V.6.6.2, there are some indications that the instantly generated impact notch has a significant damping influence on shock waves and results in a complex coupling situation between hammer and target, which makes energy dissipation rather unpredictable.
Hence, in summary, the energy dissipation process into damage cracks seems to be mainly controlled by two opposing mechanisms:

- On the one hand by shock waves, which effect a local weakening of the material and whose intensities are positively correlated with the impact energy.
- On the other hand by the depth of the impact notch, which is correlated with E_{impact} as well, and which in contrast restrains shock wave propagation, hence reducing the amount of damage crack areas and the respective surface energy.

As it is evident that the impact notch is always the first crack to appear in the HIE image sequences, it can be supposed that the second mechanism will dominate the energy dissipation process of E_{DC}.

Multivariate statistical analyses substantiate this theory, and allow the following statements about the damage crack-specific fracture energy:

- E_{DC} is influenced by E_{impact} as well as by E_{tot} with high significance: Without constraints, the corresponding results of linear correlation analyses have been $\rho = 0{,}573$; $p < 0{,}05\,\%$ and $\rho = 0{,}989$; $p < 0{,}05\,\%$, respectively.
- Target type-specific analysis confirm these distinct correlations between E_{impact}, E_{tot} and E_{DC}. For RX targets, for example, ρ is found to be 0,980 ($p < 0{,}05\,\%$).
- Yet partial correlation analyses reveal that - in contrast to E_{NC} - E_{DC} is primary correlated to E_{tot} ($\rho = 0{,}987$; $p < 0{,}05\,\%$, if controlled for E_{impact}), and that E_{impact} is even negatively correlated to E_{DC}, when the influence of E_{tot} is mathematically removed ($\rho = \text{-}0{,}486$; $p < 0{,}05\,\%$, if controlled for E_{tot}).
  These findings strongly support the conclusions about the "impact notch theory", pointed out above. Furthermore the results also explain why a similar correlation has been found for E_{frac}, as this energy term is actually dominated by E_{DC} (see Table 49).
- The amounts of E_{DC} diverge considerably even under nominally identical HIE configurations. This fact can be easily explained by the impact notch theory.
- Of course it is nearly impossible to specify the amount of the actual "effective contact area" of the hammer within the impact notch. Due to the microscopical variation of this initial constraint and the broad distribution of energy values, it is difficult to prove a general significant influence of the hammer geometry on E_{DC}. Nevertheless, it has been possible to verify a significant dependency in the case of RX targets, by means of a one-way ANOVA.
- Table 49 presents the mean values and standard deviations of E_{DC} for various target types. RX targets are characterized by significantly lower amounts. This coincides well with the above made statements that RX targets are less susceptible to shock wave induced fracture processes.
- T-tests reveal that also TK targets show significantly lower amounts of E_{DC}.

	N	$\bar{E}_{NC}$ [mJ]	$\sigma(E_{NC})$ [mJ]	$\bar{E}_{DC}$ [mJ]	$\sigma(E_{DC})$ [mJ]	R_{DC} [%]
FG	90	170,5	59,3	3025	667	95,62
T5	66	163,3	58,2	2907	627	95,33
T10	66	181,4	58,3	2956	536	95,08
TK	32	113,6	38,6	2798	436	96,10
AS	27	179,6	68,7	2885	462	94,14
RX	65	237,4	82,6	2591	461	91,62

Table 49: Overview of the normal crack-specific and of the damage crack-specific fracture energies for various target types: The corresponding sample size N, the mean values $\bar{E}_{NC}$, $\bar{E}_{DC}$ and the respective standard deviations $\sigma(E_{NC})$ and $\sigma(E_{DC})$ are presented. In the right column, R_{DC} denotes the proportion of E_{DC} in relation to E_{frac}: It is evident that E_{frac} is dominated by E_{DC}. Hence, both energy terms show the same dependencies.

- It is notable that for T10 targets $\bar{E}_{DC}$ is quite large, although they are usually marked by low damage crack extensions (see e.g. Fig. 41). Hence, a low damage crack intensity does not automatically imply low energy dissipation:
  In fact, T10 targets are characterized by comparatively large η_{DC} (see above). Thus one might also draw the conclusion that the percentage of complementary energies, which are not directly involved in the surface generation process itself, is distinctly higher in these samples than in the other float glass types.

- In general, E_{DC} does not significantly depend on the primary crack type. The only conspicuous exception has been detected for ACTs, which are characterized by significant higher amounts of damage crack-specific fracture energies. This finding is well consistent with the fact that ACTs are always associated with significant higher amounts of generated damage crack areas.
  Due to all these results, the impact notch might also explain all the features of this primary crack type:
  In some cases the randomly microscopic state of the impact notch results in a particularly effective contact condition with the hammer, which favors the initiation and propagation of shock waves.
  Thus compared to other contact situations, all damage crack zones, including Zone 1 and Zone 2, have a larger extension, effecting not only significantly higher damage crack intensities and larger amounts of energy dissipation, but also local nucleation of cracks in this "susceptible" region: As a result, normal cracks are initiated there.

In Fig. 88 the empirical interrelationship between the crack class-specific fracture areas and the corresponding amounts of energy dissipation is presented for the case of RX targets.

8.4. Comparison of the Linear FSED Models

Based on these results, it is now possible to compare the two FSED models, introduced in chapter V.4.

It is of interest that the crack class-specific FSED as well as E_{NC} and E_{DC} show pronounced differences in their dependencies. This fact itself is a strong indication that supports the theory of two different mechanisms, and hence the crack class-specific FSED model.

Due to the respective results of linear regression, the regression coefficients of both models (i.e. the corresponding FSED parameters) have been verified to be accurate by a high signif-

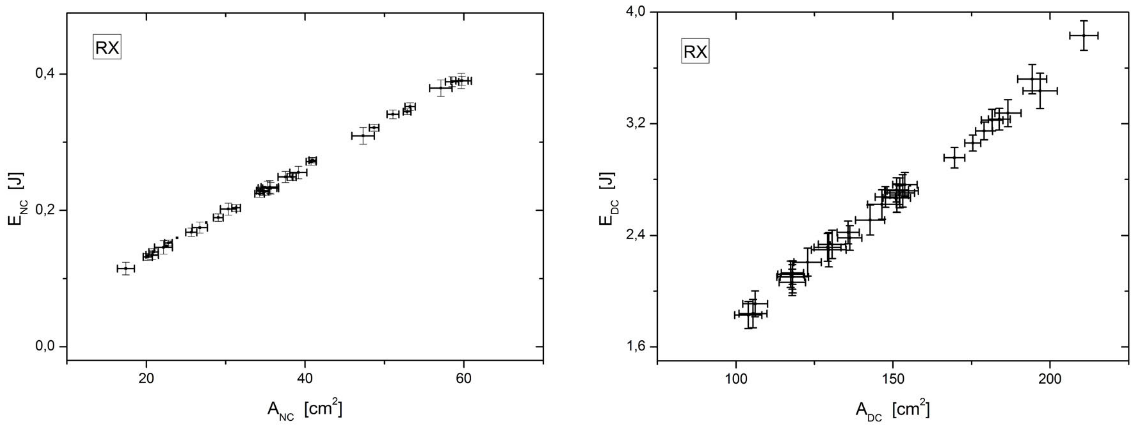

Fig. 88: Empirical coherence between crack class-specific fracture area and fracture energies for RX targets. The slope of this linear correlation is given by η_{NC} and η_{DC} respectively, which are characterized by a low variance (see Table 44 and Table 46).
A comparison with the respective result, which is based on the basic FSED model (see Fig. 84 (right)), reveals that the crack class-specific FSED model provides an enhanced and thus very accurate description of the actual interrelationship between energy dissipation and generated fracture area.

icance, with an error probability of less than 0,05 % (see Appendix H). This is an indication that both models provide a good description of the reality.

Additionally, the corresponding amounts of adjusted R^2 are examined. These parameters, which specify the quality of the models and are also denoted "adjusted coefficient of determination" [12], are listed in Table 50.

FSED model	FG	T5	T10	TK	AS	RX
basic	0,988	0,981	0,983	0,975	0,982	0,936
crack class-specific	0,998	0,998	0,997	0,997	0,995	0,996

Table 50: Resulting values of adjusted coefficients of determination R^2 for both FSED models: This parameter describes the quality of the corresponding model. Note that, although the basic FSED model is quite accurate, the crack class-specific is evidently better, especially in the case of RX targets.

For the basic FSED models, they are close to 1, which implies that these models can be seen as quite accurate.

In the case of the crack class-specific FSED models, the amounts of R^2 are even closer to the optimum value: This implies that these types of models provide an enhanced description of fracture energy dissipation.

A comparison of the plots Fig. 84 (right) and Fig. 88 gives a clear graphical impression of the superior quality of the latter model.

This improvement is most pronounced for RX targets, which coincides well with the considerations of Table 50. The reason for this is evidently the lower amount of damage crack induced areas A_{DC} in glass ceramics, which implies a higher proportion and thus a greater influence of the normal crack induced fracture processes. As a consequence, the values of η_{tot} show a significant higher variance than the specific terms η_{NC} and η_{DC}, resulting in a more scattered, but still visibly linear correlation.

In conclusion it can be stated:

- The basic FSED model provides a good description of the correlation between E_{frac} and the generated fracture surface A_{frac}, in particular if one of the two fracture mechanisms (shock wave induced damage cracks or normal cracks) distinctly dominates the fragmentation process.
- The crack-class specific FSED model, however, accurately describes the influence of both fracture mechanisms and is - although a much more elaborate method - especially appropriate in cases for which both mechanisms are relevant.

8.5. Complementary Conclusions Regarding the FSED Parameters

It is clear and coherent, that η_{NC} and η_{DC} are significantly affected by a nanocrystalline structure of the target, thus glass ceramics show distinctly different values compared to float glass targets. Also the considerable influence of the contact interface in AS targets is evident, but actually not surprising.

Most remarkable and enlightening, however, is the fact that both FSED parameters are considerably influenced by the pre-stress history of the targets: As pointed out above, it has been verified that η_{NC} and η_{DC} are significantly affected by the geometry of the resulting PSZ. Besides this similarity, both parameters show diverging dependencies.

In the case of damage cracks, a consistent explanation is provided by the above introduced impact notch theory. This explanatory model can also be enhanced by considering the conceivable fact, that pre-stresses distract or deflect propagating shock waves, which would give a reason for the slight but significant differences in η_{DC} between T5 and T10 targets.

Yet it is not so easy to explain the pre-stress specific results of η_{NC}, as they seem to conflict with the findings, that the normal crack-specific FSED are locally independent.

In fact, it is hard to explain this effect by means of a static stress (or a micro crack) model.

However, the ostensible contradiction can be easily solved by considering the *dynamic* stress situation and taking up the dual approach, which is outlined as a concept of directed and fluctuating stress in chapter II.3.3 and comprehensively studied in chapter V.3:

Keeping in mind that normal crack propagation is actually a result of interacting static and fluctuating stresses, the geometry of pre-stresses appear to specify the "global" setting of constraints within the target, which is explicitly described by the constant parameter η_{NC}.

Thus, in particular the normal crack-specific FSED gives us the possibility to quantify also dynamically the dissipation of fracture energies within a sample, despite the complex stress fluctuations in the run-up to and during fragmentation.

9. Dynamics of Fractures and Energy Dissipation

9.1. General Remarks

In principle, there is a large variety of possibilities to specify the complex development of fracture processes. The innovative approach of this thesis, however, is to reveal the interrelationship between fracture dynamics and energy dissipation by studying the dynamic extensions of fracture surface areas by means of HIE image sequences.

Thus, although the crack tip propagation is described in this chapter by using the classical defined terms of "crack velocities" (see e.g. [55, 60]) as well, the focus - in particular for normal cracks - will be primarily on the analysis of newly introduced magnitudes, which allow to quantify the amounts of dissipated energy by means of the FSED parameters.

Subsequently, the dependencies of all dynamic fracture parameters are studied by means of multivariate statistical analyses. The details of all statistical results can be found in the corresponding folder of Appendix H. Furthermore, comprehensive representative results of all mentioned dynamic magnitudes are listed in Appendix G.

9.1.1. Definitions of Dynamic Fracture Parameters

Parameters Specifying the Dynamics of Damage Cracks

It is nearly impossible to quantify the development of damage cracks in HIEs, due to the complex structure of those crack classes, and because of simultaneous fragmentation processes occurring in different located plains.

Yet, two parameters are introduced, in order to obtain at least an impression of damage crack dynamics:

- The "damage crack velocity" $v_{DC}(t)$, which specifies the propagation rate of the farthest distance $d_{DC}(t)$ between the damage crack front and the point of impact. It is defined as:

$$v_{DC}(t_2) = \frac{d_{DC}(t_2) - d_{DC}(t_1)}{t_2 - t_1} \tag{V.9-1}$$

- The "velocity of damage fracture areas" $w_{DC}(t)$, which is in fact not the rate of the actual damage fracture area, but calculated by the projected damage crack induced fracture area $\widetilde{B}_{DC}(t)$, visible on the images. The velocity of damage fracture area is defined as:

$$w_{DC}(t_2) = \frac{C_{DC}(t_2) - C_{DC}(t_1)}{t_2 - t_1} \tag{V.9-2}$$

  where $C_{DC}(t)$ is defined by:

$$C_{DC}(t) = 2 \cdot \widetilde{B}_{DC}(t) \tag{V.9-3}$$

As pointed out above, only a part of E_{DC} actually dissipates in form of damage cracks. The previous energy dissipation into impact notch and shock wave initiation cannot be determined by optical means, nor can the discrete zonal structure. However, despite these serious restrictions, v_{DC} and w_{DC} provide at least qualitative results, that will complement the whole picture of HIE fragmentation.

Parameters Specifying the Dynamics of Normal Cracks

In contrast to damage cracks, the HIE setup allows a profound “two and a half” dimensional insight into the complex dynamic processes of normal crack propagation.

Three parameters are introduced to analyze in detail the temporal evolution of normal cracks:

- The “crack tip velocity” u describes the propagation rate of a crack’s tip. In the case of branching cracks, only the longest crack branch is considered.
  This magnitude has been introduced and comprehensively applied to study cracks in FG in [40] and provides information on the behavior of a single crack tip in a sample during propagation (see e.g. Fig. 11). Especially its maximum value can be seen as a characteristic fracture parameter of a certain material.
  The crack tip velocity $u(t)$ is simply determined by:
  $$u_{i\,j}(t_2) = \frac{l_{max}(t_2) - l_{max}(t_1)}{t_2 - t_1} \tag{V.9-4}$$
  where $l_{max}(t)$ is the (longest) crack length at the time t. The index i specifies the crack type or subtype (for abbreviations see Table 9), j denotes the side (l: left, r: right).

- In contrast, the “crack velocity” $v(t)$ focusses on the length of *all* crack branches, which are summed up to $l_{total}(t)$. Therefore this parameter is defined by:
  $$v_{i\,j}(t_2) = \frac{l_{total}(t_2) - l_{total}(t_1)}{t_2 - t_1} \tag{V.9-5}$$
  This magnitude quantifies the temporal evolution of fragmentation in the target.
  In particular the following crack velocities have been used for multivariate statistical analyses: $v_{A\,r}(t)$, $v_{A\,l}(t)$ (crack velocities, considering all A-crack branches on the right and left side, respectively), $v_A(t)$ (considering the sum of all A-cracks), $v_C(t)$ (taking into account all centrical cracks - i.e. SCMs, BCMs and TCMs), $v_S(t)$ (subsuming all secondary cracks), $v_W(t)$ (considering all W-cracks) and $v_{NC}(t)$ (crack velocities, taking into account the total length of all normal cracks).

- The most interesting parameter is the fracture area velocity $w(t)$ (also denoted FAV, see chapter II.3.1), which allows - by means of the crack class-specific FSED model - to make concrete quantitative statements about the dynamics of energy dissipation into normal cracks. The FAV is defined by:
  $$w_{i\,j}(t_2) = \frac{A(t_2) - A(t_1)}{t_2 - t_1} \tag{V.9-6}$$
  where $A(t)$ denotes the fracture surface area, which is determined by OPC.

- In principle, it would be possible to specify also a *crack tip-specific* FAV, for which only the area of a single crack tip is observed. However, as this thesis focusses on the energetic aspects of the whole fragmentation process, it is more useful to quantify and study the *accumulative* FAVs, for which the areas of all crack branches are considered.

- The following *accumulative* FAVs have been calculated in order to conduct multivariate statistical analyses: $w_{A\,r}(t)$ and $w_{A\,l}(t)$ (which describe the rate of the temporal evolution of the total fracture areas, belonging to the right and left A-cracks, respectively),

$w_A(t)$ (considering the sum of all A-crack areas), $w_C(t)$ (taking into account the fracture areas of all centrical cracks), $w_S(t)$ (describing the sum of all secondary crack fracture areas), $w_W(t)$ (considering the fracture areas of all W-cracks) and $w_{NC}(t)$ (FAV of all normal cracks).

- With $w(t)$ it is then easily possible to calculate the corresponding fracture energy dissipation rate $e(t)$ by means of the crack class-specific linear FSED model. It is calculated by:

$$e(t) = \eta_{NC} \cdot w(t) \qquad \text{(V.9-7)}$$

For these magnitudes, the identical index is used as for the FAV. Thus, for example, $e_S(t) = \eta_{NC} \cdot w_s(t)$ denotes the fracture energy dissipation rate at the moment t, which drives the evolution of secondary cracks.

- Finally, the amount of the dissipated fracture energy in the period between t_0 and t_1 can be specified by:

$$E(t_1) = \int_{t_0}^{t_1} e(t)dt \qquad \text{(V.9-8)}$$

For t_0 always the moment of the earliest HIE record (i.e. the time of the first image) is selected.

9.1.2. Applied Statistical Parameters

All these dynamic parameters listed before are characterized by distinct temporal fluctuations. In order to achieve supportable and reliable assertions, it is necessary to study the statistical measures of central tendency as well as dispersion parameters.

In particular, the following statistical magnitudes are calculated and subsequently analyzed:

1. The arithmetic mean: This parameter is especially useful for HIEs, whose image sequence depicts the total process of crack development from start to finish. In these cases, the arithmetic mean can be applied as a meaningful measure of comparison. In other cases, it is only possible to compare specific stages (e.g. the stage of crack acceleration). The mean values are marked by a crossed letter, e.g. $\bar{w}_C(t)$ denotes the mean value of several centrical crack FAVs.

2. The median: This measure of central tendency is less sensitive towards outliers [110], and thus more useful for comparative analysis of strongly fluctuating data sets. Yet, for this parameter the same restrictions have to be considered as for the arithmetic mean: It is solely possible to compare median values describing the identical stage of crack development. A median value is marked by a tilde ($\tilde{\ }$), e.g. $\tilde{v}_{DC}(t)$ denotes the median of all damage crack velocities.

3. In the case of damage cracks, it is useful to study also the "genuine" average values of $v_{DC}(t)$, for which interfering influences are omitted (see also next section). These values are determined by means of a linear regression based on a least squares approach and are denoted $v_{avg\,DC}$.

4. Standard deviation σ: This important dispersion parameter is used to quantify the degree of fluctuation.

5. Maximum value, which is abbreviated by "Max ()": This parameter is by far the most interesting magnitude, as it specifies the stability limit of propagating cracks within a sample, as well as the highest rate of fragmentation and the largest amount of dissipated

fracture energy per time, which could be expected under specifically defined conditions. In particular the last magnitude is of distinct importance for volcanological research, as it can be used for example for energetic "worst case scenario" calculations. Therefore the determination and analysis of $\mathrm{Max}\,(e(t))$ will be particular interesting.

9.2. Dynamics of Damage Cracks

A typical evolution of damage cracks is illustrated in Fig. 89, which presents the propagation of a damage crack front as well as the development of the respective visible fracture area $C_{DC}(t)$. Fig. 90 shows the corresponding dynamic parameters, i.e. the damage crack velocity $v_{DC}(t)$ and the approximated velocity of damage fracture areas $w_{DC}(t)$.

9.2.1. Definition of the Average Damage Crack Velocity $v_{avg\,DC}$

In contrast to high velocity impact experiments [112, 127, 128] the crack front in HIEs appears not to move at a constant terminal speed, but with significant fluctuations. An explanation for this effect can be found by having a closer look at the corresponding image sequence, which is presented in Fig. 91: At the moment, when the tips of the ACB reaches the damage crack vicinity (i.e. between 112 and 132 µs after impact), the visible fracture area C_{DC} considerably increases.

It is evident, that the concentration of stress located at the normal crack tips has been the reason for this "boost", which drives the advance of the damage crack. Evidently, there are strong interactions between normal cracks and damage cracks, resulting in distinct energy exchanges.

Hence, it can be theoretically presumed that in fact the crack front propagates with an average speed $v_{avg\,DC}$ (marked in the example of Fig. 89 (left) by a continuous line), that is distinctly affected by the evolution of normal cracks and modulated by the complex dynamics of fluctuating stress waves, which results in large variations of the actual damage crack velocity $v_{DC}(t)$.

The values of $v_{avg\,DC}$ can be determined by means of a least square linear regression. In the example of Fig. 89 it amounts to $(144 \pm 6)\,\frac{m}{s}$. Yet, the actual propagation velocities $v_{DC}(t)$ range from crack arrest to $342\,\frac{m}{s}$, which have proven to be very typical results for damage cracks.

An additional, very conspicuous fact is presented in the illustrated example as well: In the final stage (between 162 and 172 µs after impact) $v_{DC}(t)$ significantly increases to $1244\,\frac{m}{s}$, which is an extraordinarily fast propagation for a damage crack front. The corresponding image taken by the Cranz-Schardin-camera reveals that the cause of this growth in speed is the evolution of an intermediate crack, which is in fact a combination of damage cracks and - significantly faster - normal cracks.

In order to obtain the "genuine" value of $v_{avg\,DC}$, the influence of normal cracks has to be omitted as best as possible. Thus, before applying a linear regression, all data points which apparently refer to intermediate cracks, have to be excluded.

Note that - in contrast to $v_{avg\,DC}$ - the other measures of central tendency (like the arithmetic mean $\bar{v}_{DC}$) have always been calculated on the basis of *all* data points, including those of intermediate cracks.

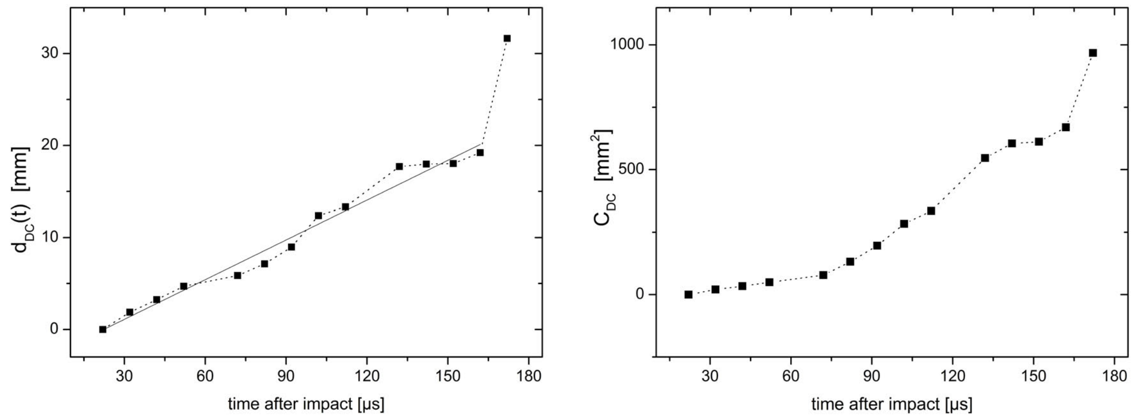

Fig. 89: Representative example showing the dynamics of damage cracks ([V233], {301}, $v_H = 2{,}14\,\frac{\mathrm{m}}{\mathrm{s}}$): On the left, a typical development of the distance $d_{DC}(t)$ between the point of impact and the farthest damage crack front is presented, the respective evolution of visible damage fracture areas $C_{DC}(t)$ is shown on the right. An excerpt of the corresponding image sequence is presented in Fig 91. In general, damage cracks propagate with an average velocity $v_{avg\,DC}$, which is distinctly affected by the evolution of normal cracks as well as by the dynamics of fluctuating stress waves. In this example $v_{avg\,DC}$ amounts to $(144 \pm 6)\ \frac{\mathrm{m}}{\mathrm{s}}$, which is determined by means of a least square linear regression (left, continuous line). The resulting adjusted coefficient of determination R^2 is 0,977.

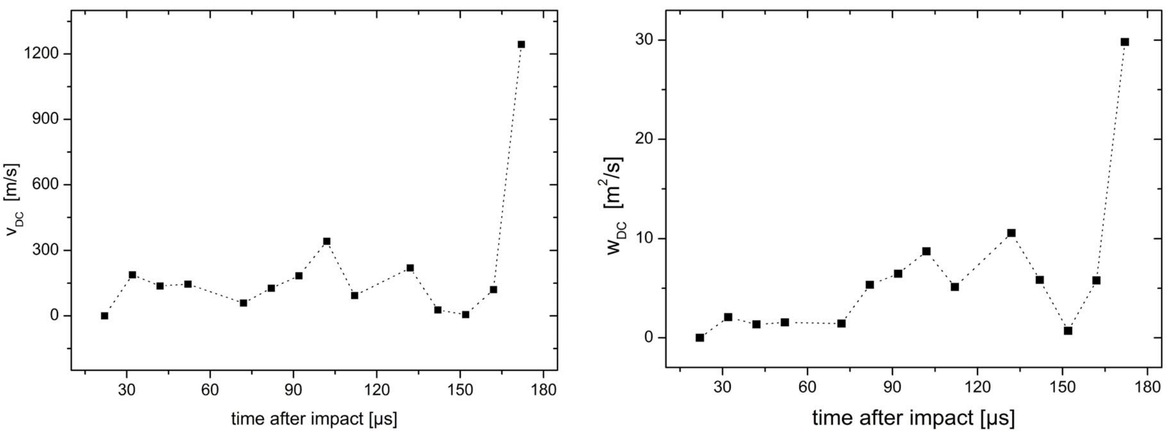

Fig. 90: Typical results of parameters describing the dynamics of damage cracks [V233]: On the left the damage crack velocity $v_{DC}(t)$ is presented, on the right the corresponding development of $w_{DC}(t)$. Both magnitudes are characterized by considerable variations due to interaction effects with normal cracks. Note that in this example the final stage of damage crack evolution is characterized by a significant increase of v_{DC} and w_{DC}, which has been the result of an initiated intermediate crack.

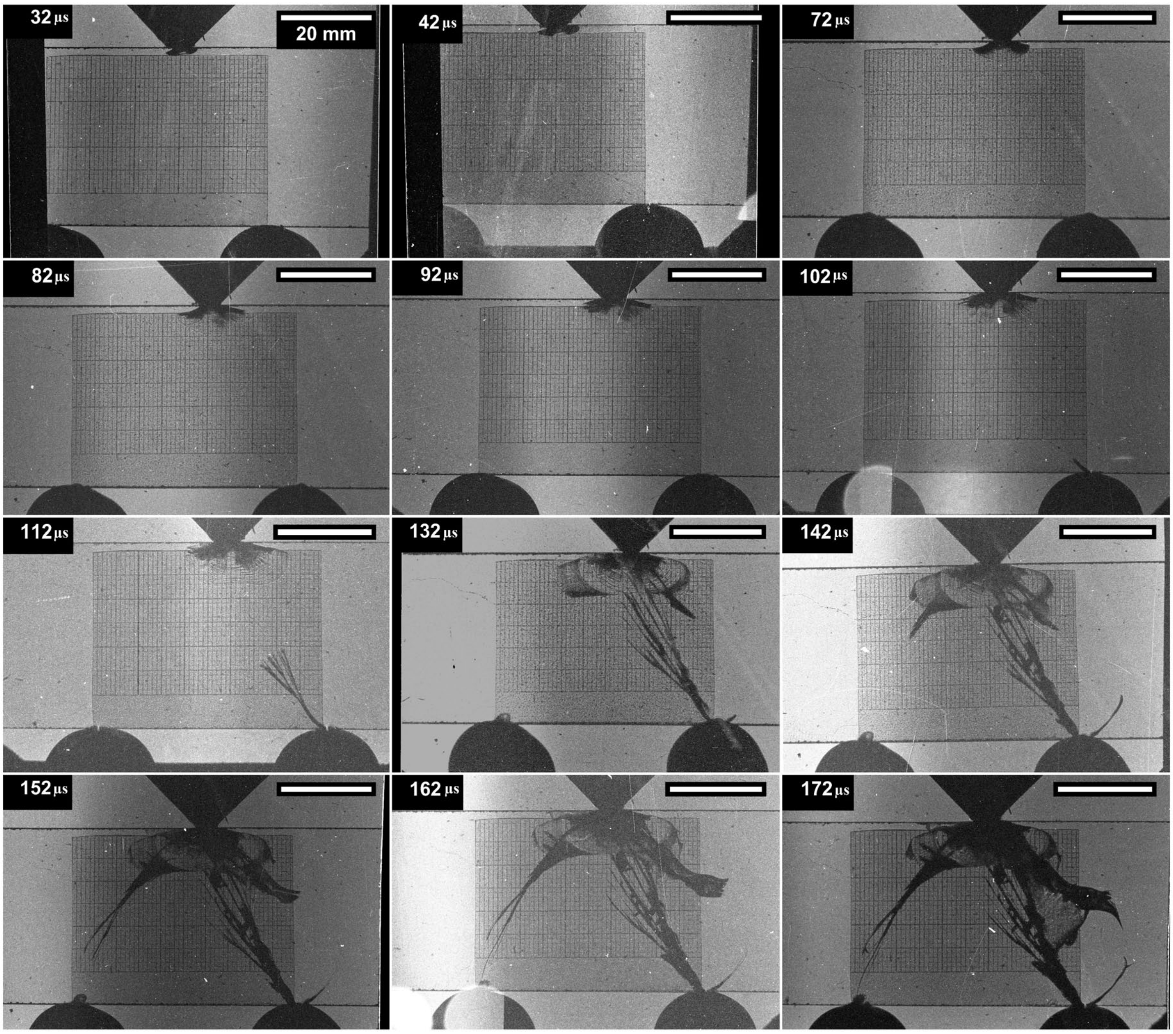

Fig. 91: Representative evolution of damage cracks (excerpt of [V233]): When the tips of the ACB arrive at the damage crack zone (between 112 and 132 µs), the damage crack area is clearly expanding. In the final stage (172 µs) a typical intermediate crack occurs, which results in a distinct increase of visible fracture areas as well as of v_{DC}. All scale bars are calibrated to 20 mm. The complete image sequence can be found in Appendix I.

9.2.2. Features of Damage Crack Velocities

Table 51 summarizes the statistical results for the maximum values $Max(v_{DC})$, the median $\widetilde{v}_{DC}$ and arithmetic mean value $\bar{v}_{DC}$ of all determined damage crack velocities as well as their genuine average values $v_{avg\,DC}$.

	$\bar{v}_{DC}$ $[m/s]$	$\widetilde{v}_{DC}$ $[m/s]$	$v_{avg\,DC}$ $[m/s]$	$v_{avg\,DC}$ HIE	$Max(v_{DC})$ $[m/s]$	$Max(v_{DC})$ HIE
minimum value	49	7	65	[V323], {303}	84	[V655], {122}
maximum value	1047	1047	632	[V208], {101}	1754	[V628], {211}
mean value	233	193	214		569	
standard deviation	176	173	120		406	

Table 51: Statistical synopsis of various characteristic values for $v_{DC}(t)$: The large standard deviations characterize the considerable variations of damage crack dynamics.

It is very interesting to compare these HIE results to published findings of edge-on impact experiments (EOIs, [127]) on float glass with blunt projectiles of high velocities ($31\,\frac{m}{s}$), for which a crack front propagation by a constant terminal velocity of $(1550 \pm 31)\,\frac{m}{s}$ is reported [112].

As already pointed out above, the velocity of damage cracks in HIEs are characterized by distinct variations. This fact is also reflected in the comparatively large standard deviations (see Table 51). In HIEs, the average evolution of shock wave induced fractures is significantly slower, and comparable propagation velocities can only be detected in rare cases and over very short periods.

The results of this comparison confirm, that fracture mechanisms significantly depend on the loading situation. Thus, the dynamics of damage cracks is evidently characterized by several influences:

- Induced shock waves: As the amounts of energy densities at the moment of impact are not comparable, it is very likely, that the effects of shock waves in HIEs and EOIs cannot be compared as well.
- The complex stress wave fluctuations during the fragmentation: These fluctuations seem to play a dominant role and actually drive the damage fracture processes in regions, which have previously been affected by shock waves. Obvious reasons for the significantly higher amount and influence of these stress variations could be the specific HIE loading geometry and moreover the longer period of contact with the hammer (see chapter IV.2).
- Furthermore, there are significant interaction and energy exchange processes with normal cracks in HIEs. In contrast, normal cracks do not occur at all in EOI [112, 127, 128], due to the different loading situation.

All these findings underpin that it is hardly possible, to compare and transfer the results and conclusions of experiments with high impact velocities to fracture situations in HIEs (and most likely also in MFCI).

Even under identical HIE configurations the parameters of damage crack evolution show distinct variations, which complicates the detection of clear dependencies by means of multivariate statistical analysis:

Therefore it is no surprise, that no significant influence of v_H or hammer geometry on $v_{avg\,DC}$, $\bar{v}_{DC}$, $\widetilde{v}_{DC}$ and $Max(v_{DC})$ can be verified by t-test or ANOVA.

Against this backdrop it is noteworthy, that the influence of the material properties (i.e. of the target type) is strong enough to effect considerable differences in $\bar{v}_{DC}$ and $\widetilde{v}_{DC}$. For example, t-tests reveal that the mean damage crack velocity in RX is significantly different from that of FG, with an error probability of $p = 2{,}8\,\%$, and the median of damage crack velocities of T5 targets differs significantly from that of FG, with an error probability of $p = 1{,}5\,\%$.

Table 52 presents the type-specific results of $\bar{v}_{DC}$ and $\widetilde{v}_{DC}$.

	FG	T5	T10	TK	RX
$\bar{v}_{DC}\ \left[\frac{m}{s}\right]$	(217 ± 151)	(167 ± 111)	(204 ± 138)	(319 ± 189)	(366 ± 299)
$\widetilde{v}_{DC}\ \left[\frac{m}{s}\right]$	(178 ± 148)	(112 ± 29)	(167 ± 136)	(281 ± 187)	(335 ± 302)

Table 52: Characteristic values of damage crack evolution: In spite of the large standard deviations, significant differences have been verified, in particular between the corresponding values of FG, T5 and RX.

9.2.3. Influences on the Fluctuation

The amount of fluctuation can be specified by the standard deviation $\sigma\left(v_{avg\,DC}\right)$ of the average "genuine" damage crack velocity. As the damage crack velocity itself, this magnitude is characterized by large variations: Its values range from 4,6 $\frac{m}{s}$ ([V265], {102}) to $163,6\,\frac{\mathrm{m}}{\mathrm{s}}$ ([V612], {112}). The mean value of $\sigma\left(v_{avg\,DC}\right)$ amounts to $26,7\,\frac{\mathrm{m}}{\mathrm{s}}$, its standard deviation is considerably large at $25,9\,\frac{\mathrm{m}}{\mathrm{s}}$.

As for $v_{avg\,DC}$, no significant influence of impact velocity and hammer geometry can be verified.

Nevertheless, there seems to be a distinct dependency on the material: The standard deviations of T10 targets, for example, are significant lower than those of RX targets, with an error probability of $p = 2{,}6\,\%$, revealed by a t-test.

Table 53 lists the target-specific mean values of $\sigma\left(v_{avg\,DC}\right)$ and their standard deviations $\sigma\left(\sigma\left(v_{avg\,DC}\right)\right)$.

	FG	T5	T10	TK	RX
$\bar{\sigma}\left(v_{avg\,DC}\right)$ $[\frac{m}{s}]$	$23{,}7 \pm 16{,}6$	$32{,}3 \pm 54{,}2$	$11{,}7 \pm 5{,}3$	$36{,}6 \pm 30{,}7$	$37{,}2 \pm 25{,}6$

Table 53: Mean values of target-specific standard deviations $\bar{\sigma}\left(v_{avg\,DC}\right)$: These magnitudes can be seen as a measure, which quantifies the fluctuation of damage crack evolution. Note, that the values for T10 are comparatively low: In those targets, damage cracks propagate with less variations.

All results indicate, that in T10 targets interaction processes with normal cracks, as well as fluctuating stress waves, have significantly less influence on $v_{avg\,DC}$ and thus on the dynamics of damage cracks, especially compared to RX and TK targets.

However, the relatively large amounts of uncertainties in particular for T5 targets, do not allow to make further reliable statistical statements.

9.2.4. Typical Velocities of Damage Fracture Areas

As pointed out above, $w_{DC}(t)$ is a parameter which describes the temporal evolution rate of the visible (i.e. projected) fracture area $C_{DC}(t)$. The real amounts of fracture areas $A_{DC}(t)$, however, are presumed to be considerably larger. Hence, an elaborate quantitative interpretation would be rather ineffective.

Nevertheless, $w_{DC}(t)$ gives a good complementary impression of the development of damage cracks: As illustrated in Fig. 90, it appears to be strongly linked to $v_{DC}(t)$ as it shows similar dependencies.

A closer look, however, reveals that the energy exchange effect of arriving normal crack tips at 132 µs is even more significant for this magnitude than for $v_{DC}(t)$: The respective value of $w_{DC}(t)$ rises from $5,1\,\frac{\mathrm{m}^2}{\mathrm{s}}$ to $10,6\,\frac{\mathrm{m}^2}{\mathrm{s}}$. This implies, that $w_{DC}(t)$ is more sensitive to interaction processes with normal cracks and stress wave dynamics.

As this interfering influence seems to be a predominant factor, it would be rather pointless to determine a "genuine" average fracture area velocity $w_{avg\,DC}$ comparable to $v_{avg\,DC}$. Instead, the arithmetic mean $\bar{w}_{DC}$ and median values $\tilde{w}_{DC}$ have been preferred as measures of central tendency for further studies.

In Fig 92 and Fig. 93 another typical example is presented, which shows the temporal evolution of damage cracks under totally different HIE configurations. In this example no intermediate crack has occurred, so that the maximum values of $v_{DC}(t)$ and $w_{DC}(t)$ have been significantly lower. Yet, these magnitudes are characterized by considerable fluctuations, ranging from $10,4\,\frac{\mathrm{m}}{\mathrm{s}}$ to $292\,\frac{\mathrm{m}}{\mathrm{s}}$ and from $0,1\,\frac{\mathrm{m}^2}{\mathrm{s}}$ to $8,7\,\frac{\mathrm{m}^2}{\mathrm{s}}$, respectively. These distinct variations are very typical for the development of damage cracks and have been observed for all targets under all studied HIE constraints.

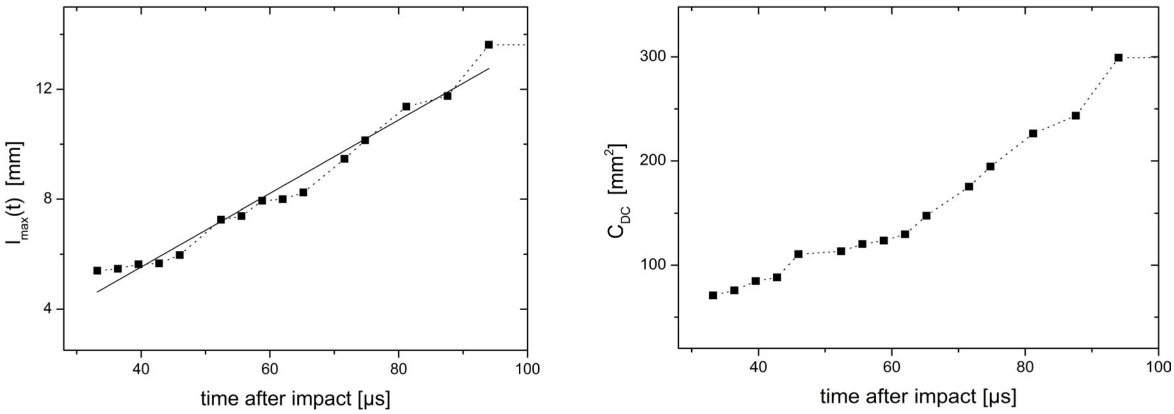

Fig. 92: Another representative example for damage crack evolution, this time for TK targets ([V677], {124}, $v_H = 1{,}79\,\frac{m}{s}$): As in this case no intermediate cracks have occurred, all data points could be taken into account in order to calculate $v_{avg\,DC}$ by least square linear regression. It amounts to $(134 \pm 6)\,\frac{m}{s}$, the resulting adjusted coefficient of determination R^2 is 0,968.

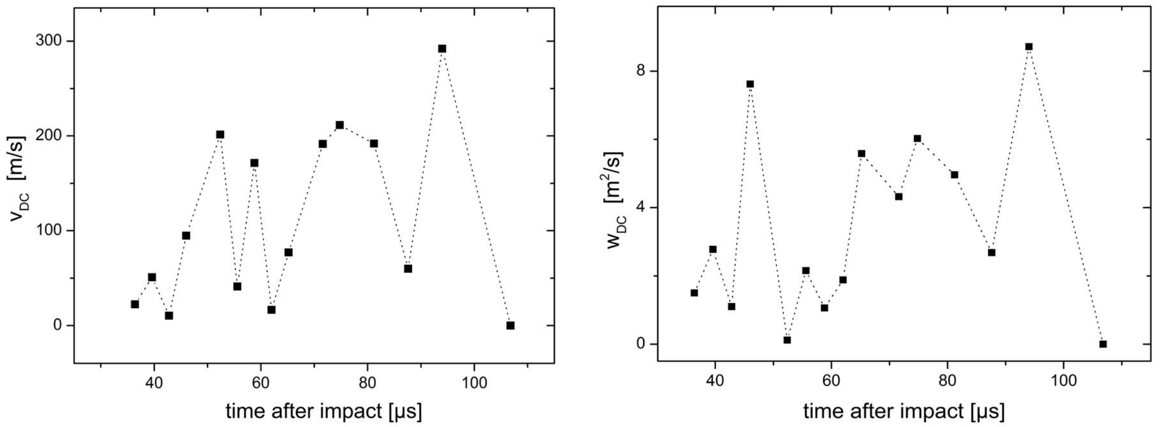

Fig. 93: Dynamic parameters corresponding to Fig. 92 [V677]: Also in this case, $v_{DC}(t)$ and $w_{DC}(t)$ show distinct variations. Yet, as in this HIE no intermediate cracks have been generated, the maximum values of both parameters have been considerably lower than those of the case presented in Fig. 90. This example clearly demonstrates the complex background of finding a comparable data set, in order to draw the correct conclusions on the basis of comparative statistical analysis.

9.2.5. Dependencies of the Temporal Evolution of Damage Fracture Areas

Table 54 presents a statistical overview of the resulting characteristic values $\bar{w}_{DC}$, $\widetilde{w}_{DC}$ and $Max\,(w_{DC})$.

Evidently, all these parameters show large variations as well, which limits the possibility to make reliable statements, based on multivariate statistical analyses. In summary, the following conclusions can be drawn:

- None of the three characteristic values show a significant dependency on v_H within the studied scope.

	$\bar{w}_{DC}$		$\widetilde{w}_{DC}$		$Max(w_{DC})$	
	$[m^2/\mathrm{s}]$	HIE	$[m^2/\mathrm{s}]$	HIE	$[m^2/\mathrm{s}]$	HIE
min.	0,9	[V228], {301}	0,2	[V223], {101}	0,9	[V228], {301}
max.	55,4	[V913], {136}	55,4	[V913], {136}	89,0	[V652], {621}
mean	8,2		6,8		19,9	
std. dev.	8,7		8,7		17,5	

Table 54: Statistical synopsis of various characteristic values for $w_{DC}(t)$: Note, that also these parameters are characterized by large standard deviations.

- The temporal evolution of damage cracks seems to be considerably affected by the contact area: Despite the large variations, a significant influence of the hammer geometry has been proven for several cases. For example for T10 targets the mean values of Max (w_{DC}) are distinctly lower in the case of a pointed hammer head $(8,6\,\frac{\mathrm{m}^2}{\mathrm{s}})$ than for a round one $(41{,}2\,\frac{m^2}{s})$, with a t-test verified significance of $p = 1{,}1\,\%$.
  Thus, it is evident, that the stress wave fluctuations which drive the damage fracture processes, are very sensitive to the conditions of mechanical coupling.
- All characteristic values substantially depend on the target type, in part with a high significance. The target-specific results of $\bar{w}_{DC}$, $\widetilde{w}_{DC}$ and $Max\,(w_{DC})$ are displayed in Table 55. Although the quantitative meaning of $w_{DC}(t)$ is quite restricted, these results

	FG	T5	T10	TK	RX
$\bar{w}_{DC}$ $[\frac{m^2}{s}]$	$7{,}2 \pm 6{,}5$	$5{,}7 \pm 2{,}8$	$9{,}3 \pm 10{,}4$	$5{,}8 \pm 4{,}5$	$15{,}9 \pm 16{,}3$
$\widetilde{w}_{DC}$ $[\frac{m^2}{s}]$	$6{,}2 \pm 6{,}6$	$4{,}5 \pm 2{,}1$	$7{,}8 \pm 10{,}7$	$2{,}3 \pm 0{,}8$	$13{,}3 \pm 16{,}2$
$Max\,(w_{DC})$ $[\frac{m^2}{s}]$	$18{,}1 \pm 16{,}6$	$13{,}2 \pm 9{,}3$	$23{,}5 \pm 19{,}2$	$23{,}2 \pm 25{,}7$	$30{,}2 \pm 19{,}6$

Table 55: Target-specific amounts of $\bar{w}_{DC}$, $\widetilde{w}_{DC}$ and $Max\,(w_{DC})$.

can be seen as proof, that the evolution of damage cracks in RX targets is significantly faster than in float glass targets. It is evident that the material has a substantial effect on the generation rate of damage fracture areas.

9.3. Fracture Energy Dissipation of Damage Cracks

According to my results, the evolution of damage cracks can be considered as a three-stage process.

Thus the dissipating damage crack energy E_{DC} can be split into three different specific components:

$$E_{DC} = E_{notch} + E_{shock} + E_{vis} \tag{V.9-9}$$

where E_{notch} denotes the energy, which dissipates into the impact notch, E_{shock} the energy of shock waves and E_{vis} the amount of energy, which visibly dissipates into damage crack structures in the final stage of damage crack evolution.

In the following, every stage is shortly summarized in order to create a model, which describes at least qualitatively the dynamics of energy dissipation.

9.3.1. First Stage: Impact Notch Generation

The motion of the hammer as well as the high speed image sequences have revealed that virtually immediately at the moment of impact, an impact notch is generated. Furthermore, it is clear that a considerable part of fracture areas is generated in this region, referred to as "Zone 0" (see chapter V.5).

As a consequence, it can be presumed that in this first stage of fracture evolution a distinct amount E_{notch} of the total damage crack fracture energy E_{DC} dissipates within a very short time period of less than 1 µs.

9.3.2. Second Stage: Shock Waves

According to the results of experiments studying the evolution of shock waves in solids [74] and water [51], it is evident that these singularities are established within the first microsecond after impact, and subsequently propagate with a velocity c_{max}, which is empirically less than 4,7 % above the level of the respective material's speed of sound c. With an increasing distance, the shock wave velocity decreases and approaches c [51, 74].

These experimental results mentioned in the literature are well consistent with the theoretical considerations, pointed out in chapter II.2.

The speed of longitudinal waves c of a specific material can be calculated by [59]:

$$c = \sqrt{\frac{E \cdot (1-\mu)}{\varrho \cdot (1-\mu-2\mu^2)}} \tag{V.9-10}$$

where E denotes the corresponding Young's modulus, ϱ the density and μ the Poisson's ratio.

By means of the respective material properties, given in Table 1, it is possible to determine the speed of sound for the used targets (see Table 56).

Furthermore the runtime t_{shock} of shock waves can be evaluated, which is the duration of shock wave propagation within a target of the height h. During this period the complete amount of shock wave energy E_{shock} dissipates into the target and causes distinct local changes in the fracture properties.

It can be estimated by:

$$t_{min} < t_{shock} < t_{max} \tag{V.9-11}$$

where t_{min} is calculated by:

$$t_{min} = \frac{h}{c_{max}} = \frac{h}{1,047 \cdot c} \tag{V.9-12}$$

and t_{max} is determined by the speed of sound c:

$$t_{max} = \frac{h}{c} \tag{V.9-13}$$

The calculated values for Robax and Optifloat targets of the (typical) height $h = 39$ mm are displayed in Table 56.

Material	c [m/s]	c_{max} [m/s]	t_{min} [µs]	t_{max} [µs]
"Optifloat®"	5818	6092	6,4	6,7
"Robax®"	6539	6847	5,7	6,0

Table 56: Shock wave propagation parameters: The speed of sound c and the maximal speed of shock waves c_{max} is given for the two glass types, used in the HIEs. Furthermore the amounts of t_{min} and t_{max} are given for a distance of 39 mm, which allows to estimate the runtime of a shock wave in a target of this height. Please note that t_{min} and t_{max} are pure run-times. Before the shock waves start to propagate it takes them about 1 µs to become established.

Thus, the process of shock wave energy dissipation is finished not later than between seven and eight microseconds after impact. According to experimental and theoretical considerations [74] it can be approximately presumed that the shock wave energy rate e_{shock} decreases with $e^{-(t/\tau)}$ where τ denotes the half-life period.

In a first approximation, a half-life period of $\tau = 1\,\mu s$ can be selected, for which e_{shock} is reduced to considerably less than 1 % of its maximum value after the run-time t_{min}.

This qualitative model is also coherent with HIE results:

Damage cracks are characterized by a discrete semi-circular shaped crack front. This fact indicates strongly that beyond that border, characterized by the distance d_{DC}, the shock wave energy density has been too low to affect the material properties in a significant way.

Fig. 94 illustrates a typical example , for which in a late stage of fragmentation the farthest distance d_{DC} between the damage crack front and the point of impact has been determined.

Using the transmission velocities listed in Table 56, it is possible to calculate the corresponding runtime.

In the case illustrated in Fig. 94, d_{DC} has amounted to 9,10 mm. Thus, a shock wave propagating in an "Optifloat" based sample passes this distance in about 1,5 to 1,6 µs. Presuming that it had previously taken 1 µs for the process of initiation, this implies that at the moment t_{DC} between 2,5 and 2,6 µs after impact, the shock wave amplitude has gone below a critical value e_{crit}, which in this example is around 20 to 22 % of the maximum energy dissipation rate. This result seems to be a very comprehensible value.

9.3.3. Third Stage: Stress Gradient Induced Fractures

The final stage of E_{DC} dissipation is characterized by the visible generation of conchoidal and intermediate crack structures within the shock wave affected zones. These cracks are driven by the alternating pressure gradients and stress fluctuations in the material. The term of energy, which dissipates in the final stage is denoted E_{vis}.

As pointed out above, it is not possible to quantify its exact value by means of HIEs due to the complex formation of damage cracks and their zonal structures.

However, in a first approximation the corresponding rate of energy that dissipates into visible conchoidal and intermediate cracks e_{vis} can be estimated by:

$$e_{vis}(t) \sim w_{DC}(t) \qquad \text{(V.9-14)}$$

9.3.4. Resulting Model

According to the conclusions of chapter V.8.3.2 it is evident that shock waves play an important role in HIE fragmentation processes.

In MFCI roughly 40 to 60 % of the total energy input dissipates into shock waves [18] (see Table 38). It has to be mentioned that the coupling conditions in HIEs can be presumed to be even more effective than in thermohydraulic driven MFCI fragmentation, so that these values can be considered as minimum estimated values.

In a coarse valuation the following ratio can be chosen:

$$E_{notch} : E_{shock} : E_{vis} \approx 30\,\% : 50\,\% : 20\,\% \qquad \text{(V.9-15)}$$

In order to gain an impression of the dynamics of the dissipating damage fracture energies, all considerations and results pointed out above are fused together in a semi-quantitative model, which is depicted for a representative example in Fig. 95.

Please note that the damping effect of Zone 0 as well as the large influences of the effective coupling conditions with the hammer (see part V.8.3.2) are *not* considered in this basic shock

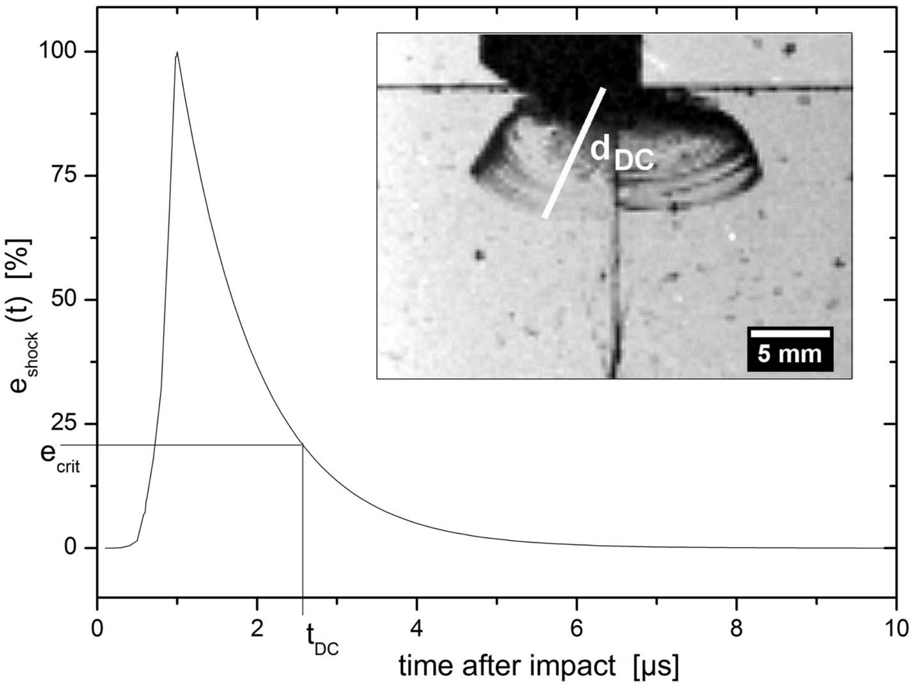

Fig. 94: Temporal evolution of shock wave energy rates $e_{shock}(t)$, scaled to their maximum value: For this model, it is presumed that a shock wave is established 1 µs after impact. The corresponding energy rate decreases with $e^{-(t/\tau)}$, where $\tau = 1$ µs is selected. In the depicted example ([V677], {124}), the farthest distance between the point of impact and the damage crack front d_{DC} has been determined to be 9,10 mm. The shock wave has passed this distance in $t_{DC} \approx 2,55$ µs. Beyond the corresponding critical value e_{crit} of about 21 % of the maximum amplitude, the energy rate has been too low to affect the material in a significant way.

wave model, although both effects -with the utmost probability- considerably affect energetic dissipation processes of damage crack evolution.

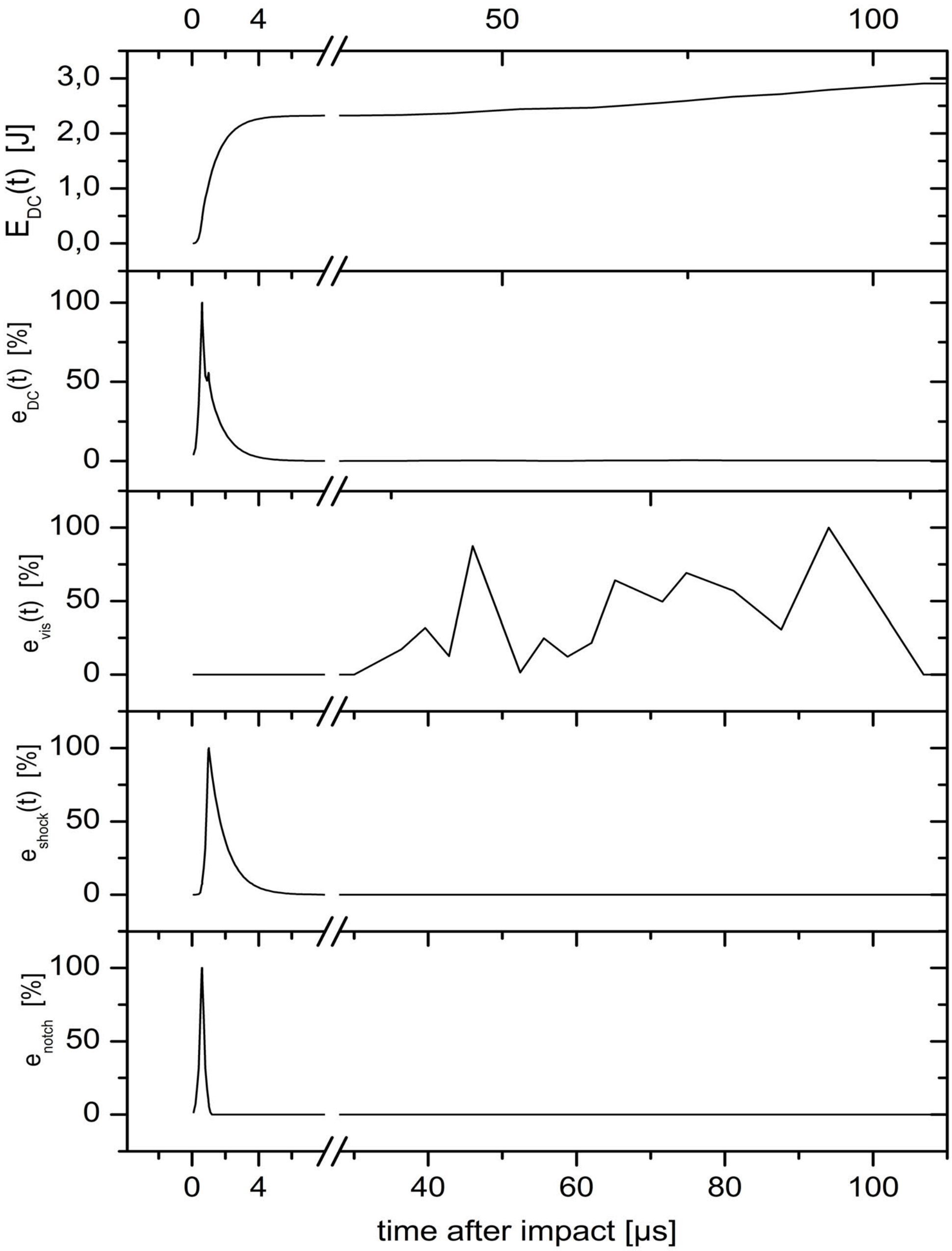

Fig. 95: Semi-quantitative model describing the dynamics of the three relevant energy rates, which are responsible for damage cracks:
Again the example of Fig. 94 is examined ([V677], {124}). The dynamic rate of energy, which dissipates into the nucleation of the impact notch $e_{notch}(t)$, the shock wave energy rate $e_{shock}(t)$, and the energy rate which finally dissipates into the visible conchoidal and intermediate crack structures $e_{vis}(t)$ have been standardized to their respective maximum values and are displayed.
The time integrals of these energy rates are weighted by the ratio (V.9-15) and calibrated to the final amount of E_{DC}, which is 2,91 J for the observed case. The resulting curve approximately describes the dynamics of $E_{DC}(t)$ and is displayed at the top.
In addition, the corresponding total damage crack energy rate $e_{DC}(t)$, which is the temporal derivative of $E_{DC}(t)$ is standardized to its maximum value and plotted. Note that the influence of $e_{vis}(t)$ on $e_{DC}(t)$ cannot be resolved in this graph.

9.4. Normal Crack Tip Velocities

In Appendix G, characteristic results of crack tip velocities are presented. When examining crack tip velocities it is useful to consider the specific speed of shear waves c_T in the studied material. This magnitude can be calculated by [59]:

$$c_T = \sqrt{\frac{E}{2 \cdot \varrho \cdot (\mu + 1)}} \tag{V.9-16}$$

Thus, for "Optifloat" float glass targets, the resulting value of c_T is 3445 $\frac{m}{s}$, for "Robax" glass ceramics, it is 3786 $\frac{m}{s}$.

A comprehensive description of the occurring crack tip velocities $u(t)$ would be far beyond the scope of this thesis. Instead, their most pronounced features are summarized as follows:

- Under various HIE conditions, a significant linear correlation between v_H and the maximum crack tip velocity $\mathrm{Max}(u(t))$ can be verified. For example under {X02} the Pearson correlation coefficient ρ amounts to 0,947 with a significance of 0,1 %. Hence, the limit of crack stability in a certain target - among other factors - depends on the impact velocity.
- For several cases, the maximum as well as the mean crack tip velocities show significant differences, depending on the hammer geometry. Thus, both parameters, $\mathrm{Max}(u(t))$ and $\bar{u}$ seem to be distinctly affected by the mechanical coupling conditions at the moment of impact.
- Evidently, there is a significant correlation between the target type and the maximum values of maximal normal crack tip velocities $\mathrm{Max}[\mathrm{Max}\,(u(t))]$. This parameter can be seen as the maximum possible propagation rate of a single crack tip and seems to be a particularly useful material-specific characteristic value.
  Its empirically determined values are presented in Table. 57.

		FG	T5	T10	TK	AS	RX
$\mathrm{Max}[\mathrm{Max}\,(u(t))]$	$[\frac{m}{s}]$	1852	2252	2153	2733	1511	3266
$\mathrm{Max}[\mathrm{Max}\,(u(t))]/c_T$	[%]	53,8	65,4	62,5	79,3	43,9	86,3
$\overline{\mathrm{Max}}\,(u(t))$	$[\frac{m}{s}]$	1497	1654	1693	1842	1384	2381
$\sigma\,(\mathrm{Max}\,(u(t)))$	$[\frac{m}{s}]$	194	229	284	470	196	423

Table 57: Target type-specific maximal crack tip velocities: Their maximum values $\mathrm{Max}[\mathrm{Max}\,(u(t))]$ are presented as well as their mean values $\overline{\mathrm{Max}}\,(u(t))$ and standard deviations $\sigma\,(\mathrm{Max}\,(u(t)))$. These results can be seen as characteristic values, which specify the stability limit of crack propagation. Note that $\mathrm{Max}[\mathrm{Max}\,(u(t))]$ and $\overline{\mathrm{Max}}\,(u(t))$ show similar material-specific dependencies.

- It is clear that the values of the maximum crack tip velocities in RX targets are distinctly higher than in FG targets (verified by a t-test significance of $p < 0{,}05\,\%$). Even if the crack tip velocity is standardized to the respective value of c_T, crack tips in RX targets are moving distinctly faster than in targets which are made of "Optifloat" float glass .
- Furthermore the results indicate that thermal pre-stresses cause a significant increase of the characteristic values $\mathrm{Max}[\mathrm{Max}\,(u(t))]$ and $\overline{\mathrm{Max}}\,(u(t))$ within float glasses, of which TK targets feature the highest maximum crack tip velocities.
- In contrast, the additional interfaces of AS targets appear to reduce the maximum crack tip velocity.

- ACBs and BCMs are characterized by high average and maximum values of $u(t)$ and in most cases no significant differences have been detected between the dynamics of both crack types. For example for RX $\bar{u}_{ACB} = (2000 \pm 308)\ \frac{\text{m}}{\text{s}}$, while $\bar{u}_{BCM} = (2090 \pm 214)\ \frac{\text{m}}{\text{s}}$. Thus, all results indicate that under identical HIE configurations:
  $\bar{u}_{ACB} = \bar{u}_{BCM}$,
  $\text{Max}(u_{ACB}(t)) = \text{Max}\,(u_{BCM}(t))$
  and $\sigma\,(u_{ACB}(t)) = \sigma\,(u_{BCM}(t))$.

- The crack tip velocities of ACBs and BCMs show comparatively low standard deviations: For example for RX targets $\sigma\,(u_{ACB}(t))$ amounts to $484\,\frac{\text{m}}{\text{s}}$, which is 24,2 % of the corresponding average velocity. Their determined value of $\sigma\,(u_{BCM}(t))$ is $440\,\frac{\text{m}}{\text{s}}$, (21,1 % of the corresponding amount of $\bar{u}_{BCM}$).

- In contrast, ACTs are usually characterized by highly significant lower crack tip velocities (e.g. for HIEs of the configuration $\{626\}$ is $\text{Max}(u_{ACB}) = (2463 \pm 11)\ \frac{\text{m}}{\text{s}}$ and $\text{Max}(u_{ACT}) = (1850 \pm 6)\ \frac{\text{m}}{\text{s}}$). Evidently, the large damage crack fracture areas which are typically associated with the initiation of ACTs affect the propagating normal cracks. In this regard, it is of interest that the dynamic fluctuations of ACTs are significantly higher than those of ACBs or BCMs: For example $\sigma\,(u_{ACT}(t))$ has been determined to be $500\,\frac{\text{m}}{\text{s}}$, which is 54,0 % of the corresponding value of $\bar{u}_{ACT}$.
  This is another strong evidence for a distinct dynamic influence of evolving damage cracks on ACTs.

- SCMs, which are virtually exclusively observed in TK targets, can propagate at very high velocities (the determined maximum values have amounted up to $2733\,\frac{\text{m}}{\text{s}}$, which is the highest crack tip velocity observed in a float glass target), but the average amount of $u_{SCM}(t)$ has been comparatively low: $\bar{u}_{SCM}(t) = (1415 \pm 336)\ \frac{\text{m}}{\text{s}}$. This indicates that these cracks feature considerable dynamic variations, which is of interest, as the crack tips of SCMs - by definition - do not show visible instabilities in form of branching.

- W-cracks propagate at comparatively low maximal and average crack tip velocities, but they also show a distinct variation in their dynamics (e.g. for RX: $\sigma\,(u_W(t)) = 501\,\frac{\text{m}}{\text{s}}$, which is 36,1 % of the corresponding amount of $\bar{u}_W$).

- Secondary cracks propagate with distinctly lower crack tip velocities. Furthermore, these cracks are also characterized by *crack arrests* (this term describes the phenomenon that a fast propagating fracture suddenly stops its evolution [55]). All these characteristics can be explained by reduced stress intensities in the late stage of fragmentation.

9.5. Normal Crack Velocities

As pointed out above, for the calculation of crack velocities all simultaneous propagating crack tips are taken into account in a body. Thus, this magnitude provides useful information about the over-all state of fragmentation at a particular point in time and has therefore been examined for significant influences by means of multivariate statistical methods (see Appendix H).

Please note that characteristic results are also presented in detail in Appendix G.

9.5.1. Statistical Overview

A statistical summary of the determined normal crack velocities $v_{NC}(t)$ is given in Table 58, in order to obtain an impression of the amounts of this magnitude, which is more abstract than the crack tip velocity $u_{NC}(t)$, but also more meaningful from the energetic point of view.

	minimum value	maximum value	mean value	standard deviation
$\bar{v}_{NC}$	$241\,\frac{\mathrm{m}}{\mathrm{s}}$	$8778\,\frac{\mathrm{m}}{\mathrm{s}}$	$2812\,\frac{\mathrm{m}}{\mathrm{s}}$	$1761\,\frac{\mathrm{m}}{\mathrm{s}}$
HIE	[V224], {101}	[V249], {501}		
$\widetilde{v}_{NC}$	$213\,\frac{\mathrm{m}}{\mathrm{s}}$	$7720\,\frac{\mathrm{m}}{\mathrm{s}}$	$2230\,\frac{\mathrm{m}}{\mathrm{s}}$	$1552\,\frac{\mathrm{m}}{\mathrm{s}}$
HIE	[V224], {101}	[V611], {613}		
$\mathrm{Max}(v_{NC}(t))$	$367\,\frac{\mathrm{m}}{\mathrm{s}}$	$26695\,\frac{\mathrm{m}}{\mathrm{s}}$	$7434\,\frac{\mathrm{m}}{\mathrm{s}}$	$5201\,\frac{\mathrm{m}}{\mathrm{s}}$
HIE	[V228], {301}	[V248], {601}		
$\sigma(v_{NC}(t))$	$105\,\frac{\mathrm{m}}{\mathrm{s}}$	$9270\,\frac{\mathrm{m}}{\mathrm{s}}$	$2393\,\frac{\mathrm{m}}{\mathrm{s}}$	$1814\,\frac{\mathrm{m}}{\mathrm{s}}$
HIE	[V224], {101}	[V248], {601}		

Table 58: Overview of the resulting normal crack velocities: The corresponding HIE number and configuration is displayed as well. Note that the highest standard deviations are associated with the highest maximum values $\mathrm{Max}(v_{NC}(t))$. Both parameters are characteristic values for the dynamic fracture stability: Higher values indicate a more unstable evolution of cracks and consequently a higher fluctuation of crack propagation rates.

9.5.2. Influences of the Hammer Impact Velocity

The following facts have been revealed by correlation analyses:

- For many cases - especially for FG and T5 targets - highly significant linear correlations between the maximum values of normal crack velocities and v_H have been verified (see also Table 59).

$\rho(v_H; ...)$		$\mathrm{Max}(v_{NC}(t))$	$\mathrm{Max}(v_A(t))$	$\mathrm{Max}(v_C(t))$	$\mathrm{Max}(v_W(t))$	$\mathrm{Max}(v_S(t))$
FG	ρ	0,443	0,427	(-)	0,438	(-)
	p	0,3 %	1,2 %	(-)	2,5 %	(-)
T5	ρ	0,737	0,804	(-)	(-)	(-)
	p	1,0 %	0,5 %	(-)	(-)	(-)

Table 59: Linear correlation for FG and T5 targets between the maximum values of crack velocities and the impact velocity v_H. Results that are not significant, are marked by "(-)". Note that no linear correlation has been verified for $\mathrm{Max}(v_C(t))$ and $\mathrm{Max}(v_S(t))$, respectively.

- It is of interest that in no case any significant correlation has been revealed for $\mathrm{Max}(v_C(t))$ and $\mathrm{Max}(v_S(t))$.
  In contrast, cracks which propagate within the PSZ (i.e. A-cracks and to some extent also W-cracks) show a significant dependency of v_H.
  Thus, all findings indicate that $\mathrm{Max}(v(t))$ distinctly depends - unlike the FSED parameter η_{NC} - on the amount of the local stress.

- Another evident fact which supports this theory is that the linear correlation is more pronounced for pre-stressed T5 than in FG samples, indicated by significantly higher Pearson correlation coefficients.
  It has to be kept in mind that the resulting PSZ in those targets is in fact a superposition of two identical stress-fields (the pre-stressed regions and the zones of directed stresses). Hence the local stress intensities within the resulting PSZ are expected to be significantly higher than for example in stress released FG targets.
  As a consequence the considerable local dependency of crack dynamics in T5 targets is well explainable.

- Very similar results are revealed by linear correlation analyses between v_H and the mean values of crack velocities: Significant linear correlations with v_H are not found for $\bar{v}_C$ and $\bar{v}_S$, but for $\bar{v}_A$ and partly for $\bar{v}_W$. For example $\rho(v_H; \bar{v}_A)$ amounts for FG targets to 0,339 ($p = 5{,}0\,\%$) and for T5 samples to 0,739 ($p = 1{,}5\,\%$).

- Per definition high maximum values of crack velocities indicate intensified crack branching and hence growing fracture instabilities.
  Thus, it can be seen as a consistent result that also the standard deviations show very comparable dependencies: For example $\rho(v_H; \sigma\,(v_A))$ amounts to 0,478 ($p = 0{,}5\,\%$) for FG and to 0,760 ($p = 1{,}1\,\%$) for T5.

In conclusion, it can be stated that crack velocities show a significant linear dependency of v_H, particularly in regions of distinct stress anisotropies. These zones are identical with the resulting PSZ, which is the superposition of pre-stressed regions and areas of directed stresses.

Due to the specific local stress situation, this effect is most pronounced for FG and T5 targets.

In these targets, a higher impact velocity causes a more rapid fracture evolution, which in turn brings about increasing dynamic instabilities, resulting in more pronounced crack branching and hence considerable higher variations of crack velocities.

9.5.3. Additional Correlations

- No systematic significant dependency of the hammer geometry has been detected for any kind of crack velocities, except for the case below.

- The only notable exception has been verified for A-crack velocities in T10 targets under specific conditions: For example for low impact velocities $\bar{v}_A$ is distinctly higher for a 4,5 mm wide than for a pointed hammer head, featuring a t-test significance of 3,0 %. Yet, due to low sample sizes (N = 6), this result should not be overrated.

- It is not surprising that all characteristic values of crack velocities significantly depend on the properties and the pre-stress situation of the targets. Table 60 gives a target type-specific overview.

	FG	T5	T10	TK	RX
$\bar{v}_{NC}(t)$ $[\frac{\text{m}}{\text{s}}]$	2943 ± 1688	2230 ± 952	3737 ± 2667	1234 ± 623	3115 ± 1833
$\overline{\text{Max}}\,(v_{NC}(t))$ $[\frac{\text{m}}{\text{s}}]$	7445 ± 4904	6304 ± 2915	9476 ± 7339	2966 ± 1276	9350 ± 6208
$\overline{\sigma}\,(v_{NC}(t))$ $[\frac{\text{m}}{\text{s}}]$	2513 ± 1879	1949 ± 966	2834 ± 2119	862 ± 349	2877 ± 2071

Table 60: Target type-specific mean values and standard deviations of $v_{NC}(t)$, $\text{Max}(v_{NC}(t))$ and $\sigma(v_{NC}(t))$: It is evident that all three characteristic parameters are correlated: A rapid fragmentation is associated with high amounts of $\overline{\text{Max}}\,(v_{NC}(t))$ and $\overline{\sigma}\,(v_{NC}(t))$. Both parameters indicate an increase in dynamic fracture instabilities.

- The lowest average amounts of normal crack velocities are determined for TK targets: For example, t-tests have verified by a high significance ($p = 0{,}2\,\%$) that in these samples crack fragmentation proceeds distinctly slower than in RX targets. As the propagation rate of cracks is always correlated with their dynamic stability, it coincides well that $\overline{\text{Max}}\,(v_{NC}(t))$ and $\overline{\sigma}\,(v_{NC}(t))$ show significantly lower values, too.

- Also the specific stress situation in T5 targets seems to effect a reduction in the observed parameters, compared to stress-released FG samples.

- In contrast, the pre-stresses in T10 targets effect a highly significant increase in the evolution rate of normal cracks. It is notable that for these samples the characteristic values of normal crack velocities are even higher than for RX targets.

- The great amounts of normal crack velocities in RX targets are not surprising, as in these materials cracks propagate with distinctly higher maximum crack tip velocities, as pointed out above.

- Table 61 presents various crack velocities for FG, T5 and RX targets:

	$\bar{v}_A(t)$ $[\frac{\text{m}}{\text{s}}]$	$\bar{v}_C(t)$ $[\frac{\text{m}}{\text{s}}]$	$\bar{v}_W(t)$ $[\frac{\text{m}}{\text{s}}]$	$\bar{v}_S(t)$ $[\frac{\text{m}}{\text{s}}]$
FG	4048	4769	756	1715
T5	2481	1583	944	1077
RX	2790	8050	955	1779

Table 61: Results of average crack velocities in FG, T5 and RX targets.

- Instabilities in form of bifurcations have never been observed in W-cracks. This explains, why for all targets $\bar{v}_W(t)$ is significantly lower than for example $\bar{v}_A(t)$.

- Due to the lower amplitudes of stress waves in the late stage of fragmentation, also significantly lower secondary crack velocities are expected. In fact, for all targets the amounts of $\bar{v}_S(t)$ are characterized by highly significant lower values, compared to primary crack velocities.

- For RX targets, centrical crack induced fragmentation is more rapid than the evolution of A-cracks. In this case $\bar{v}_C(t)$ amounts to $8050\,\frac{\text{m}}{\text{s}}$, while $\bar{v}_A(t)$ has been determined to be $2790\,\frac{\text{m}}{\text{s}}$ (see Table 61). $\text{Max}(\bar{v}_C)$ and $\sigma\,(\bar{v}_C)$ show similar differences. Evidently, in glass ceramics directed stresses ensure a more stable evolution of cracks within the PSZ. The consequences of these insightful findings will be dealt with in the next section.

- A similar effect has been found for FG, although it is not so prominent as for RX.

- It is very interesting that T5 targets show the opposite behavior: In this case, $\bar{v}_A(t)$ has been verified to be considerably higher than $\bar{v}_C(t)$.
  Nevertheless, the A-crack velocities in T5 targets generally show significantly lower values, compared to those in FG samples. This important finding is no coincidence and quite enlightening, as we will see in the next section.

In summary, crack velocities have proven to be useful parameters to specify the dynamics of crack evolution. Their mean and maximum values as well as their standard deviations are good indications of how stable and how fast fragmentation proceeds in a target.

Furthermore, it has been verified that different types of cracks show significantly different development rates depending on the local stress intensities.

This fact makes it difficult to use crack velocities for a general fragmentation model.

Instead, the above introduced fracture area velocities (FAVs) are determined and analyzed, in order to calculate the energy dissipation rates by means of the FSED approach.

9.6. FAVs and Energy Dissipation Rates of Normal Cracks

9.6.1. Representative Dynamic Fracture Energy Dissipation Profiles

By means of (V.9-6), (V.9-7) and (V.9-8), it is now possible to reconstruct individually for each HIE the exact temporal and energetic contribution of a definite normal crack type on the basis of the crack type-specific linear FSED model.

In the following, the dynamics of the FAV $w(t)$, the energy dissipation rates $e(t)$ (briefly: "energy rates") and the amount of the dissipated fracture energy $E(t)$ are presented for representative cases, in order to obtain an impression of the general behavior and the energetic influences of these magnitudes.

The corresponding HIE image sequences to these dynamic fracture energy dissipation profiles can be found on the attached DVD in Appendix I.

Fig. 96 shows the resulting FAVs (on the left axis) and energy rates (on the right axis) of all crack types that have occured in a T5 target, which had been hit by a pointed hammer with an impact velocity of $v_H = 2,47\,\frac{\mathrm{m}}{\mathrm{s}}$. The temporal evolution of the corresponding fracture energies are displayed in Fig. 97 on the opposite page. It is evident that in this case the highest amount of energy has been dissipated into an A-crack on the right side.

Similar to the crack velocities, high FAVs and energy dissipation rates are typically characterized by distinct fluctuations, which are correlated with the stability of the crack tip. Fig. 98 illustrates this correlation between crack branching and $e_{A\,r}(t)$:

Before a branching appears, the crack tips form bulges and $e_{A\,r}(t)$ is drastically reduced. This result consists well with the similar behavior of the dynamic magnitudes $u(t)$ and $v(t)$ (and of course $w(t)$), which had also been found for stress-relieved FG targets in my spadeworks [40] (see also chapter II.3.2). It is a very interesting fact that this is apparently a typical phenomenon at least for glasses, as it has been observed for *all* targets studied in HIEs.

It has to be mentioned that the presented examples also indicate two principal restrictions of the applied concept:

- Of course, it is only possible to make a "snapshot" of the actual energy dissipation processes, as the time slot of the analyzed image sequence is very limited.
- Plus, in the case of distinct and rapid fluctuations, the dynamic magnitudes significantly depend on the specific time base. This implies that for statistical analyses a large number of records is needed to obtain reliable results.

Fig. 99, Fig. 100 and Fig. 101 display the dynamic energy dissipation profiles of HIEs with FG targets. Note that in the first case, the energy dissipation of a developing ACT is examined at a high time resolution. In contrast, Fig. 100 shows the energy dissipation of an evolving ACB and Fig. 101 that of a propagating BCM.

Fig. 102 and Fig. 103 show the typical dynamics of fracture energy dissipation in a T10 target. Note that the amount of energy $E_{A\,r}(t)$, which has dissipated into the first A-crack (from the right bearing) has been distinctly higher than that of the fracture energy $E_{A\,l}(t)$, which has been transformed into the fracture surface area of the subsequent A-crack on the left. This result is coherent with the fact that the concentration of stress reaches its maximum at the tip of the first initiated crack.

Representative dynamic energy dissipation profiles of TK targets are presented in Fig. 104 and Fig. 105. Fracture processes in these targets are uniformly characterized by occuring SCMs and subsequent secondary cracks. The period between the end of the last primary and the onset of the first secondary cracks can be easily specified in the first example: Fracture energy dissipation into normal cracks has been at a "standstill" over a period of 50 µs. In this specific experiment v_H had amounted to 1,79 $\frac{\mathrm{m}}{\mathrm{s}}$. The impact velocity of the HIE illustrated in Fig. 105, however, had been considerably higher ($v_H = 2{,}44\,\frac{\mathrm{m}}{\mathrm{s}}$). Maybe this has been the reason why there, the secondary cracks have been initiated significantly earlier. As a consequence, the resulting energy dissipation curves show notable differences.

Finally, the representative example of Fig. 106 and Fig. 107 illustrates the dynamic fracture energy dissipation in a RX target. In the depicted case, a combination of primary cracks (an ACB and a BCM) had been initiated. Note that the energy dissipation rate of the BCM $e_C(t)$ has shown to be considerably larger than that of the simultaneously propagating ACB $e_A(t)$. This phenomenon is no coincidence, as we will see in the following sections.

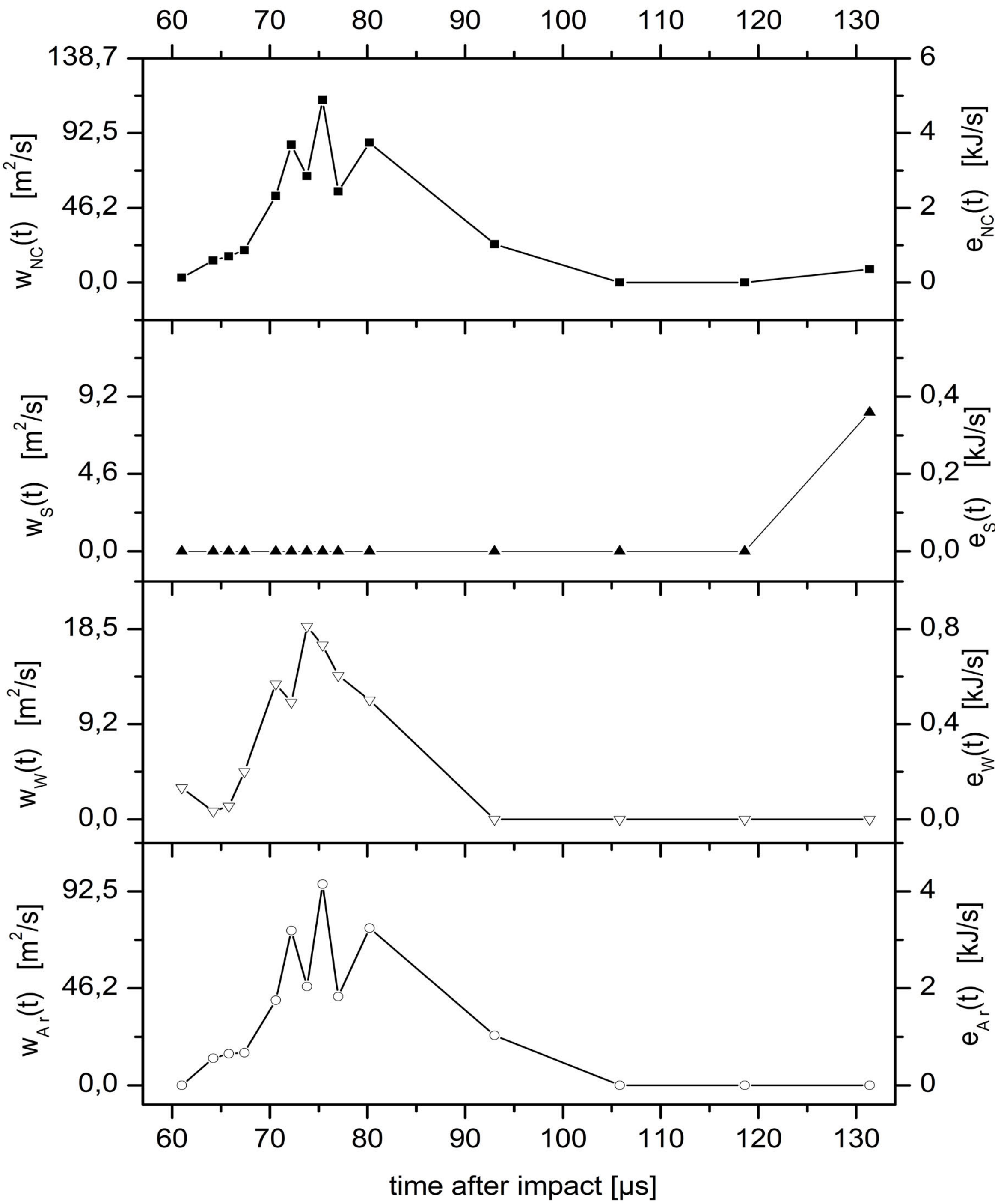

Fig. 96: Representative example, presenting the FAVs (on the left axis) and energy rates (on the right axis) of all crack types that have occured in a T5 target ([V355], {602}, $v_H = 2,47\,\frac{\text{m}}{\text{s}}$): A-, W- and secondary cracks. Additionally $w_{NC}(t)$ and $e_{NC}(t)$ are displayed, which are the sums of these magnitudes. The corresponding image sequence of this experiment can be found in Appendix I.
The magnitudes $e(t)$ are calculated out of the respective FAVs by means of the crack-specific linear FSED model. In this case η_{NC} has amounted to $43,26\,\frac{\text{J}}{\text{m}^2}$.
Note that the energy rate of the A-crack (which has developed in the PSZ) has been considerably larger than that of the W-crack. The energy dissipation diagram of $e_{Ar}(t)$ is also presented in detail in Fig. 98.

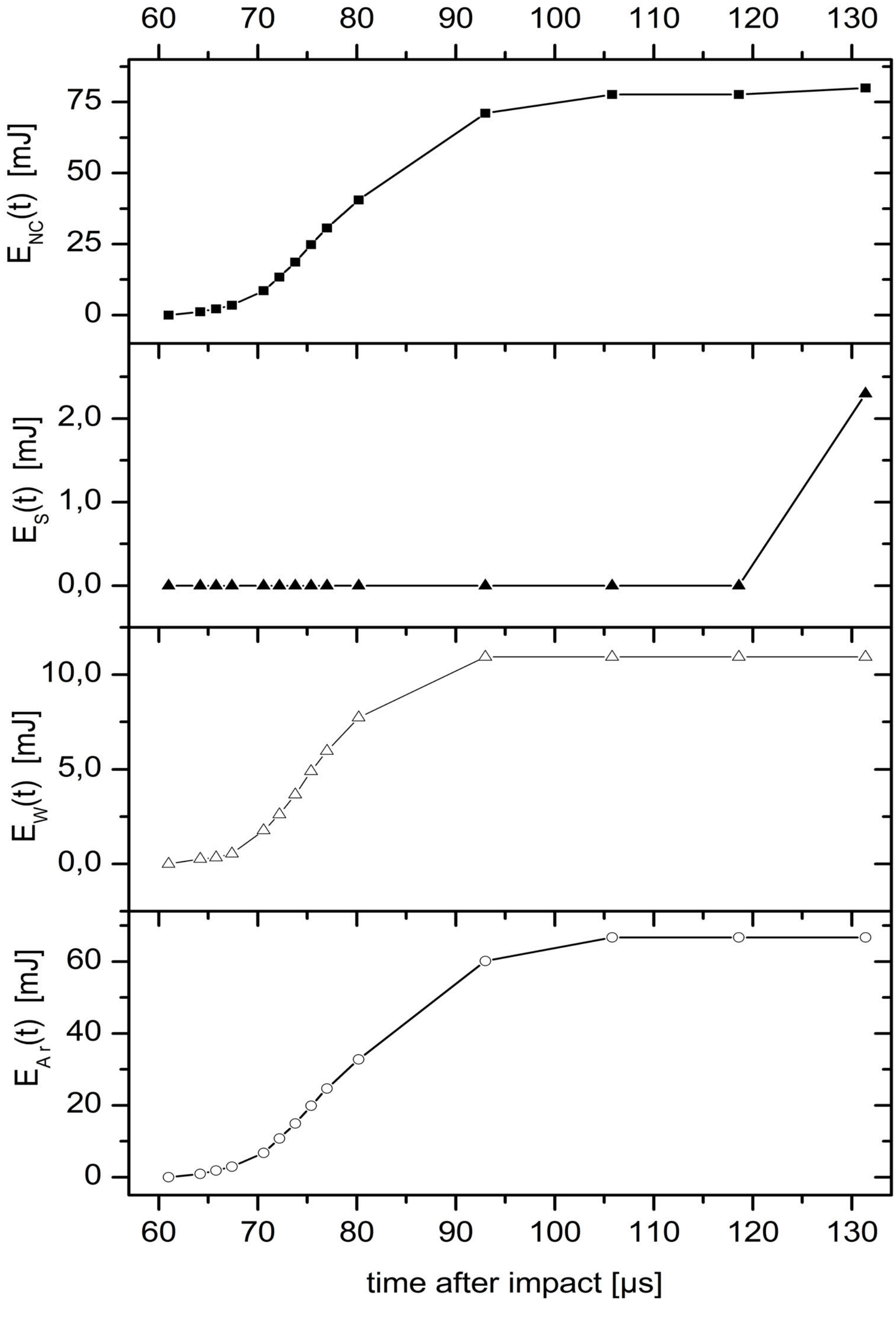

Fig. 97: Temporal development of the dissipating fracture energies during the fragmentation process corresponding to Fig. 96 [V355]: This energy profile provides information on all relevant energetic contributions in the first stages of fragmentation. Please note that - as the time slot is limited - it was only possible to record the initial phase of secondary crack evolution.

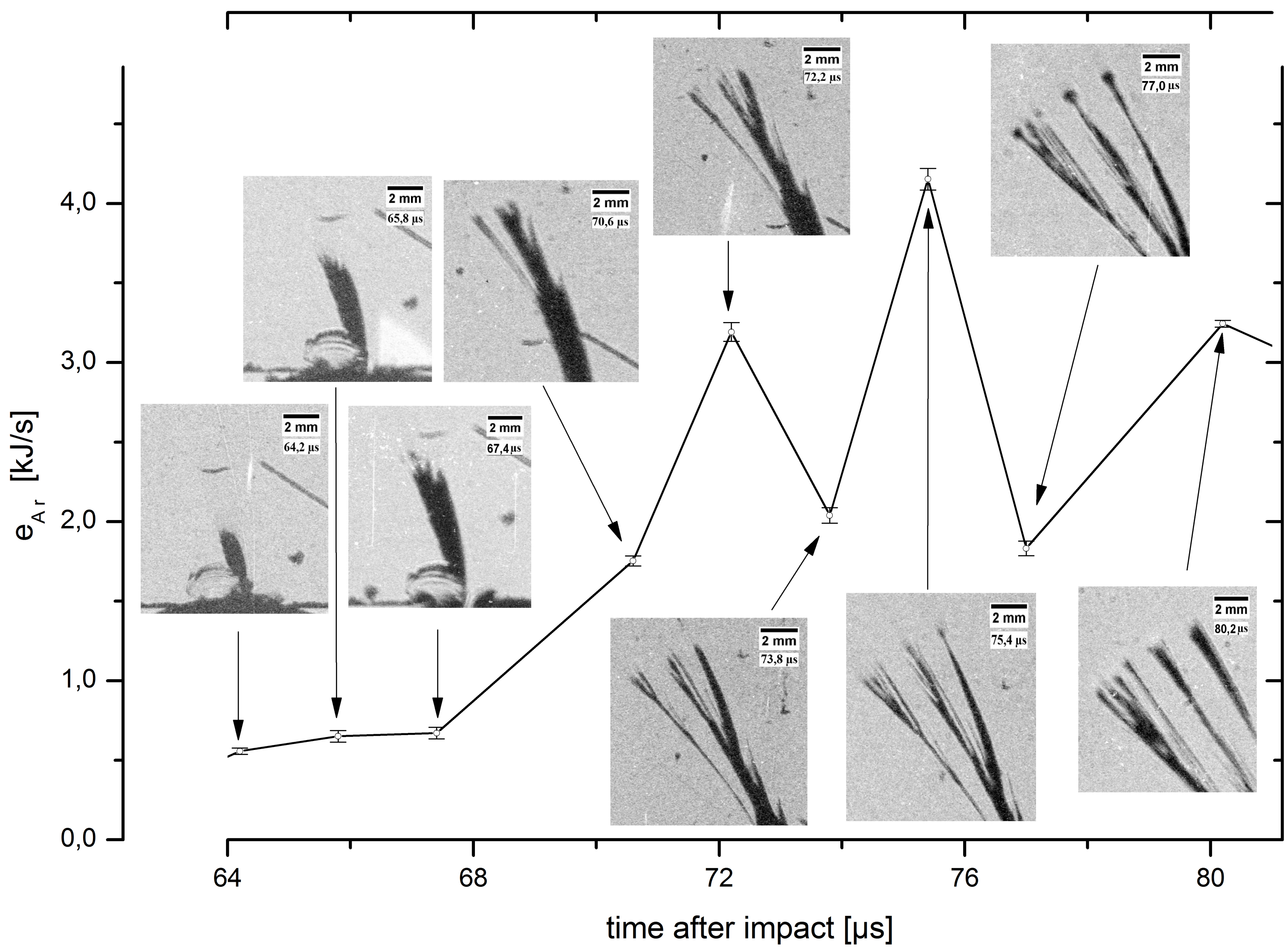

Fig. 98: Correlation between crack stability and the energy dissipation rate [V355]: For each data point, the corresponding crack tips of the examined ACB are presented. When $e_{Ar}(t)$ exceeds a certain limit (roughly between 0,67 and $1,75\,\frac{\mathrm{kJ}}{\mathrm{s}}$ in the depicted case), fracture evolution becomes an unstable process, characterized by large variations of $e(t)$ and by crack branching events.

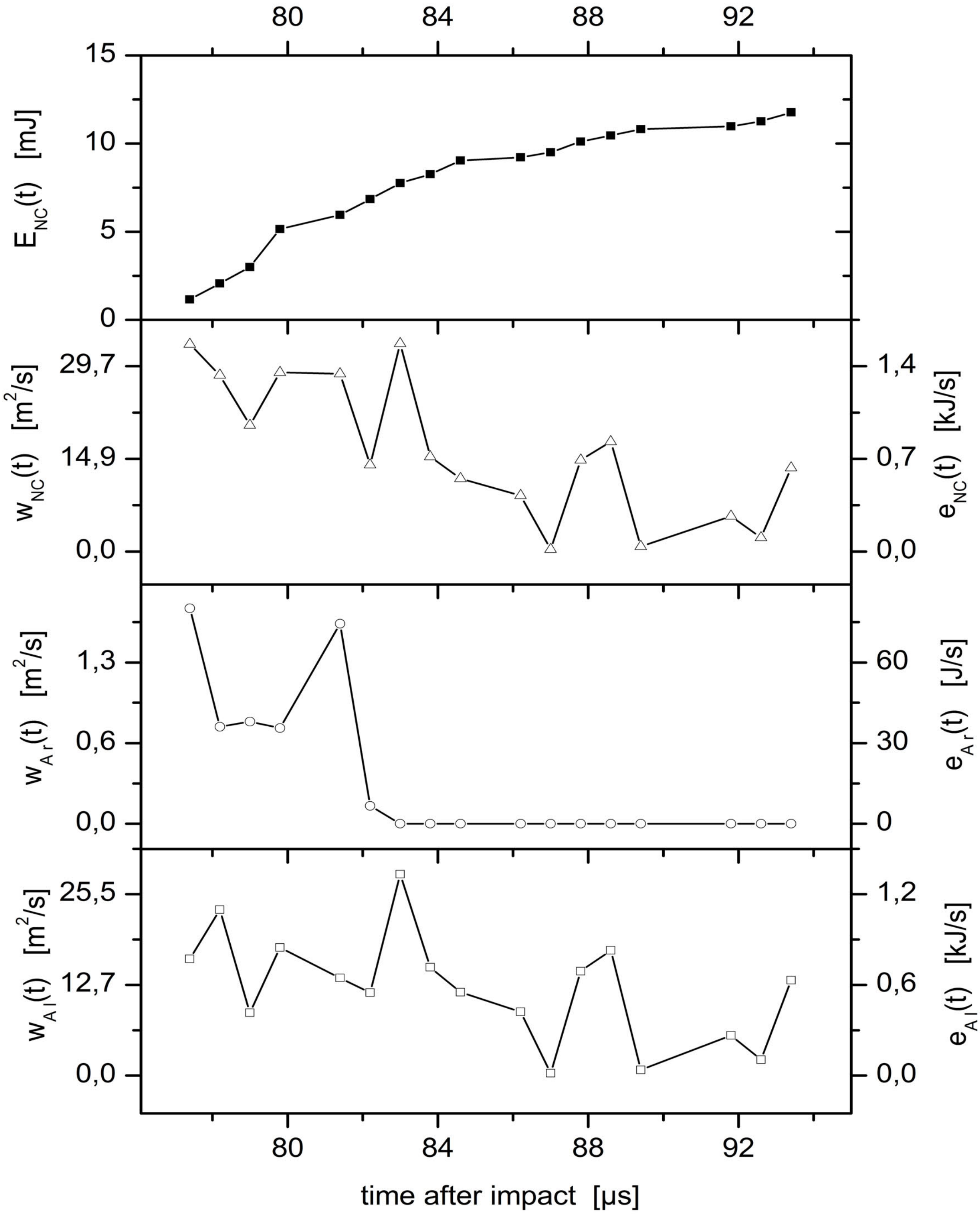

Fig. 99: Dynamic fracture energy dissipation profile in the case of FG ([V208], {101}, $v_H = 1,78\,\frac{\mathrm{m}}{\mathrm{s}}$, $\eta_{NC} = 47,10\,\frac{\mathrm{J}}{\mathrm{m}^2}$): In this example, A-cracks in form of ACTs have been initiated on both sides. Their evolution has been recorded with a high time resolution. Note that the dynamics of these cracks show considerable fluctuations and even crack arrest (at $t = 87\,\mu\mathrm{s}$). Yet, as the maximum energy rates have been comparatively low, the cracks did not bifurcate.

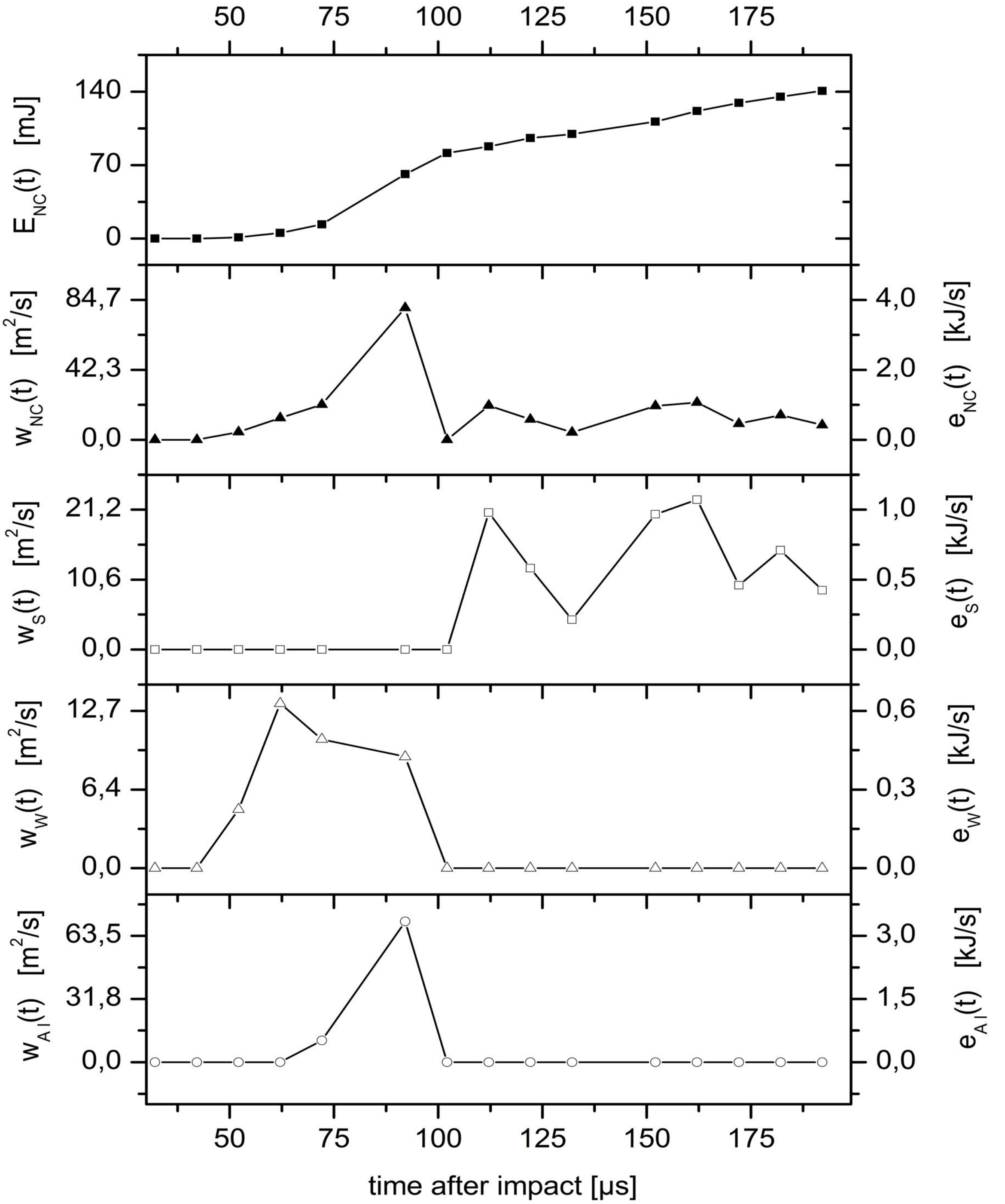

Fig. 100: Another typical fracture energy dissipation profile of a breaking FG target ([V244], {601}, $v_H = 2{,}43\,\frac{\mathrm{m}}{\mathrm{s}}$, $\eta_{NC} = 47,24\,\frac{\mathrm{J}}{\mathrm{m}^2}$): In contrast to the example of Fig. 99, an A-crack in form of an ACB has been detected.
As a lower frame rate has been chosen for the depicted experiment, it is not possible to specify the fluctuations of $e_{AI}(t)$.
However, also considerable parts of the secondary crack energy rate $e_S(t)$ have been recorded. The frequencies of these variations are in the range of 20 to 50 kHz.

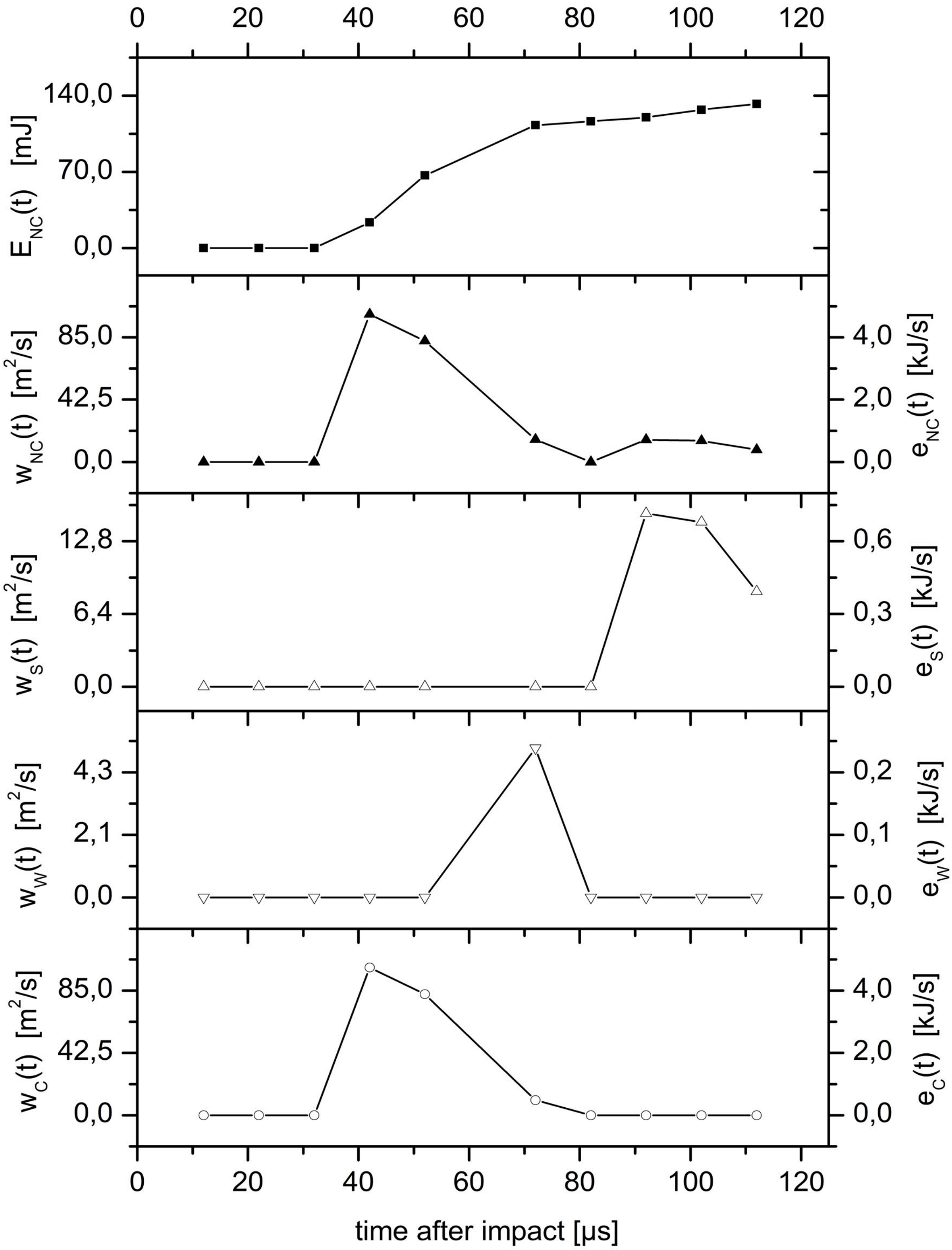

Fig. 101: Fracture energy dissipation profile of a FG sample, in which a BCM had been initiated as a primary crack type ([V226], {101}, $v_H = 1{,}79\,\frac{\mathrm{m}}{\mathrm{s}}$, $\eta_{NC} = 47{,}05\,\frac{\mathrm{J}}{\mathrm{m}^2}$).

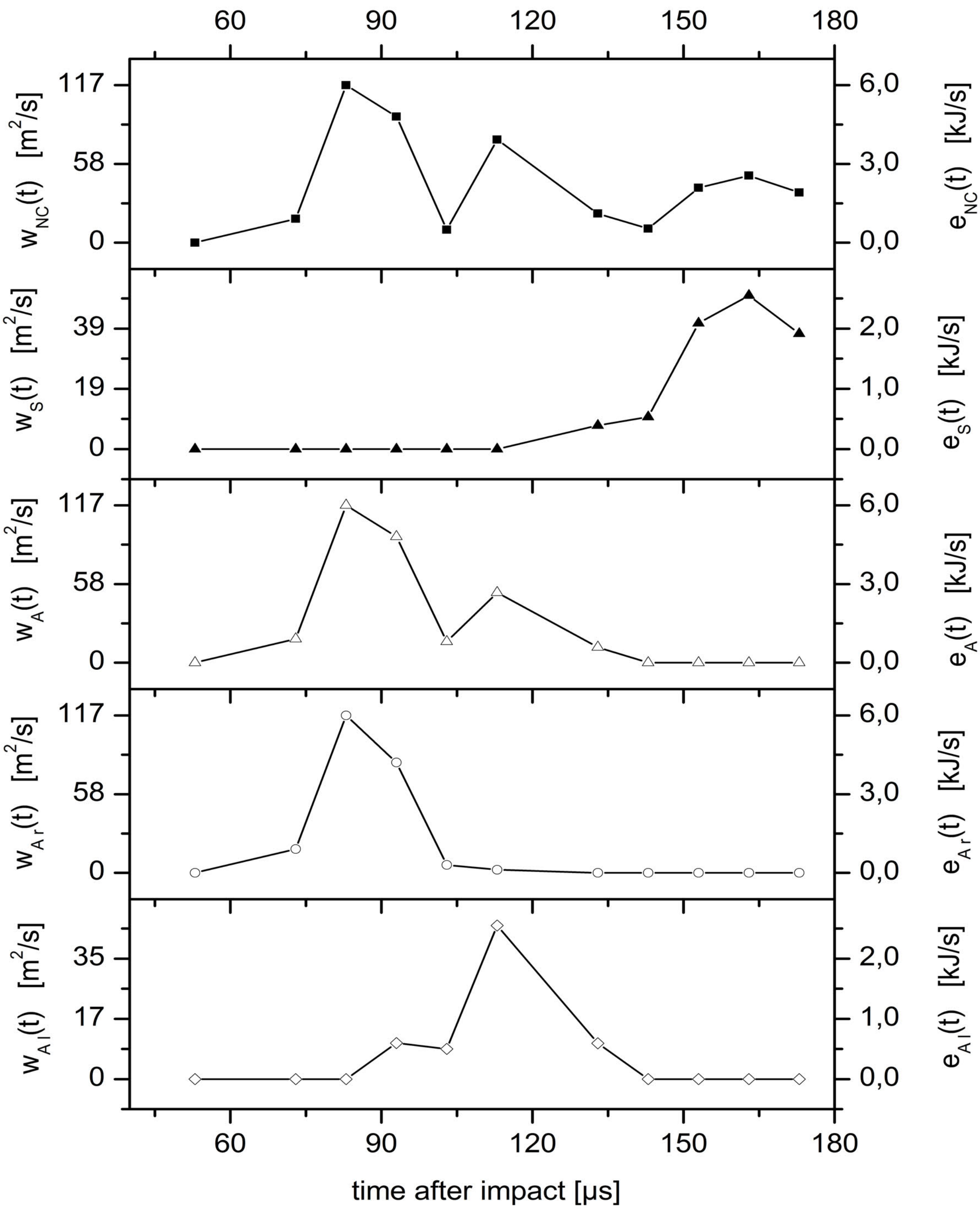

Fig. 102: This example presents the temporal evolution of FAVs and energy rates in a T10 target ([V320], {303}, $v_H = 2{,}07\,\frac{\mathrm{m}}{\mathrm{s}}$, $\eta_{NC} = 52{,}30\,\frac{\mathrm{J}}{\mathrm{m}^2}$): Note that the A-crack, which has started at the right bearing (specified by $w_{A\,r}(t)$ and $e_{A\,r}(t)$) has been initiated 10 µs before the left ACB (specified by $w_{A\,l}(t)$ and $e_{A\,l}(t)$). Evidently the first crack is characterized by a significantly higher energy rate.

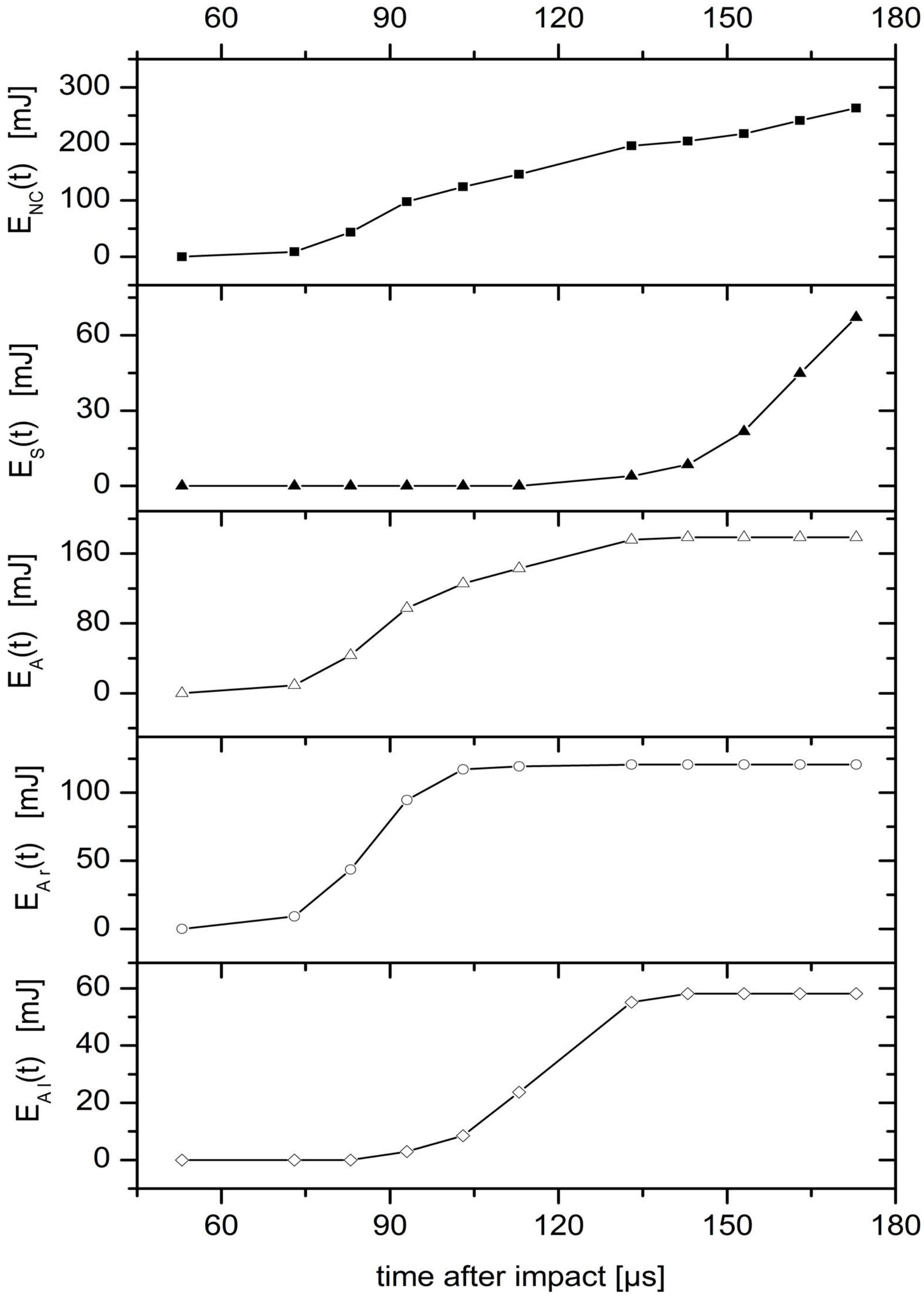

Fig. 103: Temporal development of the dissipating fracture energies during fragmentation in a T10 target, corresponding to the example illustrated in Fig. 102 [V320].

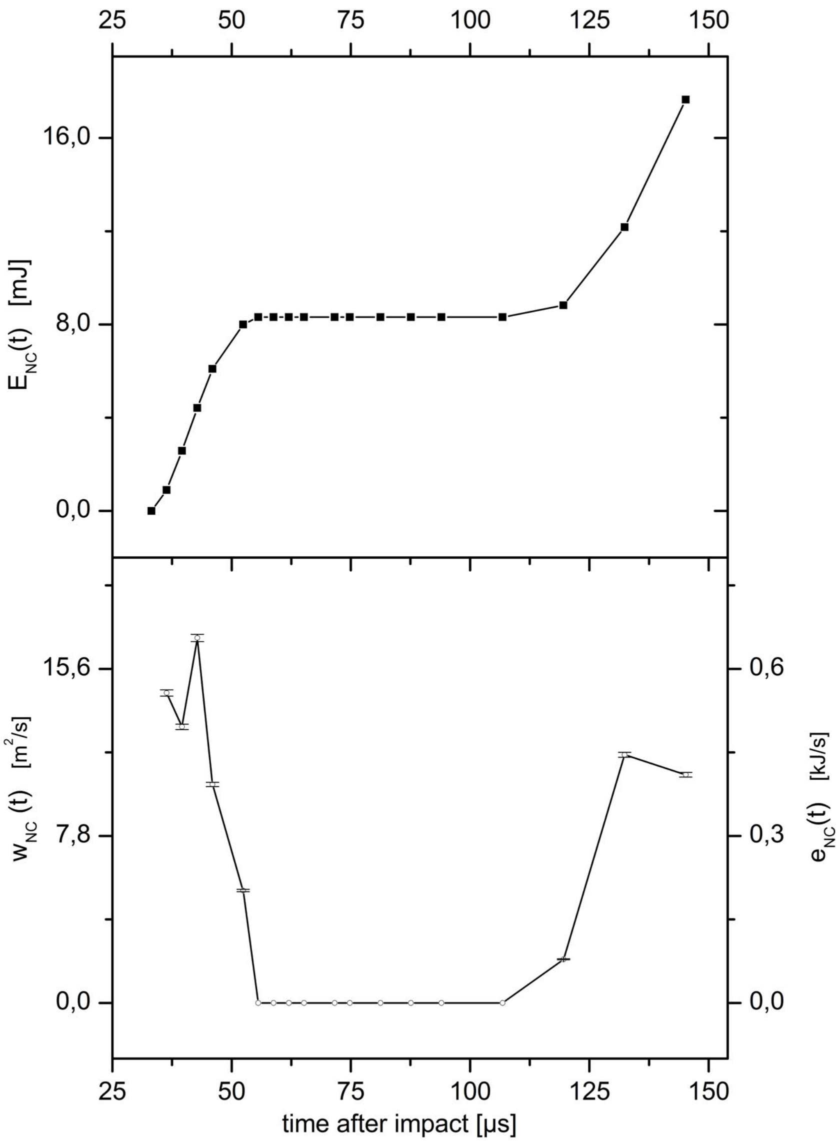

Fig. 104: Dynamic fracture energy dissipation profile of a HIE with a TK target ([V677], {124}, $v_H = 1{,}79\,\frac{\mathrm{m}}{\mathrm{s}}$, $\eta_{NC} = 38{,}46\,\frac{\mathrm{J}}{\mathrm{m}^2}$): These targets are virtually always characterized by SCMs as primary cracks and subsequent secondary cracks. Hence, only a cumulative dissipation profile of $e_{NC}(t)$ and $E_{NC}(t)$ is displayed, in which the first peak is effected by the propagating SCM and the second one by subsequently developing secondary cracks. Between both events, over a period of 50 µs, energy dissipation into normal cracks has been at a standstill.
As in this stage of fragmentation $e_{vis}(t)$ shows large variations (see the corresponding damage crack energy profile, illustrated in Fig. 95) it is evident that during this period considerable amounts of energies dissipate into visible damage crack structures.

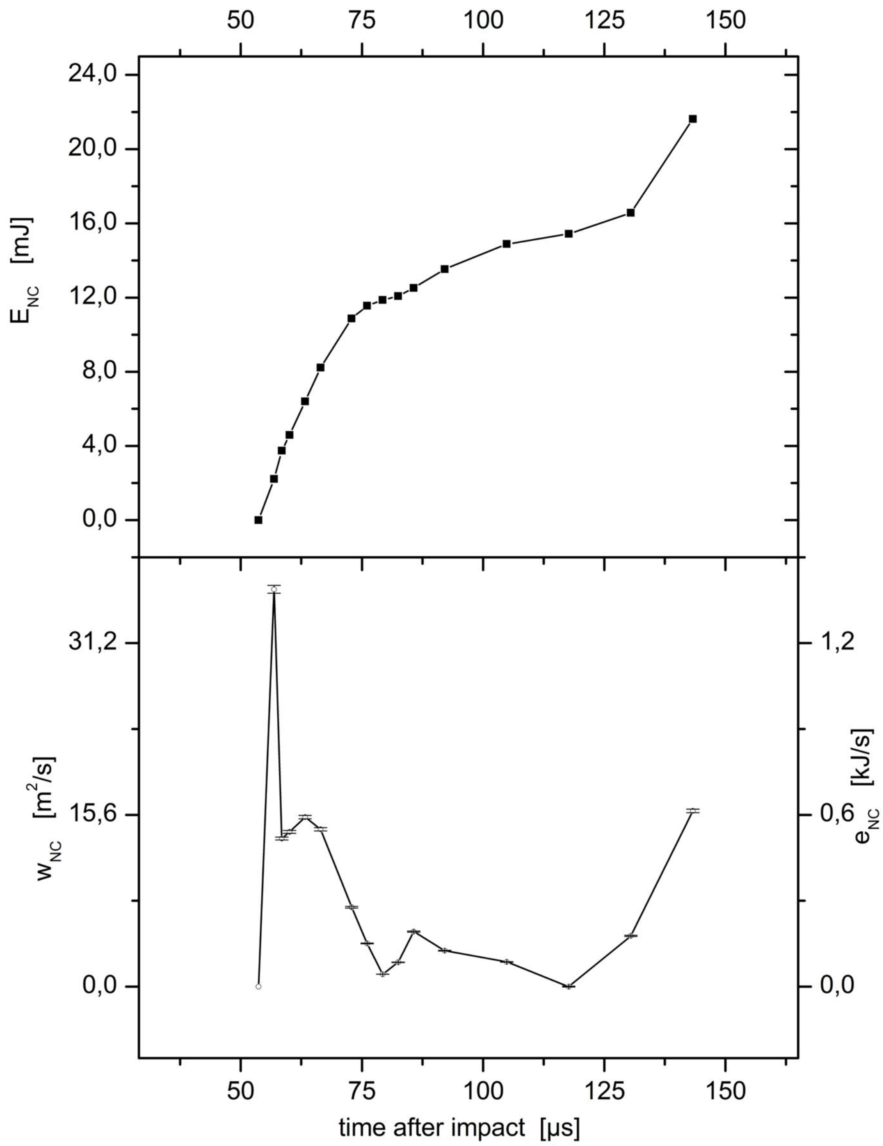

Fig. 105: Dynamic fracture energy dissipation profile of another impacted TK target, this time under a higher impact velocity ([V685], {624}, $v_H = 2{,}44\,\frac{\mathrm{m}}{\mathrm{s}}$, $\eta_{NC} = 38{,}49\,\frac{\mathrm{J}}{\mathrm{m}^2}$): In this case, the evolution of primary and secondary cracks are temporarily closer together. As a consequence, the resulting energy dissipation curve does not show such a pronounced "plateau" as in the case of Fig. 104.
Note that the amounts of energies dissipating into SCMs are always significantly lower than the fracture energies of any other primary crack type.

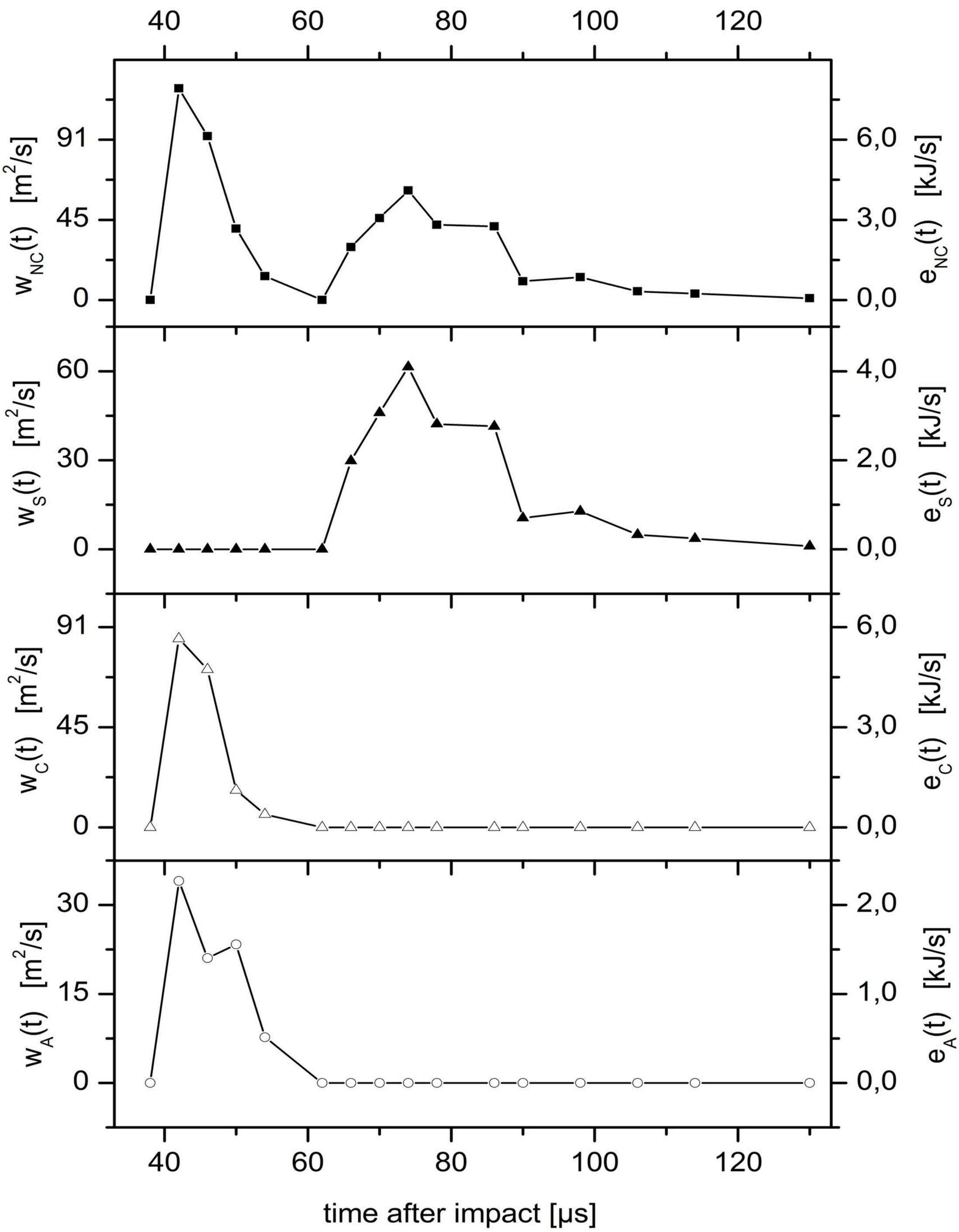

Fig. 106: Example, presenting the FAVs and energy rates of all crack types that have occured in a RX target ([V405], {106}, v_H = 1,82 $\frac{\text{m}}{\text{s}}$, η_{NC} = 66,13 $\frac{\text{J}}{\text{m}^2}$): In this case a combination of primary cracks (an ACB and a BCM) has been recorded. The energy dissipation rate of the BCM $e_C(t)$ shows considerably larger amounts than that of the simultaneously propagating ACB $e_A(t)$.
Furthermore, it is of interest that in RX the maximum values of the FAV $w_S(t)$ as well as the secondary crack energy rates $e_S(t)$ seem to be significantly higher, compared to those of the other targets. This phenomenon is also verified by the results of multivariate statistical analyses.

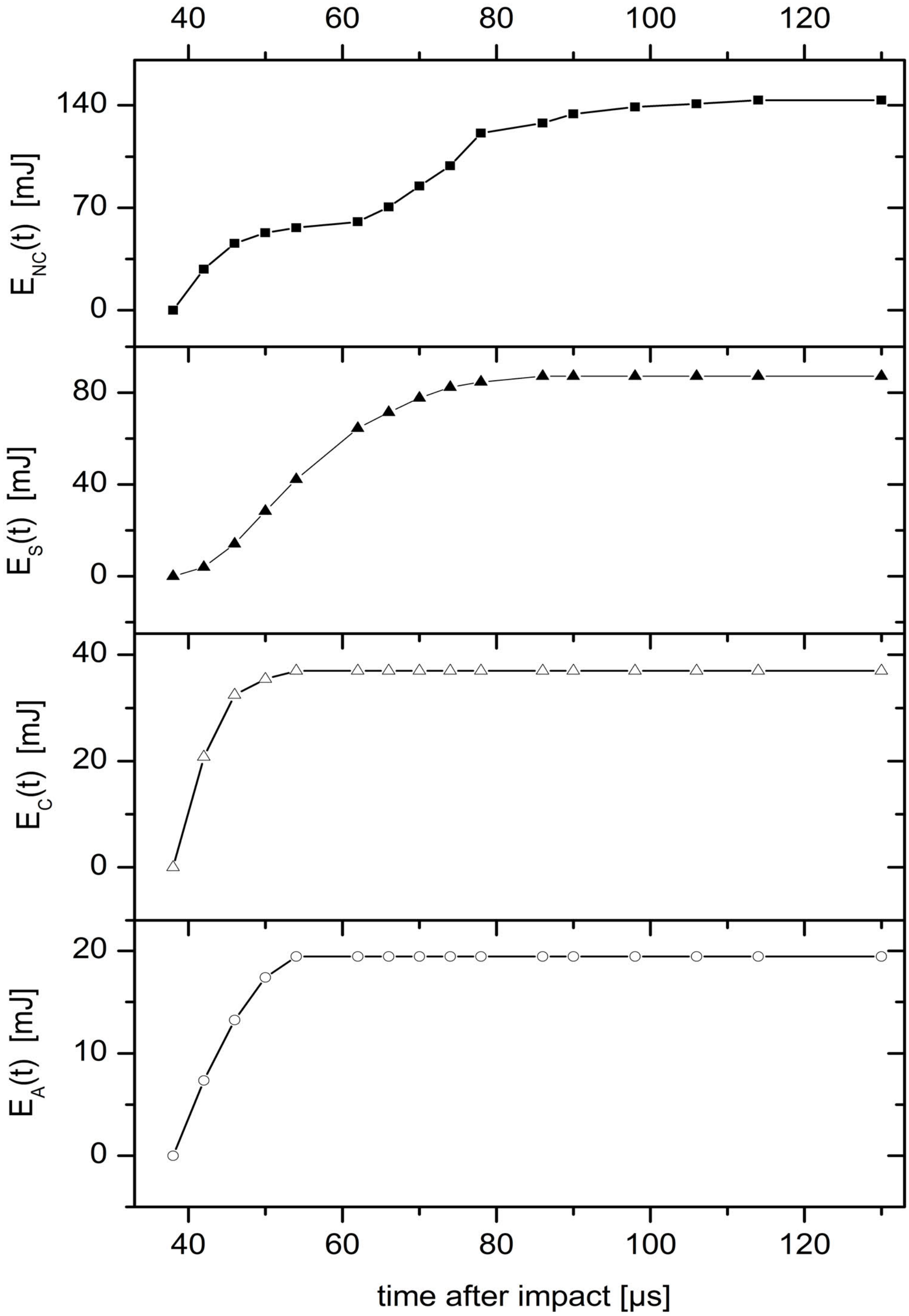

Fig. 107: Temporal development of the dissipating fracture energies during the fragmentation process in a RX target, corresponding to the example illustrated in Fig. 106 [V405].

9.6.2. Statistical Overview of the dynamic fracture parameters

Maximum Values

As mentioned in V.9.1.2, it is particularly useful to study the maximum values of the introduced dynamic fracture parameters:

Max($w(t)$) quantifies the peak value of generated fracture area per time and thus provides information about the maximum possible "speed of fragmentation" and the stability of fracture.

Max($e(t)$) is even more important - especially from the volcanological point of view. It specifies the highest possible rate of dissipating fracture energies within a target, and is hence a quantity which describes the maximum "power of fragmentation" by normal cracks within the studied material, a value that cannot be exceeded under the studied constraints.

Please note that for statistical analysis, care must be taken to use quantities on the basis of a comparable time scale.

In the case of the HIEs the maximum sample rate has been 2,5 MHz. Due to the dynamic instabilites of rapid cracks, however, it cannot be entirely ruled out that in shorter terms, the presented maximum values of $e(t)$ and $w(t)$ are exceeded.

Again, all results of multivariate statistics, which are referred to in this chapter, are presented in Appendix H.

Table 62 presents a statistical overview of the FAVs, detected for various normal crack types.

In general, the amounts of FAVs for primary cracks are significantly higher than those for secondary cracks. Note also that W-cracks - which virtually never show crack branching - are characterized by considerably less FAV peak values than centrical or A-cracks.

SI	Max($w_A(t)$) [m^2/s]	Max($w_C(t)$) [m^2/s]	Max($w_W(t)$) [m^2/s]	Max($w_S(t)$) [m^2/s]	Max($w_{NC}(t)$) [m^2/s]
minimum	8,5	9,3	3,5	4,4	3,6
maximum	244,9	177,6	107,4	91,6	262,4
mean	65,3	61,3	17,1	27,8	70,9
std. dev.	41,6	46,4	18,8	19,5	49,1

Table 62: Statistical synopsis of characteristic maximum FAV values: minimum, maximum and mean values as well as the standard deviations of the maximum FAV values are given.

The statistical values of the maximum energy dissipation rates are given in Table 63, in which also the corresponding sample rate is given. It is noteworthy that Max($e_A(t)$) and Max($e_{NC}(t)$) as well as Max($e_W(t)$) and Max($e_S(t)$) show their peak values for a comparable time resolution.

Mean Values and Medians

It has to be kept in mind that each image sequence individually describes the fracture process at a specific stage of fragmentation, and thus provides only a selective insight into the dynamic situation. This fact is quite inconvenient, due to the pronounced dynamic variations of $w(t)$ and $e(t)$.

Yet, their mean values have proven to be very useful complementary magnitudes, which give a quantitative impression of the rapidity of fragmentation and energy dissipation in an overloaded material.

Table 64 presents a synopsis of the statistical characteristics concerning the average FAVs, and Table 65 displays the statistical values of the energy dissipation rates.

	SI	$\text{Max}(e_A(t))$	$\text{Max}(e_C(t))$	$\text{Max}(e_W(t))$	$\text{Max}(e_S(t))$	$\text{Max}(e_{NC}(t))$
minimum	[J/s]	402	355	166	210	173
time res.	[µs]	10,0	6,4	10,0	10,0	20,0
HIE No.		[V231]	[V747]	[V225]	[V234]	[V228]
HIE config.		{301}	{634}	{101}	{301}	{301}
maximum	[J/s]	11344	11704	4980	5994	12155
time res.	[µs]	10,0	0,4	3,2	3,2	10,0
HIE No.		[V248]	[V415]	[V624]	[V809]	[V248]
HIE config.		{601}	{601}	{611}	{316}	{601}
mean	[J/s]	3231	3239	849	1383	3558
std. dev.	[J/s]	2026	3155	927	1055	2618

Table 63: Characteristic statistical values of maximum fracture energy dissipation rates: Additionally, also the configuration and the sample rate (time resolution) of the corresponding HIE is presented, in order to obtain an impression of the dependency of the time scale.

SI	$\bar{w}_A(t)$ [m²/s]	$\bar{w}_C(t)$ [m²/s]	$\bar{w}_W(t)$ [m²/s]	$\bar{w}_S(t)$ [m²/s]	$\bar{w}_{NC}(t)$ [m²/s]	$\widetilde{w}_{NC}(t)$ [m²/s]
minimum	4,9	6,4	1,4	1,8	2,4	1,3
maximum	131,2	115,4	19,0	60,0	86,9	74,13
mean	35,1	34,1	7,7	16,2	25,8	19,8
std. dev.	23,0	27,6	4,7	10,2	16,4	14,4

Table 64: Statistical overview of characteristic average fracture area velocities for various normal crack types: The minimum, maximum and mean values as well as the standard deviations of the average FAVs are given. Furthermore, the medians of the normal crack FAVs, $\widetilde{w}_{NC}(t)$ are presented.

Note that the statistical values for these magnitudes show very similar tendencies to those of the maximum values, presented in Table 62 and Table 63:

On average, $\bar{w}_A(t)$ is comparable to $\bar{w}_C(t)$ as well as $\text{Max}(w_A(t))$ being comparable to $\text{Max}(w_C(t))$, the corresponding values for secondary cracks are considerably lower, and W-cracks show the lowest values of all crack types.

For the energy dissipation rates, the average amount of $\bar{e}_C(t)$ is quite close to the mean value of $\bar{e}_A(t)$, but its standard deviation is considerably higher. The same characteristics can be observed for $\text{Max}(e_C(t))$ and $\text{Max}(e_A(t))$.

This large difference in their variations might explain, why the corresponding crack velocities of both crack types have proven to be significantly different (see above).

The corresponding medians show exactly the same tendencies. A list of their results for all crack types are presented in the corresponding folder of Appendix H.

SI	$\bar{e}_A(t)$ [J/s]	$\bar{e}_C(t)$ [J/s]	$\bar{e}_W(t)$ [J/s]	$\bar{e}_S(t)$ [J/s]	$\bar{e}_{NC}(t)$ [J/s]	$\widetilde{e}_{NC}(t)$ [J/s]
minimum	232	243	91	91	112	61,5
maximum	6077	7533	946	2795	4188	3898
mean	1736	1785	380	800	1285	987
std. dev.	1125	1791	242	511	856	761

Table 65: Characteristic statistical values of average fracture energy dissipation rates for various normal crack types: Additionally, the statistical results for $\widetilde{e}_{NC}(t)$ are listed.

Standard Deviations

As fluctuations play a decisive role during the process of energy dissipation, it is useful to analyze also the standard deviations of the dynamic fracture parameters, which allow to specify their degree of variation.

Table 66 presents a statistical summary of the characteristic values of FAVs. The corresponding values of the energy dissipation rates are given in Table 67.

SI	$\sigma(w_A(t))$ [m²/s]	$\sigma(w_C(t))$ [m²/s]	$\sigma(w_W(t))$ [m²/s]	$\sigma(w_S(t))$ [m²/s]	$\sigma(w_{NC}(t))$ [m²/s]
minimum	0,7	2,3	0,5	0,5	1,0
maximum	102,6	67,6	39,1	30,4	91,0
mean	25,1	24,1	6,1	9,7	22,7
std. dev.	19,1	18,2	7,0	7,2	17,1

Table 66: Characteristic statistical values concerning the standard deviations of fracture area velocities for various crack types: The minimum, maximum and mean values as well as the standard deviations are presented.

It is evident that the presented statistical magnitudes show similar tendencies as pointed out for the respective mean and maximum values.

SI	$\sigma(e_A(t))$ [J/s]	$\sigma(e_C(t))$ [J/s]	$\sigma(e_W(t))$ [J/s]	$\sigma(e_S(t))$ [J/s]	$\sigma(e_{NC}(t))$ [J/s]
minimum	31	87	22	21	49
maximum	4752	4412	1811	1866	4216
mean	1228	1280	302	484	1137
std. dev.	906	1191	340	387	892

Table 67: Characteristic statistical values concerning the standard deviations of the fracture energy dissipation rates for various normal crack types.

In conclusion, all results indicate that the studied statistical magnitudes of the fracture parameters are correlated with a high significance:

Fractures, which evolve at higher average energy dissipation rates are characterized by larger variations and by higher peak values.

This finding is also coherent with the results of linear correalation analyses: In the case of RX, for example the Pearson's correlation coefficient ρ between $\mathrm{Max}(w_{NC}(t))$ and $\sigma(e_{NC}(t))$ amounts to 0,979 with an error probability of $p < 0{,}05\,\%$.

9.6.3. Influence of the Impact Velocity

The presented peak values for $\mathrm{Max}(e_A(t))$, $\mathrm{Max}(e_W(t))$ and $\mathrm{Max}(e_{NC}(t))$ in Tab. 63 indicate that there might be a general dependency on the impact velocity.

This conjecture is confirmed by many highly significant results of linear correlation analyses: The resulting statistical parameters concerning A- and W-cracks as well as $w_{NC}(t)$ and $e_{NC}(t)$ have been verified to be linearly correlated by high significance with v_H, particularly in FG and T5, but also in some cases for T10 and RX targets.

It is of interest that only the primary cracks, which are located within the PSZ, are affected by v_H.

In this respect, it is especially insightful to compare FG with T5 (see Table 68):

	$\sigma(e_A(t))$		$\sigma(e_W(t))$		$\sigma(e_{NC}(t))$	
	ρ	p	ρ	p	ρ	p
FG	0,476	0,5 %	0,444	3,4 %	0,364	1,5 %
T5	0,769	0,9 %	(-)	(-)	0,735	1,0 %

Table 68: Results of linear correlation analyses, testing the influence of v_H on $\sigma(e_A(t))$, $\sigma(e_W(t))$ and $\sigma(e_{NC}(t))$ for FG and T5 targets: The Pearson's correlation coefficients ρ are presented as well as the corresponding error probabilities p. Note that A-cracks in T5 targets are characterized by distinctly higher values of ρ. This might indicate that the stress intensity within the PSZ significantly affects the dependency of the impact velocity.
These results are coherent with the findings of the corresponding crack velocities (cf. Table 59).
("(-)" indicates that the sample size has been too small for reliable results.)

As pointed out before, the shapes and locations of the PSZ are identical in both target types, but it can be presumed that within the PSZ of T5 targets, distinctly higher stress intensities occur right before and while primary cracks are propagating.

Hence the following conclusions can be drawn:

It is evident that the dynamic fracture parameters depend on the stress intensities.

This correlation clearly becomes especially significant within the PSZ, which is the zone of "directed stresses".

A strong anisotropy (effected by high amplitudes of directed pre-stresses within the PSZ) increases the dependency of v_H and thus the influence of the loading stress situation, an effect which is coherent with the findings of V.9.5.2.

In contrast, for example BCMs and secondary cracks are not significantly affected by v_H as they propagate over long periods outside the PSZ.

Considering the dual concept of directed and fluctuating stress (see II. 3.3), one can conclude that these crack types are mainly driven by the latter stress components.

W-cracks can be seen as a special case, as they start their evolution within the PSZ (see e.g. Fig. 43), but then they leave the regions of directed stresses. Hence these cracks change their behavior during propagation, which explains why many W-cracks are characterized by crack arrests: They often stop halfway and remain "uncompleted" (see e.g. Fig. 91).

9.6.4. Influence of the Hammer Geometry

Comprehensive multivariate statistical analyses have revealed no systematic significant correlations between the statistical values of the dynamic fracture parameters and the hammer geometry.

Thus it can be concluded that - within the studied scope - the hammer geometry has no effect on the energetic dissipation dynamics of evolving normal cracks.

9.6.5. The Local Stress Anisotropy Effect

Table 69 shows the target-specific maximum values of FAVs and energy dissipation rates for various crack types.

It is evident that there is a distinct dependency between the studied magnitudes and the material properties, which include not only the respective values of c_T and η_{NC}, but also the geometries of the corresponding pre-stressed zones.

The depicted tendencies are representative for all characteristic values for the dynamic fracture parameters $w(t)$ and $e(t)$, which are presented in detail in Appendix H.

	SI	FG	T5	T10	TK	RX
$\overline{\text{Max}}\,(w_A(t))$	[m²/s]	70,0	55,3	82,6		45,6
$\overline{\text{Max}}\,(w_C(t))$	[m²/s]	63,7	74,0		25,3	126,0
$\overline{\text{Max}}\,(w_W(t))$	[m²/s]	16,2	24,9	12,4		19,1
$\overline{\text{Max}}\,(w_S(t))$	[m²/s]	32,6	19,4	25,5	15,4	26,7
$\overline{\text{Max}}\,(w_{NC}(t))$	[m²/s]	77,0	61,1	83,5	27,0	77,2
$\overline{\text{Max}}\,(e_A(t))$	[kJ/s]	3,30	2,39	4,30		3,00
$\overline{\text{Max}}\,(e_C(t))$	[kJ/s]	2,98	3,18		0,96	8,27
$\overline{\text{Max}}\,(e_W(t))$	[kJ/s]	0,76	1,07	0,65		1,25
$\overline{\text{Max}}\,(e_S(t))$	[kJ/s]	1,53	0,84	1,33	0,59	1,75
$\overline{\text{Max}}\,(e_{NC}(t))$	[kJ/s]	3,62	2,63	4,35	1,03	5,07

Table 69: Material-specific results of the average maximum FAV values and the energy densities for various crack types: The corresponding standard deviations as well as further characteristic results of the dynamic fracture parameters can be found in the corresponding folder of Appendix H.

The following aspects are particularly notable and will finally lead us to a fundamental principle concerning the nature of fracture energy dissipation:

- The lowest values for primary cracks are detected for TK targets, which are characterized by non-branching SCMs.
- On average, the highest peak values of energy dissipation rates $e_{NC}(t)$ have been detected for RX targets. It is notable that this is solely the consequence of the significantly higher amount of η_{NC} for RX, as those targets are characterized by very similar FAVs to those of FG.
- T10 targets also show very high average peak values of $e_{NC}(t)$. The empirical range of the maximum energy dissipation rate has been remarkably large with values between $0,91\,\frac{\text{kJ}}{\text{s}}$ and $8,78\,\frac{\text{kJ}}{\text{s}}$.
- In FG and T5 targets, the variations of $w(t)$ and $e(t)$ for A- and centrical cracks are too large to prove significant differences between both crack-types.
- Yet, in RX targets, there is evidently a highly significant difference between the energy dissipation rates of A-cracks and those of centrical cracks.
  This finding is coherent with the results for the corresponding crack velocities mentioned in V.9.5.3.
  Thus, it is evident that in RX targets the high gradients of locally directed stresses within the PSZ distinctly affect the stability, the dynamics as well as the energy dissipation rates of fractures.
- It is remarkable that the consequences of the local anisotropies on the resulting dynamic fracture parameters are so pronounced that the amounts of $w_A(t)$ and $e_A(t)$ in RX targets are even lower than the corresponding values of FG. This is although they are made up of (in comparison to the latter samples characterized by clearly higher c_T) distinctly higher amounts of maximum crack tip velocities $\overline{\text{Max}}\,(u(t))$ and considerably higher values for η_{NC}, as outlined in the sections before.
- These findings indicate that there is a significant correlation between the local anisotropy of the directed stress field in which a crack is developing, its evolution stability and its

resulting dynamic energy dissipation behavior.
This crucial principle is referred to as "the local stress anisotropy effect".

- In this regard, it is again very useful to compare target types with similar material properties but different PSZ:
  As pointed out above it can be presumed that in T5 samples the local stress anisotropy within the PSZ is distinctly higher than that in FG targets.
  In contrast, T10 targets are characterized by a widened PSZ, where the inflicted stress is partly deflected from the zone of A-cracks (see V.3.5).
  If the described effect of local anisotropies in RX targets is a transfereable fundamental principle for amorphous silicate materials, it can be expected that the amounts of FAVs and energy dissipation rates of A-cracks will be lower in T5 targets than in FG targets, and clearly higher in T10 targets.
  According to this principal, the assumed order can be formally expressed by:
  $$[w_A(t)]_{T5} < [w_A(t)]_{FG} < [w_A(t)]_{T10} \tag{V.9-17}$$
  and
  $$[e_A(t)]_{T5} < [e_A(t)]_{FG} < [e_A(t)]_{T10} \tag{V.9-18}$$
  In fact, these presumptions have been empirically confirmed without exception (see Table 69 and Appendix H) by all statistical results for $w(t)$ and $e(t)$: The average A-crack fracture energy dissipation rate $\overline{e_A(t)}$, for example, is $1,05\,\frac{\mathrm{kJ}}{\mathrm{s}}$ for T5, $1,84\,\frac{\mathrm{kJ}}{\mathrm{s}}$ for FG and $2,43\,\frac{\mathrm{kJ}}{\mathrm{s}}$ for T10 targets.
- Also the dispersion parameters show the same behavior: For example $\sigma\,(e_A(t))$ is $0,86\,\frac{\mathrm{kJ}}{\mathrm{s}}$ for T5, $1,39\,\frac{\mathrm{kJ}}{\mathrm{s}}$ for FG and $1,46\,\frac{\mathrm{kJ}}{\mathrm{s}}$ for T10.
- The statistical parameters of $w_{NC}(t)$ and $e_{NC}(t)$ are affected by the local anisotropy effect in a very similar way.
- It is evident that cracks, which partially or completely propagate *outside* the PSZ, are *not* affected by the anisotropy principle.
  This is well consistent with the findings for the dynamic fracture parameters of W-cracks and centrical cracks.
- Important exceptions are the above mentioned results for TK targets: Following the principle of local stress anisotropies and considering the conclusions of chapter V.3.6 concerning their specific PSZ geometries, it is evident that in those targets the *centrical cracks* run in a zone of considerable high directed stress gradients.
  Now it can be explained, why those specific crack types (SCMs) are significantly different to the "usual" centrical cracks (BCMs): Evidently, the resulting stress-field gradient in the center of a TK sample causes a much more stable crack evolution. As a consequence, the resulting characteristic values of $w_C(t)$ an $e_C(t)$ are considerably lower.

Conclusions

It is a well known fact that the dynamic evolution of a crack becomes increasingly unstable at higher propagation velocities (see II.1.3.6).
According to my findings, this interrelationship can also be inverted:

By ensuring a high local stress gradient within the primary fracture zone, it is possible to "channel" and to stabilize the evolving crack, which consequently reduces the corresponding fracture area velocities $w(t)$ and energy dissipation rates $e(t)$.

Thus, for the dynamics of energy dissipation in float glasses, it can generally be stated:

$$[e_C(t)]_{TK} < [e_A(t)]_{T5} < [e_A(t)]_{FG} < [e_A(t)]_{T10} \tag{V.9-19}$$

As verified for Robax glass ceramics, a nanocrystalline structure seems to significantly enhance the local stress anisotropy effect.

10. All Influences on Fracture Dynamics in a Nutshell

In summary, all findings gained so far are illustrated in two float charts:

Fig. 108 presents the three stages of damage crack energy dissipation (into impact notch, shock waves and visible damage cracks) plus their dynamic correlations and dependencies.

The newly introduced and quantified FSED parameter η_{DC} specifies the complete process of fracture energy dissipation into damage cracks. It includes all relevant fracture mechanical parameters and properties (e.g. the specific speed of shear waves c_T, the Young's modulus E, the mass density ϱ, the fracture toughness K_{Ic} etc.) of the respective material, as well as the locations and intensities of existing pre-stresses.

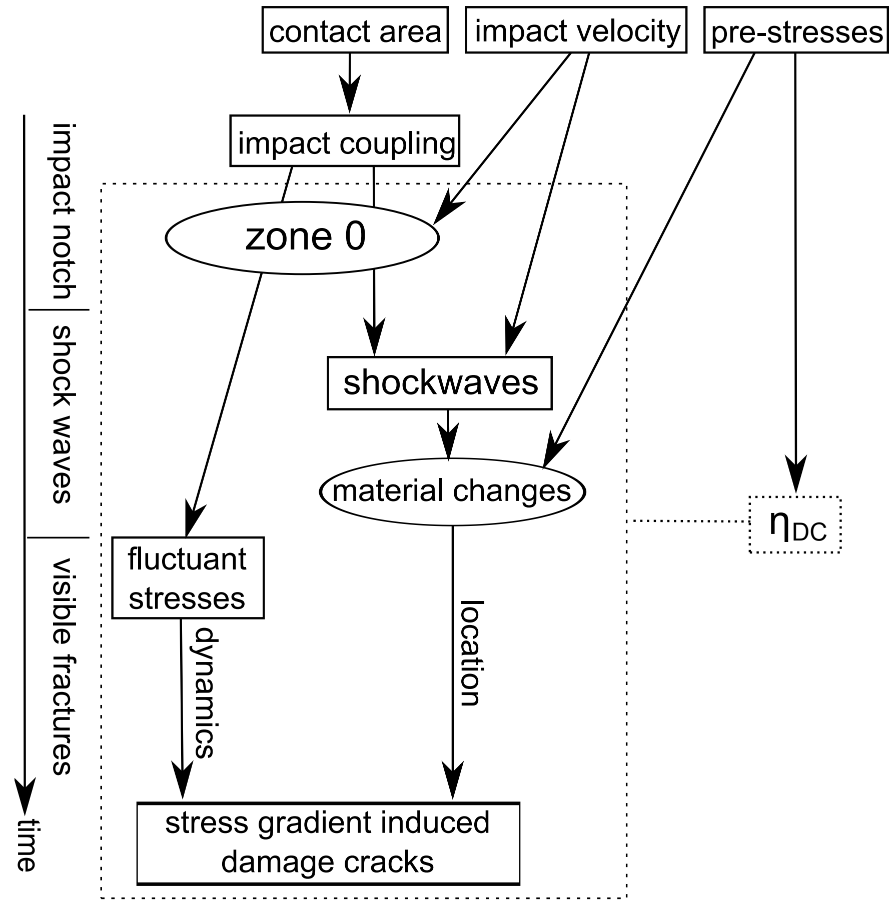

Fig. 108: Float chart describing the correlations and dependencies of energy dissipation processes, which finally result in damage cracks: Please note that all relevant material properties are implied in the essential FSED parameter η_{DC}, which allows to specify the complete process of fracture energy dissipation into damage cracks.

Fig. 109 illustrates the correlations and interdependencies which control the energy dissipation processes of propagating normal cracks.

Evidently no time-line can be displayed in this diagram, due to the complex interactions between the influencing factors (characterized by double-arrows).

All fracture mechanical parameters and material properties relevant for normal crack evolution are specified by the normal crack-specific FSED parameter η_{NC}.

Please note that (within the studied scope) η_{NC} has been verified to be a global, i.e. location-independent, material parameter, which is completely decoupled from the amplitudes of fluctuating stress waves. This fact allows to determine the exact amount of $e(t)$ at any time t.

Finally it is important to keep in mind that the two types of energy dissipation processes are interlocked, as they both depend fundamentally on the dynamics of fluctuating stress waves.

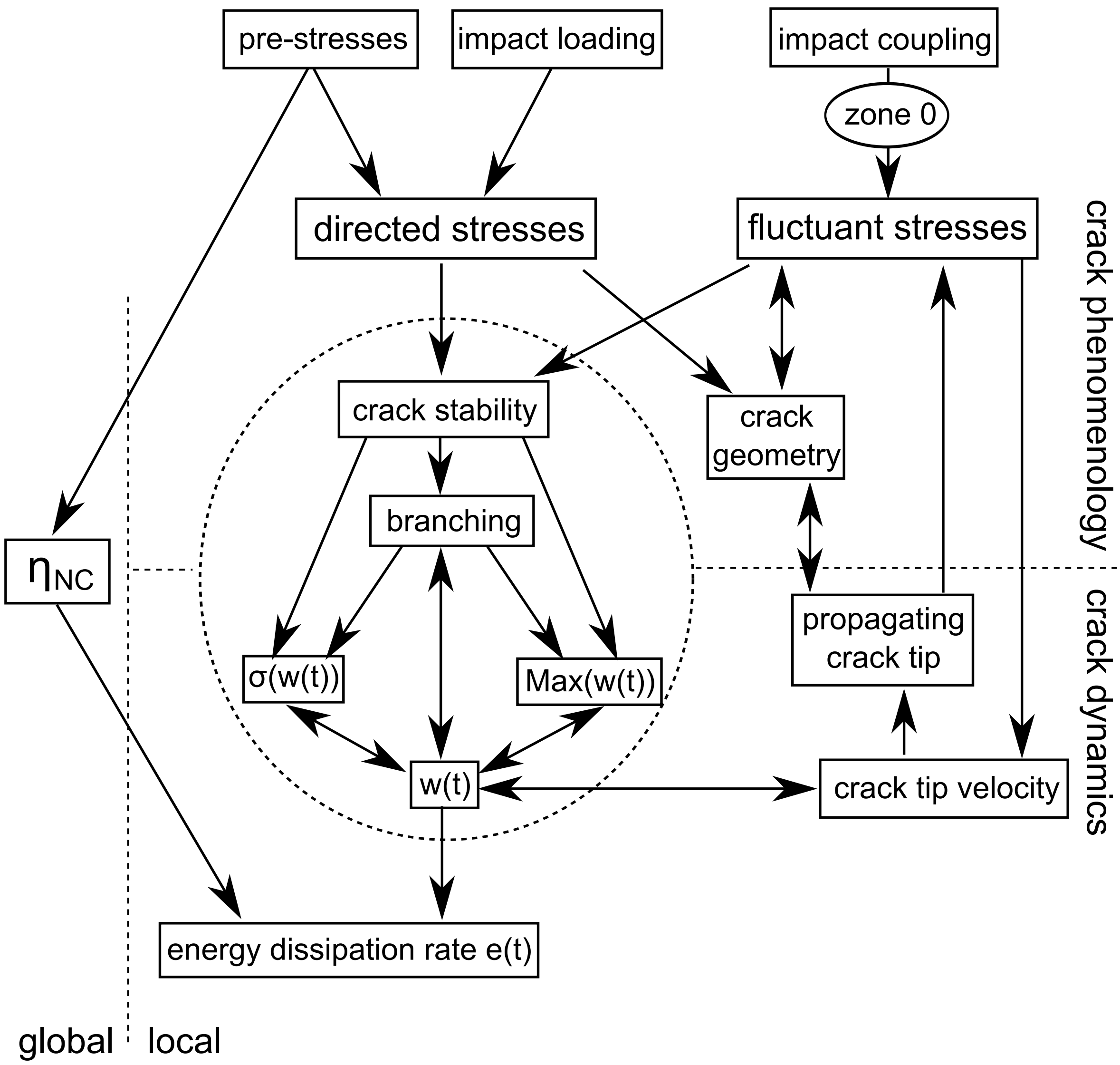

Fig. 109: Schematic diagram of correlations and interdependencies, which control the dynamics of normal cracks: This model is based on the considerably enhanced “dual” approach of directed and fluctuating stress waves, my emprical findings and the linear crack-specific FSED concept. All relevant material properties are included in η_{NC}, which has proven to be a location-independent parameter. The dynamic process of fracture area generation is marked by a dotted circle. It controls the amount of dissipating fracture energy per time $e(t)$.

Part VI.

Volcanological Implementation of the Findings

1. Comparative Particle Analysis

1.1. General Remarks

The results of the energy balances let assume that HIE fragmentation processes within the studied glass targets are similar to those of MFCI processes (see Table 38 in chapter V.6.6.1).

Furthermore, there is another elegant way to win information about the comparability of the respective fracture mechanisms:

As the resulting fragments can be seen as "eye-witnesses" of their specific generation processes [15, 32], it is useful to conduct comparative analyses between the shape of HIE fragments and experimental volcanic ash particles produced under controlled conditions on the one side, as well as natural volcanic ash particles on the other side.

Again, image particle analysis (IPA) has been used (cf. [15, 32, 140], see also V.4.3) as a meaningful tool which allows quantitative comparisons in particle shape.

The basic idea behind this procedure is that fragments of significantly similar shapes indicate a genesis by comparable fragmentation mechanisms.

Thus, it is finally possible to determine under which volcanic conditions as well as which magmatic materials the presented HIE results can be transferred to. That way, completing the chain of proof for a specific magmatic melt allows to obtain new insights in the crucial but otherwise inaccessible mechanisms of fracture dynamics in this material, at the decisive moment of failure.

1.2. Studied Reference Materials

All resulting particles have been analyzed under the SEM in the Departement of Geomineralogy, at Bari University, Italy.

1.2.1. HIE Particles

IPA has been comprehensively conducted for three different types of HIE fragments (see also V.5.4.3):

- FG particles
- Fragments of T10 samples
- RX particles

1.2.2. Natural Volcanic Ash Particles

In volcanology the term "volcanic ash" subsumes fragmented pyroclastic particles less than 2 mm in size [2, 117].

All described comparative analyses with volcanic reference materials are based on IPA results of natural and experimental volcanic ash particles, which have been gathered and kindly allocated by Dr. Daniela Mele[1].

[1] Dr. Daniela Mele, Dipartimento Geomineralogico, Università degli Studi di Bari, Italy

In this thesis, two different types of natural volcanic fragments have been compared to the HIE particles (only glass particles have been selected):

- Basaltic ash particles from the Grimsvötn eruption 2004, Iceland. Detailed background information on this representative MORB (mid ocean ridge basalt) material are presented in [4, 28]. In this thesis, Grimsvötn material is referred to as "Grim", the natural Grimsvötn ash particles are denoted "Grim nat".
- Rhyolitic ash particles from Tepexitl Tuff ring, Mexico (cf. [5, 6]). Particles originating from this material are abbreviated as "Tep", the natural Tepexitl ash particles are referred to as "Tep nat".

	SiO_2 [wt. %]	TiO_2 [wt. %]	Al_2O_3 [wt. %]	Fe_2O_3/FeO [wt. %]	MnO [wt. %]
Grim nat	48,25	2,60	14,00	12,04	0,12
Tep nat	74,11	0,02	13,76	1,28	0,04

	MgO [wt. %]	CaO [wt. %]	Na_2O [wt. %]	K_2O [wt. %]	P_2O_5 [wt. %]
Grim nat	7,80	8,94	5,94	0,32	$<$0,01
Tep nat	0,17	0,72	4,37	4,21	0,06

Table 70: Major elements of Grimsvötn (2004) melt (according to non standardized EDX, performed by Prof. Pierfrancesco Dellino, University of Bari) referred to as "Grim nat". Additionally the main chemical composition of Tepexitl obsidian material ("Tep nat") is presented (data from [5]).

1.2.3. Experimental Volcanic Ash Particles

In representative experiments, which had been performed in the Physikalisch Vulkanologisches Labor, University of Würzburg, these natural magmatic materials had been melted and exposed to various controlled conditions, which has resulted in fragmentation and thus in the generation of ash particles.

For the comparative particle analyses, fragments gathered from three different types of experiments have been used:

Thermal Granulation:

The magmatic melt is poured into a water basin [6]. As a result, due to thermal stresses, the melt fragments. The resulting particles are denoted "therm":

- For the HIE comparison studies, thermal granular Tepexitl particles have been used and are referred to as "Tep therm".
- Furthermore experimental thermal granular Grimsvötn ash particles have been analyzed, denoted "Grim therm".

Blowout Experiments:

The melt is fragmented under quasi isothermal conditions by an injected high pressurized air volume [16, 98, 138]. Particles which result from these type of experiments are denoted "blow". The following types of experimental fragments are compared to HIE particles:

- Experimental Grimsvötn (2004) blowout ash particles [4, 28], denoted "Grim blow".
- Fragments from two Tepexitl blowout experiments [6], referred to as "Tep blow 1" and "Tep blow 2".
- The latter particles are also studied as a cumulated data set as "Tep blow tot", in order to increase the sample size.

MFCI experiments:

In these important thermohydraulic fragmentation experiments, which are already described in part I, water is involved and phreatomagmatic explosions occur [17, 18, 19, 50, 138]. The resulting fragments are referred to as "MFCI". The following MFCI particles have been used for comparative analyses:

- Experimental Grimsvötn (2004) MFCI particles [4], which are denoted "Grim MFCI".
- Experimental Tepexitl MFCI ash particles [6], referred to as "Tep MFCI".

1.3. Applied Statistical Methods

By comparing the corresponding IPA parameters of the particles (elongation *elo*, rectangularity *rec*, compactness *com* and circularity *cir*, see III.4.3), it is possible to find out significant differences and similarities.

Therefore, as a well established tool [15], t-tests have been applied.

If, in the case of two subsets, none of the four average parameters show significant differences, it can be seen as a strong indication that the compared sets of particles are "similar".

For these cases also equivalence tests (ETs) have been performed in order to substantiate these findings statistically, as pointed out in III.6.

The applied values for the maximal difference range D are presented in Table 71. Furthermore, an error probability p of 0,05 has been chosen for all ETs.

	rec	*com*	*elo*	*cir*
D	0,70	0,10	0,90	0,90

Table 71: Difference range values D used for the equivalence tests.

1.4. Analyzed Grain-Size Spectra

By regarding the grain size of the studied natural and experimental particles it has to be considered that coarser volcanic fragments are affected by post-eruptive thermal fractures as well as by transportation, deposition and erosion processes [15].

In order to avoid the influences of these *secondary fragmentation mechanisms*, it is sensible to use rather fine particles of the fractions $3 \leq \phi \leq 5$ for comparative analyses.

HIE fragmentation processes, however, run under isothermal conditions. Thus, HIE fragments are not affected at all by thermal fractures. As a matter of fact, secondary fracture processes can be neglected for these particles.

As self-similarity of HIE fragments is verified (see V.5.4.3) and in order to meet the requirements for t-tests (i.e. selection at random, drawn from a normally distributed population, see III.6), samples of the fractions $0 \leq \phi \leq 2$ have been used for comparison, which include the bulk of all particles.

1.5. The Subpopulation Problem

Yet, one aggravating aspect has still to be considered:

As pointed out in V.5.4.3, HIE particles can be subdivided in different subpopulation classes.

In particular, the presence of subpopulation B class particles which are most probably produced under very anisotropic stress conditions, are a major problem for comparative IPA studies, for two reasons:

- First of all, due to their elongated, acicular shape these kind of fragments are very vulnerable towards secondary fragmentation mechanisms. This fact becomes significantly relevant for natural and experimental volcanic ash particles: Even if subpopulation B class particles are originally generated, these type of fragments cannot be detected at later stages, as they have altered in the meantime by quenching, transportation and erosion processes.

- Furthermore, one observes large stochastical variations, due to erratic effects: In principal, it is sufficient to study small amounts of samples by means of IPA to achieve significant and representative results [32]. However, in the case of low sample sizes a single B-class particle drawn at random could totally distort the average elongation value.

In order to avoid these undesirable effects, it is more beneficial to analyze homogenized data sets. This is done by omitting the data of all identified class B and class C particles. Thus for comparative particle analyses only class A particles are taken into account.

2. Results of Comparative IPA Studies

Representative examples of the studied HIE fragments are depicted in Fig. 110, as well as in Fig. 74, Fig. 75 and Fig. 76.

Representative natural and experimental Grimsvötn (2004) particles are presented in Fig. 111.

The resulting particles of a blowout experiment using a basaltic Grimsvötn melt of comparatively low viscosity are characterized by elongated or spherical, bulbous shapes, which are typical for ductile fragmentation mechanisms. Evidently, these particles are completely different to any HIE fragments, so the corresponding data set can be ruled out for further studies.

Grimsvötn particles gathered from thermal granulation experiments are characterized by a platy, smooth surface and angular contour. In contrast, the "active" MFCI particles (i.e. ash particles which are produced in the thermohydraulic phase [15]) are blocky and angular, with irregular contours and stepped surfaces.

Representative examples of ash particles originating from rhyolitic Tepexitl melts are illustrated in Fig. 112. Those melts are highly viscous [6], and all blow out ash particles are evidently generated by brittle fragmentation mechanisms. Note that in some of these particles, vesicles are visible.

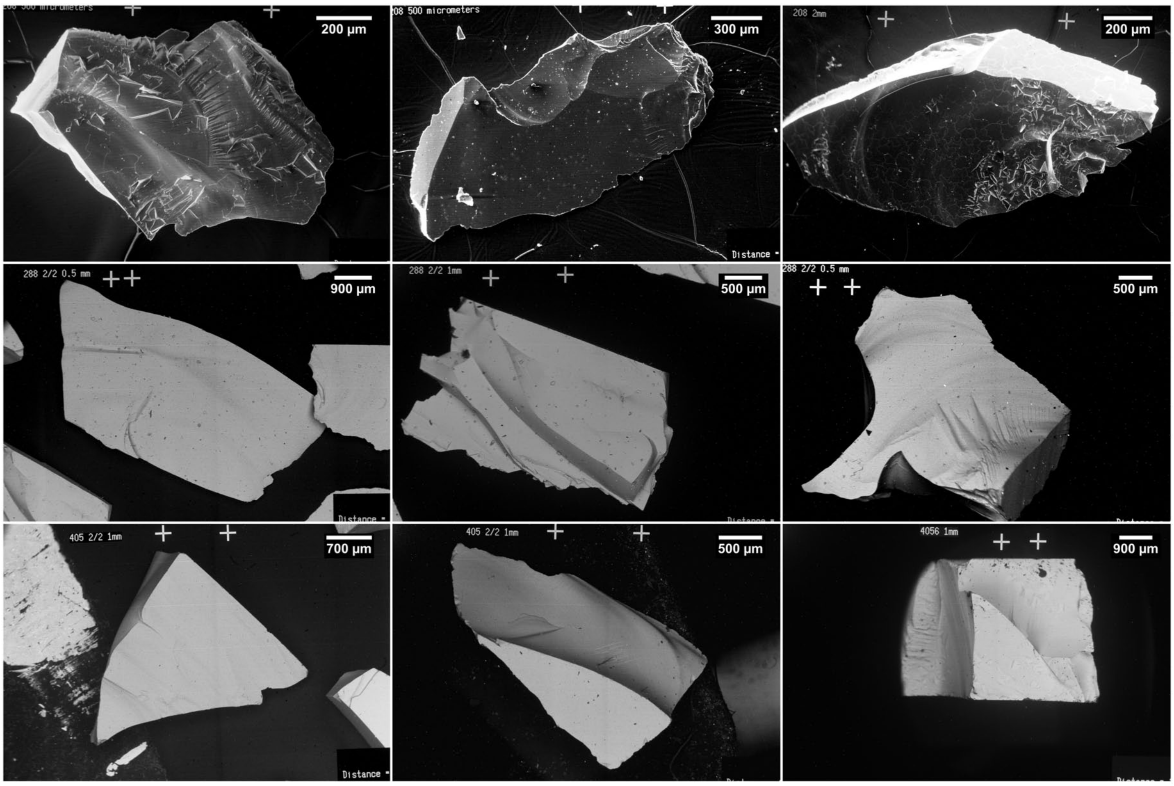

Fig. 110: HIE particles: Line by line, representative SEM images of the following fragments are presented: FG (top row, SE images, see also Fig. 74), T10 (center row, BSE images, further particles are presented in Fig. 75) and RX (bottom row, BSE images, cf. Fig. 76).

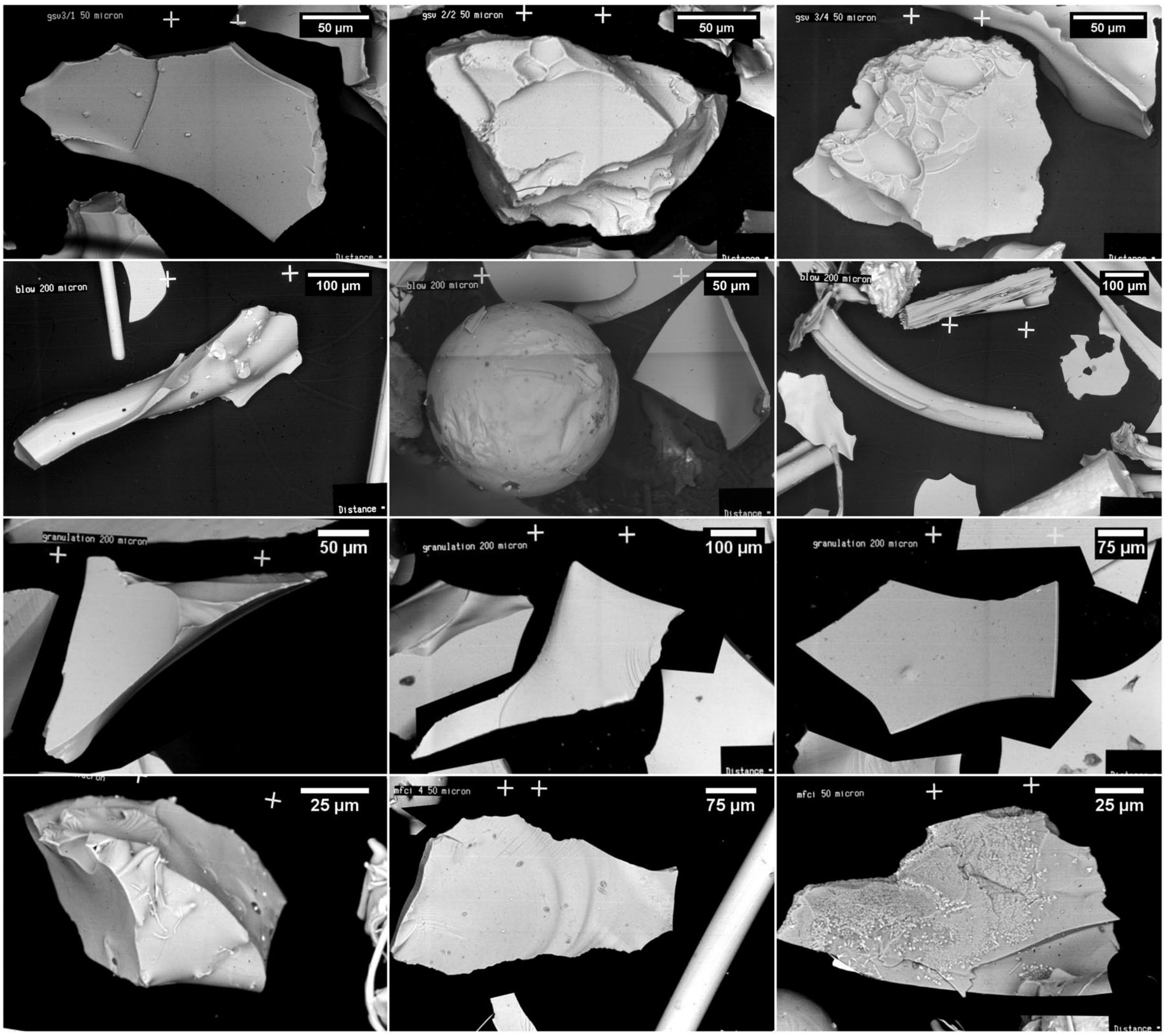

Fig. 111: Grimsvötn (2004) particles: From top to bottom, representative SEM (BSE) images of the following ash particles are presented line by line: Grim nat (top row), Grim blow (second row), Grim therm (third row) and Grim MFCI (bottom row). These SEM images have been kindly provided by Prof. Dellino and Dr. Mele, University of Bari.

The results of the comparative t-tests with FG fragments are given in Table 72, in which the error probabilities for rejecting the null hypothesis of equal mean values are presented. Thus, a low value signals that it is very likely that both data sets are different in this parameter. Using the 5%- level for significance, all results which show "significant" differences are highlighted in gray.

Table 73 provides the t-test results for HIE particles originating from T10 targets, and the results of comparative t-tests with RX fragments are presented in Table 74.

Finally, the results of t-tests for natural Tepexitl ash particles are presented in Table 75. Note that all results as well as the complete list of the studied data sets can be found in the corresponding folder of Appendix H.

T-test with FG	Rect	Comp	Elon	Circ
T10	0,948	0,541	0,077	0,803
RX	0,655	0,147	0,020	0,457
Grim MFCI	0,221	0,108	0,501	0,223
Grim therm	0,023 (s)	0,003	0,001 (s)	0,184
Grim nat	0,123	0,663	0,016	0,204
Tep nat	0,032	0,845	0,081	0,082
Tep MFCI	$<0{,}0005$	0,518	0,683	0,001
Tep therm	0,001	0,018	0,007	$<0{,}0005$
Tep blow 1	0,200	0,987	0,080	0,295
Tep blow 2	0,153	0,426	0,849	0,150
Tep blow tot	0,120	0,641	0,295	0,161

Table 72: Results of t-test, using the average IPA parameters of FG fragments as the reference data set: The presented values denote the according significances p. An average IPA parameter of a data set is proven to be "significantly different" to that of FG fragments, if p drops below 5 %. These values are highlighted in gray. Results of separate variance t-tests (see III.6) are marked by "(s)".

T-test with T10	Rect	Comp	Elon	Circ
FG	0,948	0,541	0,077	0,803
RX	0,724	0,061	0,002	0,400
Grim MFCI	0,310	0,023	0,097	0,163
Grim therm	0,017	0,001	$<0{,}0005$ (s)	0,363
Grim nat	0,213	0,221	0,892	0,127
Tep nat	0,096	0,612 (s)	0,886	0,057
Tep MFCI	0,003	0,277	0,278	0,001
Tep therm	0,003	0,011	0,001	$<0{,}0005$
Tep blow 1	0,288	0,0472	0,931	0,237
Tep blow 2	0,248	0,215	0,132	0,127
Tep blow tot	0,185	0,228	0,372	0,125

Table 73: T-test results, using the average IPA parameters of T10 fragments as the reference data set: The presented values denote the according significances p. Values, which indicate a significant difference are highlighted in gray. Results of separate variance t-tests are marked by "(s)".

T-test with RX	Rect	Comp	Elon	Circ
FG	0,655	0,147	0,020	0,457
T10	0,724	0,061	0,002	0,400
Grim MFCI	0,757	0,581	0,027	0,290
Grim therm	0,241 (s)	0,204	0,285	0,340 (s)
Grim nat	0,709	0,103	0,007 (s)	0,872 (s)
Tep nat	0,458	0,045	0,004	0,858
Tep MFCI	0,075	0,443	0,028 (s)	0,153
Tep therm	0,069	0,123	0,547	0,052
Tep blow 1	0,668	0,048	0,002	0,989
Tep blow 2	0,614	0,564	0,109	0,758
Tep blow tot	0,561	0,116	0,003	0,858

Table 74: T-test results, using the average IPA parameters of RX fragments as reference data set: The presented values denote the according significances p. Values, which indicate a significant difference are highlighted in gray. Results of separate variance t-tests are marked by "(s)".

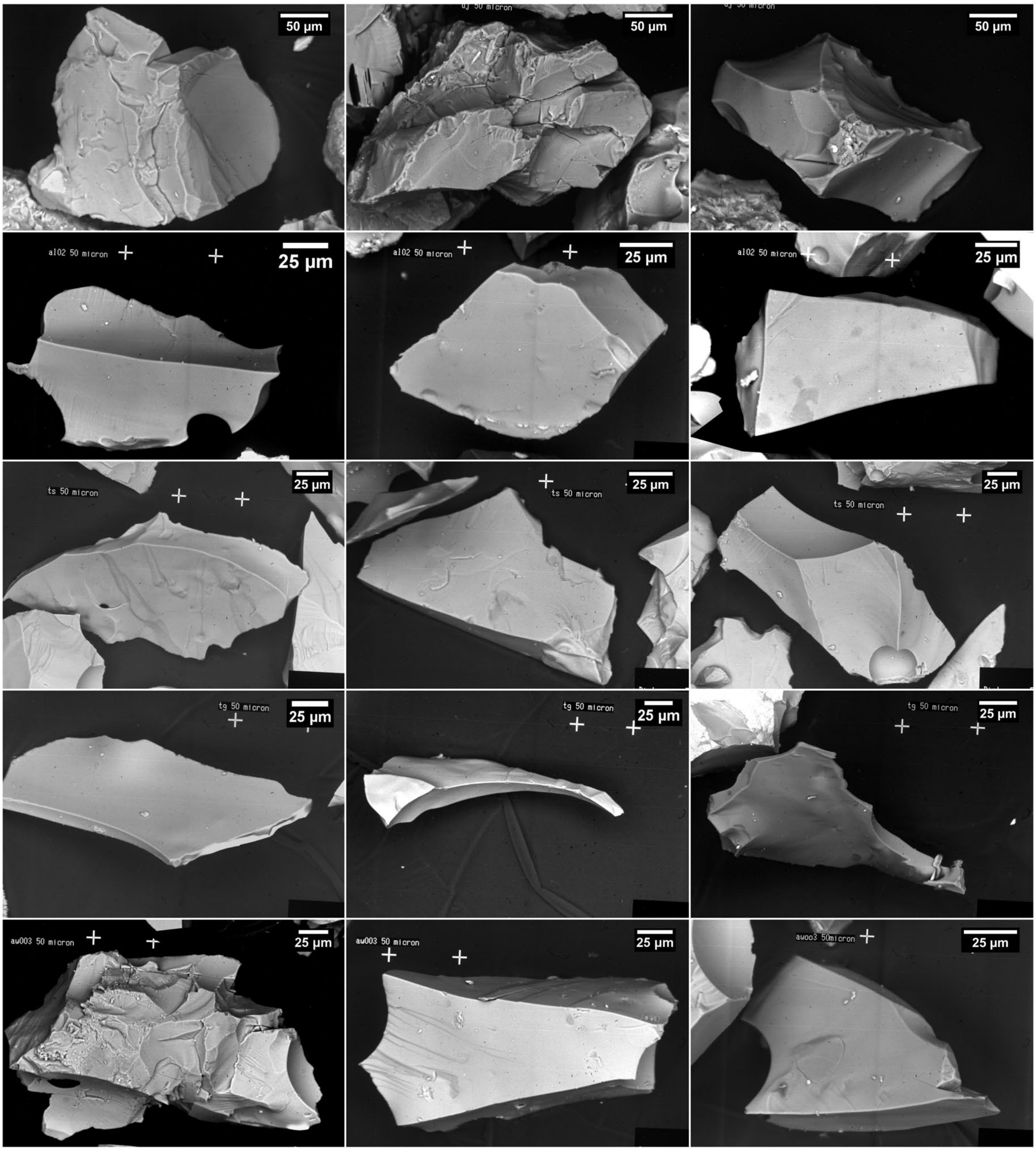

Fig. 112: Tepexitl particles: From top to bottom, representative SEM (BSE) images of the following ash particles are presented line by line: Tep nat (top row), Tep blow 1 (second row), Tep blow 2 (third row), Tep therm (fourth row) and Tep MFCI (bottom row). These SEM images have been kindly provided by Prof. Dellino and Dr. Mele, University of Bari.

T-test with Tep nat	Rect	Comp	Elon	Circ
Grim nat	0,277	0,453	0,950	0,322
Grim MFCI	0,422	0,036	0,084	0,577 (s)
Grim therm	<0,0005	<0,0005 (s)	<0,0005 (s)	<0,0005
Tep blow 1	0,732	0,763	0,810	0,806
Tep blow 2	0,923	0,222	0,135	0,135
Tep blow tot	0,788	0,401	0,339	0,993 (s)
Tep therm	0,109 (s)	0,004	0,002	0,063 (s)
Tep MFCI	0,004	0,207	0,148 (s)	0,001

Table 75: T-test results, using the average IPA parameters of natural Tepexitl ash particles as reference data set: The presented values denote the according significances p. Values, which indicate a significant difference are highlighted in gray. Results of separate variance t-tests are marked by "(s)".

It is particularly noteworthy that FG and T10 particles show no significant differences in their IPA parameters, if only subpopulation A class particles are considered. However, those type of fragments originating from RX targets are characterized by significant higher elongation values ($3{,}47 \pm 0{,}72$) compared to FG particles ($2{,}69 \pm 0{,}52$) and T10 fragments ($2{,}27 \pm 0{,}51$).

According to the t-test results, the following pairs of data sets show *no* significant differences in any of the four IPA parameters:

- FG - T10
- FG - Grim MFCI
- FG - Tep blow 1
- FG - Tep blow 2
- FG - Tep blow tot
- T10 - Grim nat
- T10 - Tep nat
- T10 - Tep blow 1
- T10 - Tep blow 2
- T10 - Tep blow tot
- RX - Grim therm
- RX - Tep therm
- RX - Tep blow 2
- Tep nat - Grim nat
- Tep nat - Tep blow 1
- Tep nat - Tep blow 2
- Tep nat - Tep blow tot

In a second step, these pairs of data sets have been checked by means of equivalence tests (ETs). The corresponding results are presented in Table 76, Table 77, Table 78 and Table 79.

ETs with FG	Rect 1	Rect 2	Comp 1	Comp 2	Elon 1	Elon 2	Circ 1	Circ 2
T10	yes	yes	yes	yes	yes	yes	yes	yes
Grim MFCI	yes	yes	yes	yes	yes	yes	yes	yes
Tep blow 1	yes	yes	no	( )	yes	yes	yes	yes
Tep blow 2	yes	no (0,71)	yes	no (0,12)	yes	yes	yes	no (1,14)
Tep blow tot	yes	yes	yes	yes	yes	yes	yes	no (0,91)

Table 76: ET results for FG particles: As the applied equivalence tests only provide reliable results for two data sets of equal variances, additional F-tests have been carried out.
1: A "yes" in the first column indicates that both data sets are of equal variances, and that the necessary condition for the subsequent ET is satisfied.
2: In the second column the results of the corresponding ETs are revealed: A "yes" indicates a verified similarity to FG particles. If a data set failed the ET, and a similarity can be rejected, the corresponding value of D is presented under which the result of the ET would have been positive.

ETs with T10	Rect 1	Rect 2	Comp 1	Comp 2	Elon 1	Elon 2	Circ 1	Circ 2
Grim nat	yes	yes	yes	yes	yes	yes	yes	yes
Tep nat	yes	yes	yes	yes	yes	yes	yes	yes
Tep blow 1	yes	yes	no	( )	yes	yes	yes	no (0,94)
Tep blow 2	yes	no (0,77)	yes	no (0,12)	yes	no (1,01)	yes	no (1,23)
Tep blow tot	yes	yes	yes	yes	yes	yes	yes	no (0,97)

Table 77: ET results for T10 particles: Additionally, F-tests have been carried out.
1: A "yes" in the first column indicates that both data sets are of equal variances, and that the necessary condition for the subsequent ET is satisfied.
2: In the second column the results of the corresponding ETs are revealed: A "yes" indicates a verified similarity to T10 particles. If a data set failed the ET and a similarity can be rejected, the corresponding value of D is presented, under which the result of the ET would have been positive.

ETs with RX	Rect 1	Rect 2	Comp 1	Comp 2	Elon 1	Elon 2	Circ 1	Circ 2
Grim therm	yes	no (0,71)	yes	no (0,14)	yes	no (1,74)	no	( )
Tep therm	yes	no (1,97)	yes	no (0,20)	yes	no (1,18)	yes	no (3,35)
Tep blow 2	yes	no (0,93)	yes	no (0,11)	yes	no (1,48)	yes	no (1,39)

Table 78: ET results for RX particles: Additionally, F-tests have been carried out.
1: A "yes" in the first column indicates that both data sets are of equal variances, and that the necessary condition for the subsequent ET is satisfied.
2: In the second column the results of the corresponding ETs are revealed: A "yes" indicates a verified similarity to RX particles. If a data set failed the ET and a similarity can be rejected, the corresponding value of D is presented, under which the result of the ET would have been positive.

ETs	Rect		Comp		Elon		Circ	
with Tep nat	1	2	1	2	1	2	1	2
Grim nat	yes	yes	yes	yes	yes	yes	yes	yes
Tep blow 1	no	( )	yes	yes	yes	yes	no	( )
Tep blow 2	yes	yes	yes	no (0,11)	yes	no (1,09)	no	( )
Tep blow tot	yes	yes	yes	yes	yes	yes	no	( )

Table 79: ET results for natural Tepexitl ash particles: Additionally, F-tests have been carried out. 1: A "yes" in the first column indicates that both data sets are of equal variances, and that the necessary condition for the subsequent ET is satisfied.
2: In the second column the results of the corresponding ETs are revealed: A "yes" indicates a verified similarity to Tep nat particles. If a data set failed the ET, and a similarity can be rejected, the corresponding value of D is presented, under which the result of the ET would have been positive.

In summary, the following pairs of data sets have significant similarities in all four IPA parameters:

- FG - T10
- FG - Grim MFCI
- T10 - Grim nat
- T10 - Tep nat
- Tep nat - Grim nat

Clearly visible similarities in the surface morphology of those particles (see also Fig. 113) substantiate these findings.

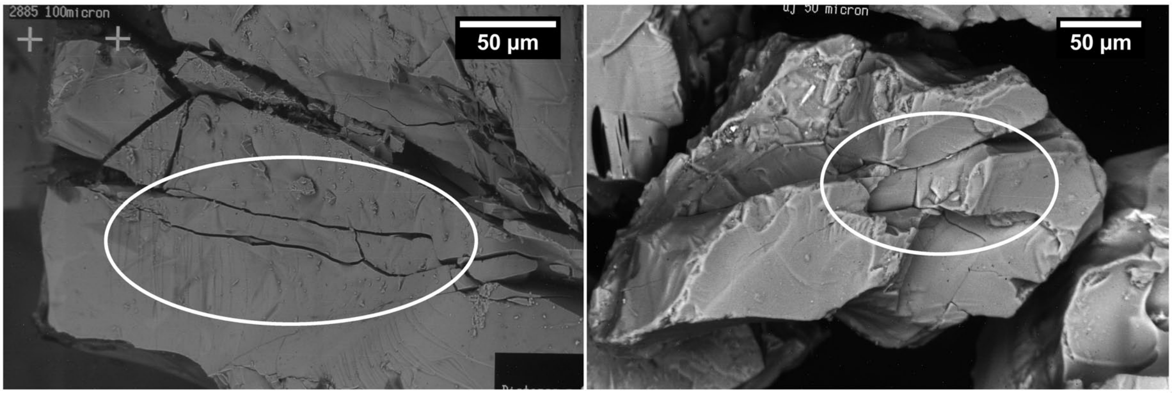

Fig. 113: Similarities in the surface morphologies: On the left, a T10 fragment is presented. The morphology of this particle is characterized by significant rift structures (marked by a white ellipse). On the right, a natural Tepexitl ash particle is depicted, which shows a comparable surface morphology.

3. Volcanological Conclusions

Focussing on volcanological aspects, the following conclusions can be drawn according to the findings of comparative IPA:

1. The fact that Tep nat and Grim nat ash particles are clearly similar - even despite their considerably different chemical composition (see Table 70) and the distinctly divergent rheology of their melts [4, 5, 64] - strongly suggests that the shape of a particle is highly correlated to the generating fracture mechanism, rather than to its rheological or chemical material properties. This conclusion confirms the applied "eye-witness" approach (see VI.1.1) of comparative IPA as a fracture analysis tool of great significance.

2. Evidently, both volcanic events have been characterized by similar fragmentation processes.

3. Natural Grimsvötn (2004) as well as natural Tepexitl ash particles show significant similarities to T10 fragments, which is a strong indication that in both events the melts had been pre-loaded under uniaxial stresses before the "actual" fragmentation has been initiated. These pre-stresses can be easily explained by the specific loading situation of a magmatic melt due to friction in the conduit.

4. In order to describe the fracture processes of those natural volcanic fragmentation events, one can refer - at least qualitatively - to the HIE fracture study results of pre-stressed T10 targets presented in this thesis.

5. Particularly, this includes the general transferability of the crack class-specific FSED model.

6. In contrast to the production of Grim nat and Tep nat, the basaltic melts in the MFCI experiment (Grim MFCI) evidently have been without any pre-stresses. Consequently, their fracture processes can be better described by transferring the corresponding findings of stress-relieved FG targets.

7. The damage crack-specific FSED value of T10 targets is considerably higher than that of FG samples (see Table 46). As a consequence, one can conclude that the corresponding FSED parameters of pre-stressed magmatic melts are distinctly higher, if compared to unloaded melts.
   Thus, empirically determined FSEDs provided by MFCI experiments could be used as a *minimum* estimation of the actual FSED values which characterize natural volcanic fracture processes of pre-stressed melts.

Part VII.

Conclusion

According to the results of edge-on hammer impact experiments (HIEs), the complex mechanisms of fragmentation can be fundamentally explained by the evolution of stresses in the target:

On the one hand, the target is loaded by *directed stresses*, which can be located in the target under a polariscope as "principal stress zones" (PSZs), that are distinctly affected by the geometry of pre-stresses.

On the other hand, at the moment of impact *fluctuating stress waves* are initiated, which rush through the sample and cause stochastic effects on the evolving cracks.

An innovative method - the FSED concept - has been introduced which allows to quantify the energy dissipation rates into new fracture areas.

The centerpiece of this model is the definition of the fracture energy E_{frac} which subsumes all energy terms possibly relevant for fragmentation, including the dissipation into heat and (generally) into ductile deformation.

In particular, the FSED concept considers the fact that in HIE targets, two classes of fractures can be identified showing distinctly different characteristics and denoted "damage cracks" and "normal cracks", respectively.

Thus, E_{frac} can be described as a linear combination of the energies dissipating into damage cracks E_{DC} and into normal cracks E_{NC}. According to the model, these crack class-specific fracture energies are linearly correlated with the corresponding fracture areas. The respective proportionality constants are denoted "fracture surface energy densities" η_{DC} and η_{NC}.

Damage cracks are characterized by complex conchoidal structures, resulting in fine particles of a grain size smaller than 4 mm. All experimental results strongly suggest that these fractures are primarily initiated by preceding shock waves, which cause local changes in the material, making it susceptible towards fluctuating stress waves propagating through the sample after impact.

In the shock wave affected surface areas, at least four discrete zones can be identified:

"Zone 0" denotes the impact notch, which is generated in the very first microseconds after impact. It considerably affects the coupling situation between hammer and target, and significantly restrains the further propagation of shock waves.

According to the "impact notch theory", a higher impact energy causes greater shock wave intensities, but also larger extensions of the shock wave restraining Zone 0: Thus, the amount of fracture energy E_{DC} dissipating into new damage crack areas is controlled by these two opposing mechanisms.

"Zone 1" is marked by fragments of a characteristic jagged shape. The fraction of the finest particles $\phi > 1$ is dominated by particles originating from the first two zones.

The surface of the next zone, referred to as "Zone 2", is characterized by fine shallow tessellate cracks. "Zone 3", which is farthest from the point of impact, does not show any of these characteristics.

The energy transfer in form of damage crack surfaces is comprehensively determined by the FSED parameter η_{DC}, which - at least in the studied scope - has shown no local dependencies.

The experimentally determined values of η_{DC} are in the range between $104,60\,\frac{\mathrm{J}}{\mathrm{m}^2}$ (for AS) and $181,85\,\frac{\mathrm{J}}{\mathrm{m}^2}$ (for RX). The damage-crack specific FSEDs significantly depend on the material properties as well as the geometry of pre-stresses, but not on hammer geometry and impact velocity.

Normal cracks are marked by a propagation perpendicular to the plane of view. The generated fragments are comparatively coarse. This fracture class includes a large variety of different crack types, characterized by specific locations as well as by distinct dynamic behaviors. The most prominent crack types are ACB and BCM.

The measured values of η_{NC} range between $37,46\,\frac{\mathrm{J}}{\mathrm{m}^2}$ (for TK) and $67,02\,\frac{\mathrm{J}}{\mathrm{m}^2}$ (for RX). Like η_{DC}, the normal crack-specific FSED η_{NC} shows no significant and systematic dependency on hammer geometry and impact velocity, but is considerably affected by the material properties and the pre-stress geometry of the target: Samples with a broader PSZ (T10), for example, are characterized by distinctly larger values of η_{NC}.

By determining the fracture area of a specific crack frame by frame, the "fracture area velocity" (FAV) could be quantified.

As η_{NC} is locally independent, it was possible to calculate the respective energy dissipation rate $e_{NC}(t)$ of the evolving cracks. By studying the energy dissipation profiles a comprehensive insight into the energetic dynamics has been gained and a crucial principle of fracture dynamics has been revealed, denoted the "local anisotropy effect":

High local stress gradients significantly stabilize the evolution of cracks and consequently cause a reduction of FAVs and energy dissipation rates. Thus the local anisotropy of the directed stress field in which a crack is developing, distinctly affects the crack's propagation stability and its resulting dynamic energy dissipation behavior. This model consistently explains the diverging fracture dynamics of different crack types as well as those of targets with different PSZ geometries.

Finally, by means of image particle analyses it was possible to compare the HIE fragments with natural and experimental volcanic ash particles, showing clear similarities for specific cases.

The results of these comparative studies strongly indicate that HIEs are a very suitable method to reproduce the MFCI loading conditions in silicate melts.

Furthermore the FSED model is substantiated as a well transferable concept to describe also volcanic fragmentation processes: In particular the experimental findings of pre-stressed T10 targets can be used to explain the fracture situation of magmatic melts under an uniaxial loading, as in the Tepexitl and Grimsvötn (2004) eruptions.

Fragmentation processes of magmatic melts without uniaxial pre-loadings, however, can be better described by referring to the results of stress-relieved FG targets.

As a consequence, the explanatory models in this thesis can be regarded as general fragmentation models for amorphous silicate materials. These will allow to calculate the fracture energies and to make precise physical statements about the fragmentation processes and the mechanisms of ash production.

Just by determining the corresponding FSED parameters of a magmatic melt, an event like Eyjafjallajökull 2010 will surely never be avoided. Yet, this concept might enable volcanologists to improve their predictions on the consequences and risks of such eruptions, reducing economic losses and - much more important - saving human lives.

Bibliography

[1] Alex, Wulf (2008); KRÜMELKUNDE; Karlsruhe; scriptum (11-19-2008) retrieved 01-12-2009 from: http://www.alex-weingarten.de/skripten/kruemel.pdf

[2] Allaby, A.; Allaby, M. (eds.) (1999); A DICTIONARY OF EARTH SCIENCES; 2nd ed.; Oxford University Press, New York

[3] Allen, T. (1997); PARTICLE SIZE MEASUREMENTS; 5th ed.; Chapman and Hall, New York

[4] Andriani, C. D. (2008); INDAGINI SPERIMENTALI SUI MECCANISMI ERUTTIVI DELL'ERUZIONE DI GRIMSVÖTN 2004: ANALISI DI IMMAGINE SUI CLASTI DI VETRO; Università degli studi di Bari; final paper

[5] Austin-Erickson, A. (2007); A CASE STUDY OF TEPEXITL TUFF RING SERDAN-ORIENTAL BASIN, MEXICO; Northern Arizona University; master thesis

[6] Austin-Erickson, A.; Büttner, R.; Dellino, P.; Ort, M. H.; Zimanowski, B. (2008); PHREATOMAGMATIC EXPLOSIONS OF RHYOLITIC MAGMA: EXPERIMENTAL AND FIELD EVIDENCE.; J. Geophys. Res.; 113; B11201

[7] Bach, H.; Krause, D. (eds.) (2005); LOW THERMAL EXPANSION GLASS-CERAMICS; 2nd ed.; Springer, Berlin, Heidelberg

[8] Bargel, H.-J.; Schulze, G. (eds.) (2008); WERKSTOFFKUNDE; 10th ed.; Springer, Berlin, Heidelberg

[9] Barrow, G. M. (1984); PHYSIKALISCHE CHEMIE, TEIL 3: MISCHPHASENTHERMODYNAMIK, ELEKTROCHEMIE, REAKTIONSKINETIK; 5th ed.; Bohmann Verlag, Heidelberg

[10] Bouchbinder, E.; Procaccia, I. (2007); OSCILLATORY INSTABILITY IN TWO-DIMENSIONAL DYNAMIC FRACTURE; Phys. Rev. Lett.; 98; 124302

[11] Boudet, J.F.; Ciliberto, S.; Steinberg, V. (1996); DYNAMICS ON CRACK PROPAGATION IN BRITTLE MATERIALS; J. Phys. II; 6; pp. 1493-1516

[12] Brosius, F. (1998); SPSS 8 PROFESSIONELLE STATISTIK UNTER WINDOWS; 1st ed.; mitp-Verlag GmbH, Bonn

[13] Brunauer, S.; Emmett, P. H.; Teller, E. (1938); ADSORPTION OF GASES IN MULTIMOLECULAR LAYERS; J. Am. Chem. Soc.; 60; No. 2; pp. 309-319

[14] Buehler, M. J.; Abraham, F. F.; Gao, H. (2003); HYPERELASTICITY GOVERNS DYNAMIC FRACTURE AT A CRITICAL LENGTH SCALE; Nature, 426; pp. 141-146

[15] Büttner, R.; Dellino, P.; La Volpe, L.; Lorenz, V.; Zimanowski, B. (2002); THERMOHYDRAULIC EXPLOSIONS IN PHREATOMAGMATIC ERUPTIONS AS EVIDENCED BY THE COMPARISON BETWEEN PYROCLASTS AND PRODUCTS FROM MOLTEN FUEL COOLANT INTERACTION EXPERIMENTS; J. Geophys. Res.; 107; B11, 2277

[16] Büttner, R.; Dellino, P.; Raue, H.; Sonder, I.; Zimanowski, B. (2006); STRESS INDUCED BRITTLE FRAGMENTATION OF MAGMATIC MELTS: THEORY AND EXPERIMENTS; J. Geophys. Res.; 111; B08204

[17] Büttner, R.; Dellino, P.; Zimanowski, B. (1999); IDENTIFYING MAGMA-WATER INTERACTION FROM THE SURFACE FEATURES OF ASH PARTICLES; Nature; 401; pp. 688-690

[18] Büttner, R.; Zimanowski, B. (1998); PHYSICS OF THERMO-HYDRAULIC EXPLOSIONS; Phys. Rev. E; 57; pp. 5726-5729

[19] Büttner, R.; Zimanowski, B.; Mohrholz, C.-O.; Kümmel, R. (2005); ANALYSIS OF THERMOHYDRAULIC EXPLOSION ENERGETICS; J. Appl. Phys.; 98; 043524

[20] Burghard, Z. (2004); BEHAVIOUR OF GLASSES AND POLYMER-DERIVED AMORPHOUS CERAMICS UNDER CONTACT STRESS; Universität Stuttgart, Max-Planck Institut für Metallforschung, Stuttgart; dissertation

[21] Caffier, I. (1998); INVESTIGATIONS ON THE FRAGMENTATION OF MAGMATIC MELT BY EXPANDING GAS; Julius-Maximilians-Universität Würzburg; diploma thesis

[22] Célarié, F.; Prades, S.; Bonamy, D.; Ferrero, L.; Bouchaud, E.; Guillot, C.; Marlière, C. (2003); GLASS BREAKS LIKE METALS, BUT AT THE NANOMETER SCALE; Phys. Rev. Lett.; 90; No. 7; pp. 212-213

[23] Chau, K. T.; Wei, X. X.; Wong, R. H. C.; Yu, T. X. (2000); FRAGMENTATION OF BRITTLE SPHERES UNDER STATIC AND DYNAMIC COMPRESSIONS: EXPERIMENTS AND ANALYSES; Mech. Mater.; 32; pp. 543-554

[24] Chen, S. Y.; Farris, T. N.; Chandrasekar, S. (1997); CONTACT MECHANICS OF HERTZIAN CONE CRACKING; Int. J. Solids Structures; 32; No. 3/4; pp. 329-340

[25] Cotterell, B. (1965); VELOCITY EFFECTS IN FRACTURE PROPAGATION; Appl. Mat. Res.; 4; pp. 227-232

[26] Cotterell, B. (2002); THE PAST, PRESENT, AND FUTURE OF FRACTURE MECHANICS; Eng. Fract. Mech.; 69; pp. 533-553

[27] Cruse, T. A. (1988); BOUNDARY ELEMENT ANALYSIS IN COMPUTATIONAL FRACTURE MECHANICS; Kluwer, Dordrecht

[28] D'Addabbo, M. (2008); STUDIO DEI MECCANISMI ERUTTIVI E DEPOSIZIONALI DELL' ERUZIONE DEL GRIMSVÖTN AVVENUTA NEL 2004; Università degli studi di Bari; final paper

[29] Dander, W. (1982); EINFÜHRUNG IN DIE GRUNDLAGEN DER BRUCHMECHANIK; Z. Werkstofftech.; 13; pp. 69-76

[30] Dander, W. (1982); EINFÜHRUNG IN DIE GRUNDLAGEN DER BRUCHMECHANIK, TEIL 2: ABHÄNGIGKEIT DES BRUCHMECHANISCHEN WERKSTOFFKENNWERTES K_{Ic} VON VERSCHIEDENEN PARAMETERN; Z. Werkstofftech.; 13; pp. 85-95

[31] Davis, J. C. (2002) STATISTICS AND DATA ANALYSIS IN GEOLOGY; 3rd ed.; John Wiley, New York

[32] Dellino, P.; Isaia, R.; La Volpe, L.; Orsi, G. (2001); STATISTICAL ANALYSIS OF TEXTURAL DATA FROM COMPLEX PYROCLASTIC SEQUENCES: IMPLICATIONS FOR FRAGMENTATION PROCESSES OF THE AGNANO-MONTE SPINA TEPHRA (4.1KA), PHLEGRAEAN FIELDS, SOUTHERN ITALY; Bull. Volcanol.; 63; pp. 443-461

[33] Dellino, P.; La Volpe, L. (1996); IMAGE PROCESSING ANALYSIS IN RECONSTRUCTING FRAGMENTATION AND TRANSPORTATION MECHANISMS OF PYROCLASTIC DEPOSITS. THE CASE OF MONTE PILATO-ROCCHE ROSSE ERUPTIONS, LIPARI (AEOLIAN ISLANDS-ITALY); J. Volcanol. Geotherm. Res.; 71; pp. 13-29

[34] Deuflhard, P.; Hohmann, A. (2008); NUMERISCHE MATHEMATIK 1 - EINE ALGORITHMISCH ORIENTIERTE EINFÜHRUNG; Walter de Gruyter, Berlin, New York

[35] Deutsches Institut für Normung (1984); DIN IEC 584 (released 1/1984) in: Westerfeld, P.; THERMOELEMENTE UND WIDERSTANDSTHERMOMETER; Hartmann & Braun AG, Frankfurt a. M.

[36] Deutsches Institut für Normung (2000); DIN EN 1288 (ed. 09/2000); GLAS IM BAUWESEN – BESTIMMUNG DER BIEGEFESTIGKEIT VON GLAS

[37] Deutsches Institut für Normung (2006); DIN EN 10083 (ed. 08/2006); VERGÜTUNGSSTÄHLE

[38] Drello Ing. Paul Drewell GmbH&Co. KG (n.d.); BETRIEBSANLEITUNG: ELEKTRONISCH GESTEUERTE HOCHFREQUENZ-FUNKENZEITLUPE; BAL 1501

[39] Du Bois, P. A.; Kolling, S. (2003); MODELLING OF SAFETY GLASS FOR CRASH SIMULATION; Comp. Mat. Sci; 28; pp. 675-683

[40] Dürig, T. (2005); VISUALISIERUNG DYNAMISCHER BRUCHPROZESSE BEI GLÄSERN; Julius-Maximilians-Universität Würzburg; diploma thesis

[41] Dürig, T.; Mele, D.; Dellino, P.; Zimanowski, B. (2011); COMPARATIVE ANALYSES OF GLASS FRAGMENTS FROM BRITTLE FRACTURE EXPERIMENTS AND VOLCANIC ASH PARTICLES; Bull. Volcanol.; DOI: 10.1007/s00445-011-0562-0

[42] Dürig, T.; Sonder, I.; Zimanowski, B.; Beyrichen, H.; Büttner, R. (2011); GENERATION OF VOLCANIC ASH BY BASALTIC VOLCANISM; J. Geophys. Res.; DOI: doi:10.1029/2011JB008628

[43] Eberhart, M. (2000); WARUM MARMOR BRICHT UND EISEN NICHT; Spektr. Wiss., 1/2000; pp. 44-50

[44] Ebert, H.-P.; Hemberger, F.; Fricke, J.; Büttner, R.; Bez, S.; Zimanowski; B. (2003); THERMOPHYSICAL PROPERTIES OF A VOLCANIC ROCK MATERIAL; High Temp.-High Press.; 34; pp. 561-668

[45] Ex, W.; Schmücker, G. A. (2000); NEUERUNGEN IM ERSCHÜTTERUNGS-IMMISSIONSSCHUTZ; Spreng Info; 22; No. 1; pp. 15-25

[46] Fineberg, J.; Gross, S. P.; Marder, M. P.; Swinney, H. L. (1991); INSTABILITY IN DYNAMIC FRACTURE; Phys. Rev. Lett.; 67; No. 4; pp. 457-460

[47] Fischer-Cripps, A. C. (1997); PREDICTING HERTZIAN FRACTURE; J. Mat. Sci; 32; pp. 1277-1285

[48] Flachglas MarkenKreis GmbH (2004); GLASHANDBUCH 2004; Flachglas MarkenKreis GmbH, Gelsenkirchen

[49] Frocht, M. M. (1969); PHOTOELASTICITY; 1st ed.; Pergamon Press, Oxford

[50] Fröhlich, G.; Zimanowski, B.; Lorenz, V. (1993); EXPLOSIVE THERMAL INTERACTIONS BETWEEN MOLTEN LAVA AND WATER; Experimental Thermal and Fluid Sci.; 7; pp. 319-332

[51] Geißler, J. (1998); UNTERSUCHUNGEN ZUR ANKOPPLUNG DER KINETISCHEN ENERGIE BEI DER WECHSELWIRKUNG ZWISCHEN PROJEKTIL UND WASSEROBERFLÄCHE; Julius-Maximilians-Universität Würzburg; diploma thesis

[52] Gerthsen, C.; Vogel, H. (1997); PHYSIK; Springer, Berlin, Heidelberg, New York

[53] Glockner, W. (1992); GLAS-TECHNIKGESCHICHTE IM DEUTSCHEN MUSEUM; DEUTSCHES MUSEUM; C. H. Beck, München

[54] Griffith, A. A. (1920); THE PHENOMENA OF RUPTURE AND FLOW IN SOLIDS; Phil. Trans. Roy. Soc. London A, 221; pp. 163-198

[55] Gross, D.; Seelig, Th. (2007); BRUCHMECHANIK; 4th ed.; Springer, Berlin, Heidelberg

[56] Grüning, M. (2005); UNTERSUCHUNGEN ZUR DISKRIMINANZANALYSE MIT HOCHDIMENSIONALEN DATEN; Otto-von-Guericke-Universität Magdeburg; dissertation

[57] Gudmundsson, M. T. (2010); personal correspondence, 04-16-2010; Institute of Earth Science, University of Iceland, Reyjkjavik

[58] Habelitz, S.; Carl, G.; Rüssel, C. (2001); PROCESSING, MICROSTRUCTURE AND MECHANICAL PROPERTIES OF EXTRUDED MICA GLASS-CERAMICS; Mat. Sci. A; 307; pp. 1-14

[59] Hänsel, H.; Neumann, W. (1996); PHYSIK - MOLEKÜLE UND FESTKÖRPER; Spektrum Akademischer Verlag, Heidelberg, Berlin, Oxford

[60] Hauch, J. A.; Marder, M.P. (1998); ENERGY BALANCE IN DYNAMIC FRACTURE, INVESTIGATED BY A POTENTIAL DROP TECHNIQUE; Int. J. Fract.; 90; pp. 133-151

[61] Heckel, K. (1970); EINFÜHRUNG IN DIE TECHNISCHE ANWENDUNG DER BRUCHMECHANIK; Carl Hanser, München

[62] Hertz, H. (1881); ÜBER DIE BERÜHRUNG FESTER ELASTISCHER KÖRPER; J. rein. angew. Math.; 92; pp. 156-171

[63] Hertz, H. (1882); IN HERTZ'S MISCELLANEOUS PAPERS; MacMillan, London

[64] Hobiger, M. (2007); MESSUNG VISKOSER EIGENSCHAFTEN MAGMATISCHER SCHMELZEN; Julius-Maximilians-Universität Würzburg, diploma thesis

[65] Höland, W. (2006); GLASKERAMIK; 1st ed.; vdf Hochschulverlag, Zürich

[66] Iceland Review; (n.a.) (2010); BREAKING NEWS: AN ERUPTION STARTED BY EYJAFJALLAJÖKULL GLACIER AT MIDNIGHT; 03-21-2010; retrieved 05-13-2010 from: http://icelandreview.com/icelandreview/daily_news/?cat_id=16567&ew_0_a_id=359633

[67] Irwin, G. R. (1957); ANALYSIS OF STRESSES AND STRAINS NEAR THE END OF A CRACK TRAVERSING A PLATE; J. Appl. Mech.; 24; pp. 361-364

[68] Jaupart, C. (2000); VULKANE; 1st ed.; Lübbe, Bergisch Gladbach

[69] Kadono, T.; Arakawa, M. (2002); CRACK PROPAGATION IN THIN GLASS PLATES CAUSED BY HIGH VELOCITY IMPACT; Phys. Rev. E; 65; 035107

[70] Kerkhof, F. (1970); BRUCHVORGÄNGE IN GLÄSERN; Verlag der Deutschen Glastechnischen Gesellschaft, Frankfurt a. M.

[71] Killeen, P. R. (2005); AN ALTERNATIVE TO NULL-HYPOTHESIS SIGNIFICANCE TESTS; Psychol Sci; 16 (5); pp. 345-353

[72] Kistler Instrumente AG (n.d.); BETRIEBSANLEITUNG: LADUNGSVERSTÄRKER 5006; B11.5006d-11.79

[73] Kistler Instrumente AG (n.d.); BETRIEBSANLEITUNG: QUARZ-MESSUNTERLAGSSCHEIBEN; B06.011d-2.77

[74] Kneubuehl, B. P.; Coupland, R. M.; Rothschild, M. A.; Thali, M. J. (2008); WUNDBALLISTIK, GRUNDLAGEN UND ANWENDUNGEN; 3d ed.; Springer Medizin Verlag, Heidelberg

[75] Kohn, W. (2005); STATISTIK - TEIL III: DATENANALYSE UND WAHRSCHEINLICHKEITSRECHNUNG; Springer, Berlin, Heidelberg; pp. 482-502

[76] Küppers, H. (1964); DIE NUMERISCHE BERECHNUNG EINER SPANNUNGSVERTEILUNG IN DER UMGEBUNG EINER KERBSPITZE; Glastechnischer Bericht; 37; pp. 185-189

[77] Läpple, V. (2006); EINFÜHRUNG IN DIE FESTIGKEITSLEHRE; 1st ed.; Vieweg, Wiesbaden

[78] Landau, L. D.; Lifschitz, E. M. (1991); LEHRBUCH DER THEORETISCHEN PHYSIK -BAND VI: HYDRODYNAMIK; 5th ed.; Akademie Verlag, Berlin

[79] Lawn, B. (1975); FRACTURE OF BRITTLE SOLIDS; 1st ed.; Cambridge Press, New York

[80] Marder, M.P.; Liu, X. (1993); INSTABILITY IN LATTICE FRACTURE; Phys. Rev. Lett.; 71; No. 15; pp. 2417-2420

[81] Met Office; (n.a.) (2010); VOLCANIC ASH ADVISORY FROM LONDON - ISSUED GRAPHICS; 05-24-2010; retrieved 06-06-2010 from: http://www.metoffice.gov.uk/aviation/vaac/vaacuk_vag.html

[82] Meyers, M. A., Chawla, K. K. (1999); MECHANICAL BEHAVIOR OF MATERIALS; Prentice-Hall, New Jersey

[83] Michel, S. (1999); EINSATZ MULTIVARIATER ANALYSEVERFAHREN BEI GESTEINSMAGNETISCHEN UNTERSUCHUNGEN DES PALÄOKLIMAS: EINE EXEMPLARISCHE STUDIE; Julius-Maximilians-Universität Würzburg & Eberhard-Karls-Universität Tübingen, diploma thesis

[84] Momber, A. W. (2003); FRACTURE LANCES IN GLASS LOADED WITH SPHERICAL INDENTERS; J. Mat. Sci. Lett.; 22; pp. 1477-1481

[85] Momber, A. W. (2004); BEOBACHTUNGEN AN GESTEINEN BEI EINDRUCKVERSUCHEN MIT RUNDEN EINDRUCKKÖRPERN; Forsch. Ing.; 68; pp. 200-212

[86] Mortimer, C. E. (1996); CHEMIE; 6th ed.; Georg Thieme Verlag, Stuttgart, New York

[87] Neuber, H. (1958); KERBSPANNUNGSLEHRE; 2nd ed.; Springer, Berlin, Göttingen, Heidelberg

[88] Obrezanova, O.; Movchan, A.B.; Willis, J.R (2002).; DYNAMIC STABILITY OF A PROPAGATING CRACK; J. Mech. Phys. Solids; 50; pp. 2637-2668

[89] Orowan, E. (1949); FRACTURE AND STRENGTH OF SOLIDS; Progr. Phys.; 12; pp. 185-232

[90] Pannhorst, W. (1997); GLASS CERAMICS: STATE-OF-THE-ART; J. Non-Cryst. Solids; 219; pp.198-204

[91] Parisi, A.; Ball, R. C.; ROLE OF SURFACE WAVES ON THE RELATION BETWEEN CRACK SPEED AND THE WORK OF FRACTURE; Phys. Rev. B; 66; No. 16; pp. 5432-5445

[92] Polyakov, Z. I.; Vshivtsov, A. V.; FRACTURE OF BRITTLE MATERIALS UNDER PULSATING LOADS; Probl. Prochn.; 12; pp. 60-62 (1973)

[93] Ponton, C. B.; Rawlings, R. D. (2002); VICKERS INDENTATION FRACTURE TOUGHNESS TEST - PART 1 - REVIEW OF LITERATURE AND FORMULATION OF STANDARDIZED IDENTATION TOUGHNESS EQUATIONS; Mat. Sci. Tech.; 5; pp. 865-872 (1989)

[94] Ponton, C. B.; Rawlings, R. D. (1989); VICKERS INDENTATION FRACTURE TOUGHNESS TEST - PART 2 - APPLICATION AND EVALUATION OF STANDARDIZED IDENTATION TOUGHNESS EQUATIONS; Mat. Sci. Tech.; 5; pp. 961-976

[95] Popov, V. L. (2009); KONTAKTMECHANIK UND REIBUNG; 1st ed.; Springer, Berlin, Heidelberg

[96] Rasch, D. (ed.) (1998); VERFAHRENSBIBLIOTHEK, BAND 2; Oldenbourg Verlag, München, Wien; pp. 686ff.

[97] Raue, H. (2004); A NEW MODEL FOR THE FRACTURE ENERGY BUDGET OF PHREATOMAGMATIC EXPLOSIONS; J. Volcanol. Geotherm. Res.; 129; pp. 99-108

[98] Raue, H. (2004); MAGMENFRAGMENTATION IM BRUCHHAFTEN REGIME: EIN NEUES MODELL ZUR ENERGIEBILANZIERUNG AM BEISPIEL DER PHLEGRÄISCHEN FELDER/ITALIEN; Julius-Maximilians-Universität Würzburg, dissertation

[99] Rentzsch, W. H.; Willmann, G. (2002); EIN EINFACHES HILFSMITTEL ZUM KONSTRUIEREN MIT KERAMIK; Mat.-wiss. Werkstofftech.; 33; pp. 184-189

[100] Retsch GmbH (1993); KORNGRÖßENBESTIMMUNG (TEIL 1); die probe; 1/93

[101] Richard, H. A.; Sander, M. (2009); ERMÜDUNGSRISSE; 1st ed.; Vieweg+Teubner; Wiesbaden

[102] Riedel, W.; Hiermaier, S.; Thoma, K. (2010); TRANSIENT STRESS AND FAILURE ANALYSIS OF IMPACT EXPERIMENTS WITH CERAMICS; Mat. Sci. Eng. B; 173; pp. 139-147

[103] Roesler, F. C. (1956); BRITTLE FRACTURES NEAR EQUILIBRIUM; Proc. Phys. Soc.; 69; pp. 981-992

[104] Roesler, F. C. (1956); INDENTATION HARDNESS OF GLASS AS AN ENERGY SCALING LAW; Proc. Phys. Soc.; 69; pp. 55-60

[105] Rösler, J.; Harders, H.; Bäker, M. (2003); MECHANISCHES VERHALTEN DER WERKSTOFFE; 1st ed.; Teubner, Stuttgart, Leibzig, Wiesbaden

[106] Roos, E.; Maile, K. (2005); WERKSTOFFKUNDE FÜR INGENIEURE; 2nd ed.; Springer, Berlin, Heidelberg

[107] Sack, W. (1965); GLAS, GLASKERAMIK UND SINTERGLASKERAMIK (1965); Chem. Ing. Tech.; 37; pp. 1154-1165

[108] Schadwinkel, A. (2010); EINE COMPUTERSIMULATION IST ZU WENIG; Zeit Online; 04-20-2010; retrieved 05-13-2010 from: http://www.zeit.de/wissen/2010-04/messung-asche-wolke

[109] Schaller, A. (2002); WERKSTOFFE DER MEDIZINTECHNIK, TEIL2- KONSTRUKTIONSWERKSTOFFE; Technische Fachhochschule Berlin, scriptum

[110] Schlittgen, R. (2003); EINFÜHRUNG IN DIE STATISTIK; 10th ed.; Oldenbourg Wissenschaftsverlag, München

[111] Scholze, H. (1988); GLAS. NATUR, STRUKTUR UND EIGENSCHAFTEN; 3rd ed.; Springer, Berlin, Heidelberg, New York

[112] Senf, H.; Strassburger, E.; Rothenhäusler, H. (1994); STRESS WAVE INDUCED DAMAGE AND FRACTURE IN IMPACTED GLASSES; J. Phys. IV; 4; pp. 741-746

[113] Sharon, E.; Gross, S.; Fineberg, J. (1996); ENERGY DISSIPATION IN DYNAMIC FRACTURE; Phys. Rev. Lett.; 76; No. 12; pp. 2117-2120

[114] Sharon, E.; Fineberg, J. (1996); MICROBRANCHING INSTABILITY AND THE DYNAMIC FRACTURE OF BRITTLE MATERIALS; Phys. Rev. B; 54; No. 10; pp. 7128-7139

[115] Sharon, E.; Fineberg, J. (1999); CONFIRMING THE CONTINUUM THEORY OF BRITTLE FRACTURE FOR FAST CRACKS; Nature; 397; pp. 333-335

[116] Sigmundsson, F.; Gudmundsson, M. T.; Larsen, G.; Hreinsdottir, S.; Einarsson, P.; Jónsdóttir, I.; Jakobsdóttir, S.; Vogfjord, K.; Hjaltadottir, S. Gudmundsson, G. B. (2010); ERUPTION IN ICELAND AT THE EYJAFJALLAJÖKULL VOLCANIC SYSTEM BEGINS 20 MARCH 2010; Institute of Earth Science, University of Iceland; (n.d.); retrieved 05-13-2010 from: http://www.earthice.hi.is/page/ies_activity_Eyjafjallajokull

[117] Sigurdsson, H.; Houghton, B.; McNutt, S.; Rymer, H.; Stix, J. (eds.) (1999); ENCYCLOPEDIA OF VOLCANOES; Academic Press, San Diego

[118] Smekal, A. (1936); BRUCHTHEORIE SPRÖDER KÖRPER; Zeitschr. Phys.; 103; pp. 495-525

[119] Smithsonian National Museum of Natural History; (n.a.) (2010); EYJAFJALLAJÖKULL; retrieved 05-13-2010 from: http://www.volcano.si.edu/world/volcano.cfm?vnum=1702-02=&volpage=weekly

[120] Sonder, I. (2010); VISCOUS PROPERTIES OF MAGMATIC MELTS; Julius-Maximilians-Universität Würzburg; dissertation

[121] Spiegel, M. R.; Stephens, L. J. (2003); STATISTIK; 1st ed.; mitp-Verlag GmbH; Bonn

[122] Spiegel Online; (n.a.) (2010); ALLE INTERNATIONALEN AIRPORTS IN DEUTSCHLAND GESCHLOSSEN; 04-16-2010; retrieved 05-13-2010 from: http://www.spiegel.de/reise/aktuell/0,1518,689300,00.html

[123] Spieler, O.; Dingwell, D. B.; Alidibirov, M. (2004); MAGMA FRAGMENTATION SPEED: AN EXPERIMENTAL DETERMINATION; J. Volcanol. Geotherm. Res.; 129; pp. 109-123

[124] Stern.de; (n.a.) (2010); KONSEQUENZEN AUS DEM FLUGCHAOS: DIE EU WILL DEN EINHEITSHIMMEL; 04-27-2010; retrieved 05-13-2010 from: http://www.stern.de/reise/service/konsequenzen-aus-dem-flugchaos-die-eu-will-den-einheitshimmel-1561977.html

[125] Stieß, M. (2009); MECHANISCHE VERFAHRENSTECHNIK - PARTIKELTECHNOLOGIE 1; 3rd ed.; Springer, Berlin, Heidelberg

[126] Stöcker, H. (2000); TASCHENBUCH DER PHYSIK; 4th ed.; Harri Deutsch, Thun, Frankfurt a. M.

[127] Strassburger, E. (2004); VISUALIZATION OF IMPACT DAMAGE IN CERAMICS USING THE EDGE-ON IMPACT TECHNIQUE; Int. J. Ceram. Tech.; 1; pp. 235-242

[128] Strassburger, E.; Senf, H.; Rothenhäusler, H. (1994); FRACTURE PROPAGATION DURING IMPACT IN THREE TYPES OF CERAMICS; J. Phys. IV; 4; pp. 653-658

[129] Taddeucci, J.; Scarlato, P. ; Andronico, D. ; Cristaldi, A.; Büttner, R.; Zimanowski, B. Küppers, U. (2007); ADVANCES IN THE STUDY OF VOLCANIC ASH; EOS Trans. AGU; 88; No. 24; pp. 253-256

[130] Trepte, A. (2003); RISSE DURCHBRECHEN DIE SCHALLMAUER; press release from 11/12/2003; C29/2003 (140); Max-Planck-Gesellschaft, München

[131] Waldschmidt, H. (2008); personal correspondence, 06-16-2008; Systems and Projects, Schott AG, Mainz

[132] Wegst, C. W. (1989); STAHLSCHLÜSSEL; Stahlschlüssel Wegst GmbH, Marbach am Neckar

[133] Will, P. (1993); R-KURVEN VON ENERGIEDISSIPATIVEN WERKSTOFFEN MIT SCHÄDIGUNGSZONE - TEIL 1: ENERGIEUMSATZ AM RISS; Mat.-wiss. Werkstofftech.; 24; pp. 327-330

[134] Will, P. (1993); R-KURVEN VON ENERGIEDISSIPATIVEN WERKSTOFFEN MIT SCHÄDIGUNGSZONE - TEIL 2: EXPERIMENTELLE ERMITTLUNG VON J-R KURVEN; Mat.-wiss. Werkstofftech.; 24; pp. 362-366

[135] Wohletz, K. H.; Zimanowski, B. (2000); ERUPTION PHYSICS; Terra Nostra; 6; pp. 515-523, 535-543

[136] Zachariasen, W. H. (1932); THE ATOMIC ARRANGEMENT IN GLASS; J. Chem. Soc.; 54; pp. 3841-3851

[137] Zimanowski, B. (1998); PHREATOMAGMATIC EXPLOSIONS in: Freundt, A.; Rosi, M.; FROM MAGMA TO TEPHRA; 1st ed.; Elsevier, Amsterdam; pp. 25-54

[138] Zimanowski, B.; Büttner, R.; Lorenz, V., Häfele, H.-G. (1997); FRAGMENTATION OF BASALTIC MELT IN THE COURSE OF EXPLOSIVE VOLCANISM; J. Geophys. Res.; 102; B1; pp. 803-814

[139] Zimanowski, B.; Fröhlich, G.; Lorenz, V. (1991); QUANTITATIVE EXPERIMENTS ON PHREATOMAGMATIC EXPLOSIONS; J. Volcanol. Geotherm. Res.; 48; pp. 341-358

[140] Zimanowski, B.; Wohletz, K.; Dellino, P.; Büttner, R. (2003); THE VOLCANIC ASH PROBLEM; J. Volcanol. Geotherm. Res.; 122; pp. 1-5

A. Error Analyses

A.1. Fragmentation and Particle Analysis

A.1.1. Mass Determination

The measuring accuracy of the scale used for particle analysis has been ±0,005 g.

A.1.2. Crack Velocities and Crack Tip Velocities

As a fine grained film has been used in the HIEs, the maximum spatial resolution of an image scanned at 3600 x 3600 dpi results to 17,6 µm per pixel. These optimal values are achieved for clearly detectable crack tips. At higher propagation rates, however, a localization is more difficult due to motion blur. Thus, usually an actual maximum spatial resolution of $\triangle x = 25\,\mu\text{m}$ is reckoned. Yet it has to be stressed that this value can also be modified on a case-by-case basis.

The temporal resolution of the Cranz-Schardin camera is $\triangle t = 17\,\text{ns}$.

With $v = \frac{x_2(t_2)-x_1(t_1)}{t_2-t_1}$ results according to the law of error propagation :

$$\triangle v = \left[\frac{(t_1-t_2)^2 \cdot \left((\triangle x_1)^2 + (\triangle x_2)^2 \right) + 2 \cdot (\triangle t)^2 \cdot (x_1 - x_2)^2}{(t_1-t_2)^4} \right]^{\frac{1}{2}} \tag{A.1}$$

where Δv is the accuracy of the crack tip velocity which has been determined by analyzing two subsequent images $i = 1, 2$ with a spatial resolution of $\triangle x_i$. Note that this equation can also be used to specify the uncertainties of crack velocities.

A.1.3. Accuracy of Area Quantification Methods

A.1.3.1. OPC

This method allows to quantify the amount of normal crack areas by measuring the projected areas in a photo and using the fundamental determination equation (III.5-15). As described above, the maximum uncertainty of spatial resolution in the plane of view is 25 µm for most cases. Thus, the accuracy of the projected fracture areas $\triangle \widetilde{B}$ is assumed to be $625\,\mu\text{m}^2$. The thickness d of a target has been determined by a micrometer caliper with a maximum error of $\triangle d = \pm 1\,\mu\text{m}$. According to the law of error propagation, the error of the actual fracture area A is given by:

$$\triangle A = \sqrt{\left(\frac{2 \cdot d^2}{\sqrt{d^2 + \frac{\widetilde{B}^2}{l^2}}} \cdot \triangle l \right)^2 + \left(\frac{2 \cdot d \cdot l}{\sqrt{d^2 + \frac{\widetilde{B}^2}{l^2}}} \cdot \triangle d \right)^2 + \left(\frac{2 \cdot \widetilde{B}}{l \cdot \sqrt{d^2 + \frac{\widetilde{B}^2}{l^2}}} \cdot \triangle \widetilde{B} \right)^2} \tag{A.2}$$

By inserting typical values, for example for a total fracture area A of $2760\,\text{mm}^2$, $\triangle A$ amounts to approximately $\pm 2{,}6\,\text{mm}^2$, which is a relative error of less than 0,1 %.

Yet one has to consider that the assumptions of the OPC - i.e. that normal crack surfaces consist of even, non-curved planes - are not always satisfied. This could imply that OPC measurements provide too low values. Nevertheless, the results of comparative analyses with TEH and CAD indicate that the relative errors of fracture areas determined by means of OPC are always below 1 %. This makes OPC a very reliable and precise tool for area quantification.

A.1.3.2. Projected Damage Crack Areas

As damage cracks are characterized by complex structures, which do not allow to quantify the actual areas A_{DC} by optical means, the projected area $\widetilde{B}_{DC}$ has been used to describe their dynamics. The uncertainty of these projected areas $\triangle\widetilde{B}_{DC}$ is assumed to be 625 µm^2.

A.1.3.3. OPT

The fragments have been photographed with a Canon EOS 350 D. The error of lengths determined by OPT is less than 125 µm, thus the digital resolution of areas is assumed to be $1{,}56{\cdot}10^{-2}$ mm^2.

A.1.3.4. BET

In this thesis, BET was used as a method to quantify the surface areas of the finest particles ($\phi > 1$). According to manufacturer's data, the measurement uncertainty of the applied gas sorption analyzer type NOVA 1200 is $\pm 0{,}01\ \frac{\mathrm{m}^2}{g}$ for particles of this grain size. A comparison between $B^{(BET)}_{IV,\phi>1}$ and $B^{(TEH)}_{IV,\phi>1}$ has revealed no distinct deviations, with just one exception: particles stemming from RX targets. This result can be explained by the nanocrystalline surface morphology of these glass ceramics, which can clearly be better resolved by nitrogen sorption than by a macroscopic liquid film used in TEH.

As a fundamental conclusion one can therefore state that - at least for RX particles - it is always preferable to compare area results achieved by identical methods.

A.1.3.5. TEH

In the scope of this thesis, TEH has been chosen as the standard tool for area quantification, as it has been verified to be a well applicable and reliable method for all targets and grain-sizes. A too complex fracture structure, however, reduces the accuracy of TEH, as those surfaces are not covered uniformly by the adhesive saline solution.

Additionally, it has to be considered that the measurement uncertainties become increasingly significant for high currents, due to the decreasing slope of the calibration curves. Therefore, the currents effectively used for TEH have always been restricted to a certain limit I_{max}.

Depending on the specific grain-size of the analyzed fragments, two different calibrations have been applied.

TEH measurements of coarse particles: The TEH measurements of class I and class II fragments are based on calibration curves for which a standard sample of 64 mm^2 has been used. Best results have been achieved with currents below 1500 µA. The measurement accuracy has been determined by the corresponding calibration curves. As a chi-square fit has been used to find out the calibration parameters, it was also possible to specify the respective standard errors and the maximum uncertainties (see e.g. Figure 27). Furthermore, the reproducibility of the TEH results has been confirmed by a number of additional comparative analyses. The empirically determined relative errors have ranged between 0,13 % and 1,1 %. Taking also the uncertainties for complex fractures surfaces - in particular of class II fragments - into account, a maximum uncertainty of 2,2 % was assumed.

TEH measurements of fine particles: In order to obtain calibration curves for the TEH area quantification of class IV fragments, glass beads with 2, 1 or 0,5 mm diameter have been used and a maximum current of $I_{max} = 240\,\mu A$ has been chosen. Fine particles have been analyzed by repetitive (usually four) measurements. Subsequently, the results have been averaged. This procedure reduces the uncertainties and allows also to determine the standard deviations as parameters of reproducibility. Empirically, these values have never exceeded 1,7 % of $B_{IV}^{(TEH)}$. Considering also the uncertainties due to complex surface structures, a maximum error of 2,2 % was assumed for most of the fractions.

For the finest fraction $\phi > 1$, however, the measurement uncertainty is considered to be distinctly larger, because these fragments tend to cluster which makes it difficult to ensure a uniform wetting of all surfaces: According to the results of comparative BET analysis, the maximum relative error of $B_{IV,\phi>1}^{(TEH)}$ was estimated 4,5 %.

A.1.4. Fracture Area Velocities

The uncertainty $\triangle w$ of the fracture area velocity (FAV) determined by two images $i = 1,2$ is calculated by:

$$\triangle w = \left[\frac{\left((\triangle A_1)^2 + (\triangle A_2)^2\right) \cdot (t_1 - t_2)^2 + 2 \cdot (\triangle t)^2 \cdot (A_1 - A_2)^2}{(t_1 - t_2)^4} \right]^{\frac{1}{2}} \tag{A.3}$$

where $\triangle t = 17\,\text{ns}$ and the values of $\triangle A_i$ are given by the equation (A.2). Note that the accuracy of w significantly depends on the sampling rate $1/|t_1 - t_2|$ which is the frame rate of the corresponding image sequence. To illustrate this influence, representative values of the maximum relative errors $\left(\frac{\triangle w}{w}\right)_{Max}$ are approximated by:

$$\left(\frac{\triangle w}{w}\right)_{Max} \leq \sqrt{\frac{(\triangle A_1)^2 + (\triangle A_2)^2}{(A_1 - A_2)^2}} + \sqrt{2} \cdot \frac{\triangle t}{|t_1 - t_2|} \tag{A.4}$$

and presented in Table A.1.

time period	[µs]	0,40	0,80	1,60	3,20	6,40	10,00
$\left(\frac{\triangle w}{w}\right)_{Max}$	[%]	≤13,2	≤6,6	≤3,3	≤1,7	≤0,9	≤0,6

Table A.1.: Dependency of $\left(\frac{\triangle w}{w}\right)_{Max}$ on the sampling rate of the corresponding image sequence: The maximum relative errors are computed by (A.4). A propagating crack with a fracture area velocity of $w = 25\,\frac{m^2}{s}$ is considered under various frame rates. In order to obtain a representative maximum approximation, typical values ($\triangle A_i/A_i = 0{,}1\,\%$, $\triangle t = 17\,\text{ns}$, $A_1 = 500\,\text{mm}^2$) are assumed.

According to these results, the uncertainties become significant for sampling rates over 1 MHz.

Nevertheless it has to be stressed that (A.4) and Table A.1 provide just *maximum* approximations. The *actual* values of $\triangle w/w$ have been individually calculated by (A.3). Mostly they have proven to be considerably lower. Empirically, even for HIEs with frame rates of 2,5 MHz, no uncertainty has exceeded 11,4 %.

A.2. Energy Balances

A.2.1. Total Energy Input E_{tot}

The total energy input is specified by $E_{tot} = \frac{1}{2} \cdot m_H \cdot \left(v_H^2 - v_b^2\right)$, thus its measurement uncertainty is according to the law of error propagation:

$$\triangle E_{tot} = \sqrt{m_H^2 \cdot \left(v_H^2 + v_b^2\right) (\triangle v)^2 + \frac{1}{4} \cdot \left(v_H^2 - v_b^2\right)^2 \cdot (\triangle m_H)^2} \tag{A.5}$$

where the fault tolerance of the applied loading mass $\triangle m_H$ has been 5 g. The propagation velocity of the hammer can be determined with at least $\triangle v = 0{,}01 \, \frac{\mathrm{m}}{\mathrm{s}}$ accuracy.

A.2.2. Kinetic Energies of Fragments E_{kin}

As pointed out in chapter V.6.2, the bulk of E_{kin} causes the motion of coarse HIE fragments ($\phi < -2$), which is detected by a digital infrared video camera. Under these circumstances, due to the relatively low spatial resolution, the accuracy of a translational particle velocity $v_{\phi<-2}$ is approximately given by:

$$\triangle v_{\phi<-2} = 0{,}02 \, \frac{m}{s} \tag{A.6}$$

It has to be considered, that the plane of rotation is not necessarily identical to the plane of view. Therefore the angular particle velocity $\omega_{\phi<-2}$ of a coarse fragment can only be determined with a tolerance of:

$$\triangle \omega_{\phi<-2} = 0{,}1 \, \frac{1}{s} \tag{A.7}$$

According to the law of error propagation the uncertainties of the translational and rotational energies are:

$$\triangle E_{trans,\phi<-2} = \sqrt{\left(0,5 \cdot v_{\phi<-2}^2 \cdot \triangle m_{\phi<-2}\right)^2 + \left(m_{\phi<-2} \cdot v_{\phi<-2} \cdot \triangle v_{\phi<-2}\right)^2} \tag{A.8}$$

$$\triangle E_{rot,\phi<-2} = \sqrt{\left(0,5 \cdot \omega_{\phi<-2}^2 \cdot \triangle \Theta_{\phi<-2}\right)^2 + \left(\Theta_{\phi<-2} \cdot \omega \cdot \triangle \omega_{\phi<-2}\right)^2} \tag{A.9}$$

Furthermore it can be assumed that $\triangle \Theta_{\phi<-2} = \pm 1 \cdot 10^{-8} \mathrm{kg\,m}^2$ and $\triangle m_{\phi<-2} = 0{,}005 \, \mathrm{g}$ (see A.1.1).

In HIEs the amount of $\triangle E_{trans,\phi<-2}$ has been between one and three orders of magnitude larger than $\triangle E_{rot,\phi<-2}$. Empirically, the total uncertainty $\triangle E_{kin,\phi<-2}$ has always been between 1,0 % and 6,4 % of E_{kin}.

According to V.6.2, two approaches have been made to determine the kinetic energy of HIE fragments, referred to as the “three-level valuation model” and the “two-level valuation model”.

As comparative error analyses have revealed that the latter one provides results of higher accuracy this method has been used as a standard method to quantify E_{kin}.

In the two-level valuation model $E_{kin,\phi\geq-2}$ is computed by:

$$E_{kin,\phi\geq-2} = e_{resi} \cdot m_{\phi\geq-2} \tag{A.10}$$

Note that also for fine fragments the particle mass has a tolerance of 0,005 g. This implies that the uncertainty $\triangle E_{kin,\phi\geq-2}$ is dominated by the considerable large variation $\triangle e_{resi} = 0{,}30 \frac{\mathrm{mJ}}{\mathrm{g}}$:

$$\triangle E_{kin,\phi\geq-2} = \left[\frac{\triangle e_{resi}}{e_{resi}} + \frac{\triangle m_{\phi\geq-2}}{m_{\phi\geq-2}}\right] \cdot E_{kin,\phi\geq-2} \approx \frac{\triangle e_{resi}}{e_{resi}} \cdot E_{kin,\phi\geq-2} \tag{A.11}$$

The maximum total uncertainty is given by:

$$\triangle E_{kin} = \triangle E_{trans,\phi<-2} + \triangle E_{rot,\phi<-2} + \triangle E_{kin,\phi\geq-2}$$

It has to be stressed that the two-level validation model provides just a rough approximation of $E_{kin,\phi\geq-2}$, based on statistical data. Nevertheless, the large uncertainties of this method are still acceptable, as the kinetic energies of coarse particles are dominant ($E_{kin,\phi<-2}/E_{kin} \gtrsim 95\,\%$).

A.2.3. Energies Dissipating into the Setup E_{setup}

The percentage of the energies E_{setup} which have dissipated into the setup is - compared to the other energy terms - nearly negligible. Nevertheless, for the sake of completeness, the amounts of E_{setup} have been quantified in the experiments. The corresponding uncertainties $\triangle E_{setup}$ can be assumed to be 50 % without any significant consequences on the total energy balance.

A.2.4. Plastic Deformation Energies E_{def}

The notch depth of the hammer head can be measured with a tolerance of 10 µm. As pointed out in chapter V.6.4, the measurement uncertainty of the plastic deformation energy can be estimated:

$$\triangle E_{def} = \pm 2\,\mathrm{mJ} \tag{A.12}$$

A.2.5. Acoustic Energies E_{air}

As E_{air} has been estimated on the basis of literature values, the uncertainty has been assumed comparatively large. Thus the relative error is reckoned to be 10 %. Hence:

$$\triangle E_{air} = 10\,\% \cdot E_{air} = 0{,}005 \cdot E_{tot} \tag{A.13}$$

A.2.6. Fracture Energies E_{frac}

Finally, the maximum uncertainty of E_{frac} can be approximated by:

$$\triangle E_{frac} \leq \triangle E_{tot} + \triangle E_{kin} + \triangle E_{setup} + \triangle E_{def} + \triangle E_{air} \tag{A.14}$$

A.3. Energy Dissipation Rates $e(t)$

According to chapter V.9 the energy dissipation rates are defined by:

$$e(t) = \eta \cdot w(t) \tag{A.15}$$

Hence the uncertainty Δe is:

$$\Delta e = e(t) \cdot \sqrt{\left(\frac{\Delta\eta}{\eta}\right)^2 + \left(\frac{\Delta w}{w(t)}\right)^2} \tag{A.16}$$

Note that Δw can be computed by (A.3). The values of $\triangle\eta$ have been determined by means of the corresponding standard errors and standard deviations, presented in Table 44 and Table 46.

Danksagung

Ich möchte mich bei all denjenigen ganz herzlich bedanken, die mit Rat, Tat und gutem Willen zum Gelingen dieser Arbeit beigetragen haben. Insbesondere möchte ich danken:

- *Prof. Vladimir Dyakonov* für seine Bereitschaft diese interdisziplinäre Arbeit zu betreuen.

- *Prof. Bernd Zimanowski* für seine stets motivierende und hilfsbereite Unterstützung und Betreuung. Die vielen fruchtbaren und stets hilfreichen Diskussionen mit ihm waren nicht nur für meine Arbeit ein unschätzbarer Gewinn.

- *Prof. Pierfrancesco Dellino*, *Prof. Luigi La Volpe*, *Dr. Daniela Mele*, *Fabio Dioguardi*, *Dr. Rosanna Bonasia* und *Dr. Vincenzo Festa* für die herzliche Gastfreundschaft an der Universität Bari und die fruchtbare Zusammenarbeit unter anderem auf dem Gebiet der vergleichenden Partikelanalysen.

- *Prof. Georg Reents,* dessen hilfreiche Tipps zur Entwicklung der TEH entscheidend beigetragen haben.

- *Prof. Volker Lorenz* für die vielen spannenden und aufschlussreichen Einblicke in die Vulkanologie - im Labor und im Gelände.

- *Anton Uttinger* für die technische Unterstützung und *Rupert Wassermann* für das Präparieren der Glasproben.

- *Günter Friedrich* von der Kreisbildstelle Aschaffenburg und *Prof. Peter Bradl* von der FH Würzburg-Schweinfurt für die freundliche Zurverfügungstellung hochauflösender Scanner.

- Allen aktuellen und ehemaligen Mitgliedern des PVL mit denen ich zusammenarbeiten durfte, namentlich *Dr. Ingo Sonder* für seine unerschütterliche Hilfsbereitschaft und die vielen anregenden Diskussionen, *Prof. Ralf Büttner* für seine hilfsbereite Unterstützung, sowie *Hermann Beyrichen, Andrea Bosmans*, *Michael Eitel*, *Daniel Hendel*, *Manuel Hobiger*, *Jenny Di Leo, Simone Jordan, Phillip Revilak, Andrea Schmid*, *Rolf Seegelken*, *Thorsten Seehaus, Katharina Willmes* und *Werner Wittmann* für die kollegiale und freundschaftliche Arbeitsatmosphäre.

- *Jutta Lingstädt* und *Dr. Frank Holzförster,* sowie allen Mitgliedern des Geologischen Institutes für die vielen sonnigen Stunden und die unerschrockene Tapferkeit auf den Decks der Titanic.

- *Prof. Magnús Guðmundsson* und *Björn Oddsson* für die vielen interessanten Gespräche und für die fürsorgliche Versorgung mit Brennivín.

- *Dr. David Foster* für sein entgegenkommendes Korrekturlesen dieser Arbeit.

- Der Friedrich-Ebert-Stiftung, von deren Unterstützung ich nicht nur finanziell, ideell und promotionsbezogen profitiert habe, sondern auch menschlich. In diesem Zusammenhang möchte ich auch ganz herzlich allen Mitgliedern "meiner" ehemaligen Hochschulgruppe für ihre tatkräftige Mitarbeit danken. Mein dickes Dankeschön gilt dabei auch *Dr. Nico Jannicke* für die freundschaftlichen Statistik-Lektionen am Rhein (welche einen signifikanten Einfluss auf mich und meine Arbeit hatten!) und *Dr. Valentina Knezevic* für ihre stete moralische Unterstützung und die schönen Tage an der Spree.

- Ganz besonders lieben Dank meinen Eltern, die mich über all die Jahre hinweg in jeglicher Hinsicht unterstützt haben, und meinen Geschwistern *Lucie* und *Johannes*. Meine Familie stand mir in allen Lagen mit Rat und Tat zur Seite. Euch zu haben sehe ich als Beleg dafür, dass am alten Sprichwort "Scherben bringen Glück" etwas dran sein muss...

- Und "last but not least" *Kurt Heisel*, meinem Großvater, dem ich diese Arbeit widmen möchte.

Lebenslauf

Name:	Tobias Christian Dürig
geboren am:	30.04.1979
Geburtsort:	Aschaffenburg

Schulbildung:

09/1985 - 07/1989:	Gutenberg-Grundschule (Aschaffenburg)
09/1989 - 06/1998:	Karl-Theodor-v.-Dalberg-Gymnasium (Aschaffenburg)
06/1998:	Abschluss: Abitur

Wehrdienst:

07/1998 - 04/1999:	Grundwehrdienst als Flugbetriebsspezialist

Studium und Promotion:

05/1999 - 02/2005:	Physikstudium an der Universität Würzburg
02/2004 - 02/2005:	Diplomarbeit: *Visualisierung dynamischer Bruchprozesse bei Gläsern*
02/2005:	Studienabschluss: Diplom
03/2005 - 12/2005:	Einarbeitung in geologische und vulkanologische Grundlagen am Geologischen Institut der Universität Würzburg
seit 12/2005:	Promotion
07/2006 – 07/2009:	Graduierten-Stipendium der Friedrich-Ebert-Stiftung (FES)
12/2006:	Wilhelm-Conrad-Röntgen Studienpreis der Universität Würzburg

Studien- und promotionsbegleitende Tätigkeiten:

08/2002 - 09/2002:	Praktikum im Physikalischen Zentrallabor des Kriminaltechnischen Institutes im Bundeskriminalamt (KT 11)
04/2006 - 07/2011:	Lehraufträge am Physikalisch Vulkanologischen Labor, Universität Würzburg

Forschungsaufenthalte im Ausland:

05/2008 - 08/2008:	Dipartimento Geomineralogico, Universität Bari (Italien)
05/2009 - 08/2009:	Dipartimento Geomineralogico, Universität Bari (Italien)

Würzburg, ______________

____
Tobias Dürig

List of Own Publications in Peer-reviewed Journals

- Dürig, T.; Mele, D.; Dellino, P.; Zimanowski, B. (2011);
  COMPARATIVE ANALYSES OF GLASS FRAGMENTS FROM BRITTLE FRACTURE EXPERIMENTS AND VOLCANIC ASH PARTICLES;
  Bull. Volcanol.; 74 (3); p. 691. DOI: 10.1007/s00445-011-0562-0
- Dürig, T.; Sonder, I.; Zimanowski, B.; Beyrichen, H.; Büttner, R. (2011);
  GENERATION OF VOLCANIC ASH BY BASALTIC VOLCANISM;
  J. Geophys. Res.; 117; p. B01204. DOI: 10.1029/2011JB008628
- Dürig, T.; Dioguardi, F.; Büttner, R.; Dellino, P.; Mele, D.; Zimanowski, B. (2011);
  A NEW METHOD FOR THE DETERMINATION OF THE SPECIFIC KINETIC ENERGY (SKE) RELEASED TO PYROCLASTIC PARTICLES AT MAGMATIC FRAGMENTATION: THEORY AND FIRST EXPERIMENTAL RESULTS;
  Bull. Volcanol.; 74 (4); p. 895. DOI: 10.1007/s00445-011-0574-9
- Dürig, T.; Zimanowski, B. (2012);
  "BREAKING NEWS" ON THE FORMATION OF VOLCANIC ASH: FRACTURE DYNAMICS IN SILICATE GLASS;
  Earth Planet. Sci. Lett.; 335-336; p. 1. DOI: 10.1016/j.epsl.2012.05.001

Versicherung an Eides statt

gemäß § 5 Abs. 2 Ziff. 2

der Promotionsordnung der Fakultät für Physik und Astronomie

der Universität Würzburg

Hiermit versichere ich an Eides statt, dass ich die vorliegende Dissertation selbstständig verfasst und ohne die Hilfe eines Promotionsberaters angefertigt habe sowie keine anderen als die angegebenen Quellen und Hilfsmittel verwendet habe.

Die Dissertation wurde bisher weder vollständig noch teilweise einer anderen Hochschule oder in einem anderen Prüfungsfach mit dem Ziel vorgelegt, einen akademischen Grad zu erwerben.

Am 08. März 2005 wurde mir von der Universität Würzburg der akademische Grad „Diplom- Physiker (Univ.) verliehen. Weitere akademische Grade habe ich weder erworben noch versucht zu erwerben.

Würzburg, ______________

____

Tobias Dürig

B. Daisy Chain Discriminant Analysis Procedures

B.1. The Influence of the Impact Velocity

Figure B.1 presents the maximum force amplitudes of each first peak group in correlation to the impact velocities. As the hammer has been released from six different positions, the data points are not continuously distributed. Although a positive correlation between the maximum peaks and the velocities can be observed, other influencing parameters seem to have bigger effects. This conclusion is confirmed by the results of correlation analyses, which are presented in Table B.1: The corresponding Pearson correlation coefficients are given by 0,302 resp. 0,303.

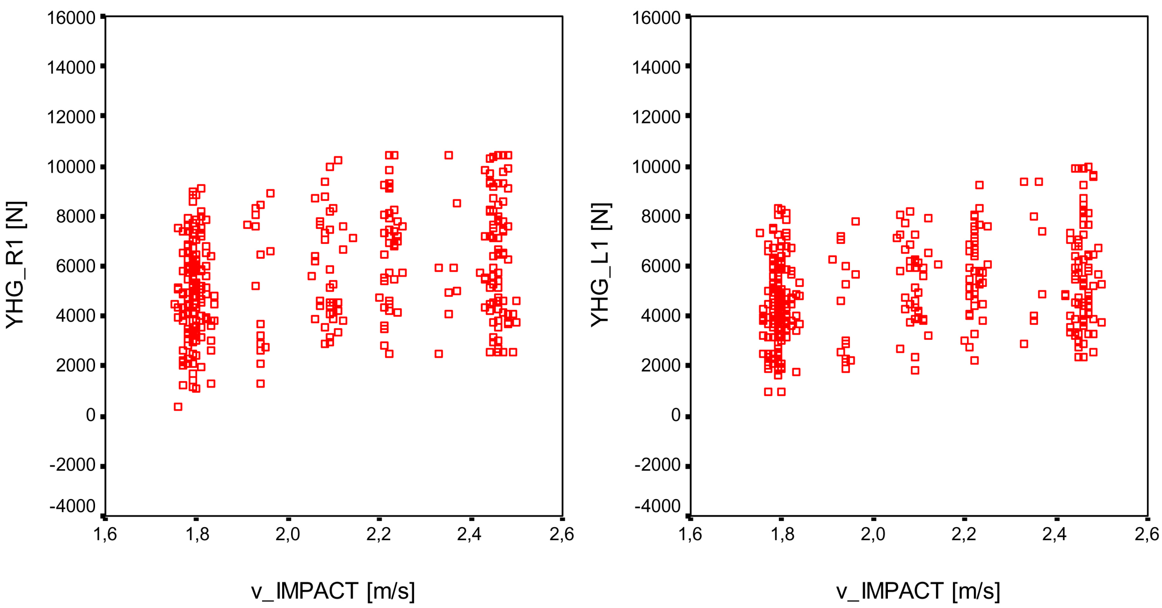

Figure B.1.: Maximum peaks: The maximum values of force amplitudes detected by the right (YHG_R1) and by the left (YHG_L1) force sensor are plotted over impact velocities.

B.2. Parametrization of the Force Signal

For the parametrization only signals are considered, which occur in a period of 200 µs after the first slope. All force signals have been characterized by determining a number of significant parameters, which are also listed in Table B.2:

- The number of peak groups (left and right signal: 2 parameters)

		V_HAMMER	YHG_L1
V_HAMMER	Pearson Correlation	1	,302**
	Sig. (2-tailed)	,	,000
	N	273	273
YHG_L1	Pearson Correlation	,302**	1
	Sig. (2-tailed)	,000	,
	N	273	273

**. Correlation is significant at the 0.01 level (2-tailed).

		peakhöhe	V_HAMMER
peakhöhe	Pearson Correlation	1	,303**
	Sig. (2-tailed)	,	,000
	N	273	273
V_HAMMER	Pearson Correlation	,303**	1
	Sig. (2-tailed)	,000	,
	N	273	273

**. Correlation is significant at the 0.01 level (2-tailed).

Table B.1.: Results of correlation analyses: These tests reveal highly significant correlations between v_H (denoted as "V_HAMMER") and YHG_L1 as well as between v_H and YHG_R1 (referred to as "peakhöhe").

- The maximum amplitude in each peak group (three peak groups for each signal: 6 parameters)
- The center of the maximum peaks in each peak group (6 parameters)
- The area under each peak group (6 parameters)
- The centroids of each peak group (6 parameters)
- Full width at half maximum (FWHM) of each peak group (6 parameters)
- Time interval at the foot of each peak group ("foot width", 6 parameters)
- Left and right width at half maximum of each peak group (12 parameters)
- Number of peaks in each peak group (6 parameters)
- Maximum and minimum time intervals between two peaks within a peak group (12 parameters)
- Area under each peak group per foot width (6 parameters)
- The ratio between the sum of all areas and the total foot width (2 parameters)
- The ratio between the maximum amplitude in each peak group and its respective foot width (6 parameters)
- The ratio between the sum of all maximum amplitudes in each peak group and the total foot width (2 parameters)
- Special characteristics of the force signal, revealed by the SFA (see next section, 5 parameters).

Hence, each data set characterizes the force signals by 89 parameters, which are subsequently z-standardized [11].

All statistical operations have been performed by means of SPSS 11.0.

It is important to note that not all of the parameters can be presumed as linearly independent, which however is a crucial prerequisite for discriminant analysis [11, 52, 71].

Thus, one has to check the dependencies of each variable first, in order to omit all linearly dependent parameters for the subsequent discriminant analysis. This operation is done as a standard test by SPSS, before finding the most suitable parameters for the discriminant functions.

	all	_R1	_R2	_R3	_L1	_L2	_L3
number of peak groups	anzhgrr, anzhgrl						
max. peak group amplitudes		yhg	yhg	yhg	yhg	yhg	yhg
peak center		xpc	xpc	xpc	xpc	xpc	xpc
area under the curve		a	a	a	a	a	a
centroid		xc	xc	xc	xc	xc	xc
full width at half maximum		hw	hw	hw	hw	hw	hw
foot width		do	do	do	do	do	do
left WHM		lhw	lhw	lhw	lhw	lhw	lhw
right WHM		rhw	rhw	rhw	rhw	rhw	rhw
number of peaks		zp	zp	zp	zp	zp	zp
max. time interval between 2 peaks		mx2p	mx2p	mx2p	mx2p	mx2p	mx2p
min. time interval between 2 Peaks		mi2p	mi2p	mi2p	mi2p	mi2p	mi2p
area under peak group per foot width		apf	apf	apf	apf	apf	apf
total area per total time	fpg_r, fpg_l						
yhg per foot width		hpf	hpf	hpf	hpf	hpf	hpf
sum of all yhg per total time	mpg_r, mpg_l						
special characteristics	m_sp, m_fp, m_2gr, m_ap, m_x						

Table B.2.: Survey and identifiers of characteristic signal parameters: Basically, the suffix R (L) denotes the parameter of the right (left) signal, the attached number indicates the peak group. Thus, for example the parameter “zp_L2” gives the number of peaks in the second peak group of the left signal.

B.3. Signal Form Analysis (SFA)

At first, the signals are categorized according to their form by plotting the curves and checking them for distinct anomalies.

By this visual inspections the force signal can be characterized as "normal" or "abnormal". The latter signals can be subdivided into several characteristic types, which are illustrated in Figure B.2.

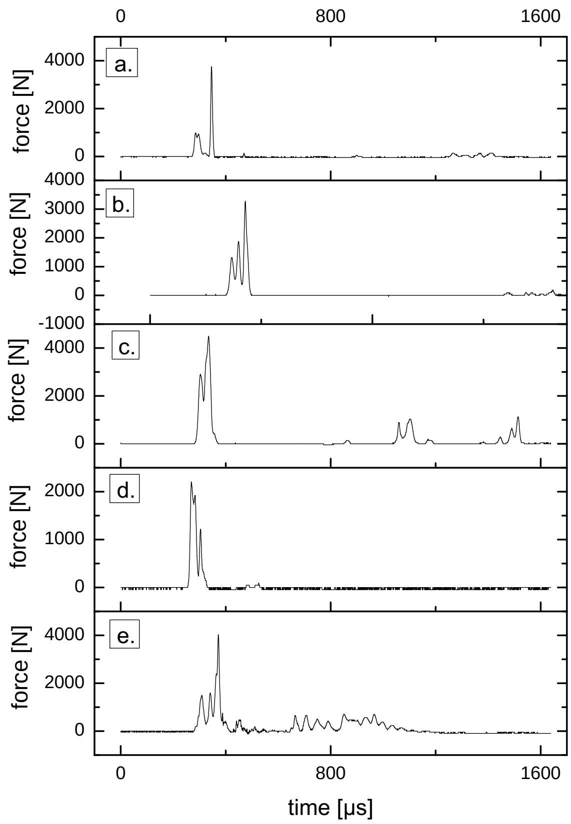

Figure B.2.: Examples for "abnormal" signal curves: In the following the corresponding characteristic parameters are given in square brackets. The shown subtypes are referred to as "precursor peak signal" [m_2gr] (a.), "broken peak signal" [m_ap] (b.), "aftershock peak signal" [m_sp] (c.), "shallow peak signal" [m_fp] (d.) and "strange peak signal" [m_x] (e.).

The empirical frequency of each signal form is given by Table B.3. Note that a data set of an abnormal signal often shows a superposition of several special forms.

Signals classified as "normal" allows the appliance of a PCDA (see B.8) without restrictions. Also in the case of "abnormal" signal forms, it has been experimentally verified, that a PCDA provides useful results, but only for FG, T5 or T10 targets.

As the database for the other target types (TK, AS, RX) has been too low to conduct a highly reliable discriminant analysis, those cases have to be filtered out. However, many indications suggest that the principle of abnormal signal form PCDA could also be transferred to the "missing" target types by broadening the empirical database.

normal	abnormal	precursor	aftershock	broken	shallow	strange	jammed
89,4 %	10,6 %	0,4 %	4,4 %	7,0 %	0,8 %	0,3 %	4,2 %

Table B.3.: Frequency of signal forms, related to the total number of data sets: About 4,2 % of the data records have to be omitted, because they correspond to "jammed" HIE. Those signals are characterized by peaks of high amplitude occurring more than 200 µs after the first slope.

B.4. General Procedure to Test and Optimize Discriminant Analysis Operations

In general, the statistic analysis program SPSS allows several variations of discriminant analysis. (For further details, see [11].) To find a method providing the most reliable results, all possibilities have been tested and compared by "hit-miss" classification tables (the final "hit-miss" results are summarized in Table 10) in addition to further statistical key figures:

- The number of discriminant coefficients in comparison to the number of data sets: An essential precondition for a reliable discriminant analysis is, that the number of discriminating variables in the discriminant function is lower than the applied sample size [52], which in our case totaled 357.
- Discriminant functions of high quality are characterized by the fact, that their mean values differ significantly for each group [52]. In order to check if this is the case, the eigenvalues are computed. This value also allows to determine the corresponding canonical correlation coefficient and Wilk's lambda as additional characteristic values. Eigenvalues are also denominated "discriminant criteria" and are given by the quotients of the variation between the groups and the variation within the groups [11]. Thus, a high eigenvalue (as well as a high value for the canonical correlation coefficient and a low value for Wilk's lambda) indicates a good discriminatory power of the tested model. Therefore, the results for all these key figures are displayed for each discriminant analysis.
- Another possibility to check the discriminatory power of a model is to analyze the function values at the group centroids: A good model is characterized by significantly different values.

B.5. Conchoidal Crack Discriminant Analysis (CCDA)

B.5.1. CCDA Settings

In the case of a CCDA the optimal settings are:

- Analysis: CCDA
- Number of classes: 5
- Method: Stepwise optimization of the Mahalanobis distance
- F-value Entry: 0,07; removal: 0,15 (F describes the error probability for the model [11].)
- Prior Probabilities: Computed from group size

- Used covariance matrix: Separate groups
- Used variables: hstufe, (a parameter describing the position of hammer release) plus all characteristic parameters listed in Table B.2 except of m_sp, m_fp, m_2gr, m_ap and m_x

The following SPSS script code was used:

```
DISCRIMINANT
/GROUPS=startmr(0 4)
/VARIABLES=hstufe zanzhg_r zanzhg_l zyhg_r1 zyhg_r2 zyhg_r3 zyhg_l1 zyhg_l2 zyhg_l3 za_r1 za_r2 za_r3 za_l1 za_l2 za_l3 znc_r1 znc_r2 znc_r3 znc_l1 znc_l2 znc_l3 znpc_r1 znpc_r2 znpc_r3 znpc_l1 znpc_l2 znpc_l3 zfwhm_r1 zfhwm_r2 zfhwm_r3 zfwhm_l1 zfwhm_l2 zfwhm_l3 zlhw_r1 zlhw_r2 zlhw_r3 zlhw_l1 zlhw_l2 zlhw_l3 zrhw_r1 zrhw_r2 zrhw_r3 zrhw_l1 zrhw_l2 zrhw_l3 zdo_r1 zdo_r2 zdo_r3 zdo_l1 zdo_l2 zdo_l3 zzp_r1 zzp_r2 zzp_r3 zzp_l1 zzp_l2 zzp_l3 zmx2p_r1 zmx2p_r2 zmx2p_r3 zmx2p_l1 zmx2p_l2 zmx2p_l3 zmi2p_r1 zmi2p_r2 zmi2p_r3 zmi2p_l1 zmi2p_l2 zmi2p_l3 zhpf_r1 zhpf_r2 zhpf_r3 zhpf_l1 zhpf_l2 zhpf_l3 zmpg_r zmpg_l zapf_r1 zapf_r2 zapf_r3 zapf_l1 zapf_l2 zapf_l3 zfpg_r zfpg_l
/ANALYSIS ALL
/SAVE=CLASS SCORES PROBS
/METHOD=MAHAL
/PIN= .07
/POUT= .15
/PRIORS SIZE
/HISTORY
/STATISTICS=UNIVF BOXM COEFF RAW TCOV TABLE
/PLOT=COMBINED SEPARATE MAP
/CLASSIFY=NONMISSING SEPARATE .
```

B.5.2. CCDA Results

To document the results of the material-specific CCDAs, the canonical discriminant function coefficients are shown in Table B.4.

Canonical Discriminant Function Coefficients

TARGET		Function 1	2	3	4
FG	HSTUFE	-,434	,496	,277	-,021
	Zscore(LHW_R2)	-,356	-,372	-,046	,515
	Zscore(YHG_L1)	,575	-,576	,613	,461
	Zscore: peakhöhe	,627	,801	-,862	,105
	Zscore(ZP_R2)	,852	-,213	,460	-,246
	Zscore(ZP_R3)	-,865	-,254	-,492	,369
	(Constant)	,802	-1,679	-,898	-,177
T5	Zscore(A_L1)	,856	,494	,495	
	Zscore(DO_R3)	-,732	,579	,747	
	Zscore(ZP_R3)	,921	,176	-1,342	
	(Constant)	,145	-,101	-,018	
T10	Zscore(APF_L3)	,515	-2,108	-,018	
	Zscore(APF_R1)	,137	,468	1,215	
	Zscore(APF_R2)	,154	,335	1,700	
	Zscore(A_L2)	4,716	1,388	-,653	
	Zscore(DO_L2)	-2,476	,601	,187	
	Zscore: Fußbreite	-,107	1,146	1,289	
	Zscore(HPF_L3)	2,075	,229	,225	
	Zscore(MI2P_L1)	-6,709	1,483	,637	
	Zscore: min Peakabstand	1,356	1,188	-,213	
	Zscore(NC_L2)	8,229	-3,913	3,565	
	Zscore(NPC_L2)	-6,908	3,236	-3,748	
	Zscore(YHG_L3)	-3,912	1,471	-,419	
	Zscore(ZP_L3)	2,549	-1,034	,495	
	Zscore: Anzahl Peaks	,684	-,894	-,901	
	(Constant)	-,955	,492	,216	
TK	Zscore: max Peakabstand	1,293	,588	,255	1,154
	Zscore: Centroid	-2,830	5,689	-5,481	-3,897
	Zscore: PeakCenter	4,828	-4,722	2,676	1,242
	Zscore(RHW_L1)	1,276	2,184	1,946	,059
	Zscore(YHG_L1)	,423	2,582	-,490	,078
	(Constant)	1,244	,837	-,664	-,566
AS	Zscore: Halbwertsbreite	-1,767	1,309	-,529	-,135
	Zscore(MX2P_L2)	1,465	-1,206	,112	1,465
	Zscore(MX2P_R3)	-1,758	-,497	,466	-,059
	Zscore(RHW_L2)	,890	-,092	,617	-,768
	Zscore(ZP_R3)	2,480	1,617	1,178	,524
	(Constant)	1,737	-,718	,310	,400
RX	HSTUFE	,211	,503	,125	-,130
	Zscore(APF_R1)	-,623	,825	-,529	1,308
	Zscore(A_R2)	-3,467	-1,529	2,253	-,574
	Zscore(DO_L1)	,240	-1,296	-1,535	,106
	Zscore(DO_R3)	,807	-,818	1,168	,150
	Zscore: Halbwertsbreite	,333	,593	1,008	-,656
	Zscore(HPF_L1)	2,684	-4,585	-1,508	3,872
	Zscore(MI2P_R2)	-,775	,864	,790	,600
	Zscore(MPG_R)	2,280	,204	,390	-1,416
	Zscore(MX2P_R2)	6,965	2,269	-1,248	1,541
	Zscore(YHG_L1)	-,912	2,477	-,247	-1,612
	Zscore: peakhöhe	-1,492	-1,633	1,007	,212
	Zscore(ZP_L1)	,893	-,083	,213	,660
	(Constant)	,096	-2,080	-,547	,490

Table B.4.: Canonical discriminant function coefficients of CCDAs.

In this table one can identify all parameters, which are relevant for the discriminant procedure. However, these coefficients are not yet standardized. Those values are shown in Table B.5, which allows to get a quantitative impression of each coefficient's influence.

TARGET		Function 1	2	3	4
FG	HSTUFE	-,770	,879	,490	-,037
	Zscore: peakhöhe	,610	,780	-,839	,102
	Zscore(YHG_L1)	,671	-,672	,716	,538
	Zscore(LHW_R2)	-,451	-,471	-,058	,652
	Zscore(ZP_R2)	,847	-,211	,457	-,244
	Zscore(ZP_R3)	-,884	-,259	-,503	,377
T5	Zscore(ZP_R3)	,972	,186	-1,416	
	Zscore(A_L1)	,795	,459	,460	
	Zscore(DO_R3)	-1,051	,832	1,072	
T10	Zscore(YHG_L3)	-4,197	1,578	-,449	
	Zscore(A_L2)	2,467	,726	-,342	
	Zscore(NC_L2)	7,307	-3,474	3,165	
	Zscore(NPC_L2)	-6,207	2,908	-3,368	
	Zscore: Fußbreite	-,080	,853	,959	
	Zscore(DO_L2)	-2,468	,599	,186	
	Zscore: Anzahl Peaks	,573	-,750	-,756	
	Zscore(ZP_L3)	2,655	-1,077	,516	
	Zscore: min Peakabstand	,758	,664	-,119	
	Zscore(MI2P_L1)	-1,230	,272	,117	
	Zscore(HPF_L3)	,720	,080	,078	
	Zscore(APF_R1)	,127	,434	1,126	
	Zscore(APF_R2)	,110	,240	1,216	
	Zscore(APF_L3)	,413	-1,692	-,015	
TK	Zscore(YHG_L1)	,260	1,586	-,301	,048
	Zscore: Centroid	-,725	1,457	-1,404	-,998
	Zscore: PeakCenter	1,406	-1,375	,779	,362
	Zscore(RHW_L1)	,560	,959	,855	,026
	Zscore: max Peakabstand	,983	,447	,194	,878
AS	Zscore(ZP_R3)	1,276	,832	,606	,270
	Zscore: Halbwertsbreite	-1,150	,852	-,344	-,088
	Zscore(RHW_L2)	,776	-,080	,538	-,670
	Zscore(MX2P_R3)	-1,552	-,439	,411	-,052
	Zscore(MX2P_L2)	,724	-,596	,055	,724
RX	HSTUFE	,450	1,071	,266	-,277
	Zscore: peakhöhe	-1,314	-1,439	,888	,187
	Zscore(YHG_L1)	-,738	2,005	-,200	-1,305
	Zscore(DO_R3)	,447	-,453	,647	,083
	Zscore(APF_R1)	-,515	,682	-,438	1,081
	Zscore: Halbwertsbreite	,393	,699	1,188	-,773
	Zscore(A_R2)	-1,694	-,747	1,101	-,280
	Zscore(DO_L1)	,229	-1,235	-1,462	,101
	Zscore(ZP_L1)	,906	-,085	,216	,669
	Zscore(MX2P_R2)	1,834	,597	-,329	,406
	Zscore(MI2P_R2)	-,649	,724	,662	,503
	Zscore(HPF_L1)	1,071	-1,829	-,602	1,544
	Zscore(MPG_R)	2,035	,182	,348	-1,264

Table B.5.: Standardized canonical discriminant function coefficients of CCDAs.

The results of CCDAs indicate that conchoidal cracks have a very complex influence, which is distinctly depending on the target type. The number of discriminant variables varies between 3 and 14 (see also Table B.6), which is significantly lower than the number of classified cases (i.e. 357). Thus, a basic precondition for a high quality discriminant analysis is satisfied.

	FG	T5	T10	TK	AS	RX
functions	4	3	3	4	4	4
variables	6	3	14	5	5	13

Table B.6.: Number of variables and functions of CCDAs.

Additionally the calculated eigenvalues, the canonical correlation coefficients and the corresponding Wilk's lambdas are listed (see Table B.7 and B.8) to check the discriminatory power of the CCDAs.

TARGET	Function	Eigenvalue	% of Variance	Cumulative %	Canonical Correlation
FG	1	1,008[a]	71,4	71,4	,709
	2	,316[a]	22,4	93,8	,490
	3	,072[a]	5,1	98,9	,258
	4	,016[a]	1,1	100,0	,125
T5	1	,432[b]	58,7	58,7	,549
	2	,273[b]	37,1	95,7	,463
	3	,031[b]	4,3	100,0	,174
T10	1	3,675[c]	67,9	67,9	,887
	2	1,227[c]	22,7	90,6	,742
	3	,511[c]	9,4	100,0	,581
TK	1	2,616[d]	51,8	51,8	,851
	2	1,992[d]	39,4	91,2	,816
	3	,408[d]	8,1	99,3	,538
	4	,038[d]	,7	100,0	,190
AS	1	5,848[e]	61,5	61,5	,924
	2	2,017[e]	21,2	82,8	,818
	3	1,226[e]	12,9	95,7	,742
	4	,412[e]	4,3	100,0	,540
RX	1	3,918[f]	56,8	56,8	,893
	2	2,170[f]	31,5	88,3	,827
	3	,663[f]	9,6	97,9	,631
	4	,146[f]	2,1	100,0	,357

Table B.7.: Eigenvalues and canonical correlation coefficients of CCDAs.

TARGET	Test of Function(s)	Wilks' Lambda	Chi-square	df	Sig.
FG	1 through 4	,348	75,557	24	,000
	2 through 4	,698	25,710	15	,041
	3 through 4	,919	6,075	8	,639
	4	,984	1,134	3	,769
T5	1 through 3	,532	36,602	12	,000
	2 through 3	,762	15,783	6	,015
	3	,970	1,789	2	,409
T10	1 through 3	,064	135,020	42	,000
	2 through 3	,297	59,449	26	,000
	3	,662	20,216	12	,063
TK	1 through 4	,063	55,200	20	,000
	2 through 4	,229	29,494	12	,003
	3 through 4	,685	7,577	6	,271
	4	,964	,738	2	,691
AS	1 through 4	,015	62,603	20	,000
	2 through 4	,105	33,743	12	,001
	3 through 4	,318	17,179	6	,009
	4	,708	5,179	2	,075
RX	1 through 4	,034	166,167	52	,000
	2 through 4	,166	88,113	36	,000
	3 through 4	,525	31,576	22	,085
	4	,873	6,661	10	,757

Table B.8.: Wilk's lambda calculated for the functions of CCDAs.

The high values for the canonical correlation coefficients and for the eigenvalues indicate an excellent discriminatory power of the discriminant functions found by CCDAs. In Table B.8 also the results of Chi square tests are shown, testing the null hypothesis: "All means of the discriminant function values are identical." The last column ("Sig.") presents the corresponding error probabilities by rejecting this hypothesis (in SPSS defined as "significance" [11]).

Particularly the results for which all discriminant functions are taken into consideration are relevant. These values are listed in the first row for each material.

In the case of CCDAs, the null hypothesis can be rejected with an error probability of less than 0,05 %. In other words: The mean values are characterized by highly significant differences. Thus, the results confirm a high discriminatory quality. This is substantiated by the values of Table B.9, which prove distinct differences in the function values of group centroids.

		Function			
TARGET	STARTMR	1	2	3	4
FG	0	1,489	-,679	,213	-,215
	1	1,359	,105	-,817	2,127E-02
	2	,465	,282	,158	,111
	3	-1,060	-,367	-5,39E-02	-1,37E-05
	4	-,862	1,589	-6,08E-03	-,281
T5	0	1,203	,320	1,189	
	1	1,031	,611	2,314E-02	
	2	,311	8,403E-02	-,121	
	3	-,319	-,432	4,379E-02	
	4	-1,664	1,390	5,103E-02	
T10	1	1,652	2,677	-,419	
	2	,461	-,849	-,869	
	3	,107	-,208	,641	
	4	-7,721	1,003	-,429	
TK	0	3,365	,162	7,906E-02	5,659E-02
	1	-,842	2,052	,640	-9,93E-03
	2	-,354	,111	-,685	-,152
	3	-,798	-1,043	3,962E-02	,196
	4	-3,51E-02	-3,445	1,649	-,533
AS	0	1,424	3,032	1,060	,764
	1	-1,784	,458	-,793	-,178
	2	1,946	-,368	,548	-,624
	3	1,387	-1,440	-,533	,825
	4	-5,799	-1,757	3,065	,346
RX	0	-2,16E-02	2,318	,148	-,696
	1	-,375	1,404	-7,93E-02	,502
	2	-1,026	-1,207	,804	-3,94E-02
	3	,396	-1,049	-1,172	-9,83E-02
	4	9,673	-,465	1,148	,130

Table B.9.: Function values at group centroids (CCDAs).

As outlined above, many indications suggest that damage cracks are not detected directly, but by the scattering effects, which interfere with the specific force signals resulting from normal crack propagation. Under this aspect, the empirical “hit ratios” show a remarkably good accuracy (see Table 10).

Furthermore, this model explains why it is useful to carry out damage crack-specific PCDAs (see B.8).

B.6. W-crack Discriminant Analysis (WCDA)

Settings:

In the following, the settings of the WCDAs are listed:

- Analysis: WCDA
- Examined cases: Occurring W-cracks (1: yes; 0: no)
- Number of classes: 2

- Method: Stepwise optimization of the Mahalanobis distance
- F-value Entry: 0,07; removal: 0,15
- Prior Probabilities: Computed from group size
- Used covariance matrix: Separate groups
- Used variables: all characteristic parameters listed in Table B.2 except of m_2gr, m_ap and m_x

The WCDA script code is:

```
DISCRIMINANT
/GROUPS=startwr(0 1)
/VARIABLES=zanzhg_r zanzhg_l zyhg_r1 zyhg_r2 zyhg_r3 zyhg_l1 zyhg_l2 zyhg_l3
za_r1 za_r2 za_r3 za_l1 za_l2 za_l3 znc_r1 znc_r2 znc_r3 znc_l1 znc_l2 znc_l3 znpc_r1
znpc_r2 znpc_r3 znpc_l1 znpc_l2 znpc_l3 zfwhm_r1 zfhwm_r2 zfhwm_r3 zfwhm_l1 zfwhm_l2
zfwhm_l3 zlhw_r1 zlhw_r2 zlhw_r3 zlhw_l1 zlhw_l2 zlhw_l3 zrhw_r1 zrhw_r2 zrhw_r3
zrhw_l1 zrhw_l2 zrhw_l3 zdo_r1 zdo_r2 zdo_r3 zdo_l1 zdo_l2 zdo_l3 zzp_r1 zzp_r2
zzp_r3 zzp_l1 zzp_l2 zzp_l3 zmx2p_r1 zmx2p_r2 zmx2p_r3 zmx2p_l1 zmx2p_l2 zmx2p_l3
zmi2p_r1 zmi2p_r2 zmi2p_r3 zmi2p_l1 zmi2p_l2 zmi2p_l3 zymx_r1 zymx_r2 zymx_r3
zymx_l1 zymx_l2 zymx_l3 zhpf_r1 zhpf_r2 zhpf_r3 zhpf_l1 zhpf_l2 zhpf_l3 zmpg_r
zmpg_l zapf_r1 zapf_r2 zapf_r3 zapf_l1 zapf_l2 zapf_l3 zfpg_r zfpg_l m_sp m_fp hstufe
/ANALYSIS ALL
/METHOD=MAHAL
/PIN= .07
/POUT= .15
/PRIORS SIZE
/HISTORY
/STATISTICS=UNIVF BOXM COEFF RAW CORR COV GCOV TCOV TABLE
/PLOT=COMBINED SEPARATE MAP
/PLOT=CASES
/CLASSIFY=NONMISSING SEPARATE .
```

Results of Material-Specific WCDAs:

TARGET	Function	Eigenvalue	% of Variance	Cumulative %	Canonical Correlation
FG	1	,793[a]	100,0	100,0	,665
T5	1	,947[b]	100,0	100,0	,697
T10	1	1,395[c]	100,0	100,0	,763
RX	1	,463[d]	100,0	100,0	,563

Table B.10.: Eigenvalues and canonical correlation coefficients of WCDAs.

TARGET	Test of Function(s)	Wilks' Lambda	Chi-square	df	Sig.
FG	1 through 2	,000	71,608	16	,000
	2	,064	20,579	7	,004
T5	1 through 2	,034	21,904	4	,000
	2	,841	1,125	1	,289
T10	1	,000	15,876	2	,000
RX	1 through 2	,000	85,965	22	,000
	2	,058	25,642	10	,004

Table B.11.: Wilk's lambda calculated for the functions of WCDAs.

	FG	T5	T10	RX
functions	1	1	1	1
variables	6	5	9	4
accuracy [%]	97,0	94,4	100	97,1

Table B.12.: Number of variables and functions of WCDAs. In the last row the empirical "hit ratio" is given as a measure of accuracy.

TARGET		Function 1
FG	HSTUFE	,240
	spätpeaks	1,874
	Zscore(APF_R2)	-,825
	Zscore(LHW_L2)	,739
	Zscore(MI2P_L3)	,600
	Zscore(MPG_R)	,604
	(Constant)	-1,389
T5	spätpeaks	,963
	Zscore: Halbwertsbreite	,726
	Zscore(LHW_L1)	,998
	Zscore: min Peakabstand	-1,228
	Zscore: peakhöhe	,707
	(Constant)	-,203
T10	HSTUFE	,310
	Zscore(ANZHG_L)	-,507
	Zscore(DO_L3)	-1,207
	Zscore(FPG_R)	-1,580
	Zscore(MPG_R)	1,502
	Zscore(MX2P_L1)	,562
	Zscore(MX2P_L3)	2,002
	Zscore(ZP_L2)	,969
	Zscore(ZP_R3)	-,569
	(Constant)	-,717
RX	Zscore(APF_L2)	,772
	Zscore(HPF_R3)	-1,176
	Zscore(NPC_L1)	1,100
	Zscore: max Peakhöhe	1,375
	(Constant)	,084

Table B.13.: Canonical discriminant function coefficients of WCDAs.

TARGET		Function 1
FG	Zscore(LHW_L2)	,351
	Zscore(MI2P_L3)	,511
	Zscore(MPG_R)	,668
	Zscore(APF_R2)	-,494
	spätpeaks	,664
	HSTUFE	,423
T5	spätpeaks	,413
	Zscore: peakhöhe	,707
	Zscore: Halbwertsbreite	,686
	Zscore(LHW_L1)	,760
	Zscore: min Peakabstand	-1,004
T10	Zscore(MPG_R)	1,267
	HSTUFE	,571
	Zscore(ANZHG_L)	-,480
	Zscore(DO_L3)	-1,988
	Zscore(ZP_R3)	-,607
	Zscore(ZP_L2)	,862
	Zscore(MX2P_L1)	,519
	Zscore(MX2P_L3)	2,446
	Zscore(FPG_R)	-1,491
RX	Zscore(NPC_L1)	,777
	Zscore: max Peakhöhe	1,127
	Zscore(HPF_R3)	-,573
	Zscore(APF_L2)	,821

Table B.14.: Standardized canonical discriminant function coefficients of WCDAs.

TARGET	STARTWR	Function 1
FG	0	-,408
	1	1,894
T5	0	-,416
	1	2,205
T10	0	-,313
	1	4,305
RX	0	-,421
	1	1,064

Table B.15.: Function values at group centroids (WCDAs).

B.7. W-crack Bearing Analysis (WCBA)

Settings:

- Analysis: WCBA
- Examined cases: Location of occurring W-cracks (1: right side; 2: left side; 3: both sides)
- Number of classes: 3
- Method: Stepwise optimization of the Mahalanobis distance
- F-value Entry: 0,08; removal: 0,15
- Prior Probabilities: Computed from group size
- Used covariance matrix: Within groups
- Used variables: hstufe, plus all characteristic parameters listed in Table B.2 except of m_sp, m_fp, m_2gr, m_ap and m_x

WCBA script code:

```
DISCRIMINANT
/GROUPS=wrseite(1 3)
/VARIABLES=zanzhg_r zanzhg_l zyhg_r1 zyhg_r2 zyhg_r3 zyhg_l1 zyhg_l2 zyhg_l3
za_r1 za_r2 za_r3 za_l1 za_l2 za_l3 znc_r1 znc_r2 znc_r3 znc_l1 znc_l2 znc_l3 znpc_r1
znpc_r2 znpc_r3 znpc_l1 znpc_l2 znpc_l3 zfwhm_r1 zfhwm_r2 zfhwm_r3 zfwhm_l1 zfwhm_l2
zfwhm_l3 zlhw_r1 zlhw_r2 zlhw_r3 zlhw_l1 zlhw_l2 zlhw_l3 zrhw_r1 zrhw_r2 zrhw_r3
zrhw_l1 zrhw_l2 zrhw_l3 zdo_r1 zdo_r2 zdo_r3 zdo_l1 zdo_l2 zdo_l3 zzp_r1 zzp_r2
zzp_r3 zzp_l1 zzp_l2 zzp_l3 zmx2p_r1 zmx2p_r2 zmx2p_r3 zmx2p_l1 zmx2p_l2 zmx2p_l3
zmi2p_r1 zmi2p_r2 zmi2p_r3 zmi2p_l1 zmi2p_l2 zmi2p_l3 zymx_r1 zymx_r2 zymx_r3
zymx_l1 zymx_l2 zymx_l3 zhpf_r1 zhpf_r2 zhpf_r3 zhpf_l1 zhpf_l2 zhpf_l3 zmpg_r
zmpg_l zapf_r1 zapf_r2 zapf_r3 zapf_l1 zapf_l2 zapf_l3 zfpg_r zfpg_l hstufe
/ANALYSIS ALL
/SAVE=CLASS SCORES PROBS
/METHOD=MAHAL
/PIN= .08
/POUT= .15
/PRIORS SIZE
/HISTORY
/STATISTICS=RAW TABLE
/PLOT=MAP
/PLOT=CASES
/CLASSIFY=NONMISSING POOLED .
```

Results of Material-Specific WCBA:

TARGET	Function	Eigenvalue	% of Variance	Cumulative %	Canonical Correlation
FG	1	900,363[a]	98,4	98,4	,999
	2	14,547[a]	1,6	100,0	,967
T5	1	23,455[b]	99,2	99,2	,979
	2	,189[b]	,8	100,0	,399
T10	1	7852659,5[c]	100,0	100,0	1,000
RX	1	813,454[d]	98,0	98,0	,999
	2	16,272[d]	2,0	100,0	,971

Table B.16.: Eigenvalues and canonical correlation coefficients of WCBAs.

TARGET	Test of Function(s)	Wilks' Lambda	Chi-square	df	Sig.
FG	1 through 2	,000	71,608	16	,000
	2	,064	20,579	7	,004
T5	1 through 2	,034	21,904	4	,000
	2	,841	1,125	1	,289
T10	1	,000	15,876	2	,000
RX	1 through 2	,000	85,965	22	,000
	2	,058	25,642	10	,004

Table B.17.: Wilk's lambda calculated for the functions of WCBAs.

	FG	T5	T10	RX
functions	2	2	1	2
variables	8	2	2	11
WCBA accuracy	100 %	100 %	100 %	100 %

Table B.18.: Number of variables and functions of WCBAs. The empirical "hit ratio" suggest, that the WCBA model is flawless.

TARGET		Function 1	Function 2
FG	Zscore(APF_L1)	-3,698	7,239
	Zscore(APF_R3)	58,652	6,813
	Zscore: Flächeninhalt	6,233	-12,214
	Zscore(A_R2)	24,738	13,399
	Zscore(DO_L2)	7,048	4,248
	Zscore(LHW_R2)	-12,445	-,687
	Zscore(RHW_L2)	-33,770	4,609
	Zscore(RHW_L3)	-9,336	-12,515
	(Constant)	7,107	-6,943
T5	HSTUFE	1,318	,306
	Zscore: max Peakhöhe	3,258	-,605
	(Constant)	-7,258	-,910
T10	Zscore(LHW_R1)	26,481	
	Zscore(NC_R3)	2575,583	
	(Constant)	-331,434	
RX	HSTUFE	14,730	-,993
	Zscore(ANZHG_L)	-26,231	3,030
	Zscore(APF_L1)	1,461	-4,397
	Zscore(APF_L3)	33,616	8,078
	Zscore(DO_L3)	80,203	5,953
	Zscore(DO_R2)	-16,041	4,418
	Zscore(FPG_L)	5,886	7,736
	Zscore(MI2P_L1)	7,114	4,340
	Zscore(MX2P_L1)	-18,982	-,880
	Zscore: PeakCenter	3,485	2,004
	Zscore(RHW_R1)	21,376	2,110
	(Constant)	-36,060	7,322

Table B.19.: Canonical discriminant function coefficients of WCBAs.

TARGET		Function 1	Function 2
FG	Zscore: Flächeninhalt	2,376	-4,655
	Zscore(A_R2)	12,320	6,673
	Zscore(LHW_R2)	-10,044	-,554
	Zscore(RHW_L2)	-17,879	2,440
	Zscore(RHW_L3)	-5,682	-7,617
	Zscore(DO_L2)	4,383	2,642
	Zscore(APF_R3)	17,974	2,088
	Zscore(APF_L1)	-3,259	6,380
T5	Zscore: max Peakhöhe	2,456	-,456
	HSTUFE	2,433	,565
T10	Zscore(NC_R3)	22,018	
	Zscore(LHW_R1)	21,995	
RX	Zscore(APF_L1)	,753	-2,265
	HSTUFE	26,083	-1,758
	Zscore(ANZHG_L)	-23,230	2,683
	Zscore: PeakCenter	3,821	2,197
	Zscore(RHW_R1)	23,288	2,299
	Zscore(DO_R2)	-9,626	2,651
	Zscore(DO_L3)	24,739	1,836
	Zscore(MX2P_L1)	-19,581	-,908
	Zscore(MI2P_L1)	4,908	2,994
	Zscore(APF_L3)	12,879	3,095
	Zscore(FPG_L)	6,069	7,977

Table B.20.: Standardized canonical discriminant function coefficients of WCBAs.

TARGET	WRSEITE	Function 1	Function 2
FG	1	13,255	1,317
	2	19,927	-11,924
	3	-50,826	-,414
T5	1	-3,338	-,206
	2	,685	,552
	3	7,317	-,313
T10	1	-1981,497	
	2	1981,497	
RX	1	-1,099	-3,059
	2	-33,317	4,620
	3	48,084	4,036

Table B.21.: Function values at group centroids (WCBAs).

B.8. Primary Crack Discriminant Analysis (PCDA)

For the subsequent classification by means of PCDA, two cases have to be distinguished: "normal" ($M_R < 3$) and "particularly pronounced" ($M_R \geq 3$) damage crack intensities.

For each case separate discrimination analyses have been carried out.

B.8.1. PCDAs in Case of Normal Crack Intensities ($M_R < 3$)

Settings:

- Analysis: PCDA (for $M_R < 3$)
- Examined cases: Type of occurring primary cracks (1: ACB; 2: ACT; 3: SCM; 4: BCM; 5: TCM; 6: Combination of crack types)
- Number of classes: 6
- Method: Stepwise optimization of the Mahalanobis distance
- F-value Entry: 0,08; removal: 0,15
- Prior Probabilities: Computed from group size
- Used covariance matrix: Within groups
- Used variables: hstufe, plus all characteristic parameters listed in Table B.2 except of m_x

Script code:

```
DISCRIMINANT
/GROUPS=startr(1 6)
/VARIABLES=zanzhg_r zanzhg_l zyhg_r2 zyhg_r3 zyhg_l1 zyhg_l2 zyhg_l3 za_r1
za_r2 za_r3 za_l1 za_l2 za_l3 znc_r1 znc_r2 znc_r3 znc_l1 znc_l2 znc_l3 znpc_r1
znpc_r2 znpc_r3 znpc_l1 znpc_l2 znpc_l3 zfwhm_r1 zfhwm_r2 zfhwm_r3 zfwhm_l1 zfwhm_l2
zfwhm_l3 zlhw_r1 zlhw_r2 zlhw_r3 zlhw_l1 zlhw_l2 zlhw_l3 zrhw_r1 zrhw_r2 zrhw_r3
zrhw_l1 zrhw_l2 zrhw_l3 zdo_r1 zdo_r2 zdo_r3 zdo_l1 zdo_l2 zdo_l3 zzp_r1 zzp_r2
zzp_r3 zzp_l1 zzp_l2 zzp_l3 zmx2p_r1 zmx2p_r2 zmx2p_r3 zmx2p_l1 zmx2p_l2 zmx2p_l3
zmi2p_r1 zmi2p_r2 zmi2p_r3 zmi2p_l1 zmi2p_l2 zmi2p_l3 zymx_r1 zymx_r2 zymx_r3
zymx_l1 zymx_l2 zymx_l3 zhpf_r1 zhpf_r2 zhpf_r3 zhpf_l1 zhpf_l2 zhpf_l3 zmpg_r
zmpg_l zapf_r1 zapf_r2 zapf_r3 zapf_l1 zapf_l2 zapf_l3 zfpg_r zfpg_l hstufe m_sp m_2gr
m_ap m_fp
/ANALYSIS ALL
/SAVE=CLASS SCORES PROBS
/METHOD=MAHAL
/PIN= .08
/POUT= .15
/PRIORS SIZE
/HISTORY
/STATISTICS=RAW TABLE
/PLOT=MAP
/CLASSIFY=NONMISSING POOLED .
```

Results of Material-Specific PCDAs ($M_R < 3$):

TARGET	Function	Eigenvalue	% of Variance	Cumulative %	Canonical Correlation
FG	1	2,400[a]	100,0	100,0	,840
T5	1	3,505[b]	100,0	100,0	,882
T10	1	1,975[c]	75,3	75,3	,815
	2	,647[c]	24,7	100,0	,627
TK	1	5959,228[d]	100,0	100,0	1,000
AS	1	3,058[e]	100,0	100,0	,868
RX	1	9,862[f]	62,1	62,1	,953
	2	4,185[f]	26,3	88,4	,898
	3	1,836[f]	11,6	100,0	,805

Table B.22.: Eigenvalues and canonical correlation coefficients of PCDAs ($M_R < 3$).

TARGET	Test of Function(s)	Wilks' Lambda	Chi-square	df	Sig.
FG	1	,294	43,444	7	,000
T5	1	,222	27,093	4	,000
T10	1 through 2	,204	25,428	6	,000
	2	,607	7,984	2	,018
TK	1	,000	113,007	4	,000
AS	1	,246	14,006	2	,001
RX	1 through 3	,006	136,986	36	,000
	2 through 3	,068	72,583	22	,000
	3	,353	28,149	10	,002

Table B.23.: Wilk's lambda calculated for the functions of PCDAs ($M_R < 3$).

		Function		
TARGET	STARTR	1	2	3
FG	ARU	-1,030		
	norm Mitr	2,217		
T5	ARU	,841		
	norm Mitr	-3,787		
T10	ARU	,526	-,217	
	ARO	-5,036	-1,463	
	norm Mitr	-1,124	1,644	
TK	lin MitR	33,567		
	norm Mitr	-156,646		
AS	ARU	-,464		
	norm Mitr	5,572		
RX	ARU	-1,437	,913	-,415
	ARO	5,459	3,726	4,014
	norm Mitr	,791	-2,935	,589
	KombiR	14,221	,896	-4,373

Table B.24.: Function values at group centroids (PCDAs for $M_R < 3$).

TARGET		Function 1	Function 2	Function 3
FG	spätpeaks	-1,116		
	Zscore(A_L1)	1,001		
	Zscore(FPG_L)	,653		
	Zscore(NC_L1)	-5,505		
	Zscore(RHW_R1)	1,193		
	Zscore(ZP_L1)	1,242		
	Zscore(ZP_R3)	-1,470		
	(Constant)	-1,700		
T5	Zscore(APF_L2)	1,216		
	Zscore(FWHM_L3)	-2,065		
	Zscore(LHW_R3)	1,860		
	Zscore(MX2P_L1)	1,811		
	(Constant)	-,783		
T10	HSTUFE	-1,184	-,344	
	Zscore(APF_L3)	1,198	2,661	
	Zscore(FHWM_R3)	,477	,078	
	(Constant)	2,227	,630	
TK	Zscore(APF_L2)	504,573		
	Zscore(FWHM_L2)	98,135		
	Zscore(HPF_L3)	-4,375		
	Zscore(HPF_R3)	-32,679		
	(Constant)	98,099		
AS	Zscore(APF_R1)	1,109		
	Zscore(MPG_R)	1,496		
	(Constant)	,630		
RX	HSTUFE	-,237	,317	-,251
	spätpeaks	-2,336	1,590	-,891
	Zscore(APF_L3)	-10,462	-2,399	5,559
	Zscore(APF_R1)	-,250	-2,329	,454
	Zscore(A_L3)	10,344	5,865	5,188
	Zscore(FWHM_L3)	5,365	,906	-5,708
	Zscore: Halbwertsbreite	1,236	1,625	,352
	Zscore(HPF_L3)	11,337	1,428	-6,745
	Zscore(HPF_R1)	,696	1,319	-,155
	Zscore(HPF_R3)	-1,833	-1,338	,248
	Zscore(NC_R2)	,284	-,045	,158
	Zscore(NPC_L3)	-8,499	-1,247	2,847
	(Constant)	1,567	-,718	1,569

Table B.25.: Canonical discriminant function coefficients of PCDAs ($M_R < 3$).

		Function		
TARGET		1	2	3
FG	Zscore(A_L1)	,836		
	Zscore(NC_L1)	-1,476		
	Zscore(RHW_R1)	,906		
	Zscore(ZP_R3)	-,793		
	Zscore(ZP_L1)	1,124		
	Zscore(FPG_L)	,709		
	spätpeaks	-,430		
T5	Zscore(FWHM_L3)	-1,191		
	Zscore(LHW_R3)	,995		
	Zscore(MX2P_L1)	1,086		
	Zscore(APF_L2)	,914		
T10	Zscore(FHWM_R3)	1,364	,223	
	Zscore(APF_L3)	,539	1,198	
	HSTUFE	-1,829	-,532	
TK	Zscore(APF_L2)	31,466		
	Zscore(FWHM_L2)	20,416		
	Zscore(HPF_R3)	-14,232		
	Zscore(HPF_L3)	-1,663		
AS	Zscore(MPG_R)	,644		
	Zscore(APF_R1)	,692		
RX	spätpeaks	-,982	,668	-,374
	Zscore(FWHM_L3)	1,882	,318	-2,002
	Zscore(APF_L3)	-4,494	-1,031	2,388
	HSTUFE	-,497	,664	-,525
	Zscore(HPF_R3)	-1,110	-,810	,150
	Zscore(HPF_L3)	5,190	,654	-3,088
	Zscore(APF_R1)	-,183	-1,704	,332
	Zscore(A_L3)	2,238	1,269	1,123
	Zscore(NC_R2)	,897	-,143	,500
	Zscore(NPC_L3)	-4,966	-,728	1,663
	Zscore: Halbwertsbreite	1,854	2,438	,529
	Zscore(HPF_R1)	,665	1,262	-,148

Table B.26.: Standardized canonical discriminant function coefficients of PCDAs ($M_R < 3$).

B.8.2. PCDAs in Case of Particularly Pronounced Crack Intensities ($M_R \geq 3$)

Settings:

- Analysis: PCDA (for $M_R \geq 3$)
- Examined cases: Type of occurring primary cracks (1: ACB; 2: ACT; 3: SCM; 4: BCM; 5: TCM; 6: Combination of cracks)
- Number of classes: 6
- Method: Stepwise optimization of the Mahalanobis distance
- F-value Entry: 0,08; removal: 0,15
- Prior Probabilities: Computed from group size
- Used covariance matrix: Within groups
- Used variables: hstufe, plus all characteristic parameters listed in Table B.2 except of m_x

Script code:

```
DISCRIMINANT
/GROUPS=startr(1 6)
/VARIABLES=zyhg_r1 zyhg_r2 zyhg_r3 zyhg_l1 zyhg_l2 zyhg_l3 za_r1 za_r2 za_r3
za_l1 za_l2 za_l3 znc_r1 znc_r2 znc_r3 znc_l1 znc_l2 znc_l3 znpc_r1 znpc_r2 znpc_r3
znpc_l1 znpc_l2 znpc_l3 zfwhm_r1 zfhwm_r2 zfhwm_r3 zfwhm_l1 zfwhm_l2 zfwhm_l3
zlhw_r1 zlhw_r2 zlhw_r3 zlhw_l1 zlhw_l2 zlhw_l3 zrhw_r1 zrhw_r2 zrhw_r3 zrhw_l1
zrhw_l2 zrhw_l3 zdo_r1 zdo_r2 zdo_r3 zdo_l1 zdo_l2 zdo_l3 zzp_r1 zzp_r2 zzp_r3
zzp_l1 zzp_l2 zzp_l3 zmx2p_r1 zmx2p_r2 zmx2p_r3 zmx2p_l1 zmx2p_l2 zmx2p_l3 zmi2p_r1
zmi2p_r2 zmi2p_r3 zmi2p_l1 zmi2p_l2 zmi2p_l3 zymx_r1 zymx_r2 zymx_r3 zymx_l1
zymx_l2 zymx_l3 zhpf_r1 zhpf_r2 zhpf_r3 zhpf_l1 zhpf_l2 zhpf_l3 zmpg_r zmpg_l zapf_r1
zapf_r2 zapf_r3 zapf_l1 zapf_l2 zapf_l3 zfpg_r zfpg_l zanzhg_r zanzhg_l m_sp m_fp
m_2gr m_ap hstufe
/ANALYSIS ALL
/SAVE=CLASS SCORES PROBS
/METHOD=MAHAL
/PIN= .08
/POUT= .15
/PRIORS SIZE
/HISTORY
/STATISTICS=RAW TABLE
/PLOT=MAP
/CLASSIFY=NONMISSING POOLED .
```

Results of Material-Specific PCDAs ($M_R \geq 3$):

TARGET	Function	Eigenvalue	% of Variance	Cumulative %	Canonical Correlation
FG	1	8,900[a]	74,7	74,7	,948
	2	1,963[a]	16,5	91,2	,814
	3	1,051[a]	8,8	100,0	,716
T5	1	38,995[b]	69,8	69,8	,987
	2	8,004[b]	14,3	84,1	,943
	3	6,655[b]	11,9	96,0	,932
	4	2,207[b]	4,0	100,0	,830
T10	1	4,189[c]	95,3	95,3	,898
	2	,188[c]	4,3	99,6	,398
	3	,017[c]	,4	100,0	,131
AS	1	646,777[d]	100,0	100,0	,999
RX	1	1475,981[e]	94,9	94,9	1,000
	2	62,801[e]	4,0	98,9	,992
	3	12,747[e]	,8	99,8	,963
	4	3,652[e]	,2	100,0	,886

Table B.27.: Eigenvalues and canonical correlation coefficients of PCDAs ($M_R \geq 3$).

TARGET	Test of Function(s)	Wilks' Lambda	Chi-square	df	Sig.
FG	1 through 3	,017	92,181	27	,000
	2 through 3	,165	40,599	16	,001
	3	,488	16,160	7	,024
T5	1 through 4	,000	159,028	48	,000
	2 through 4	,005	94,475	33	,000
	3 through 4	,041	56,015	20	,000
	4	,312	20,396	9	,016
T10	1 through 3	,159	39,474	9	,000
	2 through 3	,827	4,075	4	,396
	3	,983	,370	1	,543
AS	1	,002	3,237	1	,072
RX	1 through 4	,000	117,088	32	,000
	2 through 4	,000	62,355	21	,000
	3 through 4	,016	31,186	12	,002
	4	,215	11,530	5	,042

Table B.28.: Wilk's lambda calculated for the functions of PCDAs ($M_R \geq 3$).

		Function			
TARGET	STARTR	1	2	3	4
FG	ARU	1,872	,992	,652	
	ARO	-1,253	,237	-1,165	
	norm Mitr	,719	-2,523	,416	
	AROMIR	-12,999	,627	2,500	
T5	ARU	-,335	3,495	1,641	-6,22E-02
	ARO	-2,424	,204	-3,690	,527
	norm Mitr	,647	-2,863	1,976	1,648
	AROMIR	-2,445	-2,403	,589	-2,422
	KombiR	27,991	-,194	-2,096	-,973
T10	ARU	-1,49E-02	,314	4,050E-02	
	ARO	-1,622	-,487	-1,62E-02	
	lin MitR	7,343	-,870	,272	
	norm Mitr	2,930	2,369E-02	-,375	
AS	ARU	20,765			
	ARO	-10,382			
RX	ARU	-15,703	10,011	,114	-,503
	ARO	-33,769	-5,395	-3,881	,953
	norm Mitr	11,432	-4,533	1,592	-1,186
	AROMIR	97,791	4,006	-4,913	1,604
	KombiR	-2,260	-,667	6,547	4,666

Table B.29.: Function values at group centroids (PCDAs for $M_R \geq 3$).

TARGET		Function 1	2	3	4
FG	HSTUFE	-,530	,824	,180	
	flachpeaks	-3,761	1,390	2,019	
	Zscore(FHWM_R2)	,445	,553	-,034	
	Zscore(FPG_L)	,319	1,223	,122	
	Zscore(HPF_L1)	2,407	-3,395	2,002	
	Zscore(MX2P_L2)	5,979	2,413	,746	
	Zscore(MX2P_R3)	1,852	1,337	,389	
	Zscore(RHW_R1)	-3,083	-,150	1,182	
	Zscore(ZP_L2)	-1,875	-1,603	,150	
	(Constant)	2,181	-2,338	-,534	
T5	Zscore(ANZHG_L)	-1,026	-1,644	-,469	,421
	Zscore(APF_L3)	1,701	-,725	4,182	-,688
	Zscore(A_L2)	9,629	3,893	-3,563	,620
	Zscore: Flächeninhalt	3,259	-3,211	-,081	2,404
	Zscore(DO_L3)	-,550	-,119	-1,224	-,435
	Zscore(FWHM_L2)	-,434	2,298	,969	,911
	Zscore(MX2P_L2)	4,509	-6,169	2,115	-1,670
	Zscore(RHW_L1)	-1,827	-1,169	1,525	-,429
	Zscore(YHG_L1)	-2,649	-,421	,721	-,358
	Zscore(YHG_R2)	-21,234	-8,135	-12,493	3,861
	Zscore(YMX_R2)	16,710	9,566	11,742	-3,620
	Zscore: Anzahl Peaks	1,164	3,483	-,081	,075
	(Constant)	,480	-,543	,434	1,017
T10	Zscore: Flächeninhalt	3,191	,518	-1,304	
	Zscore(LHW_L1)	2,486	-1,093	2,540	
	Zscore(YMX_R2)	1,159	1,540	,445	
	(Constant)	1,546	-,144	,550	
AS	Zscore(APF_L1)	33,135			
	(Constant)	11,232			
RX	abgebrochener Peak	-46,780	7,324	4,357	,934
	Zscore(A_L1)	38,164	-16,427	2,172	-5,012
	Zscore(DO_L1)	-21,463	7,839	-,177	-1,696
	Zscore(MI2P_R2)	9,493	-1,133	,468	-,310
	Zscore(MPG_R)	7,691	2,158	2,103	1,415
	Zscore: Centroid	101,481	12,002	-2,514	7,172
	Zscore: PeakCenter	-11,715	-1,781	-,821	-,387
	Zscore(YMX_L1)	-3,054	10,600	,480	,611
	(Constant)	40,229	-1,676	-1,215	-,752

Table B.30.: Canonical discriminant function coefficients of PCDAs ($M_R \geq 3$).

TARGET		Function			
		1	2	3	4
FG	Zscore(FHWM_R2)	,510	,634	-,039	
	Zscore(RHW_R1)	-1,440	-,070	,552	
	Zscore(ZP_L2)	-1,954	-1,671	,156	
	Zscore(MX2P_R3)	1,162	,839	,244	
	Zscore(MX2P_L2)	2,515	1,015	,314	
	Zscore(HPF_L1)	,887	-1,251	,737	
	Zscore(FPG_L)	,288	1,105	,110	
	flachpeaks	-,703	,260	,378	
	HSTUFE	-,883	1,372	,299	
T5	Zscore(MX2P_L2)	1,208	-1,653	,567	-,447
	Zscore(YHG_R2)	-11,317	-4,336	-6,658	2,058
	Zscore(YHG_L1)	-1,747	-,278	,475	-,236
	Zscore: Flächeninhalt	1,376	-1,356	-,034	1,015
	Zscore(A_L2)	2,565	1,037	-,949	,165
	Zscore(FWHM_L2)	-,346	1,833	,772	,727
	Zscore(RHW_L1)	-,915	-,586	,764	-,215
	Zscore(DO_L3)	-,605	-,130	-1,346	-,478
	Zscore: Anzahl Peaks	,868	2,597	-,060	,056
	Zscore(YMX_R2)	9,663	5,532	6,790	-2,094
	Zscore(APF_L3)	,725	-,309	1,782	-,293
	Zscore(ANZHG_L)	-,890	-1,427	-,407	,365
T10	Zscore: Flächeninhalt	1,129	,183	-,461	
	Zscore(YMX_R2)	,723	,961	,277	
	Zscore(LHW_L1)	,715	-,315	,731	
AS	Zscore(APF_L1)	1,000			
RX	Zscore(A_L1)	8,995	-3,872	,512	-1,181
	Zscore: Centroid	25,549	3,022	-,633	1,806
	Zscore: PeakCenter	-4,401	-,669	-,308	-,145
	Zscore(DO_L1)	-12,693	4,636	-,105	-1,003
	Zscore(MI2P_R2)	9,182	-1,096	,453	-,300
	Zscore(YMX_L1)	-2,290	7,946	,360	,458
	Zscore(MPG_R)	5,189	1,456	1,419	,955
	abgebrochener Peak	-18,614	2,914	1,734	,372

Table B.31.: Standardized canonical discriminant function coefficients of PCDAs ($M_R \geq 3$).

		FG	T5	T10	TK	AS	RX
$M_R < 3$	functions	1	1	2	1	1	3
	variables	7	4	3	4	2	12
	hit ratio	97,6 %	100 %	95,8 %	100 %	100 %	100 %
$M_R \geq 3$	functions	3	4	3		1	3
	variables	9	12	3		1	8
	hit ratio	92,3 %	100 %	92,9 %		100 %	100 %

Table B.32.: Overview of the number of variables and functions for all PCDAs. The "hit ratios" for particularly pronounced conchoidal crack intensities are a bit lower, due to scattering effects with larger damage crack areas.

B.9. ACB Bearing Discriminant Analysis (ACBB)

Settings:

- Analysis: ACBB
- Examined cases: Location of occurring ACB (1: right side; 2: left side; 3: both sides)
- Number of classes: 3
- Method: Stepwise optimization by means of smallest F ratio
- F-value Entry: 0,10; removal: 0,17
- Prior Probabilities: Computed from group size
- Used covariance matrix: Within groups
- Used variables: hstufe, plus all characteristic parameters listed in Table B.2 except of m_fp and m_x

Script code:

```
DISCRIMINANT
/GROUPS=aruseite(1 3)
/VARIABLES=zanzhg_r zanzhg_l zyhg_r1 zyhg_r2 zyhg_r3 zyhg_l1 zyhg_l2 zyhg_l3
za_r1 za_r2 za_r3 za_l1 za_l2 za_l3 znc_r1 znc_r2 znc_r3 znc_l1 znc_l2 znc_l3 znpc_r1
znpc_r2 znpc_r3 znpc_l1 znpc_l2 znpc_l3 zfwhm_r1 zfhwm_r2 zfhwm_r3 zfwhm_l1 zfwhm_l2
zfwhm_l3 zlhw_r1 zlhw_r2 zlhw_r3 zlhw_l1 zlhw_l2 zlhw_l3 zrhw_r1 zrhw_r2 zrhw_r3
zrhw_l1 zrhw_l2 zrhw_l3 zdo_r1 zdo_r2 zdo_r3 zdo_l1 zdo_l2 zdo_l3 zzp_r1 zzp_r2
zzp_r3 zzp_l1 zzp_l2 zzp_l3 zmx2p_r1 zmx2p_r2 zmx2p_r3 zmx2p_l1 zmx2p_l2 zmx2p_l3
zmi2p_r1 zmi2p_r2 zmi2p_r3 zmi2p_l1 zmi2p_l2 zmi2p_l3 zymx_r1 zymx_r2 zymx_r3
zymx_l1 zymx_l2 zymx_l3 zhpf_r1 zhpf_r2 zhpf_r3 zhpf_l1 zhpf_l2 zhpf_l3 zmpg_r
zmpg_l zapf_r1 zapf_r2 zapf_r3 zapf_l1 zapf_l2 zapf_l3 zfpg_r zfpg_l hstufe m_2gr m_sp
m_ap
/ANALYSIS ALL
/METHOD=MAXMINF
/PIN= .10
/POUT= .19
/PRIORS SIZE
/HISTORY
```

```
/STATISTICS=RAW TABLE
/PLOT=MAP
/CLASSIFY=NONMISSING POOLED .
```

Results of Material-Specific ACBBs:

TARGET	Function	Eigenvalue	% of Variance	Cumulative %	Canonical Correlation
FG	1	17,666[a]	82,5	82,5	,973
	2	3,735[a]	17,5	100,0	,888
T5	1	96,426[b]	79,2	79,2	,995
	2	25,372[b]	20,8	100,0	,981
T10	1	19,031[c]	75,9	75,9	,975
	2	6,059[c]	24,1	100,0	,926
AS	1	1,005[d]	100,0	100,0	,708
RX	1	14,054[e]	83,2	83,2	,966
	2	2,840[e]	16,8	100,0	,860

Table B.33.: Eigenvalues and canonical correlation coefficients of ACBBs.

TARGET	Test of Function(s)	Wilks' Lambda	Chi-square	df	Sig.
FG	1 through 2	,011	136,693	28	,000
	2	,211	47,429	13	,000
T5	1 through 2	,000	129,548	28	,000
	2	,038	53,993	13	,000
T10	1 through 2	,007	99,032	34	,000
	2	,142	39,086	16	,001
AS	1	,499	6,955	2	,031
RX	1 through 2	,017	81,143	18	,000
	2	,260	26,910	8	,001

Table B.34.: Wilk's lambda calculated for the functions of ACBBs.

	FG	T5	T10	AS	RX
Functions	2	2	2	1	2
Variables	14	14	17	2	9
ACBB accuracy	100 %	100 %	100 %	72,7 %	100 %

Table B.35.: Number of variables and functions of ACBBs. Furthermore, the empirical hit ratio is given as a measure of accuracy.

TARGET		Function 1	Function 2
FG	spätpeaks	2,058	1,271
	Zscore(APF_R2)	1,877	,043
	Zscore(DO_R2)	2,365	-,797
	Zscore(HPF_L2)	,017	,327
	Zscore(LHW_R1)	1,274	3,519
	Zscore(LHW_R2)	1,518	,119
	Zscore(LHW_R3)	-7,237	2,219
	Zscore(MI2P_R2)	1,983	,502
	Zscore(MPG_R)	-,576	-,280
	Zscore(MX2P_L2)	,711	-,718
	Zscore(NPC_L2)	-,894	-,011
	Zscore(NPC_L3)	-,992	,154
	Zscore(NPC_R2)	-,712	,268
	Zscore(RHW_L2)	2,126	1,367
	(Constant)	-,055	1,530
T5	HSTUFE	,239	-2,476
	Zscore(APF_R1)	,018	-3,265
	Zscore(APF_R3)	-8,842	7,388
	Zscore(A_L3)	40,669	-1,023
	Zscore(A_R3)	-13,254	-,499
	Zscore(FPG_R)	,875	-3,114
	Zscore: Halbwertsbreite	,583	6,877
	Zscore(MPG_L)	1,722	-2,599
	Zscore(MPG_R)	-2,400	3,794
	Zscore(RHW_L2)	-,956	-,971
	Zscore: peakhöhe	1,261	8,968
	Zscore(ZP_L3)	-9,019	-4,102
	Zscore: Anzahl Peaks	,107	-2,387
	Zscore(ZP_R3)	3,172	1,918
	(Constant)	4,837	5,628
T10	Zscore(APF_R1)	2,346	2,694
	Zscore(A_L1)	-1,063	-2,199
	Zscore(FHWM_R2)	1,113	1,266
	Zscore(HPF_R2)	-1,074	2,063
	Zscore(HPF_R3)	1,539	-1,264
	Zscore(LHW_L3)	1,321	,119
	Zscore(MI2P_R2)	-1,782	3,874
	Zscore(MPG_L)	2,802	1,508
	Zscore(MPG_R)	-3,509	-3,236
	Zscore(MX2P_L1)	-,925	1,443
	Zscore(MX2P_R3)	2,555	-,577
	Zscore(NC_L2)	1,454	,935
	Zscore(NC_R2)	-57,763	25,304
	Zscore(NPC_R2)	12,267	-2,768
	Zscore(RHW_L3)	2,775	-1,292
	Zscore(YMX_R2)	-3,692	-1,363
	Zscore(ZP_R3)	-2,874	-,486
	(Constant)	1,888	-1,446
AS	Zscore(MPG_R)	4,153	
	Zscore(ZP_L1)	-1,749	
	(Constant)	2,527	
RX	HSTUFE	,803	,477
	Zscore: Flächeninhalt	-3,001	-,588
	Zscore(DO_R2)	1,481	-,172
	Zscore(HPF_R2)	10,495	-3,918
	Zscore(MI2P_L1)	3,414	-,178
	Zscore(MI2P_L3)	-24,220	5,351
	Zscore(MX2P_R3)	,790	-,356
	Zscore(NC_L2)	-,815	,083
	Zscore(NPC_L1)	,528	2,651
	(Constant)	-5,973	-1,103

Table B.36.: Canonical discriminant function coefficients of ACBBs.

TARGET		Function 1	Function 2
FG	Zscore(NPC_R2)	-1,573	,593
	Zscore(NPC_L2)	-1,079	-,013
	Zscore(NPC_L3)	-1,367	,212
	Zscore(LHW_R1)	,464	1,281
	Zscore(LHW_R2)	2,493	,195
	Zscore(LHW_R3)	-2,184	,669
	Zscore(RHW_L2)	1,363	,876
	Zscore(DO_R2)	2,746	-,926
	Zscore(MX2P_L2)	,643	-,649
	Zscore(MI2P_R2)	2,137	,541
	Zscore(HPF_L2)	,027	,513
	Zscore(MPG_R)	-,691	-,336
	Zscore(APF_R2)	,689	,016
	spätpeaks	,755	,466
T5	Zscore(RHW_L2)	-,969	-,985
	Zscore(MPG_R)	-2,031	3,212
	Zscore: peakhöhe	1,172	8,336
	Zscore(A_R3)	-6,902	-,260
	Zscore(A_L3)	13,074	-,329
	Zscore: Halbwertsbreite	,700	8,256
	Zscore: Anzahl Peaks	,118	-2,638
	Zscore(ZP_R3)	3,739	2,261
	Zscore(ZP_L3)	-7,665	-3,486
	Zscore(MPG_L)	1,196	-1,804
	Zscore(APF_R1)	,018	-3,133
	Zscore(APF_R3)	-3,192	2,667
	Zscore(FPG_R)	,857	-3,048
	HSTUFE	,536	-5,545
T10	Zscore(NPC_R2)	9,153	-2,065
	Zscore(MI2P_R2)	-1,750	3,803
	Zscore(MPG_R)	-2,822	-2,603
	Zscore(ZP_R3)	-3,462	-,585
	Zscore(MPG_L)	2,436	1,311
	Zscore(APF_R1)	2,143	2,461
	Zscore(A_L1)	-,788	-1,630
	Zscore(NC_R2)	-10,656	4,668
	Zscore(NC_L2)	1,314	,845
	Zscore(FHWM_R2)	1,012	1,151
	Zscore(LHW_L3)	1,075	,097
	Zscore(RHW_L3)	2,301	-1,072
	Zscore(MX2P_R3)	2,549	-,576
	Zscore(MX2P_L1)	-,644	1,004
	Zscore(YMX_R2)	-2,250	-,831
	Zscore(HPF_R2)	-,636	1,222
	Zscore(HPF_R3)	1,073	-,881
AS	Zscore(MPG_R)	1,632	
	Zscore(ZP_L1)	-1,265	
RX	Zscore(DO_R2)	1,913	-,223
	HSTUFE	1,583	,940
	Zscore(NC_L2)	-,714	,073
	Zscore(MX2P_R3)	,664	-,299
	Zscore(HPF_R2)	4,068	-1,519
	Zscore: Flächeninhalt	-3,418	-,669
	Zscore(NPC_L1)	,309	1,550
	Zscore(MI2P_L1)	4,304	-,224
	Zscore(MI2P_L3)	-4,080	,901

Table B.37.: Standardized canonical discriminant function coefficients of ACBBs.

		Function	
TARGET	ARUSEITE	1	2
FG	1	,265	-1,513
	2	2,011	2,358
	3	-17,253	1,646
T5	1	3,472	-5,722
	2	,733	4,040
	3	-45,708	-3,375
T10	1	-3,902	-2,259
	2	,593	2,096
	3	10,946	-3,596
AS	1	1,166	
	2	-,729	
RX	1	,688	1,749
	2	-2,885	-1,214
	3	8,789	-2,142

Table B.38.: Function values at group centroids (ACBBs).

B.10. ACT Bearing Discriminant Analysis (ACTB)

For this discriminant analysis a single, "pooled" database was used for all materials.

Settings:

- Analysis: ACTB
- Examined cases: Location of occurring ACT (1: right side; 2: left side; 3: both sides)
- Number of classes: 3
- Method: Stepwise optimization of the Mahalanobis distance
- F-value Entry: 0,10; removal: 0,19
- Prior Probabilities: Computed from group size
- Used covariance matrix: Separate groups
- Used variables: hstufe, plus all characteristic parameters listed in Table B.2 except of m_fp and m_x

Script code:

```
DISCRIMINANT
/GROUPS=aroseite(1 3)
/VARIABLES=zanzhg_r zanzhg_l zyhg_r1 zyhg_r2 zyhg_r3 zyhg_l1 zyhg_l2 zyhg_l3
za_r1 za_r2 za_r3 za_l1 za_l2 za_l3 znc_r1 znc_r2 znc_r3 znc_l1 znc_l2 znc_l3 znpc_r1
znpc_r2 znpc_r3 znpc_l1 znpc_l2 znpc_l3 zfwhm_r1 zfhwm_r2 zfhwm_r3 zfwhm_l1 zfwhm_l2
zfwhm_l3 zlhw_r1 zlhw_r2 zlhw_r3 zlhw_l1 zlhw_l2 zlhw_l3 zrhw_r1 zrhw_r2 zrhw_r3
zrhw_l1 zrhw_l2 zrhw_l3 zdo_r1 zdo_r2 zdo_r3 zdo_l1 zdo_l2 zdo_l3 zzp_r1 zzp_r2
zzp_r3 zzp_l1 zzp_l2 zzp_l3 zmx2p_r1 zmx2p_r2 zmx2p_r3 zmx2p_l1 zmx2p_l2 zmx2p_l3
zmi2p_r1 zmi2p_r2 zmi2p_r3 zmi2p_l1 zmi2p_l2 zmi2p_l3 zymx_r1 zymx_r2 zymx_r3
zymx_l1 zymx_l2 zymx_l3 zhpf_r1 zhpf_r2 zhpf_r3 zhpf_l1 zhpf_l2 zhpf_l3 zmpg_r
zmpg_l zapf_r1 zapf_r2 zapf_r3 zapf_l1 zapf_l2 zapf_l3 zfpg_r zfpg_l hstufe m_2gr m_sp
m_ap
/ANALYSIS ALL
/METHOD=MAHAL
/PIN= .10
/POUT= .19
/PRIORS SIZE
/HISTORY
/STATISTICS=RAW FPAIR TABLE
/PLOT=MAP
/PLOT=CASES
/CLASSIFY=NONMISSING SEPARATE .
```

Results of Material-Specific ACTB:

Function	Eigenvalue	% of Variance	Cumulative %	Canonical Correlation
1	2,798[a]	67,3	67,3	,858
2	1,361[a]	32,7	100,0	,759

Table B.39.: Eigenvalues and canonical correlation coefficients of the ACTB.

Test of Function(s)	Wilks' Lambda	Chi-square	df	Sig.
1 through 2	,112	58,127	20	,000
2	,424	22,765	9	,007

Table B.40.: Wilk's lambda calculated for the functions of the ACTB.

	Function	
	1	2
Zscore(A_R3)	,074	-1,822
Zscore(NC_L2)	2,239	-,578
Zscore(FWHM_L1)	-2,741	,228
Zscore(LHW_R3)	,111	2,041
Zscore(LHW_L3)	1,698	1,575
Zscore(DO_L2)	-1,904	-1,128
Zscore(MI2P_R2)	1,015	,281
Zscore(MI2P_L1)	,769	,626
spätpeaks	-1,295	1,875
abgebrochener Peak	6,144	-3,307
(Constant)	,135	-,393

Table B.41.: Canonical discriminant function coefficients of the ACTB.

	Function	
	1	2
Zscore(A_R3)	,035	-,867
Zscore(NC_L2)	1,576	-,407
Zscore(FWHM_L1)	-2,675	,222
Zscore(LHW_R3)	,080	1,459
Zscore(LHW_L3)	,468	,434
Zscore(DO_L2)	-1,067	-,632
Zscore(MI2P_R2)	,971	,269
Zscore(MI2P_L1)	,739	,602
spätpeaks	-,600	,869
abgebrochener Peak	1,425	-,767

Table B.42.: Standardized canonical discriminant function coefficients of the ACTB.

	Function	
AROSEITE	1	2
1	-2,018	-,150
2	1,436	-1,128
3	1,001	1,720

Table B.43.: Function values at group centroids (ACTB).

C. Sieving Analysis Results

V	{...}	$m_{\phi=-4}$[%]	$m_{\phi=-3}$[%]	$m_{\phi=-2}$[%]	$m_{\phi=-1}$[%]	$m_{\phi=0}$[%]	$m_{\phi=1}$[%]	$m_{\phi>1}$[%]
212	101	90,67	6,74	1,90	0,29	0,19	0,11	0,10
213	101	92,34	5,10	1,39	0,51	0,33	0,20	0,13
215	101	90,73	5,72	2,22	0,67	0,41	0,13	0,11
216	101	91,28	5,39	2,63	0,28	0,18	0,11	0,11
217	101	93,71	4,02	1,54	0,30	0,19	0,11	0,13
218	101	90,83	5,34	2,89	0,40	0,26	0,14	0,13
219	101	93,2	3,48	2,18	0,52	0,34	0,17	0,11
220	101	91,99	4,68	2,26	0,52	0,30	0,14	0,11
221	101	91,68	4,55	2,89	0,37	0,24	0,14	0,13
222	101	92,63	3,90	2,73	0,31	0,21	0,11	0,11
223	101	90,12	4,50	4,59	0,45	0,26	0,03	0,06
224	101	91,67	4,81	2,81	0,28	0,18	0,10	0,14
225	101	95,95	1,07	2,22	0,42	0,17	0,10	0,07
226	101	91,57	5,07	2,78	0,24	0,15	0,08	0,10
227	101	90,48	5,20	3,13	0,66	0,31	0,11	0,11
228	301	93,33	4,12	1,93	0,24	0,16	0,09	0,13
230	301	92,6	1,53	4,13	1,17	0,33	0,10	0,14
231	301	91,47	4,48	2,46	0,72	0,47	0,27	0,13
232	301	89,32	6,84	2,24	0,72	0,47	0,27	0,14
233	301	91,25	5,68	1,82	0,55	0,36	0,21	0,13
234	301	91,83	4,01	2,58	0,72	0,46	0,27	0,13
235	301	93,62	4,10	1,70	0,23	0,14	0,09	0,13
236	301	92,87	4,33	2,07	0,30	0,18	0,11	0,13
237	301	93,63	4,10	1,69	0,23	0,14	0,09	0,13
238	301	91,77	5,82	1,61	0,33	0,21	0,13	0,13
239	301	91,97	4,87	1,86	0,58	0,37	0,21	0,14
240	601	90,85	6,69	0,77	1,05	0,41	0,13	0,10
242	601	83,42	8,37	5,39	1,91	0,58	0,17	0,16
243	601	91,01	5,21	2,21	0,70	0,44	0,27	0,16
244	601	89,24	6,99	2,29	0,65	0,43	0,26	0,14
245	601	88,9	7,57	1,49	0,93	0,60	0,36	0,16
246	601	90,8	6,41	0,89	0,94	0,57	0,21	0,18
247	601	91,21	5,84	1,68	0,56	0,36	0,21	0,14
248	601	89,33	6,55	2,73	0,61	0,40	0,23	0,16

Table C.1.: Sieving analysis results I: Mass distribution of HIE fragments

V	{...}	$m_{\phi=-4}$[%]	$m_{\phi=-3}$[%]	$m_{\phi=-2}$[%]	$m_{\phi=-1}$[%]	$m_{\phi=0}$[%]	$m_{\phi=1}$[%]	$m_{\phi>1}$[%]
249	501	92,34	4,70	1,53	0,63	0,40	0,24	0,16
250	501	90,8	5,65	1,73	0,83	0,53	0,31	0,14
251	501	90,9	4,84	2,58	0,75	0,48	0,28	0,16
252	501	92,01	4,34	2,31	0,59	0,37	0,23	0,14
253	401	90,75	6,14	1,63	0,65	0,43	0,26	0,14
254	401	92,62	2,72	3,14	0,68	0,44	0,25	0,14
255	401	92,7	3,60	2,81	0,38	0,24	0,14	0,13
256	401	92,36	4,43	2,09	0,48	0,31	0,19	0,14
257	201	92,94	3,70	1,97	0,61	0,40	0,24	0,13
258	201	91,47	4,42	2,99	0,50	0,31	0,18	0,13
259	201	90,36	6,12	2,51	0,44	0,28	0,17	0,11
260	401	91,79	4,81	1,81	0,70	0,46	0,27	0,16
261	102	90,24	6,61	1,63	0,84	0,44	0,17	0,07
262	102	97,92	0,96	0,53	0,19	0,23	0,10	0,09
263	102	90,99	5,76	1,85	0,82	0,32	0,18	0,07
264	102	91,78	4,84	2,01	0,76	0,34	0,18	0,08
265	102	89,24	6,37	2,80	0,85	0,47	0,21	0,07
266	102	91,55	5,07	2,23	0,56	0,31	0,16	0,13
267	102	89,92	6,89	2,12	0,55	0,30	0,13	0,10
268	102	89,51	6,52	3,33	0,30	0,17	0,08	0,08
269	102	90,50	5,92	2,21	0,74	0,34	0,20	0,10
270	102	90,23	6,10	3,06	0,26	0,14	0,07	0,14
271	102	90,30	6,20	2,39	0,53	0,30	0,14	0,14
272	102	90,69	6,33	1,67	0,69	0,37	0,16	0,10
273	102	90,93	4,56	3,25	0,65	0,35	0,17	0,08
274	102	91,01	5,17	2,61	0,64	0,33	0,14	0,11
275	102	91,15	5,89	1,68	0,68	0,32	0,18	0,10
276	102	91,88	5,18	1,61	0,74	0,36	0,16	0,09
277	103	93,47	3,71	1,59	0,67	0,30	0,14	0,11
278	103	92,58	3,66	2,82	0,50	0,20	0,11	0,13
279	103	91,72	5,14	1,96	0,65	0,24	0,17	0,13
280	103	92,13	3,50	3,09	0,72	0,28	0,17	0,11
281	103	93,22	2,79	3,13	0,47	0,20	0,10	0,10
282	103	92,04	4,72	2,04	0,64	0,31	0,16	0,10
283	103	89,52	7,36	1,95	0,62	0,32	0,13	0,10
284	103	90,65	6,22	1,92	0,68	0,28	0,14	0,11
285	103	90,38	6,22	2,16	0,67	0,29	0,15	0,11
286	103	92,07	5,03	1,74	0,65	0,27	0,13	0,13
287	103	92,03	5,32	1,63	0,53	0,22	0,13	0,14
288	103	91,79	4,37	3,13	0,34	0,14	0,08	0,14
289	101	90,29	5,76	2,77	0,58	0,34	0,13	0,13
290	103	92,37	4,13	2,51	0,52	0,23	0,11	0,13

Table C.2.: Sieving analysis results II: Mass distribution of HIE fragments

V	{...}	$m_{\phi=-4}$[%]	$m_{\phi=-3}$[%]	$m_{\phi=-2}$[%]	$m_{\phi=-1}$[%]	$m_{\phi=0}$[%]	$m_{\phi=1}$[%]	$m_{\phi>1}$[%]
291	103	91,45	4,55	2,86	0,59	0,27	0,15	0,13
292	103	91,16	4,86	2,78	0,66	0,28	0,14	0,11
293	102	90,64	5,39	3,16	0,40	0,21	0,11	0,09
294	102	91,05	5,28	2,81	0,43	0,23	0,13	0,09
295	102	92,79	4,43	1,75	0,50	0,27	0,14	0,13
296	102	91,02	4,91	2,65	0,75	0,38	0,20	0,09
297	102	92,4	5,45	1,51	0,30	0,16	0,10	0,08
298	102	92,27	4,82	2,19	0,32	0,18	0,08	0,13
299	102	89,53	7,44	1,74	0,68	0,36	0,16	0,10
300	102	92,78	3,94	2,03	0,66	0,34	0,14	0,10
301	102	93,05	5,48	0,91	0,28	0,11	0,09	0,09
302	104	91,93	2,63	4,04	0,83	0,28	0,15	0,14
303	104	84,01	10,47	4,02	0,90	0,32	0,16	0,13
304	103	90,91	5,69	2,23	0,59	0,33	0,14	0,11
305	103	93,45	4,38	1,51	0,31	0,13	0,08	0,13
306	103	90,5	5,19	3,12	0,66	0,27	0,14	0,11
307	103	92,33	4,66	1,86	0,59	0,28	0,16	0,11
308	103	92,76	3,68	2,34	0,63	0,33	0,16	0,11
309	103	91,03	5,35	2,38	0,69	0,27	0,14	0,13
310	103	91,27	6,12	1,60	0,52	0,23	0,13	0,13
311	103	93,18	3,97	2,00	0,42	0,17	0,11	0,14
312	103	91,79	4,20	3,09	0,45	0,21	0,13	0,13
313	103	89,27	6,44	3,51	0,42	0,17	0,12	0,07
314	103	90,47	6,19	2,06	0,72	0,30	0,16	0,10
315	103	85,92	9,43	3,53	0,59	0,27	0,14	0,11
316	103	91,13	5,29	2,87	0,34	0,14	0,08	0,14
317	103	92,25	4,65	2,46	0,30	0,13	0,07	0,14
318	103	92,48	4,83	1,50	0,65	0,27	0,14	0,13
319	303	91,06	5,50	2,13	0,72	0,28	0,18	0,13
320	303	92,03	4,45	2,02	0,81	0,34	0,20	0,14
321	303	91,04	5,84	2,04	0,58	0,24	0,13	0,13
322	303	90,64	5,52	2,78	0,57	0,23	0,14	0,13
323	303	92,60	4,00	2,35	0,55	0,23	0,14	0,13
324	105	91,40	5,71	1,99	0,41	0,24	0,13	0,13
325	105	87,87	8,19	2,66	0,58	0,38	0,17	0,14
326	105	88,82	7,14	3,00	0,48	0,30	0,14	0,13
327	105	87,49	8,01	3,22	0,63	0,37	0,16	0,13
328	105	87,53	7,47	3,66	0,64	0,38	0,18	0,13
329	105	87,68	6,18	4,82	0,64	0,37	0,19	0,13
330	102	89,91	6,90	1,96	0,61	0,38	0,14	0,10
350	602	92,83	2,93	3,26	0,47	0,26	0,13	0,13
351	602	88,98	7,52	1,97	0,76	0,42	0,21	0,13

Table C.3.: Sieving analysis results III: Mass distribution of HIE fragments

V	{...}	$m_{\phi=-4}$[%]	$m_{\phi=-3}$[%]	$m_{\phi=-2}$[%]	$m_{\phi=-1}$[%]	$m_{\phi=0}$[%]	$m_{\phi=1}$[%]	$m_{\phi>1}$[%]
352	602	91,53	5,04	2,27	0,55	0,31	0,16	0,14
353	602	92,13	4,13	1,79	0,99	0,54	0,27	0,16
354	602	90,97	6,11	1,85	0,52	0,28	0,14	0,13
355	602	88,43	7,82	2,19	0,78	0,42	0,21	0,14
356	603	89,26	5,82	2,68	1,28	0,53	0,29	0,14
357	603	91,19	5,37	2,33	0,59	0,24	0,14	0,14
358	603	91,87	4,81	1,95	0,74	0,30	0,17	0,16
359	603	90,99	5,35	2,42	0,68	0,27	0,17	0,13
360	604	91,18	5,74	1,81	0,74	0,26	0,14	0,13
361	604	90,53	4,46	3,64	0,82	0,28	0,13	0,13
362	604	90,47	6,49	1,69	0,80	0,27	0,14	0,14
363	604	93,27	3,85	1,78	0,63	0,21	0,11	0,14
364	603	90,23	5,05	3,09	0,90	0,38	0,20	0,15
365	603	92,56	4,46	2,36	0,30	0,12	0,07	0,14
401	106	89,90	6,35	2,57	0,65	0,24	0,17	0,12
402	106	84,57	8,86	4,89	1,12	0,34	0,12	0,10
403	106	91,84	4,45	2,74	0,49	0,20	0,15	0,12
405	106	92,53	3,21	3,49	0,39	0,15	0,10	0,12
406	106	92,37	5,64	1,35	0,34	0,09	0,14	0,07
407	106	90,09	5,91	2,93	0,56	0,22	0,17	0,12
408	106	86,88	9,07	3,23	0,44	0,15	0,10	0,14
409	106	88,67	6,66	4,11	0,27	0,10	0,07	0,12
410	106	92,35	2,93	3,85	0,45	0,17	0,12	0,14
411	106	91,96	3,72	3,25	0,58	0,20	0,15	0,14
412	106	92,89	1,35	4,63	0,62	0,24	0,15	0,12
413	106	86,58	7,92	4,48	0,54	0,20	0,15	0,13
414	106	91,5	2,71	4,60	0,65	0,24	0,19	0,12
415	106	84,94	11,19	3,14	0,44	0,17	0,08	0,03
416	106	92,45	6,46	0,24	0,59	0,13	0,08	0,05

Table C.4.: Sieving analysis results IV: Mass distribution of HIE fragments

V	{...}	$m_{\phi=-4}$[%]	$m_{\phi=-3}$[%]	$m_{\phi=-2}$[%]	$m_{\phi=-1}$[%]	$m_{\phi=0}$[%]	$m_{\phi=1}$[%]	$m_{\phi>1}$[%]
417	306	91,39	3,59	4,02	0,55	0,17	0,15	0,14
418	306	86,13	9,78	3,12	0,49	0,20	0,14	0,14
419	306	87,26	8,90	2,82	0,53	0,21	0,14	0,14
420	306	90,80	3,38	4,72	0,59	0,22	0,17	0,12
421	306	91,41	3,98	3,79	0,44	0,15	0,12	0,12
422	306	86,48	8,90	3,74	0,47	0,15	0,14	0,12
423	306	91,88	2,70	4,26	0,61	0,25	0,17	0,12
424	306	90,01	6,45	2,48	0,56	0,24	0,15	0,12
425	306	86,57	9,34	2,94	0,61	0,25	0,17	0,13
426	306	87,26	7,80	3,85	0,58	0,21	0,17	0,14
427	306	88,56	6,86	3,28	0,70	0,27	0,20	0,14
428	306	91,91	2,44	4,66	0,54	0,19	0,14	0,14
429	606	77,08	15,94	5,73	0,75	0,26	0,17	0,09
430	606	85,88	8,59	4,33	0,63	0,25	0,19	0,14
431	606	93,03	1,01	4,97	0,51	0,21	0,14	0,14
432	606	87,4	7,05	4,25	0,68	0,29	0,19	0,14
433	606	89,85	4,71	4,36	0,56	0,24	0,15	0,14
434	606	93,39	4,16	1,52	0,53	0,19	0,15	0,07
500	105	88,14	8,15	2,39	0,66	0,40	0,18	0,10
501	105	91,37	2,83	4,91	0,40	0,26	0,11	0,12
502	305	90,85	5,95	2,03	0,54	0,33	0,16	0,14
503	305	91,58	4,13	3,07	0,56	0,35	0,16	0,14
504	305	90,85	5,58	2,15	0,68	0,42	0,19	0,14
505	605	88,30	5,99	4,68	0,46	0,29	0,14	0,15
506	605	89,40	5,76	3,08	0,82	0,54	0,25	0,15
507	605	89,47	6,54	2,30	0,80	0,51	0,25	0,14
510	205	88,65	5,19	4,99	0,53	0,34	0,16	0,14
511	405	88,63	8,13	2,15	0,49	0,31	0,14	0,15
512	405	90,08	6,75	1,93	0,56	0,36	0,16	0,15
514	505	90,40	5,26	3,04	0,60	0,38	0,18	0,15
515	505	88,61	5,90	4,32	0,53	0,34	0,16	0,14

Table C.5.: Sieving analysis results V: Mass distribution of HIE fragments

V	{...}	$m_{\phi=-4}$[%]	$m_{\phi=-3}$[%]	$m_{\phi=-2}$[%]	$m_{\phi=-1}$[%]	$m_{\phi=0}$[%]	$m_{\phi=1}$[%]	$m_{\phi>1}$[%]
601	113	90,99	5,27	2,75	0,51	0,22	0,12	0,12
602	113	91,30	5,29	2,33	0,58	0,25	0,14	0,12
603	113	91,50	4,71	2,60	0,64	0,28	0,15	0,11
605	114	90,77	6,36	1,52	0,81	0,25	0,15	0,14
606	114	91,34	4,31	3,00	0,81	0,29	0,14	0,12
607	114	87,10	10,56	1,37	0,65	0,19	0,10	0,04
608	114	89,67	6,45	2,43	0,88	0,29	0,16	0,12
609	114	91,71	4,56	2,31	0,86	0,29	0,14	0,14
610	114	91,88	4,00	2,81	0,78	0,27	0,12	0,14
611	613	92,35	4,06	1,76	1,02	0,43	0,23	0,15
612	112	90,16	7,13	1,68	0,52	0,28	0,14	0,10
613	112	89,01	7,24	2,57	0,62	0,35	0,12	0,08
614	112	93,53	2,44	2,77	0,65	0,36	0,14	0,11
615	612	90,60	4,90	2,70	0,93	0,50	0,25	0,14
616	312	90,65	6,22	1,67	0,72	0,40	0,20	0,14
617	312	89,32	6,92	2,18	0,79	0,43	0,21	0,14
618	612	90,73	5,46	2,35	0,73	0,40	0,20	0,13
619	111	93,14	2,78	3,14	0,40	0,25	0,16	0,13
620	211	91,20	5,32	2,51	0,42	0,27	0,16	0,13
621	111	91,42	5,44	2,14	0,51	0,25	0,13	0,11
622	111	90,60	5,95	2,20	0,71	0,30	0,14	0,10
623	111	92,18	4,84	1,63	0,69	0,38	0,18	0,10
624	611	91,76	4,43	2,29	0,67	0,43	0,25	0,17
625	611	89,43	7,50	1,78	0,58	0,37	0,21	0,14
626	311	92,03	3,42	2,98	0,70	0,45	0,27	0,14
627	311	90,84	4,62	2,97	0,71	0,46	0,26	0,14
628	211	89,73	6,60	2,09	0,71	0,46	0,28	0,13
629	411	90,40	6,11	2,18	0,58	0,37	0,23	0,14
630	511	91,80	4,17	2,82	0,53	0,34	0,21	0,13
631	511	90,62	6,02	2,11	0,54	0,35	0,21	0,14
640	121	91,01	5,65	2,15	0,56	0,36	0,19	0,07
641	121	92,56	4,34	2,00	0,50	0,32	0,17	0,11
642	121	92,13	5,35	1,51	0,44	0,28	0,17	0,12
643	121	92,14	4,74	1,88	0,61	0,35	0,18	0,11
644	221	90,50	6,38	2,30	0,34	0,22	0,14	0,12
645	221	93,00	3,32	2,73	0,41	0,25	0,15	0,14
646	221	90,24	5,24	2,91	0,73	0,47	0,29	0,13
647	421	91,21	3,85	3,33	0,72	0,47	0,28	0,14
648	421	89,95	6,78	1,70	0,70	0,45	0,27	0,15
649	421	91,95	4,82	1,55	0,75	0,49	0,29	0,14
650	621	92,29	4,75	1,62	0,58	0,37	0,23	0,16
651	621	92,37	3,72	2,30	0,73	0,47	0,27	0,14

Table C.6.: Sieving analysis results VI: Mass distribution of HIE fragments

V	{...}	$m_{\phi=-4}$[%]	$m_{\phi=-3}$[%]	$m_{\phi=-2}$[%]	$m_{\phi=-1}$[%]	$m_{\phi=0}$[%]	$m_{\phi=1}$[%]	$m_{\phi>1}$[%]
652	621	91,84	3,05	3,09	0,92	0,59	0,35	0,17
653	621	89,81	6,58	1,65	0,89	0,57	0,33	0,17
654	122	90,51	5,52	2,91	0,51	0,27	0,13	0,14
655	122	90,50	6,58	1,75	0,60	0,30	0,14	0,13
656	122	92,09	4,10	2,58	0,65	0,32	0,15	0,11
657	122	89,76	7,44	1,70	0,59	0,27	0,14	0,10
658	422	91,84	4,59	1,75	0,91	0,51	0,25	0,14
659	422	91,27	3,56	3,42	0,88	0,48	0,24	0,14
660	422	92,59	3,52	2,94	0,44	0,24	0,11	0,16
661	622	91,65	4,65	1,84	0,94	0,51	0,26	0,16
662	622	91,70	3,31	3,38	0,81	0,44	0,21	0,14
663	622	88,83	7,27	2,71	0,58	0,31	0,16	0,16
664	622	92,68	4,26	1,63	0,71	0,40	0,20	0,14
665	123	91,47	5,86	1,56	0,62	0,24	0,13	0,11
666	123	92,02	5,25	1,63	0,58	0,25	0,14	0,13
667	123	93,13	3,24	2,48	0,61	0,25	0,15	0,14
668	123	90,08	5,52	3,19	0,65	0,26	0,17	0,13
669	423	92,46	3,40	2,47	0,92	0,38	0,21	0,14
670	423	91,43	5,22	2,07	0,68	0,29	0,17	0,14
671	423	92,66	3,66	2,21	0,80	0,34	0,20	0,13
672	623	89,83	6,53	1,89	0,98	0,41	0,21	0,14
673	623	90,32	4,50	3,38	0,98	0,40	0,26	0,16
674	623	91,73	4,28	2,73	0,66	0,27	0,17	0,15
675	623	90,03	5,95	2,85	0,61	0,24	0,16	0,16

Table C.7.: Sieving analysis results VII: Mass distribution of HIE fragments

V	{...}	$m_{\phi=-4}$[%]	$m_{\phi=-3}$[%]	$m_{\phi=-2}$[%]	$m_{\phi=-1}$[%]	$m_{\phi=0}$[%]	$m_{\phi=1}$[%]	$m_{\phi>1}$[%]
676	124	91,67	4,98	2,20	0,68	0,21	0,11	0,14
677	124	89,53	7,26	1,76	0,89	0,27	0,17	0,13
678	124	90,43	5,32	3,19	0,60	0,21	0,11	0,14
680	424	88,82	6,77	2,78	0,98	0,32	0,18	0,15
681	424	93,65	3,41	1,54	0,83	0,29	0,13	0,14
682	424	91,68	5,01	1,68	1,01	0,34	0,16	0,13
683	624	90,03	4,18	3,97	1,10	0,37	0,20	0,14
684	624	92,49	1,60	3,82	1,28	0,43	0,23	0,16
685	624	92,75	3,52	2,68	0,61	0,20	0,11	0,14
686	622	90,26	6,50	1,89	0,66	0,36	0,19	0,16
687	622	90,41	6,23	1,67	0,85	0,47	0,23	0,14
688	122	89,00	6,62	3,15	0,61	0,33	0,16	0,13
689	622	89,49	5,40	3,14	1,01	0,55	0,27	0,14
690	622	91,27	4,96	2,12	0,84	0,45	0,23	0,14
692	622	90,54	4,50	2,98	1,01	0,55	0,28	0,14
693	421	92,61	3,83	2,48	0,46	0,30	0,18	0,14
694	421	91,51	5,18	2,14	0,51	0,33	0,20	0,14
695	221	91,86	5,06	1,66	0,62	0,41	0,24	0,14
696	221	91,76	6,06	1,61	0,21	0,14	0,08	0,13
697	221	91,66	4,87	2,60	0,35	0,23	0,14	0,14
700	131	90,54	6,26	1,77	0,72	0,45	0,17	0,10
701	131	92,89	4,07	2,33	0,30	0,18	0,11	0,11
702	131	91,92	4,86	1,91	0,60	0,38	0,23	0,10
703	131	91,31	5,41	2,42	0,38	0,24	0,14	0,10
704	231	91,22	5,21	2,02	0,70	0,45	0,27	0,13
705	231	91,41	6,06	1,86	0,27	0,17	0,10	0,13

Table C.8.: Sieving analysis results VIII: Mass distribution of HIE fragments

V	{...}	$m_{\phi=-4}$[%]	$m_{\phi=-3}$[%]	$m_{\phi=-2}$[%]	$m_{\phi=-1}$[%]	$m_{\phi=0}$[%]	$m_{\phi=1}$[%]	$m_{\phi>1}$[%]
706	231	92,63	4,14	1,87	0,61	0,39	0,24	0,13
707	231	90,49	7,10	1,46	0,41	0,27	0,16	0,11
708	431	92,80	2,88	2,91	0,64	0,40	0,24	0,13
709	431	91,82	5,99	1,41	0,33	0,21	0,13	0,11
710	431	91,37	4,99	2,78	0,36	0,23	0,13	0,14
711	631	92,92	2,78	3,17	0,49	0,32	0,19	0,14
712	631	91,38	4,73	2,29	0,73	0,46	0,27	0,14
713	631	91,70	5,98	1,54	0,31	0,20	0,11	0,14
714	631	89,57	7,17	1,46	0,82	0,53	0,32	0,14
715	132	89,45	6,61	2,85	0,53	0,28	0,15	0,13
716	132	89,43	7,50	2,11	0,46	0,25	0,13	0,13
717	132	91,85	5,17	2,29	0,31	0,17	0,09	0,11
718	132	91,20	4,70	3,02	0,53	0,28	0,14	0,13
719	432	91,46	4,03	2,74	0,90	0,49	0,24	0,14
720	432	89,75	5,85	2,91	0,75	0,41	0,21	0,13
721	432	91,94	3,78	3,34	0,44	0,24	0,13	0,14
722	632	92,61	3,40	2,82	0,56	0,31	0,16	0,14
723	632	92,19	2,66	3,20	1,00	0,54	0,27	0,13
724	632	91,06	5,16	2,02	0,90	0,49	0,24	0,13
725	632	89,96	5,14	3,09	0,91	0,51	0,25	0,14
726	133	91,88	4,49	2,43	0,67	0,26	0,17	0,10
727	133	91,39	4,50	2,82	0,72	0,28	0,17	0,11
728	133	92,43	4,84	1,96	0,40	0,16	0,10	0,13
729	133	90,70	5,50	2,84	0,52	0,21	0,11	0,11
730	433	90,37	5,23	2,77	0,91	0,38	0,22	0,13
731	433	92,47	4,48	1,69	0,74	0,29	0,18	0,14
732	433	90,57	5,64	2,16	0,90	0,38	0,20	0,14
733	433	92,52	4,28	1,68	0,83	0,35	0,20	0,14
734	633	89,83	6,26	2,21	0,96	0,38	0,23	0,14
735	633	90,75	4,59	3,02	0,91	0,36	0,24	0,13
736	633	91,48	4,62	2,16	0,96	0,39	0,24	0,14
737	133	92,14	4,52	2,17	0,63	0,28	0,15	0,11
738	134	93,28	1,71	3,61	0,85	0,27	0,16	0,13
739	134	91,53	4,74	2,93	0,44	0,16	0,07	0,13
740	134	92,14	4,72	2,30	0,47	0,17	0,09	0,11
741	134	90,71	4,35	3,47	0,92	0,28	0,13	0,13
742	434	90,70	4,24	3,93	0,67	0,21	0,13	0,13
743	434	93,44	3,16	2,37	0,60	0,21	0,10	0,13
744	434	90,89	5,96	2,00	0,69	0,21	0,13	0,13
745	634	91,11	5,22	2,39	0,77	0,25	0,14	0,13
746	634	91,67	5,64	1,52	0,68	0,24	0,11	0,14
747	634	90,80	3,76	3,69	1,06	0,38	0,17	0,13

Table C.9.: Sieving analysis results IX: Mass distribution of HIE fragments

V	{...}	$m_{\phi=-4}$[%]	$m_{\phi=-3}$[%]	$m_{\phi=-2}$[%]	$m_{\phi=-1}$[%]	$m_{\phi=0}$[%]	$m_{\phi=1}$[%]	$m_{\phi>1}$[%]
749	133	92,10	5,65	1,56	0,34	0,14	0,09	0,11
800	116	82,34	12,21	4,57	0,38	0,28	0,16	0,07
801	116	87,42	8,91	3,04	0,31	0,10	0,09	0,12
802	116	89,77	5,53	3,36	0,77	0,27	0,20	0,10
803	616	90,46	5,30	3,20	0,56	0,19	0,15	0,14
804	616	92,26	3,20	2,93	0,89	0,35	0,24	0,12
805	616	88,39	6,29	4,52	0,43	0,14	0,12	0,12
806	616	86,23	9,62	3,43	0,36	0,14	0,10	0,12
807	316	89,50	5,02	4,03	0,80	0,32	0,20	0,13
808	316	89,14	6,70	3,06	0,58	0,23	0,17	0,12
809	316	89,84	4,77	4,61	0,39	0,15	0,10	0,14
810	126	92,22	3,00	3,99	0,38	0,15	0,12	0,13
811	126	92,25	2,38	4,38	0,52	0,18	0,15	0,13
812	126	88,09	7,85	3,05	0,51	0,20	0,17	0,13
813	126	89,99	6,33	2,71	0,47	0,22	0,14	0,14
814	126	90,88	4,84	3,26	0,55	0,18	0,15	0,13
815	626	91,02	3,87	4,38	0,36	0,14	0,10	0,14
816	626	86,57	7,82	3,95	0,92	0,34	0,27	0,13
817	626	87,85	8,68	2,66	0,42	0,14	0,12	0,14
818	426	86,99	7,82	3,65	0,83	0,34	0,24	0,15
819	426	87,28	9,23	2,52	0,50	0,20	0,15	0,12
820	426	92,30	2,72	3,94	0,55	0,22	0,15	0,12
821	426	91,64	3,13	4,13	0,59	0,20	0,17	0,14
822	426	88,26	7,07	3,09	0,87	0,35	0,23	0,13
823	626	90,21	4,79	3,96	0,54	0,20	0,15	0,14

Table C.10.: Sieving analysis results X: Mass distribution of HIE fragments

V	{...}	$m_{\phi=-4}$[%]	$m_{\phi=-3}$[%]	$m_{\phi=-2}$[%]	$m_{\phi=-1}$[%]	$m_{\phi=0}$[%]	$m_{\phi=1}$[%]	$m_{\phi>1}$[%]
900	136	87,41	8,70	3,08	0,40	0,17	0,12	0,12
901	136	88,28	7,32	3,77	0,30	0,12	0,08	0,13
902	136	91,70	4,65	2,92	0,38	0,13	0,10	0,12
903	136	88,61	7,98	2,51	0,44	0,20	0,15	0,10
904	136	87,40	6,66	4,93	0,52	0,19	0,17	0,13
905	136	89,49	5,42	4,48	0,30	0,12	0,08	0,12
906	636	90,58	4,65	2,99	0,98	0,42	0,27	0,12
907	636	90,89	5,54	2,51	0,55	0,20	0,17	0,13
908	636	90,16	4,59	3,89	0,75	0,27	0,20	0,13
909	636	89,04	4,89	4,56	0,82	0,30	0,25	0,13
910	636	91,54	3,03	4,15	0,71	0,24	0,20	0,12
911	636	93,07	1,17	4,79	0,53	0,17	0,14	0,14
912	136	86,34	9,90	2,77	0,53	0,20	0,14	0,12
913	136	89,92	6,16	3,06	0,43	0,17	0,13	0,13
914	636	85,69	8,15	4,47	0,97	0,36	0,25	0,12
1001	135	90,10	4,63	4,27	0,46	0,30	0,13	0,11
1003	135	90,31	5,87	2,90	0,42	0,27	0,13	0,11
1005	135	90,51	5,25	2,99	0,58	0,35	0,18	0,14
1007	135	91,40	4,63	2,59	0,68	0,38	0,20	0,11
1008	135	92,54	1,99	4,05	0,73	0,42	0,16	0,12
1009	135	89,49	4,97	4,08	0,75	0,43	0,19	0,10
269B	102	90,42	5,55	3,35	0,30	0,17	0,09	0,13
H3103	105	89,23	7,16	2,75	0,38	0,23	0,11	0,14
H3601	605	86,69	6,46	4,72	1,13	0,59	0,26	0,15
L605	114	91,95	3,89	2,87	0,81	0,25	0,15	0,10
L693	421	90,38	4,86	3,21	0,75	0,44	0,23	0,14
L722	432	93,23	3,98	1,70	0,53	0,29	0,14	0,13

Table C.11.: Sieving analysis results XI: Mass distribution of HIE fragments

D. IPA Results

particle no.	circularity	elongation	compactness	rectangularity
86	1,4771	2,2771	0,7113	0,8115
91	1,7947	2,8764	0,6641	1,2344
92	1,5995	2,4771	0,7013	1,1443
93	1,8853	6,0029	0,5631	1,0534
94	1,8841	2,6739	0,7016	1,3320
95	2,9188	2,4883	0,5620	1,9156
96	1,3791	2,1589	0,6441	0,9710
97	1,2807	2,8215	0,5427	0,8175
98	1,6523	2,9019	0,7463	1,1762
99	1,7411	1,6891	0,7238	1,3096
100	1,8448	2,9006	0,7709	1,3266
101	1,7987	2,9164	0,6841	1,2443
102	1,6583	5,2743	0,7075	1,0101
103	2,8012	3,7593	0,7527	1,8935
104	1,3812	2,7987	0,8070	1,0153

Table D.1.: Determined IPA parameters for FG [V208], {101}.

particle no.	circularity	elongation	compactness	rectangularity
95A	1,8335	4,8590	0,4245	0,9938
95B	1,8226	5,9690	0,3457	0,9082
95C	1,3475	4,3971	0,5765	0,8198
95D	1,3968	4,3088	0,6873	0,8917
95E	1,7043	7,6438	0,5832	0,8920
95F	2,1427	5,6773	0,2507	0,9476

Table D.2.: Determined IPA parameters for Trichips [V208], {101}.

particle no.	circularity	elongation	compactness	rectangularity
101	1,7381	1,8965	0,6445	1,2302
103	1,5780	2,4663	0,6275	1,0839
105	1,5032	2,3236	0,7108	1,0890
107	1,7657	2,5636	0,7836	0,9565
109	1,2712	1,9239	0,7082	1,2806
113	1,3068	2,1311	0,8010	1,0037
114	3,2545	2,0059	0,8552	2,5412
115	1,5330	3,6309	0,7559	1,0458
118	1,8908	2,0324	0,6648	1,3525
120	1,6332	3,5448	0,7813	1,1299
122	1,8848	1,8079	0,5901	1,3185
125	2,4024	7,2535	0,73621	1,44251
126	1,8263	6,7352	0,70442	1,26281

Table D.3.: Determined IPA parameters for T10 [V288], {103}.

particle no.	circularity	elongation	compactness	rectangularity
1	1,7165	4,5212	0,5625	1,0327
3	2,0300	3,2494	0,7136	1,3987
4	1,3595	2,7314	0,5589	0,8779
5	1,3554	3,2655	0,6514	0,9064
6	2,3647	4,6689	0,6158	1,4475
7	4,5670	4,1878	0,6119	2,8522
8	1,8583	8,3848	0,6355	0,9579
9	2,7359	6,0909	0,6292	1,5584
10	1,9412	2,8707	0,6957	1,3562

Table D.4.: Determined IPA parameters for RX [V405], {106}.

E. Determined Fracture Areas

V	{...}	$B_{IV,\phi=-1}[mm^2]$	$B_{IV,\phi=0}[mm^2]$	$B_{IV,\phi=1}[mm^2]$	$B_{IV,\phi>1}[mm^2]$	f_H	$S_{m,\phi>1}[\frac{m^2}{kg}]$
212	101	1942	2524	3106	9472	12,13	135,3
213	101	3481	4448	5414	12029	12,09	133,7
215	101	4578	5650	3507	10799	12,18	135,0
216	101	1938	2520	3102	10756	12,12	134,5
217	101	2022	2503	3081	12005	12,04	133,4
218	101	2737	3519	3911	12108	12,22	134,5
219	101	3591	4659	4659	10737	12,13	134,2
220	101	3608	4095	3900	10713	12,19	133,9
221	101	2536	3316	3902	12116	12,19	134,6
222	101	2128	2902	3095	10705	12,09	133,8
223	101	3021	3508	780	5367	12,18	134,2
224	101	1938	2519	2713	13462	12,11	134,6
225	101	2926	2340	2731	6686	12,19	133,7
226	101	1651	2136	2330	9339	12,14	133,4
227	101	4450	4257	3096	10683	12,09	133,5
228	301	1649	2134	2328	12046	12,12	133,8
230	301	7875	4472	2722	13397	12,15	134,0
231	301	4932	6382	7349	12117	12,09	134,6
232	301	4922	6370	7335	13510	12,06	135,1
233	301	3802	4875	5850	12108	12,19	134,5
234	301	4838	6193	7354	12156	12,10	135,1
235	301	1549	1936	2323	12034	12,10	133,7
236	301	2034	2518	3099	12066	12,11	134,1
237	301	1559	1949	2338	12053	12,18	133,9
238	301	2223	2899	3479	12139	12,08	134,9
239	301	3982	5050	5827	13559	12,14	135,6
240	601	7184	5631	3495	9410	12,14	134,4
242	601	12855	7791	4675	14744	12,17	134,0
243	601	4741	5999	7353	14812	12,09	134,7
244	601	4470	5830	6996	13368	12,15	133,7
245	601	6311	8156	9709	14824	12,14	134,8
246	601	6428	7791	5844	17613	12,17	135,5
247	601	3774	4839	5807	13450	12,10	134,5
248	601	4147	5401	6172	14824	12,06	134,8
249	501	4261	5423	6585	14899	12,11	135,4
250	501	5603	7148	8501	13535	12,07	135,3

Table E.1.: Fracture area distribution of HIE class IV fragments: Additionally, the determined Heywood factor f_H for the particles of the fractions $-1 < \phi < 1$ is listed as well as the mass-specific surface area of the finest fraction $S_{m,\phi>1}$.

V	{...}	$A_{DC}[mm^2]$	$\triangle A_{DC}[mm^2]$	$A_{NC}[mm^2]$	$\triangle A_{NC}[mm^2]$	$A_{tot}[mm^2]$	$\triangle A_{tot}[mm^2]$
212	101	16653	600	3222	71	19875	671
213	101	26026	856	2187	48	28213	904
215	101	25544	816	4001	88	29546	904
216	101	18610	659	2997	66	21607	725
217	101	19481	720	3719	82	23200	801
218	101	22493	776	3765	83	26258	859
219	101	24182	800	1788	39	25969	840
220	101	23083	775	3784	83	26867	858
221	101	21710	771	3205	71	24915	841
222	101	19100	690	3744	82	22844	772
223	101	12439	406	4248	93	16686	500
224	101	20675	768	3871	85	24546	853
225	101	15310	494	3064	67	18374	561
226	101	15190	563	3591	79	18781	642
227	101	23765	780	3851	85	27616	864
228	301	18420	691	2082	46	20502	737
230	301	28019	940	3942	87	31962	1026
231	301	30605	972	1707	38	32312	1010
232	301	31685	1031	4504	99	36189	1130
233	301	26433	874	2986	66	29419	940
234	301	30746	976	2977	66	33723	1041
235	301	18052	683	2593	57	20645	740
236	301	19498	721	4428	97	23926	818
237	301	19952	723	2914	64	22866	787
238	301	20749	752	3981	88	24730	839
239	301	28348	950	3928	86	32276	1036
240	601	25630	800	2488	55	28118	855
242	601	40342	1246	5275	116	45617	1362
243	601	32564	1071	5096	112	37660	1183
244	601	30616	995	7079	156	37694	1151
245	601	38941	1218	6904	152	45845	1369
246	601	38022	1263	3803	84	41825	1347
247	601	27563	931	2895	64	30458	995
248	601	30532	1026	6644	146	37176	1172
249	501	30845	1045	4504	99	35349	1144
250	501	34601	1094	4136	91	38737	1185

Table E.2.: Fracture areas of HIE fragments: The results for A_{DC}, A_{NC} and the total fracture area A_{tot} are presented. The measurement uncertainties $\triangle A_{DC}$, $\triangle A_{NC}$ and $\triangle A_{tot}$ are listed as well.

V	{...}	$B_{IV,\phi=-1}[mm^2]$	$B_{IV,\phi=0}[mm^2]$	$B_{IV,\phi=1}[mm^2]$	$B_{IV,\phi>1}[mm^2]$	f_H	$S_{m,\phi>1}[\frac{m^2}{kg}]$
251	501	5150	6607	7773	14740	12,15	134,0
252	501	3980	5048	6213	13339	12,13	133,4
253	401	4464	5823	6987	13370	12,13	133,7
254	401	4657	6015	6985	13367	12,13	133,7
255	401	2632	3314	3899	12044	12,18	133,8
256	401	3293	4262	5037	13433	12,11	134,3
257	201	4184	5449	6617	12136	12,16	134,8
258	201	3400	4274	5051	12140	12,14	134,9
259	201	3011	3885	4662	10827	12,14	135,3
260	401	4752	6207	7371	14807	12,12	134,6
261	102	5395	5670	4389	6211	11,43	124,2
262	102	1175	2893	2532	7515	11,30	125,3
263	102	5214	4135	4675	6193	11,24	123,9
264	102	4944	4394	4761	7444	11,44	124,1
265	102	5366	5903	5366	6188	11,18	123,8
266	102	3538	3992	3992	11244	11,34	124,9
267	102	3549	3822	3276	8752	11,38	125,0
268	102	1880	2148	2148	7454	11,19	124,2
269	102	4741	4376	5105	8784	11,40	125,5
270	102	1632	1813	1813	12541	11,33	125,4
271	102	3426	3787	3606	12484	11,27	124,8
272	102	4453	4726	3999	8762	11,36	125,2
273	102	4189	4553	4371	7413	11,38	123,6
274	102	4070	4161	3618	10028	11,31	125,4
275	102	4283	4104	4640	8650	11,15	123,6
276	102	4708	4527	3984	7399	11,32	123,3
277	103	4205	3758	3579	9836	11,18	123,0
278	103	3210	2568	2935	11024	11,47	122,5
279	103	4159	3074	4340	11137	11,30	123,7
280	103	4621	3624	4349	9774	11,33	122,2
281	103	3031	2571	2571	8568	11,48	122,4
282	103	4058	3968	3968	8663	11,27	123,8
283	103	3979	4160	3255	8624	11,30	123,2
284	103	4390	3658	3658	9898	11,43	123,7
285	103	4336	3794	3974	9807	11,29	122,6
286	103	4170	3444	3263	11051	11,33	122,8

Table E.3.: Fracture area distribution of HIE class IV fragments: Additionally, the determined Heywood factor f_H for the particles of the fractions $-1 < \phi < 1$ is listed as well as the mass-specific surface area of the finest fraction $S_{m,\phi>1}$.

V	{...}	$A_{DC}[mm^2]$	$\triangle A_{DC}[mm^2]$	$A_{NC}[mm^2]$	$\triangle A_{NC}[mm^2]$	$A_{tot}[mm^2]$	$\triangle A_{tot}[mm^2]$
251	501	34275	1114	2155	47	36430	1161
252	501	28394	944	3999	88	32393	1032
253	401	31038	1013	5807	128	36846	1141
254	401	30763	1006	3678	81	34441	1087
255	401	21746	771	3809	84	25555	855
256	401	25845	892	3038	67	28883	959
257	201	27904	915	3571	79	31475	993
258	201	24792	839	2035	45	26827	884
259	201	22253	752	4277	94	26529	846
260	401	32998	1090	2414	53	35412	1143
261	102	22249	637	2051	45	24300	682
262	102	14406	512	2419	53	16825	565
263	102	23289	660	2164	48	25453	707
264	102	21925	676	3922	86	25847	763
265	102	23890	675	3440	76	27330	751
266	102	22813	774	3348	74	26162	848
267	102	20006	645	3474	76	23480	721
268	102	13469	475	3869	85	17338	561
269	102	23730	727	2070	46	25800	773
270	102	17727	681	2031	45	19758	725
271	102	23070	810	2511	55	25581	865
272	102	22562	704	2647	58	25209	763
273	102	22265	664	1923	42	24188	707
274	102	22708	734	2181	48	24889	782
275	102	22270	695	2311	51	24581	746
276	102	22827	677	3377	74	26204	751
277	103	21604	705	1971	43	23576	748
278	103	19826	705	3976	87	23802	792
279	103	23362	776	4072	90	27434	865
280	103	22931	734	2616	58	25548	792
281	103	16569	570	3880	85	20449	655
282	103	21927	686	3564	78	25490	764
283	103	22481	699	3570	79	26051	778
284	103	22273	721	2463	54	24736	776
285	103	22539	725	2903	64	25441	789
286	103	22408	757	3919	86	26328	843

Table E.4.: Fracture areas of HIE fragments: The results for A_{DC}, A_{NC} and the total fracture area A_{tot} are presented. The measurement uncertainties $\triangle A_{DC}$, $\triangle A_{NC}$ and $\triangle A_{tot}$ are listed as well.

V	{...}	$B_{IV,\phi=-1}[mm^2]$	$B_{IV,\phi=0}[mm^2]$	$B_{IV,\phi=1}[mm^2]$	$B_{IV,\phi>1}[mm^2]$	f_H	$S_{m,\phi>1}[\frac{m^2}{kg}]$
287	103	3486	2935	3302	12371	11,47	123,7
288	103	2131	1776	2131	12220	11,10	122,2
289	101	3957	4633	3475	12134	12,06	134,8
290	103	3369	2914	2914	11138	11,38	123,8
291	103	3876	3507	4061	11031	11,54	122,6
292	103	4335	3689	3689	9785	11,53	122,3
293	102	2568	2751	2935	7441	11,46	124,0
294	102	2681	2860	3218	7526	11,17	125,4
295	102	3201	3475	3658	11184	11,43	124,3
296	102	4814	4905	5087	7456	11,35	124,3
297	102	1891	1981	2521	7470	11,25	124,5
298	102	2105	2379	2196	11108	11,44	123,4
299	102	4338	4518	3976	8720	11,30	124,6
300	102	4250	4340	3617	8688	11,30	124,1
301	102	1805	1444	2166	7440	11,28	124,0
302	104	5597	3795	4174	13268	11,86	132,7
303	104	6060	4232	4232	12018	12,02	133,5
304	103	3750	4207	3658	9910	11,43	123,9
305	103	2027	1659	2212	11110	11,52	123,4
306	103	4207	3476	3659	9810	11,43	122,6
307	103	3874	3690	4059	9769	11,53	122,1
308	103	4030	4213	4030	9881	11,45	123,5
309	103	4326	3424	3605	11013	11,26	122,4
310	103	3331	2881	3241	11069	11,25	123,0
311	103	2687	2150	2867	12268	11,20	122,7
312	103	2952	2768	3321	11002	11,53	122,2
313	103	2611	2160	2881	6139	11,25	122,8
314	103	4565	3834	4017	8630	11,41	123,3
315	103	3724	3451	3633	9841	11,35	123,0
316	103	2166	1805	2166	12298	11,28	123,0
317	103	1880	1612	1791	12210	11,19	122,1
318	103	4235	3498	3683	11055	11,51	122,8
319	303	4651	3648	4742	11114	11,40	123,5
320	303	5185	4291	5006	12341	11,17	123,4
321	303	3736	3098	3281	11041	11,39	122,7
322	303	3640	2912	3640	10993	11,38	122,1

Table E.5.: Fracture area distribution of HIE class IV fragments: Additionally, the determined Heywood factor f_H for the particles of the fractions $-1 < \phi < 1$ is listed as well as the mass-specific surface area of the finest fraction $S_{m,\phi>1}$.

V	{...}	$A_{DC}[mm^2]$	$\triangle A_{DC}[mm^2]$	$A_{NC}[mm^2]$	$\triangle A_{NC}[mm^2]$	$A_{tot}[mm^2]$	$\triangle A_{tot}[mm^2]$
287	103	21790	781	3366	74	25156	855
288	103	18272	692	2812	62	21083	754
289	101	25418	844	2806	62	28223	906
290	103	20167	714	3736	82	23903	796
291	103	23947	788	3485	77	27431	865
292	103	22496	723	2737	60	25233	783
293	102	15927	536	3619	80	19546	616
294	102	16300	547	2768	61	19068	608
295	102	21988	744	3869	85	25856	829
296	102	23299	689	3750	82	27049	772
297	102	13888	486	3509	77	17397	563
298	102	17739	659	4380	96	22119	755
299	102	22796	708	4405	97	27201	805
300	102	23187	715	4420	97	27607	812
301	102	12720	472	3860	85	16580	557
302	104	27702	935	2599	57	30300	992
303	104	27017	874	2269	50	29285	924
304	103	22354	723	3566	78	25919	801
305	103	17053	639	2951	65	20004	704
306	103	21781	709	3694	81	25475	790
307	103	22924	734	2129	47	25053	780
308	103	22898	734	2786	61	25685	795
309	103	22348	768	3459	76	25807	844
310	103	20288	717	3790	83	24078	800
311	103	19848	728	2188	48	22036	776
312	103	20631	712	3604	79	24235	791
313	103	14422	480	3600	79	18022	559
314	103	22055	688	3672	81	25728	769
315	103	20730	692	3607	79	24337	771
316	103	17623	693	3470	76	21094	769
317	103	17605	675	2645	58	20250	734
318	103	21697	769	1888	42	23585	810
319	303	24078	806	2068	46	26146	852
320	303	27133	903	4955	109	32088	1012
321	303	20770	727	2010	44	22780	771
322	303	21126	731	3992	88	25119	819

Table E.6.: Fracture areas of HIE fragments: The results for A_{DC}, A_{NC} and the total fracture area A_{tot} are presented. The measurement uncertainties $\triangle A_{DC}$, $\triangle A_{NC}$ and $\triangle A_{tot}$ are listed as well.

V	{...}	$B_{IV,\phi=-1}[mm^2]$	$B_{IV,\phi=0}[mm^2]$	$B_{IV,\phi=1}[mm^2]$	$B_{IV,\phi>1}[mm^2]$	f_H	$S_{m,\phi>1}[\frac{m^2}{kg}]$
323	303	3529	2896	3620	10990	11,31	122,1
324	105	2701	3167	3353	12132	11,64	134,8
325	105	3920	5163	4590	13301	11,95	133,0
326	105	3221	3978	3789	12222	11,84	135,8
327	105	4194	4957	4194	12182	11,91	135,4
328	105	4299	5159	4968	12100	11,94	134,4
329	105	4319	4990	4990	12020	12,00	133,6
330	102	3948	4958	3673	8750	11,48	125,0
350	602	2964	3233	3233	11238	11,23	124,9
351	602	4899	5444	5444	11176	11,34	124,2
352	602	3578	4037	4037	12391	11,47	123,9
353	602	6367	6913	6913	13779	11,37	125,3
354	602	3380	3654	3654	11269	11,42	125,2
355	602	5033	5491	5491	12515	11,44	125,1
356	603	8069	6635	7173	12282	11,21	122,8
357	603	3790	3143	3698	12210	11,56	122,1
358	603	4700	3796	4338	13462	11,30	122,4
359	603	4326	3425	4326	11005	11,26	122,3
360	604	4998	3460	3845	11893	12,01	132,1
361	604	5557	3832	3449	11942	11,98	132,7
362	604	5383	3653	3845	13183	12,02	131,8
363	604	4214	2873	3065	13140	11,97	131,4
364	603	6005	5095	5459	13474	11,37	122,5
365	603	1986	1625	1805	12257	11,28	122,6
401	106	2437	1796	2566	7389	8,34	105,6
402	106	4289	2600	1820	6334	8,45	105,6
403	106	1897	1570	2355	7388	8,51	105,5
405	106	1508	1180	1574	7361	8,52	105,2
406	106	1297	648	2074	4273	8,43	106,8
407	106	2155	1698	2612	7351	8,49	105,0
408	106	1686	1167	1556	8431	8,43	105,4
409	106	1040	780	1040	7465	8,45	106,6
410	106	1711	1316	1843	8544	8,56	106,8
411	106	2212	1562	2343	8436	8,46	105,5
412	106	2336	1817	2336	7473	8,44	106,8
413	106	2107	1580	2371	8487	8,56	106,1

Table E.7.: Fracture area distribution of HIE class IV fragments: Additionally, the determined Heywood factor f_H for the particles of the fractions $-1 < \phi < 1$ is listed as well as the mass-specific surface area of the finest fraction $S_{m,\phi>1}$.

V	{...}	$A_{DC}[mm^2]$	$\triangle A_{DC}[mm^2]$	$A_{NC}[mm^2]$	$\triangle A_{NC}[mm^2]$	$A_{tot}[mm^2]$	$\triangle A_{tot}[mm^2]$
323	303	20729	725	4335	95	25065	820
324	105	21362	758	3564	78	24926	836
325	105	26943	913	1986	44	28929	957
326	105	23186	806	3194	70	26380	876
327	105	25775	862	2628	58	28403	920
328	105	27811	893	2566	56	30377	950
329	105	27414	884	2524	56	29938	939
330	102	21777	692	2380	52	24157	745
350	602	20575	719	5378	118	25953	837
351	602	26974	864	5806	128	32780	992
352	602	23951	819	6838	150	30789	969
353	602	33733	1080	3950	87	37684	1167
354	602	21846	749	3455	76	25301	825
355	602	28253	925	3237	71	31490	996
356	603	36519	1095	5665	125	42184	1219
357	603	22531	789	4037	89	26568	878
358	603	28625	946	3496	77	32121	1023
359	603	26139	836	3921	86	30060	922
360	604	24095	806	4258	94	28353	900
361	604	24675	820	3407	75	28082	895
362	604	26006	878	3240	71	29247	949
363	604	25790	872	4280	94	30070	966
364	603	33435	1048	5365	118	38799	1166
365	603	18102	689	3163	70	21265	759
401	106	14128	502	2667	59	16795	561
402	106	15560	492	4330	95	19890	588
403	106	13100	467	2610	57	15710	524
405	106	11482	430	2992	66	14473	496
406	106	8019	289	3388	75	11406	363
407	106	13942	490	2575	57	16518	547
408	106	12897	485	2181	48	15078	533
409	106	10271	400	2879	63	13150	463
410	106	13478	501	1883	41	15361	543
411	106	15385	538	2720	60	18105	598
412	106	14189	499	3913	86	18102	585
413	106	14573	531	1917	42	16490	573

Table E.8.: Fracture areas of HIE fragments: The results for A_{DC}, A_{NC} and the total fracture area A_{tot} are presented. The measurement uncertainties $\triangle A_{DC}$, $\triangle A_{NC}$ and $\triangle A_{tot}$ are listed as well.

V	{...}	$B_{IV,\phi=-1}[mm^2]$	$B_{IV,\phi=0}[mm^2]$	$B_{IV,\phi=1}[mm^2]$	$B_{IV,\phi>1}[mm^2]$	f_H	$S_{m,\phi>1}[\frac{m^2}{kg}]$
414	106	2464	1816	2854	7477	8,43	106,8
415	106	1701	1308	1308	2129	8,51	106,4
416	106	2297	1050	1312	3161	8,53	105,4
417	306	2082	1302	2343	8430	8,46	105,4
418	306	1900	1572	2097	8476	8,52	105,9
419	306	2041	1580	2107	8437	8,56	105,5
420	306	2291	1702	2619	7392	8,51	105,6
421	306	1714	1187	1846	7389	8,57	105,6
422	306	1839	1182	2102	7384	8,54	105,5
423	306	2342	1951	2602	7418	8,46	106,0
424	306	2168	1840	2365	7451	8,54	106,4
425	306	2428	1968	2625	8444	8,53	105,6
426	306	2225	1571	2618	8498	8,51	106,2
427	306	2655	2072	3108	8466	8,42	105,8
428	306	2100	1444	2100	8384	8,53	104,8
429	606	2881	1964	2619	5306	8,51	106,1
430	606	2391	1939	2844	8460	8,40	105,8
431	606	1964	1571	2095	8448	8,51	105,6
432	606	2637	2241	2900	8427	8,57	105,3
433	606	2170	1841	2368	8402	8,55	105,0
434	606	2040	1448	2369	4248	8,56	106,2
500	105	4574	5527	4955	9450	11,91	135,0
501	105	2754	3609	3039	12006	11,87	133,4
502	305	3821	4585	4585	13481	11,94	134,8
503	305	3958	5019	4633	13598	12,07	136,0
504	305	4715	5847	5281	13456	11,79	134,6
505	605	3250	4014	3823	14842	11,95	134,9
506	605	5592	7393	6825	14639	11,85	133,1
507	605	5508	7028	6838	13420	11,87	134,2
510	205	3649	4679	4492	13310	11,70	133,1
511	405	3393	4335	3770	14716	11,78	133,8
512	405	3883	4925	4546	14950	11,84	135,9
514	505	4184	5325	4945	14690	11,89	133,5
515	505	3694	4736	4547	13345	11,84	133,5

Table E.9.: Fracture area distribution of HIE class IV fragments: Additionally, the determined Heywood factor f_H for the particles of the fractions $-1 < \phi < 1$ is listed as well as the mass-specific surface area of the finest fraction $S_{m,\phi>1}$.

V	{...}	$A_{DC}[mm^2]$	$\triangle A_{DC}[mm^2]$	$A_{NC}[mm^2]$	$\triangle A_{NC}[mm^2]$	$A_{tot}[mm^2]$	$\triangle A_{tot}[mm^2]$
414	106	15478	534	3314	73	18791	607
415	106	6511	200	2377	52	8887	253
416	106	7759	264	1996	44	9755	308
417	306	17508	586	3530	78	21038	664
418	306	16406	561	4567	100	20973	661
419	306	14820	523	3785	83	18605	606
420	306	16336	534	4847	107	21183	640
421	306	14066	484	2798	62	16864	546
422	306	12368	446	4883	107	17251	553
423	306	17772	564	2451	54	20222	618
424	306	14143	492	3158	69	17301	561
425	306	15600	545	3515	77	19114	622
426	306	15100	535	2610	57	17711	593
427	306	16764	580	4268	94	21033	673
428	306	14395	519	2160	48	16555	566
429	606	12722	404	3538	78	16261	482
430	606	16119	557	4954	109	21073	666
431	606	14006	505	4554	100	18560	605
432	606	18587	622	5878	129	24465	751
433	606	15121	534	6428	141	21549	676
434	606	10675	340	6425	141	17100	482
500	105	25283	777	3096	68	28380	845
501	105	21312	754	2069	46	23381	800
502	305	26280	898	2387	53	28666	950
503	305	27090	918	5038	111	32128	1029
504	305	29211	961	4630	102	33841	1063
505	605	29108	989	5519	121	34628	1111
506	605	36461	1146	6241	137	42703	1283
507	605	34805	1080	6774	149	41578	1229
510	205	26060	887	2346	52	28406	939
511	405	26025	921	5208	115	31232	1035
512	405	31506	1042	2834	62	34341	1104
514	505	28917	989	4279	94	33195	1083
515	505	26267	887	5615	124	31882	1011

Table E.10.: Fracture areas of HIE fragments: The results for A_{DC}, A_{NC} and the total fracture area A_{tot} are presented. The measurement uncertainties $\triangle A_{DC}$, $\triangle A_{NC}$ and $\triangle A_{tot}$ are listed as well.

V	{...}	$B_{IV,\phi=-1}[mm^2]$	$B_{IV,\phi=0}[mm^2]$	$B_{IV,\phi=1}[mm^2]$	$B_{IV,\phi>1}[mm^2]$	f_H	$S_{m,\phi>1}[\frac{m^2}{kg}]$
601	113	3442	2977	3349	11084	11,63	123,2
602	113	3898	3341	3713	11029	11,60	122,5
603	113	4340	3774	4152	9767	11,79	122,1
605	114	5847	3568	4360	13172	12,39	131,7
606	114	5801	4129	3933	12005	12,29	133,4
607	114	4650	2770	2770	3967	12,37	132,2
608	114	6311	4142	4733	11963	12,33	132,9
609	114	6175	4116	3920	13241	12,25	132,4
610	114	5641	3959	3563	13328	12,37	133,3
611	613	6942	5816	6379	13451	11,73	122,3
612	112	3353	3624	3624	8643	11,33	123,5
613	112	4157	4619	3326	7465	11,55	124,4
614	112	4349	4812	3701	9889	11,57	123,6
615	612	6199	6662	6662	12443	11,57	124,4
616	312	4710	5172	5172	12538	11,55	125,4
617	312	5234	5608	5608	12381	11,68	123,8
618	612	4747	5212	5212	11277	11,63	125,3
619	111	2752	3538	4324	12195	12,29	135,5
620	211	2993	3792	4390	12017	12,47	133,5
621	111	3585	3585	3585	10846	12,45	135,6
622	111	4969	4174	3975	9347	12,42	133,5
623	111	4890	5389	5190	9355	12,47	133,6
624	611	4773	6165	7159	16115	12,43	134,3
625	611	4071	5163	5958	13491	12,41	134,9
626	311	4983	6378	7574	13402	12,46	134,0
627	311	5058	6546	7538	13432	12,40	134,3
628	211	5069	6560	7952	12109	12,42	134,5
629	411	4059	5148	6336	13486	12,38	134,9
630	511	3790	4787	5984	12017	12,47	133,5
631	511	3771	4962	5955	13444	12,41	134,4
640	121	4020	5098	5491	6722	12,26	134,4
641	121	3583	4578	4777	10674	12,44	133,4
642	121	3162	3953	4744	12051	12,35	133,9
643	121	4367	4963	5162	10819	12,41	135,2
644	221	2482	3178	3972	12178	12,41	135,3
645	221	2856	3546	4334	13561	12,31	135,6

Table E.11.: Fracture area distribution of HIE class IV fragments: Additionally, the determined Heywood factor f_H for the particles of the fractions $-1 < \phi < 1$ is listed as well as the mass-specific surface area of the finest fraction $S_{m,\phi>1}$.

V	{...}	$A_{DC}[mm^2]$	$\triangle A_{DC}[mm^2]$	$A_{NC}[mm^2]$	$\triangle A_{NC}[mm^2]$	$A_{tot}[mm^2]$	$\triangle A_{tot}[mm^2]$
601	113	20916	730	2361	52	23277	782
602	113	21899	751	2985	66	24884	816
603	113	22498	722	2567	56	25065	779
605	114	26900	909	2647	58	29548	967
606	114	26673	865	2580	57	29253	921
607	114	14071	404	2176	48	16247	452
608	114	27386	883	3120	69	30507	952
609	114	27714	928	1705	38	29419	966
610	114	26847	902	3245	71	30092	974
611	613	33051	1058	3197	70	36248	1128
612	112	19200	636	2199	48	21399	684
613	112	19558	609	3595	79	23153	688
614	112	23707	754	4409	97	28116	851
615	612	32059	1012	7032	155	39091	1167
616	312	27586	911	3956	87	31542	998
617	312	28588	926	4815	106	33403	1032
618	612	26315	853	4486	99	30801	952
619	111	23119	796	1973	43	25092	839
620	211	26259	857	3506	77	29765	934
621	111	21554	733	3096	68	24650	801
622	111	22458	714	3406	75	25864	789
623	111	25216	779	2003	44	27218	823
624	611	33986	1133	4997	110	38984	1243
625	611	28297	948	5239	115	33535	1063
626	311	32183	1031	4098	90	36281	1121
627	311	32562	1039	3118	69	35680	1108
628	211	31955	1004	3568	78	35523	1083
629	411	31176	1003	2711	60	33887	1062
630	511	29267	923	4584	101	33851	1024
631	511	27972	941	2741	60	30713	1001
640	121	22534	655	4168	92	26702	747
641	121	23502	765	3305	73	26807	838
642	121	23775	809	2469	54	26244	863
643	121	26036	827	4018	88	30054	916
644	221	21677	771	3677	81	25354	852
645	221	24154	859	3713	82	27867	940

Table E.12.: Fracture areas of HIE fragments: The results for A_{DC}, A_{NC} and the total fracture area A_{tot} are presented. The measurement uncertainties $\triangle A_{DC}$, $\triangle A_{NC}$ and $\triangle A_{tot}$ are listed as well.

V	{...}	$B_{IV,\phi=-1}[mm^2]$	$B_{IV,\phi=0}[mm^2]$	$B_{IV,\phi=1}[mm^2]$	$B_{IV,\phi>1}[mm^2]$	f_H	$S_{m,\phi>1}[\frac{m^2}{kg}]$
646	221	5060	6548	7937	12200	12,40	135,6
647	421	5030	6510	7891	13472	12,33	134,7
648	421	4964	6354	7545	14772	12,41	134,3
649	421	5338	6920	8304	13354	12,36	133,5
650	621	4039	5123	6305	14878	12,31	135,3
651	621	5036	6517	7505	13346	12,34	133,5
652	621	6533	8315	9899	16172	12,37	134,8
653	621	6302	8074	9452	16123	12,31	134,4
654	122	3338	3524	3338	12424	11,59	124,2
655	122	3912	3912	3725	11281	11,64	125,3
656	122	4209	4209	4026	9902	11,44	123,8
657	122	3890	3519	3705	8714	11,58	124,5
658	422	6068	6721	6721	12428	11,67	124,3
659	422	5762	6320	6320	12541	11,62	125,4
660	422	2848	3124	2940	13742	11,48	124,9
661	622	6051	6601	6601	13583	11,46	123,5
662	622	5251	5711	5527	12343	11,51	123,4
663	622	3787	4064	4064	13630	11,55	123,9
664	622	4554	5101	5101	12435	11,39	124,3
665	123	4127	3189	3377	9811	11,72	122,6
666	123	3878	3324	3693	11049	11,54	122,8
667	123	3971	3325	4064	12378	11,54	123,8
668	123	4239	3318	4424	11105	11,52	123,4
669	423	6038	5017	5574	12231	11,61	122,3
670	423	4402	3668	4402	12255	11,46	122,5
671	423	5265	4433	5172	11077	11,55	123,1
672	623	6283	5281	5463	12344	11,38	123,4
673	623	6404	5198	6683	13451	11,60	122,3
674	623	4292	3470	4383	13590	11,41	123,5
675	623	4011	3171	4104	13583	11,66	123,5
676	124	4702	2939	3135	13337	12,25	133,4
677	124	6257	3715	4693	11928	12,22	132,5
678	124	4194	2926	3121	13335	12,19	133,3
680	424	6764	4445	5025	14668	12,08	133,3
681	424	5794	4124	3535	13304	12,27	133,0
682	424	6951	4699	4307	11922	12,24	132,5

Table E.13.: Fracture area distribution of HIE class IV fragments: Additionally, the determined Heywood factor f_H for the particles of the fractions $-1 < \phi < 1$ is listed as well as the mass-specific surface area of the finest fraction $S_{m,\phi>1}$.

V	{...}	$A_{DC}[mm^2]$	$\triangle A_{DC}[mm^2]$	$A_{NC}[mm^2]$	$\triangle A_{NC}[mm^2]$	$A_{tot}[mm^2]$	$\triangle A_{tot}[mm^2]$
646	221	31603	997	2669	59	34272	1056
647	421	32600	1049	2546	56	35145	1105
648	421	33467	1099	3753	83	37220	1182
649	421	35790	1121	4332	95	40121	1217
650	621	30180	1021	4405	97	34585	1118
651	621	31963	1032	6199	136	38162	1168
652	621	42325	1331	4474	98	46799	1429
653	621	41528	1311	7185	158	48713	1469
654	122	22923	795	3550	78	26472	873
655	122	22973	780	4094	90	27067	870
656	122	22926	736	2924	64	25850	800
657	122	20093	646	3718	82	23811	728
658	422	32130	1015	2248	49	34378	1065
659	422	30657	983	4731	104	35388	1087
660	422	23119	846	3203	70	26323	916
661	622	32742	1055	4112	90	36854	1145
662	622	28739	932	3726	82	32465	1013
663	622	25294	885	6589	145	31883	1030
664	622	26819	893	5084	112	31903	1004
665	123	21123	694	2334	51	23457	745
666	123	21812	743	3744	82	25556	825
667	123	23637	820	2376	52	26013	872
668	123	22789	771	2535	56	25324	827
669	423	28708	933	4260	94	32967	1026
670	423	24651	833	4888	108	29539	940
671	423	26295	856	4003	88	30298	944
672	623	29656	956	5349	118	35005	1074
673	623	31475	1023	3835	84	35310	1107
674	623	27628	927	6428	141	34056	1069
675	623	24688	870	4782	105	29470	975
676	124	24324	856	2005	44	26329	900
677	124	26763	883	2103	46	28866	929
678	124	23706	843	1772	39	25478	882
680	424	31252	1048	2361	52	33614	1100
681	424	26538	904	3852	85	30390	988
682	424	28181	914	3005	66	31186	980

Table E.14.: Fracture areas of HIE fragments: The results for A_{DC}, A_{NC} and the total fracture area A_{tot} are presented. The measurement uncertainties $\triangle A_{DC}$, $\triangle A_{NC}$ and $\triangle A_{tot}$ are listed as well.

V	{...}	$B_{IV,\phi=-1}[mm^2]$	$B_{IV,\phi=0}[mm^2]$	$B_{IV,\phi=1}[mm^2]$	$B_{IV,\phi>1}[mm^2]$	f_H	$S_{m,\phi>1}[\frac{m^2}{kg}]$
683	624	7537	5090	5482	13307	12,24	133,1
684	624	8756	5837	6226	14497	12,16	131,8
685	624	4199	2734	3125	13240	12,21	132,4
686	622	4248	4617	4802	13763	11,54	125,1
687	622	5531	6084	5900	12428	11,52	124,3
688	122	4018	4298	4112	11247	11,68	125,0
689	622	6607	7258	7072	12421	11,63	124,2
690	622	5444	5905	5905	12546	11,53	125,5
692	622	6639	7192	7377	12486	11,53	124,9
693	421	3243	4127	5110	13510	12,28	135,1
694	421	3573	4566	5558	13354	12,41	133,5
695	221	4335	5714	6700	13492	12,32	134,9
696	221	1478	1971	2365	12065	12,32	134,1
697	221	2465	3155	3944	13532	12,33	135,3
700	131	4978	6247	4686	9321	12,20	133,2
701	131	2056	2545	3132	10718	12,24	134,0
702	131	4119	5296	6276	9366	12,26	133,8
703	131	2624	3305	3888	9473	12,15	135,3
704	231	4847	6204	7367	12086	12,12	134,3
705	231	1850	2337	2727	12029	12,17	133,7
706	231	4188	5455	6623	12073	12,18	134,1
707	231	2833	3712	4298	10672	12,21	133,4
708	431	4460	5624	6593	12166	12,12	135,2
709	431	2252	2938	3525	10761	12,24	134,5
710	431	2429	3109	3498	13483	12,15	134,8
711	631	3322	4299	5081	13371	12,21	133,7
712	631	4971	6238	7408	13414	12,18	134,1
713	631	2149	2735	3126	13485	12,21	134,8
714	631	5571	7233	8601	13382	12,22	133,8
715	132	3422	3602	3962	11171	11,26	124,1
716	132	3020	3294	3294	11294	11,44	125,5
717	132	1991	2172	2172	9893	11,31	123,7
718	132	3358	3630	3630	11244	11,34	124,9
719	432	5768	6309	6129	12466	11,27	124,7
720	432	4819	5273	5455	11225	11,36	124,7
721	432	2827	3101	3283	12499	11,40	125,0

Table E.15.: Fracture area distribution of HIE class IV fragments: Additionally, the determined Heywood factor f_H for the particles of the fractions $-1 < \phi < 1$ is listed as well as the mass-specific surface area of the finest fraction $S_{m,\phi>1}$.

V	{...}	$A_{DC}[mm^2]$	$\triangle A_{DC}[mm^2]$	$A_{NC}[mm^2]$	$\triangle A_{NC}[mm^2]$	$A_{tot}[mm^2]$	$\triangle A_{tot}[mm^2]$
683	624	31422	1020	2245	49	33667	1070
684	624	35303	1130	4682	103	39985	1233
685	624	23241	830	4371	96	27613	926
686	622	28951	969	5864	129	34815	1098
687	622	30479	977	2270	50	32749	1027
688	122	23599	793	4807	106	28405	899
689	622	33613	1044	6861	151	40474	1195
690	622	30135	971	3403	75	33538	1046
692	622	33578	1045	3368	74	36946	1119
693	421	25992	897	4347	96	30339	992
694	421	27217	919	2419	53	29635	972
695	221	30436	1000	2044	45	32480	1045
696	221	17752	671	2371	52	20123	723
697	221	26074	888	2486	55	28559	943
700	131	25361	777	3762	83	29123	859
701	131	18327	653	3737	82	22063	735
702	131	24991	768	3110	68	28101	836
703	131	19566	661	2724	60	22290	721
704	231	30194	964	2574	57	32769	1021
705	231	18801	693	3249	71	22050	765
706	231	27938	914	2159	47	30097	961
707	231	23865	774	2033	45	25899	818
708	431	29941	964	4943	109	34884	1073
709	431	19406	677	2769	61	22175	738
710	431	22304	809	1904	42	24208	851
711	631	25901	893	6684	147	32585	1040
712	631	32262	1041	4164	92	36426	1133
713	631	20968	784	4870	107	25838	891
714	631	35185	1107	2100	46	37286	1154
715	132	22640	764	2831	62	25470	826
716	132	21614	742	3247	71	24861	813
717	132	16334	594	2532	56	18866	650
718	132	21692	751	2439	54	24130	805
719	432	31184	993	3117	69	34301	1062
720	432	26562	865	2245	49	28808	915
721	432	21700	781	2609	57	24309	838

Table E.16.: Fracture areas of HIE fragments: The results for A_{DC}, A_{NC} and the total fracture area A_{tot} are presented. The measurement uncertainties $\triangle A_{DC}$, $\triangle A_{NC}$ and $\triangle A_{tot}$ are listed as well.

V	{...}	$B_{IV,\phi=-1}[mm^2]$	$B_{IV,\phi=0}[mm^2]$	$B_{IV,\phi=1}[mm^2]$	$B_{IV,\phi>1}[mm^2]$	f_H	$S_{m,\phi>1}[\frac{m^2}{kg}]$
722	632	3656	4021	4021	12549	11,42	125,5
723	632	6357	6902	6902	11248	11,35	125,0
724	632	5780	6322	6141	11178	11,29	124,2
725	632	5933	6572	6572	12354	11,41	123,5
726	133	4419	3498	4419	8661	11,51	123,7
727	133	4650	3647	4376	9828	11,40	122,9
728	133	2529	1987	2529	11064	11,29	122,9
729	133	3407	2763	2947	9801	11,51	122,5
730	433	5978	4967	5886	11142	11,50	123,8
731	433	4856	3848	4765	12347	11,45	123,5
732	433	5690	4877	5058	12368	11,29	123,7
733	433	5447	4616	5170	12310	11,54	123,1
734	633	6237	4953	5870	12212	11,47	122,1
735	633	5846	4677	6116	11021	11,24	122,5
736	633	6331	5138	6239	12253	11,47	122,5
737	133	4137	3677	4045	9788	11,49	122,3
738	134	5823	3688	4270	11959	12,13	132,9
739	134	2986	2119	1926	11844	12,04	131,6
740	134	3193	2322	2322	10624	12,10	132,8
741	134	6269	3858	3472	11912	12,06	132,4
742	434	4535	2894	3473	11835	12,06	131,5
743	434	4156	2900	2706	11943	12,08	132,7
744	434	4727	2894	3473	11872	12,06	131,9
745	634	5300	3469	3855	11918	12,05	132,4
746	634	4647	3292	3098	13201	12,10	132,0
747	634	7244	5216	4636	11983	12,07	133,1
748	133	4794	4056	4425	9905	11,52	123,8
749	133	2144	1787	2144	9769	11,17	122,1
800	116	1490	2168	2439	4199	8,81	105,0
801	116	1215	810	1349	7364	8,77	105,2

Table E.17.: Fracture area distribution of HIE class IV fragments: Additionally, the determined Heywood factor f_H for the particles of the fractions $-1 < \phi < 1$ is listed as well as the mass-specific surface area of the finest fraction $S_{m,\phi>1}$.

V	{...}	$A_{DC}[mm^2]$	$\triangle A_{DC}[mm^2]$	$A_{NC}[mm^2]$	$\triangle A_{NC}[mm^2]$	$A_{tot}[mm^2]$	$\triangle A_{tot}[mm^2]$
722	632	24019	831	6650	146	30670	977
723	632	31837	979	2981	66	34818	1045
724	632	29614	929	5980	132	35593	1061
725	632	31440	997	5869	129	37308	1126
726	133	21921	685	2322	51	24243	736
727	133	23157	755	1884	41	25041	796
728	133	18281	672	1976	43	20257	715
729	133	18504	649	2589	57	21092	706
730	433	28060	894	2291	50	30351	944
731	433	26367	884	4592	101	30960	985
732	433	28425	931	4969	109	33394	1040
733	433	27865	916	2305	51	30170	966
734	633	29611	952	3750	83	33361	1035
735	633	27537	880	5701	125	33238	1006
736	633	30410	977	6898	152	37308	1129
737	133	22439	723	3031	67	25470	789
738	134	26510	877	2973	65	29482	943
739	134	18912	696	2002	44	20914	740
740	134	18337	655	1814	40	20151	695
741	134	26161	870	1620	36	27781	905
742	434	22458	779	1856	41	24315	820
743	434	21620	759	3005	66	24624	825
744	434	23133	797	3007	66	26140	863
745	634	24524	823	5249	115	29772	938
746	634	24269	846	4922	108	29191	954
747	634	31105	987	3921	86	35026	1073
748	133	23502	752	2309	51	25811	803
749	133	16536	593	3103	68	19639	662
800	116	10393	339	2091	46	12484	385
801	116	10543	415	2674	59	13216	474

Table E.18.: Fracture areas of HIE fragments: The results for A_{DC}, A_{NC} and the total fracture area A_{tot} are presented. The measurement uncertainties $\triangle A_{DC}$, $\triangle A_{NC}$ and $\triangle A_{tot}$ are listed as well.

V	{...}	$B_{IV,\phi=-1}[mm^2]$	$B_{IV,\phi=0}[mm^2]$	$B_{IV,\phi=1}[mm^2]$	$B_{IV,\phi>1}[mm^2]$	f_H	$S_{m,\phi>1}[\frac{m^2}{kg}]$
802	116	3031	2155	3233	6401	8,76	106,7
803	616	2223	1482	2425	8407	8,76	105,1
804	616	3558	2820	3760	7385	8,73	105,5
805	616	1694	1084	1897	7364	8,81	105,2
806	616	1420	1082	1623	7400	8,79	105,7
807	316	3254	2576	3254	8407	8,81	105,1
808	316	2382	1906	2722	7455	8,85	106,5
809	316	1560	1221	1628	8480	8,82	106,0
810	126	1560	1221	1899	8498	8,82	106,2
811	126	2065	1465	2398	8394	8,66	104,9
812	126	2003	1603	2671	8399	8,68	105,0
813	126	1867	1733	2133	8416	8,67	105,2
814	126	2214	1476	2415	8472	8,72	105,9
815	626	1420	1082	1623	8449	8,79	105,6
816	626	3702	2692	4308	8534	8,75	106,7
817	626	1666	1066	1865	8405	8,66	105,1
818	426	3281	2679	3750	9547	8,71	106,1
819	426	2037	1629	2444	7472	8,83	106,7
820	426	2220	1749	2422	7337	8,75	104,8
821	426	2349	1611	2685	8426	8,72	105,3
822	426	3498	2825	3767	8462	8,75	105,8
823	626	2142	1606	2410	8488	8,70	106,1
900	136	1579	1316	1842	7346	8,55	104,9
901	136	1187	923	1318	8456	8,57	105,7
902	136	1526	1062	1593	7366	8,63	105,2
903	136	1699	1568	2353	6380	8,50	106,3
904	136	2021	1434	2608	8497	8,48	106,2
905	136	1180	918	1311	7395	8,52	105,6
906	636	3916	3318	4247	7356	8,63	105,1
907	636	2204	1603	2671	8474	8,68	105,9
908	636	2959	2104	3157	8511	8,55	106,4
909	636	3267	2400	4000	8396	8,67	104,9
910	636	2756	1837	3150	7407	8,53	105,8
911	636	2039	1315	2105	8465	8,55	105,8
912	136	2029	1571	2094	7395	8,51	105,6
913	136	1719	1322	2115	8416	8,59	105,2

Table E.19.: Fracture area distribution of HIE class IV fragments: Additionally, the determined Heywood factor f_H for the particles of the fractions $-1 < \phi < 1$ is listed as well as the mass-specific surface area of the finest fraction $S_{m,\phi>1}$.

V	{...}	$A_{DC}[mm^2]$	$\triangle A_{DC}[mm^2]$	$A_{NC}[mm^2]$	$\triangle A_{NC}[mm^2]$	$A_{tot}[mm^2]$	$\triangle A_{tot}[mm^2]$
802	116	15378	489	3831	84	19209	573
803	616	14757	532	5323	117	20080	650
804	616	17541	571	5106	112	22647	683
805	616	11793	444	3487	77	15280	521
806	616	11800	432	5285	116	17085	548
807	316	17899	609	4076	90	21975	699
808	316	15112	507	3428	75	18541	582
809	316	13060	495	3427	75	16487	570
810	126	12982	494	2754	61	15736	555
811	126	15296	533	2267	50	17563	583
812	126	15192	532	2387	53	17579	585
813	126	15066	529	2308	51	17374	580
814	126	15540	541	2245	49	17785	590
815	626	13040	488	4298	95	17338	583
816	626	21077	686	3566	78	24644	765
817	626	13166	497	7049	155	20215	652
818	426	19430	667	3915	86	23345	753
819	426	13624	481	2907	64	16530	545
820	426	13571	476	1743	38	15313	514
821	426	15307	544	3131	69	18438	613
822	426	18660	628	2567	56	21226	685
823	626	14650	531	3467	76	18117	608
900	136	12281	452	2018	44	14299	496
901	136	11806	456	3752	83	15558	539
902	136	11741	440	2278	50	14019	491
903	136	11796	422	2074	46	13870	467
904	136	15213	536	3555	78	18768	615
905	136	10611	412	3033	67	13645	478
906	636	19682	628	5965	131	25647	760
907	636	15121	542	4731	104	19852	646
908	636	16957	588	5710	126	22667	714
909	636	18382	618	4096	90	22478	708
910	636	15196	526	4869	107	20065	633
911	636	14272	519	5852	129	20124	648
912	136	12916	467	3526	78	16443	545
913	136	12955	500	2217	49	15172	549

Table E.20.: Fracture areas of HIE fragments: The results for A_{DC}, A_{NC} and the total fracture area A_{tot} are presented. The measurement uncertainties $\triangle A_{DC}$, $\triangle A_{NC}$ and $\triangle A_{tot}$ are listed as well.

V	{...}	$B_{IV,\phi=-1}$ [mm^2]	$B_{IV,\phi=0}$ [mm^2]	$B_{IV,\phi=1}$ [mm^2]	$B_{IV,\phi>1}$ [mm^2]	f_H	$S_{m,\phi>1}$ [$\frac{m^2}{kg}$]
914	636	3729	2748	3925	7427	8,50	106,1
1001	135	3042	3993	3422	10845	11,88	135,6
1003	135	2793	3660	3468	10701	12,04	133,8
1005	135	3935	4799	4991	13305	12,00	133,0
1007	135	4599	5174	5365	10640	11,98	133,0
1008	135	4880	5550	4210	10750	11,96	134,4
1009	135	4922	5679	4922	9388	11,83	134,1
269B	102	1916	2190	2190	11274	11,41	125,3
H3103	105	2628	3191	3003	13596	11,73	136,0
H3601	605	7863	8147	7200	14779	11,84	134,4
L605	114	5829	3557	4347	9314	12,35	133,1
L693	421	5257	6150	6348	13448	12,40	134,5
L722	432	3354	3626	3626	11229	11,33	124,8

Table E.21.: Fracture area distribution of HIE class IV fragments: Additionally, the determined Heywood factor f_H for the particles of the fractions $-1 < \phi < 1$ is listed as well as the mass-specific surface area of the finest fraction $S_{m,\phi>1}$.

V	{...}	A_{DC} [mm^2]	$\triangle A_{DC}$ [mm^2]	A_{NC} [mm^2]	$\triangle A_{NC}$ [mm^2]	A_{tot} [mm^2]	$\triangle A_{tot}$ [mm^2]
914	636	18153	593	5976	131	24129	724
1001	135	21485	735	1799	40	23284	775
1003	135	20576	706	1997	44	22573	750
1005	135	26868	911	3977	87	30845	998
1007	135	26568	834	4274	94	30842	928
1008	135	26898	846	2958	65	29856	911
1009	135	26195	806	4523	99	30718	906
269B	102	17421	650	3460	76	20881	727
H3103	105	22336	807	2919	64	25255	871
H3601	605	38240	1188	4188	92	42428	1280
L605	114	23337	737	3217	71	26554	808
L693	421	31425	1008	4635	102	36060	1110
L722	432	21794	762	5601	123	27394	885

Table E.22.: Fracture areas of HIE fragments: The results for A_{DC}, A_{NC} and the total fracture area A_{tot} are presented. The measurement uncertainties $\triangle A_{DC}$, $\triangle A_{NC}$ and $\triangle A_{tot}$ are listed as well.

F. Quantified Energies and FSED Results

V	{...}	E_{tot} [mJ]	$\triangle E_{tot}$ [mJ]	E_{kin} [mJ]	$\triangle E_{kin}$ [mJ]	E_{setup} [mJ]	$\triangle E_{setup}$ [mJ]	E_{air} [mJ]	$\triangle E_{air}$ [mJ]
212	101	2227,5	48,2	124,5	6,0	2,6	1,3	111,4	11,1
213	101	3282,2	42,1	80,4	3,1	0,1	0,1	164,1	16,4
215	101	3372,7	44,2	140,8	5,4	5,4	2,7	168,6	16,9
216	101	2482,1	46,3	139,7	6,6	1,9	1,0	124,1	12,4
217	101	2569,8	45,8	43,4	3,0	2,2	1,1	128,5	12,8
218	101	3001,2	42,7	137,7	3,1	6,2	3,1	150,1	15,0
219	101	3000,8	44,4	71,2	4,0	0,3	0,2	150,0	15,0
220	101	2947,7	44,7	55,6	3,9	0,3	0,1	147,4	14,7
221	101	2836,9	45,7	97,2	3,8	8,5	4,3	141,8	14,2
222	101	2585,7	46,6	108,3	6,5	0,4	0,2	129,3	12,9
223	101	1729,9	50,6	47,2	2,8	7,4	3,7	86,5	8,6
224	101	-	-	-	-	-	-	-	-
225	101	1960,2	49,4	54,0	2,9	-	-	98,0	9,8
226	101	2056,5	49,5	49,4	1,8	-	-	102,8	10,3
227	101	3208,6	43,0	145,4	4,8	-	-	160,4	16,0
228	301	2446,2	57,5	163,1	5,4	11,9	5,9	122,3	12,2
230	301	3633,2	53,9	134,3	6,6	5,1	2,5	181,7	18,2
231	301	3893,3	52,7	125,2	3,8	1,7	0,8	194,7	19,5
232	301	3989,3	53,2	63,9	2,8	12,8	6,4	199,5	19,9
233	301	3447,0	56,6	178,3	6,4	7,3	3,7	172,4	17,2
234	301	3881,3	51,5	128,9	4,0	3,8	1,9	194,1	19,4
235	301	2440,4	58,4	193,3	7,6	12,9	6,4	122,0	12,2
236	301	2688,2	56,2	124,8	3,0	6,9	3,4	134,4	13,4
237	301	2624,1	57,3	137,9	4,8	10,0	5,0	131,2	13,1
238	301	2831,1	58,3	133,6	5,3	7,3	3,6	141,6	14,2
239	301	3752,4	54,6	179,8	6,2	10,0	5,0	187,6	18,8
240	601	3247,4	68,4	109,9	2,9	3,6	1,8	162,4	16,2
242	601	5157,2	62,9	194,6	8,6	10,0	5,0	257,9	25,8
243	601	4174,7	67,2	105,1	3,2	14,8	7,4	208,7	20,9
244	601	4209,9	65,2	211,3	8,6	12,4	6,2	210,5	21,0
245	601	4930,1	63,0	79,5	3,4	14,0	7,0	246,5	24,7
246	601	4819,4	65,0	192,9	6,1	2,4	1,2	241,0	24,1
247	601	3594,8	67,9	138,4	6,3	11,6	5,8	179,7	18,0
248	601	4133,6	66,6	118,5	2,4	14,4	7,2	206,7	20,7
249	501	4059,5	62,9	111,1	3,5	10,3	5,1	203,0	20,3

Table F.1.: Determined energy components of HIEs: Missing or insufficient data is indicated by a dash ("-"). Detailed information about the calculation of the uncertainties are presented in Appendix A.

V	{...}	E_{def} [mJ]	$\triangle E_{def}$ [mJ]	E_{frac} [mJ]	$\triangle E_{frac}$ [mJ]	E_{NC} [mJ]	E_{DC} [mJ]	η_{tot} [J/m^2]	η_{NC} [J/m^2]	η_{DC} [J/m^2]
212	101			1989,1	66,6	152,9	1836,1	100,08	47,46	110,26
213	101			3037,5	61,7	102,6	2934,9	107,66	46,90	112,77
215	101			3057,8	69,2	188,9	2868,8	103,49	47,21	112,31
216	101			2216,3	66,3	139,9	2076,4	102,57	46,68	111,58
217	101			2395,7	62,7	175,8	2219,9	103,26	47,28	113,95
218	101			2707,3	64,0	176,6	2530,6	103,10	46,92	112,51
219	101			2779,2	63,6	84,5	2694,7	107,02	47,26	111,44
220	101			2744,4	63,5	176,0	2568,4	102,15	46,51	111,27
221	101			2589,3	68,0	152,5	2436,9	103,93	47,56	112,25
222	101			2347,7	66,2	174,8	2172,9	102,77	46,68	113,76
223	101			1588,7	65,8	202,6	1386,1	95,21	47,70	111,43
224	101			-	-	-	-	-	-	-
225	101			-	-	-	-	-	-	-
226	101			-	-	-	-	-	-	-
227	101			-	-	-	-	-	-	-
228	301			2148,9	81,1	98,8	2050,1	104,81	47,45	111,30
230	301			3312,1	81,2	186,1	3126,0	103,63	47,21	111,56
231	301			3571,8	76,8	80,4	3491,4	110,54	47,08	114,08
232	301			3713,1	82,3	210,7	3502,5	102,60	46,77	110,54
233	301			3089,1	83,9	140,7	2948,4	105,00	47,12	111,54
234	301			3554,5	76,8	142,2	3412,4	105,40	47,74	110,99
235	301			2112,2	84,6	120,2	1992,0	102,31	46,35	110,35
236	301			2422,1	76,0	207,5	2214,6	101,23	46,87	113,58
237	301			2345,0	80,2	138,8	2206,3	102,55	47,62	110,58
238	301			2548,7	81,4	186,7	2362,0	103,06	46,89	113,83
239	301			3375,0	84,5	183,1	3192,0	104,57	46,61	112,60
240	601			2971,6	89,4	116,7	2854,9	105,68	46,89	111,39
242	601			4694,9	102,3	248,4	4446,5	102,92	47,09	110,22
243	601			3846,0	98,6	241,1	3604,9	102,13	47,32	110,70
244	601			3775,8	101,0	334,4	3441,4	100,17	47,24	112,41
245	601			4590,1	98,1	321,8	4268,3	100,12	46,61	109,61
246	601			4383,1	96,3	181,5	4201,6	104,80	47,73	110,51
247	601			3265,0	98,0	135,9	3129,2	107,20	46,92	113,53
248	601			3794,0	96,8	307,7	3486,3	102,05	46,32	114,18
249	501			3735,1	91,9	214,9	3520,2	105,66	47,71	114,13

Table F.2.: The determined energy components E_{def} and E_{frac} are presented as well as the resulting FSED values η_{tot}, η_{NC} and η_{DC}. With these results and the known corresponding fracture areas A_{NC} and A_{DC}, it is now possible to quantify E_{NC} and E_{DC}, which specify the dissipated energies into normal cracks and damage cracks, respectively. Missing or insufficient data is indicated by a dash ("-"). Detailed information about the calculation of the uncertainties are presented in Appendix A.

V	{...}	E_{tot} [mJ]	$\triangle E_{tot}$ [mJ]	E_{kin} [mJ]	$\triangle E_{kin}$ [mJ]	E_{setup} [mJ]	$\triangle E_{setup}$ [mJ]	E_{air} [mJ]	$\triangle E_{air}$ [mJ]
250	501	4502,0	60,1	129,8	5,5	10,3	5,1	225,1	22,5
251	501	4273,0	62,5	134,9	2,3	10,7	5,3	213,6	21,4
252	501	3733,7	62,9	-	-	1,2	0,6	186,7	18,7
253	401	4172,4	56,6	149,6	4,2	9,4	4,7	208,6	20,9
254	401	3896,4	58,4	93,5	2,8	8,9	4,5	194,8	19,5
255	401	2901,2	62,2	135,3	9,0	9,7	4,8	145,1	14,5
256	401	3315,1	61,5	155,0	4,9	6,1	3,1	165,8	16,6
257	201	3602,0	48,7	58,0	2,5	6,3	3,2	180,1	18,0
258	201	3135,9	49,6	90,2	5,1	9,1	4,6	156,8	15,7
259	201	2942,5	50,9	75,4	2,9	8,4	4,2	147,1	14,7
260	401	4093,3	57,3	93,8	1,8	9,0	4,5	204,7	20,5
261	102	3011,7	45,2	111,8	4,6	6,4	3,2	150,6	15,1
262	102	2120,5	48,0	148,4	3,7	1,0	0,5	106,0	10,6
263	102	3163,0	43,6	102,2	4,8	2,7	1,4	158,2	15,8
264	102	3137,2	43,3	105,7	4,4	4,5	2,2	156,9	15,7
265	102	3367,5	42,1	163,8	9,6	-	-	168,4	16,8
266	102	3230,1	42,0	131,3	2,3	2,2	1,1	161,5	16,2
267	102	2813,7	45,0	87,6	1,4	5,2	2,6	140,7	14,1
268	102	1891,4	49,4		0,0	5,1	2,6	94,6	9,5
269	102	3208,6	42,9	110,9	3,4	-	-	160,4	16,0
270	102	2451,8	48,4	126,4	7,8	8,9	4,4	122,6	12,3
271	102	3274,3	42,6	143,4	1,9	8,4	4,2	163,7	16,4
272	102	3051,8	44,2	107,1	4,1	1,3	0,7	152,6	15,3
273	102	3092,9	44,4	146,2	8,5	3,4	1,7	154,6	15,5
274	102	3035,1	44,2	84,8	3,3	1,3	0,7	151,8	15,2
275	102	2997,3	45,7	49,2	1,8	2,5	1,2	149,9	15,0
276	102	3091,6	43,5	88,3	2,3	1,5	0,8	154,6	15,5
277	103	3166,4	43,2	148,3	5,6	4,2	2,1	158,3	15,8
278	103	2936,7	43,9	85,3	3,1	13,0	6,5	146,8	14,7
279	103	3331,6	43,6	65,0	3,3	1,8	0,9	166,6	16,7
280	103	3219,0	43,7	84,9	2,3	5,5	2,7	160,9	16,1
281	103	2567,0	46,2	173,2	7,0	6,7	3,4	128,3	12,8
282	103	3125,8	44,2	63,9	2,0	8,8	4,4	156,3	15,6
283	103	3315,1	42,8	67,2	4,4	2,9	1,5	165,8	16,6
284	103	3249,4	43,1	116,6	3,2	1,6	0,8	162,5	16,2

Table F.3.: Determined energy components of HIEs: Missing or insufficient data is indicated by a dash ("-"). Detailed information about the calculation of the uncertainties are presented in Appendix A.

V	{...}	E_{def} [mJ]	$\triangle E_{def}$ [mJ]	E_{frac} [mJ]	$\triangle E_{frac}$ [mJ]	E_{NC} [mJ]	E_{DC} [mJ]	η_{tot} [J/m^2]	η_{NC} [J/m^2]	η_{DC} [J/m^2]
250	501			4136,9	93,3	195,6	3941,3	106,79	47,30	113,91
251	501			3913,7	91,5	102,3	3811,4	107,43	47,47	111,20
252	501			-	-	-	-	-	-	-
253	401			3804,8	86,3	270,7	3534,1	103,26	46,61	113,86
254	401			3599,2	85,1	173,7	3425,5	104,50	47,21	111,35
255	401			2611,2	90,6	179,8	2431,3	102,18	47,21	111,81
256	401			2988,2	86,0	145,0	2843,2	103,46	47,74	110,01
257	201			3357,5	72,4	170,2	3187,3	106,67	47,66	114,23
258	201			2879,7	74,9	94,7	2785,0	107,34	46,56	112,33
259	201			2711,5	72,7	200,3	2511,2	102,21	46,84	112,85
260	401			3785,9	84,0	111,9	3674,0	106,91	46,36	111,34
261	102			2743,0	68,0	89,5	2653,5	112,88	43,64	119,26
262	102			1865,1	62,8	103,9	1761,3	110,86	42,93	122,26
263	102			2899,9	65,5	92,0	2808,0	113,93	42,49	120,57
264	102			2870,2	65,6	169,3	2700,9	111,04	43,16	123,19
265	102			-	-	-	-	-	-	-
266	102			2935,1	61,5	143,5	2791,6	112,19	42,86	122,37
267	102			2580,3	63,0	147,2	2433,1	109,89	42,36	121,62
268	102			1791,7	61,4	-	-	-		
269	102			-	-	-	-	-		
270	102			2194,0	72,9	88,2	2105,8	111,04	43,42	118,79
271	102			2958,8	65,0	108,6	2850,2	115,67	43,27	123,54
272	102			2790,8	64,2	114,9	2675,9	110,71	43,42	118,60
273	102			2788,6	70,1	83,7	2704,9	115,29	43,54	121,49
274	102			2797,2	63,4	94,3	2702,9	112,39	43,25	119,03
275	102			2795,8	63,7	99,5	2696,4	113,74	43,03	121,08
276	102			2847,2	62,0	145,3	2701,9	108,65	43,02	118,36
277	103			2855,6	66,8	101,0	2754,6	121,12	51,23	127,50
278	103			2691,5	68,3	209,0	2482,5	113,08	52,58	125,22
279	103			3098,3	64,4	210,9	2887,4	112,94	51,80	123,59
280	103			2967,7	64,8	135,8	2831,9	116,16	51,92	123,49
281	103			2258,7	69,4	198,9	2059,8	110,46	51,26	124,32
282	103			2896,8	66,2	182,5	2714,2	113,64	51,22	123,79
283	103			3079,2	65,3	186,9	2892,3	118,20	52,35	128,66
284	103			2968,8	63,4	129,5	2839,3	120,02	52,58	127,48

Table F.4.: The determined energy components E_{def} and E_{frac} are presented as well as the resulting FSED values η_{tot}, η_{NC} and η_{DC}. With these results and the known corresponding fracture areas A_{NC} and A_{DC}, it is now possible to quantify E_{NC} and E_{DC}, which specify the dissipated energies into normal cracks and damage cracks, respectively. Missing or insufficient data is indicated by a dash ("-"). Detailed information about the calculation of the uncertainties are presented in Appendix A.

V	{...}	E_{tot} [mJ]	$\triangle E_{tot}$ [mJ]	E_{kin} [mJ]	$\triangle E_{kin}$ [mJ]	E_{setup} [mJ]	$\triangle E_{setup}$ [mJ]	E_{air} [mJ]	$\triangle E_{air}$ [mJ]
285	103	3250,2	44,8	110,9	4,6	1,0	0,5	162,5	16,3
286	103	3286,6	43,6	142,9	3,0	1,5	0,7	164,3	16,4
287	103	3218,1	42,0	163,2	5,9	2,7	1,4	160,9	16,1
288	103	2708,5	48,1	132,2	5,8	3,6	1,8	135,4	13,5
289	101	3380,0	44,3	171,5	6,3	2,0	1,0	169,0	16,9
290	103	3018,3	45,3	74,9	4,1	4,6	2,3	150,9	15,1
291	103	3464,3	44,3	91,0	3,5	3,6	1,8	173,2	17,3
292	103	3231,6	44,7	62,9	1,4	5,0	2,5	161,6	16,2
293	102	2346,4	49,4	143,6	7,4	3,1	1,6	117,3	11,7
294	102	2257,9	48,2	85,6	3,8	5,6	2,8	112,9	11,3

Table F.5.: Determined energy components of HIEs: Missing or insufficient data is indicated by a dash ("-"). Detailed information about the calculation of the uncertainties are presented in Appendix A.

V	{...}	E_{def} [mJ]	$\triangle E_{def}$ [mJ]	E_{frac} [mJ]	$\triangle E_{frac}$ [mJ]	E_{NC} [mJ]	E_{DC} [mJ]	η_{tot} [J/m^2]	η_{NC} [J/m^2]	η_{DC} [J/m^2]
285	103			2975,8	66,2	150,0	2825,8	116,97	51,68	125,38
286	103			2977,9	63,7	204,9	2773,0	113,11	52,28	123,75
287	103			2891,2	65,4	177,4	2713,9	114,93	52,70	124,55
288	103			2437,2	69,2	146,4	2290,9	115,60	52,06	125,38
289	101			3037,6	68,5	133,3	2904,3	107,63	47,51	114,26
290	103			2787,8	66,8	192,9	2594,9	116,63	51,63	128,68
291	103			3196,5	67,0	183,7	3012,8	116,53	52,72	125,81
292	103			3002,1	64,7	143,3	2858,9	118,98	52,34	127,09
293	102			2082,4	70,1	154,0	1928,4	106,54	42,56	121,08
294	102			2053,8	66,1	120,5	1933,3	107,71	43,55	118,61

Table F.6.: The determined energy components E_{def} and E_{frac} are presented as well as the resulting FSED values η_{tot}, η_{NC} and η_{DC}. With these results and the known corresponding fracture areas A_{NC} and A_{DC}, it is now possible to quantify E_{NC} and E_{DC}, which specify the dissipated energies in form of normal crack fracture and damage crack fragmentation, respectively. Missing or insufficient data is indicated by a dash ("-"). Detailed information about the calculation of the uncertainties are presented in Appendix A.

V	{...}	E_{tot} [mJ]	$\triangle E_{tot}$ [mJ]	E_{kin} [mJ]	$\triangle E_{kin}$ [mJ]	E_{setup} [mJ]	$\triangle E_{setup}$ [mJ]	E_{air} [mJ]	$\triangle E_{air}$ [mJ]
295	102	3137,9	45,5	137,7	6,0	2,2	1,1	156,9	15,7
296	102	3335,7	44,5	158,6	5,0	2,1	1,0	166,8	16,7
297	102	1962,1	50,4	55,0	2,2	1,7	0,8	98,1	9,8
298	102	2572,6	46,4	87,0	4,4	2,5	1,3	128,6	12,9
299	102	3240,8	43,8	96,0	5,4	1,0	0,5	162,0	16,2
300	102	3269,7	43,6	160,8	5,9	0,4	0,2	163,5	16,3
301	102	1908,1	49,8	131,9	3,4	0,6	0,3	95,4	9,5
302	104	3359,1	42,7	53,0	2,2	2,0	1,0	168,0	16,8
303	104	3352,9	42,3	80,6	4,8	5,5	2,8	167,6	16,8
304	103	3255,3	43,7	96,9	4,4	2,5	1,3	162,8	16,3
305	103	2523,7	47,0	76,8	2,6	3,3	1,6	126,2	12,6
306	103	3306,2	42,5	160,7	6,9	4,8	2,4	165,3	16,5
307	103	3404,9	42,4	213,9	9,3	3,4	1,7	170,2	17,0
308	103	3282,1	43,9	109,2	3,6	12,6	6,3	164,1	16,4
309	103	3270,1	43,2	113,9	3,8	5,2	2,6	163,5	16,4
310	103	3098,4	43,6	140,7	5,3	7,8	3,9	154,9	15,5
311	103	2898,8	45,1	99,1	2,3	13,3	6,7	144,9	14,5
312	103	2969,6	43,5	43,4	3,0	2,8	1,4	148,5	14,8
313	103	2236,9	49,1	148,0	6,6	3,8	1,9	111,8	11,2
314	103	3164,7	44,1	47,8	2,4	1,7	0,8	158,2	15,8
315	103	3118,2	43,1	206,7	6,1	-	-	155,9	15,6
316	103	2666,5	47,8	109,7	4,8	-	-	133,3	13,3
317	103	2657,0	46,3	173,8	6,1	-	-	132,8	13,3
318	103	3050,6	43,9	112,9	6,5	6,7	3,3	152,5	15,3
319	303	3439,5	54,4	116,4	4,1	8,4	4,2	172,0	17,2
320	303	3894,5	52,0	83,6	2,4	8,8	4,4	194,7	19,5
321	303	3006,4	56,6	68,5	3,0	11,2	5,6	150,3	15,0
322	303	3054,4	56,8	59,2	1,8	8,9	4,4	152,7	15,3
323	303	3126,7	54,9	158,0	7,2	7,8	3,9	156,3	15,6
324	105	2685,3	48,2	117,3	4,9	3,1	1,5	134,3	13,4
325	105	3309,6	42,9	175,4	6,9	4,4	2,2	165,5	16,5
326	105	2904,3	45,9	144,9	6,3	4,7	2,4	145,2	14,5
327	105	3214,2	43,4	101,9	3,4	4,7	2,4	160,7	16,1
328	105	3434,9	42,7	206,7	9,6	3,0	1,5	171,7	17,2
329	105	3226,0	43,8	53,4	2,6	2,3	1,1	161,3	16,1

Table F.7.: Determined energy components of HIEs: Missing or insufficient data is indicated by a dash ("-"). Detailed information about the calculation of the uncertainties are presented in Appendix A.

V	{...}	E_{def} [mJ]	$\triangle E_{def}$ [mJ]	E_{frac} [mJ]	$\triangle E_{frac}$ [mJ]	E_{NC} [mJ]	E_{DC} [mJ]	η_{tot} [J/m^2]	η_{NC} [J/m^2]	η_{DC} [J/m^2]
295	102			2841,1	68,3	164,5	2676,6	109,88	42,53	121,73
296	102			3008,3	67,2	163,8	2844,5	111,22	43,67	122,09
297	102			1807,3	63,3	152,5	1654,8	103,88	43,45	119,16
298	102			2354,4	64,9	187,9	2166,5	106,44	42,90	122,13
299	102			2981,7	65,9	188,0	2793,7	109,62	42,69	122,55
300	102			2945,0	66,1	191,5	2753,5	106,68	43,32	118,75
301	102			1680,2	63,1	164,2	1516,1	101,34	42,53	119,19
302	104			3136,1	62,7	99,1	3037,0	103,50	38,14	109,63
303	104			3099,1	66,6	85,8	3013,3	105,82	37,83	111,53
304	103			2993,1	65,6	188,2	2804,9	115,48	52,78	125,48
305	103			2317,4	63,9	155,4	2162,0	115,85	52,66	126,78
306	103			2975,4	68,3	192,1	2783,3	116,80	52,00	127,79
307	103			3017,4	70,5	112,1	2905,2	120,44	52,68	126,73
308	103			2996,2	70,3	144,0	2852,3	116,65	51,67	124,56
309	103			2987,5	66,0	177,9	2809,6	115,76	51,43	125,72
310	103			2794,9	68,4	194,4	2600,6	116,08	51,28	128,18
311	103			2641,4	68,6	115,1	2526,3	119,87	52,61	127,28
312	103			2774,9	62,7	186,9	2588,0	114,50	51,86	125,44
313	103			1973,2	68,7	187,2	1786,0	109,49	52,01	123,84
314	103			2956,9	63,2	190,0	2767,0	114,93	51,74	125,45
315	103			-	-	-	-	-		
316	103			-	-	-	-	-		
317	103			-	-	-	-	-		
318	103			2778,5	69,0	97,9	2680,6	117,81	51,85	123,55
319	303			3142,7	79,9	106,7	3035,9	120,20	51,60	126,09
320	303			3607,4	78,3	254,2	3353,2	112,42	51,30	123,58
321	303			2776,3	80,2	104,8	2671,5	121,88	52,16	128,62
322	303			2833,6	78,3	204,8	2628,8	112,81	51,29	124,43
323	303			2804,5	81,6	228,3	2576,2	111,89	52,66	124,28
324	105			2430,6	68,1	174,2	2256,5	97,51	48,86	105,63
325	105			2964,4	68,6	98,6	2865,8	102,47	49,66	106,36
326	105			2609,5	69,0	157,0	2452,5	98,92	49,16	105,77
327	105			2946,9	65,2	128,0	2819,0	103,75	48,70	109,37
328	105			3053,5	71,0	126,6	2926,9	100,52	49,33	105,24
329	105			3009,0	63,7	123,1	2886,0	100,51	48,76	105,27

Table F.8.: The determined energy components E_{def} and E_{frac} are presented as well as the resulting FSED values η_{tot}, η_{NC} and η_{DC}. With these results and the known corresponding fracture areas A_{NC} and A_{DC}, it is now possible to quantify E_{NC} and E_{DC}, which specify the dissipated energies into normal cracks and damage cracks, respectively. Missing or insufficient data is indicated by a dash ("-"). Detailed information about the calculation of the uncertainties are presented in Appendix A.

V	{...}	E_{tot} [mJ]	$\triangle E_{tot}$ [mJ]	E_{kin} [mJ]	$\triangle E_{kin}$ [mJ]	E_{setup} [mJ]	$\triangle E_{setup}$ [mJ]	E_{air} [mJ]	$\triangle E_{air}$ [mJ]
330	102	2945,9	46,1	49,4	2,6	4,4	2,2	147,3	14,7
350	602	3065,7	69,5	130,8	4,6	4,0	2,0	153,3	15,3
351	602	3886,9	67,5	203,7	8,3	4,0	2,0	194,3	19,4
352	602	3598,2	68,9	266,0	6,6	3,9	1,9	179,9	18,0
353	602	4488,4	66,7	90,6	4,8	4,3	2,2	224,4	22,4
354	602	3066,8	70,6	132,6	4,0	1,9	1,0	153,3	15,3
355	602	3943,4	67,7	215,3	9,0	10,7	5,4	197,2	19,7
356	603	5281,3	63,1	152,8	3,0	5,5	2,7	264,1	26,4
357	603	3366,3	68,9	127,9	5,0	2,9	1,4	168,3	16,8
358	603	4147,5	67,5	196,6	5,4	2,2	1,1	207,4	20,7

Table F.9.: Determined energy components of HIEs: Missing or insufficient data is indicated by a dash ("-"). Detailed information about the calculation of the uncertainties are presented in Appendix A.

V	{...}	E_{def} [mJ]	$\triangle E_{def}$ [mJ]	E_{frac} [mJ]	$\triangle E_{frac}$ [mJ]	E_{NC} [mJ]	E_{DC} [mJ]	η_{tot} [J/m^2]	η_{NC} [J/m^2]	η_{DC} [J/m^2]
330	102			2744,7	65,6	103,7	2641,1	113,62	43,55	121,28
350	602			2777,7	91,4	230,7	2547,0	107,03	42,90	123,79
351	602			3485,0	97,2	253,3	3231,7	106,31	43,62	119,81
352	602			3148,4	95,4	294,9	2853,5	102,26	43,13	119,14
353	602			4169,1	96,1	169,3	3999,8	110,63	42,86	118,57
354	602			2778,9	90,9	149,5	2629,4	109,84	43,27	120,36
355	602			3520,1	101,8	140,0	3380,1	111,79	43,26	119,64
356	603			4859,0	95,3	298,8	4560,2	115,18	52,74	124,87
357	603			3067,2	92,2	210,4	2856,8	115,45	52,13	126,80
358	603			3741,4	94,7	182,0	3559,4	116,48	52,06	124,35

Table F.10.: The determined energy components E_{def} and E_{frac} are presented as well as the resulting FSED values η_{tot}, η_{NC} and η_{DC}. With these results and the known corresponding fracture areas A_{NC} and A_{DC}, it is now possible to quantify E_{NC} and E_{DC}, which specify the dissipated energies in form of normal crack fracture and damage crack fragmentation, respectively. Missing or insufficient data is indicated by a dash ("-"). Detailed information about the calculation of the uncertainties are presented in Appendix A.

V	{...}	E_{tot} [mJ]	$\triangle E_{tot}$ [mJ]	E_{kin} [mJ]	$\triangle E_{kin}$ [mJ]	E_{setup} [mJ]	$\triangle E_{setup}$ [mJ]	E_{air} [mJ]	$\triangle E_{air}$ [mJ]
359	603	3774,4	66,4	110,9	5,4	4,7	2,3	188,7	18,9
360	604	3121,7	69,7	204,8	12,6	1,5	0,8	156,1	15,6
361	604	3094,6	70,3	93,2	4,3	2,2	1,1	154,7	15,5
362	604	3219,3	69,8	117,9	5,4	3,6	1,8	161,0	16,1
363	604	3189,1	69,1	74,8	2,5	1,5	0,8	159,5	15,9
364	603	4929,6	64,4	202,6	7,8	5,6	2,8	246,5	24,6
365	603	2834,1	72,1	219,5	11,3	4,1	2,1	141,7	14,2
401	106	2981,2	45,5	142,9	6,8	2,6	1,3	149,1	14,9
402	106	3267,4	44,0	71,1	3,7	3,2	1,6	163,4	16,3
403	106	2860,8	45,3	219,8	6,5	5,1	2,6	143,0	14,3
405	106	2481,8	48,3	103,2	5,8	5,8	2,9	124,1	12,4
406	106	1945,9	50,9	136,7	4,5	2,4	1,2	97,3	9,7
407	106	2954,1	44,8	129,8	5,2	2,2	1,1	147,7	14,8
408	106	2720,5	46,0	125,5	5,8	3,4	1,7	136,0	13,6
409	106	2300,6	47,2	131,9	6,1	3,7	1,8	115,0	11,5
410	106	2802,8	45,9	114,2	5,0	2,4	1,2	140,1	14,0
411	106	3363,4	43,1	193,1	9,6	3,2	1,6	168,2	16,8
412	106	3312,3	42,0	-	-	1,1	0,6	165,6	16,6
413	106	3253,3	42,4	-	-	1,2	0,6	162,7	16,3
414	106	3229,2	43,0	-	-	1,7	0,9	161,5	16,1
415	106	3187,7	43,2	-	-	3,6	1,8	159,4	15,9
416	106	3374,9	42,1	-	-	4,1	2,0	168,7	16,9
417	306	3620,5	52,9	92,0	3,7	4,1	2,0	181,0	18,1
418	306	3595,3	53,4	109,4	4,6	3,1	1,6	179,8	18,0
419	306	3240,9	55,6	87,8	4,5	3,7	1,9	162,0	16,2
420	306	3561,4	54,7	146,8	2,3	3,8	1,9	178,1	17,8
421	306	2962,7	57,1	91,2	4,0	2,8	1,4	148,1	14,8
422	306	2948,6	57,6	191,5	6,2	3,5	1,8	147,4	14,7
423	306	3709,8	54,9	71,8	2,6	2,1	1,0	185,5	18,5
424	306	3088,4	55,5	92,5	3,7	3,6	1,8	154,4	15,4
425	306	3380,0	55,1	143,8	6,0	1,3	0,6	169,0	16,9
426	306	3173,5	56,4	83,0	4,1	3,8	1,9	158,7	15,9
427	306	3661,4	54,7	124,9	6,0	2,9	1,5	183,1	18,3
428	306	2979,9	57,5	59,9	2,4	2,7	1,4	149,0	14,9
429	606	2855,6	70,3	111,6	5,3	2,7	1,4	142,8	14,3

Table F.11.: Determined energy components of HIEs: Missing or insufficient data is indicated by a dash (“-”). Detailed information about the calculation of the uncertainties are presented in Appendix A.

V	{...}	E_{def} [mJ]	$\triangle E_{def}$ [mJ]	E_{frac} [mJ]	$\triangle E_{frac}$ [mJ]	E_{NC} [mJ]	E_{DC} [mJ]	η_{tot} [J/m^2]	η_{NC} [J/m^2]	η_{DC} [J/m^2]
359	603			3470,1	93,0	206,4	3263,7	115,44	52,65	124,86
360	604			2759,4	98,6	162,2	2597,1	97,32	38,10	107,79
361	604			2844,5	91,2	131,2	2713,3	101,29	38,50	109,96
362	604			2936,8	93,0	125,0	2811,9	100,42	38,57	108,12
363	604			2953,3	88,3	161,8	2791,5	98,22	37,81	108,24
364	603			4474,9	99,6	277,1	4197,8	115,33	51,65	125,55
365	603			2468,8	99,6	162,1	2306,7	116,10	51,24	127,43
401	106	37,0	2,0	2649,7	70,5	178,2	2471,5	157,77	66,82	174,94
402	106	32,0	2,0	2997,7	67,7	281,9	2715,8	150,72	65,12	174,53
403	106	34,0	2,0	2458,8	70,7	172,1	2286,7	156,51	65,95	174,56
405	106	35,0	2,0	2213,7	71,4	197,8	2015,8	152,95	66,13	175,57
406	106	38,0	2,0	1671,5	68,3	221,9	1449,6	146,54	65,49	180,79
407	106	39,0	2,0	2635,4	67,8	169,3	2466,1	159,55	65,74	176,88
408	106	31,0	2,0	2424,6	69,0	145,8	2278,8	160,80	66,83	176,70
409	106	33,0	2,0	2017,0	68,6	190,1	1826,9	153,39	66,04	177,87
410	106	28,0	2,0	2518,2	68,1	123,2	2395,0	163,94	65,44	177,70
411	106	40,0	2,0	2959,0	73,1	177,7	2781,3	163,43	65,32	180,78
412	106	43,0	2,0	-	-	-	-	-	-	-
413	106	36,0	2,0	-	-	-	-	-	-	-
414	106	34,0	2,0	-	-	-	-	-	-	-
415	106	37,0	2,0	-	-	-	-	-	-	-
416	106	45,0	2,0	-	-	-	-	-	-	-
417	306	52,0	2,0	3291,4	78,8	233,5	3057,8	156,45	66,16	174,65
418	306	49,0	2,0	3254,0	79,6	297,9	2956,1	155,15	65,23	180,18
419	306	61,0	2,0	2926,3	80,1	251,2	2675,1	157,29	66,37	180,51
420	306	58,0	2,0	3174,8	78,8	315,7	2859,1	149,88	65,13	175,02
421	306	52,0	2,0	2668,5	79,4	187,5	2481,0	158,24	67,02	176,38
422	306	59,0	2,0	2547,2	82,4	321,9	2225,2	147,66	65,93	179,92
423	306	61,0	2,0	3389,4	79,1	162,9	3226,6	167,61	66,46	181,56
424	306	57,0	2,0	2780,9	78,5	209,1	2571,8	160,74	66,21	181,85
425	306	69,0	2,0	2997,0	80,7	232,0	2764,9	156,79	66,02	177,24
426	306	61,0	2,0	2867,1	80,2	170,9	2696,2	161,88	65,47	178,55
427	306	66,0	2,0	3284,5	82,5	282,2	3002,3	156,16	66,11	179,09
428	306	52,0	2,0	2716,2	78,1	144,5	2571,7	164,08	66,91	178,66
429	606	79,0	2,0	2519,5	93,2	232,1	2287,5	154,95	65,58	179,80

Table F.12.: The determined energy components E_{def} and E_{frac} are presented as well as the resulting FSED values η_{tot}, η_{NC} and η_{DC}. With these results and the known corresponding fracture areas A_{NC} and A_{DC}, it is now possible to quantify E_{NC} and E_{DC}, which specify the dissipated energies into normal cracks and damage cracks, respectively. Missing or insufficient data is indicated by a dash ("-"). Detailed information about the calculation of the uncertainties are presented in Appendix A.

V	{...}	E_{tot} [mJ]	$\triangle E_{tot}$ [mJ]	E_{kin} [mJ]	$\triangle E_{kin}$ [mJ]	E_{setup} [mJ]	$\triangle E_{setup}$ [mJ]	E_{air} [mJ]	$\triangle E_{air}$ [mJ]
430	606	3541,7	68,8	113,6	5,1	5,2	2,6	177,1	17,7
431	606	3177,9	69,9	112,8	3,0	3,1	1,5	158,9	15,9
432	606	4225,1	68,0	186,4	1,8	2,4	1,2	211,3	21,1
433	606	3502,2	68,8	105,9	2,7	2,6	1,3	175,1	17,5
434	606	2598,6	72,6	100,4	6,1	2,0	1,0	129,9	13,0
500	105	3215,2	42,6	172,8	5,9	2,9	1,5	160,8	16,1
501	105	2700,4	45,6	164,4	5,9	3,1	1,5	135,0	13,5
502	305	3164,7	55,6	136,3	4,4	2,3	1,2	158,2	15,8
503	305	3428,0	55,3	64,0	2,7	2,9	1,5	171,4	17,1
504	305	3565,2	54,3	89,6	4,5	2,5	1,2	178,3	17,8

Table F.13.: Determined energy components of HIEs: Missing or insufficient data is indicated by a dash ("-"). Detailed information about the calculation of the uncertainties are presented in Appendix A.

V	{...}	E_{def} [mJ]	$\triangle E_{def}$ [mJ]	E_{frac} [mJ]	$\triangle E_{frac}$ [mJ]	E_{NC} [mJ]	E_{DC} [mJ]	η_{tot} [J/m^2]	η_{NC} [J/m^2]	η_{DC} [J/m^2]
430	606	74,0	2,0	3171,8	96,2	322,8	2849,0	150,51	65,16	176,75
431	606	75,0	2,0	2828,2	92,4	299,8	2528,4	152,38	65,82	180,52
432	606	79,0	2,0	3746,1	94,2	382,5	3363,5	153,12	65,08	180,96
433	606	77,0	2,0	3141,6	92,4	430,0	2711,6	145,79	66,90	179,32
434	606	80,0	2,0	2286,3	94,7	421,3	1865,0	133,71	65,57	174,71
500	105			2878,7	66,0	149,6	2729,1	101,44	48,31	107,94
501	105			2397,9	66,6	101,0	2296,9	102,56	48,81	107,77
502	305			2867,8	77,0	116,2	2751,6	100,04	48,70	104,70
503	305			3189,7	76,6	249,5	2940,2	99,28	49,52	108,54
504	305			3294,9	77,9	225,3	3069,5	97,36	48,67	105,08

Table F.14.: The determined energy components E_{def} and E_{frac} are presented as well as the resulting FSED values η_{tot}, η_{NC} and η_{DC}. With these results and the known corresponding fracture areas A_{NC} and A_{DC}, it is now possible to quantify E_{NC} and E_{DC}, which specify the dissipated energies in form of normal crack fracture and damage crack fragmentation, respectively. Missing or insufficient data is indicated by a dash ("-"). Detailed information about the calculation of the uncertainties are presented in Appendix A.

V	{...}	E_{tot} [mJ]	$\triangle E_{tot}$ [mJ]	E_{kin} [mJ]	$\triangle E_{kin}$ [mJ]	E_{setup} [mJ]	$\triangle E_{setup}$ [mJ]	E_{air} [mJ]	$\triangle E_{air}$ [mJ]
505	605	3697,4	68,2	190,5	1,6	6,3	3,2	184,9	18,5
506	605	4531,5	65,0	98,4	2,8	2,4	1,2	226,6	22,7
507	605	4369,8	67,5	75,8	3,2	4,2	2,1	218,5	21,8
510	205	3232,0	49,7	123,4	4,4	1,5	0,7	161,6	16,2
511	405	3348,1	59,9	191,1	5,0	2,5	1,2	167,4	16,7
512	405	3854,0	58,4	96,2	3,8	3,7	1,8	192,7	19,3
514	505	3747,0	63,8	203,0	5,0	2,6	1,3	187,4	18,7
515	505	3501,0	64,7	197,7	7,4	3,4	1,7	175,0	17,5
601	113	3034,3	44,0	123,4	2,0	3,3	1,7	151,7	15,2
602	113	3215,2	42,6	133,3	2,9	7,2	3,6	160,8	16,1
603	113	3359,1	42,7	168,8	5,3	3,1	1,5	168,0	16,8
605	114	3370,9	42,6	131,3	1,9	1,7	0,8	168,5	16,9
606	114	3252,4	44,1	81,6	2,8	8,3	4,2	162,6	16,3
607	114	1838,8	49,8	117,5	7,7	4,7	2,3	91,9	9,2
608	114	3366,0	43,5	110,3	2,9	7,4	3,7	168,3	16,8
609	114	3347,1	42,7	119,4	4,8	5,0	2,5	167,4	16,7
610	114	3293,9	42,6	108,6	3,3	3,6	1,8	164,7	16,5
611	613	4716,8	64,7	217,3	10,0	9,8	4,9	235,8	23,6
612	112	2594,5	46,2	45,3	2,4	5,2	2,6	129,7	13,0
613	112	2739,4	46,7	66,4	2,0	6,1	3,0	137,0	13,7
614	112	3350,7	43,2	169,4	6,3	4,5	2,3	167,5	16,8
615	612	4587,7	65,1	134,1	3,3	7,9	3,9	229,4	22,9
616	312	3901,8	52,8	153,0	5,6	7,9	3,9	195,1	19,5
617	312	4005,6	52,0	123,7	5,5	4,3	2,1	200,3	20,0
618	612	3866,4	66,6	291,2	11,3	3,5	1,8	193,3	19,3
619	111	2954,1	44,8	91,4	2,7	8,8	4,4	147,7	14,8
620	211	3319,0	49,3	74,0	3,5	1,3	0,7	166,0	16,6
621	111	2782,0	45,7	119,6	5,6	7,6	3,8	139,1	13,9
622	111	2989,8	44,6	139,9	3,8	12,5	6,3	149,5	14,9
623	111	3214,2	43,4	117,8	3,7	2,6	1,3	160,7	16,1
624	611	4409,3	66,2	153,0	5,4	16,4	8,2	220,5	22,0
625	611	3735,8	68,1	156,7	4,6	11,4	5,7	186,8	18,7
626	311	4231,6	51,4	145,7	8,1	10,3	5,1	211,6	21,2
627	311	4183,8	51,2	104,4	4,2	7,6	3,8	209,2	20,9
628	211	4034,4	45,8	116,7	6,2	1,6	0,8	201,7	20,2

Table F.15.: Determined energy components of HIEs: Missing or insufficient data is indicated by a dash ("-"). Detailed information about the calculation of the uncertainties are presented in Appendix A.

V	{...}	E_{def} [mJ]	$\triangle E_{def}$ [mJ]	E_{frac} [mJ]	$\triangle E_{frac}$ [mJ]	E_{NC} [mJ]	E_{DC} [mJ]	η_{tot} [J/m^2]	η_{NC} [J/m^2]	η_{DC} [J/m^2]
505	605			3315,7	91,5	271,1	3044,7	95,75	49,11	104,60
506	605			4204,0	91,7	306,4	3897,6	98,45	49,09	106,90
507	605			4071,3	94,7	327,0	3744,3	97,92	48,28	107,58
510	205			2945,5	70,9	115,9	2829,6	103,69	49,41	108,58
511	405			2987,1	82,9	258,8	2728,3	95,64	49,69	104,84
512	405			3561,3	83,2	137,8	3423,5	103,71	48,62	108,66
514	505			3354,0	88,8	206,5	3147,5	101,04	48,27	108,85
515	505			3124,8	91,4	272,5	2852,3	98,01	48,53	108,59
601	113			2755,8	62,8	121,9	2633,8	118,39	51,65	125,92
602	113			2913,9	65,2	154,6	2759,3	117,10	51,79	126,00
603	113			3019,3	66,3	132,7	2886,6	120,46	51,69	128,30
605	114			3069,3	62,3	99,2	2970,2	103,88	37,46	110,41
606	114			2999,8	67,3	96,7	2903,1	102,55	37,48	108,84
607	114			1624,6	69,0	83,7	1541,0	99,99	38,44	109,51
608	114			3080,0	67,0	117,3	2962,7	100,96	37,59	108,18
609	114			3055,3	66,8	65,5	2989,9	103,85	38,39	107,88
610	114			3017,0	64,1	122,0	2895,1	100,26	37,58	107,84
611	613			4253,9	103,1	168,1	4085,8	117,36	52,59	123,62
612	112			2414,3	64,2	93,9	2320,3	112,82	42,71	120,85
613	112			2530,0	65,5	156,5	2373,5	109,27	43,53	121,35
614	112			3009,3	68,5	192,4	2816,9	107,03	43,63	118,82
615	612			4216,3	95,3	302,0	3914,3	107,86	42,94	122,10
616	312			3545,9	81,9	168,9	3377,0	112,42	42,69	122,42
617	312			3677,3	79,6	207,4	3469,9	110,09	43,06	121,38
618	612			3378,4	98,9	192,5	3186,0	109,68	42,90	121,07
619	111			2706,2	66,6	93,3	2612,8	107,85	47,30	113,02
620	211			3077,8	70,0	164,3	2913,5	103,40	46,86	110,95
621	111			2515,7	69,0	146,3	2369,4	102,06	47,26	109,93
622	111			2687,9	69,6	157,9	2530,0	103,92	46,35	112,65
623	111			2933,1	64,4	95,3	2837,9	107,76	47,57	112,55
624	611			4019,4	101,8	231,7	3787,7	103,11	46,36	111,45
625	611			3380,9	97,0	245,7	3135,2	100,82	46,90	110,80
626	311			3864,1	85,9	191,4	3672,7	106,50	46,70	114,12
627	311			3862,6	80,2	147,9	3714,6	108,25	47,44	114,08
628	211			3714,4	73,0	168,4	3546,0	104,56	47,20	110,97

Table F.16.: The determined energy components E_{def} and E_{frac} are presented as well as the resulting FSED values η_{tot}, η_{NC} and η_{DC}. With these results and the known corresponding fracture areas A_{NC} and A_{DC}, it is now possible to quantify E_{NC} and E_{DC}, which specify the dissipated energies into normal cracks and damage cracks, respectively. Missing or insufficient data is indicated by a dash ("-"). Detailed information about the calculation of the uncertainties are presented in Appendix A.

V	{...}	E_{tot} [mJ]	$\triangle E_{tot}$ [mJ]	E_{kin} [mJ]	$\triangle E_{kin}$ [mJ]	E_{setup} [mJ]	$\triangle E_{setup}$ [mJ]	E_{air} [mJ]	$\triangle E_{air}$ [mJ]
629	411	3938,8	58,0	99,8	3,1	12,6	6,3	196,9	19,7
630	511	3855,1	64,2	113,2	4,8	4,1	2,0	192,8	19,3
631	511	3572,4	64,5	125,7	4,6	14,4	7,2	178,6	17,9
640	121	2902,7	43,8	49,9	2,9	3,4	1,7	145,1	14,5
641	121	3054,5	45,1	133,2	5,7	11,2	5,6	152,7	15,3
642	121	3073,2	43,4	98,4	6,3	4,1	2,1	153,7	15,4
643	121	3483,1	43,4	137,2	5,6	5,7	2,9	174,2	17,4
644	221	2866,2	50,1	122,6	5,4	8,2	4,1	143,3	14,3
645	221	3141,3	50,1	79,9	4,1	1,2	0,6	157,1	15,7
646	221	3918,6	45,9	77,9	3,5	2,9	1,5	195,9	19,6

Table F.17.: Determined energy components of HIEs: Missing or insufficient data is indicated by a dash ("-"). Detailed information about the calculation of the uncertainties are presented in Appendix A.

V	{...}	E_{def} [mJ]	$\triangle E_{def}$ [mJ]	E_{frac} [mJ]	$\triangle E_{frac}$ [mJ]	E_{NC} [mJ]	E_{DC} [mJ]	η_{tot} [J/m^2]	η_{NC} [J/m^2]	η_{DC} [J/m^2]
629	411			3629,4	87,1	126,6	3502,8	107,10	46,69	112,36
630	511			3545,1	90,3	217,2	3327,9	104,73	47,38	113,71
631	511			3253,7	94,1	128,2	3125,5	105,94	46,78	111,73
640	121			2704,3	62,9	193,2	2511,0	101,27	46,36	111,43
641	121			2757,3	71,7	152,9	2604,4	102,86	46,28	110,81
642	121			2817,0	67,1	115,4	2701,6	107,34	46,73	113,63
643	121			3166,0	69,3	191,1	2974,8	105,34	47,57	114,26
644	221			2592,0	73,9	171,3	2420,7	102,23	46,60	111,67
645	221			2903,1	70,5	174,6	2728,6	104,18	47,01	112,96
646	221			3641,9	70,5	123,9	3517,9	106,26	46,44	111,32

Table F.18.: The determined energy components E_{def} and E_{frac} are presented as well as the resulting FSED values η_{tot}, η_{NC} and η_{DC}. With these results and the known corresponding fracture areas A_{NC} and A_{DC}, it is now possible to quantify E_{NC} and E_{DC}, which specify the dissipated energies in form of normal crack fracture and damage crack fragmentation, respectively. Missing or insufficient data is indicated by a dash ("-"). Detailed information about the calculation of the uncertainties are presented in Appendix A.

V	{...}	E_{tot} [mJ]	$\triangle E_{tot}$ [mJ]	E_{kin} [mJ]	$\triangle E_{kin}$ [mJ]	E_{setup} [mJ]	$\triangle E_{setup}$ [mJ]	E_{air} [mJ]	$\triangle E_{air}$ [mJ]
647	421	4075,6	57,4	159,5	7,0	1,0	0,5	203,8	20,4
648	421	4181,5	56,6	86,8	4,9	3,6	1,8	209,1	20,9
649	421	4520,8	55,7	149,6	2,9	3,3	1,7	226,0	22,6
650	621	4090,9	67,3	215,3	12,7	14,6	7,3	204,5	20,5
651	621	4331,3	64,4	200,7	6,8	4,7	2,3	216,6	21,7
652	621	5280,3	62,7	111,5	4,0	6,3	3,2	264,0	26,4
653	621	5406,1	61,4	122,4	6,7	10,7	5,3	270,3	27,0
654	122	3240,8	43,7	150,5	7,1	2,0	1,0	162,0	16,2
655	122	3281,5	42,6	97,9	4,5	10,0	5,0	164,1	16,4
656	122	3180,4	44,1	97,4	2,5	8,1	4,0	159,0	15,9
657	122	2867,9	44,0	161,8	5,0	6,3	3,1	143,4	14,3
658	422	4305,8	56,2	113,2	4,5	4,8	2,4	215,3	21,5
659	422	4396,8	55,3	206,1	9,6	2,6	1,3	219,8	22,0
660	422	3168,8	60,9	129,8	4,8	6,2	3,1	158,4	15,8
661	622	4498,6	65,1	118,8	1,8	6,2	3,1	224,9	22,5
662	622	3924,1	67,4	139,0	5,1	7,4	3,7	196,2	19,6
663	622	3699,6	67,4	107,9	3,2	11,4	5,7	185,0	18,5
664	622	3792,2	68,3	132,0	4,4	10,5	5,2	189,6	19,0
665	123	2966,5	44,3	43,9	1,7	0,7	0,4	148,3	14,8
666	123	3270,1	43,1	114,3	6,0	3,3	1,6	163,5	16,4
667	123	3352,9	42,3	128,2	5,8	5,4	2,7	167,6	16,8
668	123	3271,8	41,8	64,0	3,8	1,3	0,7	163,6	16,4
669	423	4206,7	56,9	158,7	5,5	4,0	2,0	210,3	21,0
670	423	3686,9	58,6	126,1	4,5	5,5	2,8	184,3	18,4
671	423	3831,7	58,1	136,1	6,8	9,1	4,5	191,6	19,2
672	623	4374,8	66,3	163,4	6,5	10,8	5,4	218,7	21,9
673	623	4548,9	64,1	83,4	2,1	2,9	1,5	227,4	22,7
674	623	4157,4	66,3	90,7	5,1	5,5	2,8	207,9	20,8
675	623	3717,7	67,8	115,7	5,0	9,3	4,6	185,9	18,6
676	124	3010,0	43,6	64,0	2,5	0,8	0,4	150,5	15,0
677	124	3256,5	43,2	105,1	4,7	2,1	1,1	162,8	16,3
678	124	2917,5	45,0	56,9	3,2	3,4	1,7	145,9	14,6
680	424	3774,5	58,3	122,7	7,6	4,8	2,4	188,7	18,9
681	424	3366,6	60,2	100,7	3,8	4,3	2,2	168,3	16,8
682	424	3525,2	59,6	184,7	7,7	6,0	3,0	176,3	17,6

Table F.19.: Determined energy components of HIEs: Missing or insufficient data is indicated by a dash ("-"). Detailed information about the calculation of the uncertainties are presented in Appendix A.

V	{...}	E_{def} [mJ]	$\triangle E_{def}$ [mJ]	E_{frac} [mJ]	$\triangle E_{frac}$ [mJ]	E_{NC} [mJ]	E_{DC} [mJ]	η_{tot} [J/m^2]	η_{NC} [J/m^2]	η_{DC} [J/m^2]
647	421			3711,4	85,3	118,2	3593,2	105,60	46,41	110,22
648	421			3882,1	84,3	176,9	3705,3	104,30	47,13	110,71
649	421			4141,9	82,8	205,9	3936,0	103,23	47,54	109,98
650	621			3656,5	107,7	208,1	3448,3	105,73	47,25	114,26
651	621			3909,3	95,3	288,3	3621,0	102,44	46,51	113,29
652	621			4898,5	96,2	210,6	4687,9	104,67	47,06	110,76
653	621			5002,8	100,4	342,7	4660,1	102,70	47,70	112,21
654	122			2926,3	68,0	154,7	2771,5	110,54	43,59	120,91
655	122			3009,4	68,6	173,5	2836,0	111,19	42,37	123,45
656	122			2915,9	66,5	124,6	2791,3	112,80	42,63	121,75
657	122			2556,5	66,5	159,6	2396,8	107,36	42,94	119,28
658	422			3972,5	84,6	96,1	3876,3	115,55	42,76	120,65
659	422			3968,2	88,2	203,3	3764,9	112,14	42,97	122,81
660	422			2874,4	84,6	137,9	2736,5	109,20	43,05	118,36
661	622			4148,7	92,4	175,2	3973,5	112,57	42,61	121,36
662	622			3581,6	95,9	159,4	3422,2	110,32	42,78	119,08
663	622			3395,4	94,8	282,1	3113,3	106,49	42,81	123,08
664	622			3460,1	96,9	221,3	3238,8	108,46	43,54	120,76
665	123			2773,5	61,1	120,8	2652,7	118,24	51,77	125,58
666	123			2989,0	67,1	194,0	2795,0	116,96	51,83	128,14
667	123			3051,6	67,6	122,3	2929,3	117,31	51,50	123,93
668	123			3042,9	62,6	130,3	2912,5	120,16	51,42	127,80
669	423			3833,6	85,5	224,9	3608,7	116,29	52,80	125,70
670	423			3370,9	84,3	256,9	3114,0	114,12	52,57	126,32
671	423			3495,0	88,5	205,9	3289,1	115,35	51,43	125,08
672	623			3981,8	100,1	274,3	3707,6	113,75	51,27	125,02
673	623			4235,1	90,4	199,5	4035,7	119,94	52,02	128,22
674	623			3853,3	94,9	329,6	3523,6	113,14	51,28	127,54
675	623			3406,9	96,0	251,5	3155,4	115,60	52,59	127,81
676	124			2794,7	61,6	75,5	2719,3	106,15	37,64	111,79
677	124			2986,5	65,3	80,9	2905,6	103,46	38,46	108,57
678	124			2711,3	64,5	66,6	2644,6	106,42	37,61	111,56
680	424			3458,3	87,1	89,1	3369,2	102,88	37,71	107,81
681	424			3093,3	83,1	147,7	2945,6	101,79	38,34	111,00
682	424			3158,2	88,0	114,3	3043,9	101,27	38,04	108,01

Table F.20.: The determined energy components E_{def} and E_{frac} are presented as well as the resulting FSED values η_{tot}, η_{NC} and η_{DC}. With these results and the known corresponding fracture areas A_{NC} and A_{DC}, it is now possible to quantify E_{NC} and E_{DC}, which specify the dissipated energies into normal cracks and damage cracks, respectively. Missing or insufficient data is indicated by a dash ("-"). Detailed information about the calculation of the uncertainties are presented in Appendix A.

V	{...}	E_{tot} [mJ]	$\triangle E_{tot}$ [mJ]	E_{kin} [mJ]	$\triangle E_{kin}$ [mJ]	E_{setup} [mJ]	$\triangle E_{setup}$ [mJ]	E_{air} [mJ]	$\triangle E_{air}$ [mJ]
683	624	3943,4	67,7	234,1	15,6	3,9	1,9	197,2	19,7
684	624	4465,5	65,2	186,6	8,5	1,6	0,8	223,3	22,3
685	624	3065,7	69,5	131,6	6,3	10,5	5,3	153,3	15,3
686	622	4111,0	67,6	93,4	2,7	16,9	8,4	205,6	20,6
687	622	4227,5	66,0	147,2	5,9	0,8	0,4	211,4	21,1
688	122	3296,7	43,9	56,7	3,8	9,4	4,7	164,8	16,5
689	622	4760,9	63,7	101,2	7,0	9,4	4,7	238,0	23,8
690	622	4086,4	66,5	85,9	3,4	13,0	6,5	204,3	20,4
692	622	4709,2	65,2	195,7	6,3	8,9	4,5	235,5	23,5
693	421	3430,8	60,0	191,2	9,6	9,3	4,7	171,5	17,2

Table F.21.: Determined energy components of HIEs: Missing or insufficient data is indicated by a dash ("-"). Detailed information about the calculation of the uncertainties are presented in Appendix A.

V	{...}	E_{def} [mJ]	$\triangle E_{def}$ [mJ]	E_{frac} [mJ]	$\triangle E_{frac}$ [mJ]	E_{NC} [mJ]	E_{DC} [mJ]	η_{tot} [J/m^2]	η_{NC} [J/m^2]	η_{DC} [J/m^2]
683	624			3508,2	105,0	86,0	3422,2	104,20	38,31	108,91
684	624			4054,0	96,9	177,8	3876,2	101,39	37,98	109,80
685	624			2770,3	96,4	168,2	2602,0	100,33	38,49	111,96
686	622			3795,2	99,2	253,4	3541,9	109,01	43,21	122,34
687	622			3868,0	93,4	98,7	3769,4	118,11	43,46	123,67
688	122			3065,8	68,9	207,8	2858,0	107,93	43,23	121,11
689	622			4412,2	99,2	290,6	4121,6	109,01	42,36	122,62
690	622			3783,2	96,8	146,7	3636,5	112,80	43,10	120,67
692	622			4269,1	99,5	145,0	4124,1	115,55	43,05	122,82
693	421			3058,7	91,4	204,4	2854,3	100,81	47,02	109,81

Table F.22.: The determined energy components E_{def} and E_{frac} are presented as well as the resulting FSED values η_{tot}, η_{NC} and η_{DC}. With these results and the known corresponding fracture areas A_{NC} and A_{DC}, it is now possible to quantify E_{NC} and E_{DC}, which specify the dissipated energies in form of normal crack fracture and damage crack fragmentation, respectively. Missing or insufficient data is indicated by a dash ("-"). Detailed information about the calculation of the uncertainties are presented in Appendix A.

V	{...}	E_{tot} [mJ]	$\triangle E_{tot}$ [mJ]	E_{kin} [mJ]	$\triangle E_{kin}$ [mJ]	E_{setup} [mJ]	$\triangle E_{setup}$ [mJ]	E_{air} [mJ]	$\triangle E_{air}$ [mJ]
694	421	3587,1	59,4	164,5	6,7	13,4	6,7	179,4	17,9
695	221	3839,0	46,3	77,3	3,4	9,6	4,8	191,9	19,2
696	221	2403,6	54,1	127,1	5,6	11,6	5,8	120,2	12,0
697	221	3295,9	49,0	119,4	2,9	7,6	3,8	164,8	16,5
700	131	3420,7	43,7	177,1	9,3	4,8	2,4	171,0	17,1
701	131	2464,6	48,0	65,1	3,0	6,0	3,0	123,2	12,3
702	131	3195,8	44,0	84,4	4,9	7,2	3,6	159,8	16,0
703	131	2459,8	46,8	53,8	3,3	5,8	2,9	123,0	12,3
704	231	3699,2	47,5	52,4	2,9	0,4	0,2	185,0	18,5
705	231	2433,4	53,2	77,0	3,8	6,5	3,3	121,7	12,2
706	231	3612,7	47,9	169,3	4,4	0,7	0,3	180,6	18,1
707	231	2917,6	51,5	53,2	3,2	1,0	0,5	145,9	14,6
708	431	3927,4	58,9	177,4	8,8	7,8	3,9	196,4	19,6
709	431	2525,8	63,4	102,5	4,5	9,8	4,9	126,3	12,6
710	431	2892,2	62,0	96,5	5,9	10,1	5,0	144,6	14,5
711	631	3676,5	68,7	200,4	4,7	8,0	4,0	183,8	18,4
712	631	4127,2	67,2	172,7	5,9	9,5	4,7	206,4	20,6
713	631	2967,8	70,7	236,1	8,4	11,6	5,8	148,4	14,8
714	631	4465,5	65,1	176,7	5,7	7,1	3,6	223,3	22,3
715	132	3173,4	43,2	136,3	5,5	2,4	1,2	158,7	15,9
716	132	3058,5	44,3	154,3	5,0	5,7	2,8	152,9	15,3
717	132	2341,3	47,5	141,4	3,0	6,1	3,0	117,1	11,7
718	132	2948,9	44,4	112,9	2,6	7,1	3,6	147,4	14,7
719	432	4150,9	58,0	93,1	4,1	2,8	1,4	207,5	20,8
720	432	3501,0	60,5	78,2	4,3	6,0	3,0	175,0	17,5
721	432	3010,1	62,7	123,8	5,8	9,6	4,8	150,5	15,1
722	632	3422,5	69,2	78,8	2,7	1,2	0,6	171,1	17,1
723	632	4253,1	65,1	134,9	4,6	8,8	4,4	212,7	21,3
724	632	4248,8	66,3	198,2	5,3	4,0	2,0	212,4	21,2
725	632	4432,2	65,3	88,7	5,7	9,7	4,9	221,6	22,2
726	133	3228,6	43,4	120,4	3,3	3,5	1,7	161,4	16,1
727	133	3337,8	43,2	164,9	6,2	4,5	2,2	166,9	16,7
728	133	2637,5	46,0	94,9	4,5	4,0	2,0	131,9	13,2
729	133	2739,4	46,7	130,5	4,8	7,3	3,7	137,0	13,7
730	433	3998,0	57,3	122,1	1,2	4,3	2,2	199,9	20,0

Table F.23.: Determined energy components of HIEs: Missing or insufficient data is indicated by a dash ("-"). Detailed information about the calculation of the uncertainties are presented in Appendix A.

V	{...}	E_{def} [mJ]	$\triangle E_{def}$ [mJ]	E_{frac} [mJ]	$\triangle E_{frac}$ [mJ]	E_{NC} [mJ]	E_{DC} [mJ]	η_{tot} [J/m^2]	η_{NC} [J/m^2]	η_{DC} [J/m^2]
694	421			3229,8	90,7	114,3	3115,5	108,98	47,26	114,47
695	221			3560,1	73,8	96,4	3463,7	109,61	47,17	113,80
696	221			2144,7	77,5	112,4	2032,3	106,58	47,42	114,48
697	221			3004,1	72,1	115,8	2888,3	105,19	46,58	110,77
700	131			3067,8	72,5	176,8	2891,0	105,34	46,99	113,99
701	131			2270,3	66,4	178,3	2092,0	102,90	47,71	114,15
702	131			2944,5	68,5	147,2	2797,3	104,78	47,32	111,93
703	131			2277,3	65,3	128,3	2148,9	102,17	47,11	109,83
704	231			3461,4	69,1	120,7	3340,7	105,63	46,89	110,64
705	231			2228,1	72,4	154,9	2073,2	101,05	47,69	110,27
706	231			3262,1	70,7	101,2	3160,9	108,39	46,86	113,14
707	231			2717,4	69,8	95,7	2621,8	104,93	47,05	109,86
708	431			3545,7	91,2	234,6	3311,1	101,64	47,47	110,59
709	431			2287,2	85,3	128,3	2159,0	103,14	46,32	111,25
710	431			2641,0	87,4	88,7	2552,3	109,09	46,57	114,43
711	631			3284,3	95,8	317,4	2966,9	100,79	47,48	114,55
712	631			3738,7	98,5	196,1	3542,5	102,64	47,11	109,80
713	631			2571,8	99,7	226,9	2344,9	99,53	46,60	111,83
714	631			4058,4	96,8	99,3	3959,1	108,85	47,28	112,52
715	132			2876,0	65,7	121,0	2755,0	112,92	42,76	121,69
716	132			2745,6	67,4	140,8	2604,8	110,44	43,35	120,52
717	132			2076,8	65,1	107,6	1969,1	110,08	42,51	120,56
718	132			2681,4	65,3	105,0	2576,5	111,12	43,05	118,78
719	432			3847,4	84,2	132,5	3715,0	112,17	42,49	119,13
720	432			3241,7	85,3	96,3	3145,4	112,53	42,90	118,41
721	432			2726,2	88,4	112,3	2614,0	112,15	43,04	120,46
722	632			3171,4	89,6	282,8	2888,5	103,40	42,53	120,26
723	632			3896,8	95,4	128,3	3768,5	111,92	43,03	118,37
724	632			3834,1	95,0	255,1	3578,9	107,72	42,67	120,85
725	632			4112,1	98,0	255,9	3856,2	110,22	43,60	122,65
726	133			2943,3	64,6	122,6	2820,7	121,41	52,80	128,68
727	133			3001,5	68,4	97,7	2903,8	119,86	51,87	125,40
728	133			2406,8	65,6	101,9	2304,9	118,82	51,59	126,08
729	133			2464,6	68,9	132,9	2331,8	116,85	51,32	126,02
730	433			3671,7	80,7	119,1	3552,5	120,97	52,00	126,60

Table F.24.: The determined energy components E_{def} and E_{frac} are presented as well as the resulting FSED values η_{tot}, η_{NC} and η_{DC}. With these results and the known corresponding fracture areas A_{NC} and A_{DC}, it is now possible to quantify E_{NC} and E_{DC}, which specify the dissipated energies into normal cracks and damage cracks, respectively. Missing or insufficient data is indicated by a dash ("-"). Detailed information about the calculation of the uncertainties are presented in Appendix A.

V	{...}	E_{tot} [mJ]	$\triangle E_{tot}$ [mJ]	E_{kin} [mJ]	$\triangle E_{kin}$ [mJ]	E_{setup} [mJ]	$\triangle E_{setup}$ [mJ]	E_{air} [mJ]	$\triangle E_{air}$ [mJ]
731	433	3938,8	58,0	138,8	7,6	8,9	4,5	196,9	19,7
732	433	4177,8	57,8	101,7	5,5	6,5	3,2	208,9	20,9
733	433	3989,8	58,2	109,8	5,4	8,2	4,1	199,5	19,9
734	633	4234,7	66,8	129,5	5,4	10,7	5,3	211,7	21,2
735	633	4142,6	66,7	127,0	8,9	8,6	4,3	207,1	20,7
736	633	4508,1	64,6	172,9	7,4	2,5	1,3	225,4	22,5
737	133	3265,5	42,3	130,8	5,1	2,5	1,3	163,3	16,3
738	134	3380,5	43,9	119,5	5,7	3,6	1,8	169,0	16,9
739	134	2283,2	48,1	46,3	3,4	4,4	2,2	114,2	11,4
740	134	2365,5	47,3	129,2	6,6	5,2	2,6	118,3	11,8

Table F.25.: Determined energy components of HIEs: Missing or insufficient data is indicated by a dash ("-"). Detailed information about the calculation of the uncertainties are presented in Appendix A.

V	{...}	E_{def} [mJ]	$\triangle E_{def}$ [mJ]	E_{frac} [mJ]	$\triangle E_{frac}$ [mJ]	E_{NC} [mJ]	E_{DC} [mJ]	η_{tot} [J/m^2]	η_{NC} [J/m^2]	η_{DC} [J/m^2]
731	433			3594,2	89,7	235,2	3359,0	116,09	51,21	127,39
732	433			3860,7	87,5	256,7	3604,0	115,61	51,66	126,79
733	433			3672,3	87,6	119,3	3553,0	121,72	51,78	127,50
734	633			3882,8	98,7	195,6	3687,2	116,39	52,15	124,52
735	633			3799,9	100,7	297,5	3502,4	114,32	52,19	127,19
736	633			4107,3	95,8	354,1	3753,2	110,09	51,34	123,42
737	133			2968,9	64,9	159,3	2809,6	116,56	52,56	125,21
738	134			3088,3	68,3	114,5	2973,8	104,75	38,53	112,18
739	134			2118,4	65,1	75,6	2042,8	101,29	37,76	108,02
740	134			2112,8	68,3	68,6	2044,2	104,85	37,83	111,48

Table F.26.: The determined energy components E_{def} and E_{frac} are presented as well as the resulting FSED values η_{tot}, η_{NC} and η_{DC}. With these results and the known corresponding fracture areas A_{NC} and A_{DC}, it is now possible to quantify E_{NC} and E_{DC}, which specify the dissipated energies in form of normal crack fracture and damage crack fragmentation, respectively. Missing or insufficient data is indicated by a dash ("-"). Detailed information about the calculation of the uncertainties are presented in Appendix A.

V	{...}	E_{tot} [mJ]	$\triangle E_{tot}$ [mJ]	E_{kin} [mJ]	$\triangle E_{kin}$ [mJ]	E_{setup} [mJ]	$\triangle E_{setup}$ [mJ]	E_{air} [mJ]	$\triangle E_{air}$ [mJ]
741	134	3173,4	43,2	99,0	4,6	3,8	1,9	158,7	15,9
742	434	2907,5	62,3	207,3	8,1	4,8	2,4	145,4	14,5
743	434	2733,9	62,2	96,6	2,6	6,9	3,5	136,7	13,7
744	434	2962,7	61,7	105,4	4,4	9,7	4,9	148,1	14,8
745	634	3270,1	68,9	213,8	7,3	8,2	4,1	163,5	16,4
746	634	3245,0	69,4	203,5	7,9	7,9	3,9	162,3	16,2
747	634	3961,1	67,4	152,9	3,9	1,1	0,5	198,1	19,8
748	133	3283,5	43,1	79,4	4,1	-	-	164,2	16,4
749	133	2382,2	47,6	57,3	2,4	4,1	2,1	119,1	11,9
800	116	2156,8	49,5	76,1	3,2	5,5	2,7	107,8	10,8
801	116	2217,1	48,0	88,4	4,0	3,4	1,7	110,9	11,1
802	116	3359,1	42,7	178,7	8,3	0,7	0,4	168,0	16,8
803	616	3310,3	68,8	108,3	4,0	10,2	5,1	165,5	16,6
804	616	3773,9	68,0	171,9	5,8	11,2	5,6	188,7	18,9
805	616	2643,6	72,3	214,6	7,6	6,1	3,0	132,2	13,2
806	616	2732,9	72,1	115,4	5,0	5,6	2,8	136,6	13,7
807	316	3786,7	53,4	175,4	7,3	2,9	1,4	189,3	18,9
808	316	3297,3	55,4	174,0	5,7	5,0	2,5	164,9	16,5
809	316	2773,2	57,2	66,9	2,7	7,1	3,6	138,7	13,9
810	126	2782,0	45,7	103,0	2,4	8,1	4,1	139,1	13,9
811	126	3154,7	43,7	81,7	3,6	6,6	3,3	157,7	15,8
812	126	3158,8	43,3	115,7	3,8	5,2	2,6	157,9	15,8
813	126	3107,1	44,9	122,1	2,6	7,7	3,8	155,4	15,5
814	126	3169,9	43,7	100,0	5,6	6,2	3,1	158,5	15,8
815	626		0,0	84,4	3,4	-	-	-	-
816	626	4531,5	65,0	238,9	7,7	1,3	0,7	226,6	22,7
817	626	3177,9	69,9	213,0	9,3	-	-	158,9	15,9
818	426	4104,3	56,9	122,0	6,4	1,7	0,8	205,2	20,5
819	426	2927,5	61,9	197,6	13,4	11,8	5,9	146,4	14,6
820	426	2835,6	62,5	149,8	4,0	7,3	3,7	141,8	14,2
821	426	3202,3	60,9	109,7	5,1	11,1	5,6	160,1	16,0
822	426	3774,5	58,2	140,1	5,8	1,8	0,9	188,7	18,9
823	626	3151,0	70,4	140,6	3,6	3,4	1,7	157,6	15,8

Table F.27.: Determined energy components of HIEs: Missing or insufficient data is indicated by a dash ("-"). Detailed information about the calculation of the uncertainties are presented in Appendix A.

V	{...}	E_{def} [mJ]	$\triangle E_{def}$ [mJ]	E_{frac} [mJ]	$\triangle E_{frac}$ [mJ]	E_{NC} [mJ]	E_{DC} [mJ]	η_{tot} [J/m^2]	η_{NC} [J/m^2]	η_{DC} [J/m^2]
741	134			2911,9	65,6	61,9	2850,0	104,82	38,23	108,94
742	434			2550,0	87,4	70,4	2479,6	104,87	37,90	110,41
743	434			2493,7	81,9	115,9	2377,8	101,27	38,57	109,98
744	434			2699,4	85,8	116,1	2583,4	103,27	38,60	111,68
745	634			2884,6	96,7	200,2	2684,4	96,89	38,14	109,46
746	634			2871,4	97,5	184,7	2686,7	98,37	37,52	110,71
747	634			3609,1	91,6	149,8	3459,3	103,04	38,21	111,21
748	133			-	-	-	-	-	-	-
749	133			2201,7	64,0	163,0	2038,6	112,11	52,54	123,28
800	116			1967,4	66,2	139,0	1828,5	157,59	66,47	175,93
801	116			2014,4	64,8	175,1	1839,4	152,42	65,48	174,47
802	116			3011,7	68,2	249,0	2762,7	156,79	65,00	179,66
803	616			3026,2	94,4	352,4	2673,8	150,71	66,21	181,18
804	616			3402,2	98,2	341,0	3061,1	150,23	66,79	174,52
805	616			2290,7	96,3	227,4	2063,4	149,92	65,21	174,96
806	616			2475,3	93,6	345,0	2130,3	144,88	65,27	180,53
807	316			3419,1	81,1	271,6	3147,5	155,59	66,65	175,84
808	316			2953,4	80,1	228,8	2724,6	159,29	66,74	180,29
809	316			2560,5	77,3	224,4	2336,2	155,31	65,47	178,88
810	126			2531,7	66,0	182,4	2349,3	160,89	66,24	180,96
811	126			2908,7	66,4	148,0	2760,6	165,61	65,29	180,48
812	126			2880,1	65,5	159,9	2720,2	163,83	66,99	179,05
813	126			2822,0	66,9	153,2	2668,8	162,42	66,36	177,14
814	126			2905,2	68,3	148,1	2757,1	163,35	65,97	177,42
815	626			-	-	-	-	-	-	-
816	626			4064,6	96,0	232,4	3832,3	164,94	65,16	181,82
817	626			-	-	-	-	-	-	-
818	426			3775,4	84,7	255,5	3519,8	161,72	65,26	181,16
819	426			2571,7	95,9	189,7	2382,0	155,58	65,27	174,84
820	426			2536,7	84,4	114,9	2421,8	165,65	65,92	178,46
821	426			2921,4	87,6	203,6	2717,7	158,44	65,04	177,54
822	426			3443,8	83,8	168,2	3275,6	162,24	65,53	175,54
823	626			2849,5	91,5	228,9	2620,6	157,28	66,01	178,88

Table F.28.: The determined energy components E_{def} and E_{frac} are presented as well as the resulting FSED values η_{tot}, η_{NC} and η_{DC}. With these results and the known corresponding fracture areas A_{NC} and A_{DC}, it is now possible to quantify E_{NC} and E_{DC}, which specify the dissipated energies into normal cracks and damage cracks, respectively. Missing or insufficient data is indicated by a dash ("-"). Detailed information about the calculation of the uncertainties are presented in Appendix A.

V	{...}	E_{tot} [mJ]	$\triangle E_{tot}$ [mJ]	E_{kin} [mJ]	$\triangle E_{kin}$ [mJ]	E_{setup} [mJ]	$\triangle E_{setup}$ [mJ]	E_{air} [mJ]	$\triangle E_{air}$ [mJ]
900	136	2596,9	45,8	125,1	4,8	1,7	0,9	129,8	13,0
901	136	2564,8	47,1	78,6	4,5	6,6	3,3	128,2	12,8
902	136	2454,0	47,3	53,4	1,7	4,4	2,2	122,7	12,3
903	136	2495,1	47,5	127,9	4,9	5,6	2,8	124,8	12,5
904	136	3242,6	43,3	140,0	5,5	2,8	1,4	162,1	16,2
905	136	2341,3	47,5	108,9	3,8	4,0	2,0	117,1	11,7
906	636	4192,5	66,1	152,3	3,8	4,8	2,4	209,6	21,0
907	636	3301,3	69,5	146,6	5,0	13,0	6,5	165,1	16,5
908	636	3697,4	68,2	171,0	3,9	6,8	3,4	184,9	18,5
909	636	3848,9	68,5	138,9	4,2	11,7	5,8	192,4	19,2
910	636	3260,4	69,6	77,1	3,7	12,0	6,0	163,0	16,3
911	636	3204,2	69,4	136,1	6,0	8,7	4,4	160,2	16,0

Table F.29.: Determined energy components of HIEs: Missing or insufficient data is indicated by a dash ("-"). Detailed information about the calculation of the uncertainties are presented in Appendix A.

V	{...}	E_{def} [mJ]	$\triangle E_{def}$ [mJ]	E_{frac} [mJ]	$\triangle E_{frac}$ [mJ]	E_{NC} [mJ]	E_{DC} [mJ]	η_{tot} [J/m^2]	η_{NC} [J/m^2]	η_{DC} [J/m^2]
900	136			2340,2	64,5	132,0	2208,2	163,66	65,40	179,81
901	136			2351,3	67,7	249,0	2102,3	151,13	66,36	178,07
902	136			2273,4	63,5	152,5	2121,0	162,17	66,93	180,64
903	136			2236,8	67,7	134,9	2101,9	161,27	65,04	178,19
904	136			2937,7	66,4	234,3	2703,4	156,53	65,90	177,71
905	136			2111,3	65,0	201,9	1909,4	154,73	66,57	179,94
906	636			3825,8	93,3	390,1	3435,7	149,17	65,40	174,56
907	636			2976,6	97,5	309,5	2667,2	149,94	65,41	176,38
908	636			3334,8	94,0	379,6	2955,2	147,12	66,47	174,28
909	636			3505,9	97,7	273,5	3232,3	155,97	66,79	175,84
910	636			3008,3	95,6	321,4	2686,9	149,93	66,02	176,81
911	636			2899,1	95,8	388,9	2510,2	144,06	66,45	175,88

Table F.30.: The determined energy components E_{def} and E_{frac} are presented as well as the resulting FSED values η_{tot}, η_{NC} and η_{DC}. With these results and the known corresponding fracture areas A_{NC} and A_{DC}, it is now possible to quantify E_{NC} and E_{DC}, which specify the dissipated energies in form of normal crack fracture and damage crack fragmentation, respectively. Missing or insufficient data is indicated by a dash ("-"). Detailed information about the calculation of the uncertainties are presented in Appendix A.

V	{...}	E_{tot} [mJ]	$\triangle E_{tot}$ [mJ]	E_{kin} [mJ]	$\triangle E_{kin}$ [mJ]	E_{setup} [mJ]	$\triangle E_{setup}$ [mJ]	E_{air} [mJ]	$\triangle E_{air}$ [mJ]
912	136	2800,6	45,2	106,7	3,9	6,8	3,4	140,0	14,0
913	136	2676,4	46,6	93,9	5,3	5,3	2,6	133,8	13,4
914	636	3980,6	67,6	162,6	4,8	3,1	1,5	199,0	19,9
1001	135	2637,5	45,9	119,4	3,7	6,2	3,1	131,9	13,2
1003	135	2587,6	47,1	148,7	4,2	8,0	4,0	129,4	12,9
1005	135	3297,6	43,5	113,8	7,0	5,1	2,5	164,9	16,5
1007	135	3337,8	43,3	141,1	2,0	5,5	2,8	166,9	16,7
1008	135	3337,8	43,2	125,5	6,1	4,7	2,3	166,9	16,7
1009	135	3255,8	42,8	50,8	1,9	1,4	0,7	162,8	16,3
269B	102	2513,0	47,3	122,0	6,0	3,0	1,5	125,7	12,6
H3103	105	2740,7	46,3	86,6	5,3	6,0	3,0	137,0	13,7
H3601	605	4652,7	65,0	193,4	7,0	9,0	4,5	232,6	23,3
L605	114	3007,3	44,6	145,8	5,7	5,6	2,8	150,4	15,0
L693	421	4072,5	57,9	109,6	4,5	16,3	8,1	203,6	20,4
L722	432	3235,7	60,7	148,9	6,3	5,6	2,8	161,8	16,2

Table F.31.: Determined energy components of HIEs: Missing or insufficient data is indicated by a dash ("-"). Detailed information about the calculation of the uncertainties are presented in Appendix A.

V	{...}	E_{def} [mJ]	$\triangle E_{def}$ [mJ]	E_{frac} [mJ]	$\triangle E_{frac}$ [mJ]	E_{NC} [mJ]	E_{DC} [mJ]	η_{tot} [J/m^2]	η_{NC} [J/m^2]	η_{DC} [J/m^2]
912	136			2547,0	66,5	232,8	2314,2	154,90	66,02	179,17
913	136			2443,5	67,9	146,1	2297,4	161,05	65,88	177,34
914	636			3615,9	93,9	390,5	3225,4	149,85	65,34	177,68
1001	135			2380,1	65,9	87,3	2292,7	102,22	48,55	106,71
1003	135			2301,5	68,2	97,1	2204,4	101,96	48,59	107,14
1005	135			3013,8	69,5	192,3	2821,5	97,71	48,35	105,01
1007	135			3024,3	64,7	210,6	2813,7	98,06	49,27	105,91
1008	135			3040,7	68,4	146,5	2894,2	101,85	49,53	107,60
1009	135			3040,9	61,7	222,6	2818,3	98,99	49,22	107,59
269B	102			2262,4	67,3	151,1	2111,3	108,35	43,68	121,19
H3103	105			2511,0	68,2	143,0	2368,0	99,43	49,01	106,02
H3601	605			4217,6	99,7	204,5	4013,1	99,41	48,84	104,95
L605	114			2705,6	68,1	120,8	2584,8	101,89	37,54	110,76
L693	421			3743,0	90,9	218,6	3524,4	103,80	47,17	112,15
L722	432			2919,4	86,0	240,0	2679,4	106,57	42,84	122,95

Table F.32.: The determined energy components E_{def} and E_{frac} are presented as well as the resulting FSED values η_{tot}, η_{NC} and η_{DC}. With these results and the known corresponding fracture areas A_{NC} and A_{DC}, it is now possible to quantify E_{NC} and E_{DC}, which specify the dissipated energies in form of normal crack fracture and damage crack fragmentation, respectively. Missing or insufficient data is indicated by a dash ("-"). Detailed information about the calculation of the uncertainties are presented in Appendix A.

G. Representative Results of Dynamic Fracture Parameters

G.1. Characteristic Results of Damage Crack Evolution

V	{...}	$\bar{v}_{DC}$ [m/s]	$\widetilde{v}_{DC}$ [m/s]	$v_{avg\,DC}$ [m/s]	$\triangle v_{avg\,DC}$ [m/s]	$\sigma\,(v_{DC})$ [m/s]	Max(v_{DC}) [m/s]
208	101	833	847	632	33	449	1592
211	101			258	44		
212	101	72	72	83	10	64	192
214	101	255	279	243	16	120	427
215	101	241	282	149	28	99	312
217	101	110	66	116	8	104	311
218	101	90	7	83	14	164	448
219	101	565	404	580	64	526	1453
220	101	123	110	118	5	79	262
221	101	225	234	238	20	104	383
222	101	198	94	198	12	201	712
223	101	84	33	107	54	120	263
224	101	64	77	91	8	60	164
225	101	151	101	274	33	174	509
226	101	10		40		20	40
227	101	215	159	254	15	178	516
228	301	109	109	109			109
230	301	158	179	80	16	124	331
231	301	288	220	345	23	254	740
232	301	231	217	231	28	174	478
233	301	222	137	144	6	319	1244
234	301	211	195	177	15	137	435
235	301	64	64	64			64
236	301	115	25	214	26	164	499
238	301	80	50	68	7	87	283

Table G.1.: Characteristic values which specify the propagation of damage cracks.

V	{...}	$\bar{v}_{DC}$ [m/s]	$\widetilde{v}_{DC}$ [m/s]	$v_{avg\,DC}$ [m/s]	$\triangle v_{avg\,DC}$ [m/s]	$\sigma\,(v_{DC})$ [m/s]	Max(v_{DC}) [m/s]
239	301	120	94	168	39	91	269
242	601	160	151	181	13	121	405
243	601	92		172		195	552
244	601	110	107	98	9	74	233
245	601	166	147	129	20	153	442
246	601	243	124	206	33	239	682
247	601	330	330	330	78	190	464
248	601	240	114	201	51	236	506
249	501	307	308	280	13	71	371
252	501	68	52	196		81	196
256	401	131	81	140	17	120	372
259	201	173	125	185	22	185	475
264	102	97	108	100	8	49	144
265	102	106	88	106	5	100	293
268	102	116	119	79	13	83	211
276	102	176	152	168	11	118	431
277	103	133	107	164	13	148	502
320	303	101	88	113	5	73	296
323	303	49	44	65	6	44	103
351	602	311	164	257	40	301	802
357	603	8	2	26	7	11	34
360	604			21	2		
405	106	438	318	333	54	414	1110
411	106	188	201	295	26	176	402
431	606			170	55		

Table G.2.: Characteristic values which specify the propagation of damage cracks.

V	{...}	$\bar{v}_{DC}$ [m/s]	$\widetilde{v}_{DC}$ [m/s]	$v_{avg\,DC}$ [m/s]	$\triangle v_{avg\,DC}$ [m/s]	$\sigma\,(v_{DC})$ [m/s]	Max(v_{DC}) [m/s]
603	113	295	211	199	17	332	989
611	613	198	131	203	14	184	458
612	112	396	109	510	164	685	1617
615	612	117	109	86	5	56	198
623	111	309	302	286	26	188	699
628	211	402	227	257	14	479	1754
640	121	177	138	207	14	119	398
652	621	447	351	286	20	398	1742
655	122	84	84	84			84
677	124	117	86	134	6	91	292
683	624	202	156	224	29	191	620
685	624	451	451	122	47	412	742
714	631	340	222	411	25	324	927
726	133	190	134	198	19	221	754
736	633	462	454	382	13	207	830
739	134	505	429	416	83	373	995
747	634	411		363	53	915	2805
801	116	297	161	259	86	270	699
805	616	200	217	252	20	158	374
809	316	302	353	406	21	202	486
811	126	70	70			98	139
817	626	897	218	153	10	1334	2434
907	636	387	314	313	25	368	1113
913	136	1047	1047				1047
269B	102	99	79	95	13	82	264

Table G.3.: Characteristic values which specify the propagation of damage cracks.

V	{...}	$\bar{w}_{DC}$ [m^2/s]	$\widetilde{w}_{DC}$ [m^2/s]	$\sigma\,(w_{DC})$ [m^2/s]	Max(w_{DC}) [m^2/s]
208	101	17,2	13,9	12,5	40,3
212	101	6,6	6,8	3,4	11,0
214	101	9,4	11,2	5,0	14,0
215	101	12,2	12,3	6,0	19,3
217	101	3,8	2,3	4,0	11,6
218	101	1,0	0,3	1,5	3,7
219	101	14,4	10,0	13,0	34,2
220	101	4,4	3,8	5,4	16,9
221	101	3,7	3,1	2,4	7,7
222	101	7,2	5,8	6,5	22,2
223	101	1,3	0,2	1,7	4,0
224	101	1,1	1,1	0,8	2,1
225	101	2,4	1,4	3,1	9,8
226	101	2,9	0,8	3,5	7,6
227	101	9,5	6,6	7,2	25,8
228	301	0,9	0,9		0,9
230	301	4,2	3,3	4,3	9,1
231	301	13,2	15,6	9,9	29,5
232	301	7,0	6,0	6,4	16,4
233	301	6,5	5,3	7,6	29,8
234	301	8,4	2,4	13,7	46,0
235	301	1,1	1,1		1,1
236	301	1,3	0,2	2,4	8,3
238	301	3,2	2,7	2,9	8,7

Table G.4.: Characteristic values which specify the evolution of damage fracture areas.

V	{...}	$\bar{w}_{DC}$ $[m^2/\text{s}]$	$\widetilde{w}_{DC}$ $[m^2/\text{s}]$	$\sigma\,(w_{DC})$ $[m^2/\text{s}]$	$\text{Max}(w_{DC})$ $[m^2/\text{s}]$
239	301	2,2	2,4	1,6	4,2
242	601	8,6	6,9	6,2	21,5
243	601	2,0	0,6	3,1	10,9
244	601	1,7	0,5	2,2	5,6
245	601	4,8	1,6	5,5	13,2
246	601	8,5	5,2	7,8	21,8
247	601	6,1	6,1	1,7	7,3
248	601	3,5	2,4	3,7	10,0
249	501	12,1	12,4	7,5	19,0
252	501	8,5	9,7	5,0	13,5
256	401	3,4	2,2	3,4	9,6
259	201	2,8	1,9	3,2	10,7
264	102	3,0	2,9	0,5	3,8
265	102	6,3	3,8	6,7	21,1
268	102	3,2	2,5	2,2	7,6
276	102	7,5	5,6	6,3	18,4
277	103	6,9	5,9	4,8	18,7
320	303	3,9	3,0	2,9	8,5
323	303	1,6	1,4	1,1	3,8
351	602	9,2	8,4	4,1	15,7
357	603	1,0	0,7	1,0	3,5
405	106	16,3	10,7	15,4	51,6
411	106	12,8	12,8	10,7	29,7

Table G.5.: Characteristic values which specify the evolution of damage fracture areas.

V	{...}	$\bar{w}_{DC}$ $[m^2/\text{s}]$	$\widetilde{w}_{DC}$ $[m^2/\text{s}]$	$\sigma\,(w_{DC})$ $[m^2/\text{s}]$	$\text{Max}(w_{DC})$ $[m^2/\text{s}]$
603	113	6,0	3,3	6,1	19,5
611	613	10,9	5,2	16,0	51,6
612	112	9,6	5,5	11,4	31,7
615	612	4,8	4,2	3,3	11,0
623	111	13,5	10,6	11,6	38,9
628	211	10,9	9,4	7,6	25,5
640	121	6,1	5,6	3,7	12,8
652	621	32,4	28,7	19,7	89,0
655	122	5,7	5,7		5,7
677	124	3,6	2,7	2,6	8,7
683	624	12,9	1,9	20,1	60,6
685	624	1,4	1,4	1,7	2,6
714	631	24,1	28,8	15,7	47,2
726	133	10,5	9,8	9,0	33,3
736	633	33,3	33,3	12,5	49,1
739	134	3,5	3,1	1,0	4,8
747	634	7,5	0,0	14,2	39,3
801	116	6,0	5,5	5,0	13,9
805	616	4,5	4,8	3,0	9,1
809	316	12,0	10,1	8,7	24,1
811	126	3,7	3,7	4,8	7,1
817	626	25,1	12,7	27,1	56,2
907	636	7,4	3,8	7,8	24,6
913	136	55,4	55,4	0,0	55,4
269B	102	1,7	1,5	1,5	4,2

Table G.6.: Characteristic values which specify the evolution of damage fracture areas.

G.2. Characteristic Results of Normal Crack Tip Velocities

Crack ID	V	{...}	Crack Type	$\bar{u}$ [m/s]	Max($u(t)$) [m/s]	$\sigma\,(u(t))$ [m/s]
208	208	101	ACT	1149,6	1764,5	506,4
215	215	101	ACT	1168,0	1494,1	315,0
221	221	101	ACB	1252,9	1471,1	331,5
222	222	101	ACT	1027,9	1441,5	510,5
223	223	101	ACB	1477,6	1539,2	81,9
225	225	101	ACB	1488,5	1539,8	72,5
226	226	101	BCM	1495,6	1538,9	61,2
227	227	101	ACB	1187,0	1522,5	494,2
232	232	301	WC	871,1	1248,7	354,8
236	236	301	WC	920,1	1017,2	136,6
242	242	601	BCM	1184,7	1496,9	441,5
243	243	601	ACB	804,4	1458,4	667,5
244	244	601	WC	965,3	1391,7	443,6
248	248	601	ACB	1255,7	1509,2	358,5
249	249	501	ACB	1121,1	1561,1	716,5
250	250	501	WC	839,8	1159,0	235,5
251	251	501	ACB	1401,1	1434,5	47,3
252	252	501	ACB	1107,8	1475,4	519,9
256	256	401	WC	1069,2	1467,9	411,9
259	259	201	ACB	1509,2	1516,3	10,2
264	264	102	ACT	1184,8	1505,9	295,4
266	266	102	ACT	1279,0	1448,9	268,2
273	273	102	ACT	1386,2	1528,7	201,5
275	275	102	ACT	875,9	891,9	22,6
276	276	102	ACB	1039,5	1471,8	375,6
277	277	103	ACT	559,6	1577,2	702,7
282	282	103	ACB	1499,6	1508,9	13,1
287	287	103	ACB	1417,1	1489,2	110,7
290	290	103	ACB	1101,9	1243,6	193,3
318	318	103	BCM	1745,7	2211,5	658,8
320	320	303	ACB	1475,3		
355	355	602	WC	1582,8	1766,4	157,1
362	362	604	SCM	1585,6	1702,5	88,2
403	403	106	BCM	1444,7	2228,3	1108,2
405	405	106	ACB	1887,2	2342,0	518,6
409	409	106	BCM	1903,8	2217,0	443,0
411	411	106	ACB	2005,1	2369,4	498,6
413	413	106	ACT	367,1	1359,0	372,9
415	415	106	BCM	2439,5	3266,5	783,8
431	431	606	ACB	1742,2	2288,9	480,4

Table G.7.: Representative statistical results of crack tip velocities $u(t)$ in various targets.

Crack ID	V	{...}	Crack Type	$\bar{u}$ [m/s]	Max($u(t)$) [m/s]	$\sigma\,(u(t))$ [m/s]
503	503	305	ACB	1165,8	1511,0	529,6
510	510	205	ACB	1193,3	1460,9	378,5
511	511	405	ACB	880,5	1470,3	547,2
515	515	505	ACB	759,2	1092,0	285,4
603	603	113	ACB	1490,2	2045,4	346,9
607	607	114	SCM	701,2	1504,0	629,5
611	611	613	ACB	1421,0	2152,6	631,3
612	612	112	WC	1550,8	2120,2	384,5
613	613	112	ACB	1569,6	2252,4	313,3
615	615	612	BCM	1317,1	1501,8	181,2
622	622	111	BCM	1478,6	1580,3	111,6
623	623	111	ACT	1037,4	1539,7	353,2
624	624	611	ACB	1555,7	1742,5	162,1
625	625	611	ACB	1479,5	1498,8	27,3
628	628	211	ACT	1526,9	1621,0	87,4
629	629	411	ACB	1590,0	1852,2	143,3
640	640	121	BCM	1478,7	1748,6	172,3
641	641	121	BCM	1260,0	1474,7	303,6
642	642	121	ACB	1487,9	1731,2	152,8
643	643	121	BCM	1481,0	1669,3	112,1
649	649	421	WC	1050,0	1443,2	648,2
651	651	621	ACB	1433,3	1535,2	136,9
652	652	621	ACT	1386,9	1784,0	288,1
653	653	621	WC	1365,4	1423,2	57,3
655	655	122	ACB	1465,6	1504,7	55,3
660	660	422	BCM	1492,9	1721,0	194,7
665	665	123	WC	1481,5	1509,1	39,0
666	666	123	ACB	1131,9	1356,8	318,2
675	675	623	WC	1261,2	1607,3	489,5
677	677	124	SCM	1570,7	1809,8	227,2
681	681	424	SCM	1336,5		
683	683	624	SCM	1297,8	1483,8	263,1
685	685	624	SCM	991,1	1894,0	707,7
688	688	122	ACB	1555,2	1602,1	43,9
689	689	622	ACT	1099,5	1599,4	707,0

Table G.8.: Representative statistical results of crack tip velocities $u(t)$ in various targets.

Crack ID	V	{...}	Crack Type	$\bar{u}$ [m/s]	Max($u(t)$) [m/s]	$\sigma\,(u(t))$ [m/s]
691	691	622	BCM	1547,3	1620,6	120,6
694	694	421	BCM	1527,2	1673,7	146,1
701	701	131	ACB	1471,2	1523,7	64,2
704	704	231	ACT	1471,6	1625,9	93,7
710	710	431	WC	1360,2	1700,9	209,5
714	714	631	ACB	1574,7	1717,4	176,4
715	715	132	ACB	1383,6	1441,7	55,6
718	718	132	BCM	1531,7	1691,8	153,0
719	719	432	ACT	961,2	1428,7	661,2
721	721	432	BCM	1528,5	1555,0	37,4
722	722	632	ACB	1503,2	1518,9	22,7
723	723	632	BCM	1515,2	1545,1	26,1
727	727	133	ACT	1526,2	1664,5	119,8
731	731	433	BCM	1440,7	1521,7	112,7
735	735	633	BCM	1476,2	1538,2	89,7
739	739	134	SCM	1499,1	1571,3	62,6
740	740	134	SCM	1578,2	2380,2	578,3
743	743	434	SCM	1387,6	1645,2	165,2
745	745	634	SCM	1631,0	1947,5	447,6
746	746	634	SCM	1658,1	2299,8	504,0
747	747	634	SCM	761,9	1069,0	434,2
748	748	133	ACT	1199,7	1955,9	715,5
800	800	116	BCM	2092,1	2400,4	335,3
801	801	116	ACB	2311,9	2721,0	581,3
803	803	616	ACB	1492,9	2044,3	405,0
804	804	616	ACB	2572,2	2790,2	198,5
805	805	616	ACB	2004,2	2567,7	666,9
811	811	126	BCM	2239,4	2285,9	71,0
813	813	126	BCM	1952,6	2606,8	558,6
816	816	626	ACT	1480,4	1850,1	624,1
817	817	626	WC	1154,3	1943,6	636,8
819	819	426	WC	1163,1	2478,8	686,3
820	820	426	WC	1484,4	1698,7	139,7
821	821	426	WC	1191,0	2272,8	722,3
907	907	636	ACB	2085,7	2123,2	53,0

Table G.9.: Representative statistical results of crack tip velocities $u(t)$ in various targets.

Crack ID	V	{...}	Crack Type	$\bar{u}$ [m/s]	Max($u(t)$) [m/s]	σ ($u(t)$) [m/s]
910	910	636	ACB	2171,9	2885,1	535,8
912	912	136	ACB	2070,0	3065,3	734,3
913	913	136	ACB	1657,0	2648,3	879,3
2212	221	101	ACT	878,3	1043,0	232,9
2232	223	101	WC	763,6	1097,0	471,4
2322	232	301	ACB	1378,4	1472,5	132,9
2362	236	301	ACB	1182,7	1543,7	581,0
2432	243	601	WC	812,7	1401,8	633,8
2433	243	601	WC	656,2	1107,8	406,9
2442	244	601	ACB	1181,3	1472,4	411,7
2482	248	601	ACB	1506,9	1506,9	
2484	248	601	WC	1131,7	1131,7	
2492	249	501	ACB	1022,9	1521,2	628,0
2493	249	501	WC	702,1	1069,1	328,2
2494	249	501	WC	722,5	1051,3	308,3
2502	250	501	BCM	1502,1	1575,2	103,2
2512	251	501	WC	1057,2	1220,5	265,6
2562	256	401	ACB	1397,5	1489,2	129,7
2642	264	102	ACT	1046,4	1591,3	906,4
2698	269B	102	ACB	1239,4	1533,0	417,5
2772	277	103	ACT	918,5	1538,2	811,5
3552	355	602	ACB	1524,3	1827,1	189,8
4025	403	106	BCM	1912,2	2190,3	451,4
6122	612	112	ACB	1454,9	2147,6	357,0
6123	612	112	ACB	887,1	1589,8	579,5
6532	653	621	BCM	1150,1	1402,2	231,0
6533	653	621	ACB	1565,2	1825,2	367,7
6752	675	623	BCM	1355,0	1715,7	548,1
7102	710	431	ACB	1388,9	1625,9	170,1
7452	745	634	SCM	1587,6	1597,5	14,0
7462	746	634	SCM	1688,3	2733,1	635,0
8032	803	616	ACB	1495,5	2843,2	800,8
8172	817	626	WC	1959,6	2171,0	323,9
8173	817	626	ACB	2109,1	2463,1	263,6
8192	819	426	ACB	2135,4	2295,6	161,4

Table G.10.: Representative statistical results of crack tip velocities $u(t)$ in various targets.

G.3. Characteristic Results of Normal Crack Velocities

V	{...}	$\bar{v}_{A\,l}$ [m/s]	$\bar{v}_{A\,r}$ [m/s]	$\bar{v}_{A}$ [m/s]	$\widetilde{v}_{A\,l}$ [m/s]	$\widetilde{v}_{A\,r}$ [m/s]	$\widetilde{v}_{A}$ [m/s]
208	101	1189	46	1311	1257		1286
211	101						
212	101		3072	3072		3072	3072
214	101	6500		6500	6500		6500
215	101		2715	2715		2174	2174
217	101		5896	5896		5896	5896
218	101		3212	3212		4163	4163
219	101	1076	1393	2120	1045	1123	1810
220	101						
221	101	3757		3757	4028		4028
222	101	239	1179	1063	189	1244	1120
223	101	3283		3283	2818		2818
224	101						
225	101		2669	2669		1673	1673
226	101						
227	101	3328		3328	2166		2166
228	301						
230	301						
231	301	499		499	499		499
232	301	5007		5007	3894		3894
233	301	3796		3796	4817		4817
234	301	2954		2954	3132		3132
235	301						
236	301	6220		6220	5980		5980
238	301						

Table G.11.: Characteristic values which specify the propagation of normal cracks.

V	{...}	$\bar{v}_{A\,l}$ [m/s]	$\bar{v}_{A\,r}$ [m/s]	$\bar{v}_{A}$ [m/s]	$\widetilde{v}_{A\,l}$ [m/s]	$\widetilde{v}_{A\,r}$ [m/s]	$\widetilde{v}_{A}$ [m/s]
239	301						
242	601	4429		4429	4395		4395
243	601	2460		2460	1032		1032
244	601	4133		4133	4133		4133
245	601	3838		3838	3838		3838
246	601	3749		3749	3749		3749
247	601						
248	601	6386	6947	13333	5449	5036	10486
249	501	4883	4375	9258	5347	4884	10232
252	501	3125		3125	2287		2287
256	401	4024		4024	2254		2254
259	201	5290		5290	6824		6824
264	102	1583		1583	1504		1504
265	102	3211		3211	3952		3952
268	102	2436		2436	2065		2065
276	102	1142		1142	941		941
277	103	739	986	1479	583	1257	1306
320	303	2033	4476	5086	1115	1747	3668
323	303		8417	8417		10306	10306
351	602	3367		3367	2051		2051
357	603	1166		1166	1342		1342
360	604						
405	106		2651	2651		2715	2715
411	106	1886	1427	3312	2066	1795	3362
431	606						

Table G.12.: Characteristic values which specify the propagation of normal cracks.

V	{...}	$\bar{v}_{A\,l}$ [m/s]	$\bar{v}_{A\,r}$ [m/s]	$\bar{v}_{A}$ [m/s]	$\widetilde{v}_{A\,l}$ [m/s]	$\widetilde{v}_{A\,r}$ [m/s]	$\widetilde{v}_{A}$ [m/s]
603	113	8069		8069	6750		6750
611	613		10107	10107		8941	8941
612	112	897	1752	1614	805	1459	1264
615	612						
623	111	1933	2427	3587	1673	2499	3926
628	211	1556	1464	1997	1327	1504	1751
640	121						
652	621	1776		1776	1527		1527
655	122	2733		2733	1603		1603
677	124						
683	624						
685	624						
714	631		7145	7145		6909	6909
726	133		3030	3030		2851	2851
736	633	961		961	1089		1089
739	134						
747	634						
801	116	2190		2190	1959		1959
805	616		3046	3046		2639	2639
809	316						
811	126						
817	626	5231		5231	3328		3328
907	636	4476		4476	4659		4659
913	136	2265		2265	1473		1473
269B	102	1110		1110	848		848

Table G.13.: Characteristic values which specify the propagation of normal cracks.

V	{...}	$\sigma\,(v_{A\,l})$ [m/s]	$\sigma\,(v_{A\,r})$ [m/s]	$\sigma\,(v_A)$ [m/s]	Max($v_{A\,l}$) [m/s]	Max($v_{A\,r}$) [m/s]	Max(v_A) [m/s]
208	101	846	189	864	2963	777	2963
211	101						
212	101		52	52		3108	3108
214	101				6500		6500
215	101		1903	1903		4831	4831
217	101		1712	1712		7106	7106
218	101		2239	2239		4819	4819
219	101	643	1265	1784	1725	2771	4302
220	101						
221	101	2545		2545	6156		6156
222	101	148	836	870	415	2850	2850
223	101	3118		3118	7383		7383
224	101						
225	101		2697	2697		6228	6228
226	101						
227	101	3829		3829	8673		8673
228	301						
230	301						
231	301	529		529	873		873
232	301	2402		2402	7764		7764
233	301	2937		2937	6085		6085
234	301	660		660	3507		3507
235	301						
236	301	5094		5094	12363		12363
238	301						

Table G.14.: Characteristic values which specify the propagation of normal cracks.

V	{...}	$\sigma\,(v_{A\,l})$ [m/s]	$\sigma\,(v_{A\,r})$ [m/s]	$\sigma\,(v_A)$ [m/s]	Max$(v_{A\,l})$ [m/s]	Max$(v_{A\,r})$ [m/s]	Max(v_A) [m/s]
239	301						
242	601	1589		1589	6035		6035
243	601	3421		3421	7551		7551
244	601	4299		4299	7173		7173
245	601	4856		4856	7271		7271
246	601	3340		3340	6111		6111
247	601						
248	601	4461	5993	10441	11241	13661	24902
249	501	4367	3826	8192	9000	7921	16921
252	501	2758		2758	6205		6205
256	401	3816		3816	8404		8404
259	201	4128		4128	8432		8432
264	102	744		744	2582		2582
265	102	1655		1655	5167		5167
268	102	1796		1796	5662		5662
276	102	1117		1117	2624		2624
277	103	616	702	1306	1617	1512	3130
320	303	1976	5131	4538	4994	11637	11637
323	303		6695	6695		13966	13966
351	602	4207		4207	9136		9136
357	603	460		460	1495		1495
360	604						
405	106		1336	1336		4214	4214
411	106	417	695	990	2282	2111	4299
431	606						

Table G.15.: Characteristic values which specify the propagation of normal cracks.

V	{...}	$\sigma(v_{Al})$ [m/s]	$\sigma(v_{Ar})$ [m/s]	$\sigma(v_A)$ [m/s]	Max(v_{Al}) [m/s]	Max(v_{Ar}) [m/s]	Max(v_A) [m/s]
603	113	5070		5070	20290		20290
611	613		4113	4113		17577	17577
612	112	653	1109	1373	1983	4184	4732
615	612						
623	111	676	1536	1549	2700	4824	5200
628	211	430	361	823	2051	1862	3555
640	121						
652	621	802		802	3071		3071
655	122	3018		3018	7196		7196
677	124						
683	624						
685	624						
714	631		4577	4577		11900	11900
726	133		1617	1617		5091	5091
736	633	904		904	1793		1793
739	134						
747	634						
801	116	1479		1479	3642		3642
805	616		1225	1225		4772	4772
809	316						
811	126						
817	626	4311		4311	12338		12338
907	636	1638		1638	5929		5929
913	136	1850		1850	5109		5109
269B	102	1038		1038	2350		2350

Table G.16.: Characteristic values which specify the propagation of normal cracks.

V	{...}	$\bar{v}_C$ [m/s]	$\bar{v}_W$ [m/s]	$\widetilde{v}_C$ [m/s]	$\widetilde{v}_W$ [m/s]	$\sigma\,(v_C)$ [m/s]	$\sigma\,(v_W)$ [m/s]	Max(v_C) [m/s]	Max(v_W) [m/s]
208	101								
211	101								
212	101								
214	101		314		279		91		417
215	101							5009	
217	101		405		216		591		1581
218	101		608		571		389		1119
219	101								
220	101								
221	101		701		701				701
222	101		245		236		191		532
223	101		575		609		478		1106
224	101		241		213		105		381
225	101		322		322		44		353
226	101	4713	512	4713	512	5218		8402	512
227	101								
228	301		280		367		123		367
230	301								
231	301								
232	301		905		674		701		2161
233	301		692		692		781		1245
234	301								
235	301	6015		7459		3415		8470	
236	301		898		925		79		958
238	301	1526	508	1655	393	1131	508	2587	1485

Table G.17.: Characteristic values which specify the propagation of normal cracks.

V	{...}	$\bar{v}_C$ [m/s]	$\bar{v}_W$ [m/s]	$\widetilde{v}_C$ [m/s]	$\widetilde{v}_W$ [m/s]	$\sigma(v_C)$ [m/s]	$\sigma(v_W)$ [m/s]	Max(v_C) [m/s]	Max(v_W) [m/s]
239	301	5525		5525		3649		8105	
242	601	5387	450	3639	145	5728	587	13699	1126
243	601		1204		973		647		2397
244	601		946		979		361		1346
245	601								
246	601								
247	601		1242		1242		131		1335
248	601		1523		1429		953		2718
249	501		1835		1626		997		3092
252	501		736		542		542		1348
256	401		660		489		528		1454
259	201		832		621		818		2492
264	102								
265	102								
268	102								
276	102								
277	103								
320	303								
323	303		701		794		490		1241
351	602								
357	603								
360	604								
405	106	5478		5402		4800		10387	
411	106								
431	606								

Table G.18.: Characteristic values which specify the propagation of normal cracks.

V	{...}	$\bar{v}_C$ [m/s]	$\bar{v}_W$ [m/s]	$\widetilde{v}_C$ [m/s]	$\widetilde{v}_W$ [m/s]	$\sigma(v_C)$ [m/s]	$\sigma(v_W)$ [m/s]	Max(v_C) [m/s]	Max(v_W) [m/s]
603	113								
611	613								
612	112		1878		1457		1279		4584
615	612	3165		2377		2598		7707	
623	111								
628	211								
640	121	5448		6317		2675		7394	
652	621								
655	122								
677	124	1244		1359		467		1756	
683	624	1281		1019		1177		2936	
685	624	1025		628		1032		3762	
714	631		864		864				864
726	133								
736	633								
739	134	1764		975		2013		4724	
747	634	657		657		423		956	
801	116								
805	616		2009		1913		1453		4259
809	316								
811	126	14539		14539		8548		20584	
817	626		1656		1428		1588		5295
907	636		638		561		452		1319
913	136								
269B	102								

Table G.19.: Characteristic values which specify the propagation of normal cracks.

V	{...}	$\bar{v}_S$ [m/s]	$\bar{v}_{NC}$ [m/s]	$\widetilde{v}_S$ [m/s]	$\widetilde{v}_{NC}$ [m/s]	$\sigma(v_S)$ [m/s]	$\sigma(v_{NC})$ [m/s]	Max(v_S) [m/s]	Max(v_{NC}) [m/s]
208	101		1311		1286		864		2963
211	101								
212	101		1862		1879		927	2283	3108
214	101		2356		1807		2094	4370	6917
215	101	1251	3459	1151	1643	652	3317	2345	8207
217	101	586	1723	589	796	147	2455	796	7813
218	101	936	1861	811	1142	617	1917	1828	5402
219	101	2725	2769	2552	2790	1971	1633	5288	5288
220	101	1207	1207	1010	1010	764	764	2400	2400
221	101	3116	3444	2413	2500	2943	2553	8238	8238
222	101		987		990		831		2850
223	101	2867	3332	2181	3205	2377	2441	6075	7760
224	101		241		213		105		381
225	101	1090	1983	1084	1428	703	1887	2389	6228
226	101	1208	2462	1236	1522	366	2927	1528	8402
227	101	1662	2218	1123	1136	1414	2438	4053	8673
228	301		280		367		123		367
230	301								
231	301	888	777	446	446	1071	920	2666	2666
232	301	1384	2512	1206	1246	1049	2479	3101	8327
233	301	1708	3045	1394	2639	916	2295	3153	7109
234	301	937	3579	937	3507	713	960	1441	4573
235	301	450	4736	450	4937	213	3823	601	8470
236	301	1785	3181	1868	1950	676	3444	2758	12363
238	301	2825	2604	2751	2468	726	1178	3997	4706

Table G.20.: Characteristic values which specify the propagation of normal cracks.

V	{...}	$\bar{v}_S$ [m/s]	$\bar{v}_{NC}$ [m/s]	$\widetilde{v}_S$ [m/s]	$\widetilde{v}_{NC}$ [m/s]	$\sigma(v_S)$ [m/s]	$\sigma(v_{NC})$ [m/s]	Max(v_S) [m/s]	Max(v_{NC}) [m/s]
239	301	1790	2469	921	1980	1867	2530	4502	8105
242	601	1346	5028	1367	4054	49	4280	1380	14826
243	601	1150	2407	856	2020	765	2139	2283	7975
244	601	1336	1852	1230	1346	674	1979	2331	8076
245	601	3748	3793	3748	3748	3342	3404	6112	7271
246	601	2069	4784	2069	4784		4803	2069	8180
247	601		1242		1242		131		1335
248	601	2051	7463	2785	3019	1479	9270	3019	26695
249	501		8778		7053		8736		20013
252	501	2053	3959	1670	2231	1140	2950	3650	7768
256	401	1135	2284	671	1570	1010	2459	2938	8712
259	201	4510	4432	3468	3396	2512	3212	8142	9299
264	102		1583		1504		744		2582
265	102	1471	2198	683	2058	1284	1594	3835	5167
268	102	798	1569	677	1047	250	1467	1130	5662
276	102	1013	1050	792	792	874	906	2860	2860
277	103	181	1364	61	747	267	1154	636	3131
320	303	2712	4679	2875	3919	1760	3702	4850	11637
323	303	2120	3338	904	1083	2321	4626	5378	13966
351	602	1949	3544	1761	2808	825	2924	3057	9136
357	603	887	1069	992	1155	437	615	1490	2324
360	604								
405	106	2887	4285	1589	3613	2579	4235	7547	14601
411	106	1475	2182	1259	1871	723	1224	2687	4299
431	606								

Table G.21.: Characteristic values which specify the propagation of normal cracks.

V	{...}	$\bar{v}_S$ [m/s]	$\bar{v}_{NC}$ [m/s]	$\widetilde{v}_S$ [m/s]	$\widetilde{v}_{NC}$ [m/s]	$\sigma\,(v_S)$ [m/s]	$\sigma\,(v_{NC})$ [m/s]	Max(v_S) [m/s]	Max(v_{NC}) [m/s]
603	113	752	6697	714	6391	260	5411	1029	20290
611	613	1257	8337	1055	7720	907	5181	2247	17577
612	112		2518		2373		2087		7459
615	612	1005	2548	1005	1885	1044	2406	1743	7707
623	111	1055	2578	832	1630	702	1983	2095	5200
628	211		1997		1751		823		3555
640	121	1785	4532	1785	5507	18	2826	1797	7394
652	621	1904	1812	1904	1527	1259	835	2794	3071
655	122	781	2213	543	1447	443	2522	1293	7196
677	124	131	1089		1143	360	504	1201	1756
683	624	1188	1241	1368	1040	363	859	1425	2936
685	624	841	989	428	508	779	964	1740	3762
714	631	2246	5191	2439	3659	1687	4591	4899	14432
726	133		3030		2851		1617		5091
736	633	1255	1379	1255	1255		368	1255	1793
739	134	1900	1851	1868	1669	791	1263	3040	4724
747	634	431	326	458	287	204	345	620	956
801	116	2090	1976	2085	2014	873	1187	3316	3642
805	616	1220	2806	994	2084	701	2074	2327	6539
809	316	2945	3481	1203	2714	3498	3554	11667	11667
811	126	1894	6109	1256	3264	2057	7733	4844	20584
817	626	1354	4935	1427	3514	363	4240	1673	13682
907	636	1531	2121	1613	1613	787	1886	2363	5929
913	136	1170	2180	1041	1473	549	1722	1772	5109
269B	102	802	987	856	856	378	819	1158	2350

Table G.22.: Characteristic values which specify the propagation of normal cracks.

V	{...}	$\bar{w}_{Al}$ $[m^2/\text{s}]$	$\bar{w}_{Ar}$ $[m^2/\text{s}]$	$\bar{w}_{A}$ $[m^2/\text{s}]$	$\widetilde{w}_{Al}$ $[m^2/\text{s}]$	$\widetilde{w}_{Ar}$ $[m^2/\text{s}]$	$\widetilde{w}_{A}$ $[m^2/\text{s}]$
208	101	12,4	1,0	16,3	13,4	0,8	14,7
211	101						
212	101		30,0	30,0		30,0	30,0
214	101	63,7		63,7	63,7		63,7
215	101		26,8	26,8		21,6	21,6
217	101		58,3	58,3		58,3	58,3
218	101		31,5	31,5		40,6	40,6
219	101	8,7	13,8	17,7	7,2	11,7	11,1
220	101						
221	101	36,8		36,8	39,3		39,3
222	101	1,7	10,8	10,9	1,7	12,5	11,5
223	101	32,2		32,2	27,8		27,8
224	101						
225	101		26,5	26,5		16,7	16,7
226	101						
227	101	32,9		32,9	21,7		21,7
228	301						
230	301						
231	301	4,9		4,9	4,9		4,9
232	301	49,2		49,2	38,0		38,0
233	301	37,5		37,5	47,5		47,5
234	301	29,8		29,8	31,0		31,0
235	301						
236	301	42,0		42,0	42,0		42,0
238	301						

Table G.23.: Characteristic FAV values which specify the development of normal cracks.

V	{...}	$\bar{w}_{A\,l}$ [m^2/s]	$\bar{w}_{A\,r}$ [m^2/s]	$\bar{w}_{A}$ [m^2/s]	$\widetilde{w}_{A\,l}$ [m^2/s]	$\widetilde{w}_{A\,r}$ [m^2/s]	$\widetilde{w}_{A}$ [m^2/s]
239	301						
242	601	44,8		44,8	44,0		44,0
243	601	24,4		24,4	10,4		10,4
244	601	40,9		40,9	40,9		40,9
245	601	37,8		37,8	37,8		37,8
246	601	37,5		37,5	37,5		37,5
247	601						
248	601	62,9	68,3	131,2	53,6	49,6	103,2
249	501	48,1	43,1	91,2	52,6	48,1	100,7
252	501	30,9		30,9	22,6		22,6
256	401	39,8		39,8	22,3		22,3
259	201	52,3		52,3	67,5		67,5
264	102	15,8		15,8	14,6		14,6
265	102	31,4		31,4	38,8		38,8
268	102	24,0		24,0	21,3		21,3
276	102	11,4		11,4	9,4		9,4
277	103	8,0	10,2	15,6	6,4	12,8	13,8
320	303	20,7	37,5	51,3	11,6	11,8	36,7
323	303		84,2	84,2		103,3	103,3
351	602	33,0		33,0	20,2		20,2
357	603	12,0		12,0	13,7		13,7
360	604						
405	106		21,7	21,7		22,4	22,4
411	106	15,4	11,7	27,1	16,9	14,6	27,9
431	606						

Table G.24.: Characteristic FAV values which specify the propagation of normal cracks.

V	{...}	$\bar{w}_{Al}$ $[m^2/\mathrm{s}]$	$\bar{w}_{Ar}$ $[m^2/\mathrm{s}]$	$\bar{w}_{A}$ $[m^2/\mathrm{s}]$	$\widetilde{w}_{Al}$ $[m^2/\mathrm{s}]$	$\widetilde{w}_{Ar}$ $[m^2/\mathrm{s}]$	$\widetilde{w}_{A}$ $[m^2/\mathrm{s}]$
603	113	69,7		69,7	64,8		64,8
611	613		96,7	96,7		86,4	86,4
612	112	8,9	17,9	16,4	8,7	17,3	12,8
615	612						
623	111	18,2	22,9	33,8	15,8	23,5	37,0
628	211	15,0	14,8	19,9	12,7	15,2	17,5
640	121						
652	621	16,9		16,9	14,3		14,3
655	122	26,2		26,2	15,3		15,3
677	124						
683	624						
685	624						
714	631		69,8	69,8		67,3	67,3
726	133		29,2	29,2		27,3	27,3
736	633	14,4		14,4	14,4		14,4
739	134						
747	634						
801	116	20,1		20,1	18,1		18,1
805	616		24,0	24,0		20,7	20,7
809	316						
811	126						
817	626	40,7		40,7	27,7		27,7
907	636	38,0		38,0	37,9		37,9
913	136	20,3		20,3	12,2		12,2
269B	102	10,9		10,9	8,3		8,3

Table G.25.: Characteristic FAV values which specify the propagation of normal cracks.

V	{...}	$\sigma\,(w_{A\,l})$ $[m^2/\mathrm{s}]$	$\sigma\,(w_{A\,r})$ $[m^2/\mathrm{s}]$	$\sigma\,(w_A)$ $[m^2/\mathrm{s}]$	Max($w_{A\,l}$) $[m^2/\mathrm{s}]$	Max($w_{A\,r}$) $[m^2/\mathrm{s}]$	Max(w_A) $[m^2/\mathrm{s}]$
208	101	7,6	0,6	11,0	28,3	1,7	33,4
211	101						
212	101		0,7	0,7		30,5	30,5
214	101				63,7		63,7
215	101		18,5	18,5		47,2	47,2
217	101		16,4	16,4		69,9	69,9
218	101		21,7	21,7		47,2	47,2
219	101	5,1	12,2	17,2	15,9	26,9	42,8
220	101						
221	101	24,9		24,9	60,4		60,4
222	101	1,7	8,8	8,7	4,1	28,6	28,6
223	101	30,5		30,5	72,2		72,2
224	101						
225	101		26,7	26,7		61,9	61,9
226	101						
227	101	37,4		37,4	85,1		85,1
228	301						
230	301						
231	301	5,1		5,1	8,5		8,5
232	301	23,7		23,7	76,3		76,3
233	301	29,0		29,0	60,1		60,1
234	301	5,9		5,9	35,0		35,0
235	301						
236	301	51,4		51,4	78,4		78,4
238	301						

Table G.26.: Characteristic FAV values which specify the development of normal cracks.

V	{...}	$\sigma\,(w_{A\,l})$ $[m^2/\text{s}]$	$\sigma\,(w_{A\,r})$ $[m^2/\text{s}]$	$\sigma\,(w_A)$ $[m^2/\text{s}]$	Max($w_{A\,l}$) $[m^2/\text{s}]$	Max($w_{A\,r}$) $[m^2/\text{s}]$	Max(w_A) $[m^2/\text{s}]$
239	301						
242	601	15,9		15,9	61,0		61,0
243	601	33,8		33,8	74,6		74,6
244	601	42,4		42,4	70,9		70,9
245	601	47,8		47,8	71,6		71,6
246	601	33,5		33,5	61,2		61,2
247	601						
248	601	44,0	58,8	102,6	110,8	134,1	244,9
249	501	43,0	37,7	80,7	88,7	78,0	166,8
252	501	27,2		27,2	61,2		61,2
256	401	37,5		37,5	82,8		82,8
259	201	40,7		40,7	83,3		83,3
264	102	7,5		7,5	25,6		25,6
265	102	16,4		16,4	50,7		50,7
268	102	16,8		16,8	54,5		54,5
276	102	11,2		11,2	26,2		26,2
277	103	6,5	7,2	13,8	17,2	15,8	33,0
320	303	19,4	49,6	45,5	49,7	116,9	116,9
323	303		66,9	66,9		139,6	139,6
351	602	41,2		41,2	89,4		89,4
357	603	4,8		4,8	15,5		15,5
360	604						
405	106		10,9	10,9		34,3	34,3
411	106	3,3	5,7	8,0	18,6	17,1	34,7
431	606						

Table G.27.: Characteristic FAV values which specify the propagation of normal cracks.

V	{...}	$\sigma\left(w_{A\,l}\right)$ $[m^2/\text{s}]$	$\sigma\left(w_{A\,r}\right)$ $[m^2/\text{s}]$	$\sigma\left(w_{A}\right)$ $[m^2/\text{s}]$	Max$(w_{A\,l})$ $[m^2/\text{s}]$	Max$(w_{A\,r})$ $[m^2/\text{s}]$	Max(w_{A}) $[m^2/\text{s}]$
603	113	34,2		34,2	122,9		122,9
611	613		39,2	39,2		167,0	167,0
612	112	6,5	9,8	12,9	19,5	40,8	46,3
615	612						
623	111	6,4	14,5	14,6	25,4	45,4	49,0
628	211	4,2	3,6	8,1	19,9	18,8	35,1
640	121						
652	621	8,0		8,0	30,1		30,1
655	122	29,0		29,0	69,1		69,1
677	124						
683	624						
685	624						
714	631		44,3	44,3		116,1	116,1
726	133		14,8	14,8		48,4	48,4
736	633	4,8		4,8	17,8		17,8
739	134						
747	634						
801	116	6,4		6,4	29,3		29,3
805	616		9,0	9,0		36,2	36,2
809	316						
811	126						
817	626	32,6		32,6	95,0		95,0
907	636	16,2		16,2	55,3		55,3
913	136	18,6		18,6	59,0		59,0
269B	102	10,2		10,2	23,0		23,0

Table G.28.: Characteristic FAV values which specify the propagation of normal cracks.

V	{...}	$\bar{w}_C$ [m^2/s]	$\bar{w}_W$ [m^2/s]	$\widetilde{w}_C$ [m^2/s]	$\widetilde{w}_W$ [m^2/s]	$\sigma(w_C)$ [m^2/s]	$\sigma(w_W)$ [m^2/s]	Max(w_C) [m^2/s]	Max(w_W) [m^2/s]
208	101								
211	101								
212	101								
214	101		3,4		3,2		0,7		4,2
215	101	20,9		10,2		24,7		49,2	
217	101		4,0		2,1		5,9		15,9
218	101		6,0		5,5		3,8		10,9
219	101								
220	101								
221	101		6,8		6,8				6,8
222	101		2,6		2,4		1,9		5,2
223	101		5,6		6,0		4,7		10,7
224	101		2,4		2,1		1,0		3,8
225	101		3,2		3,2		0,5		3,5
226	101	64,5	5,1	82,5	5,1	47,9		100,8	5,1
227	101								
228	301		2,9		3,6		1,1		3,6
230	301								
231	301								
232	301		7,7		5,5		7,2		21,4
233	301		4,6		1,4		6,7		12,3
234	301								
235	301	59,1		73,1		33,6		83,4	
236	301		8,8		9,1		0,7		9,4
238	301	15,1	5,0	16,4	4,0	11,2	4,9	25,6	14,3

Table G.29.: Characteristic FAV values which specify the development of normal cracks.

V	{...}	$\bar{w}_C$ $[m^2/\mathrm{s}]$	$\bar{w}_W$ $[m^2/\mathrm{s}]$	$\widetilde{w}_C$ $[m^2/\mathrm{s}]$	$\widetilde{w}_W$ $[m^2/\mathrm{s}]$	$\sigma(w_C)$ $[m^2/\mathrm{s}]$	$\sigma(w_W)$ $[m^2/\mathrm{s}]$	$\mathrm{Max}(w_C)$ $[m^2/\mathrm{s}]$	$\mathrm{Max}(w_W)$ $[m^2/\mathrm{s}]$
239	301	54,5		54,5		36,0		79,9	
242	601	19,2	4,6	20,0	1,4	19,1	6,1	36,8	11,6
243	601		10,0		7,9		7,5		23,9
244	601		9,4		9,7		3,6		13,3
245	601								
246	601								
247	601		12,3		12,3		1,4		13,3
248	601		15,0		14,1		9,4		26,8
249	501		18,4		16,2		10,1		31,4
252	501		7,2		5,3		5,4		13,3
256	401		6,6		5,0		5,2		14,4
259	201		8,0		6,1		8,2		24,6
264	102								
265	102								
268	102								
276	102								
277	103								
320	303								
323	303		7,0		7,9		4,9		12,4
351	602								
357	603								
360	604								
405	106	44,9		44,2		39,5		85,5	
411	106								
431	606								

Table G.30.: Characteristic FAV values which specify the propagation of normal cracks.

V	{...}	$\bar{w}_C$ $[m^2/\text{s}]$	$\bar{w}_W$ $[m^2/\text{s}]$	$\widetilde{w}_C$ $[m^2/\text{s}]$	$\widetilde{w}_W$ $[m^2/\text{s}]$	$\sigma\,(w_C)$ $[m^2/\text{s}]$	$\sigma\,(w_W)$ $[m^2/\text{s}]$	Max(w_C) $[m^2/\text{s}]$	Max(w_W) $[m^2/\text{s}]$
603	113								
611	613								
612	112		15,1		14,2		8,1		31,0
615	612	30,4		22,9		24,9		74,0	
623	111								
628	211								
640	121	51,7		59,9		25,4		70,2	
652	621								
655	122								
677	124	12,0		12,9		4,5		17,0	
683	624	12,3		9,8		11,3		28,1	
685	624	9,8		6,1		9,9		36,1	
714	631		8,2		8,2				8,2
726	133								
736	633								
739	134	13,6		6,0		18,3		45,1	
747	634	6,4		6,4		4,1		9,3	
801	116								
805	616		14,5		12,1		11,7		33,6
809	316								
811	126	115,4		115,4		67,6		163,2	
817	626		13,9		11,1		12,7		42,2
907	636		5,1		4,4		3,6		10,3
913	136								
269B	102								

Table G.31.: Characteristic FAV values which specify the propagation of normal cracks.

V	{...}	$\bar{w}_S$ [m^2/s]	$\bar{w}_{NC}$ [m^2/s]	$\widetilde{w}_S$ [m^2/s]	$\widetilde{w}_{NC}$ [m^2/s]	$\sigma(w_S)$ [m^2/s]	$\sigma(w_{NC})$ [m^2/s]	Max(w_S) [m^2/s]	Max(w_{NC}) [m^2/s]
208	101		24,9		13,7		50,6		218,6
211	101								
212	101	16,0	19,0	19,5	20,1	7,8	9,1	24,3	30,5
214	101	18,1	23,6	14,6	19,2	15,2	20,6	44,5	67,9
215	101	12,5	34,2	11,4	16,6	6,2	32,4	22,9	80,3
217	101	6,2	17,2	6,5	6,9	1,0	24,4	7,0	77,3
218	101	9,5	18,3	9,3	11,2	7,0	18,7	18,1	52,9
219	101	34,3	25,5	27,5	22,6	16,1	17,0	52,7	52,7
220	101	9,9	9,9	9,1	9,1	8,5	8,5	24,2	24,2
221	101	18,2	28,9	18,7	24,7	7,8	17,0	25,8	60,4
222	101		10,8		10,2		8,2		28,6
223	101	32,1	32,7	30,0	31,5	23,0	23,9	59,8	75,9
224	101		2,4		2,1		1,0		3,8
225	101	11,8	19,7	12,6	14,1	6,7	18,7	23,6	61,9
226	101	12,7	35,3	14,4	15,2	3,8	38,9	15,2	100,8
227	101	16,6	22,0	11,5	11,7	13,7	23,8	38,9	85,1
228	301		2,9		3,6		1,1		3,6
230	301								
231	301	4,3	3,5	4,2	1,3	5,3	4,6	12,9	12,9
232	301	11,7	24,7	9,3	12,3	9,8	24,3	30,4	81,8
233	301	19,4	30,6	18,7	27,7	9,5	22,6	31,3	70,4
234	301	4,4	36,1	4,4	35,0		9,0	4,4	45,6
235	301	6,0	46,5	6,0	48,4		37,5	6,0	83,4
236	301	16,0	17,6	18,7	14,8	9,0	21,2	26,8	87,3
238	301	29,6	25,8	28,3	25,0	6,8	12,0	40,7	47,7

Table G.32.: Characteristic FAV values which specify the development of normal cracks.

V	{...}	$\bar{w}_S$ $[m^2/\mathrm{s}]$	$\bar{w}_{NC}$ $[m^2/\mathrm{s}]$	$\widetilde{w}_S$ $[m^2/\mathrm{s}]$	$\widetilde{w}_{NC}$ $[m^2/\mathrm{s}]$	$\sigma(w_S)$ $[m^2/\mathrm{s}]$	$\sigma(w_{NC})$ $[m^2/\mathrm{s}]$	$\mathrm{Max}(w_S)$ $[m^2/\mathrm{s}]$	$\mathrm{Max}(w_{NC})$ $[m^2/\mathrm{s}]$
239	301	18,8	24,5	12,4	19,8	19,4	24,9	44,4	79,9
242	601	14,8	48,6	14,8	38,2	0,5	39,7	15,1	146,6
243	601	12,3	22,0	8,7	19,1	8,9	21,3	22,4	78,9
244	601	14,3	18,4	13,7	13,3	6,5	19,6	22,7	79,9
245	601	60,0	35,1	60,0	32,4		35,8	60,0	71,6
246	601		48,5		48,5		49,1		83,2
247	601		12,3		12,3		1,4		13,3
248	601	16,9	73,6	16,9	30,4	19,0	91,0	30,4	262,4
249	501		86,9		69,7		86,4		198,2
252	501	24,3	40,3	20,3	22,1	14,1	30,5	39,9	78,5
256	401	12,7	22,6	8,6	15,7	10,4	24,2	28,9	85,9
259	201	48,4	43,9	34,9	33,7	25,7	31,7	80,6	92,2
264	102		15,8		14,6		7,5		25,6
265	102	15,9	21,8	6,8	20,4	13,4	15,8	38,8	50,7
268	102	9,9	16,5	9,8	12,3	2,8	13,4	13,5	54,5
276	102	10,8	10,8	8,5	8,4	9,5	9,2	28,9	28,9
277	103	1,8	14,3	0,3	7,7	3,2	12,3	6,5	33,0
320	303	29,2	47,4	37,3	39,0	19,0	37,0	49,7	116,9
323	303	24,2	33,4	21,5	10,8	25,6	46,3	53,7	139,6
351	602	17,2	35,7	15,7	28,5	3,8	27,9	21,4	89,4
357	603	8,6	10,8	9,8	11,4	4,6	6,1	14,6	22,9
360	604								
405	106	25,6	35,3	21,5	30,1	21,7	34,7	62,0	119,8
411	106	11,1	16,7	9,9	14,1	6,8	10,5	21,8	34,7
431	606								

Table G.33.: Characteristic FAV values which specify the propagation of normal cracks.

V	{...}	$\bar{w}_S$ [m^2/s]	$\bar{w}_{NC}$ [m^2/s]	$\widetilde{w}_S$ [m^2/s]	$\widetilde{w}_{NC}$ [m^2/s]	$\sigma\,(w_S)$ [m^2/s]	$\sigma\,(w_{NC})$ [m^2/s]	Max(w_S) [m^2/s]	Max(w_{NC}) [m^2/s]
603	113	5,8	57,7	5,8	60,7	1,5	40,1	6,8	122,9
611	613	15,9	79,6	15,9	74,1	8,1	49,7	21,7	167,0
612	112		25,0		22,3		19,5		71,9
615	612	17,7	24,6	17,7	18,2		23,1	17,7	74,0
623	111	7,8	24,5	7,0	15,4	4,2	18,6	13,3	49,0
628	211		19,9		17,5		8,1		35,1
640	121	18,1	29,9	18,1	18,1		31,3	18,1	70,2
652	621	26,3	17,3	26,3	14,3		8,1	26,3	30,1
655	122	8,9	21,4	8,9	14,0	5,3	24,2	12,6	69,1
677	124	11,1	10,5	11,1	11,1	0,7	4,9	11,6	17,0
683	624	11,4	7,2	11,4	4,6	5,1	9,1	14,9	28,1
685	624	10,3	9,5	10,3	5,0	8,0	9,2	16,0	36,1
714	631	26,4	50,8	24,6	35,7	15,1	44,5	47,6	140,8
726	133		29,2		27,3		14,8		48,4
736	633		13,6		12,1		3,7		17,8
739	134	17,9	14,1	17,0	14,1	8,2	13,1	29,1	45,1
747	634	5,4	3,9	5,4	3,2	3,4	3,9	7,8	9,3
801	116	18,3	16,1	17,7	17,0	8,1	9,7	28,0	29,3
805	616	10,5	22,3	8,5	16,7	5,4	16,1	18,3	51,8
809	316	29,6	29,6	23,7	23,7	28,5	28,5	91,6	91,6
811	126	7,8	36,3	6,6	6,6	6,8	60,9	15,2	163,2
817	626	7,7	35,8	9,3	23,3	5,4	33,2	12,1	106,0
907	636	11,4	17,6	10,7	13,0	6,3	16,4	19,0	55,3
913	136	7,0	19,5	7,0	12,2	1,5	17,3	8,0	59,0
269B	102	6,7	8,1	6,3	5,0	3,7	8,2	10,5	23,0

Table G.34.: Characteristic FAV values which specify the propagation of normal cracks.

G.4. Characteristic Results of Fracture Energy Dissipation

V	{...}	$\bar{e}_{Al}$ [J/s]	$\bar{e}_{Ar}$ [J/s]	$\bar{e}_{A}$ [J/s]	$\bar{e}_{C}$ [J/s]	$\bar{e}_{W}$ [J/s]	$\bar{e}_{S}$ [J/s]	$\bar{e}_{NC}$ [J/s]
205	101						955	955
208	101	584	45	767				1171
211	101	1578		1578		270	1585	1671
212	101		1425	1425			757	900
214	101	2999		2999		158	853	1111
215	101		1263	1263	986		590	1615
217	101		2758	2758		190	294	812
218	101		1478	1478		280	446	857
219	101	413	654	834			1619	1206
220	101						461	461
221	101	1751		1751		323	863	1373
222	101	78	503	507		122		504
223	101	1537		1537		269	1529	1561
224	101					112		112
225	101		1246	1246		151	557	928
226	101				3035	239	596	1660
227	101	1547		1547			780	1036
228	301					135		135
231	301	232		232			202	163
232	301	2299		2299		358	549	1155
233	301	1765		1765		214	916	1441
234	301	1423		1423			210	1725
235	301				2738		276	2157
236	301	1968		1968		412	752	823
238	301				709	234	1390	1212
239	301				2538		876	1141
242	601	2107		2107	904	217	696	2287
243	601	1155		1155		474	581	1041
244	601	1932		1932		442	675	870

Table G.35.: Characteristic values which specify the temporal dissipation rates of fracture energy in normal cracks.

V	{...}	$\bar{e}_{Al}$ [J/s]	$\bar{e}_{Ar}$ [J/s]	$\bar{e}_{A}$ [J/s]	$\bar{e}_{C}$ [J/s]	$\bar{e}_{W}$ [J/s]	$\bar{e}_{S}$ [J/s]	$\bar{e}_{NC}$ [J/s]
245	601	1764		1764			2795	1636
246	601	1789		1789				2314
247	601					576		576
248	601	2915	3162	6077		697	784	3409
249	501	2296	2056	4352		880		4144
252	501	1453		1453		341	1142	1894
256	401	1898		1898		313	606	1080
259	201	2451		2451		376	2266	2056
623	111	866	1087	1607			371	1164
624	611		1828	1828		881	664	1633
628	211	709	699	937				937
640	121				2398		841	1384
652	621	796		796			1239	813
701	131	1768		1768			1670	1570
714	631		3298	3298		387	1246	2402
264	102	683		683				683
265	102	1353		1353			683	938
268	102	1032		1032			428	710
276	102	491		491			466	466
351	602	1440		1440			748	1558
355	602		1856	1856		413	359	1381
612	112	381	763	699		644		1066
615	612				1306		762	1057
655	122	1111		1111			376	906
687	622	571	1329	1331			541	739
2698	102	475		475			292	353
277	103	408	522	799			91	733
320	303	1060	1924	2631			1496	2433

Table G.36.: Characteristic values which specify the temporal dissipation rates of fracture energy in normal cracks.

V	{...}	$\bar{e}_{Al}$ [J/s]	$\bar{e}_{Ar}$ [J/s]	$\bar{e}_{A}$ [J/s]	$\bar{e}_{C}$ [J/s]	$\bar{e}_{W}$ [J/s]	$\bar{e}_{S}$ [J/s]	$\bar{e}_{NC}$ [J/s]
323	303		4435	4435		368	1276	1758
357	603	623		623			450	562
603	113	3605		3605			300	2983
611	613		5087	5087			837	4188
726	133		1541	1541				1541
736	633	740		740				700
360	604				489		246	254
677	124				460		428	405
683	624				471		435	275
685	624				379		395	365
739	134				512		675	534
746	634				929		396	560
747	634				243		205	149
362	604				544			544
405	106		1435	1435	2970		1692	2336
411	106	1008	762	1770			726	1090
413	106	233	354	571				504
415	106				4368		732	3857
430	606				2197	166	970	903
431	606		1040	1040		91	1287	1111
801	116	1314		1314			1201	1051
805	616		1565	1565		946	687	1455
809	316						1937	1937
811	126				7533		512	2372
817	626	2682		2682		915	508	2361
907	636	2487		2487		331	747	1152
912	136	934		934			797	869
913	136	1336		1336			462	1282

Table G.37.: Characteristic values which specify the temporal dissipation rates of fracture energy in normal cracks.

V	{...}	$\widetilde{e}_{Al}$ [J/s]	$\widetilde{e}_{Ar}$ [J/s]	$\widetilde{e}_{A}$ [J/s]	$\widetilde{e}_{C}$ [J/s]	$\widetilde{e}_{W}$ [J/s]	$\widetilde{e}_{S}$ [J/s]	$\widetilde{e}_{NC}$ [J/s]
205	101						969	969
208	101	632	37	691				645
211	101	1633		1633		270	1378	1378
212	101		1425	1425			925	951
214	101	2999		2999		149	684	903
215	101		1022	1022	480		540	781
217	101		2758	2758		101	309	324
218	101		1904	1904		260	436	524
219	101	338	553	527			1299	1069
220	101						424	424
221	101	1871		1871		323	888	1176
222	101	78	584	536		114		476
223	101	1326		1326		286	1431	1501
224	101					99		99
225	101		785	785		151	592	664
226	101				3880	239	679	715
227	101	1020		1020			542	551
228	301					173		173
231	301	232		232			198	62
232	301	1779		1779		257	435	577
233	301	2237		2237		64	880	1305
234	301	1480		1480			210	1672
235	301				3388		276	2244
236	301	1968		1968		424	878	694
238	301				770	187	1327	1172
239	301				2538		576	921
242	601	2073		2073	942	67	696	1799
243	601	491		491		374	412	904
244	601	1932		1932		458	645	628

Table G.38.: Characteristic values which specify the temporal dissipation rates of fracture energy in normal cracks.

V	{...}	$\widetilde{e}_{Al}$ [J/s]	$\widetilde{e}_{Ar}$ [J/s]	$\widetilde{e}_{A}$ [J/s]	$\widetilde{e}_{C}$ [J/s]	$\widetilde{e}_{W}$ [J/s]	$\widetilde{e}_{S}$ [J/s]	$\widetilde{e}_{NC}$ [J/s]
245	601	1764		1764			2795	1509
246	601	1789		1789				2314
247	601					576		576
248	601	2483	2295	4778		655	784	1406
249	501	2510	2295	4804		774		3324
252	501	1063		1063		251	953	1041
256	401	1065		1065		238	412	747
259	201	3163		3163		283	1632	1580
623	111	750	1120	1759			331	731
624	611		572	572		243	667	667
628	211	601	715	825				825
640	121				2776		841	841
652	621	673		673			1239	673
701	131	1779		1779			1551	1551
714	631		3184	3184		387	1163	1689
264	102	631		631				631
265	102	1671		1671			294	878
268	102	918		918			422	529
276	102	404		404			363	361
351	602	882		882			686	1241
355	602		1792	1792		497	359	648
612	112	371	740	545		605		954
615	612				982		762	780
655	122	649		649			376	592
687	622	557	1486	711			516	513
2698	102	363		363			276	217
277	103	330	653	708			16	396
320	303	596	607	1882			1916	2003

Table G.39.: Characteristic values which specify the temporal dissipation rates of fracture energy in normal cracks.

V	{...}	$\widetilde{e}_{A\,l}$ [J/s]	$\widetilde{e}_{A\,r}$ [J/s]	$\widetilde{e}_{A}$ [J/s]	$\widetilde{e}_{C}$ [J/s]	$\widetilde{e}_{W}$ [J/s]	$\widetilde{e}_{S}$ [J/s]	$\widetilde{e}_{NC}$ [J/s]
323	303		5440	5440		417	1132	570
357	603	712		712			509	596
603	113	3349		3349			300	3135
611	613		4546	4546			837	3898
726	133		1440	1440				1440
736	633	740		740				619
360	604				527		90	175
677	124				496		428	428
683	624				375		435	177
685	624				234		395	192
739	134				226		643	532
746	634				1023		396	435
747	634				243		205	122
362	604				566			566
405	106		1480	1480	2921		1421	1987
411	106	1105	955	1823			646	923
413	106	64	158	266				215
415	106				3888		732	3727
430	606				1443	163	970	272
431	606		945	945		23	1366	1186
801	116	1182		1182			1161	1116
805	616		1348	1348		789	553	1090
809	316						1552	1552
811	126				7533		434	434
817	626	1823		1823		731	615	1533
907	636	2476		2476		287	699	850
912	136	843		843			977	843
913	136	801		801			462	801

Table G.40.: Characteristic values which specify the temporal dissipation rates of fracture energy in normal cracks.

V	{...}	$\sigma(e_{Al})$ [J/s]	$\sigma(e_{Ar})$ [J/s]	$\sigma(e_A)$ [J/s]	$\sigma(e_C)$ [J/s]	$\sigma(e_W)$ [J/s]	$\sigma(e_S)$ [J/s]	$\sigma(e_{NC})$ [J/s]
205	101						550	580
208	101	356	28	519				2381
211	101	1439		1439		52	1431	1277
212	101		31	31			369	433
214	101					35	714	968
215	101		872	872	1168		293	1528
217	101		776	776		279	47	1152
218	101		1018	1018		176	329	877
219	101	239	574	813			763	802
220	101						393	393
221	101	1186		1186			373	809
222	101	77	409	408		87		385
223	101	1455		1455		223	1097	1141
224	101					49		49
225	101		1257	1257		22	315	879
226	101				2252		177	1832
227	101	1761		1761			645	1120
228	301					53		53
231	301	241		241			248	216
232	301	1106		1106		336	458	1138
233	301	1366		1366		317	447	1064
234	301	282		282				428
235	301				1557			1740
236	301	2411		2411		35	420	994
238	301				523	229	318	562
239	301				1679		903	1160
242	601	750		750	900	286	21	1868
243	601	1598		1598		355	421	1006
244	601	2002		2002		168	309	924

Table G.41.: Characteristic values which specify the temporal dissipation rates of fracture energy in normal cracks.

V	{...}	$\sigma(e_{Al})$ [J/s]	$\sigma(e_{Ar})$ [J/s]	$\sigma(e_A)$ [J/s]	$\sigma(e_C)$ [J/s]	$\sigma(e_W)$ [J/s]	$\sigma(e_S)$ [J/s]	$\sigma(e_{NC})$ [J/s]
245	601	2227		2227				1666
246	601	1598		1598				2342
247	601					65		65
248	601	2036	2721	4752		434	880	4216
249	501	2054	1797	3850		484		4124
252	501	1278		1278		252	663	1434
256	401	1792		1792		249	495	1155
259	201	1907		1907		385	1202	1484
623	111	303	688	694			200	884
624	611		2197	2197		1811	41	2067
628	211	200	171	382				382
640	121				1177			1451
652	621	378		378				381
701	131	1355		1355			1100	1210
714	631		2095	2095			713	2104
264	102	323		323				323
265	102	704		704			578	681
268	102	725		725			121	578
276	102	479		479			406	395
351	602	1797		1797			165	1218
355	602		1290	1290		285		1573
612	112	278	419	551		347		835
615	612				1071			990
655	122	1228		1228			222	1023
687	622	165	949	1068			370	880
2698	102	443		443			159	358
277	103	335	371	708			161	628
320	303	994	2545	2335			973	1896

Table G.42.: Characteristic values which specify the temporal dissipation rates of fracture energy in normal cracks.

V	{...}	$\sigma\left(e_{Al}\right)$ [J/s]	$\sigma\left(e_{Ar}\right)$ [J/s]	$\sigma\left(e_{A}\right)$ [J/s]	$\sigma\left(e_{C}\right)$ [J/s]	$\sigma\left(e_{W}\right)$ [J/s]	$\sigma\left(e_{S}\right)$ [J/s]	$\sigma\left(e_{NC}\right)$ [J/s]
323	303		3525	3525		257	1349	2438
357	603	249		249			238	319
603	113	1767		1767			75	2070
611	613		2061	2061			427	2615
726	133		779	779				779
736	633	246		246				188
360	604				87		333	347
677	124				173		25	187
683	624				431		194	350
685	624				380		309	352
739	134				690		309	495
746	634				435		257	546
747	634				158		131	149
362	604				87			87
405	106		722	722	2611		1432	2296
411	106	212	373	525			447	685
413	106	423	516	880				845
415	106				3233			3284
430	606				2569	133		1533
431	606		736	736		129	333	530
801	116	419		419			532	637
805	616		584	584		765	350	1050
809	316						1866	1866
811	126				4412		444	3974
817	626	2148		2148		835	354	2187
907	636	1061		1061		232	409	1076
912	136	517		517			611	501
913	136	1227		1227			96	1138

Table G.43.: Characteristic values which specify the temporal dissipation rates of fracture energy in normal cracks.

V	{...}	Max(e_{Al}) [J/s]	Max(e_{Ar}) [J/s]	Max(e_A) [J/s]	Max(e_C) [J/s]	Max(e_W) [J/s]	Max(e_S) [J/s]	Max(e_{NC}) [J/s]
205	101						1892	1892
208	101	1332	80	1571				10286
211	101	2840		2840		306	4151	4151
212	101		1448	1448			1154	1448
214	101	2999		2999		196	2092	3195
215	101		2230	2230	2321		1080	3791
217	101		3307	3307		752	332	3656
218	101		2214	2214		513	849	2480
219	101	750	1272	2022			2490	2490
220	101						1123	1123
221	101	2872		2872		323	1228	2872
222	101	190	1333	1333		242		1333
223	101	3443		3443		512	2852	3621
224	101					178		178
225	101		2913	2913		166	1110	2913
226	101				4742	239	715	4742
227	101	4005		4005			1828	4005
228	301					173		173
231	301	402		402			609	609
232	301	3569		3569		1001	1420	3826
233	301	2832		2832		578	1475	3316
234	301	1672		1672			210	2177
235	301				3864		276	3864
236	301	3673		3673		439	1255	4093
238	301				1198	669	1910	2236
239	301				3726		2071	3726
242	601	2874		2874	1731	547	711	6903
243	601	3532		3532		1133	1060	3732
244	601	3347		3347		628	1071	3772

Table G.44.: Characteristic values which specify the temporal dissipation rates of fracture energy in normal cracks.

V	{...}	Max(e_{Al}) [J/s]	Max(e_{Ar}) [J/s]	Max(e_A) [J/s]	Max(e_C) [J/s]	Max(e_W) [J/s]	Max(e_S) [J/s]	Max(e_{NC}) [J/s]
245	601	3338		3338			2795	3338
246	601	2919		2919				3971
247	601					622		622
248	601	5133	6211	11344		1243	1406	12155
249	501	4234	3722	7956		1499		9455
252	501	2881		2881		625	1878	3692
256	401	3955		3955		689	1380	4100
259	201	3900		3900		1154	3777	4319
623	111	1210	2161	2330			634	2330
624	611		6083	6083		4980	703	6083
628	211	939	887	1655				1655
640	121				3254		841	3254
652	621	1418		1418			1239	1418
701	131	3713		3713			3357	3713
714	631		5491	5491		387	2249	6657
264	102	1106		1106				1106
265	102	2181		2181			1671	2181
268	102	2343		2343			582	2343
276	102	1128		1128			1243	1243
351	602	3900		3900			935	3900
355	602		4153	4153		811	359	4885
612	112	834	1744	1976		1325		3069
615	612				3177		762	3177
655	122	2928		2928			534	2928
687	622	857	2286	3143			974	3143
2698	102	1004		1004			458	1004
277	103	879	810	1689			332	1690
320	303	2550	5996	5996			2550	5996

Table G.45.: Characteristic values which specify the temporal dissipation rates of fracture energy in normal cracks.

V	{...}	Max(e_{Al}) [J/s]	Max(e_{Ar}) [J/s]	Max(e_A) [J/s]	Max(e_C) [J/s]	Max(e_W) [J/s]	Max(e_S) [J/s]	Max(e_{NC}) [J/s]
323	303		7349	7349		652	2829	7349
357	603	806		806			762	1195
603	113	6350		6350			353	6350
611	613		8782	8782			1139	8782
726	133		2554	2554				2554
736	633	914		914				914
360	604				551		1086	1086
677	124				655		446	655
683	624				1077		572	1077
685	624				1388		614	1388
739	134				1704		1098	1704
746	634				1355		578	1355
747	634				355		298	355
362	604				610			610
405	106		2270	2270	5654		4099	7923
411	106	1213	1117	2265			1422	2265
413	106	1731	1812	3543				3543
415	106				11704		732	11704
430	606				5059	385	970	5296
431	606		2006	2006		239	1696	2006
801	116	1920		1920			1831	1920
805	616		2362	2362		2189	1191	3376
809	316						5994	5994
811	126				10653		990	10653
817	626	6260		6260		2781	799	6985
907	636	3615		3615		674	1243	3615
912	136	1829		1829			1297	1829
913	136	3888		3888			530	3888

Table G.46.: Characteristic values which specify the temporal dissipation rates of fracture energy in normal cracks.